TOWARDS UNDERSTANDING THE ENERGETICS IN POLYMORPHS THROUGH CHARGE DENSITY STUDIES

Ioana Sovago

Thesis submitted to the University of Glasgow
for the degree of Doctor of Philosophy

School of Chemistry

submitted September 2012

Supervisors: Dr. Louis Farrugia
Prof. Chick Wilson

Declaration

The thesis has been written in accordance with the University and all work presented is original and performed by the author unless otherwise stated and referenced in the text.

Ioana Sovago

Abstract

The detailed study of the structure and electron density distributions of polymorphic and phase transition materials is presented. Understanding and predicting the appearance of polymorphism and phase transitions in organic and organometallic materials is of considerable interest in fields such as pharmaceutical science, solid-state chemistry, and materials science. However, the small lattice energy difference between the different molecular conformations and packing between these materials are often particularly challenging in this area. Consequently, obtaining the most accurate description of the atomic positions and the electronic distributions plays an extremely important role in obtaining the best estimation of the lattice energies. In the present work, high-resolution X-ray diffraction as well as neutron diffraction tehniques have been used in reaching these aims. For minimizing the data collection times, synchrotron sources were also used for obtaining X-ray diffraction data, including Diamond, I19 beam line and Soleil, CRYSTAL beam line. Molecular complexes of lutidine isomers and chloranilic acid are also studied, in both 1:1 and 2:1 ratios, in order to investigate their relative stabilities through hydrogen bond contributions towards stabilising stoichiometrically different 'compositional polymorphs'.

The energy stability rankings in small organic molecules and transition metal complexes which exhibit polymorphism or displacive phase transitions are calculated using experimental charge density and fully theoretical approaches. The effect of the hydrogen bonds in the rank stabilities is also investigated. The pharmaceutical sulfathiazole and piracetam compounds are identified to have very small lattice energy differences between the polymorphs studied and the ranking stability orders are not maintained in the approaches used. Studies of the coordination complex $[Ni(en)_3]^{2+}(NO_3^-)_2$ show that, contrary to expectation, the higher temperature phase is calculated to be the most stable one, showing the strongest intermolecular interaction energies. Overall, the presented studies show that current methodologies for estimating solid state lattice energies, even using high quality diffraction data and complex modeling of the electron density, are not sufficiently accurate to allow reliable estimation of polymorph energy differences. The results obtained for all studied polymorphic and phase transition materials using the experimental charge density approach show a high dependence of the lattice energies on the multipole model used.

Acknowledgements

I would like to thanks my supervisor Louis Farrugia for all his patience and help during my PhD, and the great opportunity of working on this project. I am very greateful for all the time he spend helping me understand crystallography and charge density. I would also like to thanks my co-supervisor Chick Wilson for all his support and advices with my project. I would like to thanks to Lynne Thomas for her encouragement and enormous help over the years.

I would also like to thanks to the following people: Marc Schmidtmann, Matthias Gutmann, Silvia Capelli, Grant Hill, Hans Martin Seen, Derek Middlemiss, Stuart Mackay, Andras, Gordon, Craig, Craig, Andrew Jones, Bryan, Alan, Kate, Louis, Charlotte, Andrew Farrell, Marc White, Ondra Kysilka, Flavien Labre, Michael Sparenberg.

Special friends: Eva, Vihar, Costy, Adi, Antoine

Romanian still special friends: Moni, Ralu, Lacri, Stefi, Oli, Alin, Marius.

Family: to my lovely sister Maria, Mamuca şi Tatuca (ştiți voi de ce), Bunica şi Matuşa.

And last I would like to thanks to the God of Sadness, God of Joy and God of Love.

TABLE OF CONTENTS

1. Introduction, Methods and Theory

1.1. Polymorphism

Crystal polymorphism, which embodies the ability of molecules to adopt diverse packing arrangements displaying different physical and chemical properties, is of paramount importance in different fields such as pharmacy, solid-state chemistry, and materials science.[1-6] There is considerable interest in understanding and if possible predicting the appearance of polymorphism in a particular molecular system, but the often small lattice energy differences between the different molecular conformations and packing between polymorphs offers particular challenges in this area.

The charge density approach which will be used in this work offers detailed analysis of the electron density in solid-state molecular systems and may be used to extract information on the factors involved in the differing energies of polymorphs. In this way, the exact contribution of various intermolecular interactions to the stability of crystalline materials can be evaluated. In addition, in favourable cases, it is possible to estimate the lattice energies of molecular solids from their charge densities. Another reason for using charge density as a tool for investigating the occurrence of polymorphism is that a large percentage of polymorphic materials have hydrogen bonding interactions and these are considered to be important in controlling the energetics of crystal formation.[7] In terms of the topology of electron density, hydrogen bonding can be analysed using Koch and Popelier's criteria.[8] AIM (Atoms in Molecules) analysis can also identify different types of weak inter- and intra-molecular interactions including CH$\cdots\pi$ interactions[9] and H$\cdots$H interactions,[10, 11] which may be significant energetic factors in controlling polymorph formation in some materials.

Polymorphism in materials science is defined as the ability of a solid material to exist in more than one form or crystal state; this includes conformational polymorphs, dynamic isomers or tautomerism. Due to the different arrangements of the molecules in the crystal, the polymorphs will exhibit different physical properties, for example having different melting points and solubilities. The different forms of a crystal structure will, however, lead to identical liquid and vapour states. The consequent presence of dynamic isomers implies a time factor dependence, and that kinetics as well as thermodynamics thus play a role in polymorph formation. If there is a solvent or a hydrate included in the crystal structure the pseudopolymorphism terminology is used. The relations between polymorphs and their most stable forms are classified as monotropic or enantiotropic.[12] If the polymorphs are monotropically related, transformation from the metastable form to a

stable form will occur and the process is irreversible. If the process is reversible the polymorphs are said to be related enantiotropically.

The first observation of the polymorphic nature of materials can be attributed to Mitscherlich who discovered this phenomenon in certain phosphate and arsenate crystals in 1818.[1] In the molecular solid state, polymorphs are frequently accessed through crystallization processes. At this stage of our understanding of the phenomenon, the appearance of polymorphs can be explained by Ostwald's law which says that when a system is departing from an unstable state, it does not necessarily form the most stable state, but rather arrives at the nearest metastable state.[13] This leads to the idea that during crystallization the molecules as they assemble will simply fall to the nearest minimum energy state with a loss in free energy while still searching for the most stable form. Therefore, an apparently stable structure formed initially can be transformed in the end into another form. However, this rule gives rise to questions, for instance when the experiment leads only to a single form. There is no way of answering this question definitively – the material might simply not be polymorphic or it could be "trapped" in a kinetically accessed (metastable) state and unable to transform to the thermodynamically most stable state. This can happen, for example, due to a high activation barrier to such a transformation from a metastable to the most stable state.

An attempt to understand polymorph formation is described by Bernstein using tools from thermodynamics and kinetics.[1] It was shown that there are cases when a clear distinction between thermodynamics and kinetics is not at all obvious, due to the formation of concomitant polymorphs (simultaneous appearance of polymorphs under the same conditions). A full understanding of the process of polymorphism in material formation eludes current scientific knowledge.

In some cases it is possible to observe polymorphs that exist over a period of time, which are then displaced by a more stable crystal form and are unable to be reproduced in subsequent experiments. This phenomenon is known as 'disappearing polymorphs'. Many researchers are sceptical about this subject due to the difficulty in reproducing exactly the initial experimental conditions. However, the effect is certainly observed in practice, and the effects of such a phenomenon can have substantial implications for production of important materials, notably the well-documented case of ritonavir, a drug developed for treated HIV (Human Immunodefficiency Virus).[13]

Polymorphs are usually obtained by varying the experimental conditions used in the crystallization process, such as solvents, temperature and pressure. In many cases, the appearance of a new polymorph is obtained by chance rather than by a systematic search, and some well-investigated materials are not known to exhibit polymorphism. For example, the structure of naphthalene has been extensively analysed (as can be seen from a CSD – Cambridge Structural Database[14] search, it has been determined using X-ray diffraction 37 times), but has not been identified as a polymorphic material. It may be possible that any compound can exhibit polymorphism but the necessary experimental conditions to obtain a specific polymorphic form might be unknown. The prediction of the existence of a particular polymorph, as well as the experimental conditions and methods necessary to achieve this, represent a current challenge.

Polymorphs have applications in different industrial fields such as agrochemicals, pigments, dyestuffs, foods or explosive materials. However, perhaps the most important application is in the pharmaceutical industry. The use of polymorphic materials in drugs can have direct medical implications. For example, drugs can be administrated orally in a crystalline state and their dissolution rates are entirely dependent on the crystal form. Solubility is thus an important factor in the choice of the crystalline form of a drug compound. Another important factor in pharmaceutical drug material formation is the bioavailability. This is related to the rate and extent of physiological absorption of a particular drug and can also vary with different crystal forms.

The discovery of a new polymorph of a material, as in the case of cefadroxil (a bactericidal antibiotic), can lead to an improvement in the quality of this substance over the previously known polymorph.[1] In this case, this includes higher solubility and high bulk density, allowing the production of smaller pills.

Co-crystals (crystal structures which contain two types of molecules, also known as molecular complexes or molecular salts) are also used in the pharmaceutical industry for improving physico-chemical properties such as solubility, melting and boiling points, taste, colour and so on. Co-crystals can also exhibit multiple phases as found for instance in the case of the pharmaceutical carbamazepine isonicotinamide[15] (Scheme 1.1). Co-crystals are also used in others fields such as the food industry (for example in changing the flavour / taste of food) and many others.

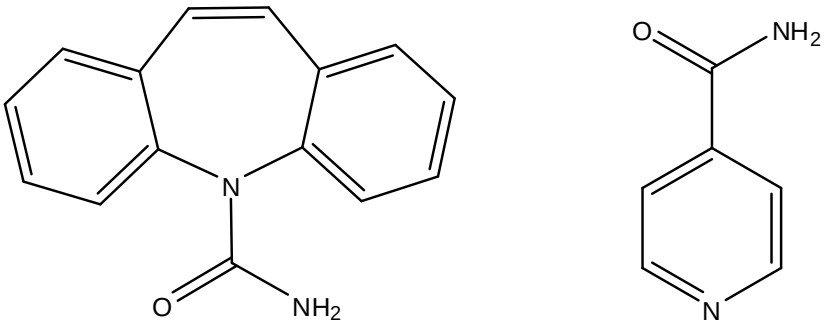

Scheme 1.1. Molecular structures of carbamazepine – isonicotinamide. The co-crystalline molecular complex of these materials is polymorphic.[15]

The organic material with the most known polymorphs is 5-methyl-2-[(2 nitrophenyl)amino]-3-thiophenecarbonitrile (ROY Scheme 1.2). The name of this compound (ROY) is due to the fact that the polymorphs can be distinguished by their different colours (red, orange and yellow). The forms are known to grow as orange needles, yellow prisms, red prisms, orange plates, yellow needles, red plates and orange-red plates.[16] There are nine polymorphs known for ROY with seven crystal structures solved that can be recrystallised from simple solvents; many of the ROY polymorphs can crystallize simultaneously from the same solution.

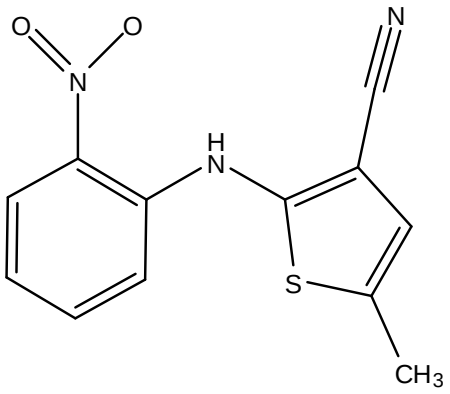

Scheme 1.2. Molecular structure of ROY

It is also possible that the same chemical composition of a solid crystalline material to present different crystal packing under high pressure conditions or different temperatures. This phenomenon is known as a phase transition. In the molecular area, the new phases obtained under high pressure are also often addressed as polymorphic forms. The phase transition process is a common phenomenon which occurs in organic, organometallic and inorganic compounds. A simple search of the CSD using the ‘phase transition’ key words gives 3448 hits.

A phase transition process is reversible and during the heating or cooling a change in the space group or unit cell parameters is often observed. A discussion of the detailed mechanism of phase transitions is beyond the scope of this work, but since it is a process that minimises the energy of a material under a given set of conditions, the approach to be adopted here of studying lattice energies and the energy of intermolecular interactions via charge density analysis will be relevant. This phenomenon will be investigated in the present work by examining the phase transition in a selection of transition metal complexes by high resolution diffraction methods.

A wide variety of techniques have been developed in the last few decades, which can be used for examining crystal structures, crystal properties and associated physical properties of solid state molecular materials. These techniques can be divided into crystallographic, spectroscopic, microscopic and thermal categories. Single crystal and powder materials are normally studied using both X-ray and neutron sources. Spectroscopic techniques include infrared and Raman spectroscopy. The microscopic techniques include hot stage and optical microscopy. The thermal techniques available are differential scanning calorimetry (DSC) and thermogravimetric analysis (TGA).

1.2. Diffraction Techniques

1.2.1. X-ray diffraction

X-ray diffraction is a common method used to determine crystal structure in the solid state. The X-ray beam, which is electromagnetic radiation, can be generated inside a vacuum tube by bombarding electrons onto a flat metal surface such as Mo or Cu. The radiation arises from the fact that the electrons of the atoms on the metal surface are ionised, especially those from K shell. This is followed by relaxation of an electron from a higher shell which emits radiation. The photons emitted in this way interact with a crystal monochromator which absorbs the unwanted wavelengths, leaving a broadly monochromatic beam, which is then directed onto the crystal. X-ray beams interact with solid state materials through the absorption and emission of radiation. The incident electromagnetic radiation scattered by the electrons in an elastic fashion is known as *Thomson scattering.* Inelastic scattering occurs when a small amount of photon energy is absorbed by electrons, this is known as the *Compton effect.*

The intensity of the X-ray beam diffracted is measured by an area detector. There are many types of area detectors such as multi-wire proportional chambers, phosphor coupled to a

TV camera, and image plates, but the most widely used in modern diffractometers are charge-coupled devices (CCDs). The diffracted X-ray enters the CCD detector through beryllium windows, and is then converted into visible light by a thin reflector phosphor. The light photons generated in this way are then reduced to the size of the CCD through a fibre optic trap which transforms the light into electrons. The signal is read out by the CCD in a binned mode which typically contains 2x2 pixels added together, is amplified by the detector, digitized in the controller and sent into computer memory producing a 2D image of the intensity of the incident X-rays on the detector surface.

The atoms in a crystalline material are arranged in a regular array which allows constructive interferences of X-ray beams, being defined by the scattering vectors. The lattice of the structure is defined by a group of atoms or molecules forming a regular array of identical points. The lattice points are equivalent to each other by translational symmetry. The unit cell of the structure is constructed by the smallest repeating volume of the lattice points. The unit cell is defined by three vectors a, b, c, and the angles between these, α, β, γ. This is depicted pictorially in Figure 1.1.

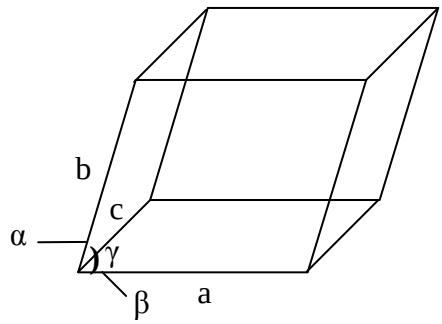

Figure 1.1. Unit cell of a crystal, showing the a, b, c, α, β, γ parameters.

Due to the various relationships between the unit cell parameters, and the number of lattice points contained within the unit cell, there are seven crystal systems and fourteen possible lattices, called the Bravais lattices (Table 1.1, Figure 1.2.).

Table 1.1. The seven crystal systems and the corresponding fourteen Bravais lattices.

Triclinic	$a \neq b \neq c$	$\alpha \neq \beta \neq \gamma \neq 90^o$	**P**
Monoclinic	$a \neq b \neq c$	$\alpha = \gamma = 90^o \beta \neq 90^o$	**P + C**
Orthorhombic	$a \neq b \neq c$	$\alpha = \beta = \gamma = 90^o$	**P + C + F + I**
Tetragonal	$a = b \neq c$	$\alpha = \beta = \gamma = 90^o$	**P + I**
Cubic	$a = b = c$	$\alpha = \beta = \gamma = 90^o$	**P + I + F**
Trigonal	$a = b \neq c$	$\alpha = \beta = 90^o \gamma = 120^o$	**R**
Or	$a = b = c$	$\alpha = \beta = \gamma < 120^o$	
Hexagonal	$a = b \neq c$	$\alpha = \beta = 90^o \gamma = 120^o$	**P**

P = primitive, **C** = centred, **I** = body-centred, **F** = face-centred, **R** = rhombohedral

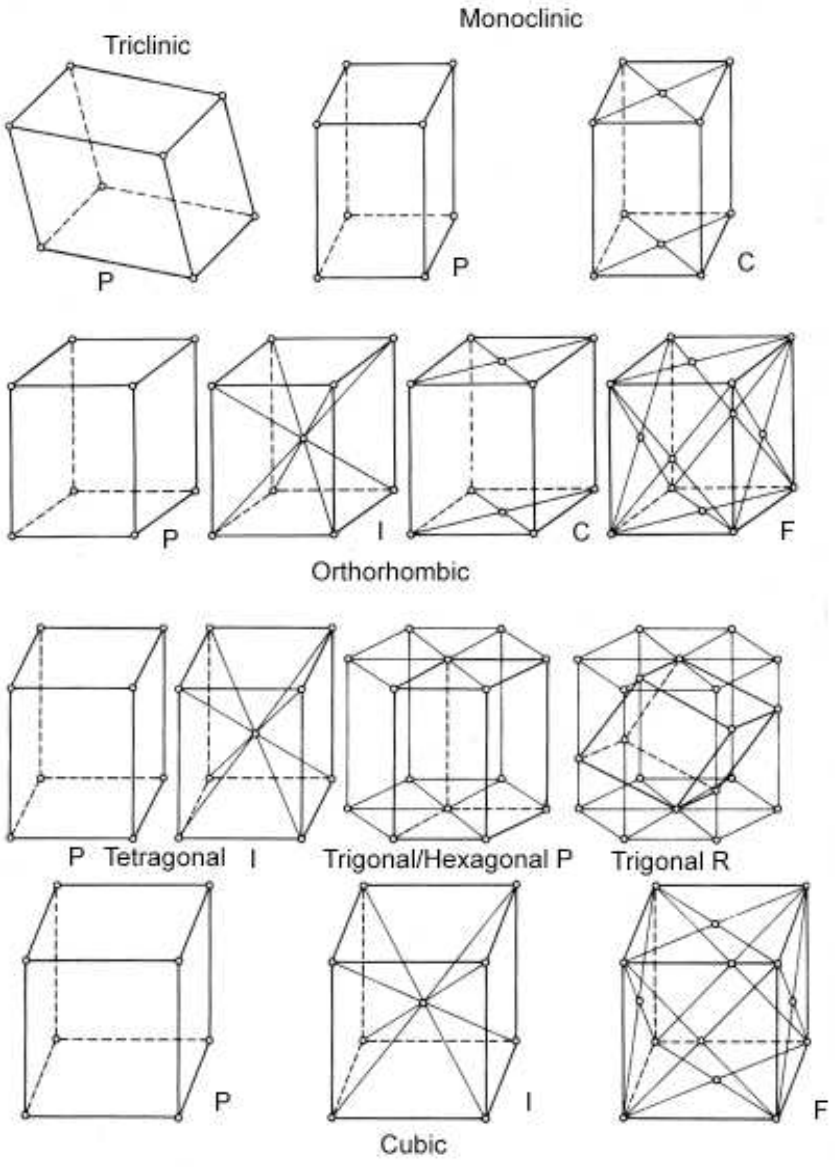

Figure 1.2. The fourteen Bravais lattices.[17]

The relationship between the lattice vectors and the geometry of diffraction can be obtained using the *Laue* and *Bragg* equations. Diffraction from a crystalline material is obtained when the diffracted X-ray beams are in phase. To ensure that the X-rays are in

phase, the difference in the path lengths of the individual rays must be equal to an integer number of wavelengths. The path difference of rays scattered by two points from the same row according to the *Laue equations* is calculated as follows (in three dimensions):

$$\text{path difference} = a\cos\psi_i - a\cos\psi_d = h\lambda \qquad \text{eq. 1.1}$$

$$\text{path difference} = b\cos\psi_i - b\cos\psi_d = k\lambda \qquad \text{eq. 1.2}$$

$$\text{path difference} = c\cos\psi_i - c\cos\psi_d = l\lambda \qquad \text{eq. 1.3}$$

where ψ_i and ψ_d are the angle of the incident and diffracted beams with respect to the row of scattering points being considered, λ is the wavelength, a,b,c are the interatomic spacing, h,k,l are three integers (see below). The Laue model of diffraction is represented in Figure 1.3 for the case of one row of regular spaced atoms. The path difference in this case is equal to AB-CD.

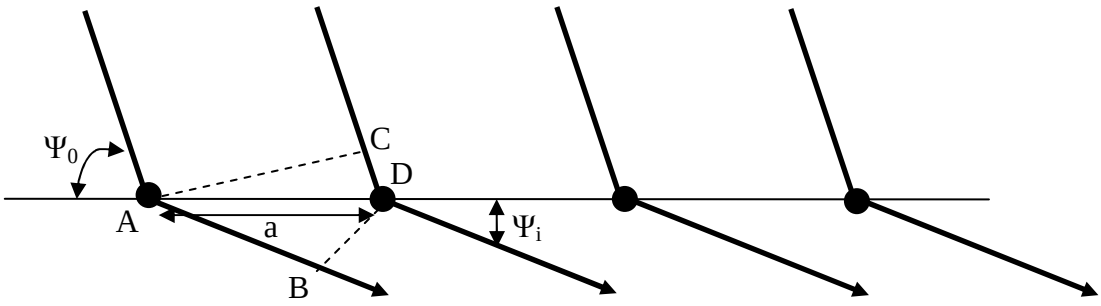

Figure 1.3. Diffraction for a single row of regular spaced atoms.

Due to the fact that in this form the three equations presented above are difficult to use from a mathematical point of view, a simpler description of the diffraction geometry was implemented by W. L. Bragg, represented in equation 1.4 and illustrated in Figure 1.4, which shows that this model is based on scattering from sets of parallel planes within the crystal.

$$n\lambda = 2d_{hkl}\sin\theta \qquad \text{eq. 1.4}$$

where n is an integer (the order of reflection), d_{hkl} is the separation between the scattering planes and θ is the angle between the incident beam and the sets of lattice planes. The path length difference has to be a multiple of wavelength in Bragg's formulation, which can be derived from Figure 1.4.

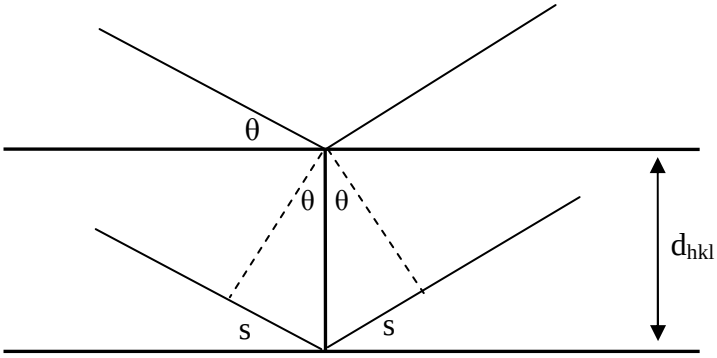

Figure 1.4. Diffraction of X-rays in the description used to derive Bragg's law.

The lattice planes defined in this model of diffraction geometry can be obtained from the unit cell vectors. These planes are constructed in a reciprocal space by the Miller indices hkl which can be calculated from the relation:

$$h : k : l = 1/a : 1/b : 1/c \qquad \text{eq. 1.5}$$

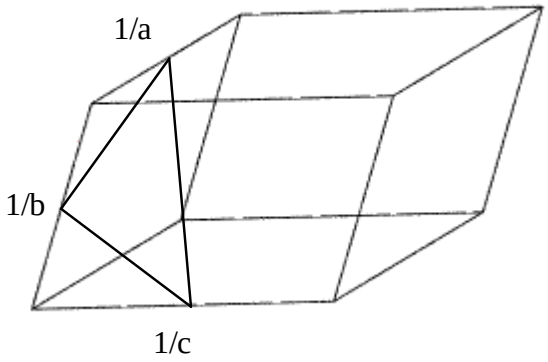

Figure 1.5. The lattice planes intercepting with the unit cell.

The h, k, l are called the Miller Indices, with integer values, and h/*a*, k/*b*, l/*c* in this case are the intersection points of the planes with the unit cell; the (1,1,1) Miller index plane is illustrated in Figure 1.5. The crystal lattice in reciprocal space is described by the *a*,b*,c*,α*,β*,γ** parameters and their relation with the direct lattice is conveniently described using vector notation:

a* = (1/V) **b** x **c; b*** = (1/V) **c** x **a; c*** = (1/V) **a** x **b;** cos**α*** = (cosβcosγ – cosα)/|sinβsinγ|; cos**β***=(cosγcosα-cosβ)/|sinγsinα|; cos**γ***=(cosαcosβ-cosγ)/|sinαsinβ| eq. 1.6

A geometrical representation in reciprocal space of Bragg's law can be represented by the *Ewald* reflecting sphere construction (Figure 1.6). The radius of the Ewald sphere as illustrated in Figure 1.6 is the reciprocal of the wavelength ($1/\lambda$). The reciprocal lattice vector lies perpendicular to the hkl plane and has a length $1/d_{hkl}$ with the origin at point O. The reciprocal lattice points need to touch the surface of the sphere in order to reach the diffraction condition. Therefore, OB is identical to $1/d_{hkl}$. For instance in triangle AOC, OC = $(1/\lambda)\sin\theta = 1/2d_{hkl}$, hence $\lambda = 2d_{hkl}\sin\theta$. For meeting these criteria during the diffraction experiments, the crystal rotating method is used – rotating the crystal also rotates the reciprocal lattice and can bring different lattice points into the scattering position on the surface of the Ewald sphere.

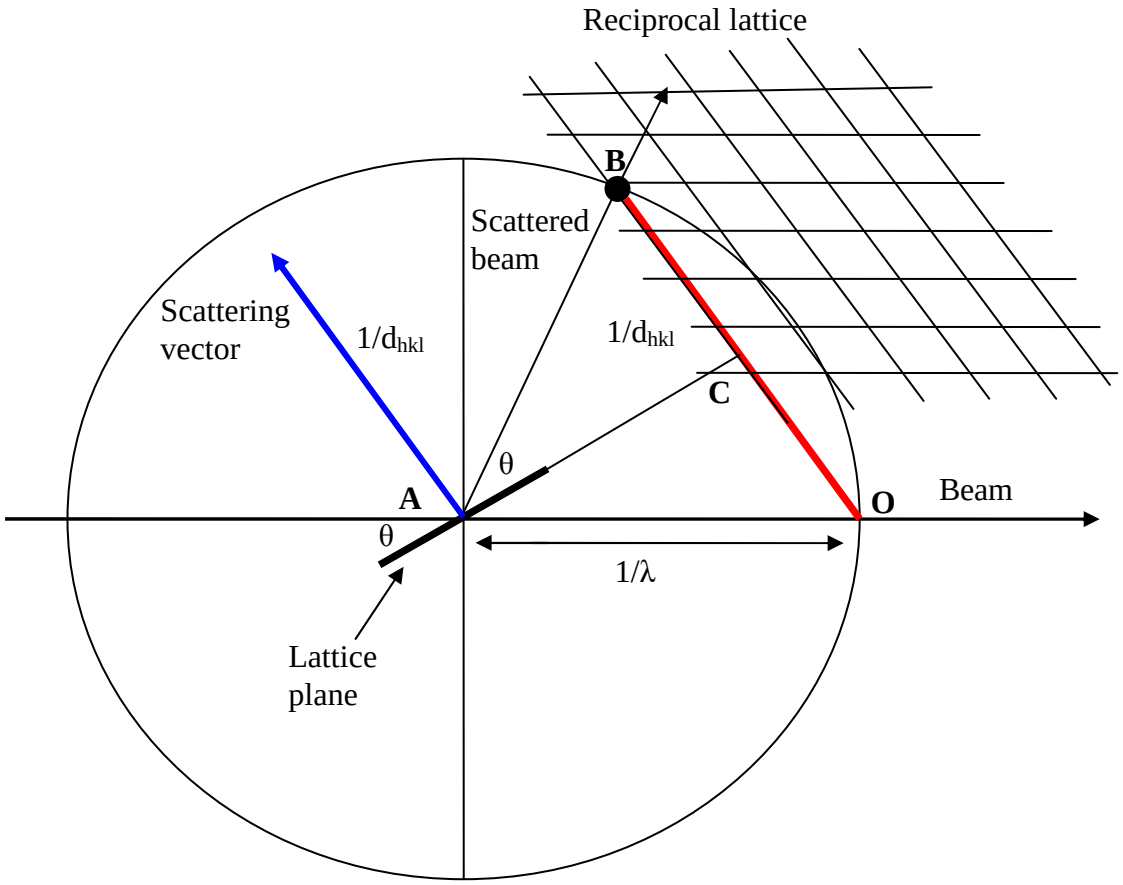

Figure 1.6. *Ewald* sphere showing the diffraction geometry in reciprocal space.

All individual waves diffracted are characterised by a structure factor – which has both an amplitude and a phase. The scattered wave can be expressed for each reflection by Fourier summation over all atoms in the unit cell which gives the structure factor F_{hkl}. This can be

described in exponential form (eq. 1.7.) or using *Euler's* rule containing a real and an imaginary part (eq. 1.8).

$$F_{hkl} = \sum_j f_j e^{2\pi i(hx_j + ky_j + lz_j)} \qquad \text{eq. 1.7}$$

$$F_{hkl} = \sum_j f_j \left[\cos 2\pi(hx_j + ky_j + lz_j) + i \sin 2\pi(hx_j + ky_j + lz_j)\right] \qquad \text{eq. 1.8}$$

Where the summation is over all atoms j in the unit cell, which have atomic scattering factor f_j and are located at position (x_j, y_j, z_j) in the cell. The phase information can not be determined directly from the experiment and there are various ways of solving this problem as described in the Section 1.2.3. The modulus of F_{hkl} can be instead obtained from the intensity measurements which are approximately proportional to the square of the structural factor amplitude:

$$I_{hkl} \propto |F_{hkl}|^2 \qquad \text{eq. 1.9}$$

The structure factor can be also expressed in terms of continuous electron density distribution by integrating the electron density over the whole unit cell volume:

$$F_{hkl} = \int_V \rho_{xyz} e^{2\pi i(hx+ky+lz)} \mathrm{d}V \qquad \text{eq. 1.10}$$

The electron density at any point (x, y, z) and hence the crystal structure can be obtained from the reverse *Fourier synthesis*:

$$\rho_{xyz} = \frac{1}{V} \sum_{hkl} F_{hkl} e^{-2\pi i(hx+ky+lz)} \qquad \text{eq. 1.11}$$

or

$$\rho_{xyz} = \frac{1}{V} \sum_{hkl} |F_{hkl}| e^{i\Phi(hkl)} e^{-2\pi i(hx+ky+lz)} \qquad \text{eq. 1.12}$$

where Φ_{hkl} is the phase of the structure factor F_{hkl}. The scattering factor f_j in equation 1.7 represents the scattering power from atom j, and shows a variation of value with the scattering angle. This is usually represented as a function of $\sin\theta/\lambda$ and it is measured in units of electrons. As the atoms are manifesting thermal motion vibration, the scattering

factor is multiplied by a term containing an isotropic (or anisotropic) displacement parameter U_j (eq. 1.13). The displacement parameter is calculated from the mean-square amplitude of the vibration and measures the amount of vibration of an atom about its equilibrium position in the crystal structure.

$$f'(\theta) = f(\theta)\exp\left(-\frac{8\pi U_j \sin^2\theta}{\lambda^2}\right) \qquad \text{eq. 1.13}$$

The $f(\theta)$ for each atom is included in most crystallographic programs and the values are taken from International Tables for Crystallography Volume C, Table 6.1.1.1-5.[18] The atomic scattering power decreases with an increase of the diffraction angle. Therefore, as can be seen from Figure 1.8., the intensity falls off as the resolution $\sin\theta/\lambda$ is increased.

1.2.2. Synchrotron and neutron sources

Synchrotron radiation

Another method of producing radiation, instead of using X-ray tubes, involves accelerating charged particles (electrons) in a synchrotron. The electrons are accelerated in this installation at almost the speed of light, and when they are changed in direction by the application of electromagnetic fields, they emit radiation. The advantage of synchrotron radiation is that it produces a very high intensity primary beam which is almost completely polarized. In a diffraction experiment at such a source, a small crystal must be used which minimises the extinction and absorption and the data are collected faster. Synchrotron radiation contains tunable wavelengths and selected monochromatic frequencies are used. The main applications of the synchrotron source radiation are for structure determination of macromolecules such as proteins or for the case where only very small crystals can be obtained. An important advantage of a synchrotron source over laboratory X-ray diffraction is that data collection time will be significantly reduced; for high resolution charge density studies, the data collection time can be reduced from between 5 to 7 days in a normal laboratory experiment, to a few hours at the synchrotron. Another advantage will be in obtaining measurable diffraction intensities at higher scattering angle – and hence higher resolution – due to the much higher intensity of the beam.

Neutron Scattering

In a neutron diffraction experiment, the neutrons are scattered by the atomic nuclei, not by the electronic shells as in X-ray diffraction. The positions of the nuclei are located directly from the neutron diffraction, which provide more accurate atom position information. In the X-ray diffraction experiment, the electron density distribution is used to locate the

atoms, which will be affected by bonding density effects and the scattering power is strongly dependent on the number of electrons and hence the atomic number Z. Therefore, it is difficult to see light atoms in presence of heavy ones or distinguish between neighboring atoms in the periodic table. The neutron scattering factors, on the other hand, are not proportional to Z and they are not scattering angle dependent as in the case of X-ray diffraction (Figure 1.7). They vary from one element to another and even from one isotope to another e.g. ^{1}H, b = –3.74, ^{2}H, b = +6.67 (Figure 1.8). It can be seen from Figure 1.8 (left) that the scattering factor for hydrogen is of average magnitude, and hence neutrons can determine H atom parameters to similar accuracy to those of the other atoms present.

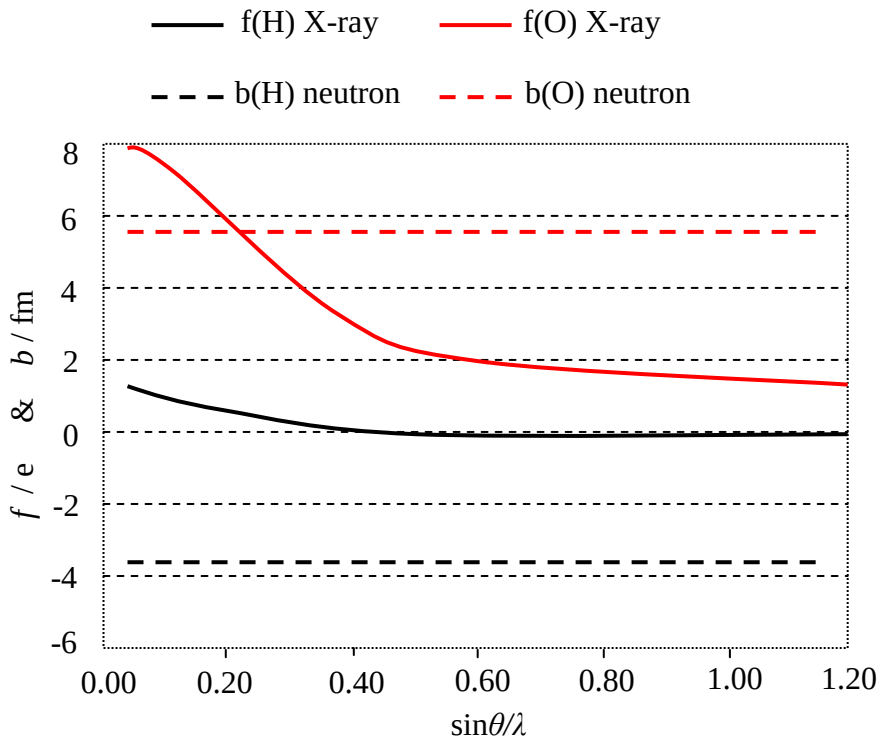

Figure 1.7. X-ray scattering factors and neutron scattering lengths plotted against $\sin\theta/\lambda$ for the elements hydrogen and oxygen.

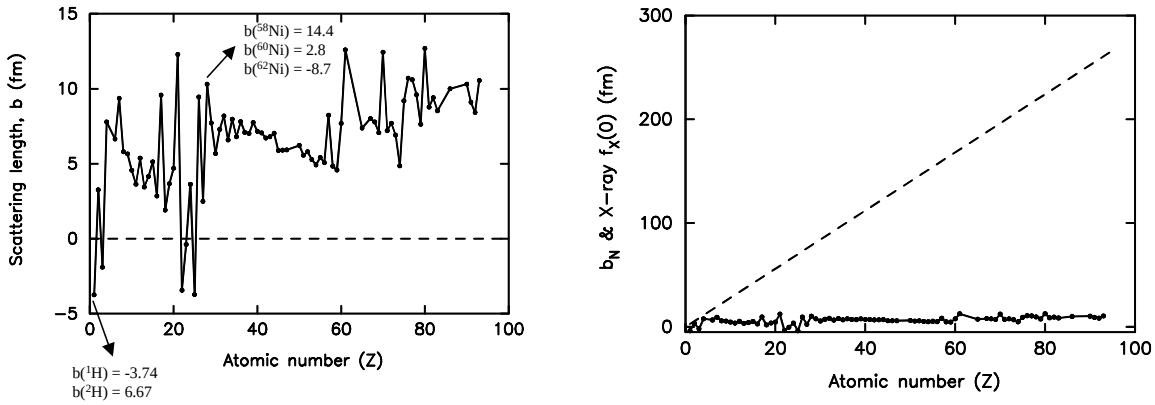

Figure 1.8. Scattering factors for neutron diffraction (left) and in comparison with X-ray diffraction (right).[19]

In this study an understanding of the influence of hydrogen bond formation in the polymorphs and also in determining accurately the rank stability of studied materials will be pursued. Knowing the precise location of hydrogen atoms plays an extremely important role in reaching these aims, hence neutron diffraction has been employed.

Neutrons for scattering experiments can be generated using two main procedures: one is based on nuclear fission and is produced using a nuclear reactor, while the other is obtained through a spallation process. In the last case the neutrons are obtained by bombarding a heavy metal target with pulses of highly energetic protons resulting in particle collisions. The protons are previously accelerated using both a linear accelerator and a synchrotron ring. As the beam is produced in pulses, it is possible to use the time-sorted (time-of-flight) Laue data collection technique. An example of this type of neutron facility (ISIS, Rutherford Appleton Laboratory) which was used in the experimental work presented here, is illustrated schematically in Figure 1.9.[20] The D19 beam at the Institut Laue-Langevin (ILL), which is based at a nuclear reactor source, was also used for experimental data collection. A fixed wavelength was used in this case.

One of the main disadvantages in using neutron diffraction is that much larger crystals are needed, typically several mm^3 in volume.

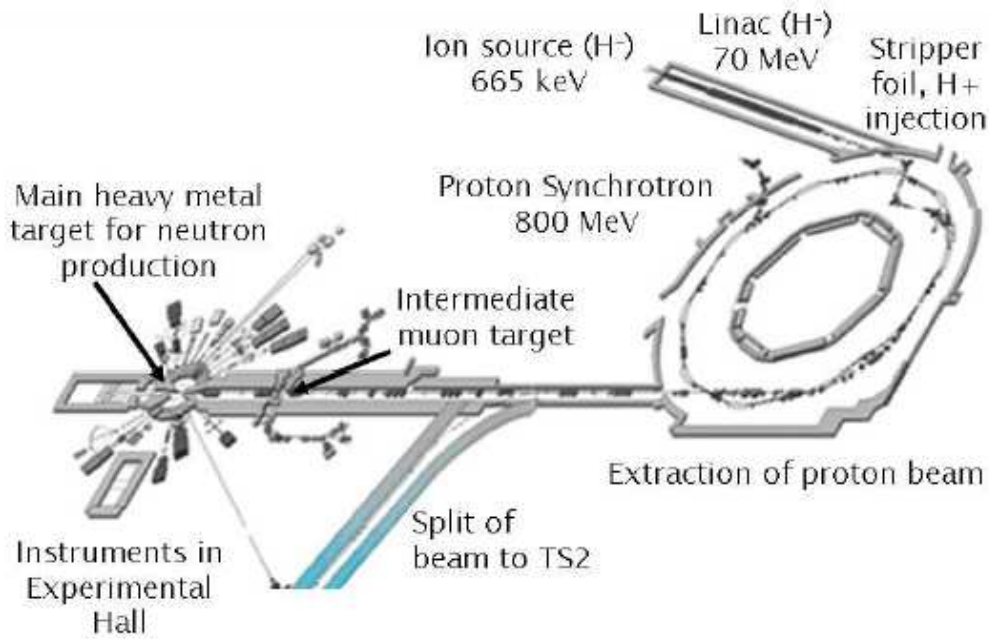

Figure 1.9. Schematic representation of the ISIS neutron facility source.[20]

1.2.3. Structure solution and refinement

Structure solution. As described above, the crystal structure can be obtained by converting the measured diffraction patterns using the Fourier transformation into an electron density map (eq. 1.14).

$$\rho(xyz) = \frac{1}{V}\sum_{hkl}\left|F(hkl)\right|\exp[i\,\Phi(hkl)]\exp[-2\pi i(hx+ky+lz)] \qquad \text{eq. 1.14}$$

The amplitudes $|F(hkl)|$ can be extracted directly from the experiment, but the phase information, $\Phi(hkl)$, is lost. It is therefore not possible to carry out the Fourier synthesis directly. There are many methods to obtain the missing phase information and hence the structure, but the two most widely used are the Patterson method and Direct methods.

The Patterson synthesis

The Patterson method is actually another version of equation 1.14 which works directly with the squared amplitudes F_0^2 and all phases set equal to zero. From this the interatomic

vectors may be obtained and in favourable situations this can be interpreted to reveal the positions for some of the atoms in the structure.

$$P_{uvw} = \frac{1}{V^2} \sum_{hkl} F_{hkl}^2 e^{-2\pi i(hu+kv+lw)} \qquad \text{eq. 1.15}$$

The use of the *uvw* distance vectors is to emphasise the difference within the real *xyz* space. The result of this transformation does not give the electron density and hence atomic positions, but rather the vectors between these positions, with a height that is the product of the two positions related by that vector. Thus, the peaks in the Patterson map are represented by vectors between pairs of atoms in the structure (i.e. the positions of atoms relative to each other) and do not correspond to the positions of individual atoms (i.e. the positions of atoms relative to the unit cell origin as expressed in their coordinates x, y, z). For every pair of atoms in the structure with coordinates (x_1, y_1, z_1) and (x_2, y_2, z_2) there will be a peak in the Patterson map at the position (x_1-x_2, y_1-y_2, z_1-z_2) and another one at the position (x_2-x_1, y_2-y_1, z_2-z_1), since each atom gives a vector to the other. However interpreting the Patterson map can sometimes be difficult especially for organic compounds, and the Patterson method is mostly used for crystal structures containing heavy atoms. Since the height of the peak corresponding to a vector is proportional to the product of the scattering from both atoms involved, the larger Patterson peaks are attributed to the vectors between the heavy atoms. These atomic positions can thus be extracted and are used as a model structure from which an approximate set of phases can be deduced and used in further Fourier synthesis development of the structure.

Direct methods

This method is used to obtain approximate reflection phases directly from the measured intensities. The crystal structure is determined in the direct method by using the convolution theorem which gives:

$$\begin{array}{ccccccc} |F(h)| & \text{x} & \exp(i\Phi(h)) & = & F(h) & & \text{eq. 1.16} \\ \Updownarrow \text{F.T.} & & \Updownarrow \text{F.T.} & & \Updownarrow \text{F.T.} & & \\ \text{amplitude synthesis} & * & \text{phase synthesis} & = & \text{electron density} & & \end{array}$$

From this equation it can be deduced that the amplitudes and phases are not independent of each other but are related through the knowledge of the electron density. The amplitude

synthesis is similar to the Patterson function and will give a large peak at the origin. By adding the phase synthesis the peak from the origin will be located at the site of each peak in the phase synthesis. The phase synthesis contains peaks at the atomic site in the convolution operation which gives the electron density. Therefore the atomic positions obtained from the density map are given by the phase rather than the amplitude.

Obtaining the correct electron density implies that a mathematical constraint has to be applied on the function ρ to be determined. For instance the intensities need to be normalized due to their dependence on the scattering angle. This procedure consists in scaling the intensities to an average values determined for different resolution ranges. Thus F_o is converted to E, the normalized structure factor. Another constraint applied to the density function is the fact that the electron density in a structure can never be negative. This was expressed in the Sayre relationship which states that the structure factor for any reflection hkl can be obtained from the sum of the products of the structure factors of all pairs of reflections of which the indices sum to it, e.g.:

$$E_{321} = E_{100} \cdot E_{221} + E_{110} \cdot E_{211} + E_{111} \cdot E_{210} + \cdot\cdot \qquad \text{eq. 1.17}$$

This was further developed by Karle and Hauptman into a practical method called the triplet relation in which the phase problem is reduced to a ‘sign problem’. In case of a centrosymmetric structure it is given by:

$$E_{hkl} = E_{h',k',l'} \cdot E_{h-h',k-k',l-l'} \qquad \text{eq. 1.18}$$

Thus, the E_{hkl} has a positive sign if $E_{\mathrm{h'k'l'}}$ and $E_{\mathrm{h'\text{-}h,\ k'\text{-}k,\ l'\text{-}l}}$ both have the same sign; and is negative if they both have different signs. Similar relationships can be deduced for phase relationships in non-centrosymmetric structures.

Structure Refinement

The Patterson and direct methods serve only to provide an initial model in determining the crystal structure. In order to complete the basic structure, the next step consists in refining the model. This procedure involves calculating the structure factor F_c for each *hkl* observed reflection of the model structure. This is used in the least-squares approach in which it is compared with the observed diffraction pattern, represented by the observed structure

factor amplitudes $|F_o|$. The "best fit" of the two sets of amplitudes will be that which minimizes the least-squares sum:

$$\sum w(|F_o| - |F_c|)^2 \qquad \text{eq. 1.19}$$

$$\text{or} \quad \sum w(F_o^2 - F_c^2)^2 \qquad \text{eq. 1.20}$$

Early refinement strategies were based on F, however recently the F^2 refinement has been shown to be more appropriate as it is in many ways superior. In the F refinement, the very weak data gives problems as the background can be sometimes estimated to be stronger than the peak. Also, negative values of the intensity can not be included in the F_o, and information from these intensities are usually not considered in the refinement. Using the F_o^2 data will solve this problem and all measured data can be included in the refinement, even those with negative values. The term w in equation 1.19 and 1.20 refers to the weights which are given to the observations $w = 1/(\sigma(F_{obs}))^2$ and $w = 1/(\sigma(F_{obs}^2))^2$ respectively. For a direct comparison of the observed and calculated amplitudes, a scale factor needs to be calculated after every change:

$$k_1 = \frac{\sum |F_o|}{\sum |F_c|} \qquad \text{or} \qquad k_2 = \frac{\sum F_o^2}{\sum F_c^2} \qquad \text{eq. 1.21}$$

The quality of the refined model can be judged with the help of the residual factors (R-factor) which are defined as:

$$R = \frac{\sum \| F_o - | F_c | \|}{\sum | F_o |} \qquad \text{eq. 1.22}$$

or through the more recently used equation:

$$wR^2 = \sqrt{\frac{\sum w(F_o^2 - F_c^2)^2}{\sum w(F_o^2)^2}} \qquad \text{eq. 1.23}$$

1.2.3. X-ray Charge Density Analysis

In the usual X-ray crystal structure analysis the electron density is described as a spherical atomic density following the thermal motion of the nuclei. This formalism does not take

into consideration the static deformation from the chemical bonding region which affects the accurate estimation of the parameters in the least square refinement. There are several possibilities for solving the inadequate description of the spherical atom formalism. One method consists in obtaining a higher order of diffraction. This is based on the fact that at high Bragg angle, the density from the core region has considerable contribution to the diffraction patterns. The valence bond density is more diffuse at the high angle and can be neglected. Therefore, a spherical-atom refinement will be in this case more realistic and the atomic parameters will therefore be described more accurately. Another possibility to increase the accuracy of the parameters involves the incorporation of the aspherical density model into the fit of experimental data. There are several methods[21, 22] which can be applied to the aspherical model formalism and the one which will be used in this work has been developed by Hansen & Coppens[23], referred to as multipole refinement. The electron density is divided in this formalism into three parts: spherical core density (ρ_c), spherical valence density (ρ_v) and aspherical deformation density (ρ_d) as described in equation 1.24.

$$\rho(\mathbf{r}) = P_c\rho_c(r) + P_v\kappa^3\rho_v(\kappa r) + \rho_d(\kappa' r) \qquad \text{eq. 1.24}$$

where the deformation valence densities are defined using:

$$\rho(\kappa'\mathbf{r}) = \sum_{l=0} \kappa^3 R_l(\kappa' r)\sum_{m=0}^{l} P_{lm\pm} y_{lm\pm}(\mathbf{r}/r) \qquad \text{eq.1.25}$$

The $y_{lm\pm}$ parameter represents the density-normalized real spherical harmonics, P_v are the valence population parameters and $P_{lm\pm}$ are the multipolar populations, κ and κ' are contraction–expansion parameters for the valence densities. The radial density functions $R_l(\kappa' r)$ are described in terms of a normalized single Slater-type and has the expression:

$$R_l(\kappa'_l r) = (\kappa'_l \alpha_l)^3 \frac{(\kappa'_l \alpha_l r)^{n(l)}}{[n(l)+2]!}\exp(-\kappa'_l \alpha_l r) \qquad \text{eq. 1.26}$$

where α_l values are obtained from the Hartree-Fock optimized single-ζ exponents of the valence-orbital wavefunctions calculated for free atoms.[24-27] The core and spherical valence density are calculated from Hartree-Fock atomic wavefunctions expanded also as Slater functions:

$$O_l = [(2n(l)!]^{-1/2}(2\zeta_l)^{n(l)+1/2,n(l)} \exp(-\zeta r) \qquad \text{eq. 1.27}$$

The corresponding scattering factor is:

$$f(h) = f_c(H) + P_v f_v(\frac{h}{k}) + \sum_l \left\langle J(\frac{h}{k'})_l \right\rangle \sum_{m=l}^{l} P_{lm} y_{lm}(\frac{h}{h}) \qquad \text{eq. 1.28}$$

Where $\langle J_l \rangle$ is a Fourier-Bessel transformation function of R_l:

$$\langle J_l \rangle = 4\pi i^l \int j_l(2\pi Hr) R_l(r) r^2 dr \qquad \text{eq. 1.29}$$

The local coordinate system

In the multipole refinement, local symmetry can be attributed to some of the atoms in the molecules. This local symmetry is not related to the crystallographic symmetry apart for the cases where the atoms lie on a crystallographic symmetry (element special position). The local symmetry of an atom is determined using the neighbour bonded atoms. For example in case of the carboxylate anion and carboxylic acid group, we can consider both groups are planar (m_1) for simplicity. The local symmetry in the case of the C_1 atom highlighted in red for the carboxylate anion in Scheme 1.3. (left) will be *mm*2. This local symmetry is applied due to the possibility of a second mirror plane that can exist (m_2), which is perpendicular to m_1. These two planes are intersecting along the C2-C1 bond and a two-fold axis is formed in this case. The carboxylic acid group has only m_1 in the plane of the molecule; hence for the C_1 atom local mirror symmetry will be applied.

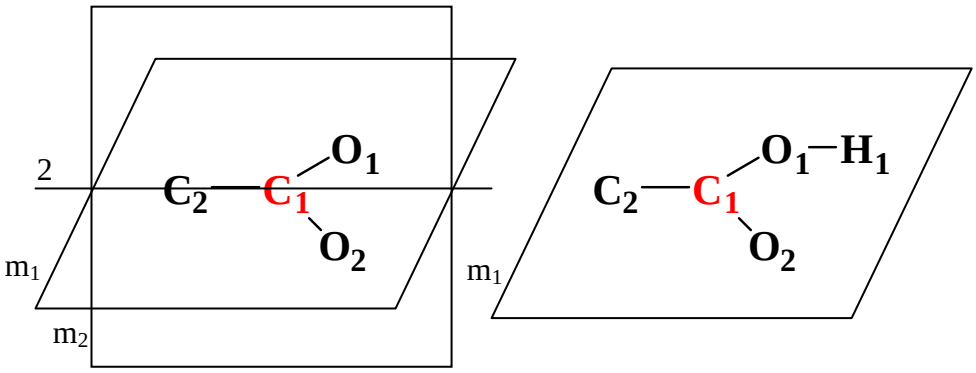

Scheme 1.3. The local symmetry determination for C_1 in carboxylate anion (left) and carboxylic acid (right) group.

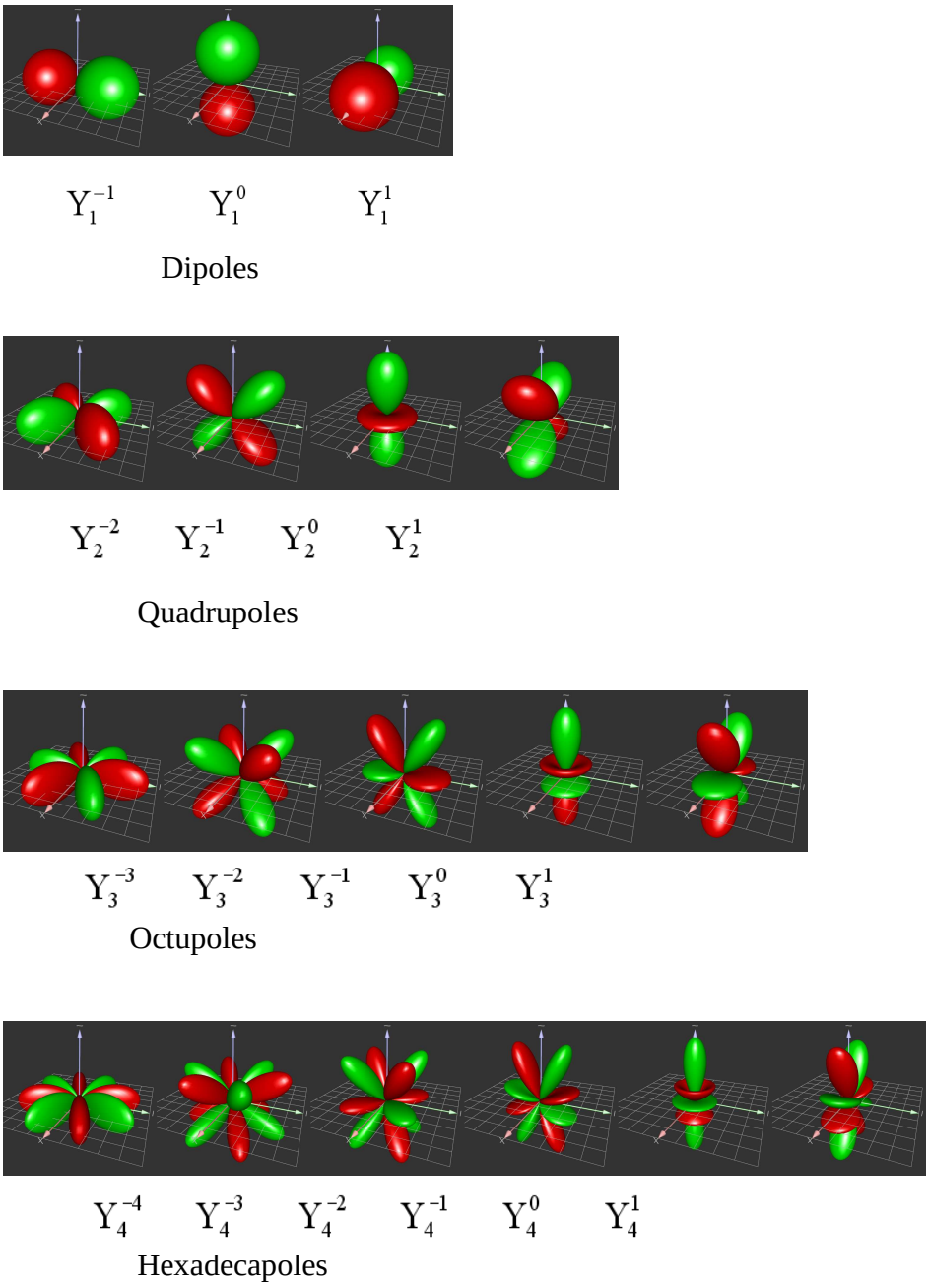

Fig 1.10. Some dipolar, quadrupolar, octupolar and hexadecapole functions.

The local axis has to be choosen for the atoms which local symmetry constraints are to be applied, and according to this it will in turn be determined which multipolar functions will be refined or not. This can be calculated using the Index Picking Rules of Site-Symmetric Sphecial Harmonics Table.[28] For local mirror symmetry the choice of coordinate axes is made in such a way that the mirror plane is perpendicular to the z axis. Therefore, for the dipole functions, the refinement of the spherical harmonics along *x* and *y* axes are allowed whereas for the Y_1^0, which lies along the *z* axis, the refinement is forbidden (Figure 1.10).

1.3. Quantum mechanics calculations

As the experimental charge density study results will be compared to theoretical calculations, this section addresses the necessary quantum mechanics theory.

Theoretical methods are classified into empirical and ab-initio approaches. The empirical approach combines classical mechanics and empirical data, while the ab-initio approach uses only theoretical calculations from first principles including the quantum mechanics laws. Quantum mechanics calculations are based on the non-relativistic and time-independent *Schrödinger equation*:

$$H\psi = E\psi \qquad \text{eq. 1.30}$$

where H represents the *Hamiltonian* operator, ψ is the wavefunction and E is the total observable energy of the system. The *Hamiltonian* in equation 1.30 is given by the kinetic and potential energy:

$$H = T_e + T_n + V_{ne} + V_{ee} + V_{nn} \qquad \text{eq. 1.31}$$

Where T_e and T_n are the kinetic energy of the electrons and nuclei respectively, the V_{ne} stands for the nuclear-electron Coulomb attraction, V_{ee} and V_{nn} are the electron-electron and nuclear-nucrear repulsion respectively. A more detailed representation of equation 1.31 for a system containing M nuclei and N electrons is written as:

$$H = \sum_{i=1}^{N} \frac{\hbar}{2m_e} \nabla_i^2 + \sum_{A=1}^{M} \frac{\hbar^2}{2M_A} \nabla_A^2 - \sum_{i=1}^{N} \sum_{A=1}^{M} \frac{e^2 Z_A}{r_{iA}} + \sum_{i=1}^{N} \sum_{j>i}^{N} \frac{e^2}{r_{ij}} + \sum_{A=1}^{M} \sum_{B>A}^{M} \frac{e^2 Z_A Z_B}{R_{AB}} \qquad \text{eq. 1.32}$$

In this case M_A is the mass of the nucleus, Z is the atomic number, $\hbar$ is Planck's constant, m_e is the mass of the electron, r_{iA}, r_{ij} and R_{AB} are the distances between two particles. The ∇_i^2 symbol is the Laplacian defined for Cartesian coordinates by:

$$\nabla_i^2 = \frac{\partial^2}{\partial x_i^2} + \frac{\partial^2}{\partial y_i^2} + \frac{\partial^2}{\partial z_i^2} \qquad \text{eq. 1.33}$$

From the Schrödinger equation, the total energy can be estimated as an expectation value of the Hamiltonian *H* as:

$$E = \langle H \rangle = \frac{\int \Psi^* H \Psi d\tau}{\int \Psi^* \Psi d\tau} \qquad \text{eq. 1.34}$$

The Schrödinger equation includes 3^N spatial variables and N spin variables (for electrons). Therefore, it is difficult to find an exact solution to this equation and approximation approaches must be used.

The Born-Oppenheimer approximation

The fundamental approximation used in quantum chemistry is the Born-Oppenheimer concept. This approximation is based on the fact that the nuclei are moving much slower in comparison with the electrons. Consequently, the nuclei can be considered fixed in to their position and only electron motion is taken into account. The Hamiltonian is then reduced to the kinetic and potential energy applied only to the electrons:

$$H = T_e + V_{ne} + V_{ee} \qquad \text{eq 1.35}$$

$$H = \sum_{i=1}^{N} \frac{\hbar}{2m_e} \nabla_i^2 - \sum_{i=1}^{N} \sum_{A=1}^{M} \frac{e^2 Z_A}{r_{iA}} + \sum_{i=1}^{N} \sum_{j>i}^{N} \frac{e^2}{r_{ij}} \qquad \text{eq. 1.36}$$

The potential V_{nn} energy is omitted in equation 1.35 as it is now a constant. The total energy in this case will be a sum of the energy of the electrons and the constant value of the potential energy of the nuclei:

$$E_{tot} = E_{elec} + V_{nn} \qquad \text{eq. 1.37}$$

At this stage, the calculations are still difficult to proceed with and can be applied only to small systems. Therefore further simplifications are demanded for larger system applications.

Antisymmetry principle

The wavefunction of a many-electron system is a function of the electron positions $\Psi(r_1, r_2, \ldots)$ and also depends on their spin occupancy. The overall wavefunction which

describes the electrons in the system can be written as $\Psi(r_1)\Psi(r_2)\ldots$ The spin occupancy is attributed by the quantum number ± ½ and described by α and β functions which have to be orthogonal:

$$\langle\alpha\,|\,\alpha\rangle = 1; \qquad \langle\beta\,|\,\beta\rangle = 1; \qquad \langle\alpha\,|\,\beta\rangle = 0; \qquad \langle\beta\,|\,\alpha\rangle = 0 \qquad \text{eq. 1.38}$$

The alpha spin (α) notation is considered a 'spin-up' and the beta spin (β) is the 'spin-down' notation. The electrons need to satisfy the Pauli exclusion principle which states that two electrons occupying the same spatial orbitals are required to have different spin functions. The wavefunction therefore needs to satisfy the antisymmetric principle. To simplify the notation we will refer to $\Psi(r_1)\Psi(r_2)\ldots$ as $\Psi(1)\Psi(2)\ldots$, and if we assume that electron 1 with spin α occupies the molecular orbital Ψ_a and electron 2 with spin β occupies the same orbital Ψ_a, then the many-electrons wavefunction will be a product of $\Psi = \psi_a^{\alpha}(1)\psi_a^{\beta}(2)\ldots$, where each wavefunction is a function of a spatial and spin state, (e.g. $\psi_a^{\alpha}(1) = \psi_a(1)\alpha(1)$). In order to satisfy the Pauli principle the wavefunction has to be described as a sum of all possible spin occupancies, varying the signs appropriately:

$$\Psi = \psi_a^{\alpha}(1)\psi_a^{\beta}(2)\ldots\psi_z^{\beta}(N_e) - \psi_a^{\alpha}(2)\psi_a^{\beta}(1)\ldots\psi_z^{\beta}(N_e) + \ldots \qquad \text{eq. 1.39}$$

This sum can be mathematically represented by the *Slater determinant* for N_e electrons:

$$\Psi = \frac{1}{\sqrt{N_e!}}\begin{vmatrix} \psi_a^{\alpha}(1)\psi_a^{\beta}(1)\cdots\psi_z^{\beta}(1) \\ \psi_a^{\alpha}(2)\psi_a^{\beta}(2)\cdots\psi_z^{\beta}(2) \\ \vdots \\ \psi_a^{\alpha}(N_e)\psi_a^{\beta}(N_e)\cdots\psi_z^{\beta}(N_e) \end{vmatrix} \qquad \text{eq. 1.40}$$

where the $1/\sqrt{N_e!}$ term is used for normalizing the wavefunction.

Hartree-Fock (HF) theory

The Hartree-Fock method is an approximation which describes each electron movement independently. The electron correlation is only treated in this case approximately and it is more useful to apply to ionic systems rather than to systems which involve covalent interactions.

Perturbation methods

The perturbation method uses the idea of finding a correlation between two systems – a system that only differs slightly from one which is already solved. The Hamiltonian in this case is expressed as a sum of the reference model $\hat{H}^{(0)}$ and the perturbed $\hat{H}^{(1)}$:

$$\hat{H} = \hat{H}^{(0)} + \hat{H}^{(1)} \qquad \text{eq.1.41}$$

One choice for the under-treated model can be the Fock operators (from HF method) and the pre-treated system will be then given by the difference between the Fock operator and the complete many-electron Hamiltonian. This method is called Møller-Plesset (MP) perturbation theory. The correction that needs to be applied will depend on the quality of the HF wavefunction, therefore for a less accurate description of the wavefunction larger correction terms are required. This implies that more terms need to be added in order to obtain a satisfactory level of accuracy.

Coupled Cluster method

The coupled cluster method makes use of electronic correlation (as in the MP method), but in addition these corrections are applied to an infinite order. The wavefunction is described in the coupled cluster approach as a product of the Slater determinant Φ_0 and the exponential ansatz:

$$|\Psi\rangle = e^{T} |\Phi_0\rangle \qquad \text{eq. 1.42}$$

Where T is the excitation operator and has the form:

$$T = T_1 + T_2 + T_3 + \ldots \qquad \text{eq. 1.43}$$

The T_1, T_2 and T_3 are the operators for the singlet, doublet and triplet state, respectively. The abbreviation for the coupled cluster theory CCSDTQ is related to the single S, double D, triple T and quadrupole Q excitations. Usually CCSDT and CCSDTQ approaches are only used for small molecules at high-accuracy level of calculations.

Density functional theory (DFT)

One of the most used methods in computational chemistry is density functional theory (DFT). The advantage of this method is that it is less computationally intensive than other

methods whilst retaining high accuracy, comparable in some cases to more computationally-expensive HF based approaches. In this method, the energy of the system is a function of the electron density E[ρ] which is a function of the wavefunction. The ρ can be expressed in terms of a contribution of each electron present in the molecule:

$$\rho(r) = \sum_{i=1}^{N_e} |\psi_i(r)|^2 \qquad \text{eq. 1.44}$$

This concept was implemented by Kohn and Sham[29] and the total energy expression is given in equation 1.45:

$$E_{KS} = T[\rho] + \int dr V_{ext}(r)\rho(r) + E_{Hartree}[\rho] + E_{xc}[\rho] \qquad \text{eq. 1.45}$$

where E_{Hartree} is the classical electrostatic energy of the density, and E_{xc} the exchange–correlation. The most used functions for E_{xc} are the *local density approximation* (LDA) and the *generalised gradient approximation* (GGA). In LDA, E_{xc} is expressed as a function of the local density ρ, while the gradient $\nabla\rho$ of the density is also included in the GGA. A combination of the Hartree-Fock exchange energy and the exchange-correlation energy is also possible, this is known as a hybrid functional (the most widely used is the B3LYP[30] functional that is widely implemented).

Solid state calculations

The quantum chemistry calculations can obviously be applied to the gas, liquid and solid state, but different calculation methods will of course be applied to each phase. For instance in the gaseous phase the molecule is isolated, while in the solid form the intermolecular interactions have to be taken into account. The *plane wave* (PW) and *atomic orbital* (AO) approaches are the most commonly used in the DFT calculations for the solid phase.

In the PW method the electronic structure is a function of the plane wave basis sets independent of the atomic nuclei and has to satisfy the periodic boundary conditions determined by the unique building block of the periodic structure. The electron density is therefore constructed from a linear combination of the plane waves.

In the AO method the electron density is calculated using the atom centred orbitals which are described by *Gaussian* or *Slater* type functions. In our work the AO calculations have been used, as incorporated in the CRYSTAL09[31] software.

All the calculations are based on the *self consisted field* (SCF) method in which the initial form of the orbitals is guessed and used to calculate the potential energy of the system. This energy is then used to calculate a new wavefunction and the calculations are considered to be converged when the energy is minimised.

Basis sets

Basis sets are the representation of the molecular orbitals. There are two different types of these basis sets: Slater type orbitals (STO)[32] and Gaussian type orbitals (GTO).[33] The STO obritals use spherical coordination and are centred on each atomic nucleus (Equation 1.46):

$$\chi = Nr^{a}e^{-br}Y_{lm_l}(\theta,\Phi) \qquad \text{eq. 1.46}$$

where N is a normalization constant, a and b are (non-negative) parameters, Y_{lm_l} is a spherical harmonic which describes the shape of the orbitals, (r, θ, Φ) are the spherical polar coordinates describing the position of the electron relative to the nucleus, l and m are the angular momentum and magnetic quantum numbers respectively. The STO orbitals are more accurate but more computationally demanding.

The GTO description of the orbitals uses Cartesian Gaussian functions centred at the atomic nuclei:

$$\chi = Nx^{i}y^{j}z^{k}e^{-\alpha r^{2}} \qquad \text{eq. 1.47}$$

where (x,y,z) are the Cartesian coordinates of the electron at the distance r from the nucleus; i,j and k are non-negative integers, α is a positive constant. The advantage of the GTO orbitals is that there is a reduction in required computational processing time due to the fact that the product of two Gaussian functions on different centres gives one Gaussian function located at a point between the two centres. This allows, for example, a two-electron integral of three or four centres to be reduced to an integral over two centres.

The smallest basis set is called a minimal basis set, in which only one basis function is used for each atomic orbital. An example of a minimal basis set is STO-NG, N being the number of Gaussian functions involved in the calculation. This type of basis sets is called single-zeta (SZ). In more sophisticated basis sets such as double-zeta (DZ) there will be two functions representing each atomic orbital, triple-zeta basis sets will be represented by three functions. There are also split-valence (SV) basis sets in which each inner-shell is represented by one function and each valence atomic orbital by two. For obtaining a better accuracy in the description of the atomic orbitals, a polarization function can also be used. This type of basis set also includes a function to represent the unoccupied orbitals. An example of an SV basis set is m-npG, were m is one function representation of each core atomic orbital, the valence shell is represented by two functions; one being a linear combination of n Gaussian and the other of p Gaussian functions. The polarization function is represented by adding d and p polarization type functions which correspond to the m-npG** notation. In m-npq-G basis sets each valence shell is represented by three functions (n,p,q). Diffuse basis sets use small α values and are written as m-npq+G which use diffuse functions for hydrogen atom.

The correlation consistent basis sets adds shells of function to the core of the atomic orbitals.[34-36] They also usually converge to the complete basis set (CBS) limit using extrapolation techniques. The cc-pVDZ (correlation consistent – polarized valence double zeta) basis set adds extra 1s, 1p and 1d functions.

1.4. Atoms in molecules

The atoms in molecules (AIM) concept which has been developed by Bader and co-workers[37, 38] will be described in this section. The main idea in this concept is to define and study the atoms inside a molecule. This makes it possible to study charge transfer from one atom to another, to study the acidic regions of the molecule, and to understand chemical processes such as nucleophilic attack, for example.

The electron density $\rho(r)$ is used as a source of information in Bader's Quantum Theory of Atoms In Molecules[37] (QTAIM). The main advantage of examining the electron density is that this property may be obtained from both experiment and theoretical calculations. The quantity can therefore be analysed in an identical fashion in both cases. The accuracy of the interpretation of the results will be highly dependent on the quality of the electron density. In order to extract the information hidden in $\rho(r)$ due to the enormous contributions of the nuclear core regions to the electron density, a few decades ago

crystallographers introduced the concept of the standard deformation density. In the deformation density map, the promolecule density is extracted from the total density. The promolecule here represents the superposition of the spherical ground-state atoms. This promolecule violates the Pauli exclusion principle, nonetheless the method is still widely used and provides information about bond regions as well as lone-pairs regions. However, in terms of AIM it is not necessary to introduce an external reference density at all, since the original molecular electron density itself can be used in this approach.

For this proposal the gradient vectors, $\nabla\rho(r)$, defined as the first derivative of the charge density, was introduced. The gradient field can be represented by small vectors which are perpendicular to the surface of the constant electron density. The gradient path will be constructed by following the trajectory of these small vectors. As the gradient path can be considered as a succession of small segments of gradient vectors, then it will adopt the property of the gradient vector itself. Another property of the gradient path is that at a given point there will be only one gradient path passing through it and at that point $\nabla\rho(r) \neq 0$. Therefore, the gradient paths never overlap apart from the points at which $\nabla\rho(r) = 0$. An important property of the gradient paths is that all have a beginning and an end. In a molecule, usually most of the gradient paths will start at infinity and terminate at a nucleus. If we take as an example the electron density of methanal in Figure 1.11[38], which is a 2D contour map, and build the entire gradient vector from it, we will obtain a picture such as that in Figure 1.12.[38] The infinite collection of the gradient paths is basically forming the gradient vector field. In practice only a finite number of gradient paths are drawn to represent the gradient vector field.

The initial points that will give a complete vector field plot are selected from an equal spaced set of a small circle at the nucleus and from there the paths are traced. Obviously, the electron density has a zero gradient at the nuclear position. The gradient vector field partitions the electron density into regions that actually describe the atoms included in the molecule. These regions are called the atomic basin and the atom is defined in the AIM concept as a union between the attractor and its atomic basin. The atoms from the molecule are called molecular atoms and are different compared to free or isolated atoms. The gradient paths attracted to a nucleus never cross the part of space which is dominated by another nucleus. As a result the atomic basins of the atoms have sharp boundaries inside the molecules.

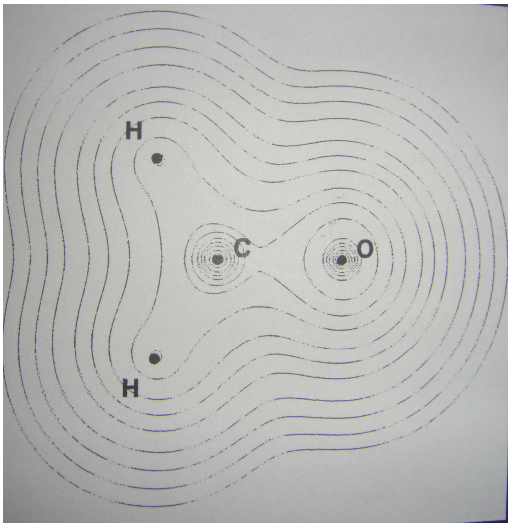

Figure 1.11. The total electron density plot of methanal. Contour line plot – outer line 0.001, next contour increases according to the pattern 2 x 10^n, 4 x 10^n, 8 x 10^n where n varies from -3 to 2.[38]

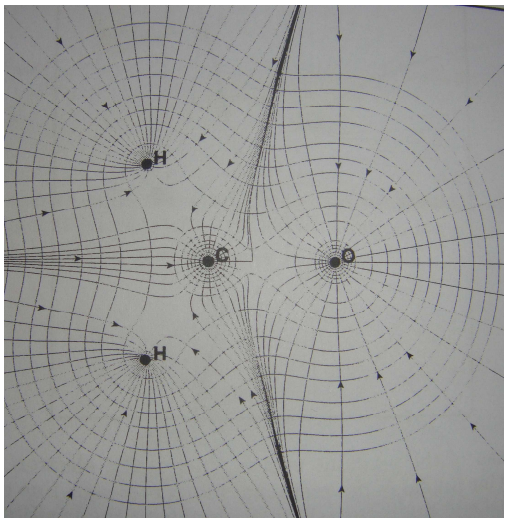

Figure 1.12. Gradient vector field representation of the electron density of methanal.[38]

The gradient $\nabla\rho(r)$ exhibits critical points (CPs) where the first derivative of $\rho(r)$ vanishes. They are indicated by a rank *r* (dimensionality) and their signature *s* (the sum of the signs of the curvature at the CP). Positive curvature has a negative sign and negative curvature has a positive sign. There are four types of these critical points in 3D space. The first case is when the curvatures in all three dimensions are positive at the CP. This is called a nuclear attractor or non-nuclear attractor (N)NA (3, -3) which represents the electron density maximum and is located normally at the atomic nucleus or at a non-nuclear attractor point. The topology of these two points can not be distinguished, hence the acronym (N)NA is used where NNA stands for non-nuclear attractors and NA for nuclear attractors. An example of a non-nuclear attractor point is plotted in Figure 1.13,[38] in the

case of an Li_2 molecule. There is a CP between the two atoms as can be observed from the illustration, where the gradient paths meet. Due to the non-nuclear attractors dominating in this region, the electronic charge is loosely bound and delocalized. This non-nuclear attractor may have an important contribution in the binding of metals and their conducting properties. The rank of the NA is 3 and the signature -3 due to the fact that the curvature is positive in all 3 dimensions at this point.

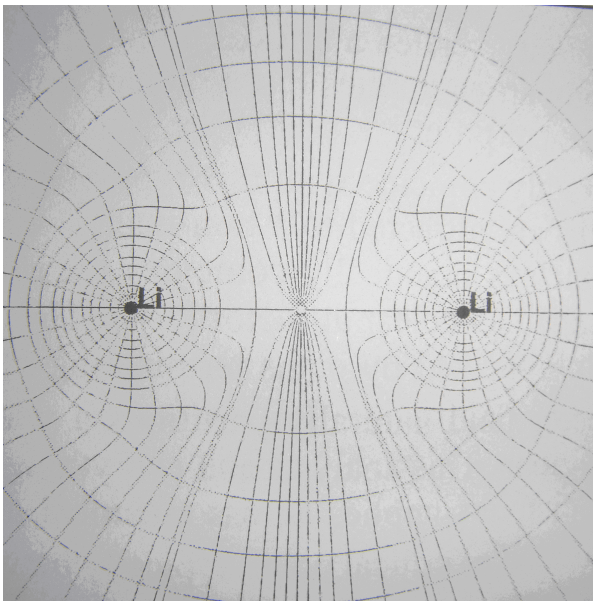

Figure 1.13. The gradient vector field map of the electron density in the Li_2 molecule[20]

The second type of CP is called a bond critical point (BCP) (3, -1) and is almost always associated with conventional covalent chemical bonds with positive curvatures in x and y, and negative curvature along the bond path. In case of BCP the gradient paths are considered to start at infinity and finish between two atoms where the electron density becomes a maximum. An example of a BCP between C and O atoms is illustrated in Figure 1.14.[38] The value of ρ at a BCP measures the strength of the bond.

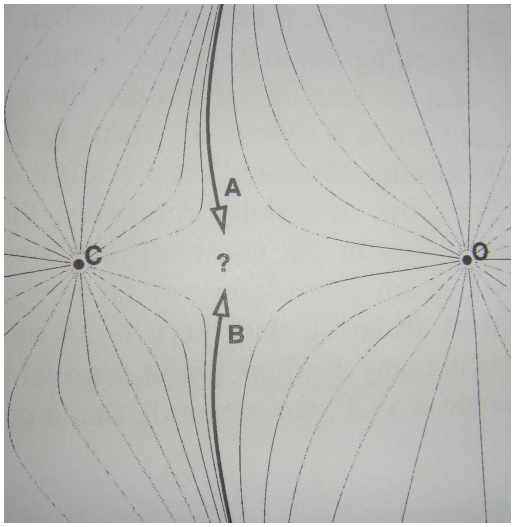

Figure 1.14. A BCP illustration between O and C nuclei.[38]

A third type of point, called a ring critical point RCP (3, +1), has positive curvature in x, and negative in z and y dimensions. The fourth critical point, called the cage critical point CCP (3, +3), has negative curvatures in all dimensions (i.e. is a minimum).

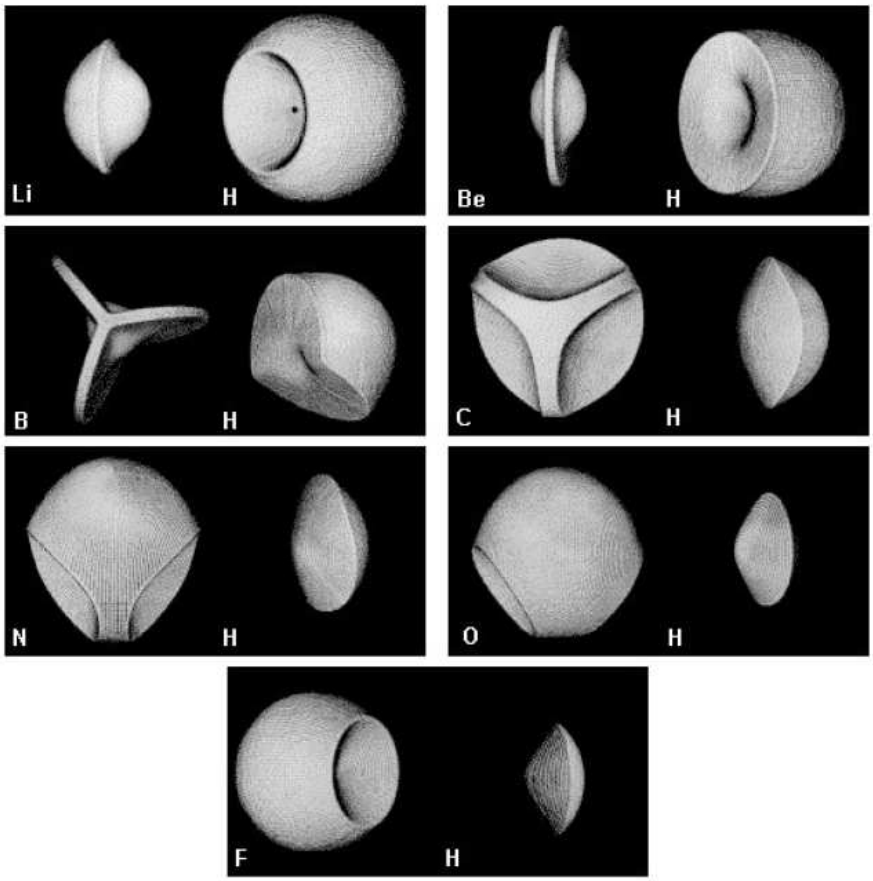

Figure 1.15. The shape of the atoms in the second-row hydrides AH_n (LiH, BeH_2, BH_3, CH_4, NH_3, H_2O and HF)[38]

The interatomic or zero-flux surface, another important concept in AIM, is defined such that at all points **r** on the surface have a normal **n** and this is orthonormal to $\nabla\rho$(r), i.e. $\mathbf{n}\cdot\nabla\rho = 0$. Therefore, the interatomic surface (IAS) is always parallel to $\nabla\rho$ but it does not contain any gradient paths which are attracted to either nucleus. It lies between two atoms and is used to define the boundary between them. The atom is hence bonded in a molecule through an IAS but in the exterior of the molecule it has the shape of an exactly isolated atom. The representation of the atom in this way is not, however, the most accurate but does represent the van der Waals envelope of the molecule. In Figure 1.15[38] a few examples of atomic shapes for the second-row hydrides AH_n are shown. It is obvious that only a part of the IAS preserves the boundary part of the atoms inside the molecule. An illustration of gradient vector field map showing the IAS and the molecular graph in the pyridine plane of the isonicotinamide-oxalic acid molecular complex (IN_2–OA) is plotted in Figure 1.16.

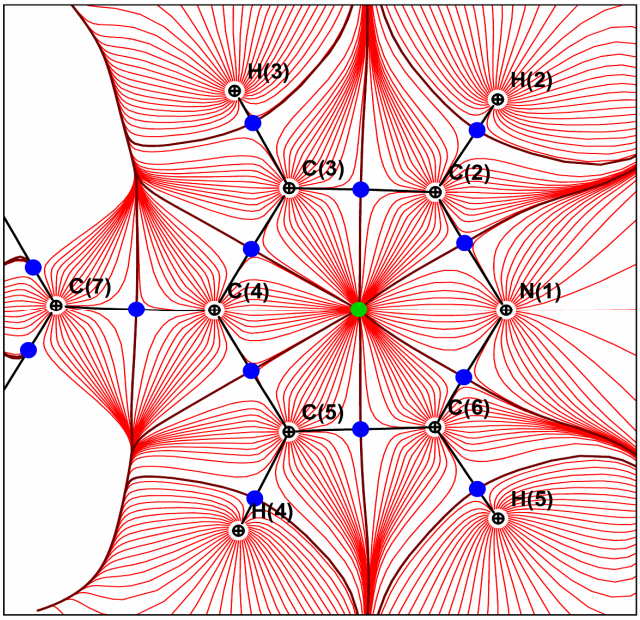

Figure 1.16. Gradient vector field map in the pyridine plane of IN_2–OA; BCP (blue), RCP (green), IAS (brown), BP (black).

The CPs for non-periodic systems are related via the Poincaré-Hopf relationship: n – b + r - c = 1 where n is the number of (N)NAs, B is the number of BCPs, r the number of RCPs and c represent the CCPs.

The second derivative of ρ(r) is called the Laplacian $\nabla^2\rho$(r) and has the mathematical expression:

$$\nabla^2\rho = \nabla \cdot \nabla\rho = \left(\frac{\partial^2\rho}{\partial x^2} + \frac{\partial^2\rho}{\partial y^2} + \frac{\partial^2\rho}{\partial z^2} \right) \qquad \text{eq. 1.48}$$

The local curvatures λ_1, λ_2 and λ_3 are determined from the diagonalisation of the 3x3 Hessian matrix which gives all possible combinations of the coordinates. The physical meaning of the Laplacian reveals areas of local charge concentration and depletion. If there is a region with $\nabla^2\rho < 0$ the density is locally concentrated, resulting in a shared interaction, while in the case of $\nabla^2\rho > 0$, the electron density is depleted, representing closed-shell interactions.

The Laplacian can be visualised for convenience as the negative Laplacian $L(r) = -\nabla^2\rho$, where the positive contours indicate charge concentration and negative values are associated with charge depletion. An example of a negative plot of the Laplacian is illustrated in Figure 1.17. The Laplacian is also useful for visualization of lone pair electron regions as the *valence shell charge concentration* (VSCC) is pronounced in these regions.

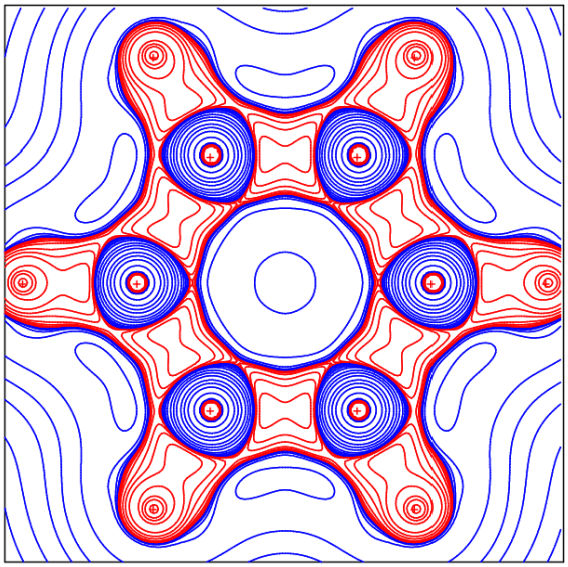

Figure 1.17. Plot of a negative Laplacian, L(r), positive contours – solid red, negative contours– solid blue (DFT/B3LYP optimised structure of benzene , 6-311G** basis).

Another successful application of the Laplacian mapping consists of the support of the well known valence shell electron pair repulsion (VSEPR) (model of Gillespie and Nyholm).[39]

The nature of the bonds can be characterised using the topological analysis by the so called ellipticity (ε). It can be calculated from the eigenvalues of the Hessian, is defined as (λ_1/ λ_2) – 1 and is applied only to the BCPs. This quantity measures the behaviour of the electron density in a plane tangential to the IAS at the BCP. Cylindrical bonds, for example in linear molecules, all present vanishing ellipticity.

A classification of the bonding interactions can be provided by topological analysis of the resultant experimental charge density $\rho(\mathbf{r})$ and its Laplacian $-\nabla^2\rho(\mathbf{r})$ in the form of the energy densities $G(\mathbf{r})$ and $H(\mathbf{r})$ [i.e. $G(\mathbf{r}) + V(\mathbf{r})$].

In addition, the hydrogen bond energies from experimental and theoretical charge densities can be evaluated in terms of the electronic kinetic energy density G(**r**) and potential energy V(**r**). The electronic kinetic energy density at the BCPs has been proposed by Abramov *et al*.[40] using the functional approximation of the electron density at a point **r**:

$$G(\mathbf{r}) = \frac{3}{10}(3\pi^2)^{2/3}\rho(\mathbf{r})^{5/3} + \frac{1}{72}\frac{\nabla\rho(\mathbf{r})^2}{\rho(\mathbf{r})} + \frac{1}{6}\nabla^2\rho(\mathbf{r}) \qquad \text{eq. 1.49}$$

Away from the nuclei (~0.5 - 2.1 Å), the calculated kinetic energy densities given by this expression are in good agreement with those calculated from Hartree-Fock wavefunctions. Using the virial theorem, the potential energy densities can be obtained from:[41]

$$V(\mathbf{r}) = \frac{\hbar^2}{4m}\nabla^2\rho(\mathbf{r}) - 2G(\mathbf{r}) \qquad \text{eq. 1.50}$$

The two equations mentioned above can be used for calculating the hydrogen bond intermolecular interactions at the BCP (E_{HB}), as shown by Espinosa *et al.*[42] (eq 1.51). The E_{HB} can be thus used to analyse the strength of the hydrogen bond interaction.

$$E_{HB} = \frac{1}{2}V(r_{CP}) \qquad \text{eq. 1.51}$$

This equation was deduced by plotting the kinetic energy density, potential energy density and dissociation energy as a function of the d(H··O) distances (Figure 1.18).

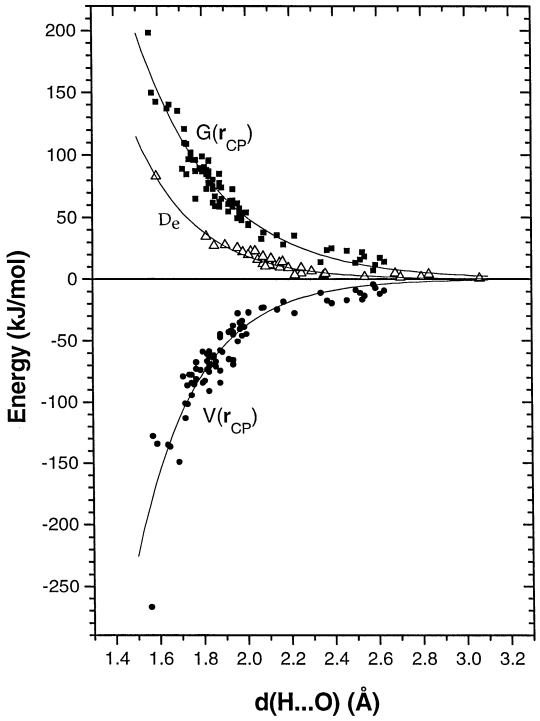

Figure 1.18. Kinetic energy density $G(\mathbf{r}_{CP})$, potential energy density $V(\mathbf{r}_{CP})$, and calculated dissociation energy D_e dependences on the H···O distance.[42]

The structure data were taken from accurate electron density experiments involving X-H···O (X = O, N, C) hydrogen bonds, with the distances ranging from 1.56 to 1.97Å, from 1.65 to 2.63 Å and from 2.28 to 2.59 Å. The dissociation energy (D_e) was determined from theoretical HF calculations. This equation is limited only to the moderate and weak hydrogen interactions as for the strong hydrogen interactions the BCPs are too close to the nuclei. The data were fitted using an exponential function which showed that the D_e is half in magnitude compared with the negative values of $V(\boldsymbol{r})$. As $E_{HB} = -D_e$, the energy at the BCP of hydrogen bond interactions can thus be calculated using equation 1.51.

AIM theory is therefore a powerful tool which can be applied for studying chemical concepts such as bond order, anti-aromaticity, ionicity, (hyper)conjugations and hydrogen bonding.

References

1. J. Bernstein, *Polymorphism in Molecular Crystals, Clarendon Press, Oxford, UK*, 2002.
2. J. Bernstein, *Conformational Polymorphism in Solid State Chemistry*, ed., G. R. Desiraju, Elsevier, Amsterdam, 1987.
3. H. G. Brittain, *Polymorphism in Pharmaceutical Solids, Marcel Dekker, New York*, 1999, **95**.
4. J. Bernstein, *Chem. Comm.*, 2005, 5007.
5. J. D. Dunitz and J. Bernstein, *Acc. Chem. Res.*, 1995, **28**, 193.
6. W. I. F. David, K. Shankland, C. R. Pulham, N. Blagden, R. J. Davey and M. Song, *Angew. Chem. Int. Ed.*, 2005, **44**, 7032.
7. J. D. Dunitz and A. Gavezzotti, *Angew. Chem. Int. Ed.*, 2005, **44**, 1766.
8. U. Koch and P. Popelier, *J. Phys. Chem.*, 1995, **99**, 9747.
9. S. Harder, *Chem. Eur. J*, 1999, **5**, 1852.
10. C. F. Matta, J. Hernández-Trujillo, T.-H. Tang and R. F. W. Bader, *Chem. Eur. J.*, 2003, **9**, 1940.
11. P. Lipkowski, S. J. Grabowski, T. L. Robinson and J. Leszczynski, *J. Phys. Chem. A.*, 2004, **108**, 10865
12. J. Dunitz, *Acta Cryst. B*, 1995, **51**, 619-631.
13. B. Rodriquez-Spong, C. P. Price, A. Jayasankar and N. Rodriguez-Hornedo, *Advanced Drug Delivery Reviews*, 2004, **56**, 241-274.
14. F. H. Allen, *Acta Cryst. B*, 2002, **58**, 380-388.
15. Joop H ter Horst and P. W. Cains, *Cryst. Grow. Des.*, 2008, **8**, 2537-2542.
16. Shuang Chen, Ilia A. Guzei and L. Yu, *J. Am. Chem. Soc.*, 2005, **127**, 9881-9885.
17. http://www.cmmp.ucl.ac.uk/~ijf/3c25/bravais.gif.
18. P. J. Brown, A. G. Fox, E. N. Maslen, M. A. O'Keefe and B. T. M. Willis, *International Tables for Crystallography, Vol. C, Chapter 6.1*, 2006, 554-595.
19. C. C. Wilson, *Single Crystal Neutron Diffraction From Molecular Crystals, World Scientific*, 2000.
20. http://www.isis.stfc.ac.uk/.
21. R. F. Stewart, *J. Chem. Phys.*, 1969, **51**, 4569-4577.
22. R. Restori, *Acta Cryst. A*, 1990, **46**, 150-151.
23. N. K. Hansen and P. Coppens, *Acta Cryst. A*, **34**, 909-921.
24. E. Clementi and D. L. Raimondi, *J. Chem. Phys*, 1963, **38**, 2686-2692.
25. E. Clementi and C. Roetti, *At. Data Nucl. Data Tables*, 1974, **14**, 177-478.

26. P. Macchi and P. Coppens, *Acta Cryst. A*, 2001, **57**, 656-662.
27. P. M. Dominiak and P. Coppens, *Acta Cryst. A*, 2006, **62**, 224-227.
28. M. Kara and K. Kurki-Suonio, *Acta Cryst. A*, 1981, **44**, 6-8.
29. W. Kohn and L. J. Sham, *Phys. Rev. A*, 1965, **140**, 1133-1138.
30. (a) A. D. Becke, *Phys. Rev. A*, 1988, **38**, 3098; (b) A. D. Becke, *J. Chem. Phys,*. 1993, **98**, 5648; (c) C. Lee, W. Yang and R. G. Parr, *Phys. Rev. B*, 1988, **37**, 785. (d) P. J. Stephens, J. F. Devlin, C. F. Chabalowski and M. J. Frisch, *J. Phys. Chem.*, 1994, **98**, 11623.
31. R. Dovesi, R. Orlando, B. Civalleri, C. Roetti, V. R. Saunders, and C. M. Zicovich-Wilson, *Z. Kristallogr.*, 2005, **220**, 571; R. Dovesi, V. R. Saunders, C. Roetti, R. Orlando, C. M. Zicovich-Wilson, F. Pascale, B. Civalleri, K. Doll, N. M. Harrison, I. J. Bush, P. D'Arco, and M. Llunell, CRYSTAL09 (CRYSTAL09 User's Manual. University of Torino, Torino, Italy, 2009).
32. J. C. Slater, *Phys. Rev.*, 1930, **30**, 57.
33. S. F. Boys, *Proc. R. Soc. London Ser. A*, 1950, **200**, 542.
34. J. Alml and P. R. Taylor, *J. Chem. Phys.*, 1997, **86**, 4070.
35. T. Hashimoto and K. H. H. Tatewaki, *Chem. Phy. Lett.*, 1995, **243**, 190.
36. T. H. Dunning, *J. Chem. Phys.*, 1989, **90**, 1007.
37. R. F. W. Bader, *Atoms in Molecules – A Quantum Theory, Oxford University Press, Oxford*, 1990.
38. P. Popelier, *Atoms in Molecules - An Introduction, Pearson Education, Harlow*, 2000.
39. R. J. Gillespie and R. S. Nyholm, *Quart. Rev.*, 1957, **11**, 339.
40. Y. A. Abramov, *Acta Cryst. A*, 1997, **53**, 264-272.
41. R. F. W. Bader and H. Essen, *J. Chem. Phys.*, 1984, **80**, 1943-1960.
42. E. Espinosa, E. Molins and C. Lecomte, *Chem. Phys. Lett.* , 1998, **285**, 170-173.

2.Sulfathiazole

2.1. Introduction

The first polymorphic material studied in this work, which will be described in this Chapter, is sulfathiazole. Sulfathiazole, [4-amino-*N*-(2-thiazolyl)benzenesulfonamide] ($C_9H_9N_3O_2S_2$) (**1**) (Scheme 2.1), is a well-known active pharmaceutical ingredient (API) and is used as an antibacterial agent. It crystallises in five polymorphic forms[1] and is one of the most examined polymorphic organic compounds (Table 2.1).

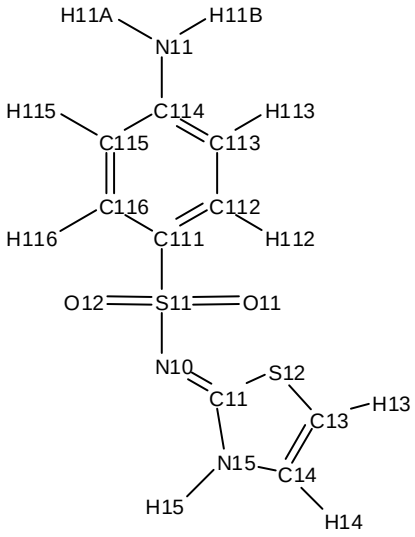

Scheme 2.1. Molecular structure and atom labelling of sulfathiazole, **1**.

The first crystal structure, now known as form II, was reported in 1971.[2] This was followed by the crystal structure of form I, first reported by the same authors in 1972.[2] The crystal structure of form IV was first analysed using X-ray diffraction in 1987,[3] reported in conjunction with form II. Form V was discovered later[4] using synchrotron X-ray powder diffraction data. Single crystal X-ray data were also obtained for this form in the same year[5], with a repeat of this experiment reported later.[1] In the case of forms I, II, III and IV the crystal structures were subsequently re-examined in a series of studies.[6,1,7,8] The last of these[8] also re-examined form V. All five forms crystallise in the monoclinic space group $P2_1/c$; though for convenience, forms IV and V are described in the non-standard setting of $P2_1/n$, to simplify refinement. This can be explained as follows: if, in the $P2_1/n$ space group, the β angle is close to 90º, then any change in the *a* component vector with respect to the *c* axis will be close to zero, hence the correlation coefficients will be small (Scheme 2.2 (a)). On the other hand, if the angle is much larger than 90º, modification of the

components of vector *a*, will result in a significant component of change along the *c* axis (Scheme 2.2 (b)). As a result of this there will be large correlations in a least-squares refinement between x and z components, which can be avoided by the choice of space group setting.

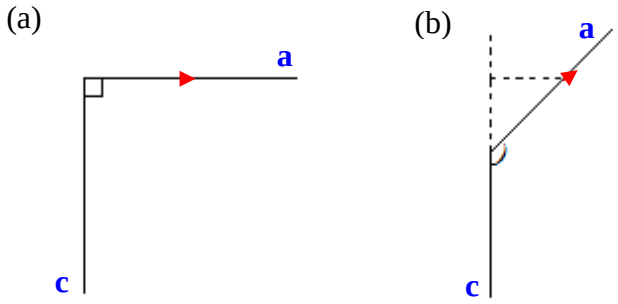

Scheme 2.2. The change of vector components of *a* axis and the correlated change in *c* axis components (a) β ~ 90º; (b) β > 90º.

Forms II and IV have one molecule per asymmetric unit while the others have two. As it was not possible to prepare sufficiently high quality single crystals of form V, only four of the forms have been characterised fully using high resolution X-ray diffraction analysis in this work. Three of the forms are also characterised for the first time using neutron diffraction, which provides more accurate description of the H atom positions. The chemical structure and the labelling scheme of **1** used in the present work are given in Scheme 2.1. In Table 2.1 the crystallographic data for forms I-IV obtained from these experiments are reported, along with those for form V[1] from the CSD. As mentioned above, each of the polymorphic forms of **1** have been characterised several times by X-ray diffraction. The corresponding reference codes from the CSD are therefore also included in Table 2.1, together with the measurement temperature: 100K, 150K or room temperature (RT, 283-303K). The data collected in this work were measured at 100K.

Table 2.1. Summary of the crystallographic data of the five polymorphs of 1. Z′- represents the number of molecules in the asymmetric unit, SP – space group, RT- room temperature

Form	I	II	III	IV	V[1]
CSD	suthaz01(RT)[2]	suthaz(RT)[2]	suthaz02(RT)[2]	suthaz04(RT)[3]	suthaz05(150K)[5]
ref.	suthaz07(100K)[6]	suthaz03(RT)[3]	suthaz11(100K)[6]	suthaz13(150K)[6]	suthaz06(RT)[4]
code	suthaz08 (RT)[6]	suthaz09(100K)[6]	suthaz12 (RT)[6]	suthaz14(RT)[6]	suthaz15(150K)[1]
	suthaz16 (150K)[1]	suthaz10 (RT)[6]	suthaz17(RT)[1]	suthaz19(150K)[1]	sutaz27(RT) [8]
	suthaz23(RT)[7]	suthaz18(150)[1]	suthaz21(RT)[7]	suthaz22(RT)[7]	
	sutaz28(RT)[8]	suthaz20(RT)[7]	sutaz25(RT) [8]	sutaz26(RT) [8]	
		sutaz24(RT) [8]			
SP	$P2_1/c$	$P2_1/c$	$P2_1/c$	$P2_1/n$	$P2_1/n$
a/ Å	10.5235(2)	8.1904(2)	17.4174(6)	10.7791(3)	10.399(2)
b/Å	12.9016(2)	8.5345(2)	8.4911(3)	8.4678(2)	15.132(3)
c/Å	17.2177(3)	15.4497(3)	15.4952(5)	11.3781(2)	14.280(3)
β/º	107.834(1)	94.155(1)	112.761(2)	91.6260(1)	91.21(3)
V/ Å^3	2225.32(7)	1077.11(4)	2113.17(12)	1038.12(4)	2246.56(6)
Z′	2	1	2	1	2
ρ/gcm^{-3}	1.524	1.574	1.605	1.634	1.51

**The presented data were collected at 100K*

In this Chapter the results from refinements based on high resolution X-ray diffraction data (θ_{max}=50°) are presented. Furthermore, more precise atomic positions and displacement parameters for the hydrogen atoms obtained from neutron diffraction are also presented. The experimental data are compared with density functional theory (DFT) calculations at the PBEPBE/cc-pVTZ level. Minor disorder was found in three forms of sulfathiazole, corresponding to a different orientation of the molecule, which had not been previously reported. Topological analysis of the theoretical electron density and best multipole models are compared in order to ascertain the effect of this minor disorder on the derived topological parameters. Multipole analyses of synthetic data derived from the periodic and aperiodic electron density are also undertaken with a view to examining the effects of the well-known deficiencies[9] of the multipole model. The intermolecular interaction energies are calculated by two different methods using different approaches and equations. The nature of the intermolecular H...H, N-H...N, NH…O, CH...π and C-H…S interactions are also examined using the Hirshfeld surface d_{norm} property.[10]

2.2. Experimental and Theoretical

2.2.1. Sample preparation

Previous successful methods for producing single crystals of the polymorphs of **1** have been described in the literature and reported details of their growth were as follows: form I can be prepared by evaporation from the solvents n-propanol[6] and n-butanol;[2,4,7] form II is reported as being obtained using the solvents n-propanol,[2] acetonitrile and methanol mixture,[5] boiling water,[11] methanol;[7] form III can be grown from water,[12] dilute aqueous ammonia,[2] ethanol-water - aqueous ammonia mixture,[6] 2-propanol;[1] form IV can be produced from an acetone-chloroform mixture,[4] boiling water[7] or ethanol;[6] form V was reported to be grown from boiling aqueous solution.[5,12]

Compound **1** was purchased as a powder from Sigma Aldrich and attempts made to obtain the forms as described in the literature. However, in the present study the following single crystal products were obtained: form I from slow evaporation of a 50:50 mixture by volume of chloroform and acetone; form II by slow evaporation of an acetonitrile solution; form III and IV were re-crystallised from dilute aqueous ammonia solvent. Crystals of form II were also found growing in solutions of **1** with dilute aqueous ammonia. Thus, three of the forms (III, IV, V) could be grown in the same solvent (dilute aqueous ammonia), while form I was grown in a different solvent compared with those reported in the literature, making the effects of solvent in controlling polymorph formation appear not straightforward.

2.2.2 Data collection and Conventional (Spherical atom) refinement

Single crystals of suitable size were selected and mounted onto a goniometer and cooled to 100K using an Oxford Cryosystems Cryostream. High resolution X-ray data were collected from forms I, II and IV (denoted IVkappa in this work) on a Bruker-Nonius Kappa CCD diffractometer (Mo K_α radiation) over a period of one week for each data collection. The Collect software was used for monitoring the data collection. The low resolution X-ray data were measured prior to the high-resolution data. The integration of intensities was carried out using the software DENZO.[13] High resolution X-ray data were collected from forms III and IV (denoted IVapex in this work) at 100K on a Bruker AXS Apex II diffractometer, using an Oxford Cryosystems Helix cooling device. Indexing, integration and scaling were performed using the Bruker APEX II software (Bruker Nonius 2009). The reflection measurements were merged and empirical absorption corrections were performed using SORTAV.[14] Data from form IV were collected on two different

diffractometers, as the scale factor for the low angle data deviated slightly from its required value of 1.0 for the data collected initially on the Bruker AXS Apex II.

The structures were solved using SIR92[15] and refined initially in the spherical-atom formalism with full-matrix least squares on F^2. The non-hydrogen atoms were allowed anisotropic thermal motion. The details of these data collections and refinements as well as neutron data are given in Table 2.2 - 2.4. Structure solution and refinement were performed using the WinGX package[16] of crystallographic programs.

Neutron diffraction data were collected for forms II, III, and IV of **1** at 100K on the SXD instrument[17] at the ISIS spallation neutron source, using the time-of-flight Laue diffraction method. Reflection intensities were reduced to structure factors using standard SXD procedures, as implemented in the computer program SXD2001.[18] Refinements were carried out using SHELXL97[19] using anisotropic displacement parameters for all atoms, including the H atoms.

Table 2.2. Experimental crystallographic data for sulfathiazole, form I and II

Compound formula	$C_9H_9N_3O_2S_2$	$C_9H_9N_3O_2S_2$	$C_9H_9N_3O_2S_2$
Form	I	II	II
M_r	255.31	255.31	255.31
Space group	$P2_1/c$	$P2_1/c$	$P2_1/c$
Crystal system	Monoclinic	Monoclinic	Monoclinic
a/ Å	10.5235(2)	8.1904(2)	8.1904(2)
b/Å	12.9016(2)	8.5345(2)	8.5345(2)
c/Å	17.2177(3)	15.4497(2)	15.4497(3)
β/deg	107.834(10)	94.1550(10)	94.155(1)
V/Å^{-3}	2225.32	1077.11(4)	107711(1)
Z	8	4	4
D_{calc}/g cm^{-3}	1.524	1.57	1.57
F(000)	1056	528	-
Radiation	Mo Kα	Mo Kα	TOF neutron
λ/Å	0.71073	0.71073	0.42-7.64
μ(Mo-K_a)/mm^{-1}	0.466	0.482	0.116
Crystal size/mm	0.13x0.35x0.56	0.19x0.24x0.43	2.0x2.0x8.0
θ range/deg	2.0-48.0	2.5-50.1	1.6-64.7
Max sin(θ)/ λ	1.045	1.079	2.15
No. of data used for merging	456552		7252
No. of unique data	21249	11293	3645
hkl range	$-21 \le h \le 20$	$-17 \le h \le 17$	$-19 \le h \le 20$
	$-26 \le k \le 0$	$0 \le k \le 18$	$0 \le k \le 25$
	$-35 \le l \le 20$	$0 \le l \le 33$	$0 \le l \le 53$
R_{int}	0.032	0.026	-
R_σ	0.0343	0.0259	0.2477
Spherical atom refinement			
No. of data in refinement	21249	11293	3645
No. of refined parameters	361	181	226
Final R [$I > 2\sigma(I)$]	0.032	0.026	0.060
R_w [$I > 2\sigma(I)$]	0.087	0.083	0.115
Goodness of fit S	1.03	1.1400	1.072
Extrema in residual map	-0.688 →1.295 eÅ^{-3}	-1.807 → 2.031eÅ^{-3}	-0.542 →0.785 fmÅ^{-3}
Max shift/esd in last cycle	0.006	0.006	
Multipole refinement			
No. of data in refinement	17353	10566	-
No. of refined parameters	443	443	-
Final R [$I > 3\sigma(I)$]	0.0242	0.0177	-
R_w [$I > 3\sigma(I)$]	0.0217	0.0249	
Goodness of fit S	1.1094	1.6494	-
Extrema in residual map/ eÅ^{-3} (all data) (data truncated to 0.8 Å^{-1})	-0.236 →0.574	-0.308→0.754	-
Max shift/esd in last cycle	0.00004	0.00007	-

Table 2.3 Experimental crystallographic for sulfathioazole, form III

Compound formula	$C_9H_9N_3O_2S_2$	$C_9H_9N_3O_2S_2$
M_r	255.31	255.31
Space group	$P2_1/c$	$P2_1/c$
Crystal system	Monoclinic	Monoclinic
a/ Å	17.4174(6)	17.4174(6)
b/Å	8.4911(3)	8.4911(3)
c/Å	15.4952(5)	15.4952(5)
β/deg	112.761(2)	112.761(2)
V/Å^{-3}	2113.17(12)	2113.17(12)
Z	8	8
D_{calc}/g cm^{-3}	1.605	1.605
F(000)	1056	-
Radiation	Mo Kα	TOF neutron
λ/Å	0.71073	0.42-7.64
μ(Mo-K$_a$)/mm^{-1}	0.491	0.118
Crystal size/mm	0.25 × 0.30 × 0.5	2×3×6
θ range/deg	1.3-57.9	1.5-64.8
Max sin(θ)/ λ	1.191	2.15
No. of data used for merging	131757	8385
No. of unique data	29858	3844
hkl range	$0 \le h \le 41$	$-43 \le h \le 31$
	$-20 \le k \le 0$	$0 \le k \le 20$
	$-36 \le l \le 34$	$0 \le l \le 54$
R_{int}	0.0331	-
R_σ	0.0307	0.0877
Spherical atom refinement		
No. of data in refinement	29858	3844
No. of refined parameters	362	451
Final R [$I > 2\sigma(I)$]	0.033	0.069
R_w [$I > 2\sigma(I)$]	0.099	0.153
Goodness of fit S	1.098	1.073
Extrema in residual map	-0.540 →0.820 eÅ^{-3}	-1.93 → 1.94 fmÅ^{-3}
Max shift/esd in last cycle	0.004	< 1.0 10^{-4}
Multipole refinement		
No. of data in refinement	18389	-
No. of refined parameters	588	-
Final R [$I > 3\sigma(I)$]	0.0258	-
R_w [$I > 3\sigma(I)$]	0.0370	
Goodness of fit S	1.9892	-
Extrema in residual map/ eÅ^{-3} (all data)	-0.473 → 0.315	-
(data truncated to 0.8 Å^{-1})		
Max shift/esd in last cycle	0.00007	-

Table 2.4 Experimental crystallographic for sulfathiazole, form IV

Compound formula	$C_9H_9N_3O_2S_2$	$C_9H_9N_3O_2S_2$	$C_9H_9N_3O_2S_2$
M_r	255.31	225.31	255.31
Space group	$P2_1/n$	$P2_1/n$	$P2_1/n$
Crystal system	Monoclinic	Monoclinic	Monoclinic
a/ Å	10.7791(3)	10.7891(2)	10.7791(3)
b/Å	8.4678(2)	8.48360(10)	8.46678(2)
c/Å	11.378(2)	11.3978(2)	11.4678(2)
β/deg	91.6260(10)	91.6425(9)	91.6260(10)
V/Å^{-3}	1038.12(4)	1042.82(3)	1038.12(4)
Z	4	4	4
D_{calc}/g cm^{-3}	1.634	1.626	1.634
F(000)	528	528	-
Radiation	Mo Kα apex	Mo Kα kappa	TOF neutron
λ/Å	0.71073	0.71073	0.42-7.64
μ(Mo-K$_a$)/mm^{-1}	0.5	0.497	0.120
Crystal size/mm	0.16x0.21x0.67	0.15x0.23x0.51	2.0x2.0x2.0
θ range/deg	2.6-56.0	2.0-50.9	2.4-54.3
Max sin(θ)/ λ	1.166	1.09	1.93
No. of data used for merging	186885	309882	3667
No. of unique data	13771	11135	1686
hkl range	$-25 \le h \le 25$	$-20 \le h \le 23$	$-20 \le h \le 27$
	$0 \le k \le 19$	$-18 \le k \le 18$	$-20 \le k \le 13$
	$0 \le l \le 26$	$-24 \le l \le 24$	$-31 \le l \le 28$
R_{int}	0.0299	0.0332	-
R_σ	0.035	0.0255	0.145
Spherical atom refinement			
No. of data in refinement	13771	11135	1686
No. of refined parameters	181	181	227
Final R [$I > 2\sigma(I)$]	0.030	0.0274	0.072
R_w [$I > 2\sigma(I)$]	0.087	0.0743	0.145
Goodness of fit S	1.0540	1.059	1.097
Extrema in residual map	-0.340→0.800 eÅ^{-3}	-0.5300→0.660eÅ^{-3}	-1.401→2.090 fmÅ^{-3}
Max shift/esd in last cycle	0.002	0.000	
Multipole refinement			
No. of data in refinement	11078	10172	-
No. of refined parameters	443	443	-
Final R [$I > 3\sigma(I)$]	0.0215	0.0141	-
R_w[$I > 3\sigma(I)$]	0.0205	0.0180	
Goodness of fit S	1.0284	1.1043	-
Extrema in residual map/ eÅ^{-3}	-0.256 →0.325	-0.196 →0.215	-
(all data)			
(data truncated to 0.8 Å^{-1})			
Max shift/esd in last cycle	0.00009	0.000009	-

$R = \Sigma (|F_o| - |F_c|)/\Sigma (F_o)$ $\quad R_w = \{\Sigma(w(F_o - F_c)^2) /\Sigma(w(F_o)^2)\}^{1/2}$

$R_{int} = \Sigma \{n/(n-1)\}^{1/2} | F_o^2 - F_o^2(mean) | / \Sigma F_o^2$ (summation is carried out only where more than one symmetry equivalent is averaged)

2.2.3 Multipole refinements

Multipole model refinements, based on the Hansen & Coppens formalism[20] to describe the aspherical atomic electron density ρ(r) (equation 1.24 Chapter 1), were performed using the XD package.[21] The radial density functions $R_l(\kappa' r)$ may be described in terms of normalized single Slater-type basis functions as given in equation 1.26 (Chapter 1). However, in the quantum-mechanical electron density formalism, the radial dependence of the multipole density deformation functions can also be represented as a product of the atomic orbitals (a HF radial function type is used in the XD program). The n_l coefficients can take any arbitrary positive values, but have to obey the condition $n_l \geq l$ in order to satisfy Poissons's electrostatic equation.[22] The ss, sp and pp type orbital products form the monopolar, dipolar and quadrupolar functions, respectively. In this case $n_l = 2$ for all three types of product functions for first-row atoms. In a similar way, the octupoles and hexadecapoles result from the 2p3d and 3d3d atomic orbital products with $n_l = 3$ and $n_l = 4$, respectively.

However, for the first-row atoms the 3d orbitals are not occupied, and hence higher multipoles are used to represent the density in the bonds around an atom. For this reason Dominiak *et al.*[23] suggested that a different scheme should be used for the first row atoms compared with second row atoms. They also showed that using more diffuse higher multipoles gives a better representation of the radial functions.[23] Due to these considerations, the (2,4,6,8) combination of *n(1,…,4)* radial function parameters of the valence deformation function were used for the sulfur atom in the multipole refinements carried out here;[23] for l = 1,2,3,4, n = 2,4,6,8. A constant value of 3.85125 bohr^{1} was attributed to the α_l parameter. For l = 0, the radial term of the deformation function was obtained from the corresponding single-ξ wave function. The standard (4,4,4,4) set was also tested, which shows slightly higher values for the R factor compared with that obtained from the (2,4,6,8) set. The multipole expansion was truncated at the octupole level for the non-H atoms, apart from the S atom for which the refinement of hexadecapoles was allowed. The multipole expansion for the H atoms was truncated at the quadrupole level. Five different multipole refinements were carried out for all studied forms of **1**. These are labelled as 1,2,…,5 and the refinement results are summarised in Table 2.12, Section 2.4.5.

An initial refinement (1) was carried out using extensive chemical constraints, incorporating an imposed local mirror plane symmetry applied for the S, N and C atoms of the thiazole ring, N(imino), S and for all the carbon atoms of the benzene ring. The

parameters obtained in this refinement were used to provide estimates of the H-atom anisotropic displacement parameters (adps) by the method of Madsen, using the SHADE (*Simple Hydrogen Anisotropic Displacement Estimator*) web interface.[24] This method combines an external rigid-body analysis of the non-hydrogen adps with the contribution of the internal atomic motion. The non-H atoms skeletal motion of the molecule can be described by a rigid-body model and the H-atoms are assumed to follow the motion of the rigid frame. Thus, the resulting rigid-body model is applied to the H atoms together with the estimated internal mean square displacements of the H atoms:

$$U^{ij} = U^{ij}_{rigid} + U^{ij}_{\text{int}ernal} \qquad \text{eq. 2.1}$$

The total internal motion is formed from all the contributions of the different internal vibrational modes. For instance, if the internal mode *k* with a mean square displacement $\langle u^2 \rangle_k$ has the direction given by the unit vector e_k, the total atomic internal motion can be expressed as:

$$U^{ij}_{\text{int}ernal} = \sum_k \langle u^2 \rangle_k e_k e_k^{\mathrm{T}} \qquad \text{eq. 2.2}$$

where e_k^{T} is the transpose of e_k, in an orthonormal coordinate system.

The SHADE[24] program uses a database for internal mean square displacements, derived from previous neutron diffraction studies of organic compounds.[25] The internal mean square displacements are calculated in the bond direction and in two perpendicular directions. The groups present in the current database are: methylene, methyl, methine, hydroxy, water and ammonium. When H atoms belonging to other types of chemical fragments are present, default values are used – typically 0.005 Å^2 in the bond direction and 0.020 Å^2 in directions perpendicular to the X-H bond. The internal mean square displacement can also be obtained from Raman spectral analysis or from theoretical *ab initio* calculations.[26]

A rigid-bond test using the Hirshfeld (1976) method[27] is applied to check the correctness of the adps. This method ensures that the atoms involved in covalent bonds have almost the same mean-square displacements in the direction of the bonds. The external vibration of the non-H framework is accounted for in terms of a TLS (translation-libration-screw) model.[28]

The calculated H-atom adps from SHADE[24] were then used as fixed parameters in a subsequent refinement (2). In the final cycles of refinement (3), the constraints imposed by local mirror symmetry were released for all atoms. The same refinement steps were followed for forms II, III and IV, except that the adps for hydrogen were obtained by scaling the neutron adp values against those from X-ray diffraction experiments (4,5). The scaling procedure takes into consideration the difference that appears between the adps from the neutron and X-ray experiments. The factors which may contribute to this difference are: the amplification of absorption and extinction effects for large crystals, possibility of temperature difference in the two experiments, thermal diffuse scattering, multiple reflection, or systematic measuring errors. The scaling value is obtained from all non-hydrogen atoms and applied to the H-atom adps. The scaling procedure was performed with the WinGX program,[16] which uses a scaling scheme proposed by Blessing (1995).[29]

The distances obtained from the neutron experiment for bonds involving hydrogen were used in all refinements. Multipole populations and κ parameters were grouped in all refinements according to the chemical similarity of the atoms.

Due to the high peaks observed on the residual map around the S12 atom – after multipole model refinements (Figure 2.1, left) – the possibility of anharmonic thermal motion for the S12 atom was examined, through a 3rd and 4th order Gram-Charlier expansion of the adps for S12. The results for form II are presented in Figure 2.1 (right) – the results for the other forms were in accordance with those for form II. It is obvious from these plots that when anharmonic refinement is used, the peaks around the sulfur atom on the residual map almost vanish. An improvement in this way can also be observed when an unrestricted multipole model is applied (model 5). Therefore, in this work the results obtained with anharmonic thermal motion refinement for S atoms were used for analysis.

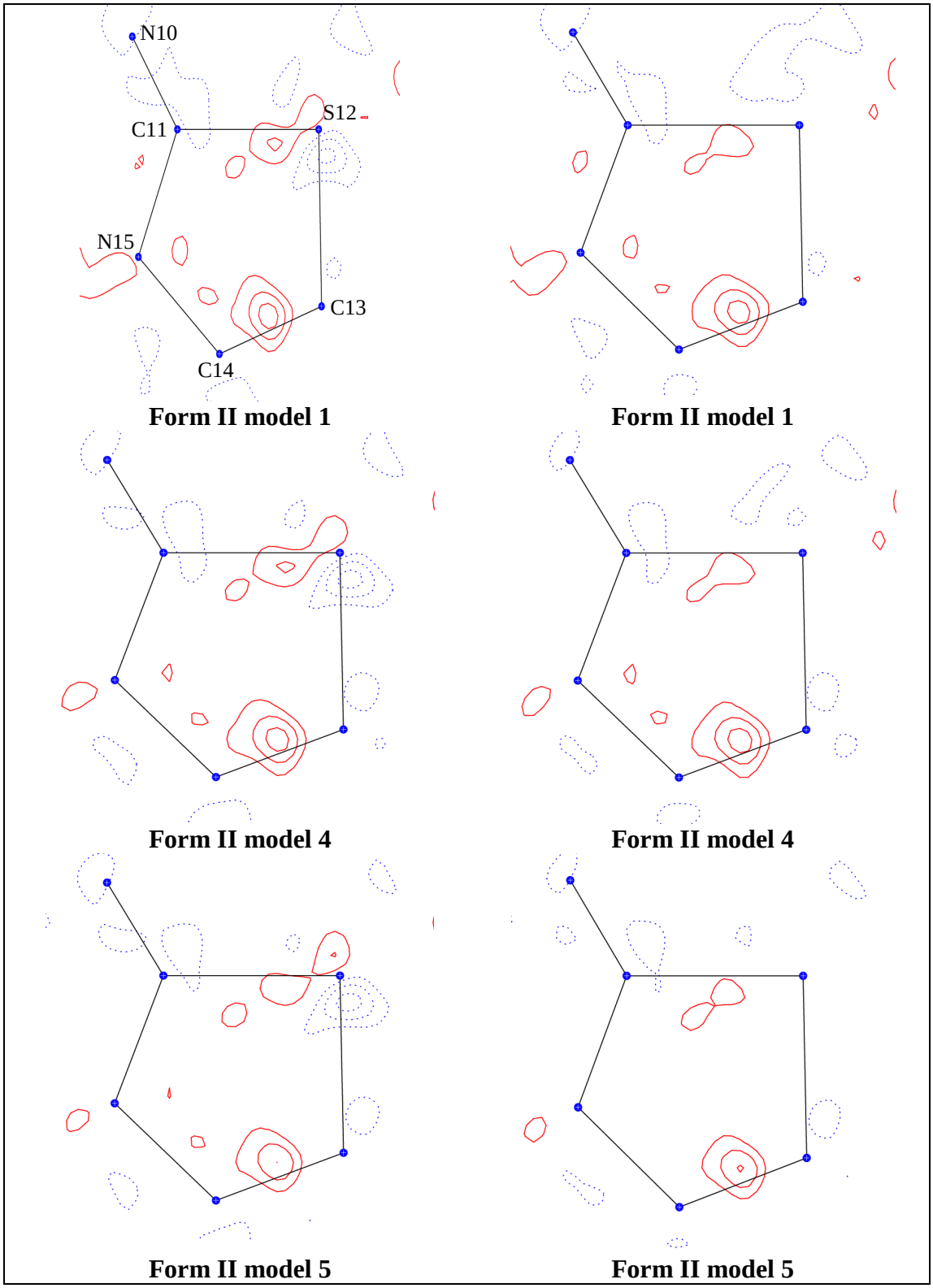

Figure 2.1. Residual density maps in the thiazole plane after the multipole refinements: harmonic atom refinement (left); anharmonic 3rd and 4th order Gram-Charlier expansion multipole refinements for the sulfur atom (right). Contour levels are at 0.1eÅ^{-3}; positive and negative contours are solid red line and broken blue lines, respectively.

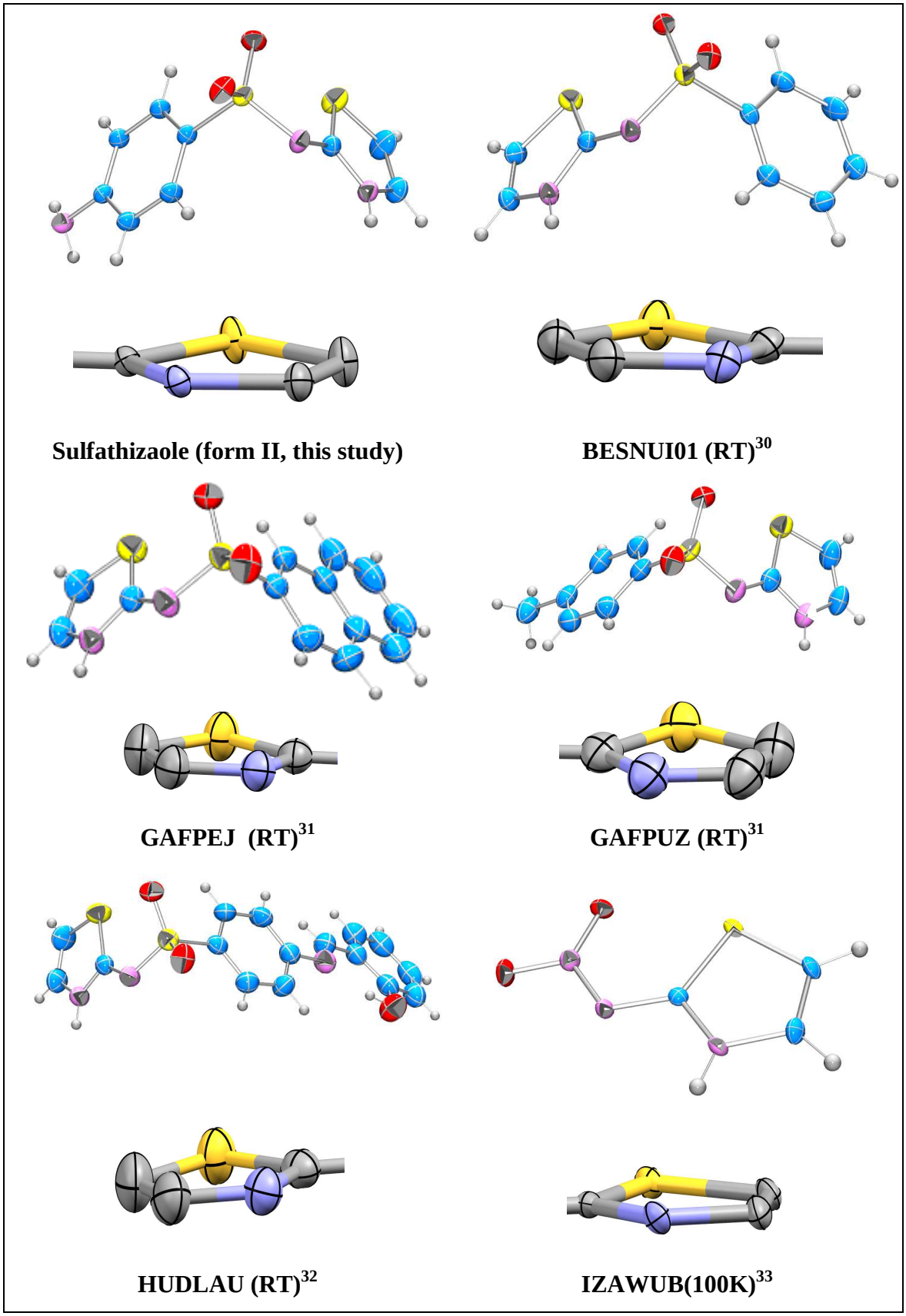

Figure 2.2. ORTEP views of crystal structures containing a thiazole ring. Atoms colour code: S-yellow, O-red, C-blue, N-purple, H-grey

Furthermore, an elongation in the shape of the thermal (adp) ellipsoid of the S12 atom perpendicular to the ring has been observed both in the X-ray (Figure 2.2) and neutron data

in the forms of **1** studied. This apparent thermal motion could be a consequence of the fact that the S atom is not exactly co-planar with the thiazole ring. Therefore, it is assumed that this elongation could be due to a slightly disordered S atom above and below the ring. In addition, the S12 adps were compared with those for S atoms in thiol rings contained in other crystal structures deposited in the CSD (Figure 2.2). A projection along the thiazole ring is also included for each structure in order to emphasise the difference in size of the ellipsoids of the atoms. All crystal structures shown in these pictures have higher thermal motion of the S atom compared with the other non-H atoms in the thiol ring.

The behavior of the S atom in a thiazole ring observed in the forms of **1** thus seems to be a common trend, which can be seen in other compounds containing the thiazole ring. One possible explanation for this is a very minor disorder in the ring system. This can be examined by carrying out data collection at variable temperature. For this purpose data were collected at seven different temperatures for form II of **1** (100K, 120K, 140K, 160K, 180K, 200K and 250K). The variation of the U11 tensor of the S12 atom with temperature is illustrated in Graph 2.1, which shows a linear dependence, confirming the likelihood of a thermal motion for the S12 atom of the thiazole ring rather than a minor disorder.

2.2.4. Theoretical calculations

Gas-phase structure optimisations were performed using DFT methods at the PBEPBE[34]/cc-pVTZ[35] level of theory, within the Gaussian03 program.[36] Basis sets were obtained from EMSL.[37] The subsequent topological analyses were performed using the AIMPAC program.[38] Theoretical structure factors were computed from the resultant wave functions and used in a multipole refinement within XD,[21] in which all thermal parameters were set to zero and all positional parameters were kept fixed. Periodic single-point quantum calculations were also performed using CRYSTAL09[39] with the DFT method at the B3LYP[40]/6-31G** level of theory. Lattice energies were also calculated using the CLP[41] software.

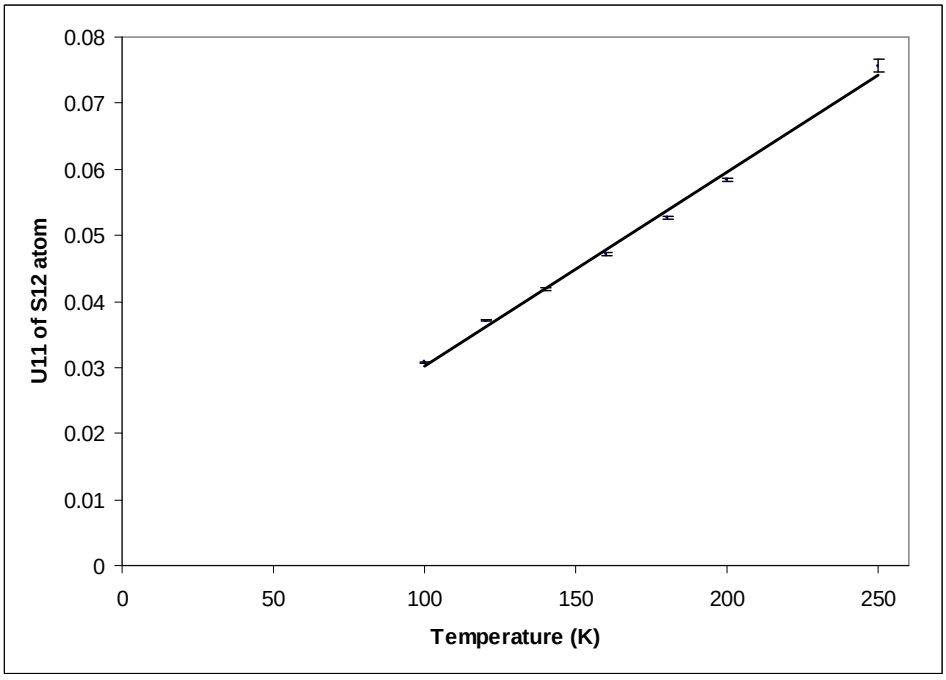

Graph 2.1. The variation of the U11 tensor of the S12 atom in sulfathiazole form II with temperature.

2.3. Results and discussion

2.3.1. Molecular structure and conformation details

The crystal structures of the polymorphs of **1** have been discussed extensively in the literature. A synopsis of this information is given here, combined with additional information from the present experimental results.

First, the differences between the four studied polymorphs will be discussed in detail in terms of their molecular geometry. The main structural difference regarding the forms of **1** relates to the orientation of the hydrogen atoms of the amine group. In form I the H atoms are pointing in the same direction as the O atoms of the SO_2 bridging group, relative to the phenyl ring, while in the other forms the hydrogen atoms are pointing in the opposite direction (Figure 2.3). The H atoms of the amine group of form V, which contains two molecules per asymmetric unit, were identified to be in the same direction as the O atoms relative to the phenyl ring for one molecule and almost in a planar orientation relative to the N (amide) atom and phenyl ring for the other molecule, in the case of suthaz05[5] and suthaz27.[8] For the suthaz06[4] data, on the other hand, the hydrogen atoms were found to be orientated in the opposite direction relative to the phenyl ring in both molecules; this is likely to be due to inaccurate X-ray determinations of hydrogen atom positions.

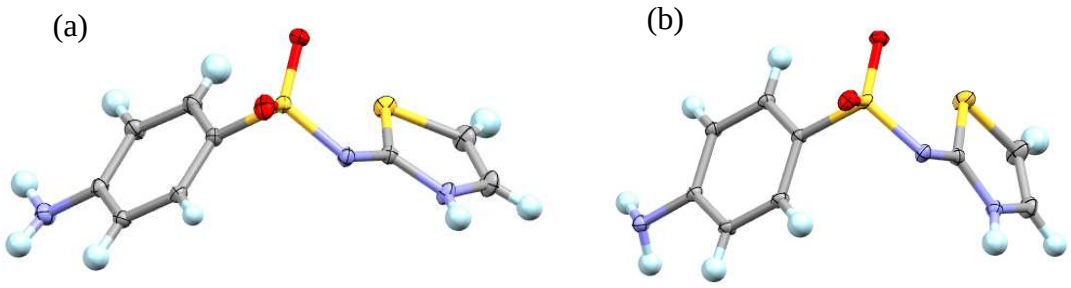

Figure 2.3. The main structural difference between form I (a) and the other forms (b) is found in the orientation of the NH_2 group (at the bottom left of each diagram).

A best-fit overlay plot of all the molecules in the asymmetric unit of the four studied forms emphasises the conformational difference between the molecules in form I and those in the other forms (Figure 2.4(a)).

The conformational similarity between the molecules of forms II, III and IV can also be observed by visual inspection of Figure 2.4 (b). The three relevant torsion angles, summarised in Table 2.5, for the four observed forms confirm the significant difference of molecular geometry of form I compared with forms II, III and IV. For example, the O11-S11-C111-C116 torsion angle of molecules a and b of form I adopts a large conformational difference compared with form II, III and IV. A significant discrepancy can also be observed between the S11-N10-C11-S12 torsion angle of the two molecules in form I (e.g. 0.26(7)°), compared with the other forms (e.g. form III a 19.57(5)°). As expected, a good agreement in the value of torsion angles can be observed between the two determined structures of form IV, IVapex and IVkappa. The apparent difference in the torsion angle O11-S11-N10-C11 in form Ib of the present experiment (−39.46(5)°), with an opposite sign when compared with the value obtained from CSD of 38.79°, is merely a consequence of the different choice of the molecular chirality in the asymmetric unit used for the refinement (the structures are all centrosymmetric).

(a)

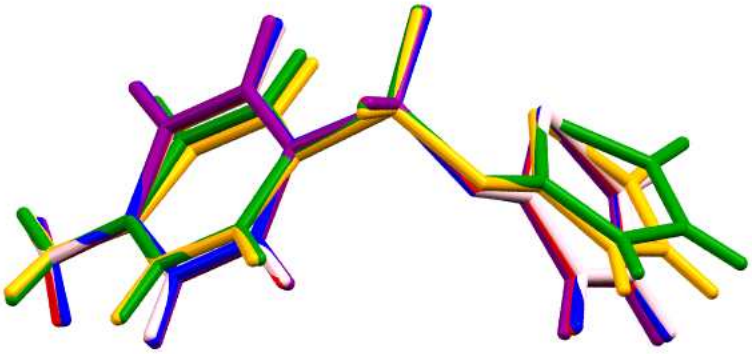

(b)

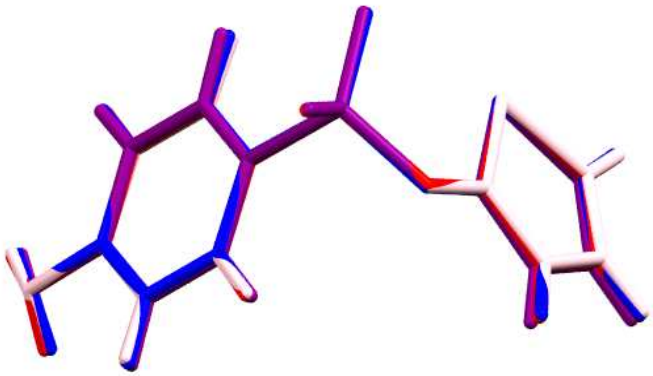

Figure 2.4. Best fit of (a) forms I,II, III and IV, (b) II, III and IV. Colour code: form I,(a)– green, (b)– yellow, form II –red, form III, molecule 1 – purple, molecule 2 –pink, form IV –blue.

Table 2.5. Experimental torsion angle data (in °) of **1,** forms I-IV

Torsion angle	This work	CSD
Form Ia		
O11-S11-C111-C116	10.01(5)	9.07
O11-S11-N10-C11	-33.46(5)	-33.81
S11-N10-C11-S12	-7.80(1)	-7.83
Form Ib		
O11-S11-C111-C116	15.29(5)	-16.37
O11-S11-N10-C11	-39.46(5)	38.79
S11-N10-C11-S12	0.26(7)	-0.02
Form II		
O11-S11-C111-C116	-6.15(3)	-6.26
O11-S11-N10-C11	-39.38(3)	-39.48
S11-N10-C11-S12	17.85(5)	17.90
Form IIIa		
O11-S11-C111-C116	-6.82(4)	-6.08
O11-S11-N10-C11	-40.03(4)	-39.50
S11-N10-C11-S12	19.57(5)	19.72
Form IIIb		
O11-S11-C111-C116	-6.20(4)	-6.11
O11-S11-N10-C11	-37.04(4)	-36.63
S11-N10-C11-S12	15.01(5)	15.10
Form IVapex		
O11-S11-C111-C116	-7.31(4)	-6.78
O11-S11-N10-C11	-37.14(4)	-36.63
S11-N10-C11-S12	15.12(5)	14.68
Form IVkappa		
O11-S11-C111-C116	-7.29(3)	-6.78
O11-S11-N10-C11	-37.13(3)	-36.63
S11-N10-C11-S12	15.09(4)	14.68

Since all polymorphs crystallise in the centrosymmetric space group $P2_1/c$ they all have two sets of enantiomerically related molecules. Thus, two different configurations of molecule **1** are observed, related to the direction of the thiazole –N-H bonds. This is imposed by a pseudo-chiral configuration at the imine nitrogen atom. The two sets of enantiomeric molecules are subsequently referred to as $\mathscr{L}$ (red) or $\mathscr{R}$ (blue). In an $\mathscr{L}$ molecule the imine –N-H bond is directed to the left when viewing the molecule down the plane of the phenyl ring, with the aniline hydrogen pointing away (Figure 2.5). The $\mathscr{R}$ -molecule has the imine –N-H bond oriented to the right if viewed down the phenyl ring plane.

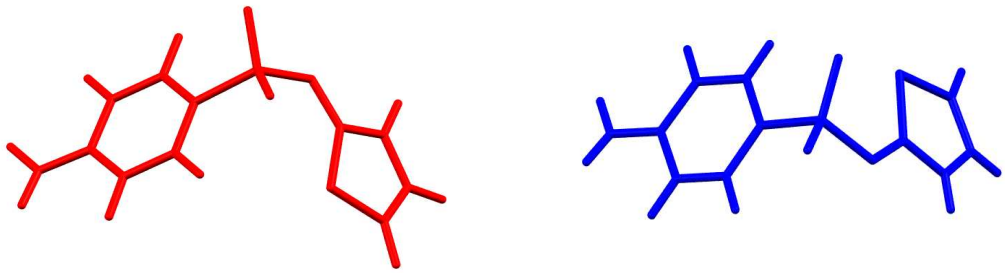

Figure 2.5. The two observed configurations adopted by **1** $\mathscr{L}$ (red) or $\mathscr{R}$ (blue)

2.3.2. Description of intermolecular interactions and crystal packing

The alternation in the unit cell of the $\mathscr{R}$ and $\mathscr{L}$ configurations in the different polymorphs of **1** are projected in Figure 2.6. The molecules are packed according to the hydrogen-bond dimers formed in forms II-IV.

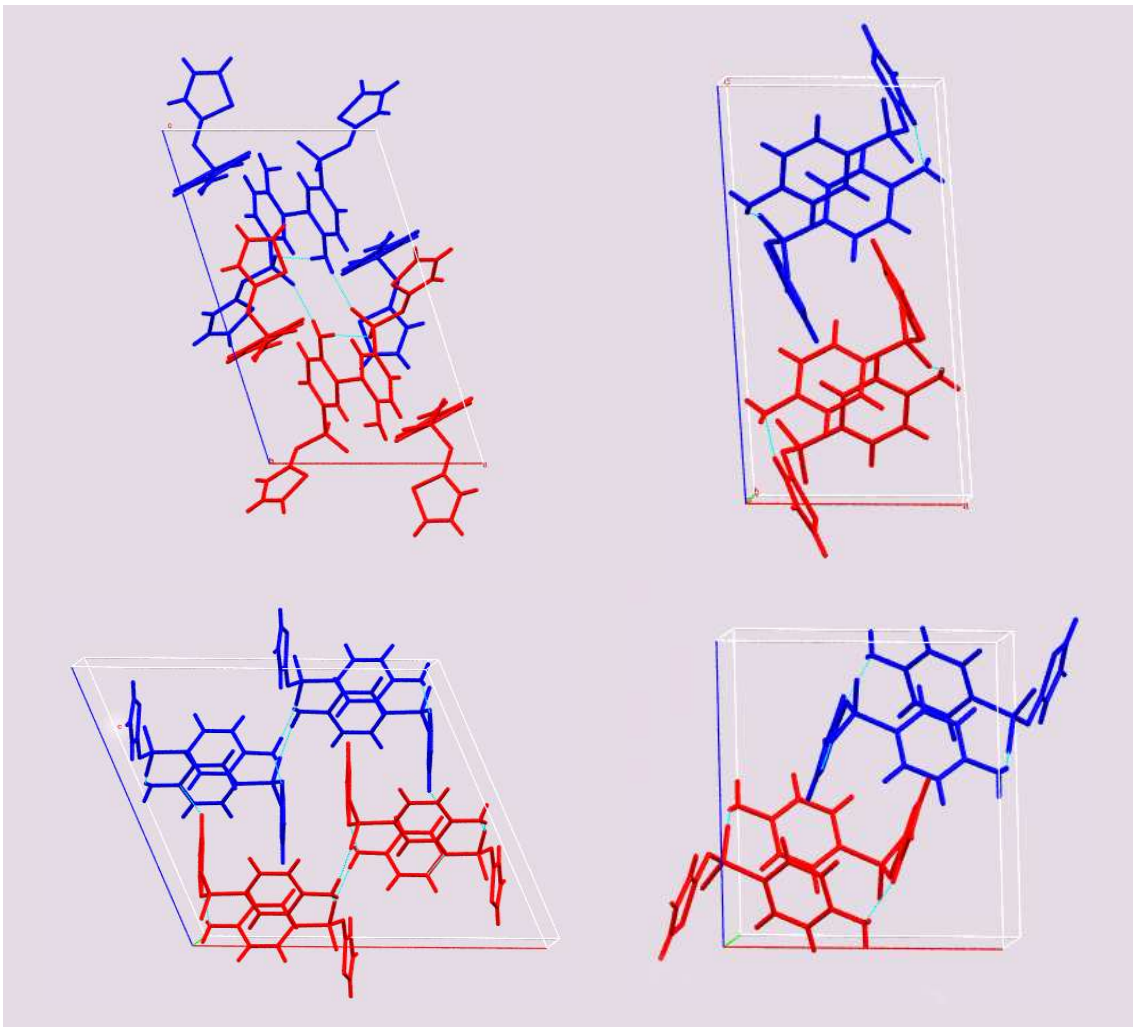

Figure 2.6. Different configurations of molecules of unit cells of the forms of **1** – the interactions forming the dimers in forms II-IV are indicated by light blue dashes.

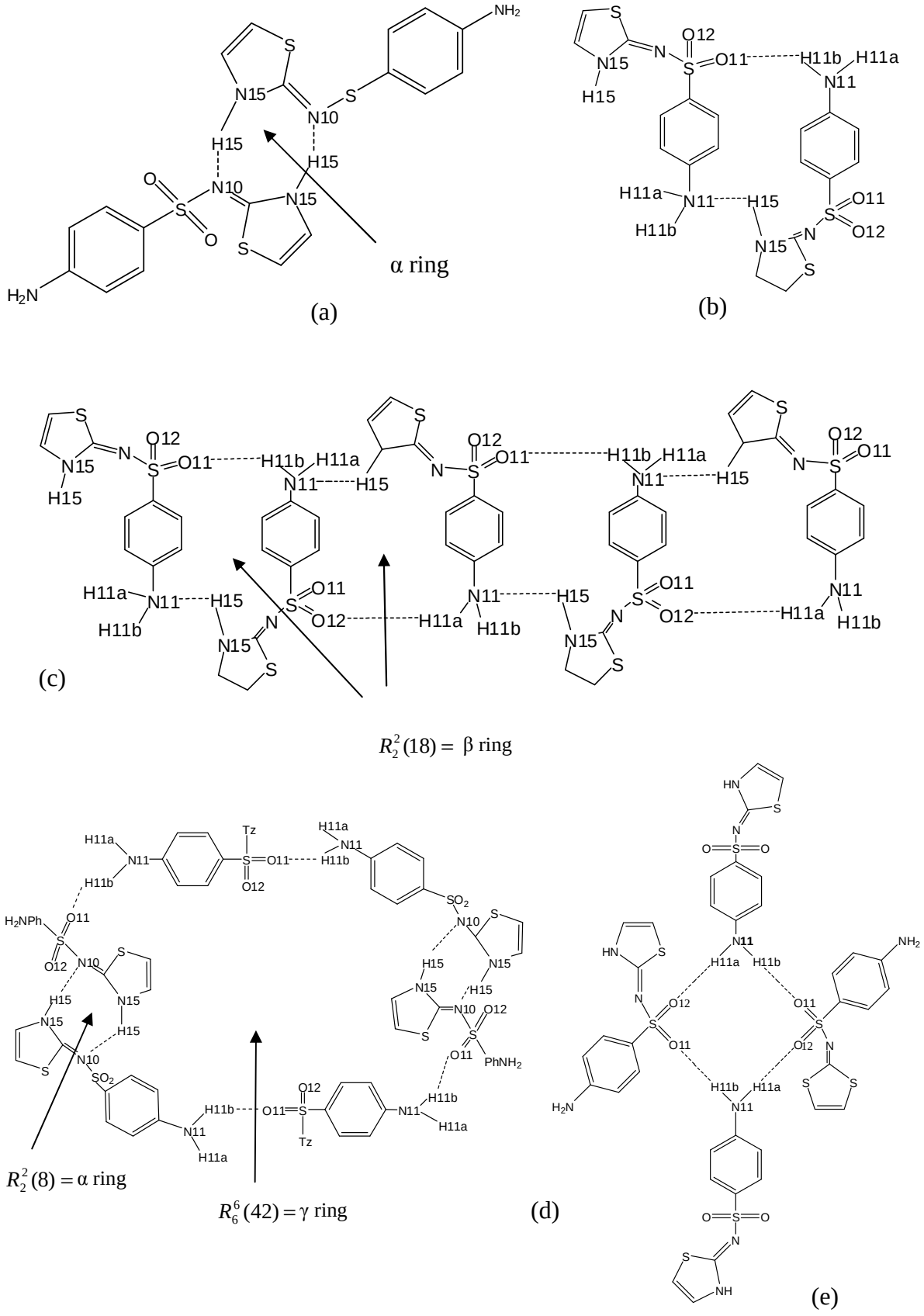

Figure 2.7. Hydrogen bonding motifs in the polymorphs of **1**. (a) Form I dimer illustrating α ring. (b) Form II, III and IV dimer illustrating the β ring. (c) C(8) [$R_2^2(18)$] dimer chain found in forms II, III and IV. (d) γ ring form in form I, (e) δ ring found in form I.

A unique dimer, designated α (Figure 2.7),[12] is found to be oriented along the *c*-axis in form I, while for forms II, III and IV, the common dimer formed and designated β (Figure 2.7)[12] is oriented along the *b*-axis.

Three different H-bond donors (two aniline N-H and one imine N-H) and four different acceptors (one aniline N, two sulfonyl O, one imido N) have been identified in all forms of **1**. The hydrogen bond motifs for all four forms were analysed and represented by graph set notation (Figure 2.7).[12] The ring symbols are notated as $R_d^a(n)$, where *n* indicates the numbers of atoms included in the ring, *d* and *a* are the numbers of donors and acceptors, respectively. In the unique α dimer found in form I the two molecules are hydrogen bonded through two imine nitrogens acting as acceptors and two amino hydrogens acting as donors, at a distance of N15···N10 = 2.8809(6)Å [Figure 2.7(a)].[12] This dimer is linked by H11···O12 interactions, forming a *C(8)* chain motif and extended into layers that provide $R_6^6(42)$ rings, designated γ [Figure 2.7(d)].[12] The six molecules included in the $R_6^6(42)$ ring alternate in an $\mathcal{LRLRLR}$ configuration for both molecules of form I. In addition, molecule b contains H(aniline)···O interactions which forms rings designated δ [Figure 2.7(e)][12] The extended structure produced through N-H···N and N-H···O hydrogen bonds (Table 2.6) in two dimensions and three dimensions is shown in Figure 2.8 and 2.9, respectively. The common dimer, designated β, found in forms II, III and IV [Figure 2.7][12] is constructed from an oxygen to an aniline hydrogen (O12···H11b) contact (II, 2.023(5) Å; III, 2.139(14), 2.150(12) Å; IV, 1.996(6) Å) and an aniline nitrogen to an amino hydrogen (N11···H15) contact (II, 1.811(4) Å; III, 2.044(13), 1.937(13) Å; IV, 1.887(8)Å).

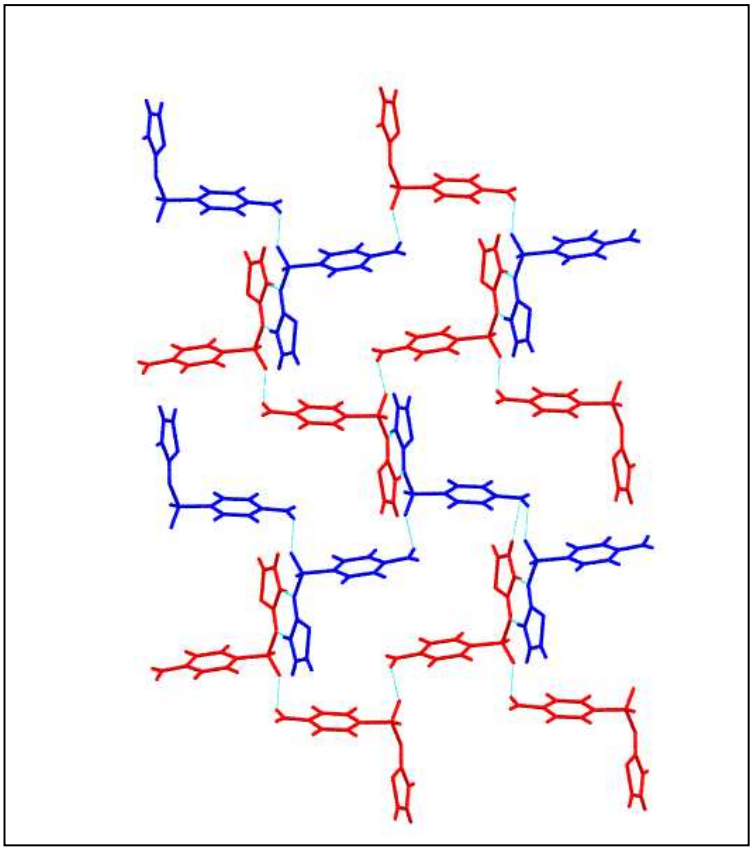

Figure 2.8. Two dimensional extended structure of **1,** form I.

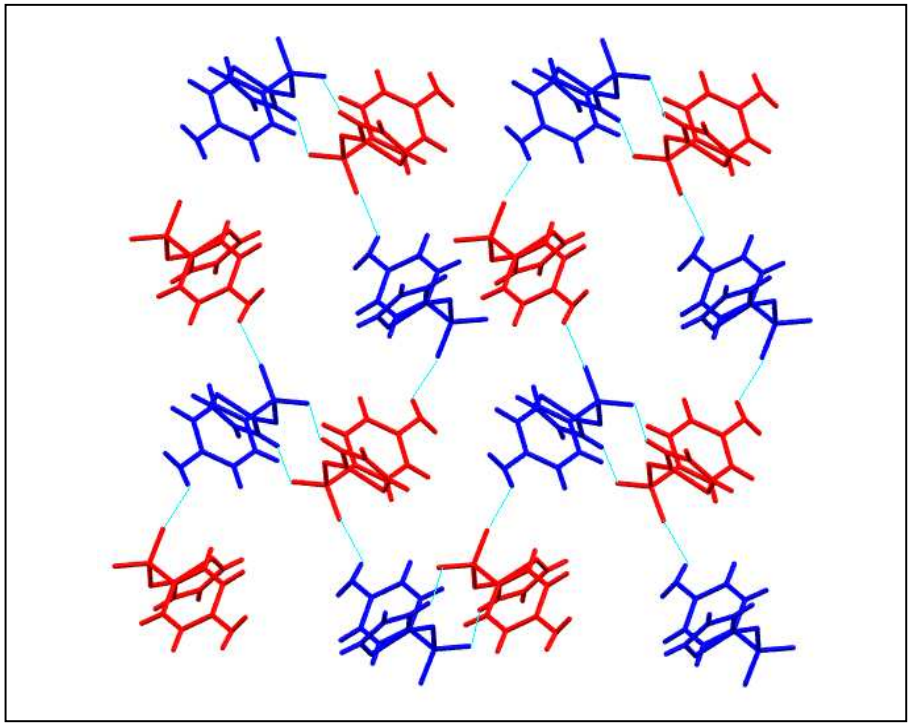

Figure 2.9. Three-dimensional extended structure of **1**, form I.

The structural differences between these three forms arise from the way in which the sheets are constructed and from their packing sequence. These different sheet constructions are shown in Figure 2.10(a)-(c).[12] The C_β chains, which are formed in each of the three forms

II, III and IV, are linked in two dimensional sheets, both in a clockwise direction and in an anticlockwise direction, forming $R_4^4(12)$ rings, designated ε,ε*,ζ, ζ*,η, η* in Figure 2.10.[12] Two types of independent sheets are found in form II, one containing $\mathscr{L}$-C_β and the other containing $\mathscr{R}$-C_β chains. These chains are connected through ε and ε* rings. In form III and IV only one sheet is found with $\mathscr{L}$-C_β and $\mathscr{R}$-C_β alternating with each other and forming ε and η rings. A summary of hydrogen bond types observed in the molecular sheets of forms I, II, III and IV is given in Table 2.6. The corresponding X-ray determined distances in form I and neutron determined distances in forms II, III and IV are displayed in Table 2.7. Obviously the hydrogen bonds in form I obtained from X-ray data are longer compared to those in form II, III and IV determined from neutron data. The H15···N11 hydrogen bond has been identified to be the shortest one in forms II, III and IV. The H11A···O12 bond included in the ε ring shows the same length in both forms II and III. Similarly, in the ζ ring the H15···N11 hydrogen bond has the same distances in forms III and IV.

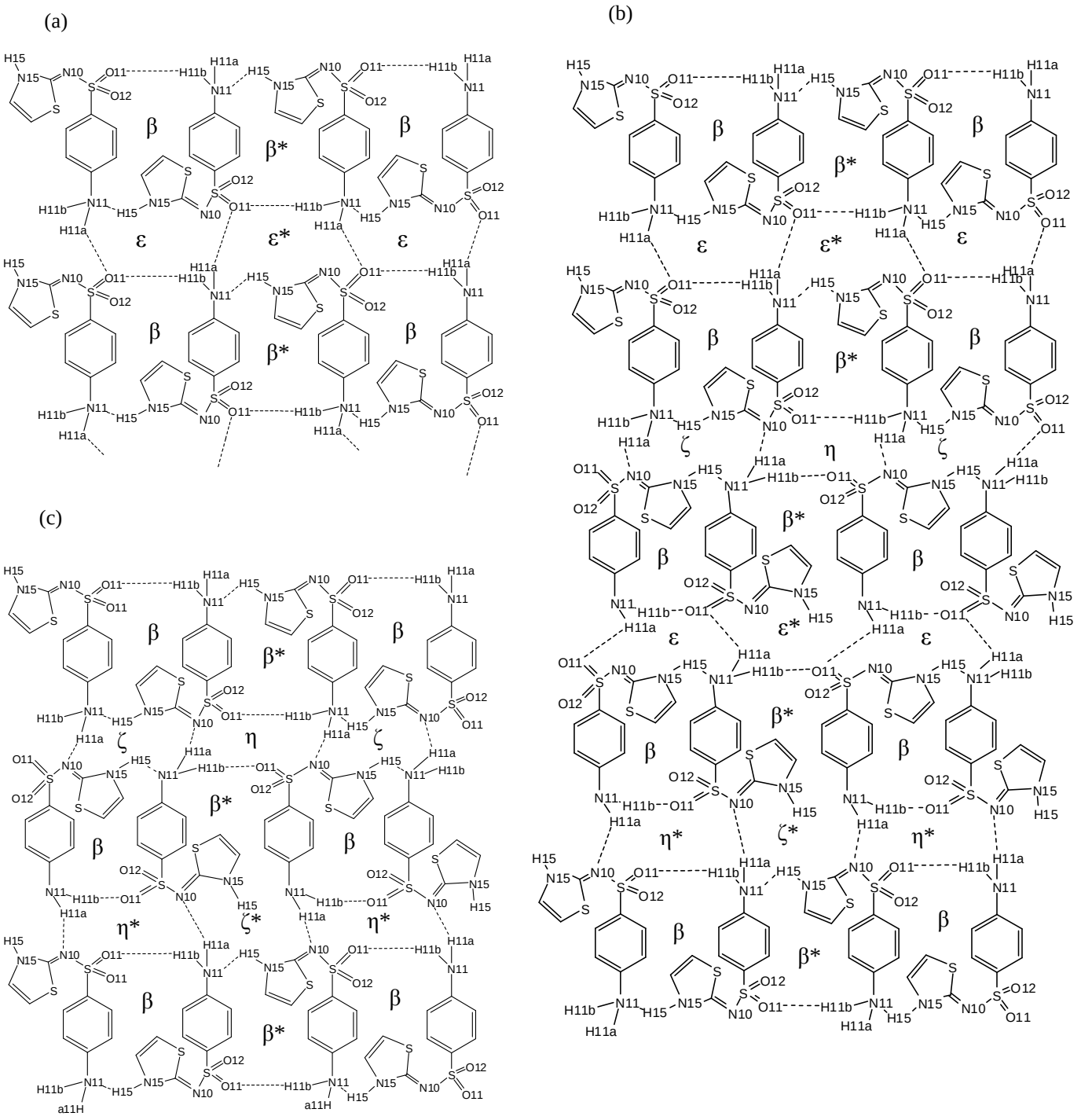

Figure 2.10. Schematic representation of sheets in (a) form II forming β, β*, ε, ε* rings, (b) form III forming β, β*, ε, ε*, η, η*, ζ and ζ* rings, (c) form IV forming β, β* η, η*, ζ and ζ* rings

Table 2.6. Hydrogen interactions form in polymorphs I, II, III and IV of **1**

Label	Symbol	Hydrogen bonds present	Form
α	$R_2^2(8)$	H15···N10 H15···N10	I
β	$R_2^2(18)$	H11B···O12 H15···N11	II, III, IV
γ	$R_6^6(42)$	H11B···O12 H11B···O12 H15···N10 H11B···O12 H11B···O12 H15···N10	I
δ	$R_4^4(12)$	H11B···O11 H11A···O12 H11B···O11 H11A···O12	I
ε	$R_4^4(12)$	H11A···O12 H15···N11 H11A···O12 H11B···O12	II III
ζ	$R_4^4(12)$	H11A···N10 H15···N11 H11A···N10 H15···N11	III IV
η	$R_4^4(12)$	H11A···N10 H11B···O12 H11A···N10 H11B···O12	III IV

Table 2.7. Hydrogen bond distances (Å) in the four studied polymorphs of **1** (parameters for form I taken from X-ray data, for forms II, III and IV from neutron data).

Hydrogen bonds present	D-H/Å	H···A/ Å	D···A/ Å	D-H···A/ º
Ia				
N11-H11A···O12	0.883(13)	2.085(13)	2.9519(7)	167.0(12)
N11-H11B···O11	0.882(12)	2.267(12)	2.9466(6)	133.8(11)
N15-H15···N10	0.890(12)	2.006(12)	2.8809(6)	167.5(12)
Ib				
N(21)-H(21B)···O(22)	0.863(13)	2.354(13)	3.0905(7)	143(11)
N(25)-H(25)···N(20)	0.862(13)	2.004(13)	2.8567(6)	170.1(12)
II				
N11-H11B···O12	1.058(4)	2.023(5)	2.980(3)	156.1(4)
N15-H15···N11	1.058(4)	1.811(4)	2.8460(18)	164.7(4)
N11-H11A···O12	1.018(4)	2.004(5)	2.999(3)	165.2(4)
III				
N11-H11B···O12	1.035(8)	2.001(8)	2.967(4)	154.2(6)
N25-H25···N11	1.048(6)	1.877(6)	2.904(3)	165.8(6)
N21-H21A···O12	1.019(7)	2.004(7)	2.004(7)	165.8(7)
N15-H15···N21	1.057(6)	1.803(6)	2.840(3)	166.1(6)
N11-H11A···N20	1.018(6)	2.219(6)	3.175(3)	155.8(6)
N11-H11B···O22	1.037(8)	1.985(8)	2.990(4)	162.4(7)
IV				
N11-H11B···O12	1.036(9)	1.996(9)	2.982(5)	158.0(6)
N15-H15···N11	1.044(7)	1.887(8)	2.907(3)	164.8(6)
N11-H11A···N10	1.014(8)	2.237(8)	3.174(3)	153.0(7)

The differences between forms II, III and IV in terms of strong hydrogen bonds are summarised in Figure 2.11.[1] In each of the forms, one molecule forms six H-bond interactions with four neighbouring molecules. The interactions drawn in red in Figure 2.11[1] are identical in all three forms. The other two hydrogen interactions in form II, formed by an aniline N-H···O contact, are drawn inblue. In form IV these interactions are shown in green. They are formed by the same donor aniline N-H, but this time the acceptor

is the amido N atom. The two independent molecules in form III contain both types of interactions found in forms II and IV (A and B). The first molecule has O atom acceptors and an H atom belonging to an aniline group acting as a donor. As a donor it uses an aniline N-H to an amido group (acceptor). The second molecule has the opposite H-bonds.

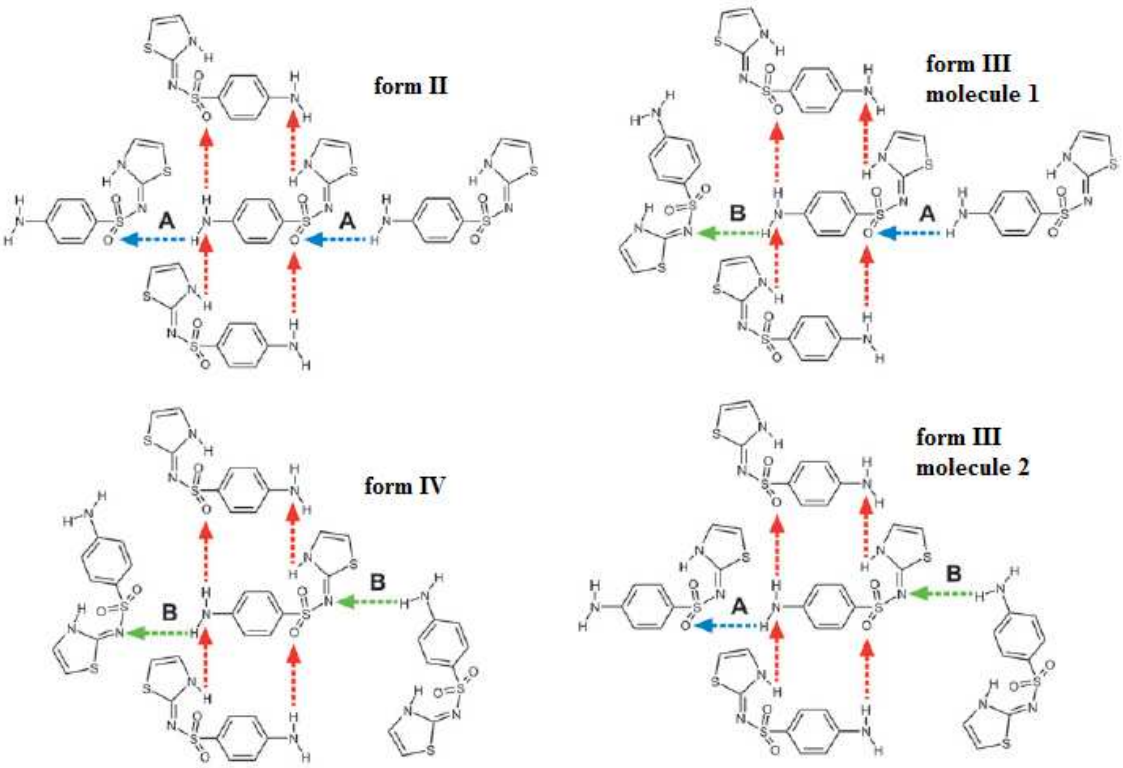

Figure 2.11. Representation of the H-bonds between **1** molecule and its four neighbouring molecules in forms II, III and IV.[1]

2.3.3. Hirshfeld surfaces and fingerprint plot analysis of the intermolecular hydrogen bond interactions

The intermolecular interactions were also studied using Hirshfeld surface plots[10] generated using the CrystalExplorer software.[42] The Hirshfeld surfaces represent the partition into molecular fragments of the total crystalline electron density. There are other partition schemes known, such as QTAIM[43] or Wigner-Seitz (WS).[44] It was shown by Spackman *et*

al.[42] that the QTAIM[43] partition gives rise to numerical integration problems due to the abrupt discontinuities of the zero-flux boundary surface. The WS[44] method also shows irregularities of the molecule surface and is strongly dependent on the atomic radii chosen. The accuracy of the molecular surface also depends on whether the partition is applied pairwise with atoms in the molecule, or if the test is made over aggregates of atoms.[45] The Hirshfeld surface is an extension of the Hirshfeld concept which divides the electron density of a molecule into continuous atomic fragments. In analogy with this concept a molecule in a crystal is defined by a weight function:[45]

$$w(\mathbf{r}) = \sum_{i \in molecule} \rho_i(r) \Big/ \sum_{i \in crystal} \rho_i(r) = \rho_{promolecule}(r) \,/\, \rho_{procrystal}(r) \qquad \text{eq. 2.3}$$

where ρ(r) is a spherically averaged Hartree-Fock atomic electron density function centered at the *i*th nucleus, and the pro-molecule and pro-crystal are the sums over the atoms belonging to a single molecule and the crystal, respectively. The w(r) function is cut off at 0.5 Å which ensures a maximum proximity of neighboring molecular volumes and prevents overlap.[15] A typical molecular Hirshfeld surface contains tens of thousands of individual points, each having a well-defined d_i and d_e pair (Figure 2.12).

In Figure 2.12, d_i represents the distance from the surface to the nearest atom in the molecule itself, and d_e the distance to the nearest atom outside the molecule. As such, they reveal details of close contacts between molecules, especially in the vicinity of hydrogen bonds. The red spots on the surface represent shorter contacts to neighbouring molecules and therefore the hydrogen bond interactions between the molecules inside the surface and the molecules which surround it. The intensity of the spots vary according to the type of interaction, the red colour will be more intense for shorter, stronger interactions. In two-dimensional fingerprint plots, which are derived from the Hirshfeld surface, the frequency of each combination of d_e and d_i is represented. A hydrogen bond acceptor corresponds to the region were $d_i > d_e$, while a hydrogen bond donor has $d_e > d_i$.

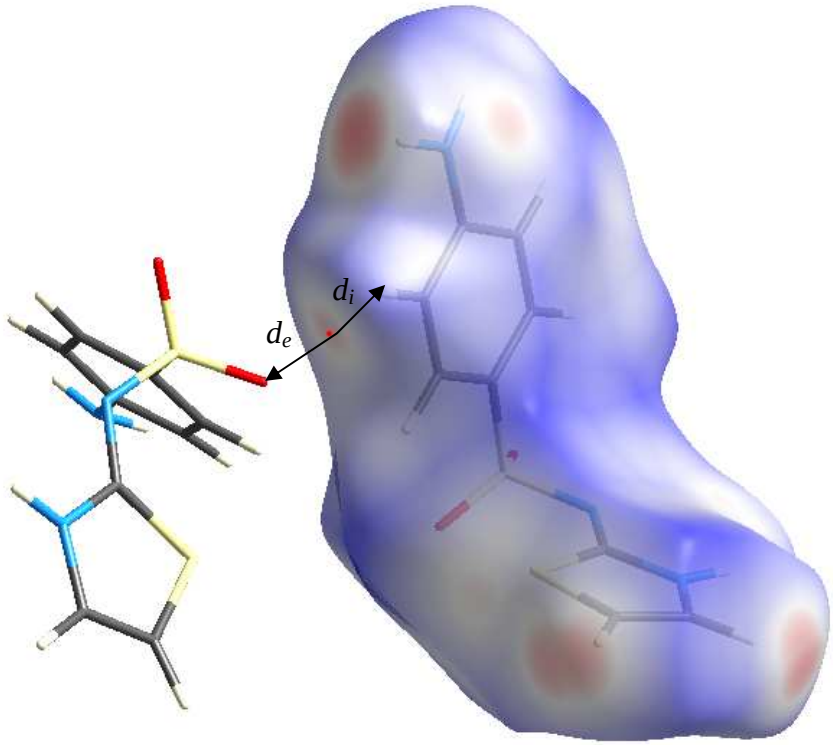

Figure 2.12. Illustration of the Hirshfeld surface of **1**, shown on the right in the transparent mode, The distances d_i and d_e are illustrated schematically for a single point (red dot).

Figure 2.13 shows the two-dimensional fingerprint plots for the four studied polymorphs of **1**, with the corresponding intermolecular interactions summarised in Table 2.8. These distances are measured approximately. Short contacts occur in all forms between hydrogen atoms on the benzene ring. There are two short H···H interactions found in the case of form I (a,b) of **1**, while for the other forms there is only one. Forms I and III contain two molecules per asymmetric unit and therefore, there are two short H···H contacts. In form III, d_i and d_e for molecules 1 and 2 are fairly similar (d_i = 1.080 Å and d_e = 1.076 Å), whereas in form I they are more dissimilar (d_i = 1.020 Å, d_e = 1.157 Å). This difference arises from the fact that in form I the H···H benzene ring interaction occurs between an H atom at the *para* position and an H atom from the *meta* position. For form III on the other hand, this peak results from two H atoms both in *meta* positions of the benzene ring (see Scheme 2.3).

Also, as a consequence, for the H…H short interaction this peak is denser in form III compared to forms II and IV.

Four uniquely strong hydrogen bond interactions (e,g. those denoted 3,4,5,6 in form I in Figure 2.13) have been found in all four studied forms, the two upper peaks in the fingerprint plots corresponding to the H-bond donor and two lower ones to the acceptor. In

all forms, the strong hydrogen bond interactions occur between N-H(thiazole)···N(imino) and N-H(aniline)···O. The 'wings' (denoted 7,8 forform I) are a typical representation of a C-H…π contact in the fingerprint plot. This type of interaction is observed between a thiazole C-H and the benzene ring in I, III and IV. In form II, the 'wings' are instead associated with C-H···S hydrogen bonds. All hydrogen bond interactions represented in the fingerprint plots for the four forms of **1** studied are summarized in Table 2.8. The different intermolecular interactions observed in **1** are a consequence of the varying molecular packing in the unit cell. The stability of these polymorphs will be influenced by the difference in the intermolecular interactions.

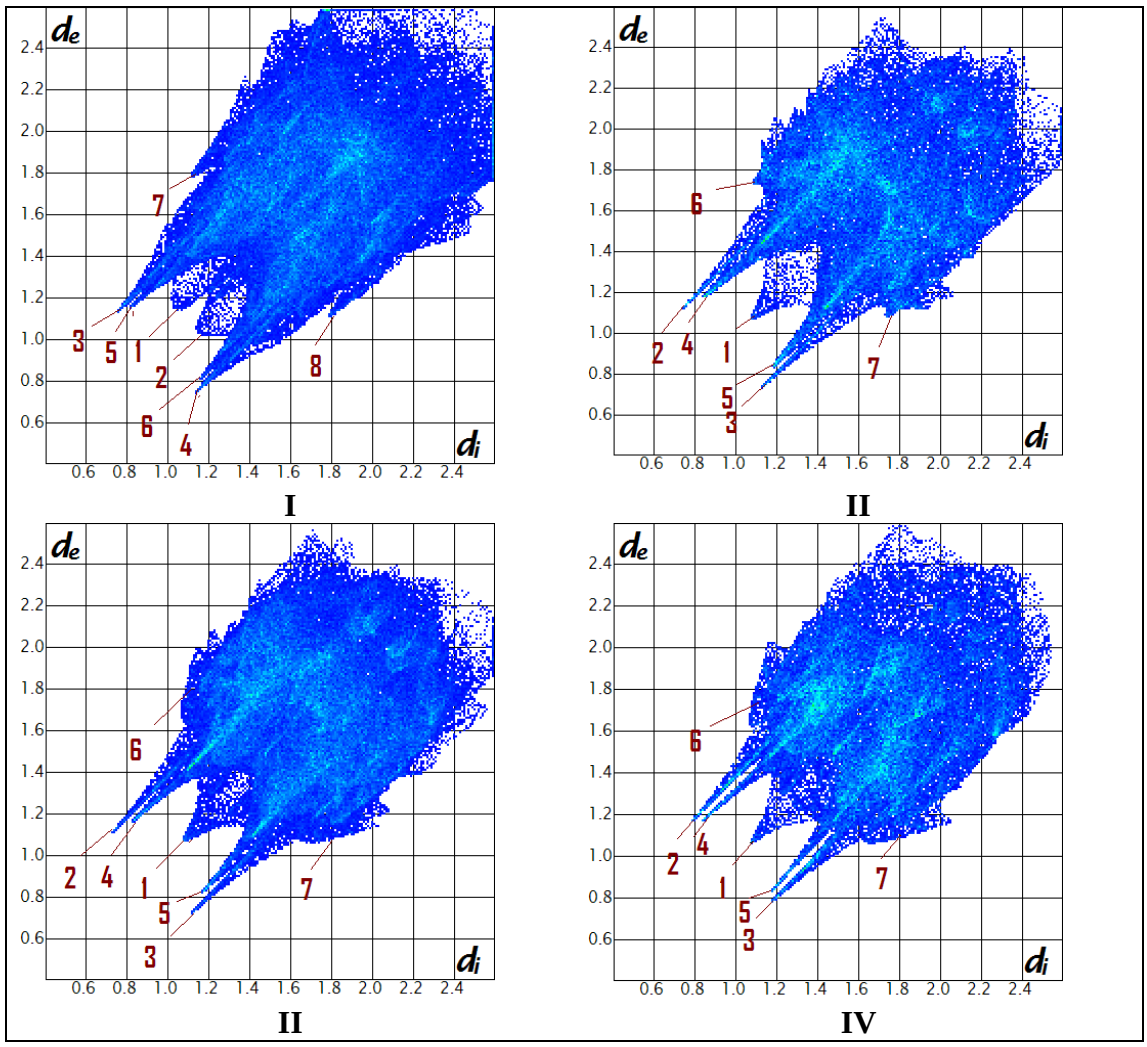

Figure 2.13. Two-dimensional fingerprint plots for four forms of **1.**

Form I	– molecule 1 (H_{para}…H_{meta}), molecule 2 (H_{meta}…H_{para})
Form III	– molecule 1 (H_{meta}…H_{meta}), molecule 2 (H_{meta}…H_{meta})

Scheme 2.3. The H···H interactions in forms I and III of**1**.

Table 2.8. The hydrogen bond interactions of the various forms of **1** obtained from the fingerprint plots generated using the CrystalExplorer[42] program.

Sulfathiazole, 1	**d_i (Å)**	**d_e (Å)**	**$d_i + d_e$ (Å)**
Form I			
H…H (benzene ring) **1**	1.020	1.157	2.177
2	1.157	1.020	2.177
N-H (thiazole)...N (imino) **3**	0.736	1.125	1.861
N (imino) ...H-N(thiazole) **4**	1.124	0.730	1.854
N- H (aniline)...O **5**	0.808	1.156	1.964
O...H-N (aniline) **6**	1.155	0.808	1.963
C-H (thiazole)...π C (benzene ring) **7**	0.986	1.575	2.561
C (benzene ring)... H-C (thiazole) **8**	0.985	1.575	2.56
Form II			
H...H (benzene ring) **1**	1.077	1.087	2.164
N-H (thiazole)... N (aniline) **2**	0.741	1.130	1.871
N (aniline)... N-H (thiazole) **3**	1.131	0.741	1.872
N-H(aniline)...O **4**	0.841	1.184	2.025
	0.849	1.187	
O... N-H(aniline) **5**	1.184	0.847	2.031
	1.184	0.841	2.025
C-H (benzene ring)…S **6**	1.091	1.742	2.833
S… C-H (benzene ring) **7**	1.741	1.092	2.833
FormIII			
H...H (benzene ring) **1**	1.075	1.080	2.155
	1.080	1.076	2.156
N-H (thiazole)... N (aniline) **2**	0.727	1.118	1.845
N (aniline)... N-H (thiazole) **3**	1.117	0.727	1.897
N-H(aniline)...O **4**	0.827	1.169	1.996
	0.832	1.177	2.009
O...H-N (aniline) **5**	1.169	0.827	1.996
	1.177	0.832	2.009
C-H (thiazole)... π C (benzene ring) **6**	1.073	1.683	2.756
C (benzene ring) π... H -C (thiazole) **7**	1.683	1.073	2.756
Form IV			
H...H (benzene ring) **1**	1.075	1.074	2.149
N-H (thiazole)... N (aniline) **2**	0.787	1.179	1.966
N (aniline)... N-H (thiazole) **3**	1.178	0.788	1.966
N-H(aniline)...O **4**	0.838	1.179	2.017
O...H-N (aniline) **5**	1.177	0.846	2.023
C-H (thiazole)... C (benzene ring) **6**	1.072	1.638	2.71
C (benzene ring) ... H -C (thiazole) **7**	1.653	1.072	2.725

2.3.4. Analysis of the crystal structures of the polymorphs of sulfathiazole, 1.

In this section, the high-resolution X-ray diffraction and neutron diffraction results of the four studied polymorphs of **1** will be examined.

Interpretation of the X-ray diffraction data revealed minor residual density peaks, which are interpreted as a minor disorder in form Ib, corresponding to a different orientation of the molecule in the unit cell (Figure 2.14 (a)). This minor disorder in form Ia corresponds to a high Q peak near the S12 of the thiazole ring. The distance between the two disordered S atoms is quite significant and the high thermal motion of the sulphur atom is consistent with the presence of such disorder. This minor disorder has not been identified in previous studies.[1-8] Another type of disorder for the sulfur atom was also identified in form III, in a low resolution data set, involving both molecules in the asymmetric unit, but when another crystal of form III was used for a high resolution data collection, no sign of disorder was found. This suggests that the problem was probably a minor twinning rather than disorder. A similar minor disorder has been also identified in form II for the full high resolution data collection, except that only one Q peak was observed in this case. The level of disorder in forms I and II was estimated at ~ 1-2% or less and only the S atom positions of the minor component could be observed as residual peaks, at a level smaller than 1.0eÅ^{-3}.

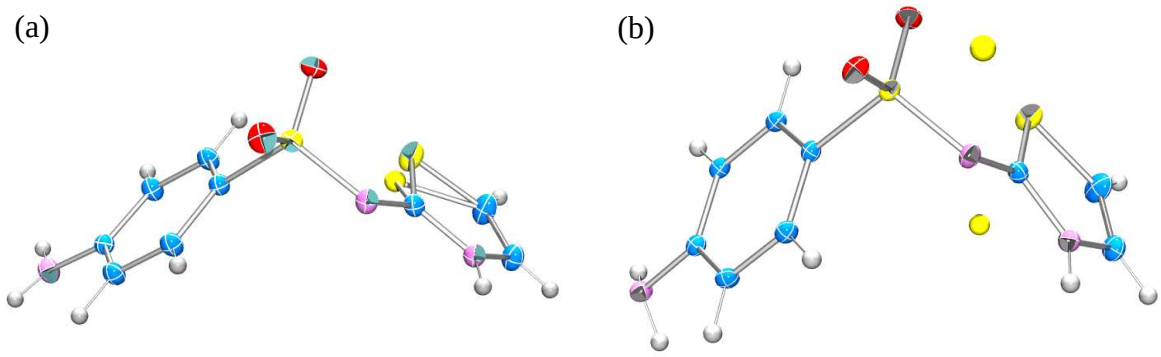

Figure 2.14. The minor disordered S atom in (a) form Ib and (b) form II of **1**.

In order to ascertain the effect of this minor disorder (or twin component) on the derived topological parameters in form Ib and II, these were compared with form III and IV, for which none of the atoms show disorder. However, it is important to mention that this disorder hypothesis is not confirmed by the neutron diffraction data, where none of the atoms show disorder. This may be a consequence of the fact that the S atom is weakly scattered by neutrons in comparison with the other atoms present in **1** (Figure 2.15).[46]

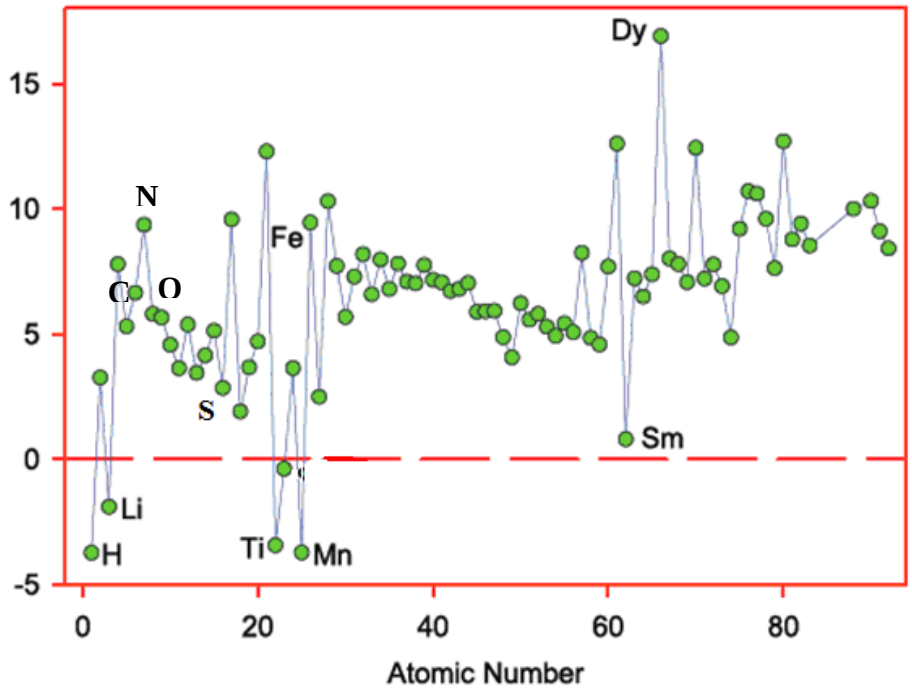

Figure 2.15. Neutron scattering length variation as a function of atomic number.[43]

2.3.4.1. Analysis of the anisotropic thermal parameters

At high diffraction angle, the core density has the most significant contribution to the reflections. The scattering by the more diffuse valence or bond density is negligible. High resolution X-ray data thus offers a more accurate description of the atomic motion. Using multipole refinement, errors which are normally included in thermal motion are minimized; hence, more accurate values for adps are obtained. Atomic motion in a crystal structure is typically based on the analyses of the form of the adps, whose values are influenced by both internal motion, which depends on the molecular vibration, and the external contributions, which depend on the lattice vibration. In the case of **1**, a difference might therefore be expected between the adps of the forms. In fact, a high degree of similarity was observed between the adps of all studied forms analysed and this can be seen qualitatively from ORTEP plots. The agreement between the adps of related atoms can be measured by calculating the similarity index S_{12} given by the expression $S_{12} = 100R_{12}$; where R_{12} measures the overlap between the probability density functions (p.d.f's) described by two displacement parameter tensors U_1 and U_2 (eq. 2.4):[47]

$$R_{12} = \int \sqrt{p_1(x)p_2(x)}\,d^3x = \frac{2^{3/2}(\det U_1^{-1}U_2^{-1})^{1/4}}{\left[\det(U_1^{-1}+U_2^{-1}\right]^{1/2}} \qquad \text{eq. 2.4}$$

If U_1 and U_2 are identical, then R_{12} = 1.00 and therefore S_{12} is measuring the difference between the two p.d.f.'s. The closer the values of S_{12} are to 100, the better is the agreement between the obtained adps. The similarity index can be calculated using the most recent version of the WinGX program.[16] The following steps are taken into consideration for calculating this similarity index: the x, y, z coordinates of the molecules studied (e.g. two different forms of **1**) are orthogonalised; the coordinates of one form are multiplied by a rotational matrix to bring them into the same orientation with the form compared; the eigenvalues and the corresponding eigenvectors of the U_{ij} tensors in the new Cartesian coordination system are calculated for each atom of both molecules. The R_{12} and S_{12} can then be calculated. In addition, a figure of merit is used in order to analyse quantitatively the results. The figure of merit includes the deviation from the principal axes of the orthogonalised U_{ij} tensor, a scale factor calculated as $U_{eq}(1)/U_{eq}(2)$, R_{12} and S_{12}.

The comparison between atoms of the studied form of **1** in terms of the adp similarity index are summarised in Table 2.9. The mean values of U_{eq} scale factor are also given here, while some of the corresponding structural and thermal ellipsoid overlays are shown in Figure 2.16. Clearly, forms II, III and IV show a high degree of similarity, with S_{12} lying between 99.58 and 99.91. The adps belonging to the two molecules of form I are slightly different, and they are also significantly different from those of form II. However, the adp similarities between Ia and Ib are slightly better (98.27) than, for instance, between Ia and II (97.70). These differences arise from the fact that their conformations are different (Figure 2.4a). The difference between the adps of form Ia – form Ib and form Ib – form II, can be easily observed from Figure 2.16, while in contrast the very good match of the adps between form II and form IIIb, and form II – form IV can also be observed clearly. The U_{eq} scale factors also have similar mean values for forms II, IIIa,b and IV. Surprisingly, comparing the adps of forms IVapex and IVkappa give a slightly higher value of the U_{eq} scale factor (1.095) in comparison with form II-form IIIa,b or form II-form IV. The figures of merit for each atom in the forms compared are listed in Table 2.10. The results emphasise the good agreement of the non-hydrogen atom adps in forms II, III and IV; as a value very close to zero is obtained for the figure of merit in most cases.

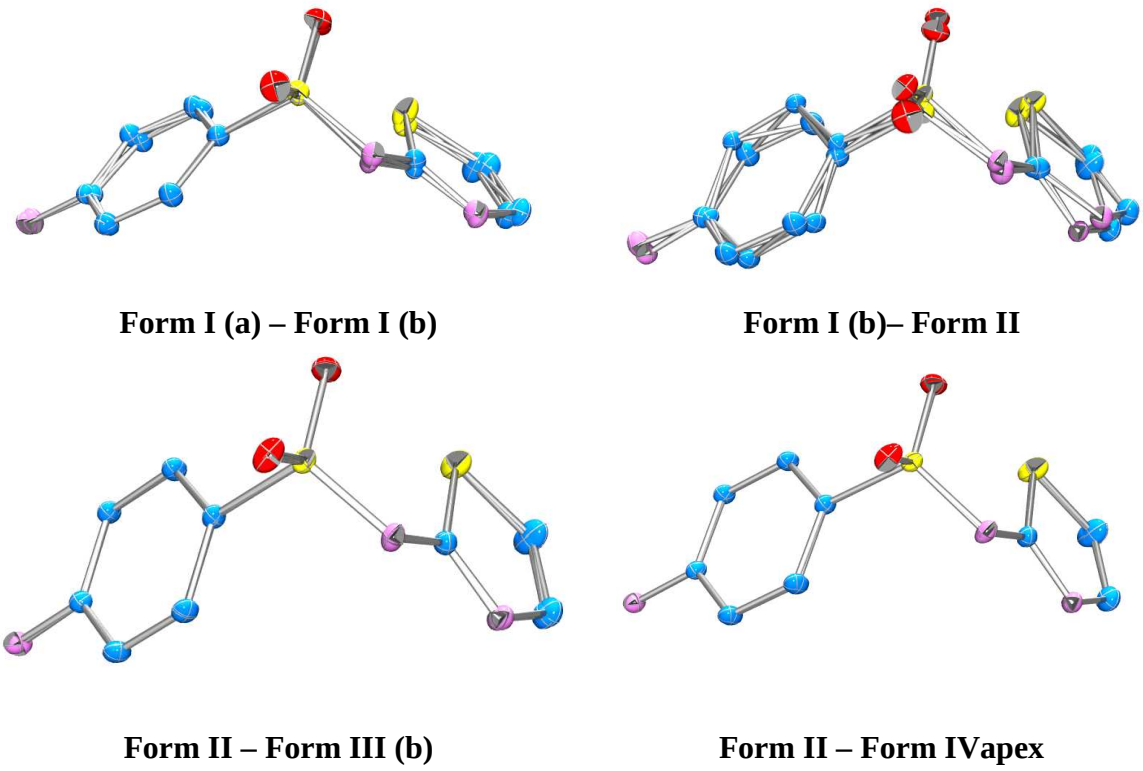

Form I (a) – Form I (b) **Form I (b)– Form II**

Form II – Form III (b) **Form II – Form IVapex**

Figure 2.16. The adp superposition between different forms of sulfathiazole, **1**.

Table 2.9. The mean values of the adp similarity index from X-ray data of compared forms of **1**

Compared forms	**Mean values of the similarity index**	**Mean value of U_{eq} scale factor**
Form I (a) - Form I (b)	98.28	0.949
Form I (a) – Form II	97.70	0.841
Form I (b) - Form II	97.33	1.27
Form II- Form III (a)	99.84	1.080
Form II- Form III (b)	99.70	1.062
Form III (a) - Form III (b)	99.74	0.984
Form III (a)– FormIVapex	99.81	0.994
Form III (b) – Form IVapex	99.91	1.011
Form IVapex – Form IVkappa	99.58	1.150

Table 2.10. The figure of merit calculated by comparing the adps for forms of **1**

Compared atoms	Figure of merit				
	Form Ia and b	Form Ib Form II	FormII Form IIIb	Form II Form IVapex	Form IIIa Form IVkappa
S11	0.164	0.146	0.018	0.140	0.056
S12	0.218	0.091	0.021	0.050	0.007
O11	0.159	0.156	0.006	0.041	0.016
O12	0.115	0.157	0.013	0.092	0.010
N10	0.093	0.122	0.021	0.109	0.023
N11	0.099	0.112	0.127	0.138	0.024
N15	0.107	0.122	0.032	0.057	0.017
C11	0.153	0.119	0.073	0.078	0.034
C13	0.175	0.099	0.021	0.043	0.006
C14	0.134	0.141	0.030	0.049	0.018
C111	0.155	0.134	0.023	0.041	0.022
C112	0.179	0.136	0.008	0.093	0.124
C113	0.124	0.129	0.042	0.088	0.018
C114	0.114	0.141	0.103	0.046	0.029
C115	0.058	0.119	0.098	0.122	0.023
C116	0.075	0.132	0.082	0.123	0.014

Good agreements were also observed (see Figure 2.17) when the adps obtained from SHADE[24] and from neutron diffraction were compared. The similarity indices for the H atoms compared are listed in Table 11, with mean values lying between 99.70 and 99.54 indicating a very good estimation of the hydrogen adps provided by SHADE.[24]

Table 2.11. The similarity index for each hydrogen atom and the corresponding mean value of similarity index in form II, III and IV comparing the neutron data with SHADE.[24]

Compared atoms	Similarity index S12			
	Form II	Form IIIa	Form IIIb	Form IV
H11a	99.36	98.61	98.46	99.39
H11b	98.65	99.47	97.95	96.07
H13	99.18	98.86	97.75	91.81
H14	98.20	99.41	99.11	93.93
H15	98.81	97.76	98.87	96.69
H112	99.41	98.04	98.74	97.29
H113	99.72	99.25	99.28	94.96
H115	99.47	99.30	99.58	97.86
H116	99.72	98.94	99.06	95.57
M.V.S.I.	99.70	99.58	99.55	98.54

M.V.S.I- mean value of similarity index

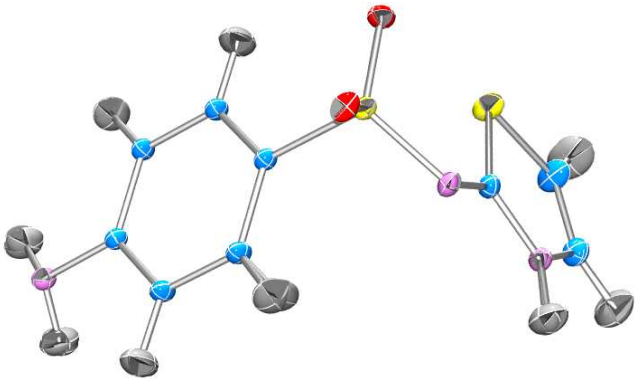

Figure 2.17. The adp superposition between neutron and SHADE[24] values for form II.

As mentioned in the first part of this section, the adp values also depend on the external motion. The high degree of similarity of the adps between forms II, III and IV may be a result of the common intermolecular interactions present in these forms as described in Section 2.3.1, Figure 2.11.

2.3.4.2. Theoretical calculation results of optimized structure of sulfathiazole, 1

The conformation of the optimized gas phase calculation using DFT methods will be compared with the experimental data in this section. Several basis sets have been tested (i.e. 6-31G, 6-311++G(2d2p), Def2-TZVPP,[48] cc-pVTZ[35]) and the optimizations were initiated from the CSD geometries. Only one optimized conformation was found from the gas phase calculations. For the 6-311++G(2d2p), Def2-TZVPP[48] and cc-pVTZ basis sets, the values of torsion angles are quite close to each other, but are slightly different for the 6-31G basis sets results. This is not surprising as the 6-31G basis set is a rather minimal basis set. However this was used as a starting point for the geometry optimisation, prior to performing calculations with larger basis set.

The hydrogen atoms of the N amino group were optimized in a planar position with the phenyl ring when the 6-31G basis set was used, which is clearly in disagreement with the experimentally determined solid state structures. The hydrogen atoms were orientated in the same direction as the O atoms relative to the phenyl ring in the optimized structures from the other basis sets apart from cc-PVTZ. In the case of more elaborate basis sets, such as cc-PVTZ, the optimized hydrogen atom positions were influenced by their starting geometry. For example, taking the geometry of form I with the H-atoms pointing in the same directions as the O atoms relative to the phenyl ring, they followed the same trend in the optimized geometry. On the other hand, if the starting geometry was selected from the

experimental structure of form II, with the hydrogen atoms pointing in the opposite direction compared with the O atoms and relative to the phenyl ring, the optimized geometry showed the same orientation of the hydrogen atoms as in the starting experimental model.

A large discrepancy can be observed between the torsion angles obtained from the experimental data and those obtained from gas phase calculations (Table 2.12, Figure 2.18). For example, the torsion angle O11-S11-C111-C116 of form II is found to be –6.26° from the experimental crystal structure data, while the optimized angle lies between 18.61° and 23.32°, depending on the functional used. This is not surprising when solid state experimental data are compared with gas phase optimisation data. For the isolated gas phase molecules, no intermolecular interactions exist but these effects clearly have an influence on the molecular conformation. The bond distances obtained from neutron diffraction data of form II and the theoretical calculations performed with different functionalities and basis sets are listed in Table 2.13. The experimental neutron diffraction data were compared with theoretical calculations and, overall, the optimized structure obtained using the PBEPBE/def2TZVPP and PBEPBE/ccpVTZ level of theory/basis set were closer to the experimental neutron structure. For this reason the wave function obtained with the PBEPBE/cc-pVTZ basis set was used for performing the topological analysis.

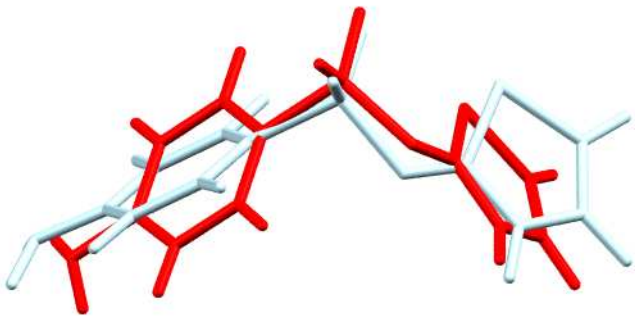

Figure 2.18. Best fit of form II with theoretical data: form II experimental model, red; theory, blue.

Table 2.12. Torsion angles obtained from theoretical calculations of sulfathiazole, **1,** forms I and II.

Torsion angle	**Starting Angle (CSD)**	**6-31G**	**6-311++G(2d2p)**	**Def2-TZVPP**	**cc-pVTZ**
Form I (a)					
B3LYP					
O11-S11-C111-C116	9.07	18.61	21.30	21.32	21.17
O11-S11-N10-C11	-33.81	28.70	5.51	5.17	6.21
S11-N10-C11-S12	-7.83	-8.74	-0.32	-0.35	-0.81
Form I (a)					
PBEPBE					
O11-S11-C111-C116	9.07	19.32	21.90	22.28	22.12
O11-S11-N10-C11	-33.81	24.07	5.04	4.74	6.30
S11-N10-C11-S12	-7.83	-8.69	-0.13	-0.22	-0.87
Form I (b)					
B3LYP					
O11-S11-C111-C116	-16.37	-15.65	-21.55	-21.33	-21.22
O11-S11-N10-C11	38.79	-26.82	-5.54	-5.19	-6.52
S11-N10-C11-S12	-0.02	8.02	0.33	0.36	0.93
Form I (b)					
PBEPBE					
O11-S11-C111-C116	-16.37	-19.18	-21.88	-22.27	-22.11
O11-S11-N10-C11	38.79	-24.04	-5.00	-4.74	-6.30
S11-N10-C11-S12	-0.02	8.67	0.11	0.23	0.86
Form II					
B3LYP					
O11-S11-C111-C116	-6.26	18.90	21.59	21.34	21.23
O11-S11-N10-C11	39.48	26.50	5.53	5.19	6.52
S11-N10-C11-S12	17.90	-8.01	-0.32	-0.6	-0.93
Form II					
PBEPBE					
O11-S11-C111-C116	-6.26	19.50	21.87	23.32	21.93
O11-S11-N10-C11	39.48	24.04	5.00	4.61	5.71
S11-N10-C11-S12	17.90	-8.68	-0.11	-0.17	-0.62

Table 2.13. Comparison of bond distances obtained using PBEPBE/def2-TZVPP and PBEPBE/cc-pVTZ level of theory and the neutron diffraction experiment of form II of sulfathiazole, **1**.

Bonds	Neutron data	B3LYP 6-311 ++G**	B3LYP def2TZ VPP	B3LYP ccp VTZ	PBEPBE 6-311 ++G**	PBEPBE def2TZ VPP	PBEPBE ccp VTZ
S(11)-O(11)	1.451(4)	1.461	1.451	1.465	1.478	1.467	1.481
S(11)-O(12)	1.451(4)	1.477	1.437	1.451	1.461	1.451	1.465
S(11)-N(10)	1.586(4)	1.654	1.641	1.658	1.667	1.653	1.673
S(11)-C(111)	1.765(4)	1.776	1.768	1.779	1.780	1.773	1.784
S(12)-C(13)	1.732(5)	1.761	1.751	1.758	1.760	1.751	1.758
S(12)-C(11)	1.745(5)	1.786	1.777	1.785	1.790	1.782	1.790
N(10)-C(11)	1.329(2)	1.291	1.291	1.290	1.302	1.301	1.301
N(11)-C(114)	1.406(2)	1.389	1.384	1.385	1.391	1.386	1.386
N(11)-H(11A)	1.018(4)	1.006	1.006	1.006	1.014	1.014	1.014
N(11)-H(11B)	1.018(5)	1.007	1.006	1.006	1.014	1.014	1.014
N(15)-C(11)	1.339(2)	1.367	1.366	1.366	1.374	1.373	1.374
N(15)-C(14)	1.383(2)	1.385	1.383	1.384	1.386	1.384	1.384
N(15)-H(15)	1.059(4)	1.007	1.007	1.007	1.014	1.015	1.015
C(13)-C(14)	1.347(3)	1.337	1.338	1.337	1.349	1.349	1.348
C(13)-H(13)	1.073(5)	1.075	1.076	1.075	1.083	1.084	1.084
C(14)-H(14)	1.100(5)	1.077	1.077	1.077	1.085	1.086	1.086
C(111)-C(116)	1.398(2)	1.392	1.393	1.391	1.399	1.399	1.398
C(111)-C(112)	1.400(2)	1.392	1.393	1.392	1.399	1.400	1.398
C(112)-C(113)	1.387(2)	1.384	1.383	1.383	1.390	1.389	1.389
C(112)-H(112)	1.088(4)	1.080	1.081	1.080	1.089	1.090	1.090
C(113)-C(114)	1.411(2)	1.403	1.403	1.403	1.410	1.410	1.410
C(113)-H(113)	1.085(4)	1.082	1.083	1.083	1.092	1.092	1.092
C(114)-C(115)	1.401(2)	1.402	1.402	1.402	1.410	1.410	1.410
C(115)-C(116)	1.398(2)	1.385	1.384	1.383	1.390	1.389	1.389
C(115)-H(115)	1.087(4)	1.082	1.083	1.083	1.092	1.092	1.092
C(116)-H(116)	1.076(4)	1.080	1.081	1.080	1.089	1.090	1.090

2.4. Analysis of the electron-density distribution

2.4.1. Description of molecular graph

The molecular graph descriptions, including the bond critical points (BCPs) formed between the atoms in the various forms of **1**, are illustrated in Figure 2.19. An unusual intramolecular BCP has been identified between O11 and S12 in each molecule of forms I, II, III and IV both in the experimental and the theoretical data (Figure 2.19). This unusual S···O interaction may be responsible for the different conformations that **1** can adopt. In Table 2.14, the torsion angles O11-S11-C11-S12 obtained from the experimental data are compared with the theoretical model. The torsion angle in the theoretical model is close to

zero, showing the co-planarity between the S11-O11 bond and the phenyl ring, while those for the experimental forms are higher (Table 2.14). A slight difference in this angle can be noticed between the molecules of form I and the others. The distance between the two atoms shows small variations between the forms, with their values lying between 2.8847(5) and 2.9847(5) Å. The optimized conformations show the shorter O11···S12 length, which is also reflected in the strength of the interactions between the atoms. The energy calculated at the bond critical point (using equation 1.51 described in Chapter 1) gives the lower energy for the optimized structure.

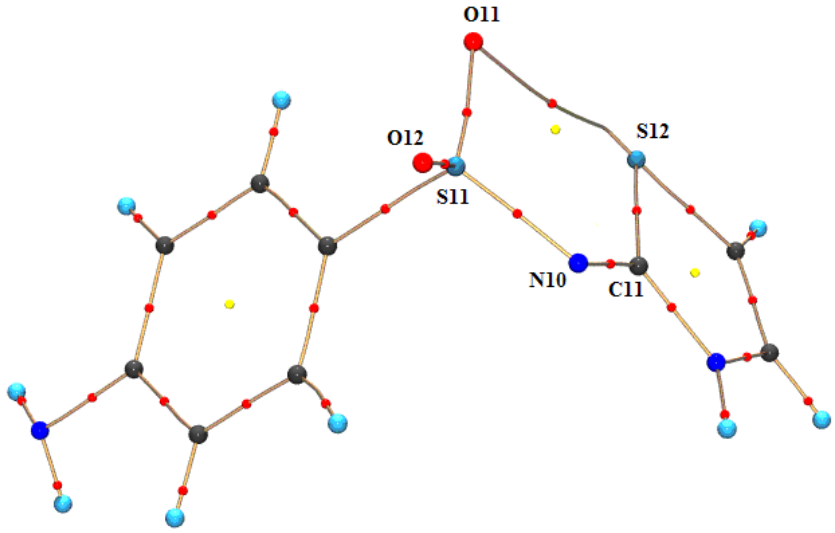

Figure 2.19. Molecular graph of sulfathiazole, **1**, from the experimental study showing the S···O bond critical point.

Table 2.14. Torsion angles, S–O bond length and the energy at the BCP obtained from experimental data and the theoretical model of the forms of **1**

	Torsion angle (˚) O(11)-S(11)-C(11)-S(12)	**Bond length (Å) O(11)-S(12)**	**Energy at the BCP (kJ/mol)**
Experimental data			
Ia	-36.73(3)	2.9847(5)	-18.8
Ib	-36.22(3)	2.9654(5)	-18.8
II	-21.76(2)	2.9160(4)	-18.8
IIIa	-20.99(2)	2.9297(4)	-18.8
IIIb	-22.15(2)	2.8734(4)	-18.8
IVapex	-22.17(2)	2.8842(4)	-15.6
IVkappa	-22.16(1)	2.8847(5)	-21.9
Theoretical model	5.56	2.708	-34.5

On the other hand, form IVapex, which shows a slightly shorter distance between the S and O atoms, has the highest energy at the BCP. Form IVkappa, on the other hand, was identified as having the lowest energy compared with the other experimental data forms.

The inconsistency between the IVapex and IVkappa may be due to the rather low quality X-ray data in the case of IVapex, which are reflected in the topological parameter results (below).

2.4.2. Laplacian representation

To examine further the nature of the S···O interactions, the negative Laplacian maps $L(\mathbf{r})$ in the O-N-S plane of **1** (four forms) and the theoretical model have been compared (Figure 2.20). They all show charge depletion on the S atoms and a continuous region of charge concentration around the O atom. The bond critical points of ρ have also been plotted and show that the path trajectory does not follow the depletion region around the S atom. The positive value of the Laplacian at the BCP between the two atoms may be an indication of the electrostatic nature of the O···S interaction and for this reason the electrostatic potential is now examined.

2.4.3. The electrostatic potential representation

The electrostatic potential is a quantity which can be measured using either X-ray diffraction or computed by *ab initio* methods. The definition of the electrostatic potential is given in equation 2.5:

$$V(r) = \sum_j \frac{Z_j}{r - R_j} - \int \frac{\rho(r)}{|r - r'|} dr' \qquad \text{eq. 2.5}$$

where R_j and Z_j represent the position and charge of the j-th nucleus, respectively. By generating the electrostatic potential on a surface or in regions of space, information about local polarity can be extracted. The electrostatic potential from a charge distribution can be expanded in terms of the electrostatic moments. A colour-coding convention is chosen for regions to depict the electrostatic surface. Mapping of a three-dimensional electrostatic potential over the molecular surface of charge densities clearly brings out the difference in electrostatic potential between the atoms.

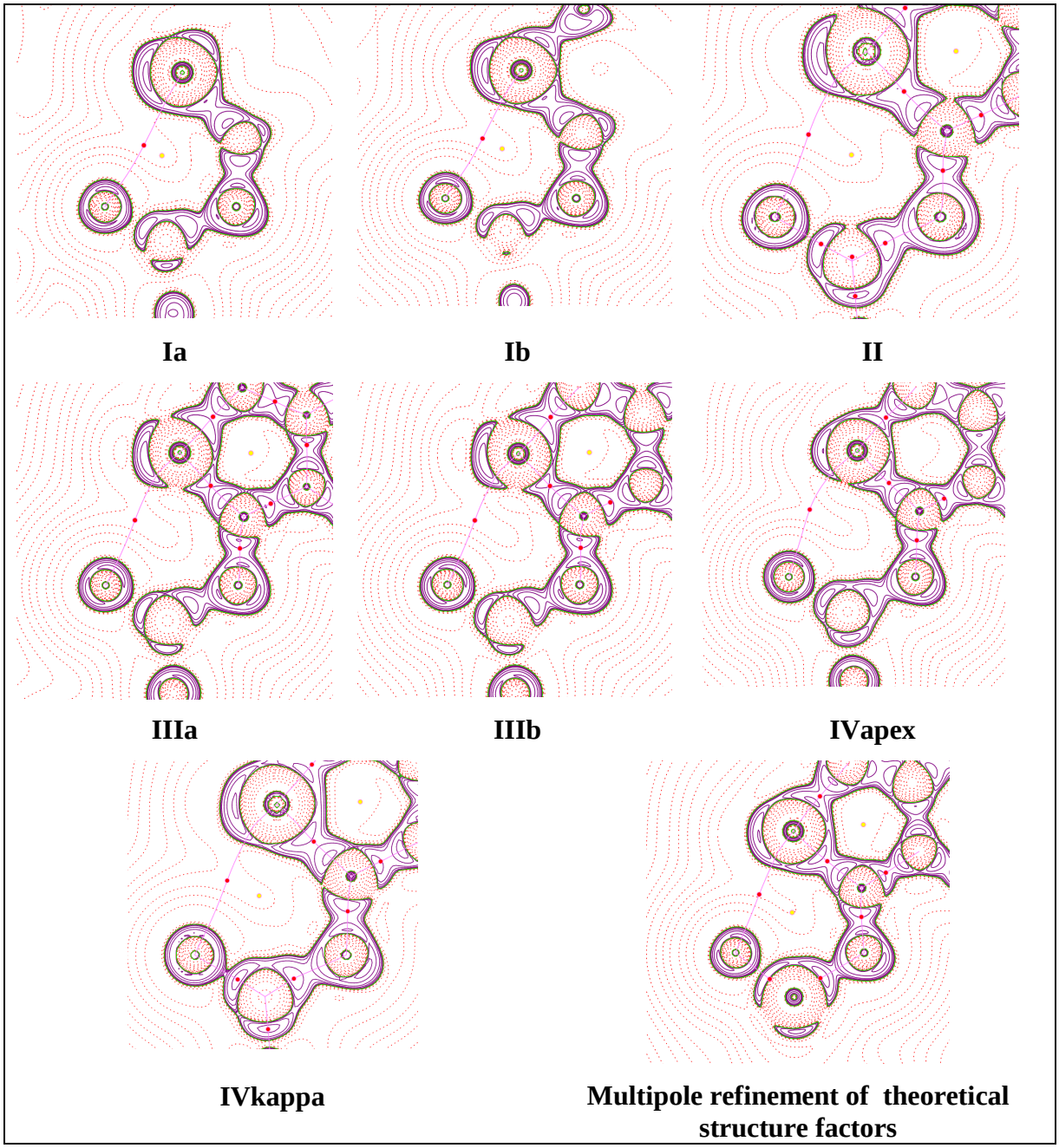

Figure 2.20. Plots of the negative Laplacian, $L(\mathbf{r})$ in the O-N-S planes of form I molecules 1 and 2, form II and the theoretical model of **1**: Positive contours – solid purple line; negative contours – dotted line. The contour levels are at -1.0 x 10^{-3}, ±2.0 x 10^{n}, ±4 x 10^{n}, ± 8 x 10^{n} (n = -3, -2, -1, 0, +1, +2) e Å^{-5}

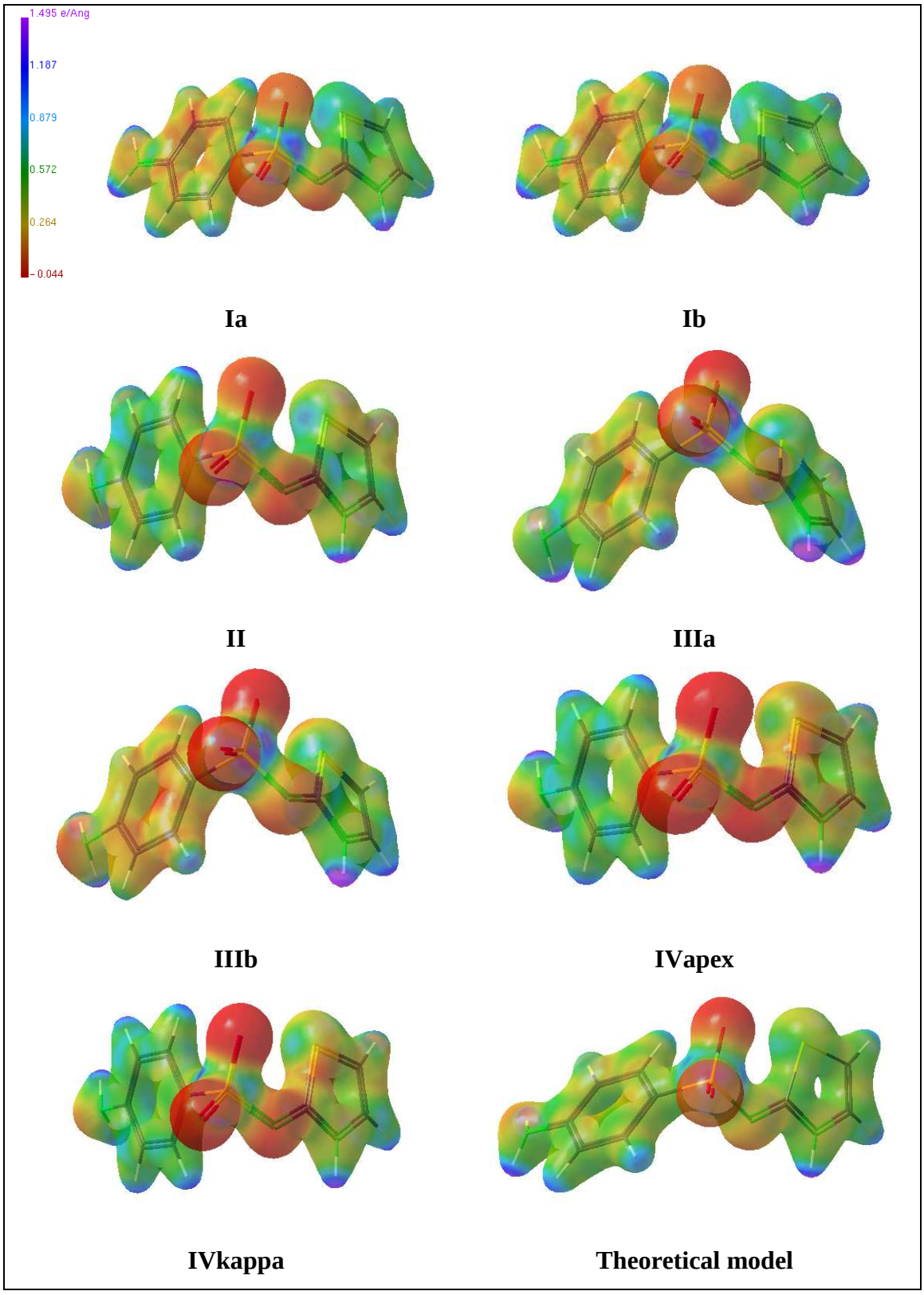

Figure 2.21. Electrostatic potential ($eÅ^{-1}$) mapped on an electron density isosurface (value of isosurface $0.5eÅ^{-3}$) (a), (b), (c), (d). The potential at $+1.49eÅ^{-1}$ is shown in blue and $-0.04eÅ^{-1}$ in red.

The electrostatic potentials are displayed for the studied forms of **1** in Figure 2.21, where the net positive potential is shown in blue and net negative potential in red, with intermediate gradation of colour i.e yellow or green. The electrostatic potential represented here for **1** has been drawn at a 0.1 a.u. isosurface and the deep red colour corresponds to the value of −0.044 a.u., whereas the deep blue colour corresponds to +1.495 a.u. The S atom region, represented by a blue surface on the electrostatic potential, indicates the positive potential area while a negative region for the oxygen atom can be observed. Therefore, the electrostatic potential indicates that the regions of S and O atoms involved in the S···O interaction show opposite electrostatic potentials. This result is consistent with the nature of the S···O interaction as an intramolecular electrostatic type.

2.4.4 Analysis of topological parameters

A detailed comparison between the topological parameters obtained from experimental data and those obtained from theory will now be given. One reason for doing this is to ascertain the effect of the minor disorder noted in the case of forms I and II.

Discrepancy between the topological parameters obtained from the experimental charge density and theory has been reported in many studies.[49-53] This discrepancy has been attributed to various effects including the inadequacy of the theoretical basis sets, the effect of the crystal lattice due to theoretical calculations being realised for isolated molecules, and deficiency in the multipole model. The topological parameters from the experimental data were compared in the present work with those directly determined from the wave functions of the gas phase calculations as well as with the multipole model based on the refinements of the theoretical structure factors.

The distance (in Å) of the BCP to the nuclei denoted by d_1 and d_2, the electron density ρ, the Laplacian at the BCP, $\nabla^2\rho$, and the three eigenvalues $\lambda_1, \lambda_2, \lambda_3$ of the Hessian matrix of selected atoms from all studied forms are listed in Table 2.15. The most affected bonds (in terms of differences between the parameters evaluated for different models) are H-N (aniline) and S-O, perhaps as a result of these atoms being involved in strong hydrogen bonding. Large discrepancies are observed for λ_3 in S(11)-O(11) bonds when experimental data of the forms are compared with topological parameters obtained from multipole refinement of the theoretical structure factors. If the density from the wave functions is taken as a reference, the λ_3 values are much closer to those obtained from experimental data. In S(11)-O(12) bonds, large differences can be seen between experimental λ_3 values

and those obtained by multipole refinement of theoretical structure factors. The values of λ_3 for all forms are closer to those obtained from the pure wave function. As a consequence, these discrepancies will also be reflected in the $\nabla^2\rho$ values, as λ_1 and λ_2 are more similar for experimental and theoretical data. The H(11A)-N(11) and H(11B)-N(11) bonds involved in strong hydrogen contacts are also more affected, as in an isolated molecule the interactions with its surroundings are negligible.

The C(111)-S(11), S(12)-C(11) and S(12)-C(13) bonds which are not involved in hydrogen bonds are less affected. The topological parameters of those atoms that are involved in non-polar interactions gave better agreement between experimental data and theoretical calculations (theoretical calculations are considered as both pure wave function and multipole refinement of the theoretical structure factors obtained from the gas phase optimization). For example, the values of ρ and $\nabla^2\rho$ of the experimental data and theory in the C113-C114 bond of form IIIa are 2.09 eÅ^{-3}, −17.87 eÅ^{-5} and 2.02 eÅ^{-3}, −15.74 eÅ^{-5}, respectively. In a polar bond such as S(11)-O(11) in the same form, these values are 2.06 eÅ^{-3}, 18.06 eÅ^{-5} and 1.96 eÅ^{-3}, 2.25 eÅ^{-3}, respectively. The fact that the S(12) atom in form I and II was identified as having disorder is not reflected in either of the S(12)-C(11) or S(12)-C(13) bonds; the experimental topological parameters for these bonds were in good agreement with theoretical data,. The experimental values of the charge density and the position of BCPs (d_1 and d_2) are more similar with the theory compared with the Laplacian values.

Table 2.15. Topological Analysis of Bond Critical Points for the polymorphs of **1**

Bond	d_1[a]	d_2[a]	$\rho(r_b)$[b]	$\nabla^2 \rho(r_b)$[c]	λ_1[c]	λ_2[c]	λ_3[c]
S(11)-O(12)	0.5714	0.8736	2.08	19.34	-12.74	-12.67	44.76
	0.5712	0.8729	2.09	19.51	-12.79	-12.68	44.98
	0.5750	0.8751	1.99	19.30	-12.23	-10.31	41.83
	0.5743	0.8745	2.06	18.06	-12.83	-11.41	42.31
	0.5748	0.8757	2.06	17.71	-12.78	-11.33	41.83
	0.5852	0.8679	2.36	3.69	-13.53	-13.23	30.44
	0.5736	0.8789	2.13	15.96	-12.92	-12.54	41.43
	0.5829	*0.8979*	*1.937*	*14.311*	*-10.960*	*-10.711*	*35.982*
	0.6098	*0.8711*	*1.96*	*2.25*	*-10.12*	*-9.91*	*22.29*
S(11)-N(10)	0.5947	1.0141	1.63	7.82	-7.71	-7.51	23.04
	0.5971	1.0223	1.62	6.51	-7.58	-7.37	21.46
	0.6099	0.9865	1.84	-3.00	-10.68	-7.78	15.45
	0.6249	0.9725	1.86	-8.83	-10.00	-8.82	9.99
	0.6318	0.9762	1.85	-10.58	-9.88	-8.72	8.01
	0.6133	0.9944	1.80	-2.87	-8.09	-7.73	12.96
	0.5951	1.0132	1.72	4.86	-8.53	-8.09	21.48
	0.7383	*0.9355*	*1.557*	*-13.893*	*-9.020*	*-8.401*	*3.528*
	0.6520	*1.0227*	*1.46*	*-7.12*	*-5.92*	*-5.67*	*4.47*
C(111)-S(11)	0.8119	0.9369	1.50	-10.98	-8.83	-7.65	5.50
	0.8117	0.9361	1.51	-11.02	-8.83	-7.67	5.48
	0.7887	0.9731	1.51	-9.94	-8.58	-8.10	6.74
	0.8188	0.9447	1.52	-11.15	-9.14	-7.69	5.68
	0.8193	0.9445	1.52	-11.16	-9.16	-7.68	5.68
	0.7768	0.9884	1.55	-10.38	-9.20	-7.96	6.77
	0.8135	0.9517	1.53	-11.24	-8.90	-8.02	5.68
	0.8262	*0.9581*	*1.381*	*-9.008*	*-8.560*	*-7.844*	*7.397*
	0.8465	*0.9378*	*1.35*	*-7.41*	*-7.25*	*-6.73*	*6.57*
C(11)-S(12)	0.8587	0.8832	1.37	-6.19	-7.34	-5.89	7.04
	0.8552	0.8822	1.38	-6.35	-7.38	-5.93	6.96
	0.8462	0.9017	1.31	-6.44	-7.17	-5.26	5.99
	0.8536	0.8934	1.29	-6.06	-6.92	-5.37	6.23
	0.8510	0.8927	1.29	-6.14	-6.94	-5.39	6.19
	0.8548	0.8921	1.44	-5.94	-8.34	-6.30	8.70
	0.8597	0.8868	1.39	-7.01	-7.57	-6.23	6.79
	0.8734	*0.9164*	*1.272*	*-6.523*	*-7.247*	*-5.787*	*6.511*
	0.8779	*0.9127*	*1.26*	*-4.93*	*-6.71*	*-5.59*	*7.37*
S(12)-C(13)	0.8517	0.8834	1.37	-6.14	-7.45	-6.03	7.35
	0.8531	0.8869	1.36	-5.95	-7.37	-6.00	7.42
	0.8439	0.9012	1.42	-5.52	-8.16	-5.93	8.56
	0.8313	0.9119	1.45	-5.81	-8.31	-6.59	9.10
	0.8300	0.9099	1.45	-5.91	-8.36	-6.62	9.07
	0.8554	0.8883	1.33	-3.78	-7.32	-5.37	8.91
	0.8493	0.8934	1.37	-5.98	-7.28	-5.97	7.27
	0.8510	*0.9070*	*1.338*	*-7.734*	*-7.485*	*-6.307*	*6.058*
	0.8758	*0.8828*	*1.27*	*-5.00*	*-6.44*	*-5.34*	*6.78*

Table 2.15. Continued

H(11A)-N(11)	0.2734	0.7467	2.20	-29.53	-28.98	-27.48	26.93
	0.2735	0.7466	2.20	-29.66	-29.10	-27.47	26.91
	0.2667	0.7516	2.26	-33.82	-30.19	-29.43	25.80
	0.2899	0.7282	2.21	-31.01	-28.39	-27.43	24.80
	0.2885	0.7296	2.22	-31.50	-28.73	-27.65	24.88
	0.2754	0.7387	2.34	-35.79	-31.40	-30.49	26.10
	0.2850	0.7266	2.23	-27.59	-28.27	-27.09	27.77
	0.2698	*0.7442*	*2.309*	*-41.386*	*-31.724*	*-30.341*	*20.680*
	0.2935	*0.7206*	*2.22*	*-24.31*	*-27.86*	*-26.08*	*29.62*
H(11B)-N(11)	0.2726	0.7474	2.20	-29.84	-29.13	-27.66	26.95
	0.2725	0.7475	2.20	-29.97	-29.21	-27.70	26.94
	0.2735	0.7438	2.21	-31.13	-28.74	-27.83	25.44
	0.2846	0.7535	2.22	-31.73	-29.18	-28.14	25.59
	0.2844	0.7517	2.22	-31.74	-29.17	-28.21	25.64
	0.2917	0.7455	2.23	-30.84	-28.44	-27.55	25.16
	0.2974	0.7407	2.13	-24.01	-26.05	-24.98	27.01
	0.2698	*0.7443*	*2.309*	*-41.388*	*-31.723*	*-30.341*	*20.676*
	0.2941	*0.7199*	*2.21*	*-24.17*	*-27.75*	*-25.97*	*29.55*
C(114)-C(113)	0.6988	0.7105	2.11	-18.64	-16.30	-13.30	10.95
	0.6987	0.7107	2.11	-18.63	-16.28	-13.31	10.96
	0.6951	0.7130	2.18	-19.89	-16.80	-14.08	10.98
	0.7004	0.7063	2.09	-17.87	-16.17	-13.00	11.30
	0.7003	0.7061	2.09	-17.90	-16.19	-13.00	11.29
	0.6942	0.7150	2.20	-20.40	-17.33	-14.27	11.21
	0.6911	0.7183	2.13	-18.63	-16.52	-13.69	11.58
	0.6801	*0.7302*	*2.067*	*-22.577*	*-16.027*	*-13.424*	*6.874*
	0.6872	*0.7230*	*2.02*	*-15.74*	*-15.35*	*-12.57*	*12.18*

First seven lines correspond to Form Ia, Form Ib, Form II, Form IIIa, Form IIIb, Form IVapex, Form IVkappa, Last two lines (italic) correspond to reference density from wave function and reference density from theoretical structure factor respectively. [a] *In units of Å.* [b] *In units of e Å*$^{-3}$. [c] *In units of e Å*$^{-5}$.

2.4.5 Analysis and comparison of the multipole refinements.

In this section the agreement improvements between the experimental data and theoretical calculations as the sophistication of the model is increased will be examined, with a particularly interest in the effects of the minor disorder on the derived parameters.

Five different multipole models refined from the experimental data (1, 2, 3, 4, 5), as described in Section 2.3, were compared with the topological parameter analysis of the wave function of the gas phase calculations (a), as well as with the multipole model based on the refinements of the theoretical structure factors (b). The charge densities and the Laplacian at the BCPs of each experimental and theoretical model were compared. As the volume of data is too large to see the trends clearly (Table 2.15), a residual factor R_{Par} was

calculated in order to describe the global measurement of the agreement between experimental and theoretical parameters, using equation 2.6:

$$R_{Par} = \frac{\sum_{i=1}^{n} (par_i(\text{mod}) - par_i(th))}{\sum_{i=1}^{n} (par_i(th))} \qquad \text{eq. 2.6}$$

where par_i is the value of the parameter being summed (i.e. ρ, $\nabla^2\rho$). The R_{val}, R_ρ and $R_{\nabla 2(\rho)}$ values for all four studied forms of **1** are summarized in Table 2.16. The R_{val} is seen to decrease in all the forms when anisotropic parameters for H atoms are used (either from Shade or neutron diffraction data). The lowest values can be observed for the unrestricted models (3 and 5). The best refinement was obtained for form IV with the lowest R_{val} (1.41 – model 5). In most of the cases, when the reference density of the wave function is used, the R_ρ values are lowest for the first model and there is a trend in the decrease of these values from model 3-2-1 and from 5-4-1. The values of $R_{\nabla 2(\rho)}$ conversely, are found to decrease from 1-2-3 or 1-4-5. A low value of R_ρ (e.g. 0.0001) proves to represent a very good agreement between experimental data and theoretical calculations. In the second case, when the multipole model of the theoretical structure factor was chosen as a reference, the same trend can be observed for R_ρ values, which are lowest for model 1 in all studied forms. The R_ρ values are lower for models 4 and 5 compared with models 2 and 3. This comparison shows that using adps from the neutron data experiment gives a slightly better agreement with theory than the refinements in which adps are taken from SHADE.[24,26] The Laplace $R_{\nabla 2(\rho)}$ values are also lowest for model 1 but in this case decrease in the model order 3-2-1 and 5-4-1. As with the R_ρ values, the Laplace $R_{\nabla 2(\rho)}$ values are smaller in models 4 and 5 than in models 3 and 2 in all the studied forms. The difference between R_{val} and R_{Par} for forms III and IV, which are ordered, are indistinguishable compared with those in forms I and II which are disordered. This indicates that the topological parameters in forms I and II are not affected by the minor disorder at the S atom.

Table 2.16. The residual factor of the experimental data vs theoretical calculations of form I (molecule 1 and 2) and II of **1**

(a) Reference density from wave function	**Model**	$\mathbf{R_{values}}$	$\mathbf{R_{\rho}}$	$\mathbf{R_{\nabla 2(\rho)}}$
Ia	1	0.0248	0.0125	0.2430
	2	0.0244	0.0009	0.2035
	3	0.0242	0.0021	0.2029
Ib	1		0.0116	0.2412
	2		0.0001	0.2020
	3		0.0031	0.2012
II	1	0.0186	0.0127	0.2847
	2	0.0183	0.0018	0.2303
	3	0.0178	0.0042	0.2053
	4	0.0183	0.0047	0.2347
	5	0.0177	0.0015	0.2096
IIIa	1	0.0262	0.0058	0.2743
	2	0.0259	0.0098	0.1983
	3	0.0258	0.0103	0.1804
	4	0.0259	0.0074	0.2069
	5	0.0258	0.0085	0.1837
IIIb	1		0.0047	0.2671
	2		0.0110	0.1907
	3		0.0114	0.1726
	4		0.0084	0.1992
	5		0.0096	0.1757
IVapex	1	0.0227	0.0087	0.2519
	2	0.0219	0.0414	0.1501
	3	0.0214	0.0459	0.1564
	4	0.0219	0.0347	0.1724
	5	0.0215	0.0390	0.1776
IVkappa	1	0.0148	0.0068	0.2775
	2	0.0142	0.0096	0.2099
	3	0.0139	0.0111	0.2065
	4	0.0144	0.0040	0.2377
	5	0.0141	0.0056	0.2318

Table 2.16. Continued

(b) Reference density from theoretical structure factor				
Form Ia	1	0.0248	0.0140	0.1670
	2	0.0244	0.0259	0.2280
	3	0.0242	0.0290	0.2288
Form Ib	1		0.0149	0.1699
	2		0.0268	0.2303
	3		0.0300	0.2316
Form II	1	0.0186	0.0138	0.1028
	2	0.0183	0.0250	0.1867
	3	0.0178	0.0312	0.2251
	4	0.0183	0.0221	0.1798
	5	0.0177	0.0284	0.2186
Form IIIa	1	0.0262	0.0209	0.1188
	2	0.0259	0.0369	0.2360
	3	0.0258	0.0374	0.2635
	4	0.0259	0.0344	0.2228
	5	0.0258	0.0356	0.2585
Form IIIb	1		0.0220	0.1298
	2		0.0382	0.2477
	3		0.0385	0.2756
	4		0.0355	0.2345
	5		0.0367	0.2707
Form IVapex	1	0.0227	0.0358	0.1533
	2	0.0219	0.0693	0.3103
	3	0.0214	0.0740	0.3006
	4	0.0219	0.0625	0.2759
	5	0.0215	0.0669	0.2679
Form IVkappa	1	0.0148	0.0199	0.1139
	2	0.0142	0.0367	0.2182
	3	0.0139	0.0383	0.2233
	4	0.0144	0.0309	0.1753
	5	0.0141	0.0326	0.1843

1 –restricted multipole refinement- isotropic adps of H atoms, 2- restricted multipole refinement –anisotropic adps from SHADE of H atoms, 3 – unrestricted multipole refinement –anisotropic adps from SHADE of H atoms, 4- restricted multipole refinement –anisotropic adps from neutron diffraction of H atoms, 5 – unrestricted multipole refinement –anisotropic adps from neutron diffraction of H atoms.

2.5. Lattice and intermolecular interaction energy calculations

The main focus of this research is to estimate lattice and intermolecular interaction energies, in order to classify the relative stability of the studied forms of **1**. Lattice energy

is the energy required to separate one molecule (or asymmetric unit) from the crystal. As such, the lattice energy is a measure of the strength of the intermolecular bonds. In the present study, the lattice energy was calculated using different approaches and different software, including experimental charge density and theoretical calculations. In the case of theoretical calculations, the lattice energy is estimated as the sum between the molecular interaction energy E1 and the molecular relaxation energy E2 introduced by Abramov *et al.*[54]

$$E_L = E1 + E2 \qquad \text{eq. 2.7}$$

where

$$E1 = E_{mol}(\text{crystal}) - E_{mol}(\text{gas,crystal geometry}) \qquad \text{eq. 2.8}$$

$$E2 = E_{mol}(\text{gas,optimized geometry}) - E_{mol}(\text{gas,crystal geometry}) \qquad \text{eq. 2.9}$$

The interaction energy has been evaluated as a difference between the energy of the molecule in the crystal (E_{mol}(crystal)) and the energy of an isolated molecule with the crystal geometry. These energies in the present work were calculated using the CRYSTAL09[39] package. Dispersion energy corrections and BSSE (basic set superposition error) corrections incorporated in the CRYSTAL09[39] program were applied.

The relaxation energy represents the difference in energy of an isolated molecule with optimized geometry and that of an isolated molecule with crystal geometry. These energies were evaluated using the Gaussian03[36] program. All the calculations were performed using the DFT method, at the B3LYP/6-31G** level. A comparison between lattice energies obtained from the experimental charge density approach and theoretical calculations on different compounds were previously presented in the literature.[54] Relatively good agreements were obtained in that work between the two approaches; the larger difference being 9.4 kJ/mol. However, no polymorphic materials were studied. Therefore, the assumption cannot be made that this method can be applied to the type of materials under study here.

The relative stabilities of a polymorphic material, arylbromic azaester - 6-butyl-2-(4′-bromophenyl)-(N-B-1,3,6,2 diozoboracane), which has two known forms, have been calculated[55] using CRYSTAL09[39] and CLP.[41] The lattice energy obtained for form I in CRYSTAL09[39] was −150.8 kJ/mol and with CLP[41], −156.2 kJ/mol. In the case of form II, a value of −277.3 kJ/mol was obtained with CRYSTAL09[39] and −293.8 kJ/mol with

CLP,[41] giving a 16 kJ/mol difference between the lattice energy values obtained using the two different programs for form II. The results, however, shows that the lattice energy difference between the forms is relatively large and thus the most stable form can be clearly distinguished as both programs shows the same trends. The same approaches as those described above and additionally the experimental charge density approach (ECD) will be used here, with the purpose of finding the most stable form of **1**.

The LATEN option in the xdprop section incorporated in the XD program[21] was used for calculating the lattice energy from the ECD. This method calculates the intermolecular interaction energy between the reference molecule in the asymmetric unit and the surrounding molecules within the crystal. The interaction energy is calculated as a sum between the electrostatic, exchange-repulsion, dispersion and induction terms:[56]

$$E_{int} = E_{es} + E_{ex\text{-}rep} + E_{disp} + E_{ind} \qquad \text{eq. 2.10}$$

The electrostatic term was obtained from a combination of the exact potential and multipole methods (EP/MM).[57] The multipole method is used for non-overlapping charge distribution with pseudoatoms in the outer region having the expression:[58,59]

$$E_{es}^{mul}(AB) = Tq_a q_b + T_\alpha (q_A \mu_{\alpha B} - q_B \mu_{\alpha A}) + T_{\alpha\beta}(\frac{1}{3} q_A \Theta_{\alpha\beta,B} + \frac{1}{3} q_b \Theta_{\alpha\beta,A} - \mu_{\alpha A}\mu_{\beta B}) + \ldots \quad \text{eq. 2.11}$$

Where q, μ_α and $\Theta_{\alpha\beta}$ are charge, dipole and quadrupole atomic electrostatic moments, and $T_{\alpha\beta\ldots\nu} = (4\pi\varepsilon_0)^{-1}\nabla_\alpha\nabla_\beta\ldots\nabla_\nu R_{AB}^{1}$ is a Cartesian tensor.

For the inner sphere the exact potential term is used (eq. 2.12) for calculating the pseudoatom – pseudoatom interactions which evaluates the exact Couloumb integral:[60]

$$E_{es} = \iint \frac{\rho^A(r_A)\rho^B(r_b)}{|r_A - r_B|} dr_A dr_B \qquad \text{eq. 2.12}$$

The electrostatic term is calculated exactly whereas the exchange-repulsion and dispersion terms were approximated by using the approximation of the atom-atom potential-energy of Williams & Cox (1984).[61] The induction term for the experimental results is incorporated in the electrostatic energy.

Table 2.17. Lattice energy (kJ/mol) of experimental charge density of the studied polymorphs of **1** obtained with the LATEN option in XD[21]

	Form	**I**	**II**	**III**	**IVapex**	**IVkappa**
Model						
1		-114.4	-116.16	-131.8	-205.19	-152.12
2		-174.91	-181.06	-217.03	-325.36	-196.60
3		-183.39	-209.17	-229.57	-336.33	-207.58
4			-176.88	-214.41	-333.74	-191.95
5			-204.96	-230.3	-353.36	-206.36

The lattice energy calculations resulting from all types of refinements used for each form are presented in Table 2.17. As can be seen from this table, the lattice energy results are influenced by the type of refinement applied. The highest values of the lattice energy were obtained when the multipoles for H atoms were refined only to the dipole level and when only κ parameters for the non-hydrogen atoms were refined. The energy decreased by refining the multipole parameters for hydrogen atoms to the quadrupole level and all κ and κ' for all atoms were refined. The unrestricted multipole model seems to give lower energy when compared with those refinements where local mirror symmetry was imposed in the multipole model. The same trend can be identified in models 2, 4 and 5, the lattice energy increasing in the order IVapex > III > IVkappa > II > I. In models 1 and 3, the order of the polymorph stability is changed to IVapex > IVkappa >III > II > I and IVapex > III > II > IVkappa > I, respectively. The difference in energy between the forms in general is quite substantial. For example, in model 2 the difference between the calculated lattice energies for forms II and IVkappa is 15 kJ/mol. However, much closer energy values were obtained for models 3 and 5 between these two forms (as low as 1.4 kJ/mol). The slightly larger difference in energies between the forms found for the experimental data, may arise from the difficulties in refinement of all the κ and κ' parameters. This can be a consequence of the repeated refinement of the x,y,z and Uij parameters, together with the multipoles, before introducing the adps from neutron data for H atoms (model 1); the initial x,y,z position of the spherical refinement was used to scale the X-ray and neutron data for obtaining the anisotropic parameters for H atoms. Therefore introducing the adps scaled from the spherical refinement after multipoles model refinement together with x,y,z and Uij parameters may have an influence on the convergence of the κ and κ' parameters. In order to investigate this problem of refinement, a set of restricted multipole model refinements were carried out, in which the positional parameters and the harmonic adps were refined only once and independently of multipoles. In the next step the adps for H atoms were added and the multipoles for the H atoms were refined at the quadrupole level.

A kappa restricted multipole model (KRMM) was also performed, in which a fixed set of κ and κ' parameters were used, obtained from the theoretical structure factor multipole refinement based on CRYSTAL09[39] calculations. The results presented in Table 2.18 contain the lattice energies obtained with the CLP[41] program, CRYSTAL09[39] and the theoretical approach, which includes the relaxation energy (E_L).

Two methods have been incorporated in the CLP[41] program for calculating the lattice energy: atom-atom energy CLP[41] (AA-CLP) and PIXEL. Both methods are based on the division of the total energy into Coulombic, polarisation, dispersion (London) and repulsion (Pauli) terms. The total energy of AA-CLP is described by equation 2.13:[41]

$$E_{ij} = 1/(4\pi\varepsilon^o)(q_i q_j) R_{i,j}^{-1} - F_P P_{i,j} R_{i,j}^{4} - F_D D_{i,j} R_{i,j}^{6} + F_R T_{i,j} R_{i,j}^{12} \qquad \text{eq. 2.13}$$

Where, $R_{i,j}$ represent the internuclear distance, $q_i = F_Q q_i^o$ is the rescaled net charge population on atom i, and F_Q, F_P, F_D, F_R are empirical disposable scaling parameters. P, D and T are coefficients calculated on the basis of the local environment of an atom on a given molecule. The Coulombic term in the AA-CLP method is represented by the local atomic point charge obtained from the Mulliken population analysis extended Hückel wave function.[62] In the second method (PIXEL) the intermolecular energy is evaluated through a distributed charge description. This requires an evaluation of the charge density by quantum chemistry methods. The charge q in the electrostatic term is evaluated as a product between the electron density and the volume, $q = \rho V$. In addition, the charge at the nucleus Z is introduced. To illustrate this, if an example molecule A is taken, with electron density ρ_k and volume V_k centred at point k and assigned charge $q_k = \rho_k V_k$; the charge of the N_A nuclei of molecule A at point j is denoted Zj. Another given molecule B is introduced with $q_i = \rho_i V_i$ at point i and charge Z_m. Thus, molecule A can generate an electrostatic potential at point i of the charge density of molecule B:[63]

$$\Phi_i = 1/4\ (\pi\varepsilon^o)[\ \Sigma_k q_k/R_{ik} + \Sigma_j Z_j/R_{ij}] \qquad \text{eq. 2.14}$$

where R_{ik} is the distance between the i and k points. The potential generated by molecule A at nucleus m of molecule B is described as:

$$\Phi_m = 1/4\ (\pi\varepsilon^o)[\ \Sigma_k q_k/R_{km} + \Sigma_j Z_j/R_{jm}] \qquad \text{eq. 2.15}$$

The total electrostatic potential energy between the two molecules is thus a sum between their electrostatic energies at point i ($E_i = q_i\Phi_i$) and at point m ($E_i = Z_m\Phi_m$). In consequence, the Couloumbic energy is a parameterless quantity, and the accuracy depends on the wavefunction description. The penetration energies are also taken into consideration, making the PIXEL method largely superior to the point-charge Couloumbic energy. The polarisation term in AA-CLP is also less accurate as the many body-field effects are neglected. The dispersion terms gave similar results as a similar approach was used in both cases. MP2/631G** and DFT/B3LYP/631G** methods were used for performing the wavefunction calculations for the studied forms of **1**.

Using the new strategy for refinement of the multipole model, in which the positional parameters and the harmonic adps were refined only once and independently of multipoles, closer agreement between the values for ECD multipole refinements of lattice energy were obtained (Table 2.18). When KRMM refinements were again applied, slightly larger differences could be observed. The atom-atom CPL results seem to be in the same range as the results obtained using ECD-KRMM. Similar results were obtained for PIXEL/MP2/631G** and PIXEL/B3LYP/ 631G** calculations, however the order of the relative stability of the forms is not maintained in comparison with the E1 results. A remarkable similarity was found between form III and IVkappa in the PIXEL calculation results, their energy difference being only 0.3 kJ/mol. Even closer energy agreement was obtained between form II and III for E_L calculations. The energy difference in this case was only 0.01 kJ/mol. Therefore, challenges arose in estimating the lattice energies even when using programs based on fully theoretical calculation methods.

Table 2.18. Lattice energy calculation results for **1**, using different programs and approaches (kJ/mol).

Form	**ECD**	**ECD -KRMM**	**atom-atom CLP[41]**	**PIXEL/ MP2/ 631G****	**PIXEL/ B3LYP/ 631G****	**E1**	**E_L**
I	-164.69	-180.01	-182.6	-212.5	-210.2	-213.08	-168.23
II	-162.42	-174.77	-170.6	-229.7	-226.0	-224.82	-179.22
III	-167.77	-191.98	-181.6	-227.5	-223.9	-225.97	-179.23
IVkappa	-163.91	-178.34	-191.4	-227.2	-223.6	-222.41	-180.19

In order to identify the best combination of ECD and theory, a very accurate intermolecular interaction energy calculation, between the two molecules in the asymmetric unit of form III, was carried out.

An MP2 complete basis set (CBS) limit was estimated using results from aug-cc-pVTZ and aug-cc-pVQZ basis sets. The HF component of the energy was extrapolated using the formula of Karton[64] and the correlation energies were extrapolated using the formula of Halkier.[65] All of these calculations included the counterpoise correction.

A correction for CCSD(T) correlation was also computed. This was performed at the DF-LCCSD(T0)/aug-cc-pVDZ level, comparing the correlation energy with that from DF-LMP2/aug-cc-pVDZ. The difference in correlation energy was then added to the MP2/CBS total energies. Counterpoise corrections were not used, as the local correlation methods are BSSE free. These calculations were carried out by Dr Grant Hill. The CPS(T) results were compared with DFT calculations at B3LYP and B97-D[66]/def2 –TZVPP level.

Table 2.19. Intermolecular interaction energy of molecules present in the asymmetric unit of form III (kJ/mol)

	ECD-KRMM	E_{int}(DFT) B3-LYP	E_{int}(DFT) B97-D	CBS(T)
Intermolecular interaction energy – form III	-30.37	-73.31	-67.58	-65.93

The CBS(T) calculations are in good agreement with those from DFT/B97-D. A slightly bigger discrepancy can be seen when B3LYP functionality was used instead (7.38 kJ/mol) (Table 2.19). The lattice energies estimated with experimental charge density gave a 35 kJ/mol difference within the CBS(T) calculations. If the x,y,z and U_{ij} parameters are kept fixed (using the x,y,z that were used in theoretical calculations) and the multipoles and kappa parameters refined again, starting from default values, the E_{int} obtained was −23.30 kJ/mol. Another cycle of refinement of the same parameters resulted in E_{int} decreasing to −32.05 kJ/mol. Two more cycles were run in which E_{int} further reduced to −41.40 and −50.71 kJ/mol. No further refinements were possible as the kappa parameters do not reach convergence criteria. As a consequence of repeating the multipole and kappa parameter refinements, the gap between theoretical calculations and ECD decreased to 15.22 kJ/mol. The total lattice energy was −222.165 kJ/mol, in the last cycle, which gave significantly better agreement with the PIXEL and E_L' results (−227.5 and −225.97 kJ/mol, respectively).

The same type of refinement was considered for the other forms as well, to confirm the results obtained for form III. Only three-repeated refinements were afforded for form I, as

the kappa parameters were not meeting the criteria for convergence in the next refinement. The E_{int} was modified in those few steps from −5.26 kJ/mol to −14.28 kJ/mol, in the last refinement. The estimation of E_{int} as −32.65 kJ/mol using DFT/B97-D/def2-TZVPP level of theory gave a discrepancy of 18.37 kJ/mole with the ECD results. The total lattice energy in this case was −198.75 kJ/mol, a difference of 14.33 kJ/mol with that from the E_L' calculations. Therefore, a less satisfactory agreement between experimental and theoretical calculations was obtained for form I. It was not possible to evaluate the repeating refinement strategy for forms II and IV, since in neither case did the kappa parameter refinement satisfy the convergence criteria after more than one cycle.

The intermolecular interaction energies between the two molecules in the asymmetric unit of forms I and III were also estimated from the multipole refinement of the theoretical structure factors obtained from the periodic calculations. The results show an excellent agreement with the gas phase calculation for both forms: −34.96 kJ/mol for form I and −62.41 kJ/mol in the case of form III. On the other hand, the lattice energy calculations for the multipole refinements of the theoretical structure factors obtained from the periodic calculations are not in accordance with the results obtained from CRYSTAL09[39] calculations (Table 2.20).

Table 2.20. Lattice energy calculation (kJ/mol) of the forms of **1** obtained from periodic calculation in CRYSTAL09[39] and multipole refinement based on theoretical structure factors.

Form	**CRYSTAL09[39]**	**XD[21]**
Form I	−213.08	−184.23
Form II	−224.82	−190.40
Form III	−225.97	−211.22
Form IV	−222.41	−213.05

A comparison has recently been presented[67] for several polymorphic organic compounds, between the lattice energy estimated using four different calculation methods and the density and potential energy at each critical point for intermolecular interactions involving hydrogen. The ranking of the relative stability of the polymorphs based on the density rule were found to be in accordance with the lattice energy calculations for only three out of the 10 organic compounds studied. Therefore, estimating the relative stability based only on the hydrogen bonding interaction strength is shown to be a problematic methodology. To

investigate the problem with this approximation, the intermolecular interactions which contribute to the total lattice energy calculations provided by the PIXEL/B3LYP/631G** method were analysed in more detail. These are summarised in Table 2.21; only the intermolecular interactions of the first shell, i.e. the closed neighbor hydrogen bond interactions, were taken into consideration.

The total intermolecular interaction energies of the first shell are greatest in form I, followed by III, IV and II. However, the total interaction energy within the crystal lattice shows a different ranking stability of II>III>IV>I. In the first shell, the intermolecular interactions were limited only to the hydrogen bonds, however, there are also repulsion interactions which contribute to the total lattice energy. In the case of form I, for example, there is a considerable strong repulsion interaction between two Ia…Ia molecules of 15.4 kJ/mol (Figure 2.22), also observed in forms III and IV, with values of 17 kJ/mol and 19.0 kJ/mol, respectively. In form II the intermolecular repulsion interaction energies are much smaller (3.9 kJ/mol). **In conclusion, it has not been found to be possible to estimate the relative stability of the polymorphic forms of sulfathiazole only on the basis of the hydrogen bond interactions.**

Table 2.21. The main hydrogen bond intermolecular interaction energies (kJ/mol) in forms I and II of sulfathiazole, **1**

	Ia		**Ib**		**II**	
	a…a	Symm Op.	**b...b**	Symm Op. No.		Symm. Op.
	-28.9	x,1/2-y, ½-z	-8.6	x,1/2-y,1/2-z	-34.1	x,1/2-y,1/2+z
	-38.5	-x, ½+y, 3/2-z	-30.0	-x,-1/2+y,3/2-z	-28.7	-1+x,y,z
	-144.5	2-x, -y, 2-z	-130.1	-x,1-y,2-z	-73.5	x,-1+y,z
	a…b		-20.1	2-x,-y,-z	-49.9	1-x,-1/2+y,2-z
	-32.5		**b...a**		-37.9	1-x,1-y,2-z
	-27.2	1+x,y,z	-30.9	x,1/2-y,1/2-z	-44.5	2-x,1-y,2-z
	-15.2	1-x,-1/2+y,3/2-z	-27.2	-1+x,y,z	-24.7	X,1/2-y,-1/2+z
	-19.9	1-x,1/2+y,3/2-z	-19.9	-x,1/2+y,3/2-z	-9.7	1+x,1/2-y,1/2+z
	-27.4	1-x,-y,2-z	-15.2	1-x,1/2+y,3/2-z		
	-35.5	1-x,1-y,2-z	-27.4	1-x,-y,2-z		
	-30.9	x,1/2-y,-1/2+z	-35.5	1-x,1-y,2-z		
	-15.4	1+x,1/2-y,1/2+z	-15.4	-1+x,1/2-y,-1/2+z		
Sum	-415.9		-360.3		-303	

Table 2.22. The main hydrogen bond intermolecular interaction energies (kJ/mol) in forms III and IV of **1**

	IIIa		**IIIb**		**IV kappa**	
	a…a	Symm Op.	**b...b**	Symm Op.		Symm. Op.
	-25.9	x,1/2-y,1/2+z	-29.3	x,-1+y,z	-71.4	½-x,1/2-y,1/2-z
	-29.4	x,-1+y,z	-16.5	2-x,-1/2+y,3/2-z	-27.6	x,-1+y,z
	-41.5	1-x,-y,2-z	-19.9	2-x,1-y,2-z	-17.1	-1/2-x,-1/2+y,1/2-z
	-22.0	2-z,1-y,2-z	-21.7	x,3/2-y,-1/2+z	-48.1	-x,1-y,-z
	a…b		**b…a**		-35.2	-x,2-y,-z
	-73.3		-70.9	x,1+y,z	-19.6	-x,2-y,1-z
	-70.9	x,-1+y,z	-33.5	1-x,1/2+y,3/2-z	-22.6	1-x,1-y,-z
	-35.6	x,1/2-y,1/2+z	-9.3	1-x,1-y,1-z	-23.5	-1/2+x,-3/2-y,-1/2+z
	-33.5	1-x,-1/2+y,3/2-z	-46.6	2-x,1-y,2-z	-45.6	-1/2+x,3/2-y,1/2+z
	-9.3	1-x,1-y,1-z	-35.6	x,1/2-y,-1/2+z		
	-46.6	2-x,1-y,2-z	-49.1	x,3/2-y,-1/2+z		
	-49.1	x,3/2-y,1/2+z				
Sum	-437.1		-332.4		-310.7	

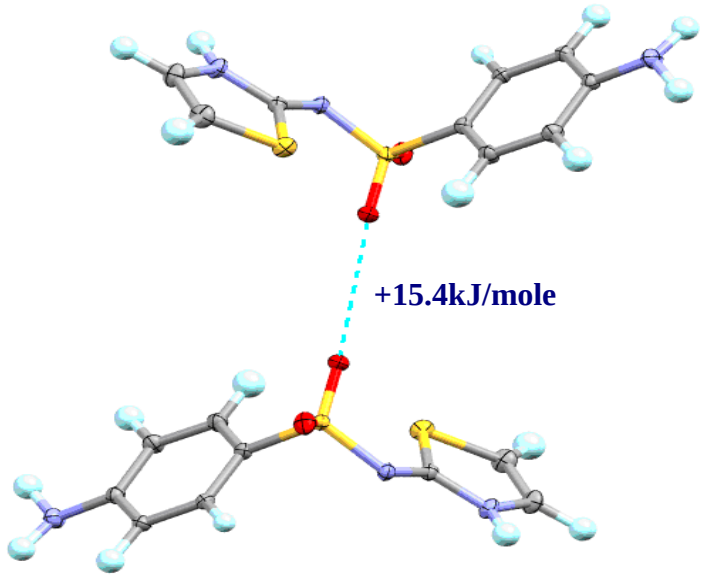

Figure 2.22. An example of the strong Ia···Ia intermolecular repulsion interactions present in form I of sulfathiazole.

2.6. Melting point determination of the forms of 1, using DSC thermal analysis

Given the problems with achieving consistent results from the proposed calculations, it was also important to investigate experimentally the relative stability of the various polymorphic forms of **1**, which can be achieved by thermal methods such as DSC (Differential Scanning Calorimetry) The experimental determination of sublimation

enthalpies, however, also introduces difficulties such as calibration of the instrument, control of the composition of the gas phase, control of partial decomposition. It is known that the expected uncertainly of such experiments are around 10%,[41] which is larger than the calculated energy differences between the polymorphs of **1**. Moreover, experimental difficulties appeared also in melting point determinations of **1**, due to the conversion between forms or the slight contamination of the sample with other forms.[11] Previous studies presented in the literature show form I melting in a range of 200.2-201ºC,[2,7] while form II was observed to melt at 196 ºC,[68] while in other cases, a transition point was observed around 173-175 ºC (the reported melting point of form III) followed by a melting point at 200.2ºC.[2] A broad transition between 150-175 ºC has also been observed for form III,[11] with similar results for Form IV.

As the melting point data presented in the literature are not entirely clear, attempts were made to redetermine the melting points of the polymorphs of **1** using DSC thermal analysis. An initial scanning of the unit cell, of the selected samples using X-ray diffractometry, was performed in order to identify the forms. The results for all four studied forms are presented in Figure 2.23. In all cases, a transformation at a range of 150-170ºC was observed, with the exception of form I, followed by a melting at 194.60ºC for form II, 199.86ºC form III and 199.92ºC for form IV. Form I shows a transformation in the 130-140ºC range and the complete melting occurs at 201.14 ºC. It is difficult to make a clear distinction between melting points of form I, III and IV, as they occur in approximately the same range. A recent report, based on DSC measurements of the forms of **1**, appeared after the current project measurements were taken,[69] which concluded that all forms were transformed into form I and thus DSC alone can not be used in a fully comprehensive way to analyse the forms of **1**.

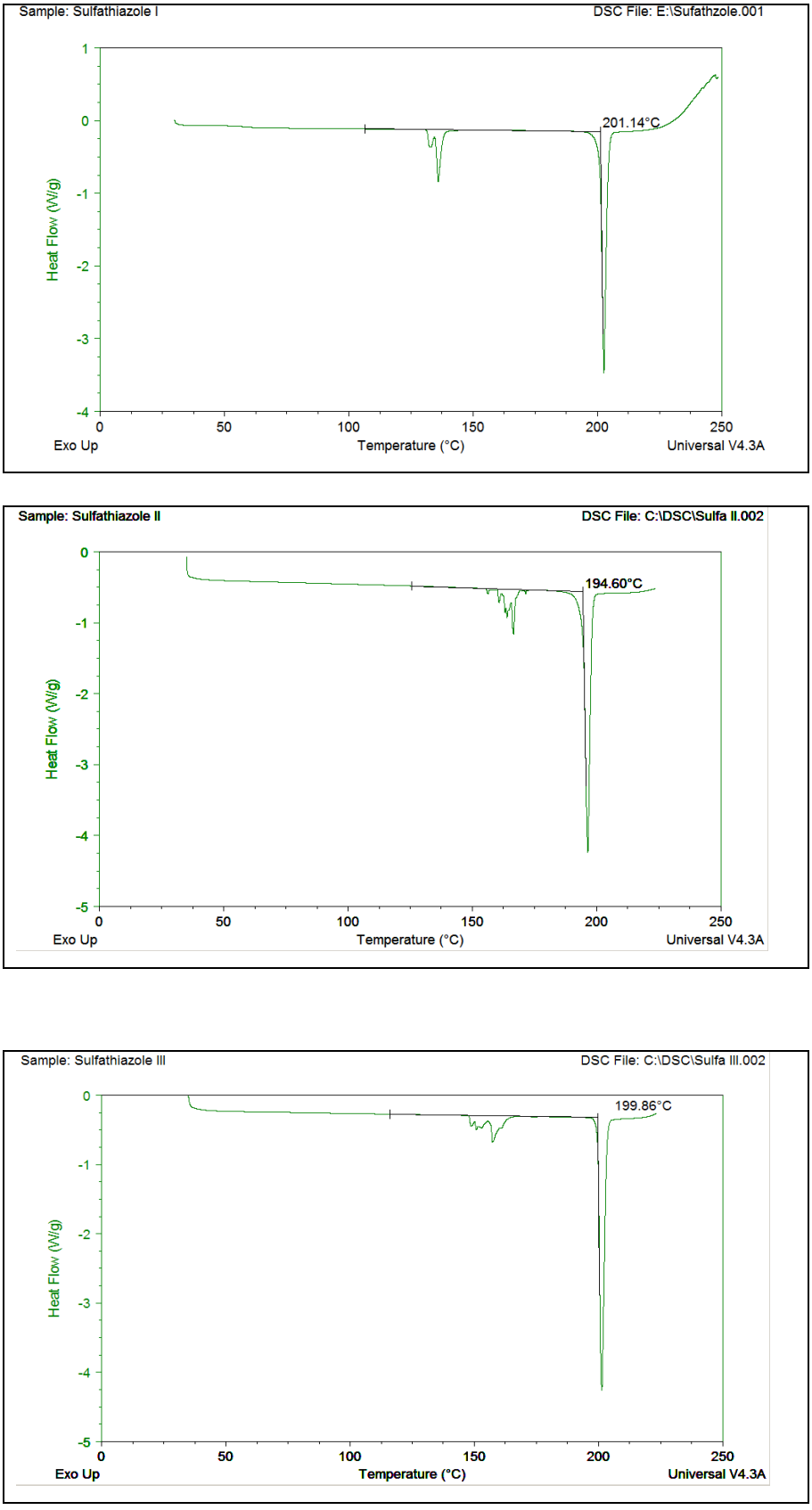

Figure 2.23. DSC curves of forms I (top), II (middle) and III (bottom) of **1** (IV shown below).

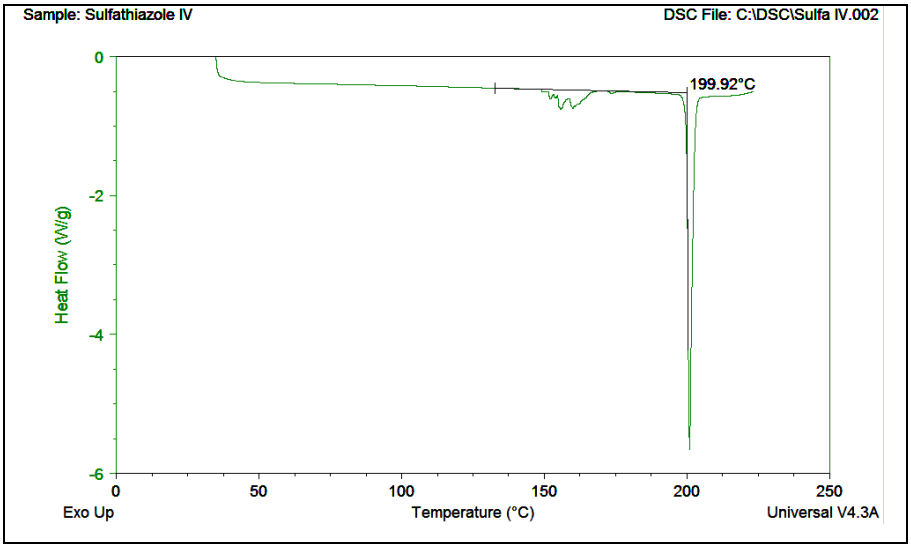

Figure 2.23 continued. DSC curves of forms IV of **1**.

2.7. Conclusions

A significant difference in conformational geometry of form I of sulfathiazole, **1**, compared with forms II, III and IV, is observed. A common dimer in the crystal packing is present in forms II, III and IV, involving an oxygen to an aniline hydrogen (O2···H2) contact and an aniline nitrogen to an amino hydrogen (N1···H3) contact. A close similarity was observed between the adps of the studied forms of **1**.

Forms I and II were identified as having a minor disorder/twin and it has been shown that this does not affect the topological parameters derived from electron density. The topological analyses show an unusual intramolecular BCP between O11 and S12 in each molecule of forms I, II, III and IV of **1,** both in the experimental data and the theoretical results. The S···O interaction was identified to be of electrostatic nature, using the electrostatic potential plots. This showed a positive region around the S atom and a negative region for the oxygen atom. The Laplacian plots also show charge depletion on the S atom and continuous contours of charge concentration at the O atom. A positive value for the Laplacian at the BCP was found, indicating the possibility of an electrostatic S··O interaction.

The topological parameters of the experimental data show large discrepancies, compared with the theoretical results. This is found to be more pronounced for the atoms involved in hydrogen bonding interactions or in the polar bonds.

Calculating the lattice energies from the experimental charge density is found to be unreliable, even when theoretical results are present. The manipulation of the refinement strategy raised a methodological problem. An ideal refinement strategy in ECD should perhaps be unique and invariable for all polymorphs of the same compound. The experimental charge density results emphasise that the lattice energy calculations are highly sensitive to the multipole model strategy applied in the refinements. Predicting the stability order of the polymorphs, which are known to present very small energy differences as small as 5 kJ/mol or less, is thus likely to be rather difficult even when using fully theoretical programs and so further investigations are necessary.

This investigation has shown also that the relative stability of sulfathiazole polymorphs cannot be estimated only on the basis of the hydrogen bond interactions; this may also be more generally the case for polymorphic materials of organic compounds. The melting point determination of the forms of **1** using DSC is rather difficult due to the transformation of the various forms to form I.

It can be concluded that at this stage predicting the most stable form of **1** with the software used in this work is not possible to achieve in a reliable manner. This is due to the fact that the forms of **1** show very close lattice energies with respect to each other. To distinguish clearly between them would thus require very accurate lattice energy calculations, which would not only be computationally time consuming, but will require further consolidation of the methodology used for the calculations. Predicting the most stable form of **1**, and of other important polymorphic organic compounds, remains a further challenge.

References

1. T. Gelbrich, D. S. Hughes, M. B. Hursthouse and T. L. Threlfall, *CrystEngComm*, 2008, **10**, 1328–1334.
2. G. J. Kruger and G. Gafner, *Acta Cryst. B*, 1971, **27**, 326.
3. F. V. Babilev, V. K. Bel'skii, Yu. A. Simonov and A. P. Arzamastsev, *Khim.-Farm. Zh. Russ. Chem. Pharm. J.,* 1987, **21**, 1275.
4. F. C. Chan, J. Anwar, R. Cernik, P. Barnes and R. McHardy Wilson, *J. Appl. Cryst.*, 1999, **32**, 436.

5. D. S. Hughes, M. B. Hursthouse, T. Threlfall and S. Tavener *Acta Cryst. C*, 1999, **55**, 1831.
6. T. N. Drebushchak, E. V. Boldyreva and M. A. Mikhailenko, *Zh.Strukt.Khim. Russ. J. Struct. Chem.*, 2008, **49**, 90.
7. M. M. Parmar, O. Khan, L. Seton and J. L. Ford *Cryst. Grow. Des.*, 2007, **7**, 1635.
8. P.McArdle, Yun Hu, A.Lyons and R.Dark, *CrystEngComm*, 2010, **12**, 3119.
9. A. Volkov, P. Coppens, *Acta Cryst. A*, 2001, **57**, 395-405.
10. M. A. Spackman and D. Jayatilaka *CrystEngComm*, 2009, **11**, 19-32.
11. J. Anwar, S.E. Tarling and P. Barnes, *J. Pharm. Sci.*, 1989, **78**(4), 337-342.
12. N. Blagden, R. J. Davey, H. F. Lieberman, L. Williams, R. Payne, R. Roberts, R. Rowe and R. Docherty, *Faraday Trans*, 1998, **94**(8), 1035-1044.
13. Z. Otwinowski, W. Minor, *Methods in Enzymology, Macromolecular Crystallography, Part A;* W. C. Carter, M.R. Sweet, *Academic Press New York*, 1997, **279**, 307-326.
14. H. R. Blessing, *J. Appl. Cryst.*, 1997, **30**, 421-426.
15. A. Altomare, G. Cascarano, C. Giacovazzo and A. Guagliardi, *J. Appl. Cryst.*, 1994, **27**, 435.
16. L. J. Farrugia, *J. Appl. Cryst.*, 1999, **32**, 837-838.
17. D. A. Keen, , M. J. Gutmann, and C. C. Wilson, *J. Appl. Cryst.*, 2006, **39**, 714–722.
18. M. J. Gutmann, *SXD2001. ISIS Facility, Rutherford Appleton Laboratory, Oxfordshire, England*, 2005.
19. G. M. Sheldrick, *Acta Cryst. A*, 2008, **64**, 112-122.
20. K.N. Hansen and P. Coppens, *Acta Cryst. A*, 1978, **34**, 909-921.
21. A. Volkov, P. Macchi, L. J. Farrugia, C. Gatti, P. R. Mallinson, T. Richter and T. Koritsanszky, *XD-2006*, 2006, http://xd.chem.buffalo.edu/.
22. R. F. Stewart and D. Feil, *Acta Cryst. A*, 1980, **36**, 503.
23. P.M. Dominiak and P. Coppens, *Acta Cryst. A* , 2006, **62**, 224-227.
24. Ø. A. Madsen, *J. Appl. Cryst*., 2006, **39**, 757-758.
25. Ø. A. Madsen, S.Mason, S. Larsen, *Acta Cryst. B*, 2003, **59**, 653-663.
26. P. Munshi, A. Ø. Madsen, M.A. Spackman, S. Larsen and R. Destro, *Acta Cryst. A*, 2008, **64**, 465-475.
27. F. L. Hirshfeld, *Acta Cryst. B*, 1976, **34**, 3623-3626.
28. V. Schomaker and K. N. Trueblood, *Acta Cryst. B*, 1968, **24**, 63-76
29. R.H. Blessing, *Acta Cryst. B*, 1995, **51**, 816-823.
30. S. J. Coles, M. B. Hursthouse, T. A. Mayer and T. L. Threlfall, University of Southampton, Crystal Structure Report Archive, 2000.

31. R. Cejudo-Marin, G. Alzuet, S. Ferrer, J. Borras, A. Castineiras, E. Monzani and L. Casella, *Inorg. Chem*., 2004, **43**, 6805.
32. Xin-Li Zhang, *Acta Cryst*. *E*, 2009, **65**, 2274.
33. J. Zaleski, G. Spaleniak and J. B. Kyziol, *Acta Cryst. C*, 2004, **60**, 627-629
34. J. P. Perdew, K. Burke and M. Ernzerhof, *Phys. Rev. Lett.*, 1996, **77**, 3865.
35. (a) T. H. Dunning, *J. Chem. Phys.*, 1989, **90**, 1007; (b) K. A. Peterson, D. Figgen, M. Dolg and H. Stoll, *J. Chem. Phys.*, 2007, **126**, 124101.
36. M. J. Frisch, G. W. Trucks, H. B. Schlegel, G. E. Scuseria, M. A. Robb, J. R. Cheeseman, J. A. Montgomery, T. V. Jr., K. N. Kudin, J. C. Burant, J. M. Millam, S. S. Iyengar, J. Tomasi, V. Barone, B. Mennucci, M. Cossi, G. Scalmani, N. Rega, G. A. Petersson, H. Nakatsuji, M. Hada, M. Ehara, K. Toyota, R. Fukuda, J. Hasegawa, M. Ishida, T. Nakajima, Y. Honda, O. Kitao, H. Nakai, M. Klene, X. Li, J. E. Knox, H. P. Hratchian, J. B. Cross, V. Bakken, C. Adamo, J. Jaramillo, R. Gomperts, R. E. Stratmann, O. Yazyev, A. J. Austin, R. Cammi, C. Pomelli, J. W. Ochterski, P. Y. Ayala, K. Morokuma, G. A. Voth, P. Salvador, J. J. Dannenberg, V. G. Zakrzewski, S. Dapprich, A. D. Daniels, M. C. Strain, O. Farkas, D. K. Malick, A. D. Rabuck, K. Raghavachari, J. B. Foresman, J. V. Ortiz, Q. Cui, A. G. Baboul, S. Clifford, J. Cioslowski, B. B. Stefanov, G. Liu, A. Liashenko, P. Piskorz, I. Komaromi, R. L. Martin, D. J. Fox, T. Keith, M. A. Al-Laham, C. Y. Peng, A. Nanayakkara, M. Challacombe, P. M. W. Gill, B. Johnson, W. Chen, M. W. Wong, C. Gonzalez and J. A. Pople, GAUSSIAN03, Wallingford, CT., US, 2004.
37. Basis sets were obtained from the Extensible Computational Chemistry Environment Basis Set Database, Version 02/25/04, as developed and distributed by the Molecular Science Computing Facility, Environmental and Molecular Science Laboratory which is part of the Pacific Northwest Laboratory, P.O. Box 999, Richland, WA 99352, U.S.A., and funded by the U.S. Department of Energy.
38. F. W. Biegler-Konig, R. F .W. Bader and T. Tang, *J. Comput. Chem*, 1982, **3**, 317.
39. R. Dovesi, R. Orlando, B. Civalleri, C. Roetti, V. R. Saunders, and C. M. Zicovich-Wilson, *Z. Kristallogr.*, 2005, **220**, 571; R. Dovesi, V. R. Saunders, C. Roetti, R. Orlando, C. M. Zicovich-Wilson, F. Pascale, B. Civalleri, K. Doll, N. M. Harrison, I. J. Bush, P. D'Arco, and M. Llunell, CRYSTAL09 (CRYSTAL09 User's Manual. University of Torino, Torino, Italy 2009).
40. (a) A. D. Becke, *Phys. Rev. A*, 1988, **38**, 3098; (b) A. D. Becke, *J. Chem. Phys.*, 1993, **98**, 5648; (c) C. Lee, W. Yang and R. G. Parr, *Phys. Rev. B*, 1988, **37**, 785.

(d) P. J. Stephens, J. F. Devlin, C. F. Chabalowski and M. J. Frisch, *J. Phys. Chem.*, 1994, **98**, 11623.

41. A. Gavezzotti, *New J. Chem*., 2011, **35**, 1360-1368.
42. CrystalExplorer (Version 3.0), *S.K. Wolff, D.J. Grimwood, J.J. McKinnon, M.J. Turner, D. Jayatilaka, M.A. Spackman*, University of Western Australia, 2010.
43. R. F. W. Bader, Atoms in Molecules – *A Quantum Theory, Oxford University Press*, Oxford 1990.
44. E. Wigner, F. Seitz, *Phys Rev*., 1933, **43**, 804.
45. M. A. Spackman and P. G. Byrom, *Chem. Phys. Lett.*, 1997, **267**, 215-220.
46. http://www.isis.stfc.ac.uk/learning/neutron-training. course/downloads/general/neutron-training-course---manual10674.pdf.
47. A. E. Whitten and M. A. Spackman, *Acta Cryst. B*, 2006, **62**, 875-888.
48. (a) F. Weigend, R. Ahlrichs, *Phys. Chem. Chem. Phys.*, 2005, **7**, 3297. (b) F. Weigend, *Phys. Chem. Chem. Phys.*, 2006, **8**, 1057.
49. A. Volkov, Y. Abramov, P. Coppens and C. Gatti, *Acta Cryst. A*, 2000, **56**, 11201-11208.
50. C. Gatti, R. Bianchi, R. Destro and F. Merati, *J. Mol. Struct*, 1992, **87**, 409-433.
51. D. E. Hibbs, J. Overgaard, C. Gatti and T. W. Hambley, *New J. Chem. Soc*, 2003, **27**, 1392-1398.
52. R. Flaig, T. Koritsanszky, B. Dittrich, A. Wagner and P. Luger, *J. Am. Chem. Soc*., 2002, **124**, 3407-3417.
53. C. Gatti, V. R. Saunders and C. Roetti, *J. Chem. Phys*, 1994, **101**, 10686-10696
54. Y. A. Abramov, A. Volkov, G. Wu and P. Coppens, *J. Phys Chem* B, 2000, **104**, 2183-2188.
55. K. Durka, A. A. Hoser, R. Kaminski, S. Lulinski, J. Serwatowski, W. Kozminski and K. Wozniak, *Cryst. Grow. Des.*, 2011, **11**, 1835-1845.
56. A. J. Stone, *The Theory of Intermolecular Forces*, Oxford: Clarendon Press, 1996
57. A. Volkov, H. F. King, P. Coppens and L. J. Farrugia, *Acta Cryst. A*, 2006, **62**, 400–408.
58. A. D. Buckingham, *Adv. Chem. Phys.*, 1967, **12**, 107.
59. P. Coppens, X-Ray Charge Densities and Chemical Bonding, *Oxford University Press*, New York, 1997.
60. M. A. Spackman, *J. Chem. Phys*, 1986, **85**, 6587.
61. D. E. Williams and S. R. Cox, *Acta Cryst. B*, 1984, **40**, 404.
62. R. Hoffmann, *J. Phys. Chem*., 1963, **39**, 1397-1412.

63. R. P. Feynman *The Feynman Lectures on Physics*; Addison-Wesley: Reading, MS, 1989; Vol. 2, chapter 11.
64. A. Karton and J. M. L. Martin, *Theor. Chem. Acc.*, 2006, **115**, 330-333.
65. A. Halkier, T. Helgaker, P. Jørgensen, W. Klopper, H. Koch, J. Olsen and A. K. Wilson, *Chem. Phys. Lett.*, 1998, **286**, 243-252.
66. S. Grimme, *J. Comput. Chem.*, 2006, **27**, 1787.
67. Y. A. Abramov, *J. Phys. Chem.*, 2011, **115**, 12809-12817.
68. M. Lagas and C.F. Lerk, *Int. J. Pharm.*, 1981, **8**, 11-24.
69. Áine Munroe, Åke C. Rasmuson, B. Kieran Hodnett, and Denise M. Croker, *Cryst. Grow. Des.*, 2012.

3. Piracetam

3.1. Introduction

The second of the organic compounds which exhibit extensive polymorphism that is analysed in this work is piracetam (2-oxo-1-pyrroloneacetamide) (**2**) (Scheme 3.1). Piracetam is a well-studied drug with pharmaceutical applications which acts as a nootropic agent and is used in the treatment of age-associated mental decline, as well as disorders of the nervous system. It is known to crystallise in five polymorphic forms, of which forms IV and V are generated under high-pressure (0.4-0.7 GPa) (Table 3.1)[1] and are therefore not studied here. There is also a hydrate form, which will also be examined in this work.

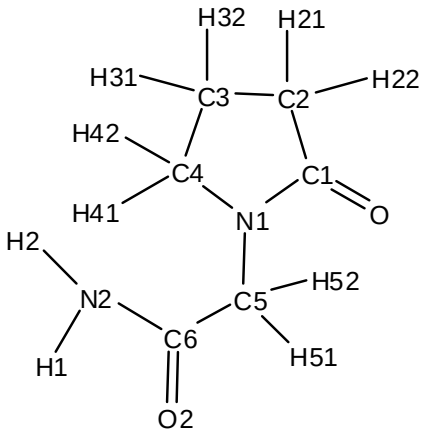

Scheme 3.1. The molecular structure and atom labelling of piracetam, **2**.

The first two crystal structures of **2** reported were those of forms II and III in 1982.[2] This was followed by the structure of form I, first reported in 1995 from powder diffraction.[3] The crystal structure of form IV was first analysed using X-ray diffraction in 2005 (obtained under high-pressure at 0.4 GPa)[4] and was reported together with form I. The structure of form V was determined for the first time in 2007[1] under various high-pressure conditions (0.7, 0.9, 2.5 and 4 GPa). At a pressure of 0.45 GPa, form II was still observed, showing there is a phase co-existence region.[1] The structure of form III has been re-examined three times[5, 6, 7], as has form II[6]. The hydrate form was first determined in 2007[1] re-examined in 2011[6].

In Table 3.1 a summary of the crystallographic data for all forms is provided (form I –III from data collected in this work, forms IV and V from CSD data). High resolution X-ray

diffraction studies of forms II and III as well as the hydrate form have previously been carried out.[6] However, the present work has added to this in various ways, including the accurate determination of the hydrogen atom parameters in forms II and III from neutron diffraction. In addition, form I has also been determined here using the high resolution X-ray diffraction technique, for the first time. For a direct comparison of the charge density analyses in the present work with those presented by Chambrier *et al.*[6], the same unit cell parameters as in that previous study were employed in the present refinements of forms II, III and hydrate form.

Table 3.1. Summary of the crystallographic data of five polymorphs of **2** (data from this work for forms I-III, CSD data for forms IV and V)

Form	I	II	III	IV (0.4 GPa)	V (0.7 GPA)
CSD	BISMEV03(RT)[3]	BISMEV(RT)[2]	BISMEV01(RT)[2]	BISMEV04	BISMEV07(RT)[1]
ref.	BISMEV05(150K)[4]	BISMEV06(RT)[1]	BISMEV02(RT)[5]	(RT)[4]	BISMEV08(RT)[1]
code		BISMEV11(100K)[6]	BISMEV12(RT)[6]		BISMEV09(RT)[1]
			BISMEV13(100K)[7]		BISMEV10(RT)[1]
SP	$P2_1/n$	$P\bar{1}$	$P2_1/n$	$P2_1/c$	$P\bar{1}$
a/ Å	6.7406(2)	6.3527(2)	6.4569(2)	8.9537(11)	6.442(2)
b/Å	13.2915(4)	6.5294(2)	6.3930(2)	5.4541(6)	6.3530(11)
c/Å	8.0195(2)	8.3727(3)	16.1994(5)	13.610(4)	8.737(3)
α/deg	90.00	80.286(1)	90.00	90.00	81.43(3)
β/deg	98.309(1)	78.198(1)	92.000(1)	104.93(2)	112.88(2)
γ/deg	90.00	89.037(1)	90.00	90.00	91.3892)
V/ Å^3	710.95(1)	334.02(1)	666.45(1)	642.2(2)	325.53(17)
Z'	1	1	1	1	1
ρ/g cm^{-3}	1.39	1.41	1.42	1.47	1.45

**The presented data were collected at 100K*

The refined models resulting from the experimental high resolution X-ray diffraction data collected in this work from forms I, II, III and the hydrate will be compared with DFT calculations at the PBEPBE/cc-pTZVP level. The topological analyses of the theoretical density and best multipole model will be compared with a view to examine the effects of the well-known deficiencies[8] of the multipole model. The intermolecular interactions and lattice energy are calculated using both experimental charge density and fully theoretical approaches in order to attempt to estimate the order of stability of the polymorphs of **2**.

3.2. Experimental and Theoretical

3.2.1 Sample preparation

The preparation conditions for the various polymorphic forms of **2** are described in the literature as follows: form I can be obtained by heating single crystals of form III to 400K, cooling to 298K, after coating with oil, and then rapidly cooling to 150K[4]; form II is reported to be obtained by recrystallisation from 2-propanol[2,6] and 1,4-dioxane[6] solvents; form III can be grown from 2-propanol,[2] methanol[6] and dichloromethane.[7] The hydrate form is reported to be grown from an equal volume solution of water-methanol.[6]

Compound **2** was purchased as a powder from Sigma Aldrich and attempts made to obtain the forms as described above. However, in this study form II (and not form I) was obtained by heating single crystals of form III to 400K, cooling to 298K, and then rapidly cooling to 150K; this was the previously reported route to form I. Form I was instead obtained by heating the starting materials at 152ºC, producing converted material that contained seeds of form I which were dispersed into isobutanol and held for 8 hours at 90ºC. The temperature was then reduced and held at 70ºC, producing block crystals of form I within a few days. Despite previous observations regarding the meta-stability of form I at room temperature,[3] the block crystals grown were stable at room temperature for a period of over six months. Form II was also observed to occur as a product of recrystallisation from 2-propanol and 1,4-dioxane. Crystals of form III were obtained from 2-propanol and methanol solutions as described in the literature.[2,6]

3.2.2 Data collection and Conventional (Spherical atom) refinement

Single crystals of suitable size were selected and mounted onto a goniometer. High resolution X-ray data of forms I, III and the hydrate were collected over a period of one week on a Bruker-Nonius Kappa CCD diffractometer (Mo K_α radiation) at 100 K, cooled by an Oxford Cryosystems Cryostream. The Collect software was used for monitoring the data collection. The low-resolution X-ray data were measured prior to the high-resolution data. Integration of intensities was carried out using the software DENZO.[9] High resolution X-ray data for form II was collected at 100K on a Bruker AXS Apex II diffractometer, with sample cooling in this case from an Oxford Cryosystems Helix. Indexing, integration and scaling were performed using the Bruker APEX II software (Bruker Nonius 2009). The reflection measurements were merged and empirical absorption corrections were performed using SORTAV.[10] The structures were solved using SIR92[11] and refined initially in the spherical-atom formalism with full-matrix least squares on F^2. The non-hydrogen atoms were refined with anisotropic displacement parameters. Structure solution

and refinement were performed using the WinGX package[12] of crystallographic programs. The H atoms for form I were added using the AFIX command in SHELXL.

Neutron diffraction data were collected for forms II and III of **2** at 100K on the SXD instrument[13] at the ISIS spallation neutron source, using the time-of-flight Laue diffraction method. Reflection intensities were reduced to structure factors using standard SXD procedures, as implemented in the computer program SXD2001.[14] Refinements were carried out using SHELXL97[15] using anisotropic displacement parameters for all atoms, including the H atoms.

The details of these data collections and refinements, including the neutron experiments, are given in Table 3.2 and 3.3. The unit cell parameters used for the refinement of forms II, III and the hydrate were taken from the literature,[6] to allow direct comparison of the electrostatic interaction energies from the present work with those reported previously[6] (Section 3.5).

3.2.3 Multipole refinement

The XD software package[16] was used to perform the multipole refinements. The multipole expansion was truncated at the octupole level for C, N and O atoms. Five different multipole refinements were performed for forms II and III, for which neutron data were also available. Where no neutron data were available, only three multipole refinements were performed. In the first refinement (model 1) extensive chemical constraints were imposed by local mirror symmetry of the C and N1 atoms. For the O and N2 atoms free multipole refinements were allowed. Only the first monopole and last dipole were refined in this model for H atoms, and these were used to estimate the H-atom adps by the method of Madsen using the SHADE web interface.[17] The calculated H-atom adps were used in subsequent refinements (model 2) as fixed parameters. In the final cycles (model 3) the multipole constraints were released. The same steps were performed in parallel refinements (for forms II and III) in which the adps for H atoms were obtained from scaled X-ray / neutron diffraction data, denoted as models 4 and 5. The hydrogen atom positions were set to the standard neutron distances in all refinements. Multipole populations and κ parameters were grouped in all refinements according to the chemical similarity of the atoms. For the disordered atoms in form I, no multipole refinements were performed.

3.2.4 Theoretical calculations

Gas-phase structure optimisations were performed using the DFT method at the PBEPBE[18]/cc-pVTZ[19] level of theory, within the Gaussian03 program.[20] Basis sets were obtained from EMSL.[21] The subsequent topological analyses were performed using the AIMPAC program.[22] Theoretical structure factors were computed from the resultant wave functions and used in a multipole refinement within XD,[16] where all thermal parameters were set to zero and all positional parameters were kept fixed. Periodic single-point quantum calculations were also performed using CRYSTAL09[23] with the DFT method at the B3LYP[24]/6-31G** level of theory. Lattice energy calculations were performed using the CLP[25] software with the DFT method at the B3LYP[24]/6-31G** level.

Table 3.2. Experimental crystallographic data for 2, form I and II

Compound formula	$C_6H_{10}N_2O_2$	$C_6H_{10}N_2O_2$	$C_6H_{10}N_2O_2$
Form	I	II	II
M_r	142.2	142.2	142.2
Space group	$P2_1/n$	$P\bar{1}$	$P\bar{1}$
Crystal system	Monoclinic	Triclinic	Triclinic
a/ Å	6.7406(2)	6.3530(2)	6.3530(2)
b/Å	13.2915(4)	6.5278(2)	6.5278(2)
c/Å	8.0195(2)	8.3716(2)	8.3716(2)
α/deg	90.00	80.297(1)	80.297(1)
β/deg	98.309(1)	78.226(1)	78.226(1)
γ/deg	90.00	89.048(1)	89.048(1)
V/Å^{-3}	710.95(1)	334.02(1)	334.02(1)
Z	4	2	2
D_{calc}/g cm^{-3}	1.33	1.41	1.41
F(000)	304	152	-
Radiation	Mo Kα	Mo Kα	TOF neutron
λ/Å	0.71073	0.71073	0.42-7.64
μ(Mo-K_a)/mm^{-1}	0.101	0.107	0.207
Crystal size/mm	0.14x0.31x0.49	0.19x0.24x0.43	2.0x2.0x8.0
θ range/deg	3.0-50.5	2.5-58.2	8.5-84.3
Max sin(θ)/ λ	1.07	1.19	
No. of data used for merging	228921	93280	3134
No. of unique data	7549	9439	2064
hkl range	$-14 \le h \le 14$	$-14 \le h \le 15$	$-12 \le h \le 5$
	$0 \le k \le 28$	$-15 \le k \le 15$	$-15 \le k \le 18$
	$0 \le l \le 17$	$0 \le l \le 19$	$-23 \le l \le 26$
R_{int}	0.0297	0.0440	-
R_σ	0.0271	0.0333	0.066
Spherical atom refinement			
No. of data in refinement	7549	9439	3134
No. of refined parameters	101	131	186
Final *R* [$I > 2\sigma(I)$]	0.043	0.031	0.069
R_w [$I > 2\sigma(I)$]	0.132	0.092	0.169
Goodness of fit *S*	0.996	1.062	1.077
Extrema in residual map	-0.230→ 0.625eÅ^{-3}	-0.244→0.797 eÅ^{-3}	-1.607→2.372 fmÅ^{-3}
Max shift/esd in last cycle	0.002	0.001	0.000
Multipole refinement			
No. of data in refinement	6457	8487	-
No. of refined parameters	258	265	-
Final *R* [$I > 3\sigma(I)$]	0.0300	0.0177	-
R_w [$I > 3\sigma(I)$]	0.0332	0.0214	
Goodness of fit *S*	1.397	1.1838	-
Extrema in residual map/ eÅ^{-3} (all data)	-0.194 → 0.318	-0.158→ 0.292	-
Max shift/esd in last cycle	0.00003	0.00001	-

Table 3.3 Experimental crystallographic data for 2, form III and the monohydrate

Compound formula	$C_6H_{10}N_2O_2$	$C_6H_{10}N_2O_2$	$C_6H_{12}N_2O_3$
Form	III	III	monohydrate
M_r	142.2	142.2	160.2
Space group	$P2_1/n$	$P2_1/n$	$P\bar{1}$
Crystal system	Monoclinic	Monoclinic	Triclinic
a/ Å	6.4539(5)	6.4539(5)	6.9340(3)
b/Å	6.3857(5)	6.3857(5)	7.4534(2)
c/Å	16.1814(1)	16.1814(1)	9.0909(2)
α/deg	90.00	90.00	97.948(1)
β/deg	92.057(5)	92.057(5)	103.971(1)
γ/deg	90.00	90.00	115.797(1)
V/Å^{-3}	666.45(1)	666.45(1)	394.26(3)
Z	4	4	2
D_{calc}/g cm^{-3}	1.42	1.42	1.35
F(000)	304	-	172
Radiation	Mo Kα	TOF neutron	Mo Kα
λ/Å	0.71073	0.42-7.64	0.71073
μ(Mo-K_a)/mm^{-1}	0.108	0.207	0.108
Crystal size/mm	0.13x0.35x0.56	2.0x2.0x8.0	0.19x0.24x0.43
θ range/deg	2.5-48.3	8.5-88.3	2.4-50.5
Max sin(θ)/ λ	1.04		
No. of data used for merging	145728	7882	169912
No. of unique data	5432	3493	8373
hkl range	$-13 \le h \le 7$	$-14 \le h \le 7$	$-14 \le h \le 14$
	$0 \le k \le 13$	$-19 \le k \le 19$	$-16 \le k \le 15$
	$0 \le l \le 33$	$-47 \le l \le 41$	$0 \le l \le 19$
R_{int}	0.0613	-	0.0225
R_σ	0.0352	0.0591	0.0277
Spherical atom refinement			
No. of data in refinement	5432	7882	8373
No. of refined parameters	132	186	149
Final R [$I > 2\sigma(I)$]	0.039	0.063	0.038
R_w [$I > 2\sigma(I)$]	0.106	0.160	0.108
Goodness of fit S	1.049	1.072	0.992
Extrema in residual map	-0.330→ 0.592eÅ^{-3}	-2.235→ 1.977fmÅ^{-3}	-0.471→0.823eÅ^{-3}
Max shift/esd in last cycle	0.000	0.001	0.001
Multipole refinement			
No. of data in refinement	5288	-	7123
No. of refined parameters	265		295
Final R [$I > 3\sigma(I)$]	0.0293	-	0.0248
R_w [$I > 3\sigma(I)$]	0.0269		0.0274
Goodness of fit S	1.3629	-	1.5168
Extrema in residual map/ eÅ^{-3} (all data)	-0.236→0.217	-	-0.280→0.351
Max shift/esd in last cycle	0.0002	-	0.0001

3.3 Results and discussion

3.3.1. Molecular structure and conformation details

The crystal structures of the polymorphs of **2** have been discussed extensively in the literature and a summary is given in this section. First, the differences between the molecular geometries of three polymorphs observed under ambient pressure and the monohydrate will be compared in detail.

Interpretation of the diffraction data reveal a disorder of some of the atoms in form I, corresponding to a different orientation of the molecule in the unit cell. The level of disorder is ~70% and this affects the occupancies of the C3 methylene group, affecting the C3, H31 and H32 atoms (Figure 3.1). In previous determinations of form I, disorder was also identified in the positions of the other two methylene groups, affecting atoms H21, H22, H41 and H42.[4]

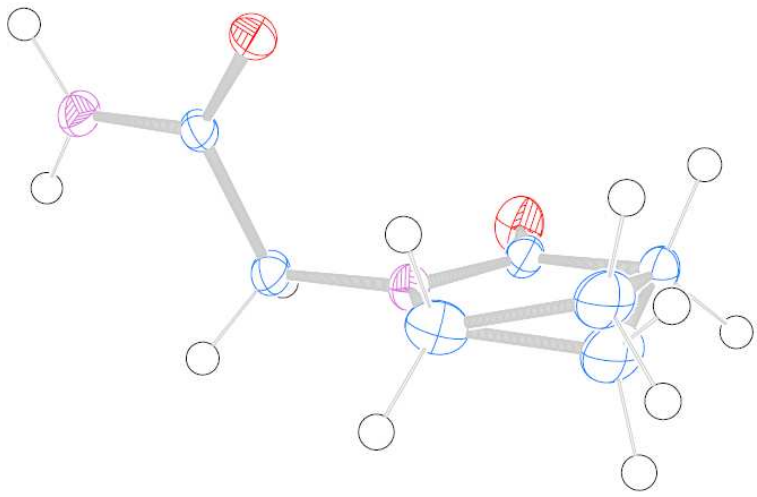

Figure 3.1. Form I of piracetam, **2**, showing the disorder of the methylene group, comprising C3, H31 and H32 atoms.

The best-fit overlay plot of the four studied polymorphs is shown in Figure 3.2. The acetamide group in both form I and the monohydrate show a slight conformational difference compared with forms II and III. The disordered methylene group (C31, H31, H32) in form I naturally shows a slight positional deviation compared with the other forms. The close conformational similarity between molecules of forms II and III can be observed by visual inspection of Figure 3.2 (b).

(a)

(b)

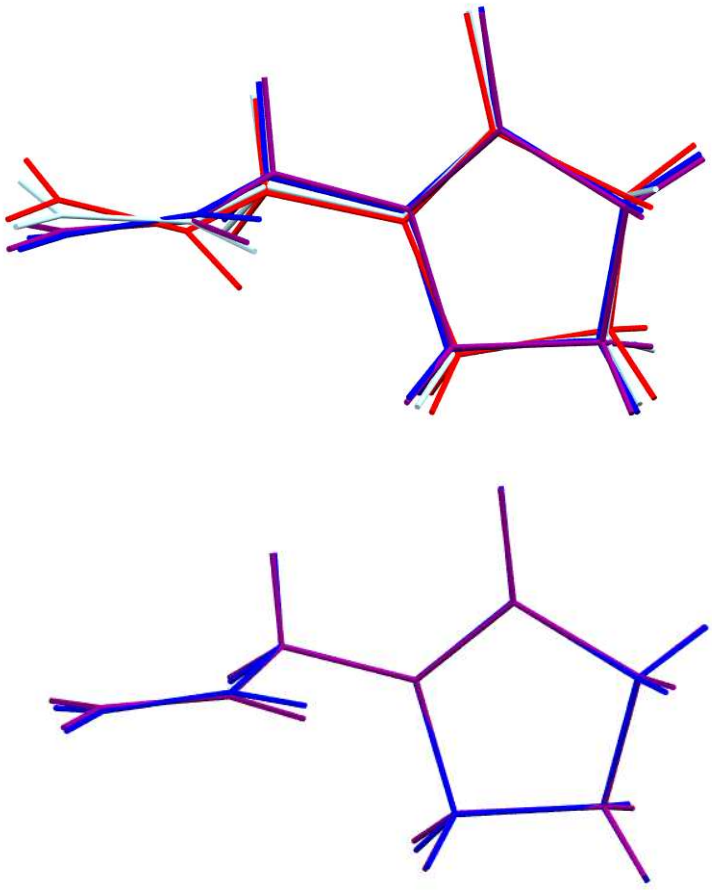

Figure 3.2. Best fit overlay plots of (a) forms I, II, III and the monohydrate, and (b) forms II and III, of piracetam, **2**. Form I - red, form II - blue, form III – purple, monohydrate - light blue.

The bond lengths for the non-hydrogen atoms of the four studied forms are listed in Table 3.2. The bond distances in the various forms are similar, except for the C2-C3 and C3-C4 bonds which are slightly different in form I (1.5134(10), 1.5498(10) Å for the major C3 site) compared with those in the other forms (e.g. 1.5287(3) and 1.5347(3) Å in form II). To examine the molecular conformations, Table 3.3 gives three selected torsion angles of the four studied forms of **2**, including also the CSD data and gas-phase optimised structure for forms II and III. The major difference lies in the N2-C6-C5-N1 torsion angle (176.95(3)º) of form I which is significantly different to that in forms II, III and the monohydrate (−154.968(18), −159.06(4) and −179.13(3)º, respectively). The discrepancies arise due to the different orientation of the acetamide group relative to the ring (Figure 3.3). The monohydrate form also shows a significant difference of the N2-C6-C5-N1 torsion angle (−179.13(3)º) compared with forms II and III (−154.968(18) and −159.06(4)º), but is in better agreement with that for the optimised structure (−178.54º). On the other hand, the C6-C5-N1-C1 and C4-N1-C1-O1 torsion angles show good

agreement between all forms and also with the optimised geometry. Overall the experimental data in this study are in excellent agreement with the previously reported data in the CSD.

Table 3.2. Bond distances (Å) involving the of non-hydrogen atoms of forms I, II, III and monohydrate of **2**. The two values of the C2-C3 and C3-C4 bond lengths in form I correspond to the two different positions (with major and minor occupancy) adopted by the disordered C3 atom.

Distance	Form I	Form II	Form III	Monohydrate
C1-O1	1.2349(5)	1.2353(2)	1.2395(6)	1.2403(4)
C6-O2	1.2367(4)	1.2342(2)	1.2363(5)	1.2409(4)
C1-N1	1.3453(4)	1.34710(2)	1.3498(6)	1.3425(4)
C4-N1	1.4608(5)	1.4621(3)	1.4600(6)	1.4594(4)
C5-N1	1.4378(4)	1.4382(2)	1.4384(6)	1.4414(4)
C6-N2	1.3361(4)	1.3353(2)	1.3363(6)	1.3353(4)
C1-C2	1.5135(5)	1.5127(3)	1.5118(6)	1.5137(5)
C2-C3	1.592(3) [minor], 1.5134(10) [major]	1.5287(3)	1.5332(7)	1.5344(6)
C3-C4	1.489(2) [minor], 1.5498(10) [major]	1.5347(3)	1.5402(7)	1.5368(6)

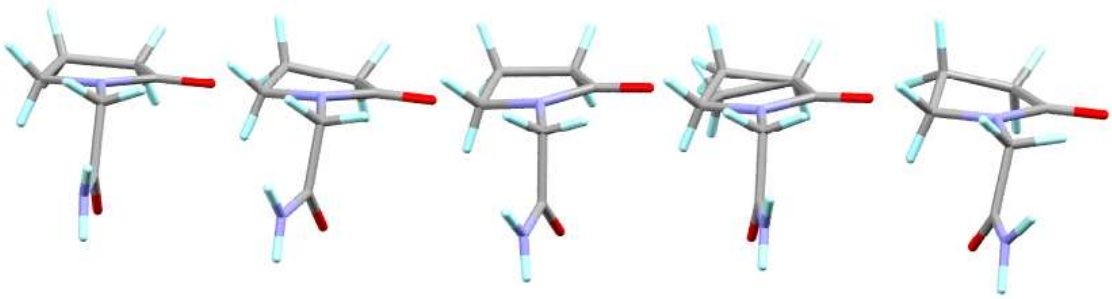

Figure 3.3. Conformation of the molecules of **2** in (from left), the monohydrate, forms II, III and I, and the optimised structure, showing the different orientation of the acetamide group relative to the ring.

Table 3.3 Three selected torsion angles (°) in forms I, II, III and the monohydrate of **2**, compared with CSD data and the optimised gas phase molecular geometry.

Torsion angle	This work	CSD	PBEPBE/cc-pVTZ
FormI			
N2-C6-C5-N1	176.95(3)	178.39	
C6-C5-N1-C1	-95.70(4)	-103.32	
C4-N1-C1-O1	-179.20(4)	-176.04	
FormII			
N2-C6-C5-N1	-154.968(18)	-155.04	-178.54
C6-C5-N1-C1	-90.60(2)	-90.45	-100.17
C4-N1-C1-O1	-174.82(2)	-174.81	-176.10
FormIII			
N2-C6-C5-N1	-159.06(4)	-159.00	-178.49
C6-C5-N1-C1	-91.13(5)	-91.23	-100.19
C4-N1-C1-O1	-174.52(4)	-174.52	-176.10
Monohydrate			
N2-C6-C5-N1	-179.13(3)	-170.11	
C6-C5-N1-C1	-91.45(3)	-91.16	
C4-N1-C1-O1	-176.27(3)	-175.98	

3.3.2. Description of intermolecular interaction and crystal packing

A common centrosymmetric dimer produced by hydrogen bond interactions between symmetry-related pairs of acetamide groups was observed in forms II, III and the monohydrate. This is designated as the $R_2^2(8)$ ring in Figure 3.4 (a) and (b). In addition, hydrogen bond interactions formed between acetamide and pyrrolidone groups give rise to $R_4^4(18)$ rings which enable a 2D expansion of forms II and III (Figure 3.4(a)). The $R_4^4(18)$ rings present in the monohydrate form contain hydrogen bond intermolecular interactions between acetamide groups and additional O-H···O and N-H···O hydrogen bonds formed between the piracetam and water molecules extend the 2D packing of the structure (Figure 3.4(b)). The crystal packing of form I is dictated by two types of intermolecular bond interactions forming a two-dimensional network (Figure 3.4(c)). The expanded network of form I reveals two types of rings, $R_4^4(18)$ and $R_4^4(22)$, as illustrated in Figure 3.4(c).

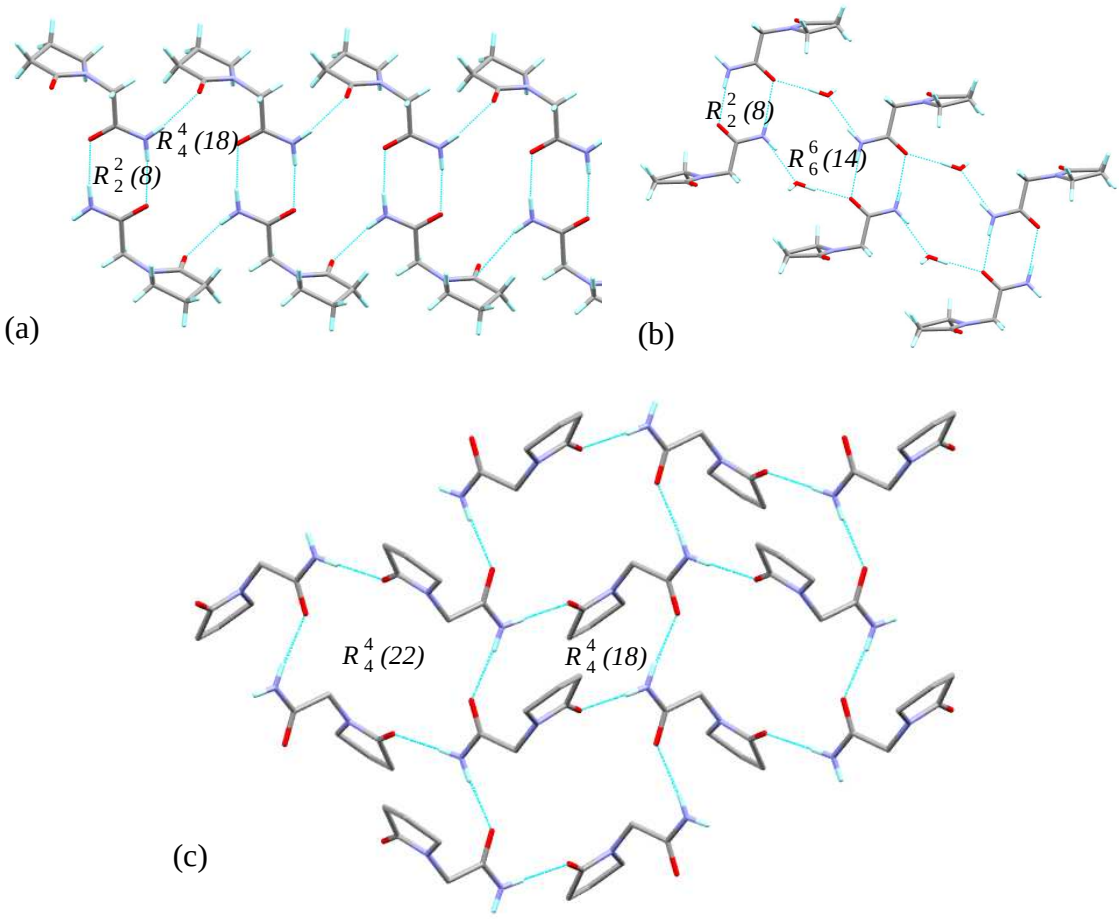

Figure 3.4. (a) Hydrogen bonded intermolecular interactions found in the studied forms of **2**: (a) form II and III, (b) monohydrate form, (c) form I.

The main hydrogen bond interactions present in the four studied forms of **2** are summarised in Table 3.4. The N-H···O hydrogen bondsformed between the two acetamide groups show good similarity between forms II, III and the monohydrate (D···A distances of 2.913(2), 2.9155(11) and 2.9526(5) Å, respectively). On the other hand, the O-H···O hydrogen bonds involving the water molecules, that are present in the $R_4^4(18)$ ring of the hydrate, are found to be shorter and stronger than those in form II and III, while in the absence of the dimer in form I, slightly shorter N2-H1···O2 and N2-H2···O1 hydrogen bonds are formed (D···A, 2.8788(5) and 2.8597(6) Å)

Table 3.4. Hydrogen bond distances (Å) in the four studied polymorphs of **2** (parameters for form I and monohydrate taken from X-ray data, for forms II and III from neutron data). For each bond, the upper line represents D···A, thelower H···A.

	Form I	**Form II**	**Form III**	**monohydrate**
N2-H1···O2	2.8788(5)	2.913(2)	2.9155(11)	2.9526(5)
	2.02*	1.895(4)	1.904(2)	2.062(12)
N2-H2···O1	2.8597(6)	2.929(2)	2.9349(13)	
	2.00*	1.937(5)	1.945(3)	
Ow-Hw1···O1				2.7348(4)
				1.873(13)
N2-H1···Ow				2.8634(5)
				1.996(11)
Ow-Hw2···O2				2.7820(5)
				1.880(15)

* H in calculated positions

3.3.3. Hirshfeld surface analysis

The derived two dimensional fingerprint plots derived from the Hirshfeld surfaces of forms I, II, III and IV have been previously analysed and discussed in the literature.[4] However, the intermolecular interactions present in forms II and III will be re-examined in this study via updated fingerprint plots calculated using experimental neutron data, available for the first time in this work. Fingerprint plots for form I and the monohydrate will also be included for comparison.

The plots show very good agreement with those described previously,[4] except for form I where a more diffuse spread of the wings can be observed in the fingerprint. The two sharp peaks correspond to N-H···C=O hydrogen bonds: the upper one represents the hydrogen bond donor and the lower one the hydrogen bond acceptor. The middle peaks correspond to the short H···H contacts and an elongation in the length of these contacts can be observed in the case of form III. For forms I and II the contacts appear in the region of d_e+d_i = 2.2 Å. The more laterally spread wings in form I represent the C-H···C weak intermolecular interactions. The shape of the wings in form III are slightly different due to the additional C-H···N(pyrrolidone ring) hydrogen bond interactions present.

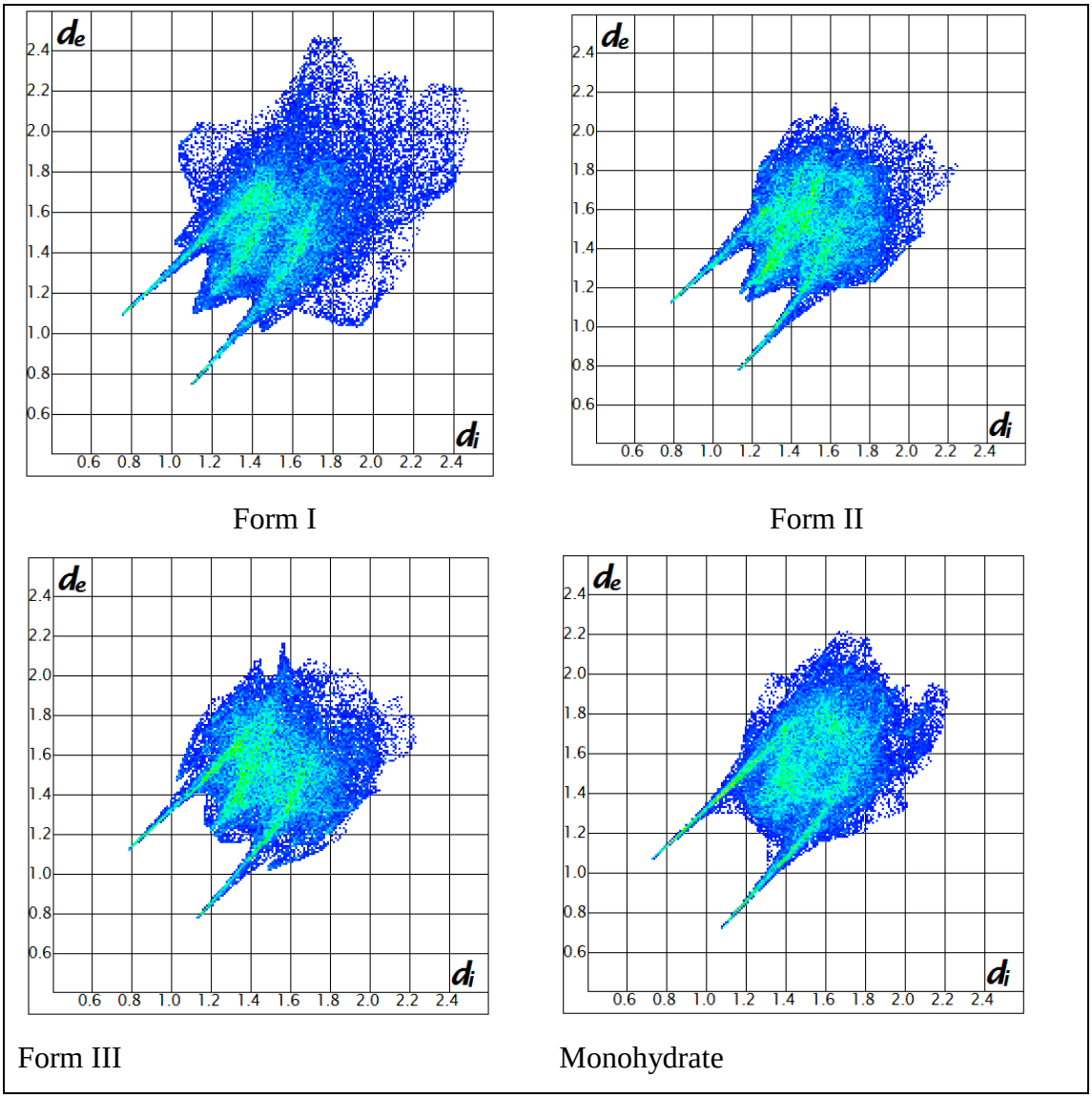

Figure 3.5. Two-dimensional fingerprint plots for the four studied forms of **2**.

3.4. Analysis of the electron-density distribution

3.4.1. Analysis of topological parameters

A comparison of topological parameters obtained from experimental charge density data with those from theory will be given in this section. The effect of the disorder on the derived topological parameters in form I of piracetam, **2**, will also be examined; it is accepted that the presence of disorder represents a real challenge in analyses such as these. The topological parameters from experimental data were compared both with those directly determined from the wave functions of the gas phase calculations and from the multipole model based on the theoretical structure factors. The distances of the BCP to the nuclei denoted by d_1 and d_2, the electron density ρ, the Laplacian at the BCP, $\nabla^2\rho$, and the three eigenvalues λ_1, λ_2, λ_3 of the Hessian matrix of all the atoms of the studied forms are listed in Table 3.5. The most affected bonds giving the poorest agreement between the experimental and calculated parameters are the H-N (aniline) bonds and this is perhaps due

to the involvement of these atoms in strong hydrogen bonds. The $\nabla^2\rho(r_b)$ parameters for the C(1)-O(1) and C(6)-O(2) bonds show better agreement with those obtained from the multipole refinements of theoretical structure factors, whereas a large discrepancy can be observed in comparison with those derived from the pure wave function. The $\nabla^2\rho(r_b)$ parameters of the methylene H31-C3 and H32-C3 bonds involved in disorder are seriously affected, as may be expected, with large discrepancies from the parameters obtained from theoretical calculations. The experimental topological parameters for the C-C and C-H bonds which are involved in non-polar shared interactions yield a better agreement with theoretical calculations. Overall the experimental values are closer to those from the theoretical calculations for the charge density and the position of BCPs (d_1 and d_2), while those for the $\nabla^2\rho(r_b)$ parameters show less good agreement.

Table 3.5. Topological Analysis of BCPs for the three studied forms of **2**

Bond		d_1[a]	d_2[a]	$\rho(r_b)$[b]	$\nabla^2\rho(r_b)$[c]	λ_1[c]	λ_2[c]	λ_3[c]
C(1)	-O(1)	0.4379	0.7989	2.86	-35.58	-27.99	-25.2	17.61
		0.4792	0.7551	3.04	-39.49	-29.37	-25.29	15.17
		0.4667	0.7722	2.92	-40.86	-27.57	-25.45	12.16
		0.425	*0.8007*	*2.745*	*-10.959*	*-25.026*	*-22.647*	*36.714*
		0.4678	*0.7579*	*2.9*	*-34.86*	*-26.48*	*-24.00*	*15.62*
C(6)	-O(2)	0.5219	0.7138	3.01	-37.65	-27.93	-24.49	14.77
		0.4723	0.7613	3.02	-41.38	-30.19	-26	14.81
		0.4517	0.7842	2.86	-38.07	-28.2	-25.19	15.32
		0.4243	*0.8*	*2.758*	*-10.826*	*-25.18*	*-22.748*	*37.102*
		0.4679	*0.7564*	*2.89*	*-33.53*	*-26.21*	*-23.44*	*16.12*
C(1)	-N(1)	0.5765	0.7686	2.44	-26.28	-20.82	-17.06	11.61
		0.5677	0.7796	2.34	-22.19	-19.94	-16.27	14.03
		0.5324	0.818	2.33	-26.56	-19.4	-15.9	8.74
		0.5277	*0.851*	*2.107*	*-20.92*	*-16.706*	*-14.131*	*9.917*
		0.5832	*0.7955*	*2.1*	*-15.87*	*-16.73*	*-13.74*	*14.6*
C(4)	-N(1)	0.5933	0.866	1.74	-11.31	-11.24	-10.45	10.38
		0.6235	0.8381	1.79	-10.48	-13.42	-11.92	14.85
		0.6111	0.8478	1.78	-12.16	-12.42	-11.51	11.77
		0.5838	*0.8753*	*1.765*	*-16.084*	*-12.247*	*-11.675*	*7.838*
		0.6388	*0.8203*	*1.71*	*-7.7*	*-11.76*	*-11.12*	*15.18*
C(5)	-N(1)	0.5956	0.8428	1.87	-15.2	-13.48	-12.96	11.24
		0.6201	0.8177	1.84	-9.93	-12.99	-12.19	15.25
		0.593	0.8442	1.88	-14.75	-13.24	-12.7	11.19
		0.5701	*0.8634*	*1.865*	*-17.854*	*-13.104*	*-12.796*	*8.046*
		0.6321	*0.8015*	*1.85*	*-10.16*	*-12.97*	*-12.77*	*15.58*
C(6)	-N(2)	0.5452	0.7921	2.3	-26.37	-20.18	-16.51	10.32
		0.5636	0.7722	2.36	-23.42	-21.07	-16.19	13.85
		0.5521	0.7864	2.41	-27.57	-20.87	-17.37	10.67
		0.5177	*0.8516*	*2.138*	*-22.009*	*-17.161*	*-14.954*	*10.106*
		0.5837	*0.7858*	*2.15*	*-17.73*	*-17.38*	*-15.00*	*14.65*
H(1)	-N(2)	0.2575	0.7427	2.3	-33.35	-32.29	-31.44	30.38
		0.2604	0.7398	2.36	-37.86	-33.52	-32.18	27.84
		0.262	0.744	2.26	-31.16	-30.51	-29.35	28.71
		0.2636	*0.7504*	*2.299*	*-42.931*	*-32.195*	*-30.813*	*20.077*
		0.2831	*0.7309*	*2.21*	*-24.86*	*-28.37*	*-26.72*	*30.23*
H(2)	-N(2)	0.2726	0.7374	2.21	-29.94	-29.67	-28.83	28.56
		0.262	0.7483	2.34	-36.7	-33.14	-31.51	27.95
		0.2587	0.7493	2.27	-31.69	-31.14	-29.74	29.19
		0.2662	*0.7467*	*2.305*	*-42.201*	*-31.922*	*-30.54*	*20.261*
		0.2846	*0.7283*	*2.2*	*-24.21*	*-28.17*	*-26.2*	*30.16*
C(2)	-C(1)	0.6987	0.814	1.67	-9.76	-10.7	-9.53	10.47
		0.7215	0.7911	1.73	-10.57	-12.33	-10.7	12.46
		0.7188	0.7947	1.77	-11.77	-12.1	-10.9	11.23
		0.7463	*0.7795*	*1.682*	*-14.39*	*-12.183*	*-11.466*	*9.259*
		0.7415	*0.7846*	*1.63*	*-8.7*	*-10.99*	*-10.01*	*12.3*

Table 3.5, continued

H(21)	-C(2)	0.3742	0.7229	1.73	-15.67	-15.76	-15.1	15.18
		0.3744	0.7232	1.9	-18.75	-18.4	-17.68	17.33
		0.3881	0.6947	1.77	-17.11	-16.26	-15.49	14.64
		0.3991	*0.7023*	*1.852*	*-24.135*	*-17.685*	*-17.45*	*11.00*
		0.3896	*0.7119*	*1.78*	*-15.26*	*-16.19*	*-15.8*	*16.72*
H(22)	-C(2)	0.3863	0.6952	1.67	-14.96	-14.82	-14.23	14.1
		0.392	0.6884	1.82	-18.08	-17.13	-16.44	15.49
		0.3893	0.7097	1.75	-16.22	-16.11	-15.03	14.92
		0.3958	*0.7003*	*1.884*	*-25.004*	*-18.215*	*-17.978*	*11.189*
		0.3848	*0.7113*	*1.82*	*-16.57*	*-16.95*	*-16.46*	*16.83*
H(41)	-C(4)	0.3679	0.7271	1.78	-16.42	-16.63	-15.33	15.55
		0.3873	0.7059	1.86	-19.19	-17.86	-17.22	15.89
		0.3838	0.7103	1.8	-17.73	-16.75	-16.04	15.06
		0.3903	*0.7112*	*1.908*	*-25.601*	*-18.996*	*-18.504*	*11.899*
		0.3831	*0.7185*	*1.83*	*-16.95*	*-17.12*	*-16.84*	*17.02*
H(42)	-C(4)	0.3636	0.7266	1.79	-16.71	-16.81	-15.79	15.89
		0.3805	0.7095	1.9	-20.16	-18.52	-17.92	16.29
		0.381	0.7106	1.81	-18.34	-17.03	-16.52	15.22
		0.3983	*0.7031*	*1.89*	*-25.193*	*-18.476*	*-18.036*	*11.319*
		0.3885	*0.7129*	*1.8*	*-16.54*	*-16.67*	*-16.44*	*16.57*
C(5)	-C(6)	0.7545	0.7786	1.71	-11.47	-12.54	-10.09	11.17
		0.7347	0.7941	1.76	-11.02	-13.03	-10.96	12.96
		0.7472	0.7821	1.68	-11.24	-11.87	-10.35	10.98
		0.7578	*0.783*	*1.645*	*-13.689*	*-12.167*	*-11.129*	*9.607*
		0.7581	*0.7828*	*1.61*	*-8.88*	*-11.22*	*-9.98*	*12.31*
H(51)	-C(5)	0.3816	0.7069	1.81	-19.79	-17.14	-16.63	13.98
		0.3695	0.7186	1.95	-20.81	-19.07	-18.66	16.93
		0.3798	0.7125	1.84	-17.94	-17.14	-16.65	15.85
		0.3848	*0.7179*	*1.884*	*-25.094*	*-18.747*	*-18.384*	*12.038*
		0.3842	*0.7186*	*1.79*	*-15.76*	*-16.38*	*-16.29*	*16.91*
H(52)	-C(5)	0.386	0.7095	1.8	-19.87	-17.36	-16.16	13.64
		0.3806	0.7144	1.89	-20.09	-18.6	-17.58	16.08
		0.3792	0.7122	1.85	-18.36	-17.38	-16.82	15.83
		0.3969	*0.7065*	*1.866*	*-24.502*	*-18.192*	*-17.641*	*11.33*
		0.3864	*0.717*	*1.79*	*-16.22*	*-16.75*	*-16.06*	*16.59*
H31-C3		0.3771	0.7133	1.61	-0.93	-12.35	-9.65	21.06
		0.3754	0.7107	1.87	-18.89	-18.25	-17.46	16.82
		0.3833	0.7168	1.77	-16.95	-16.43	-16	15.48
		0.3984	*0.6981*	*1.889*	*-25.073*	*-18.11*	*-18.056*	*11.092*
		0.3859	*0.7105*	*1.81*	*-16.36*	*-16.67*	*-16.47*	*16.78*
H32-C3		0.3810	0.7181	1.58	-0.59	-11.97	-9.43	20.81
		0.3781	0.7171	1.85	-18.26	-17.8	-17.26	16.8
		0.378	0.706	1.82	-18.14	-17.1	-16.51	15.47
		0.4007	*0.6983*	*1.881*	*-24.765*	*-17.987*	*-17.823*	*11.046*
		0.3897	*0.7093*	*1.78*	*-15.73*	*-16.18*	*-16.13*	*16.58*

First three lines correspond to Form I, Form II and Form III. Last two lines (italic) correspond to reference density from the wave function and reference density from the theoretical structure factor respectively. [a] *In units of Å.* [b] *In units of e Å*$^{-3}$. [c] *In units of e Å*$^{-5}$

3.4.2 Analysis and comparison of the multipole refinements.

In this section the agreement between the experimental data and theoretical calculations of the topological parameters are compared as the sophistication of the model is increased. Of particular interest is the effect of the disorder on the derived parameters of form I.

Five different multipole model refinements of the experimental data of forms II and III (1, 2, 3, 4, 5), as described in Section 3.2.3, were compared with the topological analysis of the wave functions of the gas phase calculations (a), as well as with the multipole model based on the refinements of the theoretical structure factors (b). For form I and the monohydrate only three multipole refinements were performed due to the absence of neutron data. The charge densities and the Laplacian at the BCPs of each experimental and theoretical model are compared. Since the volume of data prohibited the deduction of clear trends (Table 3.5), a residual factor R_{Par} (equation 2.9) was calculated in order to describe the global measurement of the agreement between experimental and theoretical parameters. The R_{val}, R_{ρ} and $R_{\nabla 2(\rho)}$ values for the studied forms of **2** are summarized in Table 3.7. An improvement of the R_{values} term can be noticed with increasing sophistication of the multipole model in forms I, II and III. In form II, the R_{values} are identical for the hydrogen adps obtained from SHADE[17] and using those from scaled X-ray data with neutron data (model 2 and 4 or 3 and 5). For form III, slightly lower R_{values} were observed when the hydrogen adps obtained from the scaled X-ray data with neutron data were implemented. No particular trends can be observed for the R_{ρ} and $R_{\nabla 2(\rho)}$ parameters.

The two different density references used are also not in agreement for each form analysed. For instance, in form I case (a), the best fit with theory of R_{ρ} is given by model 1 followed by 3 and 2, whereas in case (b) model 1 is followed by model 2 and 3. The best agreement between experimental data and theoretical calculations of the $R_{\nabla 2(\rho)}$ parameters in case (a) is given by model 3 followed by 2 and 1. In case (b) the trends are in the opposite direction, the best fit was found for model 1 followed by 2 and 3. The same trends were observed for the $R_{\nabla 2(\rho)}$ values in the case of form III. In form II, the lower $R_{\nabla 2(\rho)}$ was found for model 1 in both cases. However in case (a) it was followed by models 5, 3, 4 and 2 in that order, whereas in case (b) a shift in the trend between models 2 and 3 can be observed.

Table 3.7. The residual factor of the experimental data versus theoretical data for forms I, II and III of piracetam, **2**

(a) Reference density from wave function	**Model**	$\mathbf{R_{values}}$	$\mathbf{R_{\rho}}$	$\mathbf{R_{\nabla 2(\rho)}}$
I	1	0.0332	0.006	0.1895
	2	0.0321	0.0053	0.1301
	3	0.0300	0.0026	0.0582
II	1	0.0201	0.0065	0.1917
	2	0.0184	0.0288	0.0649
	3	0.0177	0.0325	0.0464
	4	0.0184	0.0288	0.0634
	5	0.0177	0.0335	0.0463
III	1	0.0304	0.0111	0.1749
	2	0.0299	0.0035	0.0789
	4	0.0294	0.0028	0.0757
	5	0.0298	0.0092	0.0648
	6	0.0293	0.0084	0.0624
(b) Reference density from theoretical structure factors				
I	1	0.0332	0.0115	0.0321
	2	0.0321	0.0121	0.1078
	3	0.0300	0.0202	0.1993
II	1	0.0201	0.0286	0.0690
	2	0.0184	0.0514	0.2368
	3	0.0177	0.0552	0.2612
	4	0.0184	0.0513	0.2388
	5	0.0177	0.0561	0.2613
III	1	0.0304	0.0106	0.0913
	2	0.0299	0.0255	0.2182
	3	0.0294	0.0248	0.2224
	4	0.0298	0.0314	0.2369
	5	0.0293	0.0305	0.2401

The lower values of $R_{\nabla 2(\rho)}$ in case (a) compared with case (b) suggest a better agreement between experimental data and the theoretical calculations when the reference density from the wave function is used. The $R_{\nabla 2(\rho)}$ values are more markedly lower for form I compared with forms II and III, which may be a consequence of the fact that the multipoles for atoms identified as exhibiting disorder were not refined. This implies a difference in the nature of the topological parameters between the disordered form I and the other two forms.

3.4.3. The residual density maps representations

The residual electron density maps for all studied forms of **2** are represented in Figures 3.5 and 3.6. The maps represent the Fourier calculations based on the difference between the observed and calculated structure factors, and are plotted in both acetamide and pyrrolidone planes. The remained densities in all studied forms of **2** do not exceed 0.3 eÅ^{-3}, indicating the good quality of the multipole refinements. Form I, which was identified to possess disordered atoms, shows no particularly high residual peaks on the residual density maps, though does exhibit more noise. However, similar levels of noise were also found for form II. The cleanest residual map can be observed for the monohydrate form.

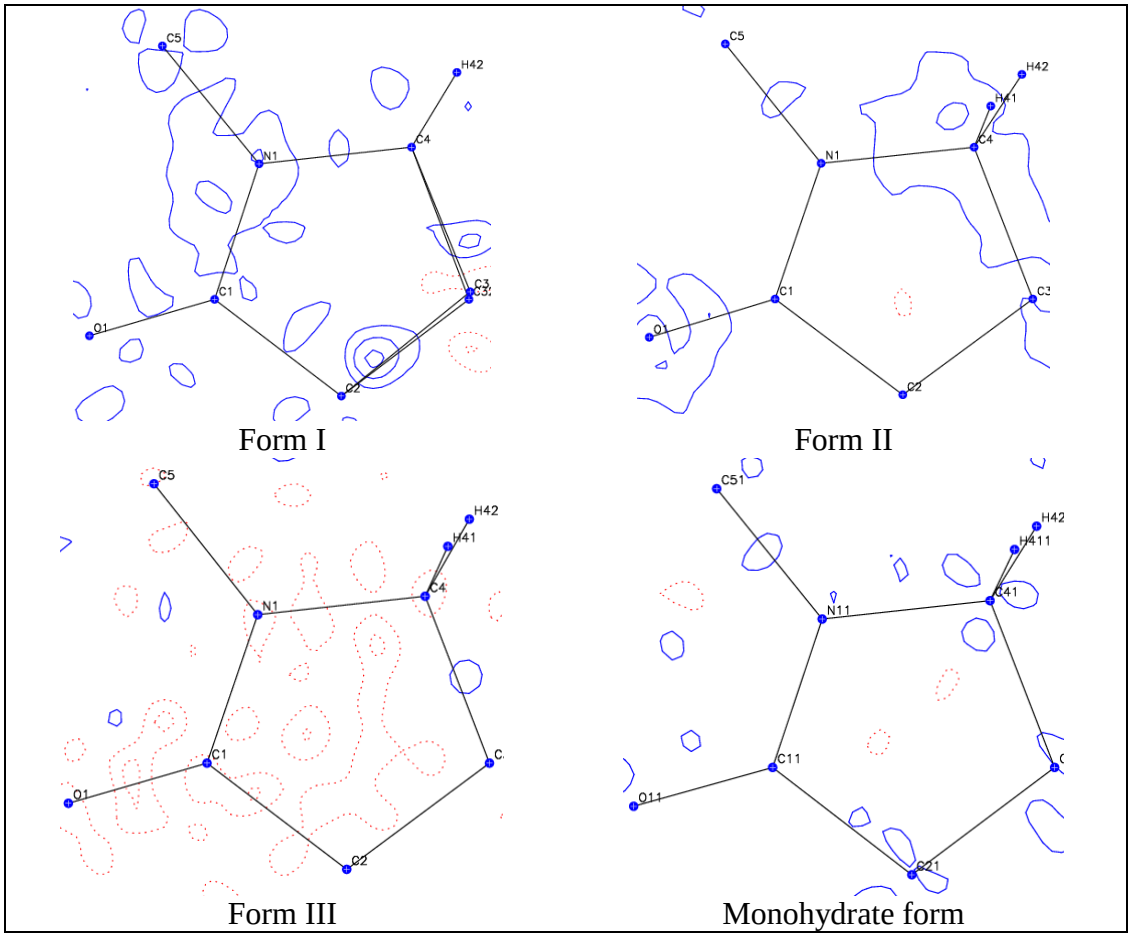

Figure 3.5. Residual electron density maps for the studied forms of **2**, in the pyrrolidone ring plane. Contours level are ±0.1e/Å^{-3}

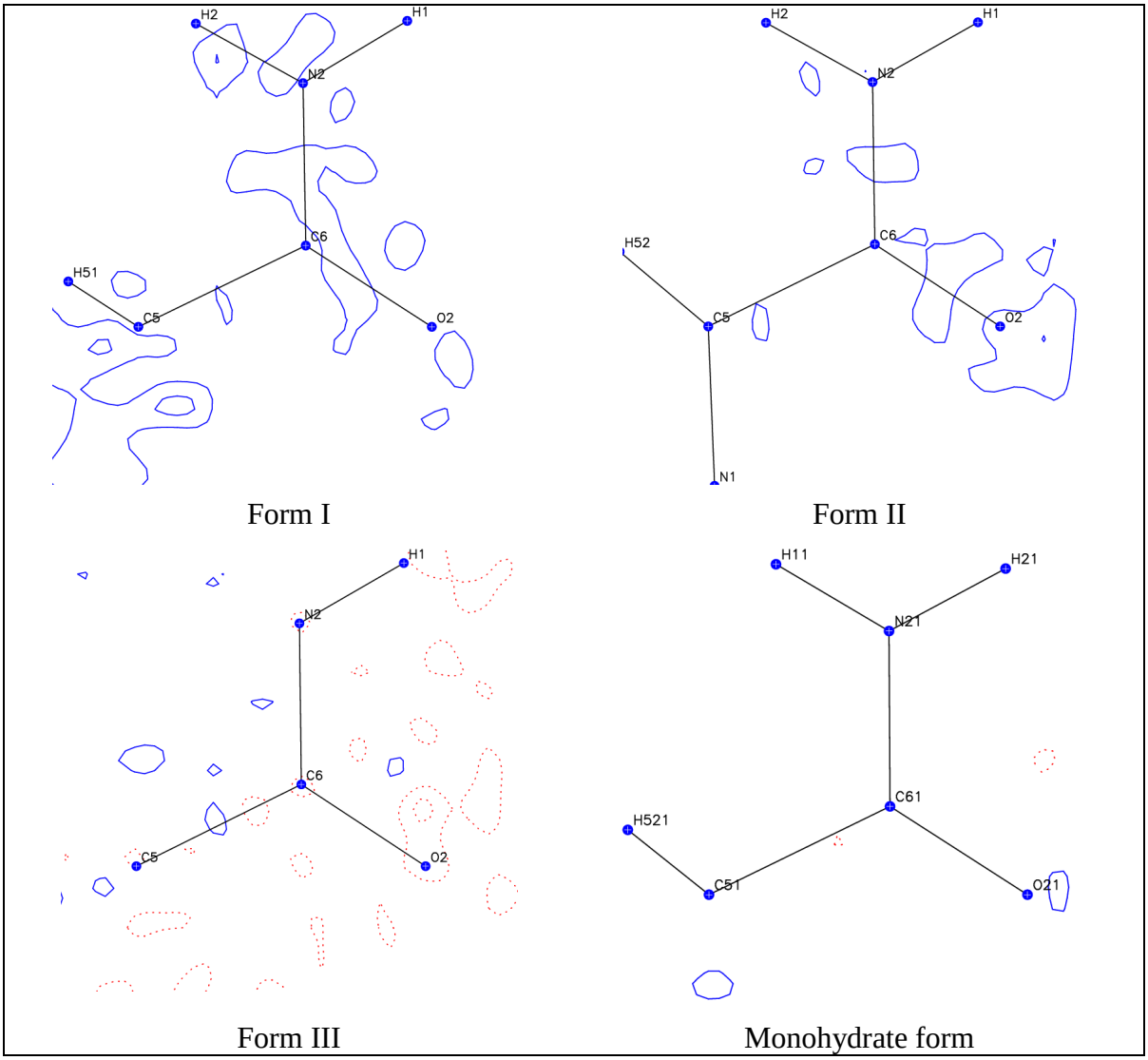

Figure 3.6. Residual electron density maps for the studied forms of **2**, in the acetamide plane. Contours level are ±0.1e/Å^{-3}

3.4.4. Deformation density maps representation

The deformation density maps in the pyrrolidone plane for the studied forms of **2** are plotted in Figures 3.7 and 3.8. The map resulting from the multipole refinement of theoretical structure factors of form II obtained from CRYSTAL09[23] calculations is also included for comparison. The maps are plotted in both pyrrolidone (Figure 3.7) and acetamide (Figure 3.8) planes. The deformation density maps of the piracetam have already been analysed in the literature for forms II, III and the monohydrate.[6] However, the results obtained in this study will be shown here, which include in addition the previously unstudied deformation density map for form I. The theoretical results do not show any particular asymmetry in the lone pair densities around the atoms in the pyrrolidone ring or acetamide planes.

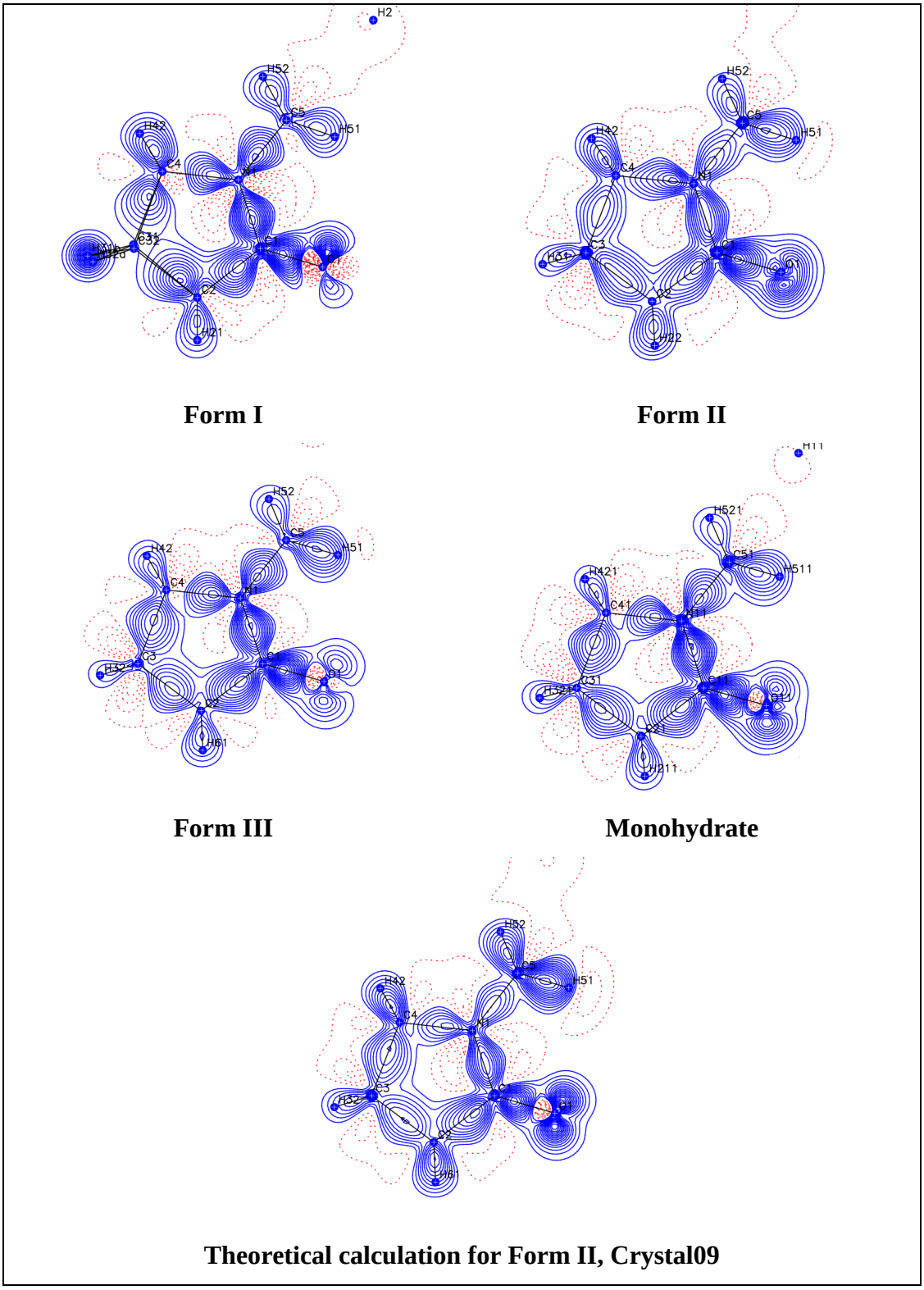

Figure 3.7. Deformation density maps representation for experimental studied forms of **2** and from the multipole refinement of theoretical structure factor of form II obtained from CRYSTAL09[23] calculations. Plotted in the pyrrolidone ring plane (negative contours - red dashed, positive contours – blue line). Contour levels at 0.08 eÅ^{-3}

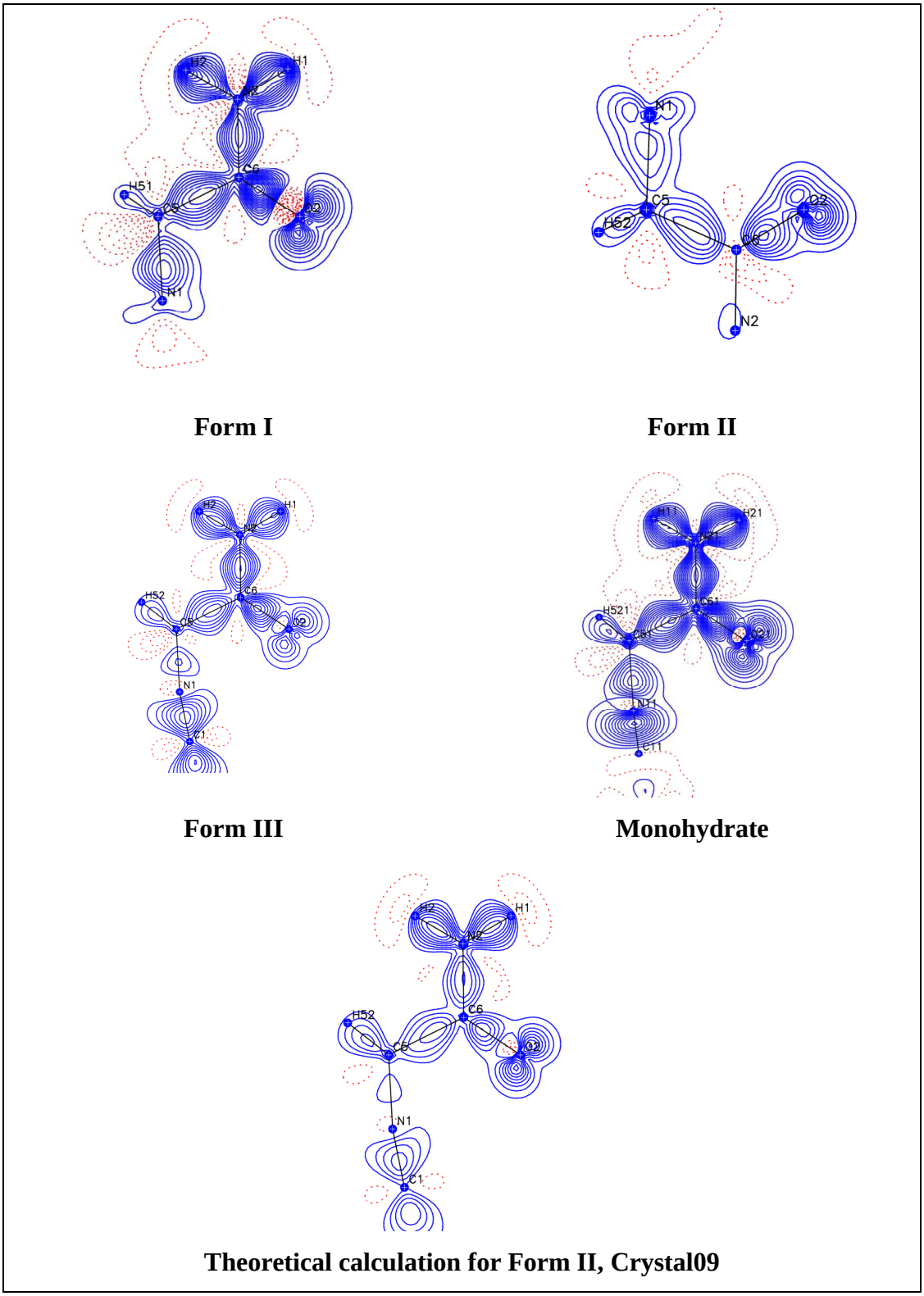

Figure 3.8. Deformation density maps representation for experimental studied forms of **2** and from the multipole refinement of theoretical structure factor of form II obtained from CRYSTAL09[23] calculations. Plotted in the acetamide plane (negative contours - red dashed, positive contours – blue line). Contour level at 0.08 eÅ^{-3}

The fact that the multipole parameters were not refined for the disordered atoms in form I is reflected in the deformation density map, with clear spherical density observed around

the relevant H atoms that is not observed in the other forms. The O1 atom in form I also shows significantly asymmetrical lone pairs in form I, compared with the other forms and the theoretical results. On the other hand O2 shows a symmetrical lone pair in form I, in agreement with the situation in form III, monohydrate and theoretical calculations. For form II, asymmetrical lone pairs for this atom were observed. The theoretical results do not show any particular asymmetry on the lone pair electrons around the atoms in either the pyrrolidone ring or acetamide planes.

3.4.5. Laplacian representation

In order to investigate the behaviour of the lone pair electrons around the O atoms in the various forms of **2**, the Laplacian maps were also plotted in both the pyrrolidone ring and acetamide planes (Figures 3.9. and 3.10). The experimental results were also compared with the Laplacian from the multipole refinement of theoretical structure factors for form II, obtained from CRYSTAL09[23] calculations. The theoretical calculations show symmetrical lone pairs around both O1 and O2 atoms. On the other hand, in the experimental results these lone pair electrons shapes vary in the different forms. For example, in form I, O1 shows a less pronounced lone pair on one side of the atom. In form II, the lone pairs around the O1 atom show unification at one side of the atom indicating a more homogeneous electron distribution. The lone pairs of the O1 atom are more symmetrical in form III, but are asymmetrical in the monohydrate. For the O2 atom the lone pair electrons are symmetrical in form I and the monohydrate, but asymmetrical in forms II and III (Figure 3.10). In form I, the atoms indentified with disorder for which no multipole refinement was carried out, shows spherical density on the Laplacian map, as expected.

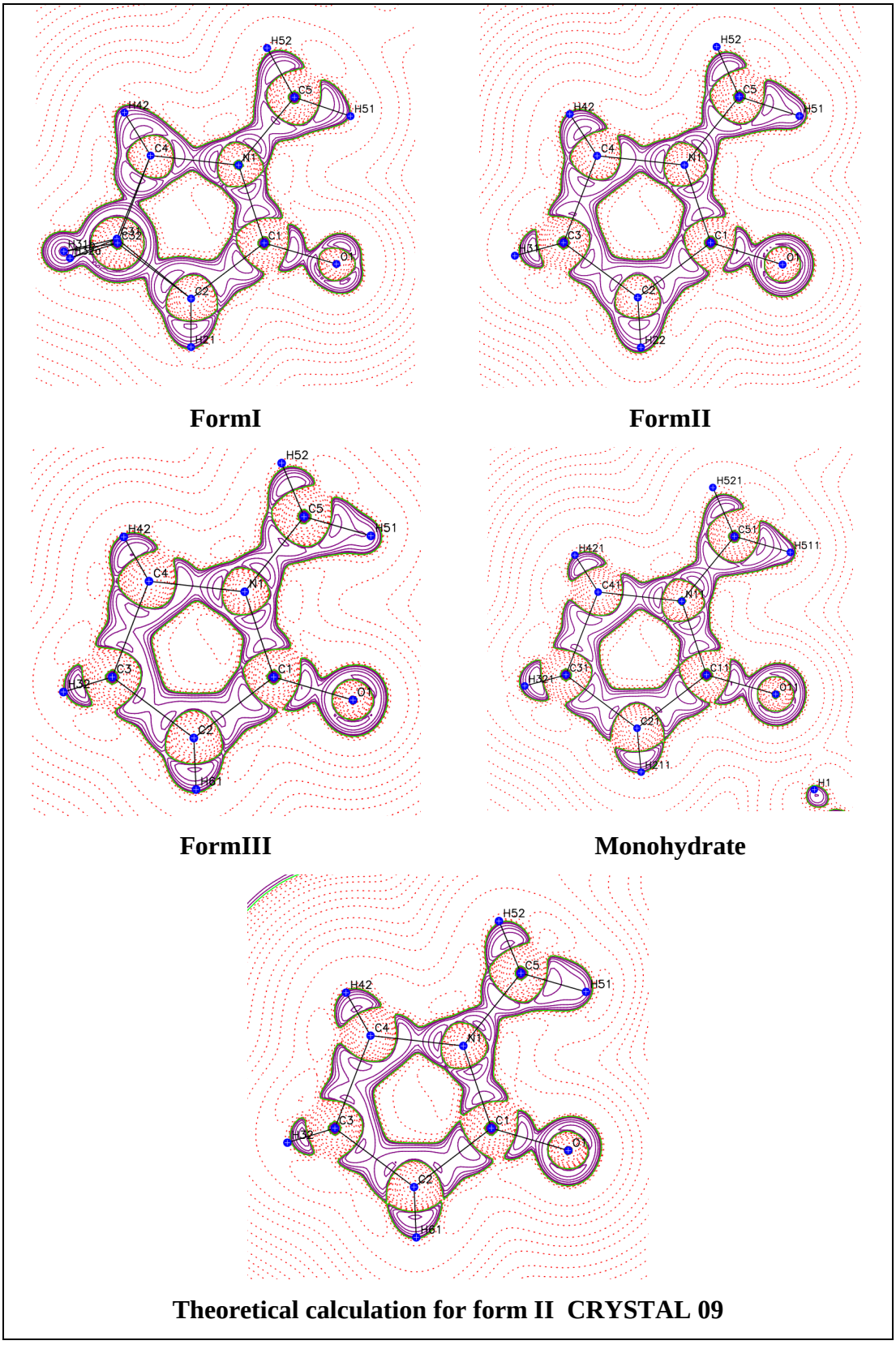

Figure 3.9. Plots of the negative Laplacian, $L(\mathbf{r})$ in the pyrrolidone plane of the forms of **2**. Positive contours – solid purple line; negative contours – dotted line. The contour levels are at -1.0 x 10^{-3}, ±2.0 x 10^{n}, ±4 x 10^{n}, ± 8 x 10^{n} (n = -3, -2, -1, 0, +1, +2) e Å^{-5}

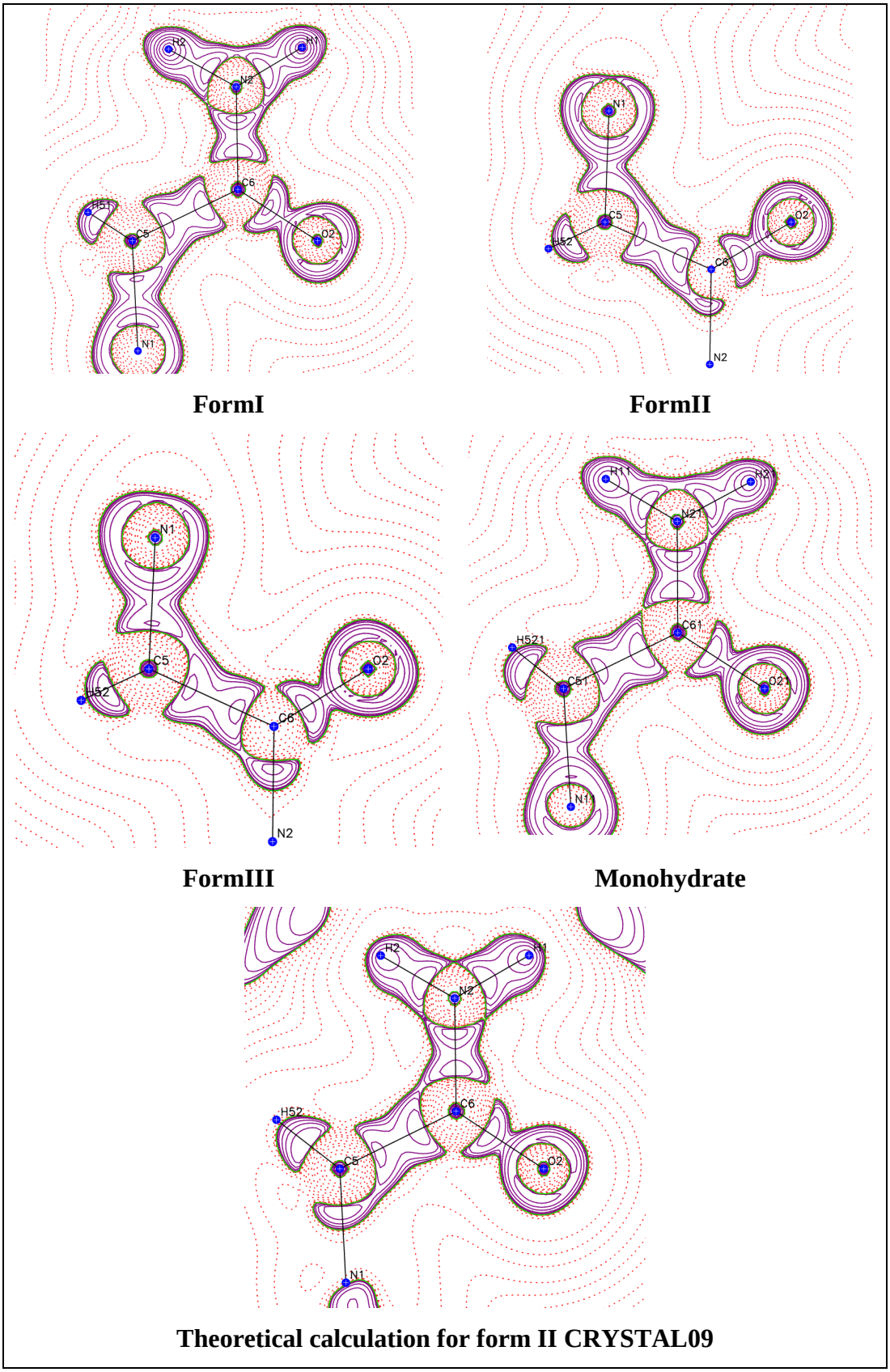

Figure 3.10. Plots of the negative Laplacian, $L(\mathbf{r})$ in the acetamide plane of the forms of **2**. Positive contours – solid purple line; negative contours – dotted line. The contour levels are at -1.0 x 10^{-3}, ±2.0 x 10^{n}, ±4 x 10^{n}, ± 8 x 10^{n} (n = -3, -2, -1, 0, +1, +2) e Å^{-5}

3.4.6. Atomic net charge calculations

The atomic net charge was calculated for the oxygen atoms in forms of **2** using the Bader's QTAIM[26] method implemented in the XD[12] program, and compared with the values from the multipole refinement of theoretical structure factors obtained from gas phase optimisation, as well as with the Mulliken charge. There is an obvious difference between the theoretical calculations, where no hydrogen bonds are present, and the experimental data. In the case of the experimental data, higher charge can be observed for atoms O1 and O2. There is also a significant difference in the Q_{QTAIM} calculation for the theoretical results and the $Q_{Mulliken\ charge}$ method. The O1 and O2 atoms are found to be more charged in forms I, II and the monohydrate, due to the shorter hydrogen bonds formed in these structures compared with those in form III (Table 3.4 and 3.8)

Table 3.8. Experimental atomic charges, Q_{QTAIM} and $Q_{Mulliken\ charge}$, for the studied forms of **2**.

	Q_{QTAIM}	
	O1	O2
Form I	-1.125	-0.883
Form II	-1.064	-1.002
Form III	-0.964	-0.958
Monohydrate	-1.082	-1.118
Theoretical calc.	-0.895	-0.869
(isolated molecule)	$Q_{Mulliken\ charge}$	
	O1	O2
	-0.319	-0.295

3.5. Lattice and intermolecular interaction energy calculations.

The lattice energy of the studied forms of **2** were calculated using different approaches and different software including XD,[12] CRYSTAL09[23] and CLP.[25] The intermolecular interactions between the molecules exhibiting hydrogen bond interactions were also calculated. The results will be discussed in this section.

The results of the lattice energy calculations using the experimental charge density approach are listed in Table 3.9. The two values given for form I correspond to the different positions that can be adopted by the disordered C3, H31 and H32 atoms. There is a high sensitivity of the lattice energies to the type of multipole model used for all studied forms. Variation in the ranking stability of the different forms can also be seen for model 1 when compared with the other models. The lattice energy is significantly lower in

magnitude for model 1 as compared with models 2, 3, 4 and 5, with form III being the most stable, followed by forms II and I. The energy is decreased by refining the multipole parameters for hydrogen atoms to the quadrupole level (model 2 and 4). The unrestricted multipole model seems to give the lowest lattice energies for all studied forms. The trends in ranking stabilities of the forms were identical for models 2, 3, 4 and 5, with form II being the most stable followed by forms I and III.

Overall, forms II and I showed close agreement in their lattice energy values, whereas form III had significantly higher values. In order to investigate the large discrepancy between the lattice energy obtained for form III and that for the other two forms, new refinements were carried out in which the x,y,z and U_{ij} parameters were refined only once and in a different block to the multipole parameters. The results were compared with the CRYSTAL09[23] and CLP[25] lattice energy calculations and are summarised in Table 3.9. The CRYSTAL09[23] and CLP[25] lattice energy calculations give the lowest lattice energy for form III, while the experimental charge density shows form II with the lowest lattice energy. In contrast with the CRYSTAL09[23] and CLP[25] lattice energy calculations in this work, previous atom-atom potential method calculations give form II the lowest energy (–99.44 kJ/mol) followed by form III (–97.30 kJ/mol) and form I (–87.29 kJ/mol).[27]

Table 3.9. Lattice energies from the experimental charge density of the studied forms of **2** (kJ/mol).

Model	**Form I**	**Form II**	**Form III**
1	-95.08 [minor] -93.78 [major]	-95.49	-99.81
2	-184.20 [minor] -184.21 [major]	-185.97	-151.67
3	-187.52 [minor] -187.55 [major]	-197.73	-148.15
4		-185.47	-145.50
5		-187.32	-142.12

Table 3.10. Lattice energy calculations from the experimental charge density approach in comparison with fully theoretical results using the CRYSTAL09[23] and CLP[25] programs (kJ/mol).

Form	XD[12] lattice energy	CLP[25]	CRYSTAL09[23]
I_1	-149.10	-122.5	-152.80
I_2	-155.94	-123.3	-152.39
II	-174.03	-126.3	-165.47
III	-150.58	-128.1	-167.26

The intermolecular interaction energies of forms II, III and the monohydrate were calculated using the INTEREN option in the xdprop section incorporated in the XD program.[12] This method calculates the intermolecular interaction energies as described in equation 2.10, using the same methodology as LATEN. The results are listed in Table 3.11. The electrostatic term is also included here for a comparison with previous calculations of these forms.[6] The nearest neighbour molecules were generated according to the hydrogen bond contacts and the short H···H contacts were also taken into consideration. The results were compared with the DFT calculations at the B-LYP/TZVPP[28] level performed with the TURBOMOLE 6.2[29] software.

Closer agreement of the intermolecular interaction energy (E_{int}) of the ECD with the theoretical calculations were obtained for model 2. In the case where dimers are present, the total electrostatic interaction between the two molecules was used, unlike the strategy used elsewhere.[6] The E_{int} of form II shows the best agreement between the results of experiment and theory, with values of –297.71 kJ/mol and –281 kJ/mol, respectively. On the other hand form III and the monohydrate show a slightly larger discrepancy between experimental and theoretical results.

Table 3.11 Intermolecular interaction energies (kJ/mol) of the studied forms of **2**

Form II **Model 2**	E_{int}	E_{es}	$E_{ex\text{-}rep}$	E_{disp}	E_{int}(DFT)	**Dispersion correction**
O2…H1-N2	-75.59	-123.73	79.34	-31.20	-69.25	-14.27
O1…H2-N2	-64.25	-77.70	43.33	-29.89	-45.92	-22.25
O1…H51-C5	-19.19	-19.89	19.22	-18.52	-36.08	-13.71
O2…H21-C2	-57.54	-47.69	19.41	-29.26	-34.72	-27.18
O2…H31-C3	-25.35	-17.14	11.66	-19.87	-14.24	-18.86
H51…H32	-39.14	-22.69	33.93	-50.38	-46.14	-48.42
H31…H1	-11.71	+0.26	10.96	-22.95	-19.47	-22.94
H31…H31	-0.61	+1.64	1.32	-3.58	-2.97	-3.66
H31…H1	+17.49	+20.74	6.26	-9.52	-3.07	-9.97
H51…H2	-21.78	-16.55	1.63	-6.86	-9.14	-7.12
Sum	-297.71	-320.76			-281.00	
FormIII **Model 2**	E_{int}	E_{es}	$E_{ex\text{-}rep}$	E_{disp}	E_{int}(DFT)	**Dispersion corrections**
O2…H1-N2	-39.30	-86.93	78.48	-30.86	-69.04	-13.94
N2-H2…O1	-39.50	-54.30	44.83	-30.02	-45.78	-22.30
O2…H32-C3	-44.13	-34.20	19.50	-29.43	-34.72	-27.21
C3-H31…O1	-23.67	-15.74	13.44	-21.38	-15.76	-20.20
C6-H61...O2	-0.39	+1.82	4.70	-6.92	-5.53	-5.92
C6…H41	-11.19	+0.32	12.13	-23.65	-19.98	-23.54
H2…H31	7.81	+10.83	6.42	-9.45	-3.12	-9.91
H32…H32	-0.10	+2.38	1.49	-3.98	-3.21	-4.07
N1…H51	-36.7	-26.52	21.36	-31.63	-38.01	-30.36
Sum	-187.29	-202.35			-235.15	
Monohydrate **Model 2**	E_{int}	E_{es}	$E_{ex\text{-}rep}$	E_{disp}	E_{int}(DFT)	**Dispersion corrections**
N2-H2…O2	-44.18	-82.16	65.68	-27.69	-65.10	-13.21
C3-H31…O1	-85.33	-68.20	29.97	-47.10	-42.08	-45.32
C4-H41…O2	-47.21	-37.92	11.22	-20.51	-21.38	-19.24
C5-H51…O1	-18.50	-15.63	13.13	-16.00	-43.36	-13.13
C2-H22…O1	-39.41	-34.21	14.48	-19.68	-21.26	-16.48
H42…N2	-2.42	-0.87	0.09	-1.65	-4.10	-1.66
H21…H32	-0.92	4.82	6.86	-12.61	-8.75	-12.70
N2…H52	-8.68	-1.40	5.51	-12.80	-7.58	-13.38
Sum	-246.65	-235.57			-213.61	
Model 2	E_{int}	E_{es}	$E_{ex\text{-}rep}$	E_{disp}	E_{int}(DFT)	**Dispersion corrections**
O2…HW2-OW	2.61	2.72	-0.11	-0.11	-36.84	-13.24
OW-HW1…O1	-28.98	-71.78	62.73	-19.93	-28.68	-6.34
N2-H1…OW	0.63	1.33	0.11	-0.81	-25.81	-9.69
HW2…H2	-3.18	-2.35	1.46	-2.29	-2.56	-2.40
Sum	-28.92	-70.08			-93.89	

There is a large discrepancy between the electrostatic term obtained for form II and the monohydrate from the present experimental results as compared with those in the literature.[6] From the experimental results of form II, the electrostatic term was found to be –320.76 kJ/mol whereas the value presented in the literature is –187.8 kJ/mol. In the monohydrate case, the electrostatic energy for the piracetam···piracetam intramolecular interactions is –235.57 kJ/mol and for piracetam···water –70.08 kJ/mol, while in the previous work the piracetam···piracetam electrostatic energy is evaluated as –199 kJ/mol, with –175.2 kJ/mol for piracetam···water interactions. These results emphasise the variation of the electrostatic energy with the model and methodology used.

3.6. Conclusions

Three forms of **2** that are stable at ambient conditions were analysed using high resolution X-ray diffraction. Additionally, the monohydrate form was also included in this study. The samples of Form I produced in this study were identified to be stable under ambient conditions over a period of six months, in contrast to previous reports. Only one carbon atom was identified with disorder compared with previous studies where two of the C atoms of the lactam ring were identified with disorder. A difference in the conformation of form I compared with the other forms was observed, in the orientation of the acetamide group relative to the ring. A common centrosymmetric dimer is present in forms II, III and the monohydrate, formed by hydrogen bond interactions between acetamide groups.

The agreement between experimental data and theoretical calculations of the topological parameters was slightly better for form I than for the other forms. This may be a consequence of the fact that the multipoles for atoms identified as exhibiting disorder were not refined. This reveals a difference in the topological parameters between the disordered form I and the other two forms.

The experimental charge density results emphasise, as found for sulfathiazole in Chapter 2, that the lattice energy calculations are highly sensitive to the multipole model strategy applied in the refinements. The fully theoretical results were, however, in agreement in this case, with form III giving the lowest lattice energy, followed by forms II and I. However the magnitudes of the lattice energies of the forms are significantly different. As in the previous chapter, it can be concluded that calculating the lattice energy from the experimental charge density is hardly possible with current methodologies even when theoretical results are present. Future investigations and developments are thus necessary.

The intermolecular interaction experimental results were found to be in good agreement with theoretical results only for form II. Large discrepancies are evident between experimental data and theoretical calculations for the other forms. A possible explanation may be that the multipole refinement for form II gives lower R_{values} compared with the other forms, suggesting that more accurate data, or better multipole model refinements are available for this form. The intermolecular interaction results were also compared with previous results from the literature.[6] The electrostatic term for form II and the monohydrate showed a large discrepancy between the present results and those present in the literature, further suggesting that substantial developments are required in this area to make such energy calculations reliable.[6]

References

1. F. P. A. Fabbiani, D. R. Allan, W. I. F. David, A. J. Davidson, A. R. Lennie, S. Parsons, C. R. Pulham and J. E. Warren, *Cryst. Grow. Des*., 2007, **7**, 1115-1124.
2. G. Admiral, J. C. Eikelenboom and A. Vos, *Acta Cryst. B*, 1982, **38**, 2600-2605.
3. D. Louer, M. Louer, V. A. Dzyabchenko, V. Agafonov and R. Ceolin, *Acta Cryst. B*, 1995, **51**, 182-187.
4. F. P. A. Fabbiani, D. R. Allan, S. Parsons and C. R. Pulham, *CrystEngComm*, 2005, **7**, 179-186.
5. Z. Galdecki and M. L. Glowka, *Pol. J. Chem*., 1983, **57**, 1307.
6. M. -H. Chambrier, N. Bouhmaida, F. Bonhomme, S. Lebegue, J. -M. Gillet, C. Jelsch and N. E. Ghermani, *Cryst. Grow. Des*., 2011, **11**, 2528-2539.
7. A. Tilborg, D. Jacquemin, B. Norberg, E. Perpete, C. Michaux and J. Wouters, *Acta Cryst. B*, 2011, **67**, 499-507.
8. A. Volkov and P. Coppens, *Acta Cryst. A*, 2001, **57**, 395-405.
9. Z. Otwinowski, W. Minor, *Methods in Enzymology, Macromolecular Crystallography, Part A;* W. C. Carter, M.R. Sweet, *Academic Press New York*, 1997, **279**, 307-326.
10. H. R. Blessing, *J. Appl. Cryst.*, 1997, **30**, 421-426.
11. A. Altomare, G. Cascarano, C. Giacovazzo and A. Guagliardi, *J. Appl. Cryst.*, 1994, **27**, 435.
12. L. J. Farrugia, *J. Appl. Cryst.*, 1999, **32**, 837-838.
13. D. A. Keen, M. J. Gutmann, and C. C. Wilson, *J. Appl. Cryst.*, 2006, **39**, 714–722.

14. M. J. Gutmann, *SXD2001. ISIS Facility, Rutherford Appleton Laboratory, Oxfordshire, England*, 2005.
15. G. M. Sheldrick, *Acta Cryst. A*, 2008, **64**, 112-122.
16. A. Volkov, P. Macchi, L. J. Farrugia, C. Gatti, P. R. Mallinson, T. Richter and T. Koritsanszky, *XD-2006*, 2006, http://xd.chem.buffalo.edu/.
17. Ø. A. Madsen, *J. Appl. Cryst.*, 2006, **39**, 757-758.
18. J. P. Perdew, K. Burke and M. Ernzerhof, *Phys. Rev. Lett.*, 1996, **77**, 3865.
19. (a) T. H. Dunning, *J. Chem. Phys.*, 1989, **90**, 1007; (b) K. A. Peterson, D. Figgen, M. Dolg and H. Stoll, *J. Chem. Phys.*, 2007, **126**, 124101.
20. M. J. Frisch, G. W. Trucks, H. B. Schlegel, G. E. Scuseria, M. A. Robb, J. R. Cheeseman, J. A. Montgomery, T. V. Jr., K. N. Kudin, J. C. Burant, J. M. Millam, S. S. Iyengar, J. Tomasi, V. Barone, B. Mennucci, M. Cossi, G. Scalmani, N. Rega, G. A. Petersson, H. Nakatsuji, M. Hada, M. Ehara, K. Toyota, R. Fukuda, J. Hasegawa, M. Ishida, T. Nakajima, Y. Honda, O. Kitao, H. Nakai, M. Klene, X. Li, J. E. Knox, H. P. Hratchian, J. B. Cross, V. Bakken, C. Adamo, J. Jaramillo, R. Gomperts, R. E. Stratmann, O. Yazyev, A. J. Austin, R. Cammi, C. Pomelli, J. W. Ochterski, P. Y. Ayala, K. Morokuma, G. A. Voth, P. Salvador, J. J. Dannenberg, V. G. Zakrzewski, S. Dapprich, A. D. Daniels, M. C. Strain, O. Farkas, D. K. Malick, A. D. Rabuck, K. Raghavachari, J. B. Foresman, J. V. Ortiz, Q. Cui, A. G. Baboul, S. Clifford, J. Cioslowski, B. B. Stefanov, G. Liu, A. Liashenko, P. Piskorz, I. Komaromi, R. L. Martin, D. J. Fox, T. Keith, M. A. Al-Laham, C. Y. Peng, A. Nanayakkara, M. Challacombe, P. M. W. Gill, B. Johnson, W. Chen, M. W. Wong, C. Gonzalez and J. A. Pople, GAUSSIAN03, Wallingford, CT., US, 2004.
21. Basis sets were obtained from the Extensible Computational Chemistry Environment Basis Set Database, Version 02/25/04, as developed and distributed by the Molecular Science Computing Facility, Environmental and Molecular Science Laboratory which is part of the Pacific Northwest Laboratory, P.O. Box 999, Richland, WA 99352, U.S.A., and funded by the U.S. Department of Energy.
22. F. W. Biegler-Konig, R. F .W. Bader, T. Tang, *J. Comput. Chem.*, 1982, **3**, 317.
23. R. Dovesi, R. Orlando, B. Civalleri, C. Roetti, V. R. Saunders, and C. M. Zicovich-Wilson, *Z. Kristallogr.*, 2005, **220**, 571; R. Dovesi, V. R. Saunders, C. Roetti, R. Orlando, C. M. Zicovich-Wilson, F. Pascale, B. Civalleri, K. Doll, N. M. Harrison, I. J. Bush, P. D'Arco, and M. Llunell, CRYSTAL09 (CRYSTAL09 User's Manual. University of Torino, Torino, Italy, 2009).

24. (a) A. D. Becke, *Phys. Rev. A*, 1988, **38**, 3098; (b) A. D. Becke, *J. Chem. Phys.*, 1993, **98**, 5648; (c) C. Lee, W. Yang and R. G. Parr, *Phys. Rev. B*, 1988, **37**, 785. (d) P. J. Stephens, J. F. Devlin, C. F. Chabalowski and M. J. Frisch, *J. Phys. Chem.*, 1994, **98**, 11623.
25. A. Gavezzotti, *New J. Chem*., 2011, **35**, 1360-1368.
26. R. F. W. Bader, *Atoms in Molecules: A Quantum Theor.*, Oxford: Claredon Press.
27. D. Louër, M. Louër, V. A. Dzyabchenko, V. Agafonov and R. Céolin, *Acta Cryst. B*, 1995, **51**, 182-187.
28. A. Schaefer, C. Huber and R. Ahlrichs, *J. Chem. Phys.*, 1994, 100, 5829-5835.
29. TURBOMOLE V6.2 2010, a development of University of Karlsruhe and Forschungszentrum Karlsruhe GmbH, 1989-2007, TURBOMOLE GmbH, since 2007; available from http://www.turbomole.com.

4. Carbamazepine

4.1. Introduction

Carbamazepine (**3**; 5*H*-dibenz[*b,f*]azepine-5-carboxiamide (Scheme 4.1.) is another extensively studied polymorphic material, which will be examined in this chapter. Carbamazepine is an anti-convulsant drug used in treatment of trigeminal neuralgia and epilepsy. It is known to crystallise in five anhydrous polymorphs,[1-5] and is one of the most examined polymorphic organic compounds. Form II was found to be a low density polymorph with large voids between the carbamazepine molecules within the crystal packing in the initial structure determination;[2] subsequent studies showed that this is, in fact, a solvated crystal structure.[6, 7] It has been shown that the solvent persists even after keeping the crystals in oven at 343 K over a period of 30 days.[6] Carbamazepine also exists in a dihydrate form, which is also studied in this work.

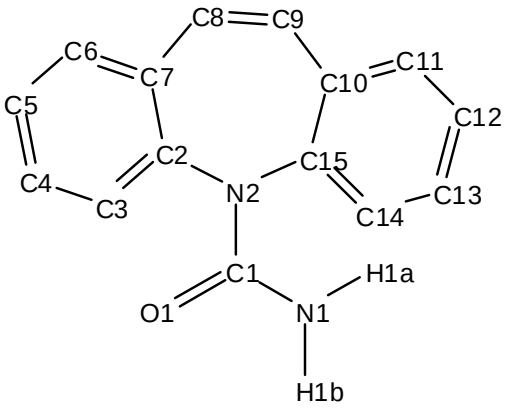

Scheme 4.1. Molecular structure and atom labelling of **3.** Some of the hydrogen atoms are omitted for clarity. However, they are labelled by way of their corresponding C atom. For instance, the H atom bonded to C3 atom is labelled H3.

The first crystal structure of carbamazepine was reported for form III in 1981.[1] This was followed by the crystal structure of form II, in 1987,[2] and by form IV in 2002.[3] The structure of form I was first determined in 2003.[4] Form III has been re-examined four times,[5, 8-10] while form I was re-determined by powder diffraction data in 2007.[11] The most recent polymorph reported, form V,[12] is formed selectively by templating the growth of carbamazepine from the vapour phase onto the surface of a crystal of the hydrogenated analogue dihydrocarbamazepine form II.

Form I is known to crystallise in a triclinic $P\bar{1}$ space group; form II in trigonal R-3, forms III and IV in monoclinic $P2_1/n$ and $C2/c$, respectively. Form V was observed to crystallise in an orthorhombic *Pbca* space group. There are four unique molecules in the asymmetric unit in form I, while in form II, III, IV and V there is only one molecule per asymmetric unit.

In Table 4.1 the crystallographic data for all forms is summarised (form III – from data in the current work, forms I, II, and IV from CSD data). The corresponding reference codes from the CSD are also included, together with the measurement temperature: 123K, 160K, 191K or room temperature (RT, 283-303K).

Table 4.1. Summary of the crystallographic data of the five polymorphs of carbamazepine, **3** (form III from the present work, CSD data for forms I, II, and IV).

Form	**I**	**II**	**III**	**IV**	**V**
CSD ref code	CBMZPN11(191K)[4] CBMZPN13(160K)[11]	CBMZPN03 (RT)[2]	CBMZPN(RT)[1] CBMZPN01(RT)[5] CBMZPN02(RT)[8] CBMZPN10(RT)[9] CBMZPN15(RT)[10]	CBMZPN12 (158K)[3]	CBMZPN16 (123K)[10]
SP	$P\bar{1}$	*R*-3	$P2_1/n$	$C2/c$	*Pbca*
a/ Å	5.171(<1)	35.454(3)	7.4893(4)	26.609(4)	9.1245(5)
b/Å	20.574(2)	35.454(3)	11.0323(5)	6.927(1)	10.4518(5)
c/Å	22.245(2)	5.253(1)	13.7640(6)	13.957(2)	24.8224(11)
α/deg	84.12(<1)	90.00	90.00	90.00	90.00
β/deg	88.01(1<)	90.00	92.953(2)	109.70(<1)	90.00
γ/deg	85.19(<1)	120.00	90.00	90	90.00
V/ Å^3	293.103	5718.321	1135.73(9)	2421.926	2367.2(2)
Z′	4	1	1	1	1
ρ/g cm^{-3}	1.339	1.235	1.382	1.296	1.326

**The presented data were collected at 100K*

The dihydrate form was first reported in 1986[13] in an orthorhombic Abam (standard setting, Cmca) space group containing disordered atoms, and has been re-examined four times[10, 14-17] . The space group was re-interpreted by Harris *et. al.*[15] (2005) as monoclinic $P2_1/c$ and solved as a twinned crystal, these results were supported by later findings (T. Gelbrich *et. al*, 2006)).[16] Subsequent interpretation of the dihydrate crystal structure form (A. Kogan *et. al*, (2008))[17] showed that there was a missing mirror plane and second glide plane in the monoclinic $P2_1/c$ space group, leading to the Cmca space group with an

orthorhombic unit cell being proposed, as reported by Florence *et al*, 2004.[14] The crystallographic data are summarised in Table 4.2 with the corresponding reference codes from the CSD and the measurement temperature.

Table 4.2. Summary of the crystallographic data of the dihydrate form of **3** (CSD data). There are two distinct space groups reported in the literature, a larger volume centred orthorhombic cell and a primitive monoclinic cell.

Form	**Dihydrate**	**Dihydrate**
CSD	FENOT[13]	FENOT02[15]
refcode	FENOT01[14]	FENOT03[16]
	FENOT05[10]	FENOT04[17]
	FENOT06[10]	FENOT07[10]
SP	*Abam/Cmca*	$P2_1/c$
a/ Å	28.659(9)	10.066(2)
b/Å	4.924(2)	28.718(5)
c/Å	19.748(5)	4.831(1)
α/deg	90.00	90.00
β/deg	90.00	103.45(1)
γ/deg	90.00	90.00
V/ Å^3	1393.388	1358.268
Z′	0.5	1
ρ/g cm^{-3}	1.298	1.332

4.2. Experimental and Theoretical

4.2.1. Sample preparation

The conditions for growth of crystals of the polymorphs of **3** are described in the literature as follows: form I can be prepared by melting commercially supplied carbamazepine at 192°C;[4] bulk crystals of form I were also obtained by heating form III at 165°C.[4] Form II is reported as being obtained by evaporation using the solvents tetrahydrofuran, chloroform and carbon tetrachloride;[2] it can be also obtained by dissolving commercial carbamazepine in ethanol at 80°C, cooling to room temperature and holding at 5°C for 5 hours.[4] Form III can be grown in from solution in ethanol,[4, 5] *sec*-butylalcohol, *i*-propyl alcohol and *n*-propyl alcohol.[2] Form IV is grown from methanol solution, in the presence of hydroxypropylcellulose.[3] Form V was found to form by templating the growth of carbamazepine from the vapour phase onto the surface of a crystal of dihydrocarbamazepine form II.[12]

Compound **3** was purchased as a powder from Sigma Aldrich and attempts made to obtain the forms using the methods described in the literature. However, in the present study, form III was obtained from ethanol solution, while the dihydrate form was obtained instead of form II, in some cases, by following the published route for the latter. When tetrahydrofuran was used in a further attempt at obtaining form II, the same unit cell was obtained as for form II described in the literature.[2] The form II crystal structure was obtained with residual electron density found in the pore regions indicating solvent inclusion in this crystal structure. However, modelling the solvent from the X-ray data collected in this study was not possible. The solvated THF form of **3** with a complete determination of the crystal structure including the disordered solvent was previously reported in literature.[6]

4.2.2. Data collection and Conventional (Spherical atom) refinement

Single crystals of a suitable size were selected and mounted onto a goniometer and cooled to 100K using a Oxford Cryosystems Helix. High resolution X-ray data for form III were collected on Bruker AXS Apex II diffractometer (Mo K_α radiation) over a period of one week. The low resolution X-ray data were measured prior to the high-resolution data. Indexing, integration and scaling were performed using the Bruker APEX II software (Bruker Nonius 2009). A multi-scan absorption correction was applied using SADABS.[18] The reflection measurements were merged using SORTAV.[19] The structures were solved using SIR92[20] and refined initially in the spherical-atom formalism, with full-matrix least squares on F^2. The non-hydrogen atoms were refined with anisotropic displacement parameters. Structure solution and refinement were performed using the WinGX package[21] of crystallographic programs. Only low angle X-ray data were collected on the dihydrate due to the disorder identified for some atoms in this crystal. As it was not possible to model precisely the solvent in form II, no high resolution X-ray data were collected in this case. Residual electron density was identified in the channels but this was disordered about a 3-fold rotation axis and could not be resolved. SQUEEZE[22] was therefore used to estimate the residual electron density and the volume of the solvent accessible voids. The total potential solvent accessible volume per unit cell was calculated to be 384.9Å^3; this volume corresponds to approximately one THF solvent molecule within each channel.

Neutron diffraction data were collected for forms III and the dihydrate of **3** at 100K on the SXD instrument at the ISIS spallation neutron source, using the time-of-flight Laue diffraction method.[23] Reflection intensities were reduced to structure factors using standard SXD procedures, as implemented in the computer program SXD2001.[24] Refinements were

carried out using SHELXL97[25] (using the X-ray determined atomic coordinates as a starting model) with anisotropic displacement parameters (adps) determined for all atoms, including the H atoms.

4.2.3 Multipole refinement

The XD software package[26] was used to perform the multipole refinements. The multipole expansion was truncated at the octupole level for C, N and O atoms. Five different multipole refinements were performed for form III of **3**. In the first refinement (model 1), extensive constraints with imposed local mirror symmetry were applied to all the atoms apart from O1 and N1. For the O1 and N1 atoms, free multipole refinements were allowed. Only the first monopole and last dipole were refined in this model for H atoms. These were used to estimate the H atoms adps by the method of Madsen using the SHADE web interface.[27] The calculated H-atom adps from SHADE[27] were used in subsequent refinements (model 2) as fixed parameters. In the final cycles (model 3) the multipole constraints were released. The same steps were taken for models that used the adps for H atoms obtained from scaled X-ray with neutron diffraction data, denoted models 4 and 5. The hydrogen atom positions were set to the standard neutron distances in all refinements. Multipole populations and κ parameters were grouped in all refinements according to the chemical similarity of the atoms.

Table 4.3. Experimental crystallographic data for carbamazepine. 3, form III

Compound formula	$C_{15}H_{12}N_2O$	$C_{15}H_{12}N_2O$
Form	III	III
M_r	236.3	236.3
Space group	$P2_1/n$	$P2_1/n$
Crystal system	Monoclinic	Monoclinic
a/ Å	7.4893(4)	7.4893(4)
b/Å	11.0323(5)	11.0323(5)
c/Å	13.7640(6)	13.7640(6)
β/deg	92.953(2)	92.953(2)
V/Å^{-3}	1135.73(9)	1135.73(9)
Z	4	4
D_{calc}/g cm^{-3}	1.38	1.38
F(000)	496	-
Radiation	Mo Kα	TOF neutron
λ/Å	0.71073	0.42-7.64
μ(Mo-K_a)/mm^{-1}	0.089	0.146
Crystal size/mm	0.13x0.35x0.56	2.0x2.0x8.0
θ range/deg	2.4-58.0	2.37-69.50
Max sin(θ)/ λ	1.19	
No. of data used for merging	72811	8277
No. of unique data	16012	3674
hkl range	$-17 \le h \le 17$	$-19 \le h \le 20$
	$0 \le k \le 26$	$0 \le k \le 25$
	$0 \le l \le 32$	$0 \le l \le 53$
R_{int}	0.0662	0.1424
R_σ	0.0343	0.1144
Spherical atom refinement		
No. of data in refinement	16012	3674
No. of refined parameters	211	276
Final *R* [$I > 2\sigma(I)$]	0.042	0.061
R_w [$I > 2\sigma(I)$]	0.123	0.122
Goodness of fit *S*	1.064	1.153
Extrema in residual map	-0.339→ 0.760 eÅ^{-3}	-1.871→1.651 fmÅ^{-3}
Max shift/esd in last cycle	0.001	0.001
Multipole refinement		
No. of data in refinement	13158	-
No. of refined parameters	510	-
Final *R* [$I > 3\sigma(I)$]	0.0256	-
R_w [$I > 3\sigma(I)$]	0.0299	
Goodness of fit *S*	1.4680	-
Extrema in residual map/ eÅ^{-3} (all data)	-0.175→ 0.199	-
(data truncated to 0.8 Å^{-1})		
Max shift/esd in last cycle	0.0003	-

Table 4.4. Experimental crystallographic data for 3, dihydrate form

Compound formula	$C_{15}H_{12}N_2O$	$C_{15}H_{12}N_2O$	$C_{15}H_{12}N_2O$
Form	dihydrate	dihydrate	Solvated (THF)
M_r	236.3	236.3	236.3
Space group	*A* c a m	*C* m c a	*R*-3
Crystal system	Orthorhombic	Orthorhombic	Trigonal
a/ Å	4.8422(19)	28.6590(9)	35.3115(13)
b/Å	19.6826(77)	4.9240(2)	35.3115(13)
c/Å	28.8648	19.7480(5)	5.1538(2)
V/Å^{-3}	2751.36(19)	2786.78(16)	5565.33(4)
Z	8	8	6
D_{calc}/g cm^{-3}	1.20	1.13	1.27
F(000)	1056	-	2232
Radiation	Mo Kα	TOF neutron	Mo Kα
λ/Å	0.71073	0.42-7.64	0.71073
μ(Mo-K$_a$)/mm^{-1}	0.088	0.119	0.081
Crystal size/mm	0.18x0.29x0.40	2.0x2.0x5.0	0.17x0.20x0.31
θ range/deg	1.4-22.0	1.4-68.8	1.1-30
Max sin(θ)/ λ	0.52		0.70
No. of data used for merging	9521	5257	34512
No. of unique data	849	1686	3372
hkl range	$0 \le h \le 5$	$0 \le h \le 70$	$-48 \le h \le 0$
	$0 \le k \le 20$	$0 \le k \le 12$	$0 \le k \le 48$
	$0 \le l \le 30$	$0 \le l \le 45$	$0 \le l \le 7$
R_{int}	0.0491	-	0.0487
R_σ	0.0430	0.3481	0.1140
Spherical atom refinement			
No. of data in refinement	849	1686	3372
No. of refined parameters	133	186	212
Final *R* [$I > 2\sigma(I)$]	0.029	0.078	0.099
R_w [$I > 2\sigma(I)$]	0.054	0.135	0.257
Goodness of fit *S*	1.047	1.097	1.069
Extrema in residual map	-0.135→0.106 eÅ^{-3}	-1.707→1.746 fmÅ^{-3}	-0.285→0.423 eÅ^{-3}
Max shift/esd in last cycle	0.001	0.00	0.003

4.2.4 Theoretical calculations

Gas-phase structure optimisations were performed using DFT methods at the PBEPBE[28]/cc-pVTZ[29] level of theory/basis set, within the Gaussian03 program.[30] Basis sets were obtained from EMSL.[31] The subsequent topological analyses were performed using the AIMPAC program.[32] Theoretical structure factors were computed from the resultant wave-functions and used in a multipole refinement within XD,[26] in which all thermal parameters were set to zero and all positional parameters were kept fixed. Periodic single-point quantum calculations were also performed using CRYSTAL09[33] with the DFT method at the B3LYP[34]/6-31G** level of theory. Lattice energy calculations were also carried out using the CLP[35] program.

4.3. Results and discussion

4.3.1. Molecular structure and conformation details.

The crystal structures of the polymorphs of **3** have been discussed extensively in the literature.[1-10] A synopsis of this information is given here, combined with the present experimental results. As it was not found possible to prepare good quality crystals for high resolution X-ray diffraction of forms I, II, IV and V, the discussion will focus more on form III, for which good data were obtained and for which the high resolution refinements provide additional important structural information. Form II solvated (THF) with a complete resolved crystal structure was obtained by Fabbiani *et al.*[6] This will be included in the discussion along with the solvated THF form obtained in this study. The dihydrate form will also be discussed. First, a detailed comparison will be given of the five polymorphs in terms of the molecular geometry.

4.3.1.1 Summary of the conformational differences between polymorphs

The best fit overlay plot of forms I, II, III, IV, form II solvated (THF) and the dihydrate of **3** is illustrated in Figure 4.1 (a). The acetamide group in both forms I[5] and the dihydrate[17] shows a slight conformational difference compared with forms II[2] and III (this study). In the case of form V,[12] there are slight differences in the positions of the amide group and O atom in comparison with form III (Figure 4.1 (b)).

The effects of the amide pyramidalization on the relative energies have been addressed previously in a crystal prediction study.[36]

The azepine ring shows good conformational agreement between forms III and V. Overall, a high degree of conformational similarity between molecules can be observed.

(a)

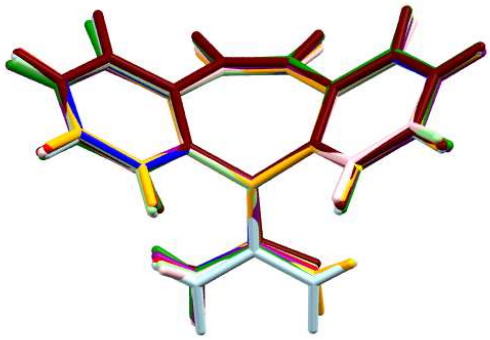

(b)

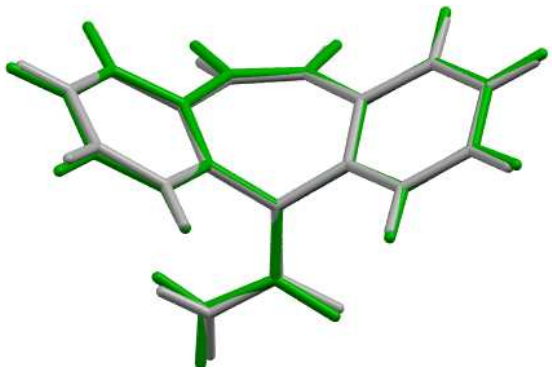

(c)

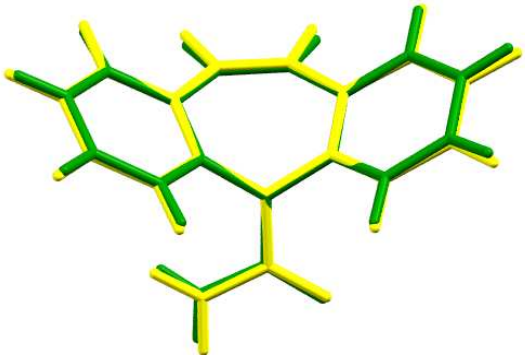

Figure 4.1. Best fit overlay plots of forms of carbamazepine, **3**: (a) forms I (4 molecules in the asymmetric unit), II, III, IV, dihydrate: (b), form III and form V; (c), form III and optimised structure. Colour code: form I - red, orange, light green, pink, form II - blue, form III - green, form IV - purple, form V - grey, dihydrate - light blue, optimised structure – yellow, form II solvated (THF) – dark red

4.3.1.2 Comparison with the gas phase calculations

Selected torsion angles of form III obtained from the present experimental data are compared with those from the CSD and the optimised gas phase calculation results from this work in Table 4.5, and show very good agreement. In particular, close similarity was observed for the O1-C1-N2-C15 torsion angle from the experimental structure and optimised gas phase molecule: −177.62(3)º and −177.64º, respectively. A slightly smaller

O1-C1-N2-C2 torsion angle was obtained for the optimised gas phase structure compared with the experimental angle: 6.63º and 9.40(4)º, respectively. The N1-C1-N2-C15 torsion angle (2.12(4)º, this work) shows an almost planar position of the amide group relative to the azepine ring. The preference of the almost planar conformation of the isolated amide group has been also observed in previous study.[36]

Overall, there are good agreements between the experimental and gas phase molecular geometry, as can be seen from Table 4.5. The best fit overlay plot also confirmed the excellent conformational agreement between the experimental structure of form III and the optimised gas phase molecule (Figure 4.1 (c)).

Table 4.5. Selected torsion angles (°) of form III in comparison with CSD data and the optimised gas phase molecule.

Torsion angle	This work	CSD	PBEPBE/cc-pVTZ
FormIII			
N1-C1-N2-C2	-170.86(3)	-170.64	-172.22
N1-C1-N2-C15	2.12(4)	2.25	3.51
O1-C1-N2-C2	9.40(4)	9.03	6.63
O1-C1-N2-C15	-177.62(3)	-178.09	-177.64

4.3.2 Disorder in Carbamazepine Dihydrate

As mentioned in the introduction, the structure of the dihydrate form was interpreted in two different ways in previous studies. The first interpretation of the structure was reported in the literature as being disordered orthorhombic, while a different interpretation of form III as a monoclinic twin was made by Harris *et al.*[15] This was justified on the basis that the previous interpretation was based on the similarity of the diffracting powers of the O and N atoms, making it hard to make a clear distinction between these two atoms using X-ray diffraction. In the present X-ray diffraction experiments, a lower R1obs value was obtained for the structure solution in the orthorhombic space group. In addition, neutron diffraction data were collected, for which the diffraction power of the O and N atoms are significantly different (b_O = 5.803 fm, b_N = 9.36 fm; Figure 2.15, Chapter 2). The results of the neutron data refinement confirmed the disordered position of the two atoms. The structure solution

and refinement in the $P2_1/c$ space group of the neutron data resulted in poor behaviour of the anisotropic displacement parameters including non-positive definite atoms indicating an incorrect assignment of the space group. Moreover, the neutron data offered a better interpretation of the hydrogen atoms of the water molecule. One hydrogen atom is ordered (H2A) and the other one was found to be disordered, flipping between two positions (H2B and H2C) (Figure 4.2). When the O atom of carbamazepine is adjacent to the water molecule, (pointing right in the molecule in Figure 4.2), one of the water hydrogen atoms will point in it's direction (H2C). On the other hand when the amide group is present instead of the O atom, the water molecules have both hydrogen atoms pointing in opposite direction to the carbamazepine molecule (H2A and H2B).

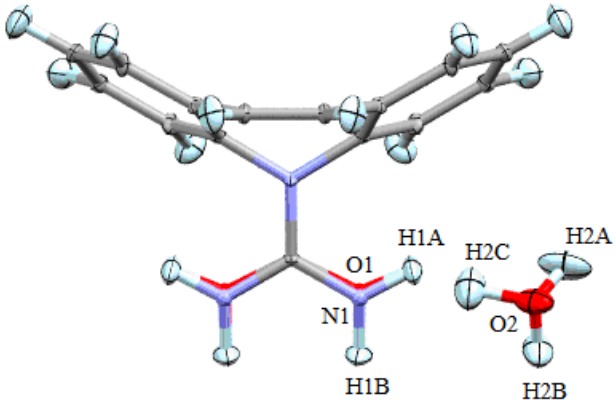

Figure 4.2. The dihydrate form of **3** showing the disordered O, N and H atoms, in both the carbamazepine and water molecules. The H2C atom of the water molecule is 50% of the time in the direction of the O1 atom (when this is 50% of the time occupying the right part of the molecule) and 50% of time occupies the H2B position (when amide group is 50% of the time occupying the right position of the molecule).

As it was concluded that the Cmca space group interpretation is more reliable (with a lower R1obs) than the $P2_1/c$ for the dihydrate form and due to the disordered atoms within the crystal packing, no high resolution X-ray data were collected in this case.

4.3.3. Description of intermolecular interaction and crystal packing

The intermolecular interactions and crystal packing of the polymorphs of **3** have been discussed extensively in the literature. A synopsis of this information is given here, combined with the present experimental results which include hydrogen bonds distances obtained from the neutron data of form III and the dihydrate.

The common dimer produced by hydrogen bond interactions between the amide groups (N1-H1B···O1 atoms) is found in all solid forms of **3** (including the dihydrate)[1-5,13-17] (Figure 4.3), apart from the recently discovered form V, which is catemeric (see below).[12] The dimers form $R_2^2(8)$ rings which are in turn held together in the crystal packing via weak C-H···O, C-H·π or π···π stacking interactions.[1-5] The difference in the packing of forms I, II, III, IV and the dihydrate, lies in the dimer unit arrangement. Two possible ways in which the aromatic rings could be arranged were found in the forms of **3**: stacked or herringbone. In the stacking arrangement the aromatic rings are aligned parallel to each other, while in the herringbone arrangement, the rings are tilted with respect to each other with tilt angles in the range 40-90°.[36] Forms I, II and the dihydrate were identified to have offset π stacking, while form III and IV show sandwich-herringbone packing (Figure 4.4).[36]

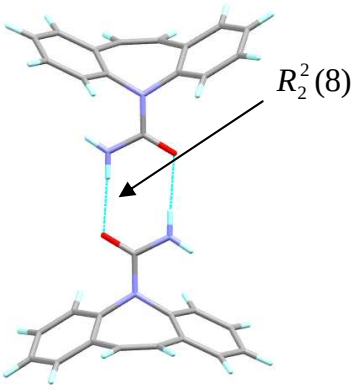

Figure 4.3 The common $R_2^2(8)$ dimer found in forms I, II, III, IV and dihydrate of **3**.

A particular difference in the packing of form II compared with the others, is that large voids are observed to form along the *c*-axis. The work of Fabbiani *et al.*[6] showed that this form contained solvent, such as tetrahydrofuran, within the pores. The solvent persists even after keeping the crystals in oven at 343 K over a period of 30 days. The geometry of the THF molecules lying within the pores is disordered and was identified to have three positions about a pivotal oxygen atom.[6] The presence of solvent, such as toluene and n-tridecane, in form II, has also been reported.[7] The residual electron density found in the pore regions indicated the presence of the solvent, however, the modeling of the solvent from the X-ray data was not possible in these cases.[7] In attempts to obtain crystals of form II in this work, a variety of solvents were used. Crystals of form II were obtained in THF, however as mentioned earlier analysing the X-ray diffraction data, residual electron density was found to be present within the voids which could not be modelled. The channels

formed along the *c* axis obtained in this study are illustrated in Figure 4.5. (a) and (b); these are the same as those found in the previous studies.[6, 7]

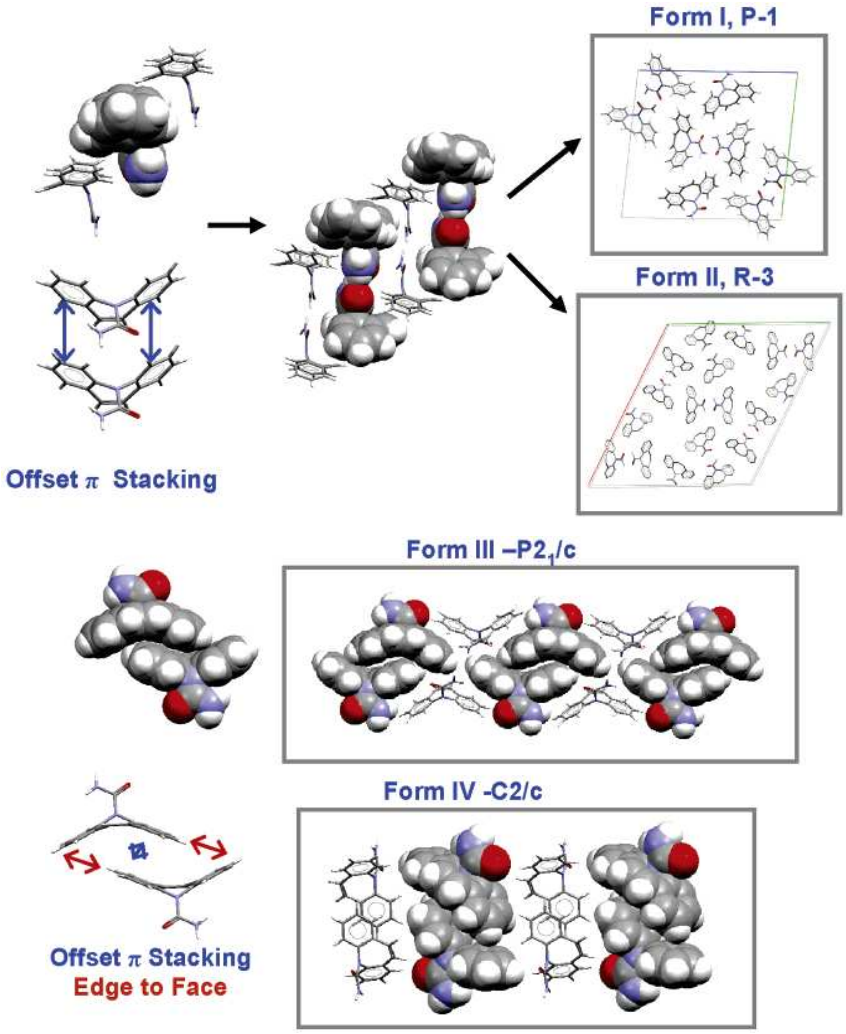

Figure 4.4. Common aromatic stacking patterns found in the forms of **3**: (top) offset π stacking packing in the trigonal, triclinic and dihydrate polymorphs; (bottom) sandwich-herringbone packing in both monoclinic crystals.[36]

(a)

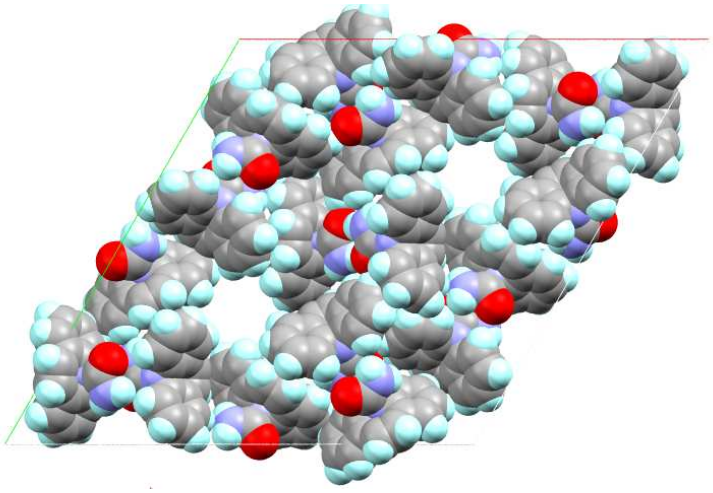

(b)

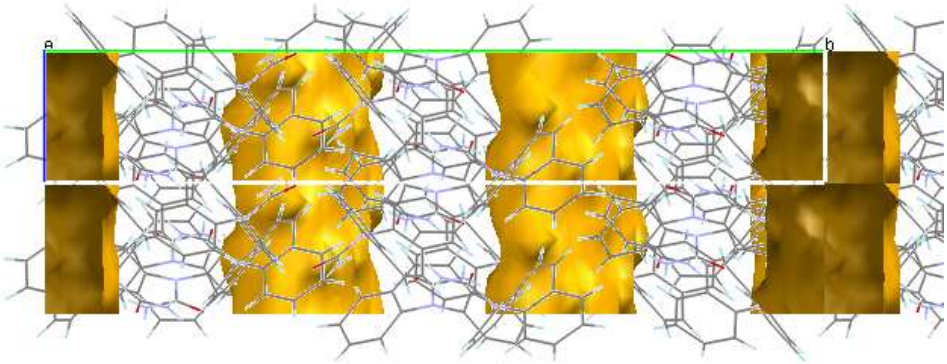

Figure 4.5. (a) Spacefill representation of form II of **3**, viewed along *c* axis taken from the data collected in this work. (b) The voids illustration formed by crystal packing of this form

The dihydrate form also shows channels along the *c*-axis, this time occupied by the water molecules (Figure 4.6). The orientation of the azepine rings in the crystal packing can also be observed from Figure 4.6. The double stacked units presented here are related to each other by a 2_1 axis, and the offset π stacking described in Figure 4.4 for form I and II is also observed in the case of the dihydrate form.[36]

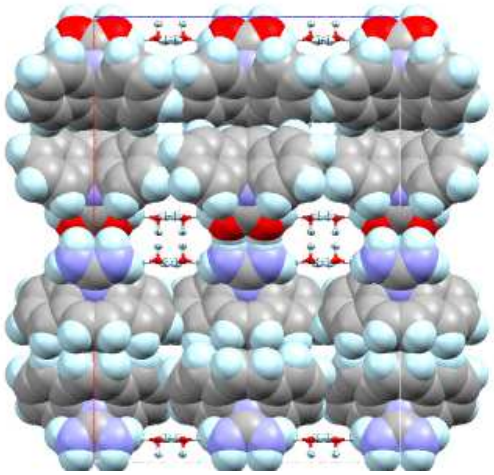

Figure 4.6. Spacefill representation of the dihydrate form of **3** showing the water molecules occupying the voids along the *c* axis taken from the neutron data.

In the recently discovered form V of carbamazepine, the primary hydrogen bond motif is no longer the $R_2^2(8)$ dimer, and the molecules are instead hydrogen bonded in a catemeric motif (Figure 4.7).[12] In addition, N-H$\cdot\cdot\pi$ weak hydrogen bonding interactions are present here and together with the weak C-H$\cdot\cdot\pi$ interactions give rise to the 3D expansion of the packing.[12]

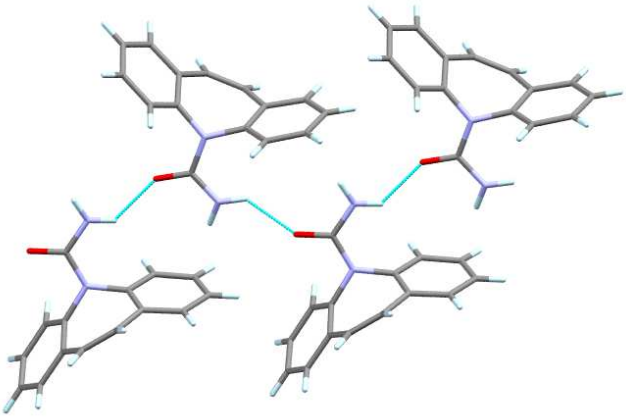

Figure 4.7. Form V of **3**, showing the catemeric hydrogen bonded motif.

The intermolecular hydrogen bond distances of the dimers in form III and the dihydrate obtained from the neutron diffraction experiments are summarized in Table 4.6. In both cases the dimers are held together through strong hydrogen bonding interactions, with the amide group acting as a donor and the carboxylate group acting as an acceptor. Both dimers are centrosymmetric, showing similar hydrogen bond lengths: form III 1.897(4) Å and dihydrate form 1.871(15) Å.

Table 4.6. Hydrogen bond distances and angles in the dimer motif in form III and dihydrate, obtained from the neutron diffraction experiment.

N2-H1B···O2 HB	Form III	Dihydrate
N2-H1B	1.017(6)	1.018(12)
N2···O1 distance (Å)	2.918(3)	2.876(7)
H1B···O1 distance (Å)	1.898(5)	1.871(15)
N1-H1B···O1 angle (°)	177.4(4)	168.6(17)

4.3.4. Hirshfeld surface analysis

The derived two-dimensional fingerprint plots from the Hirshfeld surfaces of forms III, II unsolvated and II solvated have been previously analysed in the literature.[16] A summary of these results will be given and, in addition, the intermolecular interactions of forms I, IV and V based on literature structures will be examined (Figure 4.8). The two sharp peaks found in all forms correspond to the N-H···O hydrogen interactions.[6] These were found to be within the 1.0 – 1.2 d_e and d_i region in forms I, II, III and IV where a dimer is formed. In form V, where the dimer is absent and the N-H··O bonds are slightly longer compared with the other forms, it can be seen from Figure 4.8 that d_e = 1.2Å and d_i =1.2Å. In addition, two small, sharp peaks are formed here corresponding to the weak N-H··π intermolecular interactions in the d_e/d_i = 1.5 Å region. The H···H contacts are noticeably shorter in form V, represented in the fingerprint plots by the external peaks in the 1.4 – 1.6 Å d_e/d_i region. The H···H interactions are represented inthe other forms by the external wings in the 1.6 – 2.2 Å d_e/d_i region. The 2D fingerprint plot in the case of form I shows much denser peaks, which is not surprising as there are four molecules present in the asymmetric unit and hence a larger number of distinct interatomic contacts at similar distances. The middle peaks correspond to the short H···H contacts, and for form IV this peak is sharper. This is due to the unique presence of the H14···H11 short hydrogen contact. The peaks are larger and split in forms I, II and III, due to the presence of more than one H···H short contact, for example in form **II**; H11···H13 and H14 ···H13. There is only one type of short H···H contact in form V (H5··H9), which gives a unique peak around the 1.2 – 1.4 Å d_e/d_i area.

The 2D fingerprint plot of unsolvated form II as reported previously in the literature,[6] shows a considerable number of points in the top right quarter, which correspond to the

direction of the voids in the structure (Figure 4.8). This is evidence of a large difference in the packing between form II and the others although this would be expected as this is not a true polymorph and would be better described as a solvate; in the void regions there is a lack of any close contacts between the neighbouring molecules where the disordered solvent molecules are not modelled. This is reflected in the Hirshfeld surface representation; the surfaces are elongated in the void region (Figure 4.9).[6] The diameters of the voids are over 5Å, which is enough to accommodate small solvent molecules.[6] The inclusion of the solvent in the form II crystal structure is reflected in the fingerprint plots. Most noticeably, the diffuse points at the top right are absent in the solvated form (Figure 4.9, form II solvated). The Hirshfeld surface analysis, especially the fingerprint, was highlighted as a powerful tool for rapid detection of unusual packing behaviour in a series of crystal structures by Fabbiani *et al*.[6]

The difference in the crystal packing between the catemeric form V and the others can be quickly detected from the two-dimensional fingerprint plots. The two small sharp peaks present in from V correspond to the formation of the N-H$\cdots\pi$ intermolecular interactions present only in this form.

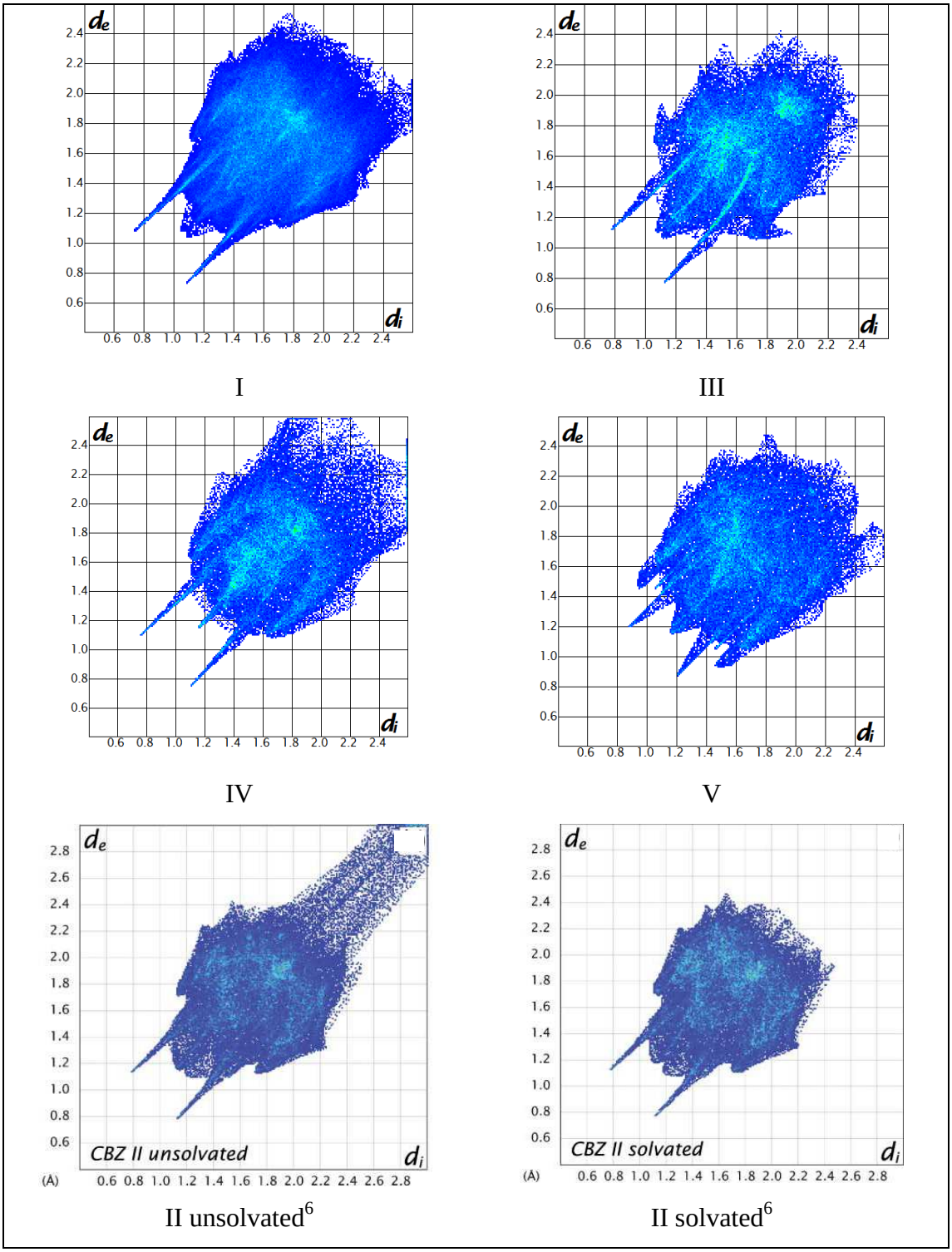

Figure 4.8. Two-dimensional fingerprint plots of the five forms of **3**. The fingerprint plots for forms I, IV and V were generated in this work and II and III were previously determined.[6]

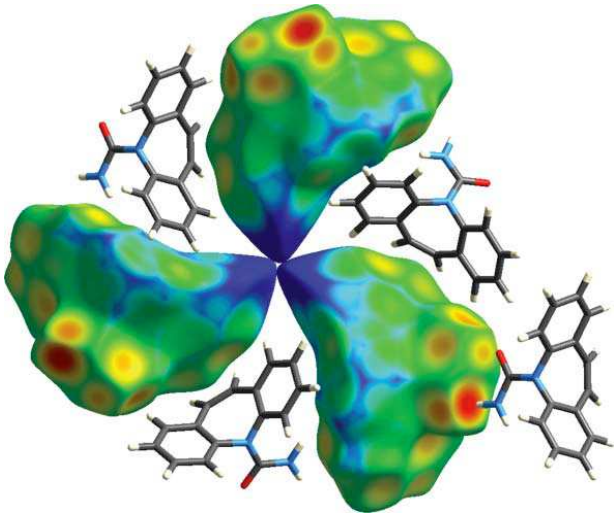

Figure 4.9. Cluster of molecules in the form II of **3** – Hirshfeld surface representation.[6] The Hirshfeld surfaces are extended towards the centre of the voids in the absence of modelling of the disordered solvent contained within them.

4.4. Analysis of the electron-density distribution

4.4.1. Analysis of topological parameters

The topological parameters from the experimental data were compared with those directly determined from the wave functions of the gas phase calculations and with the multipole model based on the theoretical structure factors. The distance of the BCP to the nuclei denoted by d_1 and d_2, ρ, the Laplacian at the BCP, $\nabla^2\rho$ and the three eigenvalues ($\lambda_1, \lambda_2, \lambda_3$) of the Hessian matrix of all the atoms of the studied forms are listed in Table 4.7. The most affected bonds, showing the largest discrepancy between the topological parameters of the experimental and theoretical data are the H-N (aniline) bonds, perhaps due to the involvement of those atoms in moderate hydrogen bonds. The $\nabla^2\rho(r_b)$ parameters of the experimental data gave better agreement with the multipole refinement of the theoretical structure factor. Overall, when the density calculated from the wave function is chosen as a reference, large discrepancies can be observed with the experimental $\nabla^2\rho(r_b)$ parameters. For instance, in the case of the C(1)-O(1) bond the $\nabla^2\rho(r_b)$ for the experimental data at the BCP is –37.32 $e\text{Å}^{-5}$, while the value of $\nabla^2\rho(r_b)$ for the density derived from the wave function and the densities from the theoretical structure factors is –13.53$e\text{Å}^{-5}$ and –33.32$e\text{Å}^{-5}$, respectively. The density and the position of BCPs (d_1 and d_2) between the bonded atoms show good agreement between experimental data and theoretical calculations.

Table 4.7 Topological Analysis of Bond Critical Points for form III of **3**

Bond	d_1[a]	d_2[a]	$\rho(r_b)$[b]	$\nabla^2\rho(r_b)$[c]	λ_1[c]	λ_2[c]	λ_3[c]
C(1)-O(1)	0.5063	0.7325	3.07	-37.32	-29.19	-26.07	17.94
	0.4281	*0.7985*	*2.77*	*-13.53*	*-25.34*	*-22.35*	*34.16*
	0.4913	*0.7353*	*2.90*	*-33.32*	*-26.07*	*-23.39*	*16.14*
C(1)-N(1)	0.6010	0.7559	2.46	-21.80	-22.38	-17.83	18.41
	0.5309	*0.8420*	*2.14*	*-22.80*	*-17.71*	*-14.73*	*9.65*
	0.5914	*0.7814*	*2.13*	*-16.96*	*-17.79*	*-14.50*	*15.33*
H(1A)-N(1)	0.2566	0.7419	2.35	-36.77	-33.73	-32.39	29.35
	0.2616	*0.7481*	*2.32*	*-43.89*	*-32.72*	*-31.16*	*19.98*
	0.2859	*0.7247*	*2.17*	*-24.83*	*-28.00*	*-25.98*	*29.14*
H(1B)-N(1)	0.2597	0.7583	2.28	-33.61	-31.94	-30.42	28.75
	0.2613	*0.7493*	*2.31*	*-43.58*	*-32.46*	*-31.00*	*19.87*
	0.2808	*0.7290*	*2.22*	*-24.43*	*-28.68*	*-26.73*	*30.98*
C(1)-N(2)	0.6143	0.7679	2.28	-17.98	-20.35	-16.33	18.70
	0.5671	*0.8418*	*1.98*	*-19.65*	*-15.96*	*-13.18*	*9.49*
	0.6193	*0.7894*	*1.95*	*-12.05*	*-15.80*	*-12.73*	*16.48*
C(2)-N(2)	0.6366	0.7934	1.98	-10.64	-15.42	-14.33	19.12
	0.5664	*0.8637*	*1.88*	*-18.55*	*-13.60*	*-12.96*	*8.00*
	0.6295	*0.8008*	*1.84*	*-10.02*	*-13.43*	*-12.64*	*16.04*
C(15)-N(2)	0.6399	0.7910	1.95	-10.59	-15.13	-14.23	18.77
	0.5713	*0.8568*	*1.89*	*-18.56*	*-13.67*	*-13.08*	*8.19*
	0.6491	*0.7791*	*1.87*	*-9.00*	*-13.50*	*-12.61*	*17.11*
C(3)-C(2)	0.6886	0.7080	2.22	-17.42	-18.00	-14.03	14.60
	0.6816	*0.7155*	*2.12*	*-23.87*	*-16.77*	*-13.79*	*6.70*
	0.6761	*0.7213*	*2.09*	*-16.89*	*-15.95*	*-13.03*	*12.08*
C(7)-C(2)	0.6973	0.7087	2.19	-17.58	-17.78	-14.28	14.48
	0.6989	*0.7139*	*2.06*	*-22.32*	*-16.13*	*-13.32*	*7.13*
	0.7035	*0.7093*	*2.02*	*-15.38*	*-15.24*	*-12.49*	*12.36*
C(3)-C(4)	0.6853	0.7077	2.20	-18.43	-17.76	-14.82	14.15
	0.6939	*0.6994*	*2.12*	*-23.89*	*-16.47*	*-13.88*	*6.46*
	0.6891	*0.7044*	*2.08*	*-16.56*	*-15.67*	*-13.07*	*12.17*
H(3)-C(3)	0.3783	0.7104	1.95	-19.34	-19.52	-18.32	18.51
	0.3872	*0.7018*	*1.93*	*-26.50*	*-19.14*	*-18.94*	*11.58*
	0.3804	*0.7086*	*1.86*	*-18.20*	*-17.84*	*-17.31*	*16.95*
H(4)-C(4)	0.3802	0.7010	1.89	-19.50	-19.06	-17.90	17.46
	0.3912	*0.6993*	*1.91*	*-26.15*	*-18.88*	*-18.62*	*11.35*
	0.3798	*0.7108*	*1.85*	*-17.32*	*-17.69*	*-16.97*	*17.34*
C(5)-C(4)	0.6981	0.6997	2.20	-18.01	-17.71	-14.58	14.28
	0.6989	*0.6995*	*2.10*	*-23.54*	*-16.31*	*-13.84*	*6.61*
	0.6944	*0.7041*	*2.06*	*-16.10*	*-15.44*	*-12.90*	*12.24*
H(5)-C(5)	0.3702	0.7148	1.91	-18.01	-19.28	-18.08	19.35
	0.3919	*0.6987*	*1.91*	*-26.09*	*-18.83*	*-18.56*	*11.30*
	0.3836	*0.7070*	*1.85*	*-17.38*	*-17.63*	*-16.75*	*17.01*
C(6)-C(5)	0.6803	0.7083	2.19	-18.04	-17.70	-14.40	14.06
	0.6909	*0.6987*	*2.14*	*-24.23*	*-16.67*	*-13.94*	*6.38*
	0.6834	*0.7066*	*2.10*	*-16.86*	*-15.86*	*-13.16*	*12.16*
C(7)-C(6)	0.7033	0.7049	2.20	-17.59	-17.63	-14.54	14.58

Table 4.7 Continued

	0.7001	*0.7106*	*2.05*	*-22.28*	*-15.78*	*-13.43*	*6.93*
	0.6983	*0.7126*	*2.01*	*-15.03*	*-14.87*	*-12.56*	*12.40*
H(6)-C(6)	0.3747	0.7148	1.90	-21.79	-19.74	-18.74	16.69
	0.3924	*0.6993*	*1.91*	*-25.91*	*-18.74*	*-18.46*	*11.29*
	0.3864	*0.7054*	*1.81*	*-16.45*	*-17.14*	*-16.31*	*16.99*
C(8)-C(7)	0.7299	0.7333	1.89	-12.76	-14.43	-12.60	14.26
	0.7279	*0.7280*	*1.88*	*-19.05*	*-14.02*	*-12.79*	*7.76*
	0.7168	*0.7393*	*1.84*	*-12.19*	*-13.06*	*-11.72*	*12.60*
C(9)-C(8)	0.6739	0.6783	2.43	-22.13	-20.52	-15.77	14.16
	0.6777	*0.6784*	*2.26*	*-26.65*	*-18.01*	*-14.06*	*5.43*
	0.6600	*0.6967*	*2.23*	*-19.14*	*-17.39*	*-13.54*	*11.79*
H(9)-C(9)	0.3699	0.7169	1.89	-20.13	-19.16	-18.57	17.60
	0.3933	*0.7001*	*1.90*	*-25.66*	*-18.65*	*-18.31*	*11.30*
	0.3888	*0.7047*	*1.80*	*-16.22*	*-16.91*	*-16.19*	*16.87*
H(8)-C(8)	0.3726	0.7273	1.88	-19.29	-18.96	-18.13	17.79
	0.3925	*0.7012*	*1.90*	*-25.76*	*-18.71*	*-18.44*	*11.38*
	0.3818	*0.7120*	*1.82*	*-16.43*	*-17.21*	*-16.59*	*17.37*
C(9)-C(10)	0.7304	0.7320	1.95	-13.61	-14.94	-13.21	14.54
	0.7209	*0.7344*	*1.88*	*-19.09*	*-14.04*	*-12.79*	*7.74*
	0.7112	*0.7447*	*1.83*	*-12.22*	*-13.10*	*-11.61*	*12.50*
C(11)-C(10)	0.7025	0.7042	2.15	-16.71	-17.12	-14.03	14.45
	0.7010	*0.7092*	*2.06*	*-22.35*	*-15.81*	*-13.47*	*6.92*
	0.6823	*0.7279*	*2.01*	*-15.14*	*-14.88*	*-12.52*	*12.26*
C(10)-C(15)	0.7021	0.7038	2.16	-16.39	-17.64	-13.40	14.65
	0.6997	*0.7153*	*2.05*	*-22.16*	*-16.05*	*-13.31*	*7.20*
	0.6979	*0.7173*	*2.02*	*-15.26*	*-15.19*	*-12.47*	*12.40*
H(11)-C(11)	0.3797	0.7086	1.92	-18.55	-18.96	-18.27	18.69
	0.3915	*0.7003*	*1.91*	*-25.97*	*-18.80*	*-18.53*	*11.36*
	0.3899	*0.7020*	*1.81*	*-16.58*	*-17.03*	*-16.24*	*16.69*
H(14)-C(14)	0.3008	0.6780	1.91	-14.36	-20.11	-19.23	24.98
	0.3889	*0.7017*	*1.91*	*-26.11*	*-18.94*	*-18.64*	*11.48*
	0.3789	*0.7118*	*1.85*	*-17.79*	*-17.76*	*-17.16*	*17.13*
C(12)-C(11)	0.6874	0.7008	2.22	-18.65	-18.32	-14.58	14.25
	0.6928	*0.6981*	*2.13*	*-24.12*	*-16.62*	*-13.91*	*6.41*
	0.6802	*0.7108*	*2.10*	*-16.78*	*-15.79*	*-13.14*	*12.14*
H(12)-C(12)	0.3688	0.7204	1.95	-18.61	-19.54	-18.43	19.36
	0.3912	*0.6993*	*1.91*	*-26.13*	*-18.87*	*-18.61*	*11.35*
	0.3937	*0.6968*	*1.79*	*-16.95*	*-16.99*	*-16.06*	*16.10*
C(13)-C(12)	0.6771	0.7202	2.16	-16.71	-17.07	-14.05	14.41
	0.6981	*0.7004*	*2.10*	*-23.51*	*-16.30*	*-13.82*	*6.61*
	0.6876	*0.7110*	*2.06*	*-16.07*	*-15.37*	*-12.91*	*12.20*
C(13)-C(14)	0.6917	0.7015	2.19	-17.64	-17.45	-14.53	14.34
	0.6934	*0.7013*	*2.11*	*-23.70*	*-16.40*	*-13.79*	*6.49*
	0.6748	*0.7199*	*2.07*	*-16.28*	*-15.54*	*-12.84*	*12.10*
H(13)-C(13)	0.3648	0.7176	1.90	-19.52	-19.40	-18.58	18.46
	0.3909	*0.6996*	*1.91*	*-26.12*	*-18.88*	*-18.60*	*11.37*
	0.3921	*0.6985*	*1.82*	*-17.07*	*-17.16*	*-16.36*	*16.45*
C(14)-C(15)	0.6908	0.7077	2.21	-18.21	-18.54	-14.17	14.49

Table 4.7 Continued

0.6886	*0.7132*	*2.10*	*-23.20*	*-16.54*	*-13.47*	*6.81*
0.6937	*0.7084*	*2.07*	*-16.05*	*-15.76*	*-12.65*	*12.35*

First line corresponds to Form III experimental data. The second and the third lines (italic) correspond to reference density from the wave function and reference density from the theoretical structure factor, respectively. [a] *In units of Å.* [b] *In units of e Å^{-3}.* [c] *In units of e Å^{-5}*

4.4.2 Analysis and comparison of the multipole refinements

This section will examine the improvements of the agreement between the experimental data and theoretical data with the increase in model sophistication. Five different multipole models were performed for the experimental data (1, 2, 3, 4, 5), as described in Section 4.2.3. These were compared with (a) the topological analysis of the wave functions of the gas phase calculations, as well as (b) with the multipole model based on the refinements of the theoretical structure factors. The charge densities and the Laplacian at the BCPs of each experimental and theoretical model are also compared. Since the volume of data is too large to see the trends clearly (Table 4.7), as before a residual factor R_{Par} was calculated, using equation 2.9, Chapter 2, in order to achieve a global measurement of the agreement between experimental and theoretical parameters. The R_{values}, R_{ρ} and $R_{\nabla 2(\rho)}$ values for form III of **3** are summarized in Table 4.8. An improvement of the R_{values} term can be noticed with the increase of the sophistication of the multipole model. A slightly better refinement was obtained when the hydrogen adps obtained from the scaled X-ray data with neutron data were implemented, compared with the use of adps for hydrogen atoms obtained from SHADE[27] in the restricted multipole model (2 and 4). When the restriction was released, the same results were obtained for both models 3 and 5. If the density from the wave function is taken as a reference, the best agreement was obtained for model 1, with the lowest R_{ρ}. The same was observed when the density from the theoretical structure factor was used. The lowest values for $R_{\nabla 2(\rho)}$ were obtained for models 2 and 4 in case (a) followed by models 3 and 5, while for (b) the lowest values of $R_{\nabla 2(\rho)}$ were obtained for model 1 followed by models 3 and 5, 2 and 4. Therefore, the trends for the $R_{\nabla 2(\rho)}$ were not the same in the two studied cases (a) and (b).

Table 4.8 The residual factors of the experimental data versus theoretical data for the various model multipole refinements of form III of **3**

(a) Reference density from wave functions	**Model**	$\mathbf{R_{values}}$	$\mathbf{R_{\rho}}$	$\mathbf{R_{\nabla 2(\rho)}}$
Form III	1	0.0275	0.0154	0.2448
	2	0.0261	0.0320	0.2019
	3	0.0256	0.0369	0.2096
	4	0.0260	0.0307	0.2055
	5	0.0256	0.0355	0.2132
(b) Reference density from theoretical structure factors				
Form III	1	0.0275	0.0435	0.1040
	2	0.0261	0.0607	0.1669
	3	0.0256	0.0656	0.1555
	4	0.0260	0.0592	0.1616
	5	0.0256	0.0642	0.1503

4.4.3. The residual map density representation

The residual electron density maps of the spherical and multipole refinements of form III of **3** are represented in Figure 3.10 for the azepine ring and the acetamide group. The maps contain very little noise in case of the multipole refinements compared with the spherical atom refinements (Figure 3.10 left) and the residual densities do not exceed 0.2 $eÅ^{-3}$. These facts indicate high quality of the multipole refinement.

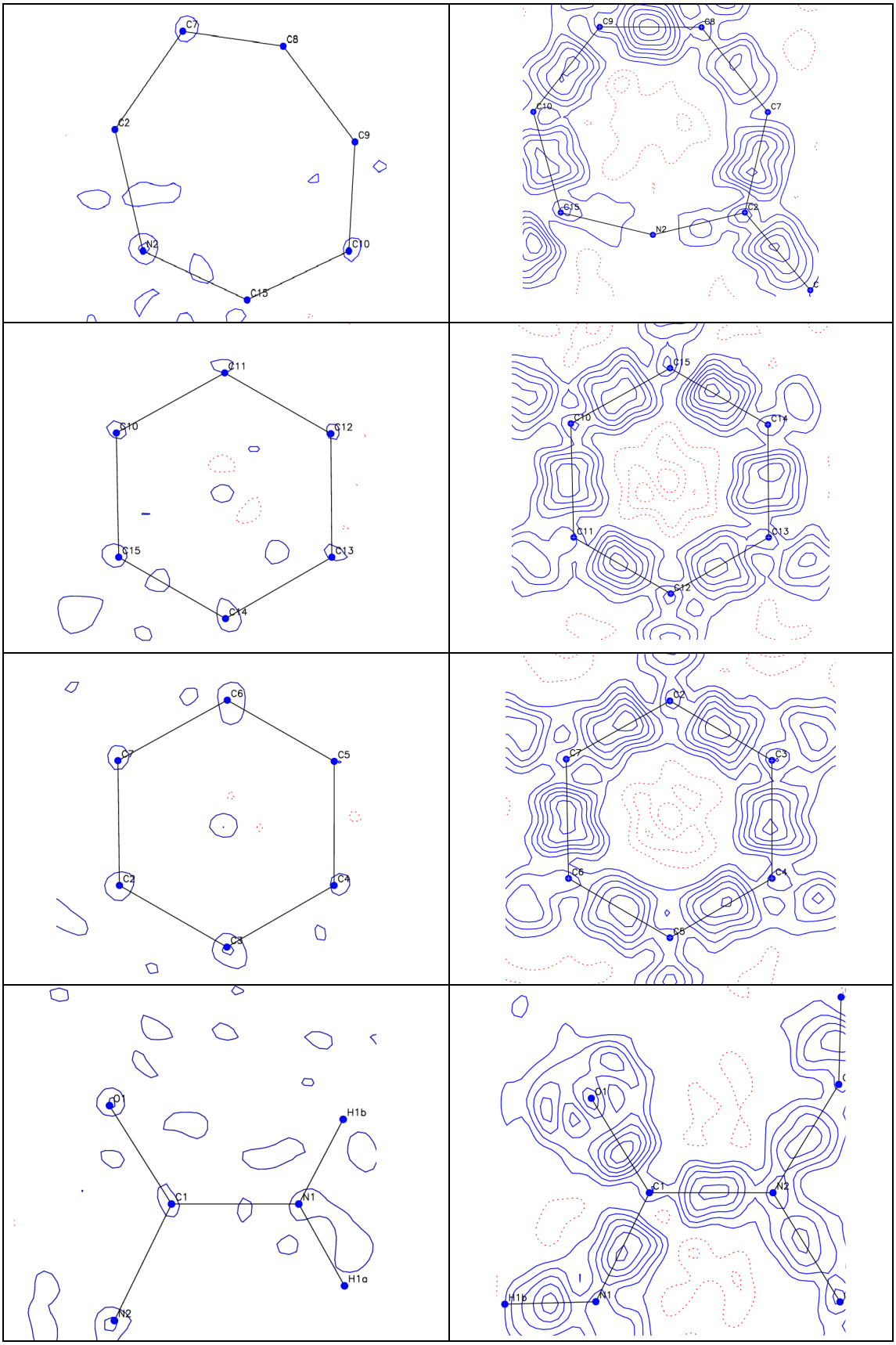

Figure 4.10. Residual electron density maps for form III of **3** – azepine rings and acetamide group (left – multipole refimentents, right –spherical atom refinements). Contours level are ±0.1e/Å^{-3}

4.4.4. Deformation density maps representation

The deformation density maps for form III and the optimised gas phase calculation of **3** are plotted in Figure 4.11. The maps are plotted in the acetamide group plane, in order to investigate the behaviour of these atoms involved in hydrogen bond interactions and compare the results with the theoretical calculations. The conformation of the molecule is clearly reflected on these maps. For the experimental data, the deformation density is less pronounced and for the O1 atom, asymmetric lone pairs can be observed. The multipole refinement of the theoretical structure factors obtained from optimised gas phase calculations shows negative deformation density at the O1 atom in the O1-C1 bond direction. The lone pair electrons for O1 are symmetrical in this case.

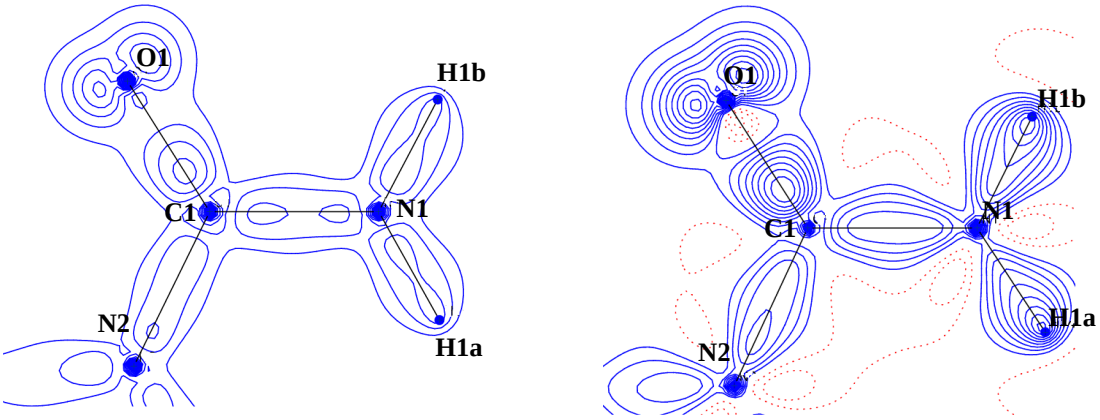

Figure 4.11. Deformation density maps representation for the experimentally studied form III of **3** (left) and from the multipole refinement of theoretical structure obtained from optimised gas phase calculations (right) in the acetamide group plane (negative contours - red dashed, positive contours – blue line) Contour level at 0.08eÅ^{-3}

The atomic net charge for O1 calculated using Bader's QTAIM implemented in XD[26] software is -1.03 e for the experimental data of form III. The multipole refinement of theoretical structure factors obtained from optimised gas phase calculations gave slightly less negative value of the charge (-0.86 e). This is perhaps due to the absence of hydrogen bonds in the theoretical calculations. The Mulliken charge extracted from the Gaussian03[30] calculations is also less negative (-0.32 e) compared with both the experimental data, and the multipole refinement of the theoretical structure factors.

4.4.5. Laplacian representation

The Laplacian maps for form III and the optimised gas phase calculation of **3** are also plotted in Figure 4.12. The experimental data shows similar trends with the theoretical results. The lone pairs of electrons at the O1 atom are symmetrical in both cases here.

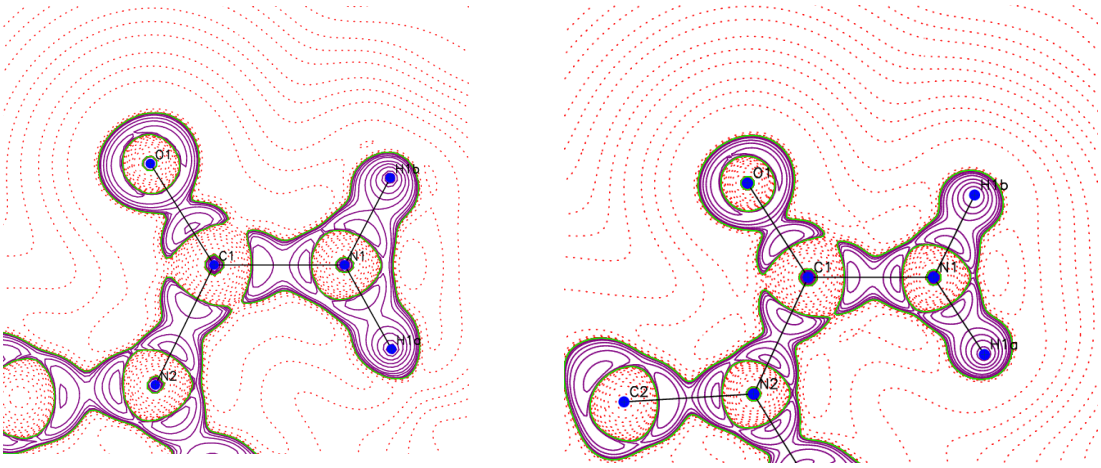

Figure 4.12. Plots of the negative Laplacian, $L(\mathbf{r})$ in the acetamide group plane of the form III (left) and from the multipole refinement of theoretical structure obtained from optimised gas phase calculations (right) of **3**. Positive contours – solid purple line; negative contours – dotted line. The contour levels are at -1.0 x 10^{-3}, ±2.0 x 10^{n}, ±4 x 10^{n}, ± 8 x 10^{n} (n = -3, -2, -1, 0, +1, +2) e Å^{-5}

4.5. Lattice and intermolecular interaction energy calculations

The lattice energy of form III was calculated using different approaches and different software including XD,[26] CRYSTAL09[33] and CLP.[35] The lattice energy calculations using the experimental charge density approach are listed in Table 4.9. As noted in the previous chapters, the lattice energy shows high sensitivity to the type of multipole model used. Lower values for the lattice energies were obtained when a more sophisticated multipole model was used, especially for the unrestricted models. The fully theoretical lattice calculation shows significant differences with the experimental results. For instance, in case of model 5 the lattice energy obtained from the experimental charge density approach is –209.12 kJ/mol, while the CRYSTAL09[33] and the CLP[35] programs gave values of –159.84 and –130.4 kJ/mol, respectively. A new multipole refinement was carried out in which the x,y,z and U_{ij} parameters were refined only once, and in a different block from the multipole parameters. In this case the lattice energies were estimated at –165.99 kJ/mol, giving a 6.15 kJ/mol difference with the CRYSTAL09[33] calculations.

Table 4.9 Lattice energies (kJ/mol) of experimental charge density of form III of **3** for various multipole refinement models.

	Form III		
Model	XD[26]	CRYSTAL09[33]	CLP[35]
1	-185.60		
2	-192.50		
3	-205.54		
4	-194.17		
5	-209.12	-159.84	-130.4

4.6. Conclusions

Form III of carbamazepine, **3**, has been analysed for the first time using high resolution X-ray diffraction. In addition, neutron diffraction data collection and refinement was performed for both form III and its dihydrate. The structure solution of the dihydrate form was interpreted in two ways in previous literature studies, and the present work has shown that the orthorhombic interpretation is the more reliable one. This assumption was made by considering the lower R1obs obtained for the orthorhombic form. The neutron data also support these results and in addition the hydrogen atoms for the water molecule were also found to be disordered. Moreover, neutron data can better distinguish between the O and N atoms due to their different scattering power. These two atoms were therefore interpreted as being disordered from the neutron data as well. The analysis of the various carbamazepine forms also support the previously interpretation[6] of form II, which is a solvated form; residual density was found in the pores of form II in this study, indicating the presence of the solvent. The best fit overlay plots show a high degree of conformational similarity between molecules of all forms.

The topological parameters from the experimental data were compared with those directly determined from the wave functions of the gas phase calculations, and also with the multipole model based on the theoretical structure factors. An improvement of the R_{values} term was noted with the increase of the sophistication of the multipole model refinement. A slightly better refinement was observed when the hydrogen adps obtained from the scaled X-ray-data with neutron data, were implemented and compared with the use of adps for hydrogen atoms obtained from SHADE[27] in the restricted multipole model (2 and 4).

As concluded in the previous chapters, the calculated lattice energies show high sensitivity to the type of multipole model used. The fully theoretical lattice calculation shows significant difference with the experimental results. There is also a considerable

discrepancy between the fully theoretical calculation approaches. Therefore, an accurate estimation of the lattice energies from the experimental charge density is not currently possible for carbamazepine, **3**. Challenges also arose in estimating the lattice energy using fully theoretical programs.

References

1. W. H. DeCamp, V. L. Himes and A. D. Mighell, *ACA Ser.2*, 1981, **9**, 27.
2. M. M. J. Lowes, M. R. Cairo, A. P. Lotter and J. G. van der Watt, *J. Pharm. Sci.*, 1987, **76**, 744.
3. M. Lang, J. W. Kampf and A. J. Matzger, *J. Pharm. Sci.*, 2002, **91**, 1186.
4. A. L. Grzesiak, Meidong Lang, Kibum Kim and A. J. Matzger, *J. Pharm. Sci.*, 2003, **92**, 2260.
5. J. P. Reboul, B. Cristau, J. C. Soyfer and J. P. Astier, *Acta Cryst. B*, 1981, **37**, 1844.
6. F. P. A. Fabbiani, L. T. Byrne, J. J. McKinnon and M. A. Spackman, *CrystEngComm*, 2007, **9**, 728-731.
7. A. J. C. Cabeza, G. M. Day, W. D. S. Motherwell and W. Jones, *Chem. Comm.*, 2007, 1600-1602.
8. J. N. Lisgarten, R. A. Palmer and J. W. Saldanha, *J. Cryst. Spectrosc. Res.*, 1989, **19**, 641.
9. V. L. Himes, A. D. Mighell and W. H. DeCamp, *Acta Cryst. B*, 1981, **37**, 2242.
10. A. Kogan, I. Popov, V. Uvarov, S. Cohen, A. Aserin and N. Garti, *Langmuir*, 2008, **24**, 722.
11. P. Fernandes, K. Shankland, A. J. Florence, N. Shankland and A. Johnston, *J. Pharm. Sci.*, 2007, **96**, 1192.
12. Jean-Baptiste Arlin, L. S. Price, S. L. Price and A. J. Florence, *Chem. Comm.*, 2011, **47**, 7074-7076.
13. G. Reck and G. Dietz, *Cryst. Res Technol.* , 1986, **21**, 1463.
14. A. J. Florence, A. R. Kennedy, N. Shankland and A. Johnston, *Private Communication*, 2004.

15. R. K. Harris, P. Y. Ghi, H. Puschmann, D. C. Apperley, U. J. Griesser, R. B. Hammond, C. Ma, K.J.Roberts, G.J.Pearce, J.R.Yates and C.J.Pickard, *Org. Process Res. Dev.*, 2005, **9**, 902.
16. T. Gelbrich and M. B. Hursthouse, *CrystEngComm.*, 2006, **8**, 448.
17. A. Kogan, I. Popov, V. Uvarov, S. Cohen, A. Aserin and N. Garti, *J. Disp. Sci. Tech.*, 2007, **28**, 1008.
18. SADABS: Area-Detector Absorption Correction; Siemens Industrial Automation, Inc.: Madison, WI, 1996. .
19. R. Blessing, *J. Appl. Cryst.*, 1997, **30**, 421-426.
20. A. Altomare, G. Cascarano, C. Giacovazzo and A. Guagliardi, *J. Appl. Cryst.*, 1994, **27**, 435.
21. L. Farrugia, *J. Appl. Cryst.*, 2012, **45**, 849-854.
22. P. v.d. Sluis and A. L. Spek, *Acta Cryst. A*, 1990, **46**, 194-201.
23. D. A. Keen, M. J. Gutmann and C. C. Wilson, *J. Appl. Cryst.*, 2006, **39**, 714-722.
24. M. J. Gutmann, *SXD2001. ISIS Facility, Rutherford Appleton Laboratory, Oxfordshire, England*, 2005.
25. G. M. Sheldrick, *Acta Cryst. A*, 2008, **64**, 112-122.
26. A. Volkov, L. J. Farrugia, C. Gatti, P. R. Mallinson, T. Richter and T. Koritsanszky, *XD-2006*, 2006, http://xd.chem.buffalo.edu/.
27. A. Madsen, *J. Appl. Cryst.*, 2006, **39**, 757-758.
28. J. P. Perdew, K. Burke and M. Ernzerhof, *Phys. Rev. Lett.*, 1996, **77**, 3865.
29. (a) T. H. Dunning, *J. Chem. Phys.*, 1989, **90**, 1007; (b) K. A. Peterson, D. Figgen, M. Dolg and H. Stoll, *J. Chem. Phys.*, 2007, **126**, 124101.
30. M. J. Frisch, G. W. Trucks, H. B. Schlegel, G. E. Scuseria, M. A. Robb, J. R. Cheeseman, J. A. Montgomery, T. V. Jr., K. N. Kudin, J. C. Burant, J. M. Millam, S. S. Iyengar, J. Tomasi, V. Barone, B. Mennucci, M. Cossi, G. Scalmani, N. Rega, G. A. Petersson, H. Nakatsuji, M. Hada, M. Ehara, K. Toyota, R. Fukuda, J. Hasegawa, M. Ishida, T. Nakajima, Y. Honda, O. Kitao, H. Nakai, M. Klene, X. Li, J. E. Knox, H. P. Hratchian, J. B. Cross, V. Bakken, C. Adamo, J. Jaramillo, R. Gomperts, R. E. Stratmann, O. Yazyev, A. J. Austin, R. Cammi, C. Pomelli, J. W. Ochterski, P. Y. Ayala, K. Morokuma, G. A. Voth, P. Salvador, J. J. Dannenberg, V. G. Zakrzewski, S. Dapprich, A. D. Daniels, M. C. Strain, O. Farkas, D. K. Malick, A. D. Rabuck, K. Raghavachari, J. B. Foresman, J. V. Ortiz, Q. Cui, A. G. Baboul, S. Clifford, J. Cioslowski, B. B. Stefanov, G. Liu, A. Liashenko, P. Piskorz, I. Komaromi, R. L. Martin, D. J. Fox, T. Keith, M. A. Al-Laham, C. Y. Peng, A. Nanayakkara, M. Challacombe, P. M. W. Gill, B. Johnson, W. Chen, M.

W. Wong, C. Gonzalez and J. A. Pople, GAUSSIAN03, Wallingford, CT., US, 2004

31. Basis sets were obtained from the Extensible Computational Chemistry Environment Basis Set Database, Version 02/25/04, as developed and distributed by the Molecular Science Computing Facility, Environmental and Molecular Science Laboratory which is part of the Pacific Northwest Laboratory, P.O. Box 999, Richland, WA 99352, U.S.A., and funded by the U.S. Department of Energy.
32. F. W. Biegler-Konig, R. F .W. Bader and T. Tang, *J. Comput. Chem.*, 1982, **3**, 317.
33. R. Dovesi, R. Orlando, B. Civalleri, C. Roetti, V. R. Saunders, and C. M. Zicovich-Wilson, *Z. Kristallogr.*, 2005, **220**, 571; R. Dovesi, V. R. Saunders, C. Roetti, R. Orlando, C. M. Zicovich-Wilson, F. Pascale, B. Civalleri, K. Doll, N. M. Harrison, I. J. Bush, P. D'Arco, and M. Llunell, CRYSTAL09 (CRYSTAL09 User's Manual. University of Torino, Torino, Italy, 2009).
34. (a) A. D. Becke, *Phys. Rev. A*, 1988, **38**, 3098; (b) A. D. Becke, *J. Chem. Phys.*, 1993, **98**, 5648; (c) C. Lee, W. Yang and R. G. Parr, *Phys. Rev. B*, 1988, **37**, 785. (d) P. J. Stephens, J. F. Devlin, C. F. Chabalowski and M. J. Frisch, *J. Phys. Chem.*, 1994, **98**, 11623.
35. A. Gavezzotti, *New J. Chem.*, 2011, **35**, 1360-1368.
36. A. J. Cruz Cabeza, G. M. Day, W. D. S. Motherwell and W. Jones, *Cryst. Grow. Des.*, 2006, **6**, 1858-1866.

5. Octakis(arylthio)naphthalenes

5.1. Introduction

This chapter addresses octakis(phenylsulfanyl)naphthalene (**4**) (Scheme 5.1), an organic compound known to crystallise in two different conformational polymorphs. It was synthesized for the first time in 1983.[1] The compound was obtained from the reaction of octafluoro-naphthalene with PhSNa in presence of 1,3-dimethyl-imidazolidin-2-one within 2 days at room temperature. The recrystallisation of compound **4** in different solvents leads to the formation of the two polymorphs, one yellow (**4a**) and one red (**4b**). An interesting solid-solid transformation was observed to occur by applying pressure to the yellow form on a glass slide. Red crystals were produced at the point of pressure application. The crystal structure of form **4b** was re-examined by X-ray diffraction at room temperature in 2003.[2] The yellow form is known to crystallise in a monoclinic crystal system with *C*2/*c* space group, while the red form was identified with a triclinic, $P\bar{1}$, space group.

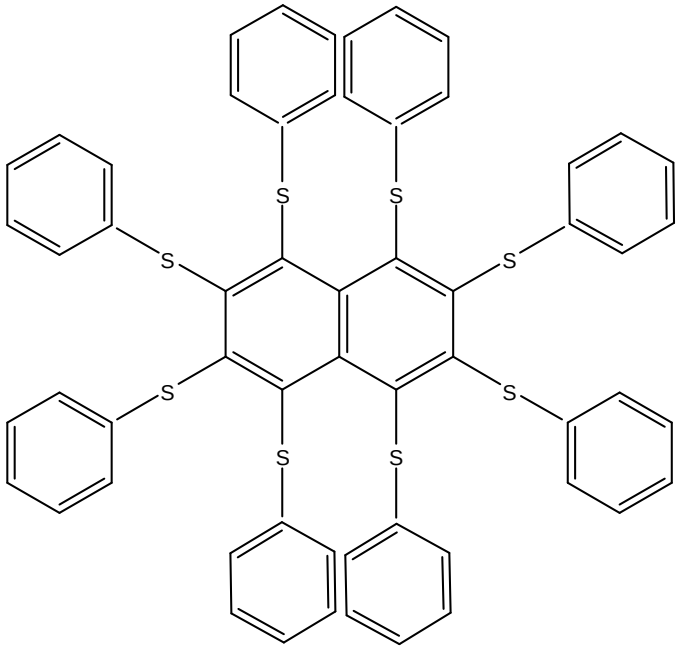

Scheme 5.1. Molecular structure of octakis(phenylsulfanyl)naphthalene, **4**

The characterisation of the two forms using charge density analysis and their ranking stability obtained by energy calculations within periodic calculations has been carried out in this work and will be described here. For this purpose, high resolution X-ray diffraction data were collected for both forms at 100 K. The crystallographic information for the two

forms are summarized in Table 5.1. The CSD reference codes from the previous data collections are also included in this table, together with the measurement temperature (RT – room temperature).

Table 5.1 Summary of the crystallographic data of the two polymorphs of **4**

Form	**4a**	**4b**
CSD ref. code	BOWWOZ(RT)[1]	BOWWOZ01(RT)[1] BOWWOZ02(200K)[2]
SP	$C2/c$	$P\bar{1}$
a/ Å	24.1754(8)	9.0541(2)
b/Å	10.4260(4)	11.393(2)
c/Å	20.1012(6)	12.3355(2)
α/degrees	90.00	100.999(1)
β/degrees	111.017(1)	96.083(1)
γ/degrees	90.00	109.640(1)
V/ Å^3	4729.5(3)	1156.32(4)
Z'	0.5	0.5
ρ/g cm^{-3}	1.395	1.427

**The presented data were collected at 100K*

5.2. Experimental and Theoretical

5.2.1 Sample preparation

The crystals of the two polymorphs of **4** are described in the literature as being grown as follows. Form **4a** was prepared using the solvents dimethylformamide[1] and diethylether,[2] while form **4b** can be grown from anisole at 50ºC[1] and from chloroform-pentane solution.[2] In attempts in this project to produce the crystals of the two forms as described above, in the majority of the cases form **4b** was produced in all the solvents used. The yellow form appeared in only one crystallization vial, in which chloroform-pentane was used as solvent.

5.2.2 Data collection and Conventional (Spherical atom) refinement

Single crystals of suitable size were selected, mounted on a diffractometer and cooled to 100 K using an Oxford Cryosystems Cryostream cooling device. High resolution X-ray data from form **4a** were collected on a Bruker-Nonius Kappa CCD diffractometer (Mo K_α radiation) over a period of one week. The Collect software was used for monitoring the data

collection. The low resolution X-ray data were measured prior to the high-resolution data. The integration of intensities was carried out using the DENZO[3] software. Data for form **4b** (denoted 4b_apex in this work) were collected initially at 100 K on a Bruker AXS ApexII diffractometer, in this case using an Oxford Cryosystems Helix cooling device. Indexing, integration and scaling were performed using the Bruker ApexII software (Bruker Nonius 2009). A multi-scan absorption correction was applied using SADABS.[4] The data collected on the Bruker AXS ApexII diffractometer for form **4b** were found to be not satisfactory for charge density analysis, showing somewhat large deviations of the scale factor. In consequence, the date for **4b** were recollected, again at 100 K, on a Bruker-Nonius Kappa CCD diffractometer (denoted 4b_kappa in this work). The reflections were merged and empirical absorption corrections were performed using SORTAV[5] program. The structures were solved using SIR92[6] and refined initially in the spherical-atom formalism with full-matrix least squares on F^2. Structure solution and refinement were performed using the WinGX[7] package of crystallographic programs. Anisotropic displacement parameters were refined for the non-hydrogen atoms. The details of these data collections and refinements are given in Table 5.2.

Table 5.1. Experimental crystallographic for the two polymorphic forms 4a and 4b.

Compound formula	$C_{58}H_{40}S_8$	$C_{58}H_{40}S_8$	$C_{58}H_{40}S_8$
Form	4a	4b_apex	4b_kappa
M_r	993.38	993.38	993.38
Space group	$C2/c$	$P\bar{1}$	$P\bar{1}$
Crystal system	Monoclinic	Triclinic	Triclinic
a/ Å	24.1754(8)	9.0497(4)	9.0541(2)
b/Å	10.4260(4)	11.3991(5)	11.3930(2)
c/Å	20.1012(6)	12.3177(5)	12.3355(2)
α/deg	90.00	100.954(2)	100.9990(10)
β/deg	111.0170(10)	96.085(2)	96.0830(10)
γ/deg	90.00	109.599(2)	109.6400(10)
V/Å^{-3}	4729.5(3)	1155.28(9)	1156.32(4)
Z	4	1	1
D_{calc}/g cm^{-3}	1.40	1.43	1.43
F(000)	2064	516	516
Radiation	Mo Kα	Mo Kα	Mo Kα
λ/Å	0.71073	0.71073	0.71073
μ(Mo-K$_a$)/mm^{-1}	0.418	0.428	0.428
Crystal size/mm	0.13x0.35x0.56	0.16x0.31x0.48	0.19x0.24x0.43
θ range/deg	1.8-50.2	1.7-50.0	1.7-50.6
Max sin(θ)/ λ	1.08	1.07	1.08
No. of data used for merging	404982	207164	382684
No. of unique data	24409	24272	24605
hkl range	$-52 \le h \le 48$	$-19 \le h \le 19$	$-19 \le h \le 19$
	$0 \le k \le 22$	$-24 \le k \le 24$	$-24 \le k \le 24$
	$0 \le l \le 42$	$0 \le l \le 26$	$0 \le l \le 26$
R_{int}	0.0400	0.0504	0.0418
R_σ	0.0410	0.0341	0.0356
Spherical atom refinement			
No. of data in refinement	24409	24272	24605
No. of refined parameters	379	378	378
Final R [$I > 2\sigma(I)$]	0.042	0.034	0.035
R_w[$I > 2\sigma(I)$]	0.116	0.097	0.102
Goodness of fit S	1.054	1.053	1.080
Extrema in residual map / eÅ^{-3}	-0.472→0.655	-0.269→0.763	-0.497→0.668
Max shift/esd in last cycle	0.002	0.001	0.002
Multipole refinement			
No. of data in refinement	18618	23564	19210
No. of refined parameters	867	866	866
Final R [$I > 3\sigma(I)$]	0.0343	0.0285	0.0271
R_w[$I > 3\sigma(I)$]	0.0311	0.0263	0.0255
Goodness of fit S	1.4063	1.1525	1.2781
Extrema in residual map/ eÅ^{-3} (all data)	-0.310→ 0.418	-0.355→ 0.713	-0.307→0.471
Max shift/esd in last cycle	0.0005	0.0006	0.0006

5.2.3 Mutipole refinement

The multipole refinements were performed using the XD[8] package. The multipole expansion was truncated at the octupole level for non-H atoms, apart from the S atom for which the refinement of hexadecapoles was allowed. In addition for the S atom, the (2,4,6,8) combination of the n(1,…4) radial function parameters of the valence deformation function were used. Three different multipole refinements were carried out for both phases. The first refinement (model 1), for **4a**, was performed applying extensive chemical constraints with an imposed local two-fold rotation axis symmetry to the C5 and C6 atoms located in a special position. This constraint is applied due to the fact that a 2 fold proper rotation axis is passing along the C5-C6 bond, which is at the centre of the core naphthalene ring in the compound. For the other non-hydrogen atoms where no such axis is present, local mirror plane symmetry was applied. For the **4b** phase, local mirror plane symmetry was applied for all non-hydrogen atoms. The resulting refined parameters were used to estimate the H-atom adps by the method of Madsen using the SHADE[9] web interface. The calculated adps for H-atom were used in subsequent refinements (model 2) as fixed parameters. In the final cycles (model 3), the multipole constraints were released. The hydrogen positions were constrained to the standard neutron-determined distance from their parent atom. Multipole populations and *k* parameters were grouped in all refinements according to the chemical similarity of the atoms.

5.2.4. Theoretical calculations

Gas phase single point calculations were performed using the DFT method at the b-p[10a,d]/ def2-TZVP[11] level of theory, performed with the TURBOMOLE 6.2[12] software, in order to reveal the difference in the energy of the molecular conformations in the two polymorphs (the conformation energy). Periodic single point quantum calculations were also performed using CRYSTAL09[13] with the DFT method at the B3LYP[10a-d]/6-31G** level of theory.

5.3 Results and discussion

5.3.1. Molecular structure and conformation details

The conformational differences between the forms of **4** and their crystal packing have already been discussed in the literature.[1,2] A brief summary of this information will be given here and in addition the discussion will be extended to the hydrogen bond

intermolecular interactions. The Mercury diagram of the forms of **4** is shown in Figure 5.1. The alternation of the external side phenyls above or below the central naphthalene ring are denoted as conformations **a** and **b.** The **4a** form contains two entiomers within the crystal packing with the external phenyl alternated in **aabbaabb** or **bbaabbaa** fashion (Figure 5.1). A slight twist of the naphthalene ring can be noticed for the **4a** form, whereas the naphthalene ring is almost flat in the **4b** form (Figure 5.2). The **aababbab** conformation was identified for the **4b** form as can clearly be seen from Figure 5.2.

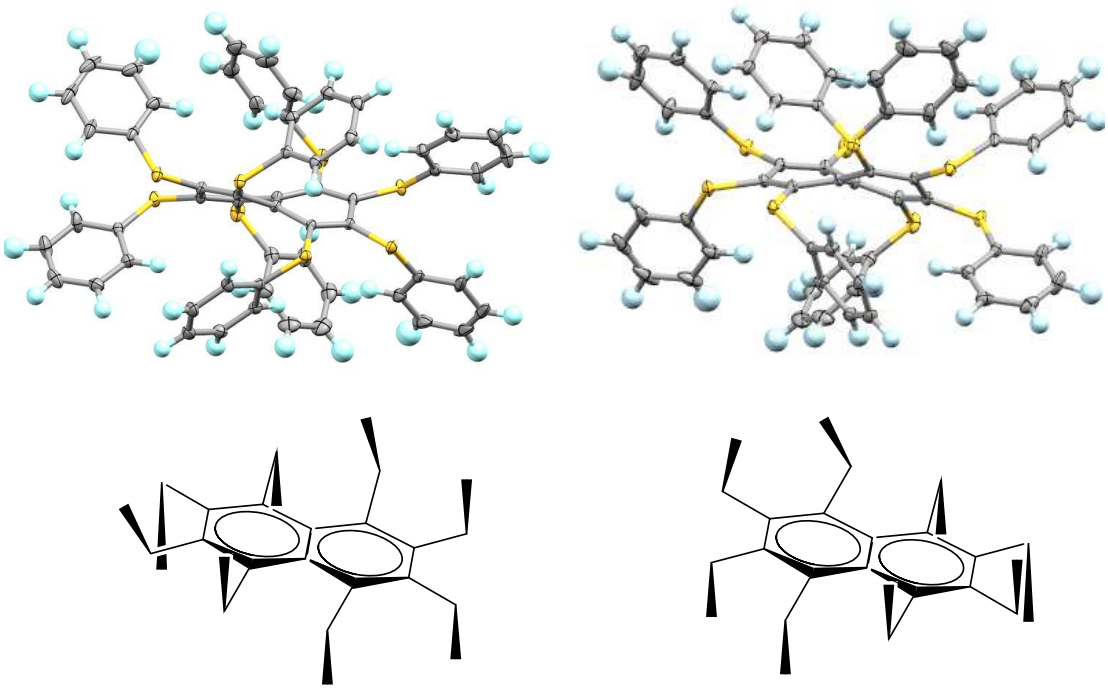

aabbaabb **bbaabbaa**

Figure 5.1. Mercury view of the **4a** form of octakis(phenylsulfanyl)naphthalene, showing the thermal ellipsoids and the different conformation adopted by the antiomers of form **4a** (**aabbaabb** and **bbaabbaa**).

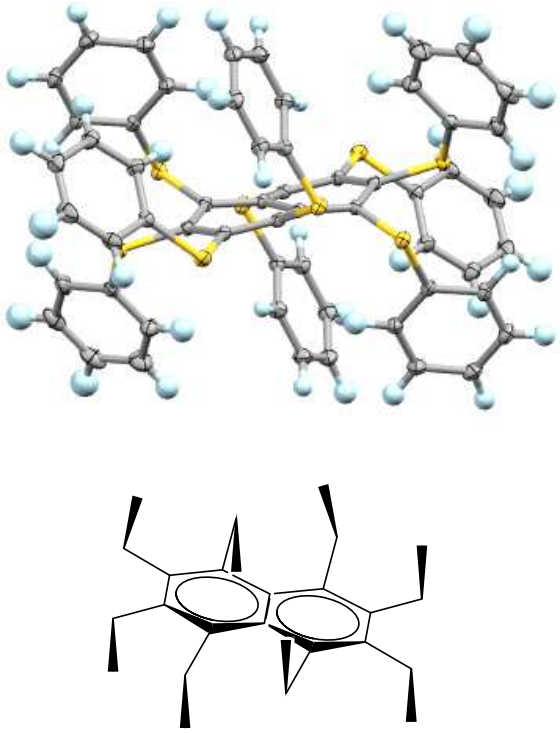

Figure 5.2. Mercury view of the **4b** form of octakis(phenylsulfanyl)naphthalene, showing the thermal ellipsoids and the conformation adopted (**aababbab).**

Selected bond lengths and bond angles for forms **4a** and **4b** from the experimental results and also those from the CSD are summarized in Table 5.3. The present experimental results are in excellent agreement with the data previously deposited. A general slight elongation of the bonds can be observed for form **4b** compared with **4a**, while on the other hand the C-S-C angles are in general smaller for form **4b** compared with form **4a**. This is a consequence of different crystal packing effects and taking the individual molecules, as noted in the paragraph below, the yellow form **4a** seems to be more stable than the red form **4b**. In both cases there are two smaller angles and two larger ones: for each of the **aa** and **bb** conformations adopted there is a small angle and a larger one. The same can be observed for the S-C bond lengths.

The gas phase optimised energy using DFT method at the b-p/ def2-TZVP level gives a difference in the conformation energy of –16.7 kJ/mol, with the yellow form (form **4a**) being the most stable.

Table 5.3 Selected bond lengths and bond angles for the **4a** and **4b** forms of octakis(phenylsulfanyl)naphthalene.

Form **4a**	Present data	CSD data
S1-C1	1.7737(5)	1.775
S2-C2	1.7592(5)	1.762
S3-C3	1.7624(5)	1.763
S4-C4	1.7753(5)	1.779
S1-C111	1.7806(5)	1.778
S2-C211	1.7661(7)	1.760
S3-C311	1.7711(6)	1.763
S4-C411	1.7826(8)	1.779
C1-S1-C111	101.50(2)	101.75
C2-S2-C211	106.50(3)	106.62
C3-S3-C311	107.90(2)	107.63
C4-S4-C411	100.43(3)	101.30

Form **4b**	Present data	CSD data
S1-C1	1.7898(4)	1.789
S2-C2	1.7651(5)	1.761
S3-C3	1.7768(5)	1.775
S8-C8	1.7806(4)	1.779
S1-C111	1.7831(5)	1.779
S2-C211	1.7706(5)	1.768
S3-C311	1.7790(5)	1.777
S8-C811	1.7843(5)	1.780
C1-S1-C111	97.12(2)	97.38
C2-S2-C211	105.54(2)	105.82
C3-S3-C311	101.30(2)	101.59
C8-S8-C811	98.67(2)	98.74

5.3.2. Hirshfeld surface analysis

The hydrogen bonds present in the **4a** and **4b** forms are generally of the weaker type. There are weak hydrogen interactions of the C-H···S type, plus other close C-H···C contacts. Examination of the fingerprint plots generated by the Crystal Explorer[14] program shows a slight difference between the two forms around the d_i = 1.0 - 1.4 Å region (Figure 5.3). This position represents the short H···H contacts. The denser region in the **4b** form is due to the presence of six short H···H contacts, four of them with distance 2.32(2) Å and two with 2.31(2) Å. In the **4a** case, there are only four H contacts with distance of 2.28(2) Å. The wings show that the C-H···S and C-H··C intermolecular contacts are almost identical for the two forms.

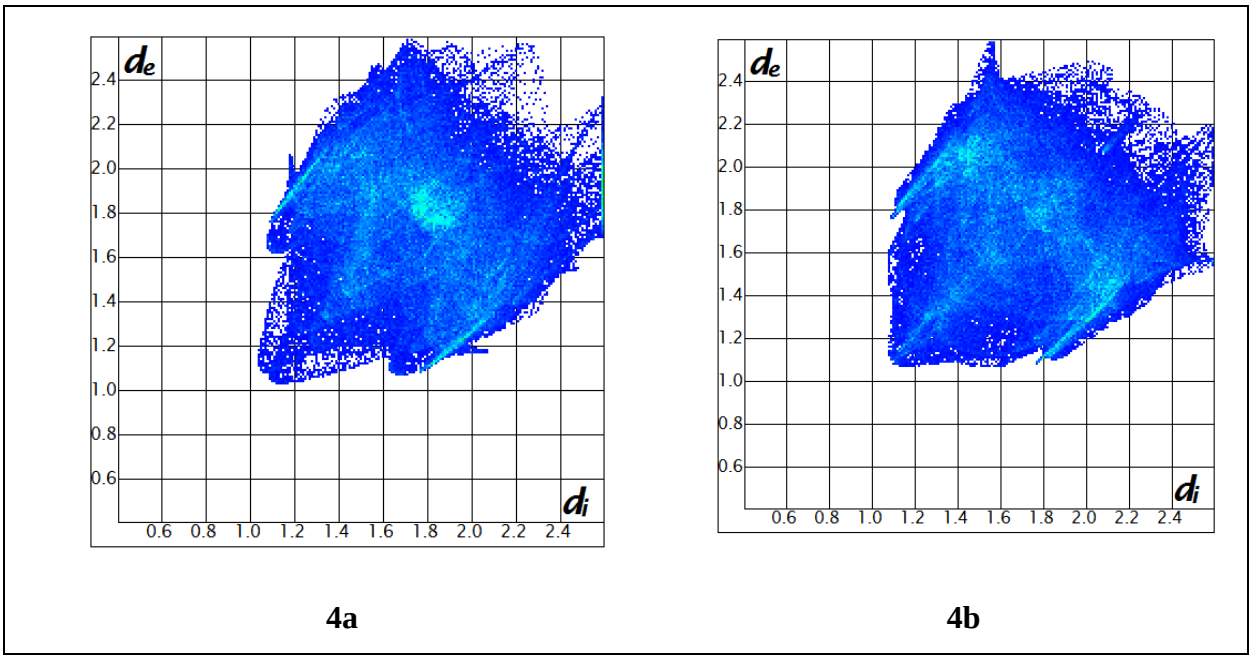

Figure 5.3. Two-dimensional fingerprint plots for the two forms of **4**.

5.4. Analysis of the electron-density distribution

5.4.1. Analysis of topological parameters

A detailed comparison is now made between the topological parameters obtained from experimental data and those obtained from multipole refinement of the theoretical structure factors derived from single point periodic calculations. The distance (Å) of the BCP to the nuclei denoted by d_1 and d_2, the electron density ρ, the Laplacian at the BCP, $\nabla^2\rho$, and the three eigenvalues ($\lambda_1, \lambda_2, \lambda_3$) of the Hessian matrix of all the atoms of the studied forms are listed in Table 5.3 and 5.4. The topological parameters presented in these tables correspond to the atoms from the asymmetric unit. Good agreement between the topological

parameters obtained from the experimental data and theoretical calculations is observed for both forms. This is not surprising as only weak hydrogen bonds are present in the studied system and the experimental data are compared with single point periodic calculations in this case.

Table 5.3. Topological Analysis of Bond Critical Points for the **4a** form

Bond	$\mathbf{d_1}^{a}$	$\mathbf{d_2}^{a}$	$\boldsymbol{\rho(r_b)}^{b}$	$\boldsymbol{\nabla^2 \rho(r_b)}^{c}$	$\boldsymbol{\lambda_1}^{c}$	$\boldsymbol{\lambda_2}^{c}$	$\boldsymbol{\lambda_3}^{c}$
C1-S1	0.8351	0.9376	1.31	-4.40	-7.44	-5.76	8.80
	0.8538	*0.9182*	*1.27*	*-5.57*	*-6.81*	*-5.73*	*6.98*
C111-S1	0.8333	0.9458	1.34	-5.43	-7.39	-6.60	8.56
	0.8520	*0.9265*	*1.26*	*-5.47*	*-6.74*	*-5.92*	*7.19*
C2-S2	0.8289	0.9311	1.36	-5.61	-8.01	-6.03	8.42
	0.8614	*0.8978*	*1.31*	*-5.99*	*-6.92*	*-5.93*	*6.87*
C211-S2	0.8236	0.9402	1.37	-6.94	-8.58	-6.30	7.94
	0.8223	*0.9409*	*1.29*	*-5.77*	*-7.29*	*-6.04*	*7.56*
C3-S3	0.8333	0.9280	1.40	-7.03	-7.95	-7.02	7.94
	0.8615	*0.8997*	*1.31*	*-5.83*	*-6.96*	*-5.84*	*6.96*
C311-S3	0.8234	0.9490	1.38	-6.50	-7.77	-6.94	8.20
	0.8457	*0.9255*	*1.28*	*-5.64*	*-7.06*	*-5.82*	*7.24*
C4-S4	0.8319	0.9454	1.34	-4.66	-7.60	-6.06	9.01
	0.8677	*0.9074*	*1.27*	*-5.56*	*-6.74*	*-5.70*	*6.87*
C411-S4	0.8358	0.9449	1.28	-3.76	-6.88	-5.83	8.95
	0.8559	*0.9246*	*1.26*	*-5.23*	*-6.70*	*-5.83*	*7.29*
C1-C2	0.6959	0.7012	2.19	-19.21	-17.15	-13.42	11.36
	0.6963	*0.7005*	*2.09*	*-16.70*	*-15.82*	*-12.48*	*11.60*
C6-C1	0.6992	0.7384	1.92	-15.92	-14.79	-11.99	10.86
	0.7066	*0.7306*	*1.91*	*-14.11*	*-14.10*	*-11.70*	*11.69*
C2-C3	0.7116	0.7280	1.94	-15.55	-14.78	-12.01	11.24
	0.7169	*0.7228*	*1.89*	*-13.37*	*-13.79*	*-11.39*	*11.81*
C4-C3	0.6952	0.7051	2.12	-18.16	-16.45	-12.76	11.05
	0.6916	*0.7089*	*2.06*	*-16.28*	*-15.67*	*-12.23*	*11.62*
C4-C5	0.7003	0.7405	1.95	-16.21	-14.55	-12.71	11.05
	0.7167	*0.7242*	*1.90*	*-14.09*	*-14.08*	*-11.66*	*11.65*
C5-C6	0.7014	0.7221	2.06	-17.92	-15.91	-13.03	11.01
	0.7028	0.7207	1.96	-15.64	-14.75	-12.27	11.38
C112-C111	0.6956	0.7016	2.16	-19.50	-16.82	-14.05	11.38
	0.6935	*0.7037*	*2.09*	*-17.12*	*-16.30*	*-13.08*	*12.26*
C116-C111	0.6656	0.7344	2.20	-20.29	-17.43	-14.16	11.31
	0.6797	*0.7202*	*2.06*	*-16.59*	*-15.84*	*-12.91*	*12.16*
H112-C112	0.3559	0.7281	1.89	-20.04	-18.85	-18.10	16.91
	0.3908	*0.6923*	*1.90*	*-20.06*	*-18.49*	*-17.47*	*15.90*

Table 5.3 Continued

H115-C115	0.3645	0.7194	1.82	-18.59	-17.72	-17.27	16.40
	0.4106	*0.6725*	*1.88*	*-19.65*	*-17.77*	*-16.74*	*14.87*
H116-C116	0.3543	0.7295	1.89	-20.04	-18.93	-18.14	17.03
	0.3732	*0.7099*	*1.88*	*-18.37*	*-18.34*	*-17.62*	*17.59*
C112-C113	0.6938	0.7041	2.23	-21.04	-17.72	-14.93	11.61
	0.6733	*0.7242*	*2.05*	*-16.99*	*-15.96*	*-12.93*	*11.90*
C114-C113	0.6846	0.7093	2.23	-20.79	-18.16	-14.35	11.72
	0.6710	*0.7228*	*2.14*	*-17.44*	*-16.37*	*-13.54*	*12.47*
H113-C113	0.3638	0.7202	1.84	-19.03	-18.06	-17.30	16.33
	0.3889	*0.6941*	*1.89*	*-19.40*	*-18.25*	*-17.40*	*16.24*
C115-C114	0.6326	0.7653	2.21	-20.44	-16.85	-14.42	10.83
	0.6909	*0.7067*	*2.09*	*-16.65*	*-15.85*	*-13.24*	*12.44*
H114-C114	0.3529	0.7313	1.89	-19.85	-19.33	-17.81	17.28
	0.4081	*0.6749*	*1.88*	*-19.49*	*-17.76*	*-16.84*	*15.10*
C116-C115	0.6833	0.7144	2.19	-18.89	-17.01	-13.74	11.86
	0.6822	*0.7154*	*2.08*	*-16.57*	*-15.98*	*-12.94*	*12.35*
C212-C211	0.6955	0.7074	2.14	-17.45	-16.07	-13.34	11.97
	0.6888	*0.7141*	*2.04*	*-16.60*	*-16.12*	*-12.63*	*12.14*
C216-C211	0.6213	0.7762	2.19	-22.06	-17.17	-14.91	10.02
	0.6342	*0.7616*	*2.08*	*-17.59*	*-15.97*	*-12.97*	*11.34*
H212-C212	0.3764	0.7092	1.70	-15.23	-15.88	-15.52	16.17
	0.3668	*0.7163*	*1.89*	*-18.69*	*-18.64*	*-17.80*	*17.75*
C213-C212	0.6707	0.7256	2.20	-18.92	-17.64	-13.48	12.21
	0.6459	*0.7507*	*1.99*	*-16.33*	*-15.65*	*-12.19*	*11.51*
H214-C214	0.3674	0.7167	1.82	-18.57	-17.86	-16.75	16.04
	0.4231	*0.6600*	*1.88*	*-19.71*	*-17.28*	*-16.58*	*14.16*
C214-C213	0.6581	0.7481	2.28	-21.28	-18.18	-14.78	11.69
	0.6059	*0.7972*	*2.18*	*-17.27*	*-15.74*	*-13.20*	*11.68*
H213-C213	0.3604	0.7277	1.85	-19.98	-19.49	-17.09	16.60
	0.4916	*0.5922*	*1.84*	*-21.35*	*-16.35*	*-14.77*	*9.78*
C215-C214	0.6922	0.7029	2.15	-19.87	-17.13	-14.14	11.40
	0.6912	*0.7014*	*2.08*	*-16.70*	*-15.88*	*-13.13*	*12.32*
H215-C215	0.3518	0.7317	1.91	-19.78	-19.08	-17.92	17.22
	0.3653	0.7177	1.89	-18.69	-18.67	-17.91	17.89
H216-C216	0.3627	0.7217	1.82	-17.54	-17.73	-16.52	16.71
	0.3708	*0.7123*	*1.90*	*-19.12*	*-18.67*	*-17.92*	*17.47*
C215-C216	0.6974	0.6978	2.16	-18.75	-17.03	-13.42	11.70
	0.6790	*0.7161*	*2.07*	*-17.04*	*-16.10*	*-12.97*	*12.03*
C312-C311	0.6967	0.7017	2.16	-18.82	-16.78	-13.59	11.54
	0.6812	*0.7173*	*2.08*	*-16.78*	*-16.14*	*-12.93*	*12.29*

Table 5.3 Continued

C316-C311	0.6922	0.7053	2.12	-19.38	-17.03	-13.54	11.19
	0.6789	*0.7180*	*2.08*	*-16.61*	*-15.89*	*-12.98*	*12.26*
H312-C312	0.3589	0.7256	1.85	-18.79	-18.30	-17.34	16.86
	0.3698	*0.7132*	*1.90*	*-19.29*	*-18.73*	*-18.01*	*17.45*
H313-C313	0.3554	0.7299	1.88	-19.83	-19.08	-17.79	17.04
	0.4090	*0.6742*	*1.87*	*-19.22*	*-17.56*	*-16.63*	*14.97*
C312-C313	0.6802	0.7165	2.20	-20.75	-17.38	-14.70	11.33
	0.6976	*0.6990*	*2.03*	*-16.47*	*-15.78*	*-12.71*	*12.02*
C313-C314	0.6960	0.7024	2.24	-20.28	-17.39	-14.59	11.70
	0.6922	*0.7057*	*2.17*	*-17.17*	*-16.26*	*-13.77*	*12.86*
H314-C314	0.3555	0.7277	1.88	-19.88	-18.87	-17.97	16.9
	0.4152	*0.6679*	*1.88*	*-19.82*	*-17.60*	*-16.78*	*14.56*
C314-C315	0.6560	0.7378	2.15	-18.87	-16.62	-13.59	11.34
	0.6509	*0.7427*	*2.11*	*-17.47*	*-16.06*	*-13.31*	*11.90*
H316-C316	0.3643	0.7206	1.82	-18.19	-17.83	-16.84	16.47
	0.3796	*0.7035*	*1.89*	*-18.95*	*-18.28*	*-17.57*	*16.91*
C316-C315	0.6749	0.7214	2.21	-19.93	-17.24	-14.23	11.53
	0.6876	*0.7087*	*2.07*	*-16.40*	*-16.00*	*-12.77*	*12.37*
H315-C315	0.3659	0.7176	1.83	-19.25	-17.99	-17.35	16.10
	0.4215	*0.6615*	*1.88*	*-20.46*	*-17.81*	*-16.59*	*13.94*
C412-C411	0.6960	0.7054	2.18	-19.10	-16.86	-14.09	11.85
	0.6909	*0.7104*	*2.09*	*-16.45*	*-15.99*	*-12.99*	*12.53*
C416-C411	0.6935	0.7056	2.14	-19.47	-16.90	-13.77	11.20
	0.6939	*0.7053*	*2.07*	*-16.71*	*-16.03*	*-12.96*	*12.28*
H416-C416	0.3382	0.7457	2.00	-22.66	-20.89	-19.87	18.11
	0.3641	*0.7189*	*1.89*	*-18.82*	*-18.75*	*-18.03*	*17.97*
C413-C412	0.6678	0.7248	2.04	-15.46	-15.08	-12.22	11.83
	0.6864	*0.7057*	*2.10*	*-16.98*	*-16.25*	*-13.02*	*12.29*
H412-C412	0.3666	0.7171	1.81	-18.21	-17.84	-16.66	16.29
	0.3983	*0.6847*	*1.90*	*-19.99*	*-18.17*	*-17.30*	*15.48*
H413-C413	0.3856	0.6980	1.67	-15.16	-15.44	-15.00	15.28
	0.4293	*0.6537*	*1.87*	*-20.15*	*-17.38*	*-16.24*	*13.47*
H414-C414	0.3721	0.7197	1.75	-17.19	-17.30	-16.10	16.22
	0.3953	0.6878	1.89	-19.46	-17.90	-17.30	15.74
C414-C413	0.5943	0.8029	2.11	-20.14	-16.98	-12.45	9.29
	0.6228	*0.7730*	*2.04*	*-17.44*	*-15.82*	*-12.57*	*10.95*
C415-C414	0.5599	0.8424	2.19	-21.18	-18.47	-12.31	9.61
	0.3916	*0.6914*	*1.88*	*-18.94*	*-17.93*	*-17.25*	*16.25*
C416-C415	0.6123	0.7936	2.09	-20.02	-16.57	-13.08	9.64
	0.6611	*0.7430*	*2.07*	*-16.50*	*-15.79*	*-12.87*	*12.15*

First lines correspond to 4b. The second line (italic) correspond to the multipole refinement of the theoretical structure factor obtained from single point periodic calculations. [a] *In units of Å.* [b] *In units of e Å^{-3}.* [c] *In units of e Å^{-5}*

Table 5.4. Topological Analysis of Bond Critical Points for the **4b** form

Bond	d_1[b]	d_2[b]	$\rho(r_b)$[c]	$\nabla^2 \rho(r_b)$[d]	λ_1[d]	λ_2[d]	λ_3[d]
S8-S1	1.4807	1.5601	0.15	0.94	-0.47	-0.39	1.80
	1.4645	*1.4961*	*0.16*	*1.39*	*-0.45*	*-0.33*	*2.17*
C1-S1	0.8729	0.9175	1.23	-4.06	-6.10	-5.62	7.66
	0.8772	*0.9127*	*1.23*	*-4.62*	*-6.18*	*-5.61*	*7.17*
C111-S1	0.8359	0.9460	1.29	-4.48	-6.89	-5.91	8.32
	0.8600	*0.9219*	*1.26*	*-5.13*	*-6.47*	*-5.89*	*7.23*
C2-S2	0.8697	0.8961	1.27	-4.64	-6.55	-5.61	7.53
	0.8685	*0.8962*	*1.28*	*-5.45*	*-6.63*	*-5.80*	*6.98*
C211-S2	0.8404	0.9291	1.33	-5.88	-7.50	-6.06	7.68
	0.8517	*0.9173*	*1.28*	*-5.36*	*-6.94*	*-5.72*	*7.30*
C3-S3	0.8577	0.9179	1.32	-5.40	-7.33	-5.92	7.85
	0.8650	*0.9104*	*1.26*	*-5.18*	*-6.65*	*-5.68*	*7.15*
C8-S8	0.8739	0.9069	1.30	-5.40	-6.93	-5.99	7.52
	0.8671	*0.9127*	*1.25*	*-4.90*	*-6.43*	*-5.69*	*7.21*
C811-S8	0.8789	0.9044	1.27	-5.63	-6.52	-5.86	6.75
	0.8680	*0.9149*	*1.25*	*-4.91*	*-6.42*	*-5.71*	*7.22*
C1-C2	0.6792	0.7193	2.18	-19.17	-17.20	-13.63	11.66
	0.6954	*0.7031*	*2.07*	*-16.39*	*-15.59*	*-12.39*	*11.59*
C1-C9	0.7116	0.7195	1.94	-14.71	-14.72	-11.95	11.96
	0.7155	*0.7157*	*1.94*	*-14.91*	*-14.50*	*-12.07*	*11.66*
C3-C2	0.7013	0.7278	1.96	-15.69	-15.14	-12.05	11.50
	0.7126	*0.7168*	*1.94*	*-14.53*	*-14.42*	*-11.78*	*11.68*
C9-C8	0.7105	0.7202	2.01	-16.16	-15.14	-13.00	11.98
	0.7135	*0.7172*	*1.93*	*-14.98*	*-14.56*	*-12.00*	*11.58*
C111-C112	0.6854	0.7146	2.20	-18.80	-16.89	-14.20	12.29
	0.6953	*0.7047*	*2.08*	*-17.12*	*-15.73*	*-12.86*	*11.47*
C111-C116	0.6968	0.6978	2.10	-18.00	-16.24	-13.36	11.60
	0.6847	*0.7099*	*2.10*	*-17.52*	*-15.94*	*-12.97*	*11.39*
H112-C112	0.3573	0.7279	1.77	-17.01	-17.48	-16.68	17.15
	0.3889	*0.6941*	*1.88*	*-19.14*	*-17.94*	*-17.09*	*15.89*
C112-C113	0.6782	0.7141	2.19	-19.27	-17.46	-13.76	11.95
	0.6934	*0.6989*	*2.10*	*-17.42*	*-15.90*	*-12.96*	*11.44*
H113-C113	0.3547	0.7286	1.79	-17.67	-17.96	-16.95	17.25
	0.3868	*0.6962*	*1.89*	*-19.03*	*-17.95*	*-17.16*	*16.09*
C113-C114	0.6867	0.7078	2.10	-19.39	-16.64	-13.96	11.20
	0.6972	*0.6973*	*2.09*	*-17.39*	*-15.80*	*-13.04*	*11.45*
H114-C114	0.3498	0.7337	1.82	-18.34	-18.54	-17.40	17.61
	0.3862	*0.6968*	*1.88*	*-18.98*	*-17.96*	*-17.15*	*16.13*
C115-C114	0.6766	0.7163	2.28	-21.83	-18.32	-15.42	11.91
	0.6956	*0.6971*	*2.10*	*-17.59*	*-15.88*	*-13.10*	*11.38*

Table 5.4 Continued

H115-C115	0.3585	0.7245	1.78	-17.44	-17.58	-16.70	16.84
	0.3842	*0.6987*	*1.89*	*-19.12*	*-18.08*	*-17.23*	*16.18*
C116-C115	0.6758	0.7231	2.15	-19.04	-16.99	-13.83	11.78
	0.6958	*0.7030*	*2.07*	*-17.16*	*-15.70*	*-12.92*	*11.46*
H116-C116	0.3558	0.7283	1.78	-17.53	-17.76	-16.94	17.18
	0.3820	*0.7010*	*1.90*	*-19.84*	*-18.35*	*-17.53*	*16.04*
C212-C211	0.6657	0.7311	2.17	-19.33	-16.80	-14.39	11.85
	0.6832	*0.7136*	*2.08*	*-16.97*	*-15.64*	*-12.76*	*11.43*
C212-C216	0.6979	0.7000	2.15	-18.55	-16.93	-13.58	11.95
	0.6880	*0.7099*	*2.07*	*-16.98*	*-15.63*	*-12.80*	*11.45*
H216-C216	0.3504	0.7337	1.81	-18.16	-18.30	-17.50	17.65
	0.3861	*0.6969*	*1.90*	*-19.60*	*-18.21*	*-17.27*	*15.87*
C212-C213	0.6944	0.7007	2.15	-17.95	-16.68	-13.39	12.12
	0.6961	*0.6989*	*2.08*	*-17.22*	*-15.78*	*-12.85*	*11.41*
H212-C212	0.3616	0.7220	1.74	-15.76	-16.79	-15.89	16.92
	0.3845	*0.6985*	*1.90*	*-19.67*	*-18.26*	*-17.37*	*15.96*
H213-C213	0.3472	0.7366	1.84	-18.50	-18.61	-17.74	17.84
	0.3859	*0.6971*	*1.89*	*-19.44*	*-18.14*	*-17.32*	*16.02*
C213-C214	0.6882	0.7016	2.17	-19.43	-16.83	-14.19	11.59
	0.6936	*0.6962*	*2.12*	*-18.00*	*-16.14*	*-13.19*	*11.33*
H214-C214	0.3583	0.7247	1.77	-16.94	-17.45	-16.48	16.98
	0.3881	*0.6950*	*1.88*	*-18.83*	*-17.86*	*-16.97*	*16.00*
C214-C215	0.6576	0.7378	2.28	-20.95	-18.01	-15.02	12.07
	0.6951	*0.6997*	*2.09*	*-17.41*	*-15.79*	*-13.05*	*11.43*
C215-C216	0.6757	0.7172	2.15	-18.81	-16.98	-13.68	11.85
	0.6953	*0.6976*	*2.08*	*-17.22*	*-15.80*	*-12.83*	*11.41*
H215-C215	0.3633	0.7216	1.74	-16.80	-17.17	-16.21	16.59
	0.3884	*0.6948*	*1.88*	*-18.97*	*-17.85*	*-17.09*	*15.97*
C312-C311	0.6805	0.7137	2.18	-19.03	-17.31	-13.64	11.92
	0.6872	*0.7071*	*2.10*	*-17.51*	*-15.94*	*-12.99*	*11.42*
C311-C316	0.6986	0.6988	2.17	-18.45	-16.91	-13.67	12.14
	0.6900	*0.7073*	*2.08*	*-17.07*	*-15.70*	*-12.83*	*11.45*
H312-C312	0.3477	0.7374	1.84	-18.96	-18.75	-18.00	17.80
	0.3863	*0.6967*	*1.88*	*-19.10*	*-18.02*	*-17.12*	*16.04*
C313-C312	0.6620	0.7368	2.10	-17.92	-16.24	-13.36	11.67
	0.6949	*0.7031*	*2.08*	*-17.18*	*-15.71*	*-12.93*	*11.46*
C313-C314	0.6925	0.7053	2.23	-19.13	-17.60	-14.37	12.83
	0.6961	*0.7015*	*2.08*	*-17.12*	*-15.73*	*-12.89*	*11.50*
H313-C313	0.3637	0.7228	1.72	-15.52	-16.52	-15.90	16.91
	0.3863	*0.6967*	*1.89*	*-19.32*	*-18.06*	*-17.27*	*16.01*

Table 5.4 Continued

H314-C314	0.3594	0.7247	1.78	-18.09	-17.77	-16.99	16.66
	0.3857	*0.6973*	*1.90*	*-19.76*	*-18.23*	*-17.42*	*15.89*
C315-C314	0.6960	0.6969	2.19	-19.14	-17.10	-14.18	12.15
	0.6946	*0.6977*	*2.10*	*-17.61*	*-15.92*	*-13.10*	*11.41*
C315-C316	0.6926	0.6982	2.13	-18.57	-16.05	-14.19	11.68
	0.6926	*0.6981*	*2.10*	*-17.60*	*-15.98*	*-12.99*	*11.37*
H316-C316	0.3564	0.7268	1.78	-16.76	-17.68	-16.27	17.19
	0.3867	*0.6963*	*1.88*	*-19.00*	*-17.96*	*-17.10*	*16.05*
H316-C316	0.3564	0.7268	1.78	-16.76	-17.68	-16.27	17.19
	0.3867	*0.6963*	*1.88*	*-19.00*	*-17.96*	*-17.10*	*16.05*
C811-C812	0.6879	0.7113	2.13	-18.11	-16.43	-13.67	11.99
	0.6919	*0.7072*	*2.07*	*-17.05*	*-15.68*	*-12.82*	*11.46*
C811-C816	0.6917	0.7061	2.13	-18.32	-16.65	-13.54	11.86
	0.6908	*0.7071*	*2.08*	*-17.14*	*-15.78*	*-12.82*	*11.46*
H812-C812	0.3588	0.7261	1.76	-16.51	-17.18	-16.46	17.14
	0.3882	*0.6948*	*1.90*	*-19.77*	*-18.16*	*-17.31*	*15.71*
H816-C816	0.3438	0.7397	1.87	-19.31	-19.10	-18.21	17.99
	0.3872	*0.6958*	*1.89*	*-19.26*	*-18.05*	*-17.14*	*15.93*
C812-C813	0.6756	0.7193	2.08	-17.34	-15.71	-13.23	11.60
	0.6960	*0.6989*	*2.09*	*-17.48*	*-15.88*	*-13.01*	*11.41*
H813-C813	0.3576	0.7261	1.77	-17.21	-17.53	-16.76	17.08
	0.3862	*0.6968*	*1.88*	*-18.90*	*-17.92*	*-17.10*	*16.12*
C813-C814	0.6937	0.7023	2.13	-19.32	-16.85	-14.05	11.58
	0.6947	*0.7013*	*2.09*	*-17.26*	*-15.73*	*-13.00*	*11.46*
C815-C814	0.6751	0.7181	2.21	-20.15	-17.83	-14.23	11.91
	0.6965	*0.6965*	*2.09*	*-17.35*	*-15.85*	*-12.93*	*11.43*
H814-C814	0.3571	0.7268	1.78	-17.80	-18.00	-16.75	16.96
	0.3840	*0.6991*	*1.89*	*-19.25*	*-18.08*	*-17.33*	*16.17*
H815-C815	0.3520	0.7315	1.82	-18.53	-18.24	-17.62	17.33
	0.3873	*0.6957*	*1.88*	*-19.00*	*-17.90*	*-17.09*	*15.99*
C816-C815	0.6920	0.7021	2.12	-18.65	-16.70	-13.54	11.60
	0.6942	*0.6999*	*2.10*	*-17.55*	*-15.86*	*-13.08*	*11.39*

First lines correspond to 4b. The second line (italic) correspond to the multipole refinement of the theoretical structure factor obtained from single point periodic calculations. [a] *In units of Å.* [b] *In units of e Å*$^{-3}$. [c] *In units of e Å*$^{-5}$

5.4.2 Analysis and comparison of the multipole refinements

In this section the improvements of the agreement between the experimental and theoretical data with the increase of model sophistication will be analysed. Refinements

using three different multipole models were performed for the experimental data (1, 2, 3), as described in Section 5.2.3; these were compared with the topological analysis of the multipole model based on the refinements of the theoretical structure factors derived from periodic single point calculations. The charge densities and the Laplacian at the BCPs of each experimental and theoretical model are compared. Since the volume of data prohibited the deduction of clear trends (Tables 5.3 and 5.4), a residual factor R_{Par} was calculated in order to describe the global agreement between experimental and theoretical parameters using equation 2.9, Chapter 2. The R_{val}, R_{ρ} and $R_{\nabla 2(\rho)}$ values of the forms **4a** and **4b_kappa** are summarized in Table 5.5. For both forms, an improvement of the R_{val} term can be noticed with the increase of the sophistication of the multipole model. For form **4a**, the best agreement between the experimental data and theoretical calculations of the charge density and Laplacian were obtained for model 1 followed by 2 and 3. The lowest R_{ρ} for **4b_kappa** was obtained for model 1 followed by 3 and 2. On the other hand, for the $R_{\nabla 2(\rho)}$ the lowest value was obtained for model 3 followed by 2 and 1. Therefore, the trends between the two forms are not in agreement.

Table 5.5. The residual factor of the experimental data versus theoretical data of forms **4a** and **4b_kappa** of **4**

Reference density from theoretical structure factor	**Model**	$\mathbf{R_{val}}$	$\mathbf{R_{\rho}}$	$\mathbf{R_{\nabla 2(\rho)}}$
4a	1	3.53	0.0182	0.0306
	2	3.50	0.0190	0.0554
	3	3.43	0.0208	0.0724
4b_kappa	1	2.75	0.0079	0.0058
	2	2.73	0.0090	0.0040
	3	2.71	0.0077	0.0012

5.4.3. The residual density maps representations

The residual electron density maps for the forms of **4** are represented in Figures 3.5 and 3.6. The maps are plotted in the naphthalene and C-S-C planes. The residual densities in both forms of **4** do not exceed 0.4 $eÅ^{-3}$, indicating the good quality of the multipole refinements. Some noise can be noticed in the maps for both forms, particularly around the S atom. However no further investigations were made in this case, such as testing anharmonic thermal motion refinements, as was carried out for the forms of compound **1** (in which the residual densities were higher, with values of around $0.8eÅ^{-3}$)

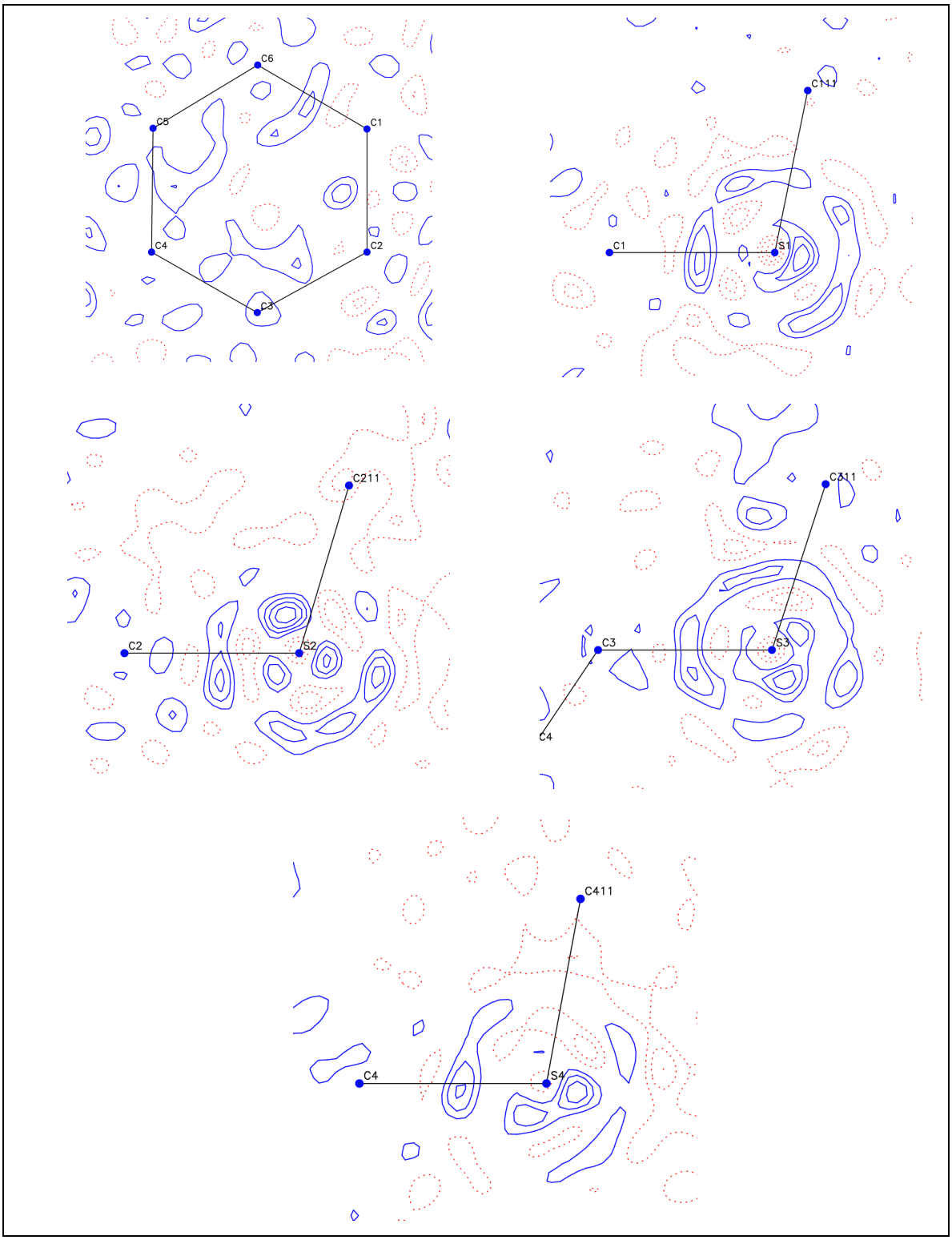

Figure 5.4. Residual electron density maps for form **4a –** in the naphthalene ring plane (top left), and the various C-S-C planes. Contours level are ±0.1e/Å^{-3}

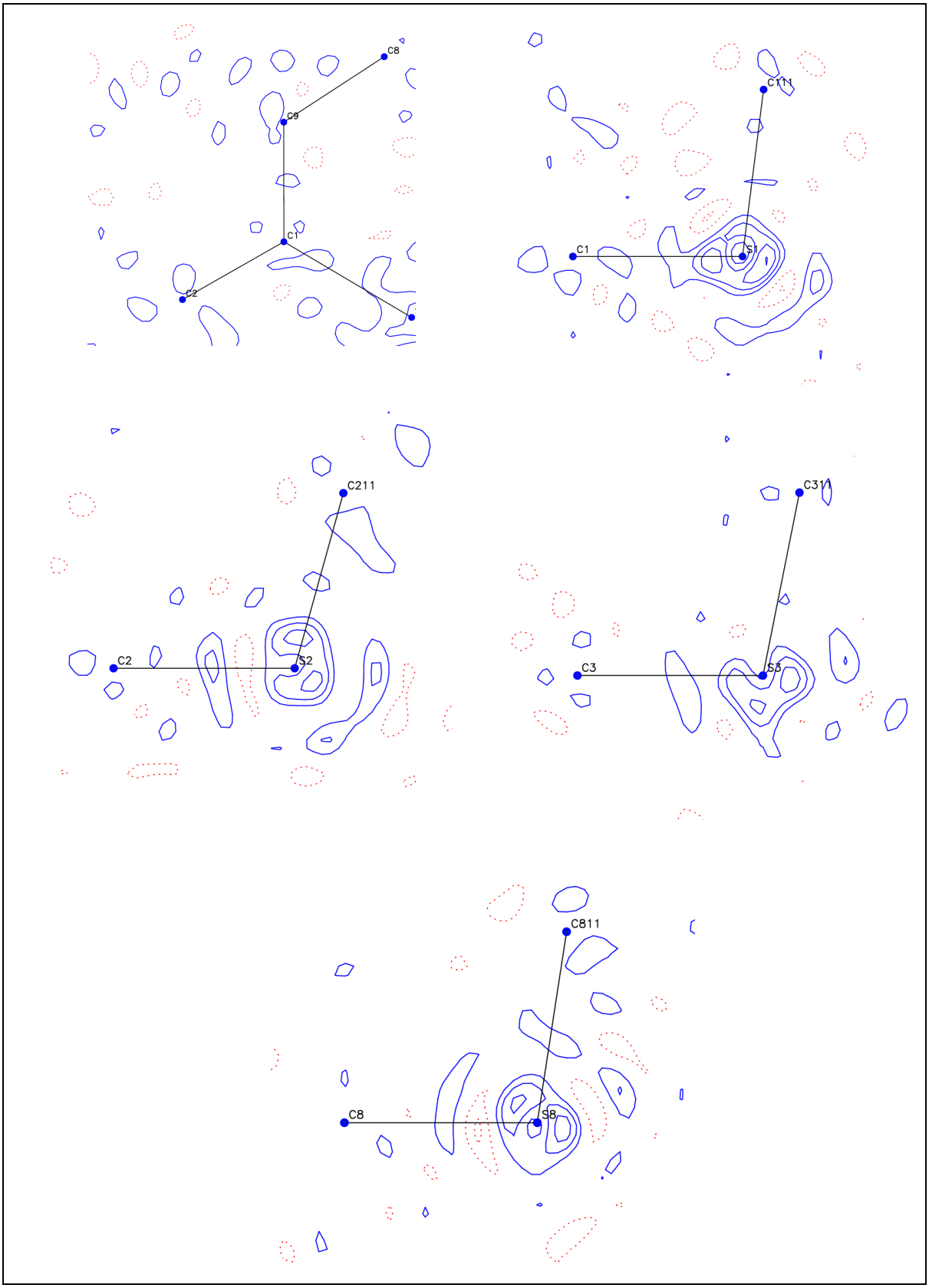

Figure 5.5. Residual electron density maps for form **4b –** in the naphthalene ring plane (top left), and the various C-S-C planes. Contours level at ±0.1e/Å^{-3}

5.4.4 Description of molecular graphs

The molecular graphs description, including BCPs formed between the atoms in forms **4a** and **4b**, are illustrated in Figures 5.6 and 5.7, respectively. Only the molecular graphs for the asymmetric unit are plotted, for clarity. Two additional BCPs were observed in form **4a** between the S atom and the C-C bond while in form **4b** only one BCP of this type was observed. In addition, in form **4b**, an intramolecular BCP was observed between the S1 and S8 atoms. In order to investigate this unusual BCP within the S1···S8 intramolecular interaction, the distances between the S atoms were calculated for both **4a** and **4b** forms (Table 5.6). The distances S···S of both forms **4a** and **4b** are found to be in the range 2.9481(2) to 3.3951(2) Å range, and are thus shorter than the sum of the van der Waals radii (3.70 Å). However a BCP is observed only between atoms S1···S8, which is the intramolecular S···S interaction with the shortest distance (2.9481(2)Å).

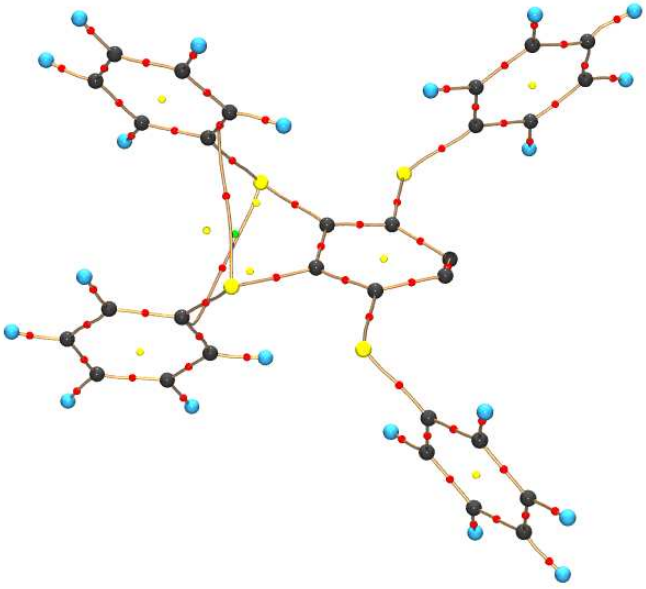

Figure 5.6. Molecular graph of form **4a** showing the BCPs between the atoms in the asymmetric unit. Atoms colour code: C-grey, S-yellow, H-light blue. The BCPs between the atoms are represented by red spheres.

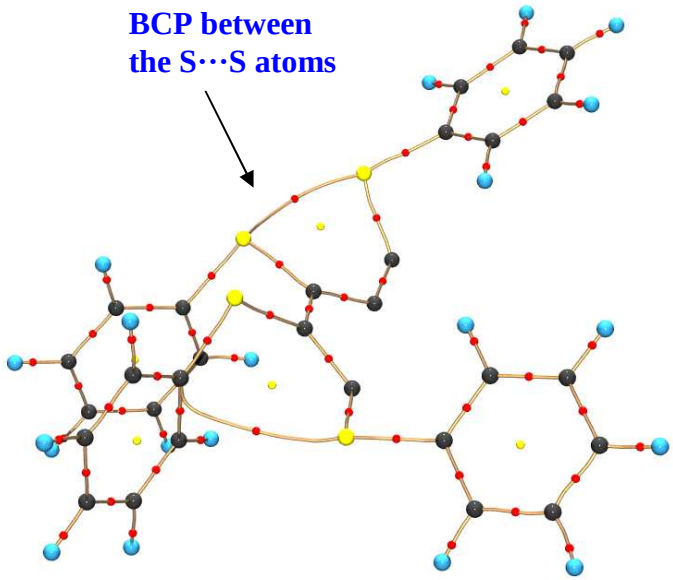

Figure 5.7. Molecular graph of form **4b** showing the BCPs between the atoms in the asymmetric unit. Atoms colour code: C-grey, S-yellow H-light blue. The BCPs between the atoms are represented by red spheres.

Table 5.6. The S···S interatomic distances in forms **4a** and **4b** (Å). The shortest of these (S1···S8) contains a BCP

4a		**4b**	
S1···S2	3.0703(2)	S1···S2	3.1765(2)
S2···S3	3.3951(2)	S2···S3	3.285(2)
S3···S4	3.0739(2)	S1···S8	2.9481(2)

5.4.5. Laplacian representation

In order to investigate the unusual BCP formed between the S1 and S8 atoms the Laplacian map was plotted in the S8···S1-C1 plane. Charge depletion can be observed at the S8 atom in the direction of the S1 atom, while the lone pair at the S1 atom is slightly orientated to the S8 atom. The BCP path also follows the depletion region at S8 and the concentration region at S1.

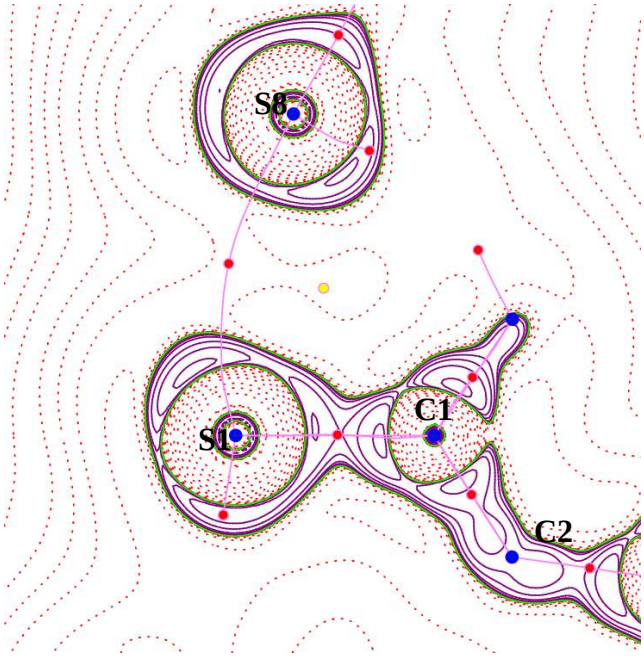

Figure 5.8. Plots of the negative Laplacian, $L(\mathbf{r})$ in the S8···S1-C1 plane of form **4b**,with the BCPs indicated as red dots. Positive contours – solid purple line; negative contours – dotted line. The contour levels are at -1.0 x 10^{-3}, ±2.0 x 10^{n}, ±4 x 10^{n}, ± 8 x 10^{n} (n = -3, -2, -1, 0, +1, +2) e Å^{-5}

5.5. Lattice and intermolecular interaction energy calculations.

The lattice energies of the forms of **4** were calculated using different approaches and different software including XD[7] and CRYSTAL09.[10] The results are discussed in this section.

The lattice energy calculations evaluated using the experimental charge density approach are listed in Table 5.7. Form **4b** was found to be the most stable, showing the lowest lattice energy in case of both data collections, **4b_kappa** and **4b_apex**. However, considerable discrepancy was obtained for the two different data collections of **4b**. Variation of the lattice energy with the different multipole models used can also be noticed here, as in the previous cases studied in this work.

The CRYSTAL09[10] lattice energy calculations are in agreement with the results obtained from the experimental charge density approach. The calculations were carried out using the atom coordinates from the best multipole model refinement (model 3). For form **4b** only the results for form **4b_kappa** were used for estimating the lattice energy using

the CRYSTAL09[10] software. The best fit between the ECD approach and CRYSTAL09[10] lattice energy calculations for **4a** was obtained for model 2, with a difference of 11.24 kJ/mol. In the case of **4b_kappa** the best fit was obtained for model 1 with significantly larger differences of 51.35 kJ/mol. The results are in accord with the thermal analysis studies, with form **4b** having the highest melting point.[2]

Table 5.7. Lattice energies calculated from experimental charge density of the two polymorphs of **4** (kJ/mol)

Model	**4a**	**4b_kappa**	**4b_apex**
1	–535.49	–676.61	–726.40
2	–562.83	–706.39	–763.17
3	–565.15	–740.75	–843.90

Table 5.8. Lattice energy calculations of the polymorphs of **4** using the CRYSTAL09[10] software (kJ/mol).

4a	**4b_kappa**
–551.59	–624.65

5.6. Conclusions

The two conformational polymorphs of **4** compound were analysed for the first time using high resolution X-ray diffraction. The crystals of the forms can be distinguished by their different colour. The yellow form is known to crystallise in a monoclinic crystal system with *C*2/*c* space group, while the red form was identified with a triclinic, $P\bar{1}$ space group.

The **4a** form contains two isomers within the crystal packing, distinguished by the configuration of the external phenyl groups that alternate in an **aabbaabb** or **bbaabbaa** fashion. The **aababbab** conformation of the phenyl groups was identified for the **4b** form.

The gas phase optimized energy using the DFT method at b-p/ def2-TZVP level of theory gives a difference in the conformation energy of –16.7 kJ/mol between the molecules in the two forms, with the yellow form being the most stable one.

The molecular graph description of **4a** and **4b** shows an intramolecular BCP between S atom and the C-C bond of the benzene ring. In addition, in form **4b** a BCP is observed between atoms S1···S8. The distance between these two atoms is found to be the shortest of the S···S distances present in the forms of **4**. The Laplacian map plotted in the S8···S1-C1 plane also confirm a charge depletion at atom S8 and charge concentration at atom S1.

The lattice energies of the forms of **4** were calculated using different approaches and different software including XD[7] and CRYSTAL09.[10] Form **4b** was found to be the most stable form, showing the lowest lattice energy from both XD[7] and CRYSTAL09.[10] Variation of the lattice energy with the different multipole model used can also be noticed here, as in the previous cases studied.

References

1. R. H. Barbour, A. A. Freer and D. D. MacNicol, *Chem. Comm.*, 1983, 362-363.
2. Y. Suenaga, A. Ueda, T. Kuroda-Sowa and M. Maekawa, *Thermochim. Acta*, 2003, **400**, 87-94.
3. Z. Otwinowski and W. Minor, *Methods in Enzymology* 1997, **279**, 307-326.
4. SADABS: Area-Detector Absorption Correction; Siemens Industrial Automation, Inc.: Madison, WI, 1996
5. R. Blessing, *J. Appl. Cryst.*, 1997, **30**, 421-426.
6. A. Altomare, G. Cascarano, C. Giacovazzo and A. Guagliardi, *J. Appl. Cryst.*, 1994, **27**, 435.
7. L. Farrugia, *J. Appl. Cryst.*, 2012, **45**, 849-854.
8. A. Volkov, L. J. Farrugia, C. Gatti, P. R. Mallinson, T. Richter and T. Koritsanszky, *XD-2006*, 2006, http://xd.chem.buffalo.edu/.

9. Ø. A. Madsen, *J. Appl. Cryst.*, 2006, **39**, 757-758.

10. (a) A. D. Becke, *Phys. Rev. A*, 1988, **38**, 3098; (b) A. D. Becke, *J. Chem. Phys.*, 1993, **98**, 5648; (c) C. Lee, W. Yang and R. G. Parr, *Phys. Rev. B*, 1988, **37**, 785. (d) P. J. Stephens, J. F. Devlin, C. F. Chabalowski and M. J. Frisch, *J. Phys. Chem.*, 1994, **98**, 11623.

11. (a) F. Weigend and R. Ahlrichs, *Phys. Chem. Chem. Phys.*, 2005, **7**, 3297; (b) F. Weigend, *Phys. Chem. Chem. Phys.*, 2006, **8**, 1057.

12. TURBOMOLE V6.2 2010, a development of University of Karlsruhe and Forschungszentrum Karlsruhe GmbH, 1989-2007, TURBOMOLE GmbH, since 2007 http://www.turbomole.com.

13. R. Dovesi, R. Orlando, B. Civalleri, C. Roetti, V. R. Saunders, and C. M. Zicovich-Wilson, *Z. Kristallogr.*, 2005, **220**, 571; R. Dovesi, V. R. Saunders, C. Roetti, R. Orlando, C. M. Zicovich-Wilson, F. Pascale, B. Civalleri, K. Doll, N. M. Harrison, I. J. Bush, P. D'Arco, and M. Llunell, CRYSTAL09 (CRYSTAL09 User's Manual. University of Torino, Torino, Italy, 2009).

14. S. K. Wolff, D. J. Grimwood, J. J. McKinnon, M. J. Turner, D. Jayatilaka and M. A. Spackman, 2010, University of Western Australia, CrystalExplorer (Version 3.0).

6. Molecular Complexes of Chloranilic Acid with Lutidines

6.1. Introduction

Interest in the nature of polymorphic materials extends also to molecular complexes and their relative stabilities through hydrogen bond contributions towards stabilising stoichiometrically different 'compositional polymorphs'. In this chapter, molecular complexes of the isomers of lutidines (dimethylpyridine) with chloranilic acid (2,5-dichloro-3,6-dihydroxy-*p*-benzoquinone) will be presented and analysed using charge density studies.

6.1.1. Crystal Engineering

Crystal engineering represents a field for designing and synthesising molecular solid state complexes with the aim on building materials with particular desired properties. The 'crystal engineering' term was first mentioned by Schmidt *et al.*[1] on his work related to the topochemical reactions of crystalline cinnamic acids in 1971. Since then the crystal engineering field has evolved and developed in many ways.[2] The most two important design strategies used in this field are based on hydrogen bonding and coordination complexation[2] but there are examples of other types of intermolecular interactions such as π··π[3,4] and halogen···halogen,[5-9] being explored. The formation of a specific supramolecular synthon can be predicted from the intermolecular interaction preference of the functional groups used. The architecture of the molecules in the crystal and their self-assembly represent therefore the core of the crystal engineering. In coordination complexes, the interactions are formed between metal centres and ligands or metal clusters, e.g. metal organic frameworks (MOFs)[10-13] (which have applications in areas such as gas storage)[14,15] and polyoxometalates (POMs).[16,17]

Crystal engineering takes advantage of knowledge of the preferred intermolecular bonding patterns that a functional group will adopt. This includes both strong and weak interactions that a system can form. Understanding the intermolecular interactions of simple organic molecular crystals may lead to a better understanding of the interactions which occur in larger biomolecular complexes. For example Sakaki *et al.*[18] investigated the π··π interactions in thiamine-tryptophane molecular complexes which are the basis of the thiamine coenzyme and tryptophenyl residual interactions in apoenzymes. The crystallographic studies of the thiamine indole-3-propinate compounds showed three types of π··π stacking interactions: indole-pyrimidinium, indole-thiazolium and indole-

pyrimidine. All the rings are almost parallel with interplanar distances ranging between 3.4 and 3.6 Å.

Computational methods available at the moment which are used for predicting molecular crystal packing interactions require a large amount of computational power and hence time and is consequently restricted to relatively small, rigid molecules;[2,19] usually a systematic experimental approach for tuning supramolecular motifs using similar functional groups is more effective.

Charge density analysis also plays an important role in understanding the nature of intermolecular interactions and therefore represents a powerful tool in the crystal engineering field.[20]

6.1.2. p*K*a Matching

A current challenge in crystal engineering is the ability to predict proton transfer between molecular fragments in molecular complexes. There are various methods which have been applied to try and predict the likelihood of proton transfer in molecular complexes. The most widely applied approach is consideration of the acid dissociation constant (pK_a) values. The pK_a is equal to $-\log_{10}K_a$ (eq. 6.1.) and can be used to measure the strength of the acids and bases in solution, $HA \Leftrightarrow A^- + H^+$

$$K_a = \frac{[A^-][H^+]}{[HA]} \qquad \text{eq. 6.1}$$

High values are associated with weak acids and therefore the proton is more difficult to be removed. Whilst pKas are solution based values, there is a surprising level of transferability into the solid-state. A commonly applied rule of thumb as described by Childs *et al.*[21] states that proton transfer is expected to occur between an acid and a base if the ΔpK_a value (ΔpK_a = pK_a(base) – pK_a(acid)) is greater than 3. Hence, when the pK_a values of the basic molecule is considerably higher then the acid, the proton is expected to be bound to the molecule with the higher pK_a. A salt is expected to be produced if the ΔpK_a is greater than 3.[21] When $\Delta pK_a < 0$, no proton transfer is expected, the molecules remain neutral and a co-crystal is formed.[22] Between 0 and 3, it is difficult to predict whether proton transfer will occur or not and thus this rule is inadequate to be used in salt or co-crystal prediction between this region.[21] Because of this difficulty, in most of cases this methodology is only applied to acid-base complexes which give a ΔpK_a smaller than 1 or greater than 3; hence the 0-3 region represents a narrow area of research results. The rule

for the values of the ΔpK_a varies in the literature with the molecular complexes studies. For instance B. R. Bhogala *et al.*[22] suggested according to their results for pyridine base and carboxylic acid complexes that when ΔpK_a <0 a neutral O-H···N hydrogen bond results, between 0 and 3.75 an intermediate character of the O-H···N/ N-H$^+$···O$^-$ bond was observed; and for ΔpK_a greater then 3.75 proton transfer occurs with the N-H$^+$···O$^-$ intermolecular interaction formation. The ΔpK_a rule was also found to be inadequate for predicting O-H···N/ N-H$^+$···O bond formation in presence of other polar functional groups in the system (e.g. 3-, 4-hydroxybenzoic acid, 3,5-dihydroxybenzoic acid, 3-fluoro-4-hydroxybenzoic acid, 3-chloro-4-hydroxybenzoic acid, 3,5-dimethyl-4-hydroxybenzoic acid 3-, 4-aminopyridine).[23] Neutral hydrogen bonds and proton transfer were observed simultaneously to form in the range of 0-4 values of ΔpK_a for these systems. In the case of pyridine phenol pairs, salt formation was shown to occur for ΔpK_a values greater than 2.95.[24]

The application of the ΔpK_a values rule is highly influenced by the compounds studied, but there is also the issue of the accuracies of the pK_a measurements when transferred from the solution state to the solid state is often inaccurate.

6.1.3. Chloranilic Acid and Molecular Complexes of Chloranilic Acid

Chloranilic acid or 2,5-dichloro-3,6-dihydroxy-*p*-benzoquinone in combination with other molecules can exist in neutral, singly deprotonated or doubly deprotonated forms (Scheme 6.1). It can also act as a proton acceptor in acid base reactions and crystallisation.[25] The deprotonation or oxidation of chloranilic acid depends on the basicity of the co-molecules present in the system. In the neutral and CA^{2-} forms, the chloranilic acid molecule has an inversion centre due to the symmetry of the molecule and consequently only half of these molecules are often present in the asymmetric unit. Due to the hydrogen bond formation and proton transfer abilities, chloranilic acid represents a good candidate for crystal engineering studies; therefore the behaviour in molecular complexes with different stoichiometries will be investigated in this work.

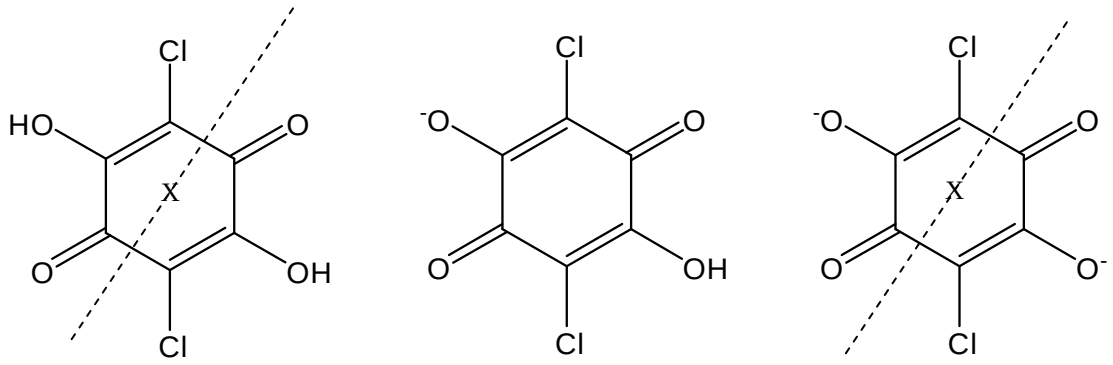

Scheme 6.1. The three possible charge states of chloranilic acid: left - neutral H_2CA; middle - partially deprotonated HCA^-; and right - fully deprotonated CA^{2-} and the inversion centre are shown for the neutral H_2CA and CA^2

Chloranilic acid is known to crystallise in only one anhydrous form, determined for the first time in 1967 by E.K. Anderson.[26] Moderate O-H···O hydrogen bonds (O···O distances 2.752Å) and close Cl···Cl halogen interactions areformed between molecules (Figure 6.1). A dihydrate form was determined in the same year 1967 by E.K. Anderson.[27] The chloranilic acid molecules form hydrogen bonds with water molecules; each chloranilic acid molecule is surrounded by four water molecules. The waters molecules also form H bonds between each other creating chains (Figure 6.2).

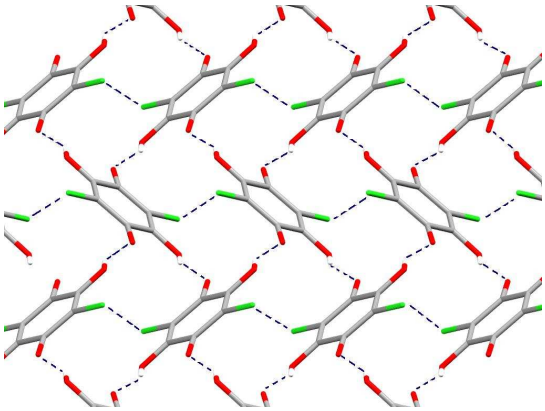

Figure 6.1. The hydrogen bonds and halogen-halogen Cl···Cl interactions in the chloranilic acid crystal structure.

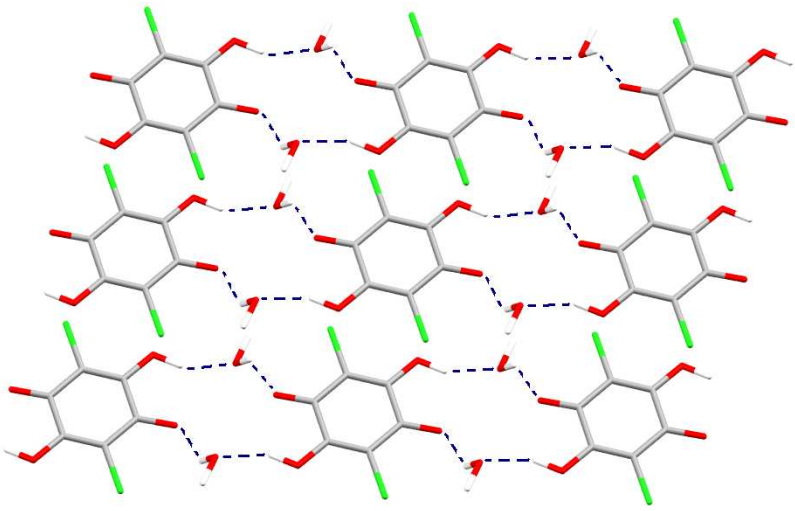

Figure 6.2. Intermolecular hydrogen bonds in the crystal structure of chloranilic acid dihydrate resulting in a 3-dimensional hydrogen bonded network.

Chloranilic acid has previously been shown to readily form molecular complexes with nitrogen bases such as pyridine and pyridine derivatives (e.g. picolines,[28,29] 4,4′-bipyridine[30]) or heterocyclic rings incorporating more then one N atom (e.g. pyrazine,[31] pyrimidine,[21] cytosine,[32] benzamidazole,[33] imidazole[34]). In these cases, proton transfer from chloranilic acid to the N atom of the co-molecule frequently occurs. Different stoichiometries of the molecular complex formed can result in different protonation states for the chloranilic acid molecules.[28] A study of picoline-chloranilic acid molecular complexes in both 1:1 and 2:1 stoichiometries revealed salt formation for all picoline isomers and for both molecular ratios.[28] In general, the chloranilic acid molecule loses one proton in the 1:1 case (HCA^-) and forms a hydrogen-bonded supramolecular unit with picoline in P:C:C:P fashion (P-picoline, C-chloranilic acid). For the 2:1 stoichiometry, the chloranilic acid tends to become doubly deprotonated (CA^{2-}) and forms P:C:P synthon units through hydrogen bond interactions.

The hydrogen bond patterns have been classified for the 1:1 chloranilic acid-amine systems into three categories by S. Ishida *et al.*[35] In the first type the amide chloranilic acid molecules build molecular chains through O-H···N or N-H···O hydrogen bond alternation. The chloranilic acid molecule can be in this case either neutral or singly deprotonated (H_2CA, HCA^-) In the second type, chains of chloranilate ions (HCA^-) are formed via O-H···O hydrogen bonds and are linked together by N-H···O hydrogen bonds. The third type contains dimers formed by chloranilic acid via O-H···O bonds. The singly deprotonated dimers are connected to the amine base by N-H···O hydrogen bonds allowing three different types of amine arrangements (Figure 6.3).

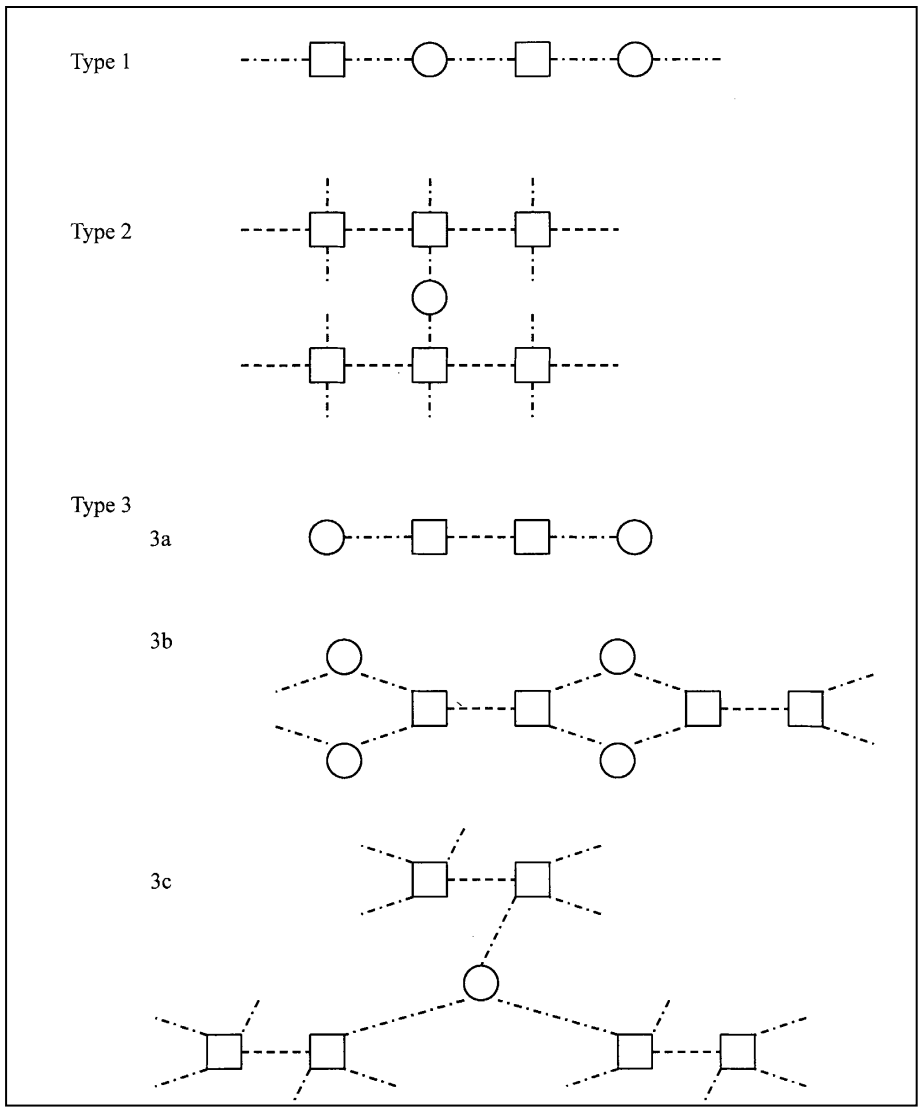

Figure 6.3. The three possible hydrogen bonds formation by 1:1 complexes of chloranilic acid with co-molecules containing amine groups.[35] The square symbols represent H_2CA or HCA^-, the circles represent the amine and the N-H···O, N···H-O and O-H···O hydrogen bonds are indicated by dashed-and-dotted and dashed lines. Type 1: linear tapes of chloranilic acid with amines via O-H···N or N-H···O hydrogen bond alternation. Type 2: chains of chloranilic acid connected into sheets by hydrogen bonding with the amines. Type 3: dimers forms between chloranilic acid molecules (a) linear tapes of chloranilic acid with amines, (b) and (c) the dimers of chloranilic acid connected intro sheets by hydrogen bonding with the amides

The behaviour of the colour of chloranilic acid molecules in neutral, singly and doubly deprotonated in both the solution and solid phases was studied by K. Molcanov *et al.*[29] Crystallisations of chloranilic acid with a series of five organic nitrogen bases molecules were examined such as: dimethylamine, 2-methylpyridine, 2,6-dimethyl-4-amino-pyrimidine, *R,S*-tryptophane and 5,6-phenantroline. It was shown that no proton transfer

occurs between chloranilic acid and 5,6-phenantroline. In this case where the neutral chloranilic acid molecules were present, a light red solution and crystals were observed. A single deprotonation of the chloranilic acid molecules was observed when 2-methyl pyridine, *R,S*-tryptophenone and dimethylamine were used. The solution and crystals formed were dark violet and opaque. In the 2-methylpyridine chloranilic acid molecular complex, two protons were lost by the chloranilic acid molecule. The doubly deprotonated chloranilic acid molecules also give a dark violet colour but the solution was less opaque. A search of the Cambridge Structural Database (CSD)[36] reveals equal occurrences of singly and doubly deprotonated chloranilic acid molecules in molecular complexes with organic compounds. There are approximately 43 crystal structures containing singly deprotonated chloranilic acid molecules complexed with nitrogen containing bases. There are 39 examples of doubly deprotonated chloranilic acid molecules.

Proton transfer can be also influenced by temperature as has been shown for instance in case of phenazine – chloranilic acid (1:1).[37] At 170 K, no proton transfer occurs between chloranilic acid and phenazine molecules. However, as the temperature is decreased to 93K, the chloranilic acid molecule becomes singly deprotonated and the H atom is transferred to one N atom of the phenazine ring.[37] This is a case where the ΔpK_a value is between 0 and 3. The neutral phenazine chloranilic acid molecular complex has been shown to have ferroelectric properties,[38] which have potential applications in electronic and photonic devices.

6.1.4. Molecular Complexes of Lutidines

There are six different isomers of lutidine or dimethylpyridine (C_7H_9N) differentiated by the positions of the methyl groups: 2,3-, 2,4-, 2,5-, 2,6-, 3,4- and 3,5- substituted. The lutidines are known to form either co-crystals or salts with organic acid functional groups.[39-41] In favourable cases with ΔpK_a greater then 3, lutidines show an affinity for protons acting as a H^+ ion absorber. For instance, it was shown that the 2,3- , 2,4-, 2,5 and 3,4 lutidines form salts in all the cases with pamoate acid.[39] Another example of organic molecular complexes presented in literature is pentachlorophenol with the lutidine isomers.[40] The ΔpK_a values in this case varied from 1.45 to 2.29. This is an interesting case where for 3,4-, 3,5-lutidine – pentachlorophenol 1:1 molecular complexes (with ΔpK_a values of 1.76 and 1.45, respectively) no proton transfer was observed while for the 2:1 stoichiometric ratios proton transfer occurs (with ΔpK_a 1.76 and 1.45 respectively). For the

2,3-lutidine – pentachlorophenol molecular complex only crystals in a 1:1 molecular ratio were obtained and no proton transfer was observed (ΔpK_a = 1.87). Two forms were obtained for 1:1 2,6-lutidine pentachlorophenol molecular complexes; in form I no proton transfer was observed while in form II a 50% proton transfer occurs. 100% proton transfer was determined in the 1:1 2,4-lutidine pentachlorophenol molecular complex with ΔpK_a = 2.29. Only the 2:1 2,5-lutidine pentachlorophenol molecular complex showed 100% proton transfer. Therefore, the proton transfer showed a high dependence on the stoichiometry.

A case with the ΔpK_a in a 0-3 range was presented in literature using for crystallisation with lutidines with succinic or fumaric acid.[41] Neutral co-crystal formations were found for all six lutidine isomers with succinic acid in a 2:1 stoichiometry, while the complexes with fumaric acid formed salts in all cases.

In the molecular complex of 2,6 lutidine – 2,4 dihydroxybenzoate,[42] one 2,6-lutidine cation, one 2,4 dihydroxybenzoate and one neutral 2,6-lutidine molecule are found in a 1:1:1 ratio. Hence, there are two 2,6-lutidine molecules in the asymmetric unit, one protonated and one non-protonated effectively making a 2:1 lutidine:benzoic acid molecular complex. This highlights the difficulty in applying the p*K*a rule when the stoichiometry differs from 1:1.

6.1.5. Molecular Complexes of Chloranilic Acid with Lutidines

The crystal structures of the 1:1 molecular complexes of chloranilic acid with 2,4-, 2,5-, 2,6- and 3,4–lutidine have been previously determined by H. Ishida *et al.*[35] (CSD codes: WUXYUJ, WUXZAQ, WUXZEU, WUXZIY). Molecular complexes of chloranilic acid with 2,3-, 2,4-, 2,5- and 2,6–lutidine in a 2:1 molar ratio have also been previously determined.[27] Two polymorphs were found in the case of 2,4 – lutidine (2:1) and two hydrate forms for 3,4- and 3,5– lutidine (2:1).[43] In all cases, the lutidine is protonated and almost all of the time, the chloranilic acid exists in either the singly deprotonated or doubly deprotonated forms depending on the stoichiometry.

In an attempt to obtain new forms of lutidinium chloranilates and also analyse the known forms using charge density tools and neutron diffraction to extract additional information on the energetics of the hydrogen bonds formed in these complexes, new crystallizations were set up for all six isomers of lutidine with chloranilic acid in 1:1 and 2:1 ratios. New molecular complexes of chloranilic acid with 2,3- and 3,5- lutidine (1:1 ratio) and 3,4–lutidine (2:1 ratio) and a new hydrate form of 2:1 2,4-lutidine with chloranilic acid were found. Molecular complexes containing neutral chloranilic acid coexisting with deprotonated CA^- were also found for 2,4- and 3,5-lutidine.

In the case of the 1:1 molecular complexes, five crystal structures were collected using high resolution X-ray diffraction: 2,4-, 2,5-, 2,6-, 3,4- and 3,5-lutidine with chloranilic acid. The crystal size of the molecular complex of 2,3-lutidine chloranilic acid meant that it was not suitable for high resolution diffraction measurements. For the 2:1 molecular complexes, data on five out of the six possible crystal structures (2,3-, 2,4-, 2,5-, 2,6- and 3,4-lutidine with chloranilic acid) were collected to high resolution using X-ray diffraction. Crystals of a 3,5-lutidine chloranilic acid 2:1 molecular complex were not found and a crystal structure has not been previously reported for this.

Proton transfer across from the oxygen to the nitrogen atom would be expected in chloranilic acid – lutidine molecular complexes as lutidine has a significantly higher pK_a (e.g. 2,6-lutidine pK_a = 6.6[44]) compared with chloranilic acid (pK_{a1} = 0.58, pK_{a2} = 3.18[45]). The ΔpK_a values (6.02 and 3.42) show that is easiest to remove the first proton than to remove two from the chloranilic acid molecule although in both cases, the difference is greater than three, so the lutidine molecule would always be expected to be protonated.

6.2. Experimental and Theoretical Section

6.2.1 Sample Preparation

Crystallisations of chloranilic acid and all six isomers of lutidine were prepared in 1:1 and 2:1 ratios using two different solvents, acetonitrile or methanol. Dark red crystals were formed as the solution slowly evaporated for the 2:1 molecular ratio. In the 1:1 molecular ratio case, the crystals were still red but slightly lighter compared with 2:1 molar ratio and for the hydrate forms, purple crystals were observed to grow. This is not consistent with the colour allocation described by K. Molčanov *et al.*[29] for the relevant protonation state of the chloranilic acid molecule. In some cases in addition to the molecular complex, crystals of the starting material, chloranilic acid, were observed to form concomitantly (Figure 6.4).

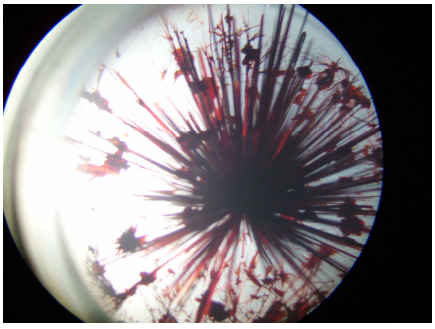

Figure 6.4. Crystals of the 1:1 molecular complex of chloranilic acid 2,3-lutidine (needles) and chloranilic acid (prisms).

6.2.2 Data Collection

Single crystals of suitable size and quality were selected and data were collected at 100K either on a Bruker-Nonius Kappa CCD or a Bruker Apex II difractometer (Mo K_α radiation). In most of the cases, good quality crystals were obtained and collected at a high resolution (~sinθ/λ 1.1 $Å^{-1}$). The reflections measured were merged using SORTAV.[46] The structures were solved using SIR92[47] and refined initially in the spherical-atom formalism with full-matrix least squares on F^2. The non-hydrogen atoms were refined with anisotropic displacement parameters. Structure solution and refinements were performed within the WinGX[48] program. The H112 and H126 atoms of the chloranilic acid and lutidine molecules, respectively in the 2,3-lutidine chloranilic acid molecular complex were placed on calculated positions and refined as riding on the atoms to which they were bonded; all other H atoms were found from difference Fourier maps.

Four of the chloranilic acid – lutidine molecular complexes were measured using neutron diffraction at the ILL using monochromatic radiation on D19; 2,4-lutidine (1:1) 2,5-lutidine (1:1), 2,6-lutidine (1:1 and (2:1)). The 3,4-lutidine chloranilic acid molecular complex (1:1) was also measured using a synchrotron radiation source using I19 at Diamond Light Source. However the quality of the data were not satisfactory for charge density studies due to the high R1obs value obtained from a standard spherical refinement, indicating poor quality of the data. The results from the laboratory source X-ray diffraction measurements were more suitable for the purpose of charge density analysis. The crystallographic information for all of the crystal structures determined in this work using X-ray and neutron diffraction are presented in Tables 6.1-6.7.

Table 6.1. Crystallographic data for the 1:1 molecular complexes of chloranilic acid with 2,3-, 2,4-, and 2,5-lutidine

Compound formula	$C_{13}H_{11}Cl_2NO_4$	$C_{13}H_{11}Cl_2NO_4$	$C_{13}H_{11}Cl_2NO_4$
Isomer	2,3-lutidine 1:1	2,4-lutidine1:1	2,5-lutidine 1:1
M_r	316.13	316.13	316.1
Space group	$P\bar{1}$	$P\bar{1}$	$P2_1/c$
Crystal system	Triclinic	Triclinic	Monoclinic
a/ Å	3.8653(4)	5.0687(2)	7.7415(2)
b/ Å	11.5522(12)	11.2561(4)	11.0538(3)
c/Å	14.4711(14)	11.6281(3)	15.4495(3)
α/deg	98.976(6)	96.274(2)	90.00
β/deg	93.377(5)	91.960(2)	95.514(1)
γ/deg	91.025(6)	90.609(1)	90.00
V/Å^{-3}	636.91(7)	659.00(2)	1315.94(1)
Z	2	2	4
D_{calc}/g cm^{-3}	1.65	1.59	1.60
F(000)	324	324	648
Radiation	Mo Kα	Mo Kα	Mo Kα
λ/Å	0.71073	0.71073	0.71073
μ(Mo-K$_a$)/mm^{-1}	0.522	0.504	0.505
Crystal size/mm	0.18x0.21x0.34	0.17x0.20x0.41	0.12x0.31x0.39
θ range/deg	1.4 – 30.4	2.4-50.7	2.3-50.6
Max sin(θ)/ λ	0.72	1.1	1.1
No. of data used for merging	24317	281388	500656
No. of unique data	3793	13978	14007
hkl range	$-5 \le h \le 5$	$-10 \le h \le 10$	$-16 \le h \le 16$
	$-16 \le k \le 16$	$-24 \le k \le 24$	$0 \le k \le 23$
	$0 \le l \le 20$	$0 \le l \le 25$	$0 \le l \le 33$
R_{int}	0.0702	0.0194	0.0331
R_σ	0.0727	0.259	0.0291
Spherical atom refinement			
No. of data in refinement	3793	13978	14007
No. of refined parameters	217	225	225
Final R [$I > 2\sigma(I)$]	0.045	0.025	0.027
R_w [$I > 2\sigma(I)$]	0.089	0.076	0.082
Goodness of fit *S*	1.021	1.039	1.049
Extrema in residual map/eÅ^{-3}	-0.317 →0.434	-0.406→0.642	-0.408→0.619
Max shift/esd in last cycle	0.000	0.004	0.002
Multipole refinement			
No. of data in refinement	-	12502	11797
No. of refined parameters	-	543	543
Final R [$I > 3\sigma(I)$]	-	0.0164	0.0190
R_w [$I > 3\sigma(I)$]	-	0.0200	0.0205
Goodness of fit *S*	-	1.2038	1.1312
Extrema in residual map/ eÅ^{-3} (all data)	-	-0.310→0.183	-0.302→0.254
Max shift/esd in last cycle	-	0.0009	0.0003

Table 6.2. Crystallographic data for the 1:1 molecular complexes of chloranilic acid with 2,6-, 3,4-, and 3,5-lutidine

Compound formula	$C_{13}H_{11}Cl_2NO_4$	$C_{13}H_{11}Cl_2NO_4$	$C_{13}H_{11}Cl_2NO_4$
Isomer	2,6-lutidine 1:1	3.4-lutidine 1:1	3.5-lutidine 1:1
M_r	316.1	316.1	316.1
Space group	$P\bar{1}$	$P2_1/n$	$P2_1/c$
Crystal system	Triclinic	Monoclinic	Monoclinic
a/ Å	9.0071(3)	10.6010(2)	11.3192(4)
b/ Å	9.0326(3)	5.167(1)	10.2762(4)
c/Å	9.0768(3)	24.3363(4)	11.7534(4)
α/deg	93.526(2)	90.00	90.00
β/deg	104.359(2)	97.199(1)	100.198(2)
γ/deg	110.821(2)	90.00	90.00
V/Å^{-3}	659.48(8)	1322.75(2)	1345.54(5)
Z	2	4	4
D_{calc}/g cm^{-3}	1.59	1.59	1.56
F(000)	324	648	648
Radiation	Mo Kα	Mo Kα	Mo Kα
λ/Å	0.71073	0.71073	0.71073
μ(Mo-K_a)/mm^{-1}	0.504	0.503	0.494
Crystal size/mm	0.20x0.25x0.36	0.16x0.22x0.35	0.20x0.20x0.27
θ range/deg	2.3-50.5	2.4-50.6	2.7-50.4
Max sin(θ)/ λ	1.1	1.08	1.08
No. of data used for merging	284210	238608	276447
No. of unique data	14002	13865	14184
hkl range	$-19 \le h \le 18$	$-22 \le h \le 22$	$-24 \le h \le 23$
	$-19 \le k \le 19$	$0 \le k \le 11$	$0 \le k \le 22$
	$0 \le l \le 19$	$0 \le l \le 52$	$0 \le l \le 25$
R_{int}	0.0261	0.0240	0.0331
R_σ	0.0295	0.0403	0.0283
Spherical atom refinement			
No. of data in refinement	14002	13865	14184
No. of refined parameters	225	225	225
Final R [$I > 2\sigma(I)$]	0.026	0.033	0.034
R_w [$I > 2\sigma(I)$]	0.080	0.091	0.089
Goodness of fit *S*	1.031	1.020	1.032
Extrema in residual map/eÅ^{-3}	-0.387→0.719	-0.314→0.690	-0.529→0.672
Max shift/esd in last cycle	0.003	0.001	0.002
Multipole refinement			
No. of data in refinement	11968	10959	12092
No. of refined parameters	543	542	542
Final R [$I > 3\sigma(I)$]	0.0183	0.0268	0.0258
R_w [$I > 3\sigma(I)$]	0.0203	0.0240	0.0278
Goodness of fit *S*	1.0882	1.0935	1.5751
Extrema in residual map/ eÅ^{-3} (all data)	-0.239→0.235	-0.378→0.265	-0.342→0.269
Max shift/esd in last cycle	0.0003	0.0004	0.0004

Table 6.3. Crystallographic data for the 2:1 molecular complexes of chloranilic acid with 2,3-, 2,4-, and 2,5-lutidine

Compound formula	$C_{20}H_{20}Cl_2N_2O_4$	$C_{20}H_{20}Cl_2N_2O_4$	$C_{20}H_{20}Cl_2N_2O_4$
Isomer	2,3-lutidine 2:1	2,4-lutidine 2:1	2,5-lutidine 2:1
M_r	423.28	423.28	423.28
Space group	$P\bar{1}$	*Pcab*	$P2_1/c$
Crystal system	Triclinic	Orthorhombic	Monoclinic
a/ Å	7.6305(2)	7.5644(5)	8.0870(3)
b/ Å	8.3081(2)	15.7136(10)	11.4214(5)
c/Å	8.4348(2)	16.6651(11)	10.3253(4)
α/deg	65.839(1)	90.00	90.00
β/deg	80.610(2)	90.00	100.451(2)
γ/deg	88.280(1)	90.00	90.00
V/Å^{-3}	480.94(3)	1980.88(2)	937.87(4)
Z	1	4	2
D_{calc}/g cm^{-3}	1.46	1.42	1.50
F(000)	220	880	440
Radiation	Mo Kα	Mo Kα	Mo Kα
λ/Å	0.71073	0.71073	0.71073
μ(Mo-K_a)/mm^{-1}	0.368	0.357	0.377
Crystal size/mm	0.20x0.25x0.35	0.18x0.24x0.36	0.21x0.42x0.50
θ range/deg	2.7-50.4	2.4-50.2	2.6-50.6
Max sin(θ)/ λ	1.08	1.08	1.1
No. of data used for merging	199231	388485	365776
No. of unique data	10134	9962	10037
hkl range	$-16 \le h \le 16$	$0 \le h \le 16$	$-17 \le h \le 17$
	$-15 \le k \le 17$	$0 \le k \le 33$	$0 \le k \le 24$
	$0 \le l \le 18$	$0 \le l \le 35$	$0 \le l \le 22$
R_{int}	0.0290	0.0540	0.0267
R_σ	0.0255	0.0328	0.0261
Spherical atom refinement			
No. of data in refinement	10134	9962	10037
No. of refined parameters	167	167	167
Final R [$I > 2\sigma(I)$]	0.027	0.036	0.025
R_w [$I > 2\sigma(I)$]	0.083	0.100	0.083
Goodness of fit *S*	1.073	1.028	1.056
Extrema in residual map/eÅ^{-3}	-0.283→0.661	-0.479→0.595	-0.417→0.583
Max shift/esd in last cycle	0.003	0.002	0.005
Multipole refinement			
No. of data in refinement	9384	10401	8919
No. of refined parameters	378	378	379
Final R [$I > 3\sigma(I)$]	0.0173	0.0291	0.0155
R_w [$I > 3\sigma(I)$]	0.0217	0.0277	0.0190
Goodness of fit *S*	1.3299	1.4468	1.1711
Extrema in residual map/ eÅ^{-3} (all data)	-0.148→0.216	-0.305→0.253	-0.250→0.271
Max shift/esd in last cycle	0.0004	0.0006	0.0009

Table 6.4. Crystallographic data for the 2:1 molecular complexes of chloranilic acid with 2,6-, and 3,4-lutidine

Compound formula	$C_{20}H_{20}Cl_2N_2O_4$	$C_{20}H_{20}Cl_2N_2O_4$
Isomer	2,6-lutidine 2:1	3,4-lutidine 2:1
M_r	423.28	423.28
Space group	$P2_1/c$	$P2_1/n$
Crystal system	Monoclinic	Monoclinic
a/ Å	7.1427(3)	7.0429(2)
b/ Å	9.3025(4)	9.3113(2)
c/Å	14.7753(6)	14.6210(3)
α/deg	90.00	90.00
β/deg	94.526(2)	90.303(1)
γ/deg	90.00	90.00
V/Å^{-3}	978.28(2)	958.81(0)
Z	2	2
D_{calc}/g cm^{-3}	1.44	1.47
F(000)	440	440
Radiation	Mo Kα	Mo Kα
λ/Å	0.71073	0.71073
μ(Mo-K_a)/mm^{-1}	0.361	0.369
Crystal size/mm	0.15x0.21x0.35	0.18x0.26x0.36
θ range/deg	2.6-53.4	2.6-53.9
Max sin(θ)/ λ	1.1	1.1
No. of data used for merging	168711	312677
No. of unique data	11814	11674
hkl range	$-16 \leq h \leq 16$	$-15 \leq h \leq 15$
	$0 \leq k \leq 20$	$0 \leq k \leq 20$
	$0 \leq l \leq 33$	$0 \leq l \leq 33$
R_{int}	0.0470	0.0231
R_σ	0.0466	0.0254
Spherical atom refinement		
No. of data in refinement	11814	11674
No. of refined parameters	167	167
Final *R* [$I > 2\sigma(I)$]	0.035	0.033
R_w^2 [$I > 2\sigma(I)$]	0.094	0.103
Goodness of fit *S*	1.017	
Extrema in residual map/eÅ^{-3}	-0.300→0.690	-0.874→0.739
Max shift/esd in last cycle	0.003	0.002
Multipole refinement		
No. of data in refinement	9143	10232
No. of refined parameters	378	379
Final *R* [$I > 3\sigma(I)$]	0.0280	0.0240
R_w [$I > 3\sigma(I)$]	0.0263	0.0335
Goodness of fit *S*	1.1554	2.0459
Extrema in residual map/ eÅ^{-3} (all data)	-0.242→0.367	-0.666→0.471
Max shift/esd in last cycle	0.0009	0.0002

Table 6.5. Crystallographic data for the 1:1 molecular complexes of chloranilic acid with 2,4-, 2,5-, and 2,6-lutidine and the 2 :1 molecular complex with 2,6-lutidine determined using neutron diffraction.

Compound formula	$C_{13}H_{11}Cl_2NO_4$	$C_{13}H_{11}Cl_2NO_4$	$C_{13}H_{11}Cl_2NO_4$	$C_{20}H_{20}Cl_2N_2O_4$
Isomer	2,4-lutidine 1:1	2,5-lutidine1:1	2,6-lutidine1:1	2,6-lutidine2:1
M_r	316.13	316.1	316.1	423.28
Space group	$P\bar{1}$	$P2_1/c$	$P\bar{1}$	$P2_1/c$
Crystal system	Triclinic	Monoclinic	Triclinic	Monoclinic
a/ Å	5.0687(2)	7.7415(2)	9.0071(3)	7.1427(3)
b/ Å	11.2561(4)	11.0538(3)	9.0326(3)	9.3025(4)
c/Å	11.6281(3)	15.4495(3)	9.0768(3)	14.7753(6)
α/deg	96.274(2)	90.00	93.526(2)	90.00
β/deg	91.960(2)	95.514(1)	104.359(2)	94.526(2)
γ/deg	90.609(1)	90.00	110.821(2)	90.00
V/Å^{-3}	659.00(2)	1315.94(1)	659.48(8)	978.28(2)
Z	2	4	2	2
D_{calc}/g cm^{-3}	1.59	1.60	1.59	1.44
Radiation	Neutrons	Neutrons	Neutrons	Neutrons
λ/Å	0.94840	0.94840	0.94840	0.94840
μ(Mo-K_a)/mm^{-1}	0.142	0.142	0.142	0.166
Crystal size/mm	1.8x2x5	1.9x1.9x6	2x2x7	2.1x2.1x6
θ range/deg	3.2-62.1	3.0-61.7	3.1-61.7	3.5-61.9
Max sin(θ)/ λ	0.93	0.92	0.92	0.93
No. of data used for merging	20076	34129	19566	18005
No. of unique data	7503	7915	7399	5216
hkl range	-8≤ *h* ≤ 8	-12≤ *h* ≤12	-16≤ *h* ≤15	-12≤ *h* ≤11
	-20≤ *k* ≤20	0≤ *k* ≤20	-16≤ *k* ≤16	0≤ *k* ≤17
	0≤ *l* ≤21	0≤ *l* ≤28	0≤ *l* ≤16	0≤ *l* ≤27
R_{int}	0.0422	0.0484	0.0294	0.0666
R_σ	0.0529	0.0584	0.0486	0.1004
Spherical atom refinement				
No. of data in refinement	7503	7915	7399	5216
No. of refined parameters	281	309	309	218
Final *R* [$I > 2\sigma(I)$]	0.031	0.038	0.034	0.089
R_w [$I > 2\sigma(I)$]	0.091	0.089	0.080	0.223
Goodness of fit *S*	1.127	0.091	1.118	0.990
Extrema in residual map/ fmÅ^{-3}	-1.255→1.15	-1.039→0.775	-0.965→0.976	-2.213→4.152
Max shift/esd in last cycle	0.001	0.000	0.001	0.000

Table 6.6. Crystallographic data for the hydrate molecular complexes of chloranilic acid with 2,4- and 3,5-lutidine 1:2

Compound formula	$C_{20}H_{28}Cl_2N_2O_8$	$C_{20}H_{26}Cl_2N_2O_7$
Isomer	2:1 2,4-lutidine dihydrate	2:1 3,5-lutidine trihydrate
M_r	495.34	477.33
Space group	$P\bar{1}$	$P2_1/n$
Crystal system	Triclinic	Monoclinic
a/ Å	7.9413(3)	10.6104(4)
b/ Å	8.9010(4)	17.7659(7)
c/Å	9.0838(3)	12.3211(5)
α/deg	71.310(2)	90
β/deg	70.3580(10)	108.6810(10)
γ/deg	76.061(2)	90
V/Å^{-3}	566.42(4)	2200.21(15)
Z	1	4
D_{calc}/g cm^{-3}	1.452	1.441
F(000)	332	1000
Radiation	Mo Kα	Mo Kα
λ/Å	0.71073	0.71073
μ(Mo-K_a)/mm^{-1}	0.336	0.340
Crystal size/mm	0.20x0.22x0.31	0.19x0.24x0.29
θ range/deg	2.4-51.3	2.1-50.4
Max sin(θ)/ λ	1.09	1.08
No. of data used for merging	241193	426309
No. of unique data	12074	23249
hkl range	$-15 \leq h \leq 17$	$-22 \leq h \leq 21$
	$-17 \leq k \leq 19$	$0 \leq k \leq 38$
	$0 \leq l \leq 19$	$0 \leq l \leq 26$
R_{int}	0.0260	0.0279
R_σ	0.0272	0.0296
Spherical atom refinement		
No. of data in refinement	12074	23249
No. of refined parameters	201	384
Final *R* [$I > 2\sigma(I)$]	0.029	0.033
R_w^2 [$I > 2\sigma(I)$]	0.088	0.096
Goodness of fit *S*	1.026	1.048
Extrema in residual map/ eÅ^{-3}	-0.297→0.603	-0.582→0.602
Max shift/esd in last cycle	0.001	0.002

Table 6.7. Crystallographic data for the molecular complexes of chloranilic acid with 2,4-, 3,5- lutidine (other stoichiometries 2:3 and 4:5) and 2,6-di-tert-butyl-4-methylpyridine (1:1)

Compound formula	$C_{16}H_{11}Cl_3NO_6$	$C_{16}H_{12}Cl_3NO_6$	$C_{29}H_{23}Cl_5N_2O_{10}$	$C_{20}H_{25}Cl_2NO_4$
Isomer	2,4-lutidine 2:3	3,5-lutidine 2:3	3,5-lutidine 4:5	2,6-di-tert-butil-4-methylpyridine 1:1
M_r	419.60	420.62	736.74	414.31
Space group	$P\bar{1}$	$P2_1/c$	$P\bar{1}$	$P2_1/n$
Crystal system	Triclinic	Monoclinic	Triclinic	Monoclinic
a/ Å	8.0154(3)	18.330(5)	8.4477(3)	11.7516(11)
b/ Å	9.3997(3)	4.9542(1)	10.5046(3)	11.5488(12)
c/Å	11.8524(5)	19.8433(5)	18.2834(4)	15.4398(15)
α/deg	71.632(2)	90	99.0840(16)	90
β/deg	88.044(2)	110.869(1)	93.6611(17)	95.931(6)
γ/deg	86.436(2)	90	91.1015(12)	90
V/Å^{-3}	845.75(5)	1684.62(7)	1598.14(8)	2084.2(4)
Z	2	4	2	4
D_{calc}/g cm^{-3}	1.652	1.661	1.531	1.32
F(000)	426	856	752	872
Radiation	Mo Kα	Mo Kα	Mo Kα	Mo Kα
λ/Å	0.71073	0.71073	0.71073	0.71073
μ(Mo-K$_a$)/mm^{-1}	0.577	0.580	0.513	0.336
Crystal size/mm	0.20x0.22x0.31	0.17x0.22x0.27	0.27x0.21x0.17	0.18x0.21x0.32
θ range/deg	1.8-30.2	1.2-30.3	1.1-30.1	2.1-32.2
Max sin(θ)/ λ	0.70	0.70	0.70	0.74
No. of data used for merging	42591	9339	74680	140003
No. of unique data	4974	4950	9371	7363
hkl range	-11≤ *h* ≤11	-25≤ *h* ≤24	-11≤ *h* ≤11	-17≤ *h* ≤17
	-12≤ *k* ≤13	0≤ *k* ≤6	-14≤ *k* ≤14	0≤ *k* ≤17
	0≤ *l* ≤16	0≤ *l* ≤27	0≤ *l* ≤25	0≤ *l* ≤23
R_{int}	0.0438	0.0314	0.0468	0.079
R_σ	0.0380	0.0274	0.0570	0.0809
Spherical atom refinement				
No. of data in refinement	4974	4950	9371	7363
No. of refined parameters	279	283	507	340
Final *R* [*I* > 2σ(*I*)]	0.034	0.025	0.034	0.042
R_w [*I* > 2σ(*I*)]	0.080	0.081	0.081	0.093
Goodness of fit *S*	1.047	1.127	1.049	1.006
Extrema in residual map/ eÅ^{-3}	-0.508→0.627	-0.276→0.718	-0.235→0.397	-0.329→0.500
Max shift/esd in last cycle	0.000	0.001	0.001	0.001

6.2.3. Multipole Refinements

The XD[49] software package was used for performing the multipole refinements. The multipole expansion was truncated at the octupole level for C, N and O atoms. The hexadecapole level was allowed only for Cl atoms. Five different multipole refinements were performed for the molecular complexes for which neutron data were available. Where no neutron data were available, only three multipole refinements were carried out. In the first refinement (model 1) extensive constraints imposed by local mirror symmetry were applied to the atoms included in the lutidine and chloranilic acid rings for the 1:1 molecular complexes. For the atoms attached to the rings such as Cl, O, C (methyl group), free multipole refinements were allowed. Only the first monopole and last dipole were refined in this model for H atoms. These were used to estimate the H-atom adps by the method of Madsen using the SHADE[50] web interface. The calculated H-atom adps were used in subsequent refinements (model 2) as fixed parameters. In the final cycles (model 3) the multipole constraints were released. The same steps were taken with the inclusion of the adps for H atoms obtained from neutron diffraction result in models 4 and 5. The hydrogen atoms were placed at standard neutrons distances in all refinements, apart for the data for which neutron data were available. Multipole populations and κ parameters were grouped in all refinements according to the chemical similarity of the atoms.

6.2.4. Theoretical Calculations

Single point periodic calculations were performed using the DFT method at B3LYP[51]/6-31G** level of theory/basis set using the CRYSTAL09[52] software. The lattice energies for the 1:1 molecular complexes were estimated using the CLP[53] program.

6.3. Results and Discussion

The crystal structures of the 1:1 chloranilic acid and 2,4-, 2,5-, 2,6- and 3,4-lutidine molecular complexes have been discussed previously in the literature.[35] The structural details of the 2:1 2,3-, 2,4-, 2,5- and 2,6-lutidine molecular complexes and two hydrate forms of 3,4- and 3,5-lutidine have also been discussed previously.[43] A complete overview of the structural details and intermolecular interactions of all the crystal structures, which were determined in this work, will be described in this section.

The two common supramolecular units formed by chloranilic acid and lutidine in both 1:1 and 2:1 ratios are illustrated in Scheme 6.2. In the 1:1 molecular complexes, the chloranilic acid is only singly deprotonated (HCA^-), whereas in the 2:1 complexes, each chloranilic acid loses both protons (CA^{2-}). In both the 1:1 and 2:1 molecular complexes, the chloranilic acid and lutidine molecules are linked by N-H···O bifurcated hydrogen bonds

apart from the 2,3-lutitine 1:1 molecular complex where no bifurcated hydrogen bond is found. In the 1:1 complexes, there are additional O-H···O hydrogen bonds linking dimers of chloranilic acid molecules, forming LCCL units (L-lutidine, C- chloranilic acid) (Scheme 6.2 (a)). In the 2:1 complexes, only three molecules are present in the hydrogen bonded unit (LCL). The formation of dimers between the chloranilic acid molecules in the molecular complexes differs from the connectivity of pure chloranilic acid.[26]

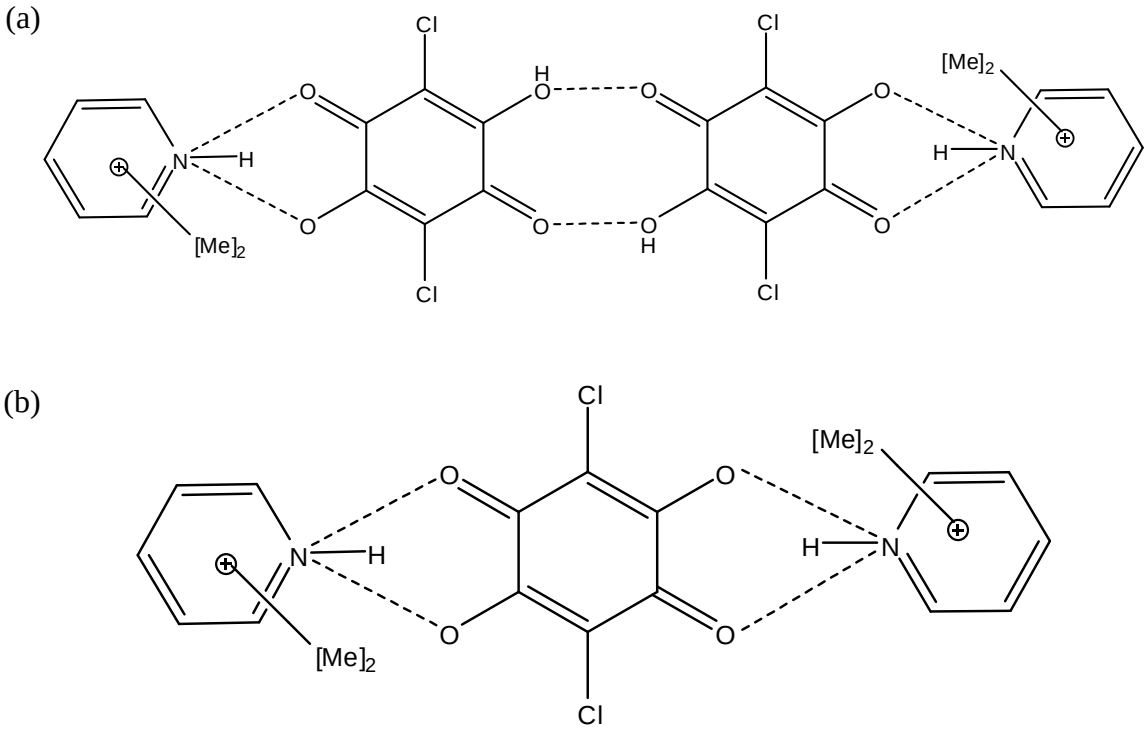

Scheme 6.2. The supramolecular synthon units formed by chloranilic acid and lutidine in (a) 1:1 (LCCL) and (b) 2:1 (LCL) molecular complexes.

6.3.1. A Comparison of the Molecular Geometry of H_2CA, HCA^- and CA^{2-}

The deprotonation of the chloranilic acid molecule leads to a charge delocalisation, thus a change in bond distances are expected for both singly and doubly deprotonated molecules. In order to investigate these changes, the bonds lengths of singly and doubly deprotonated chloranilic acid molecules will be compared with the neutral form[54] (Table 6.8). Most commonly, the effect of singly deprotonating the chloranilic acid molecule is a distribution of the negative charge along the O2-C112-C111-C116-O6 part of the molecule (Scheme 6.3. HCA^-).[29] For most doubly deprotonated chloranilic acid molecules, the negative

charge formed is distributed on both sides of the molecule[29] along O2-C112-C111-C116-O6 and O3-C113-C114-C115-O5 (Scheme 6.3. CA^{2-}).

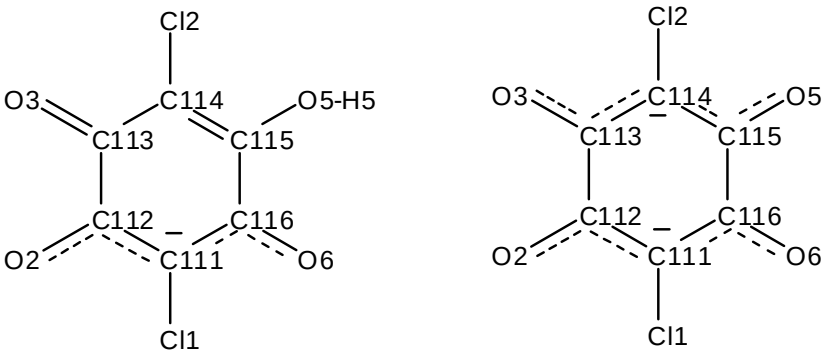

Scheme 6.3. Charge delocalization in the singly (left) and doubly (right) deprotonated chloranilic acid molecule.

If this delocalization occurs, an equalisation of the C111-C112 and C111-C116 bond lengths would be expected. An elongation of the double bond (C111-C112) and a shortening of the single bond (C111-C116) is observed to the extent where these two bond lengths are effectively the same in both the singly and doubly deprotonated chloranilic acid molecules compared to the neutral molecule. Due to the loss of both protons in the doubly deprotonated molecule (CA^{2-}), this effect is symmetrical on both sides of the molecule; the bonds C114-C113 and C114-C115 retain their single and double bond character, respectively, in the singly deprotonated form (HCA^{-}). On deprotonation, the C112-O2 and C113-O3 bonds becomes more equalized (the double bond becomes longer and the single bond shorter) and significantly shorter compared to C115-O5 bond of the singly deprotonated molecule which is still protonated. The charge accumulation around the C111 and C114 atoms is also reflected in the elongation of the C-Cl bonds for partially and fully deprotonated chloranilic acid molecules (Tables 6.9 and 6.10).

Table 6.8. Bond lengths for the neutral chloranilic acid molecule.[53]

Chloranilic acid	
Cl1-C111	1.717
C111-C112	1.349
C112-C113	1.508
C113-C114	1.450
C112-O2	1.322
C113-O3	1.224
O5-H5	0.819

Table 6.9. Bond lengths for the singly deprotonated chloranilic acid molecule in the 1:1 molecular complexes with the lutidines

1:1	2,3-lutidine	2,4-lutidine	2,5-Lutidine	2,6-lutidine	3,4-lutidine	3,5-lutidine
Cl1-C111	1.7393(18)	1.7293(3)	1.7331(3)	1.7318(3)	1.7336(4)	1.7337(5)
Cl2-C114	1.7259(18)	1.7275(3)	1.7243(3)	1.7210(3)	1.7269(4)	1.7255(5)
C111-C112	1.399(2)	1.3978(4)	1.4094(5)	1.4005(4)	1.3956(6)	1.4066(6)
C112-C113	1.545(2)	1.5448(4)	1.5506(5)	1.5466(4)	1.5664(6)	1.5473(6)
C113-C114	1.460(2)	1.4559(4)	1.4513(5)	1.4554(4)	1.4517(6)	1.4531(6)
C114-C115	1.353(2)	1.3586(4)	1.3594(5)	1.3568(5)	1.3522(6)	1.3587(6)
C115-C116	1.516(2)	1.5155(4)	1.5152(5)	1.5143(5)	1.5194(6)	1.5170(6)
C116-C111	1.413(2)	1.4127(4)	1.4053(5)	1.4157(4)	1.4136(6)	1.4081(6)
C112-O2	1.246(2)	1.2554(3)	1.2444(5)	1.2546(4)	1.2485(5)	1.2484(5)
C113-O3	1.216(2)	1.2250(4)	1.2289(5)	1.2236(4)	1.2254(5)	1.2254(5)
C115-O5	1.328(2)	1.3238(4)	1.3243(4)	1.3252(4)	1.3247(5)	1.3244(5)
C116-O6	1.246(2)	1.2460(4)	1.2533(4)	1.2481(4)	1.2502(5)	1.2503(5)
O5-H5	0.79(3)	0.910(12)	0.815(14)	0.884(12)	0.870(13)	0.888(14)

Table 6.10. Bond lengths for the doubly deprotonated chloranilic acid molecule in the 1:2 molecular complexes with the lutidines

2:1	2,3-lutidine	2,4-lutidine	2,5-lutidine	2,6-lutidine	3,4-lutidine
Cl1-C111	1.7444(3)	1.7381(4)	1.7430(3)	1.7374(3)	1.7378(3)
C111-C112	1.3954(4)	1.3947(5)	1.3966(4)	1.3987(5)	1.4050(4)
C112-C113	1.5458(4)	1.5427(5)	1.5473(4)	1.5443(5)	1.5468(4)
C112-O2	1.2595(4)	1.2588(5)	1.2613(4)	1.2586(5)	1.2506(4)
C113-O3	1.2389(3)	1.2411(5)	1.2423(4)	1.2428(4)	1.2494(4)

6.3.2 The Supramolecular Units

6.3.2.1. 1:1 Molecular Complexes

All of the 1:1 molecular complexes presented here exhibit the singly deprotonated chloranilic acid molecule and the hydrogen bonded LCCL unit (Figure 6.5 and 6.6). The labelling scheme used in this work is shown in Figures 6.5 and 6.6. Within this series of molecular complexes, the lutidine ring is almost coplanar with the chloranilic acid ring in the case of 2,3-, 2,5- and 3,5-lutidines whereas for the 2,4-, 2,6- and 3,4-lutidines, the rings are twisted relative to one another. A summary of the relative planarity of the lutidine and chloranilic acid rings is given in Table 6.11. Approximately planar geometries were considered to be where the angles between the molecular planes of the lutidine and chloranilic acid were smaller than 15º. The molecular complexes with an angle between the planes larger than 45º were considered to adopt a twisted position of the molecular geometries. In general, when the two lutidine and chloranilic acid rings lies approximately coplanar to each other, a symmetrical bifurcated hydrogen bond is formed (2,5- and 3,5-lutidine); when the lutidine ring is twisted with respect to the chloranilic acid molecule, an asymmetric bifurcated hydrogen bond is found (2,4-, 2,6- and 3,4-lutidine). For instance

the intermolecular bond distances for 2,5-lutidine N125···O2 and N125···O3 are 2.9203(5)Å and 2.94701(9)Å, respectively. In the case of twisted molecules such as 2,4-lutidine, the N125···O2 and N123···O3 intermolecular hydrogen bond distances are 2.6962(4)Å and 3.1956(4)Å, respectively. Besides the strong intermolecular interactions, there are some important C-H···O and C-H···Cl weak hydrogen bonds which may contribute to the planarity of the lutidine ring with respect to the chloranilic acid molecule.

Table 6.11. Summary of the twisted or coplanar nature of the chloranilic acid and lutidine rings in the supramolecular units formed in the 1:1 and 2:1 lutidine chloranilic acid molecular complexes.

Form	1:1(˚)		2:1(˚)	
2,3-lutidine	10.04(7)	Planar	77.97(2)	Twisted
2,4-lutidine	58.05(1)	Twisted	1.60(6)	Planar
2,5-lutidine	13.66(2)	Planar	88.27(2)	Twisted
2,6-lutidine	77.91(1)	Twisted	70.38(2)	Twisted
3,4-lutidine	87.24(1)	Twisted	2.77(3)	Planar
3,5-lutidine	33.21(2)	Planar		

The 2,3-lutidine 1:1 molecular complex represents an anomaly. Whilst the LCCL unit is still formed, it does not show a bifurcated hydrogen bond involving the protonated N atom of the pyridine ring. Instead, additional C-H(methyl)···O (C···O distance, 3.224(3) Å) and C-H···Cl (C···Cl distance, 3.865(2)Å) weak hydrogen bonds are formed and these may have an influence on the consequent coplanar rings of the lutidine and chloranilic acid molecules. In a twisted case such as 2,4-lutidine chloranilic acid, the same C-H(methyl)···O weak hydrogen bond interaction is longer and therefore weaker (C···O distance, 3.3421(4) Å). The 2,5- and 3,5-lutidine complexes (coplanar rings) show also shorter C-H(methyl)···O or C-H···O intermolecular hydrogen bonds. An exception is found in the 3,4-lutidine case, where despite the formation of a relatively short C-H···O intermolecular hydrogen bond (C···O distance, 3.240(7) Å) which issimilar in length to those found where the LCCL unit is approximately planar, only one such hydrogen bond is formed rather than two and the LCCL unit is twisted. In the other cases two C-H···O weak hydrogen bonds are typically formed between the lutidine chloranilic acid molecules in the LCCL and LCL units. The twisted position of the 2,6-lutidine rings relative to the chloranilic acid molecule, with relatively short C-H···O weak hydrogen bonds (3.1947(5)Å), may be a consequence of the steric repulsion between the methyl groups and the O atoms of chloranilic acid.

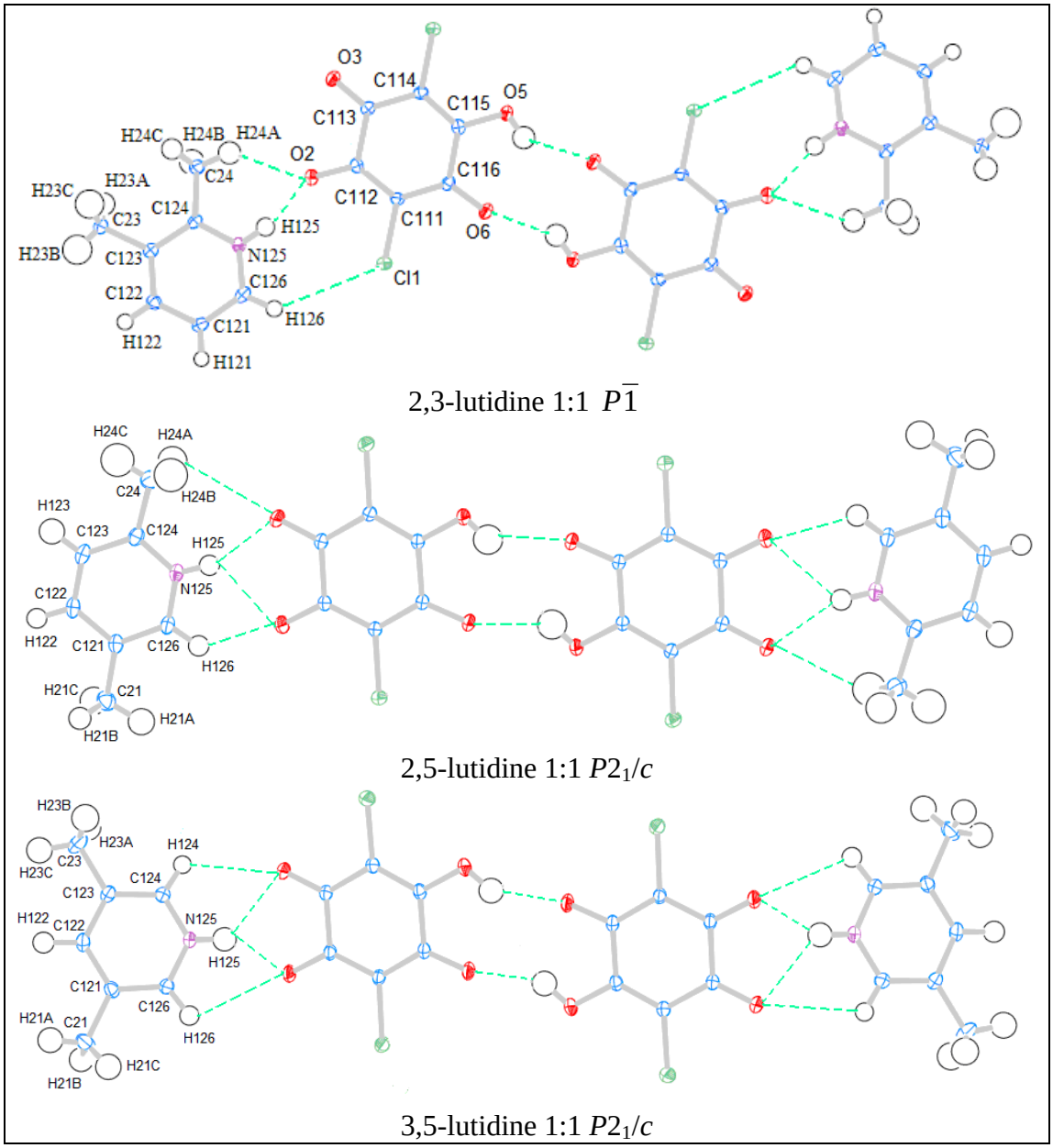

Figure 6.5. Ortep plots of the 1:1 chloranilic acid 2,3-, 2,5- and 3,5-lutidine molecular complexes showing their connection through intermolecular hydrogen bonds and the co-planar position of the lutidine ring relative to the chloranilic acid molecules. Ellipsoids are shown at the 50% probability level.

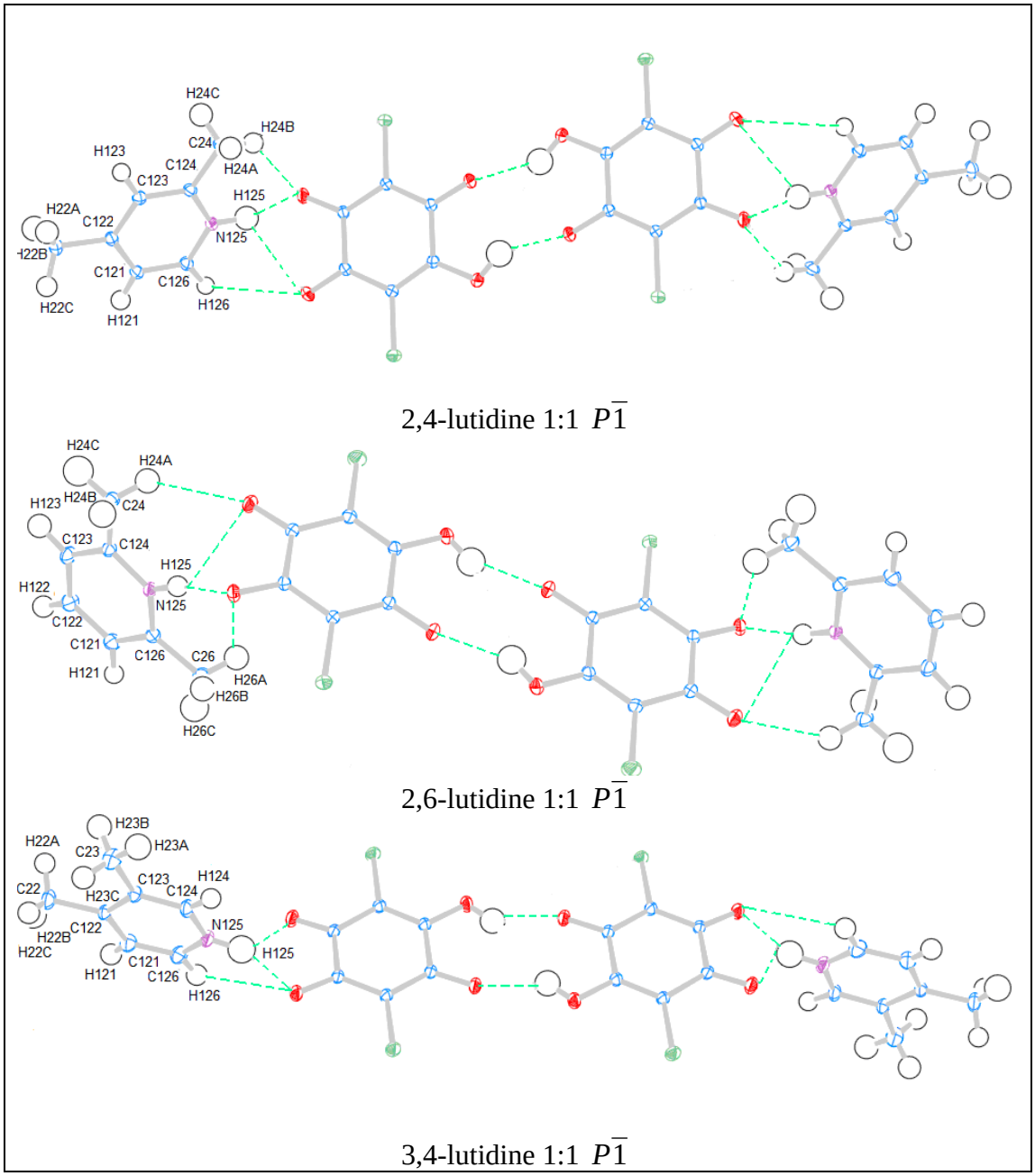

Figure 6.6. Ortep plots of the 1:1 chloranilic acid 2,4-, 2,6- and 3.4-lutidine molecular complexes showing their connection through intermolecular hydrogen bonds and the twisted position of the lutidine ring relative to the chloranilic acid molecules. Ellipsoids are shown at the 50% probability level.

6.3.2.2 2:1 Molecular Complexes

In the case of the 2:1 molecular complexes, the lutidine ring lies in the same plane as the chloranilic acid for the 2,4- and 3,4-lutidines whereas for 2,3-, 2,5- and 2,6-lutidine the rings are twisted.

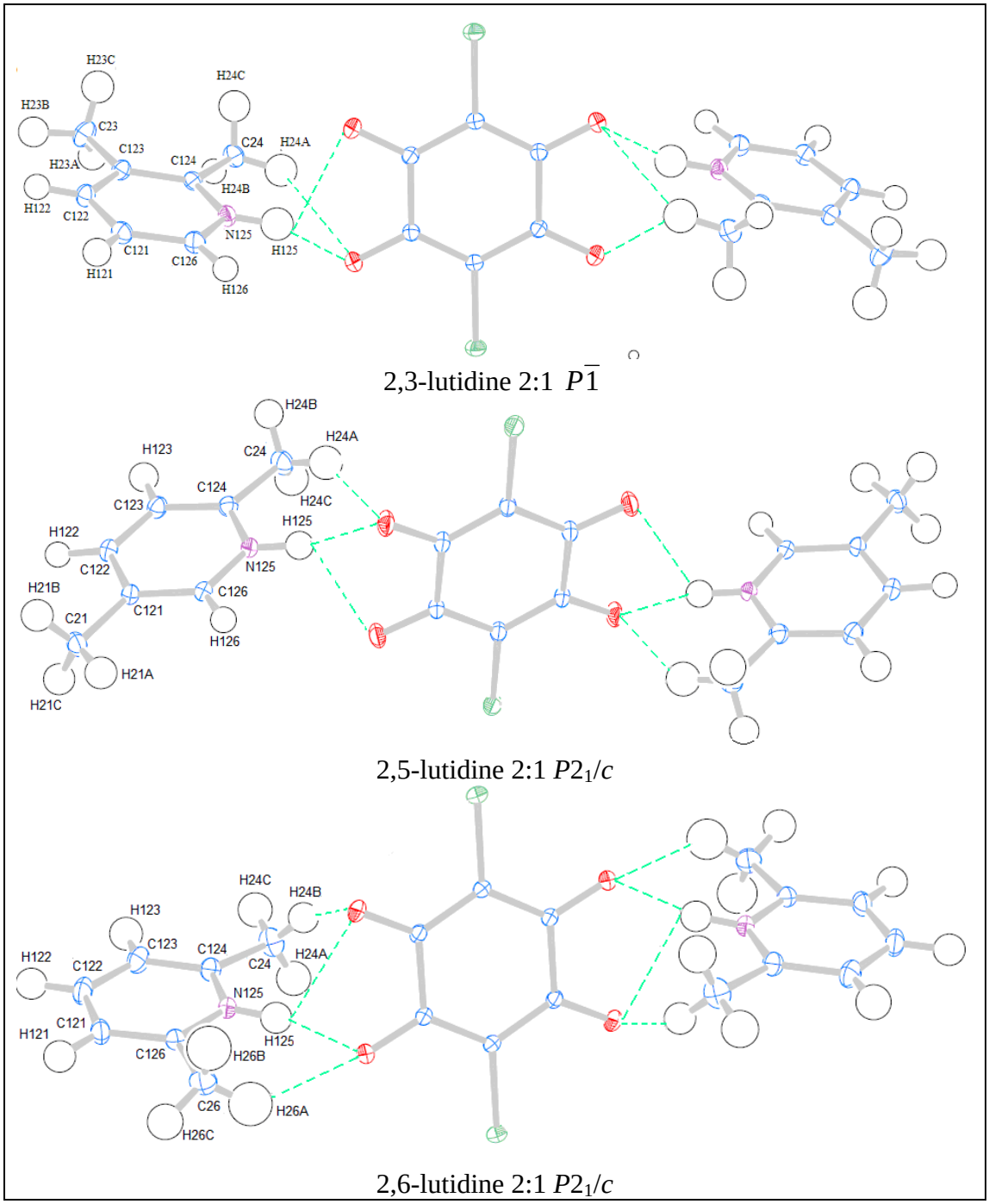

Figure 6.7. Ortep plots of the 1:2 chloranilic acid 2,3-, 2,5- and 2,6-lutidine molecular complexes showing their connection through intermolecular hydrogen bonds and the twisted position of the lutidine ring relative to the chloranilic acid molecule.. The ellipsoids are shown at the 50% probability level

The 3,4-lutidine chloranilic acid molecular complex (coplanar rings) forms symmetrical bifurcated hydrogen bonds as was also observed in case of 1:1 molecular complexes containing coplanar rings. An exception to this was found in the 2,4-lutidine molecular complex for which the NH group points almost directly at a single oxygen atom and a very asymmetric bifurcated hydrogen bond is formed. The C-H(methyl)···O and C-H···O

hydrogen bond interactions are shorter when the lutidine lies coplanar to the chloranilic acid ring in all cases. A summary of the twisted or coplanar rings formed in the 2:1 molar complexes is given in Table 6.11.

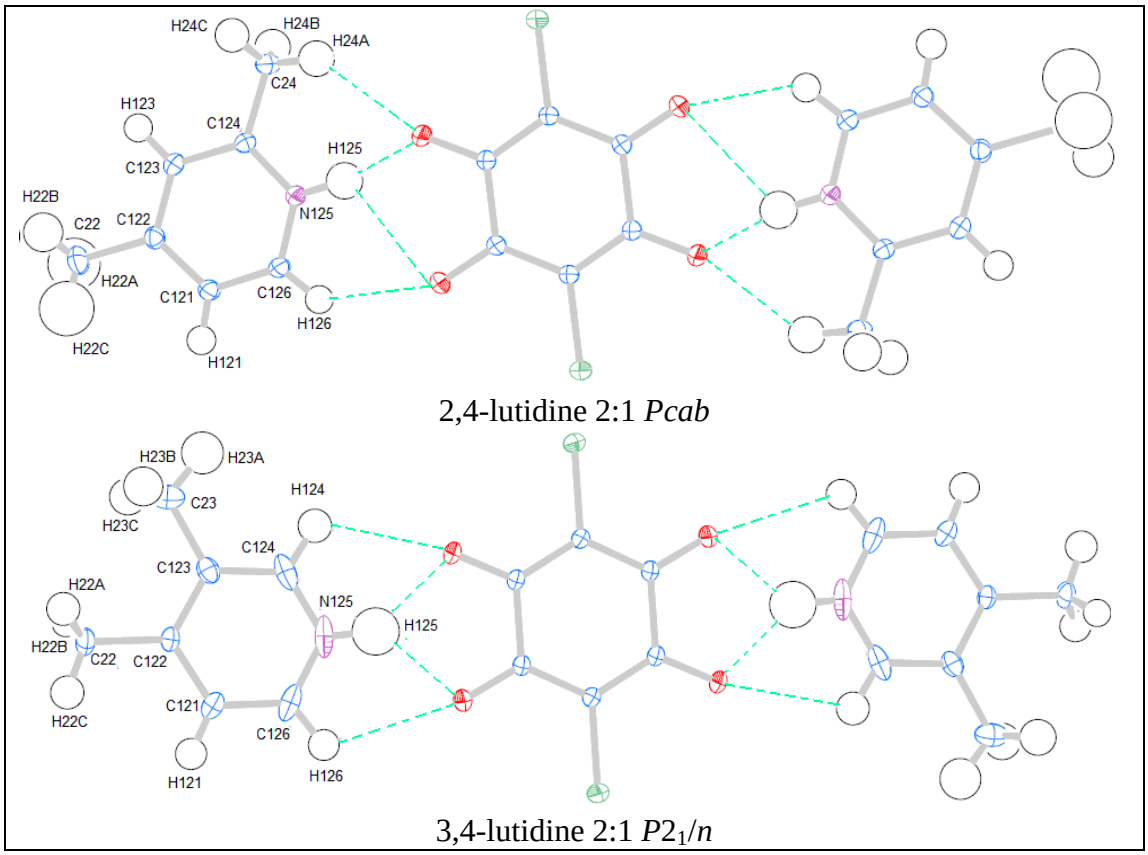

Figure 6.8. Ortep plots of the 1:2 chloranilic acid 2,4- and 3,5-lutidine molecular complexes showing their connection through intermolecular hydrogen bonds and the co-planar position of the lutidine ring relative to the chloranilic acid molecule. The ellipsoids are shown at the 50% probability level

6.3.2.3 Steric Effects on the Supramolecular Units

Steric effects clearly have a significant influence on the relative planarity of the LCCL or LCL units (i.e. the twisting of the lutidine rings relative to the chloranilic acid molecules) in both the 1:1 and 2:1 molecular complexes of 2,6-lutidine with chloranilic acid. To introduce further steric side groups in the 2- and 6- positions, chloranilic acid was co-crystallised with 2,6-di-tert-butyl-4-methylpyridine (Figure 6.9). The presence of tert-butyl groups in the 2- and 6- positions should introduce further steric repulsion with the oxygen atoms of chloranilic acid and a significantly twisted arrangement for the LCCL unit would be expected. An angle of 87.52(5)° is found between the 2,6-di-tert-butyl-4-methylpyridine

pyridine ring and chloranilic acid planes. The 2,6-lutidine molecule is twisted by 77.91(1)º relative to the chloranilic acid molecule. The increase in the degree twist of 2,6-di-tert-butyl-4-methylpyridine molecule relative to the chloranilic acid by approximately 10º can be attributed to the elongation of the of the bifurcated hydrogen. These bonds are significantly longer in this interaction compared with the 2,6-lutidine molecular complex.

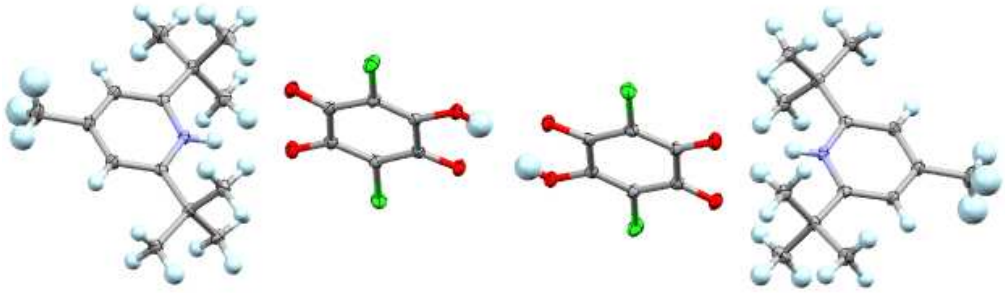

Figure 6.9. 1:1 2,6-tert-butyl-4methyl-pyridine chloranilic acid molecular complex showing the twisted arrangement of the rings of the LCCL synthon units formed.

The elongation of the bifurcated N-H···O bond (N···O distances, 3.0447(15)Å, 3.7696(15)Å) compared with the lutidine systems (N···O distances 2.6-2.7Å) is induced by the presence of the tert-butyl groups. The twisting of the 2,6-tert-butyl-4methyl-pyridine ring relative to the chloranilic acid molecules allows the two oxygen atoms (O2 and O3) of the chloranilic acid molecule to form weak hydrogen bonds with the methyl groups of the tert-butyl groups located in both the 2- and 6- positions. The O2 atom accepts three C-H(methyl)···O weak hydrogen bonds, two with H atoms of two different methyl groups in the 6- position and one with of a methyl group located in the 2 position. The O3 atom accepts only two C-H(methyl)···O weak hydrogen bonds with two different methyl groups one in the 2- position and one in the 6- position.

6.3.2.4. Comparison of the LCL and LCCL units

In terms of the same methyl substituent positions of the lutidines, there is no agreement between the 1:1 and 2:1 molecular complexes regarding the relative orientations of the lutidine relative to the chloranilic acid ring; in fact the only complexes where the twisting is consistent between the two stoichiometries is where two bulky side groups are present next to the NH group in 2,6-lutidine. Neither is there an increased likelihood for planarity of the LCL units over the LCCL units or vice versa.

The relative orientations of the two chloranilic acid molecules within the LCCL units show also slight deviations from co-planarity in some of the molecular complexes such as 2,3-lutidine (1.61(3)) or 3,4-lutidine (2.35(2). A summary of the angles formed between the planes of the chloranilic acid molecules are listed in Table 6.12. These deviations from co-planarity of the chloranilic acid molecules shows no particular trend with the nature of the bifurcated hydrogen bond (symmetrical or asymmetrical) or with the position of the lutidine ring relative to the chloranilic acid molecules. The relative geometries of the rings are therefore significantly influenced by other weak interactions with the surrounding units.

Table 6.12. The angles formed between the planes of the chloranilic acid molecules in the LCCL unit.

	Angle (º)
2,3-lutidine	1.61(13)
2,4-lutidine	0.74(5)
2,5-lutidine	0.25(7)
2,6-lutidine	1.45(2)
3,4-lutidine	2.35(2)
3,5-lutidine	1.17(6)

In the 1:1 and 2:1 molecular complexes of 2,3-lutidine and chloranilic acid, the 2:1 structure contains two lutidine molecules above and below the chloranilic acid molecule orientated with the methyl groups in the chloranilic acid molecule direction (Figure 6.10 (a)). Therefore weak hydrogen bonds form between the π bonds in the chloranilic acid molecule and the methyl groups of the lutidine keeping the chloranilic acid in a twisted position relative to the lutidine rings. For the 1:1 stoichiometry no such hydrogen bonds are present, the chloranilic acid molecules are surrounded by other chloranilic acid molecules from adjacent LCCL layers forming π··π interactions (Figure 6.10 (b)). In addition, the 1:1 molecular complex contains no bifurcated hydrogen bond in the LCCL synthon unit creating, in this particular case, a different packing arrangement compared with the 2:1 stoichiometry molecular complex.

(a)

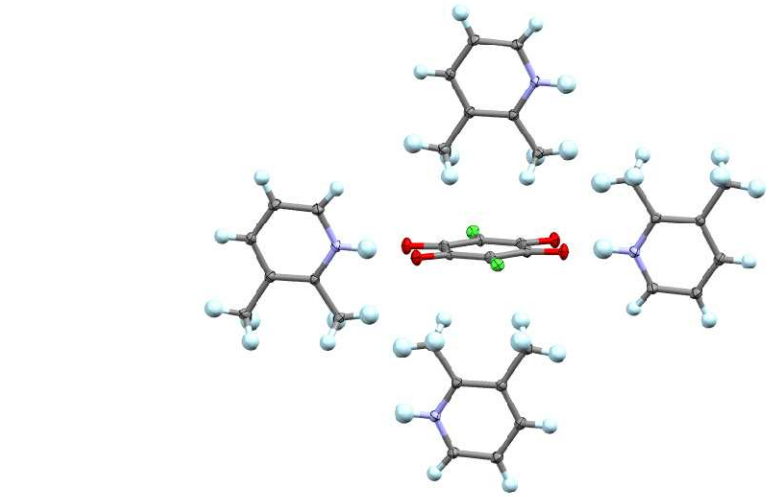

(b)

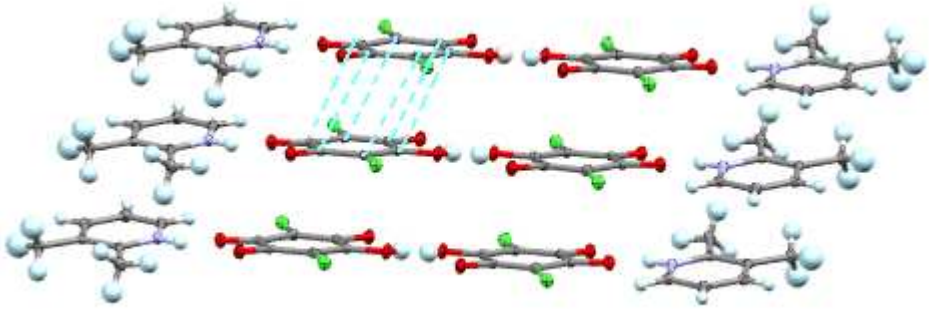

Figure 6.10. (a) The weak C-H··π hydrogen bonds between the methyl groups of the lutidine molecules and the chloranilic acid ring creating a twisted motif in the 2:1 molecular complex of 2,3-lutidine with chloranilic acid. (b) The π··π interactions formed between the chloranilic acid molecules within LCCL layers in the 1:1 molecular complex of 2,3-lutidine with chloranilic acid.

Contrary to the 2,3-lutidine molecular complexes, in the 2,4-lutidine chloranilic acid complexes, the rings lie twisted in the 1:1 stoichiometry and co-planar in the 2:1. An illustration of the degree of twisting in the 2,4-lutidine and chloranilic acid molecular planes (1:1) in comparison to co-planar planes of the 2:1 stoichiometry is shown in Figure 6.11.

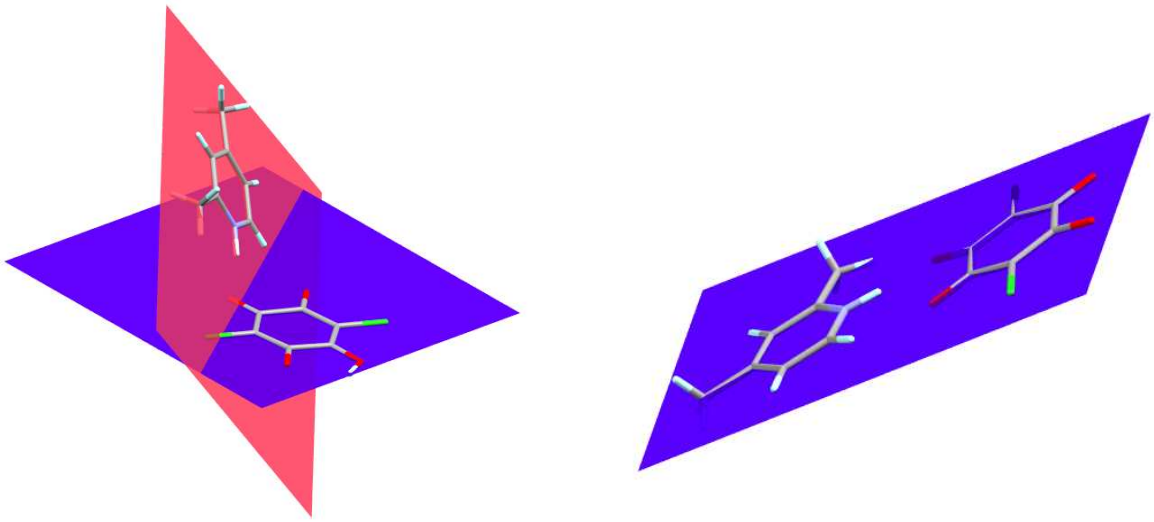

(a) (b)

Figure 6.11. The planes of the rings of 2,4-lutidine with chloranilic acid: (a) 1:1 ratio - the rings lying in different planes; (b) 2:1 ratio – the rings ling in the same plane.

The twisting of the lutidine ring relative to the chloranilic acid ring in the 1:1 case can be attributed to the weak C-H(methyl)···O, C-H···O, ad C-H(methyl)···Cl hydrogen bonds formed in the region of the methyl groups. In the 2:1 complex, the lutidine molecule is surrounded by five others molecules with which it forms weak hydrogen bonds and a co-planar position of the lutidine molecule relative to the chloranilic acid ring is formed.

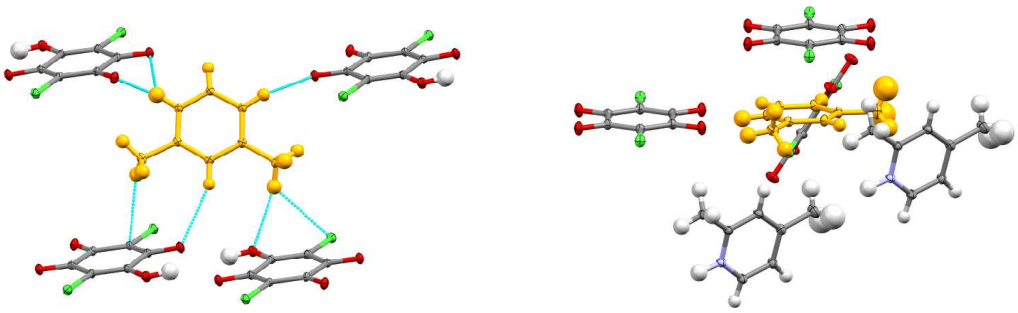

(a) (b)

Figure 6.12. The neighboring molecules showing the influence on the position of the 2,4-lutidine molecule relative to the chloranilic acid through weak hydrogen bonds (a) 1:1, (b) 2:1. The lutidine molecule is shown in yellow.

For the 2,5-lutidine complexes show a similar behaviour of the lutidine ring relative to the chloranilic acid ring as that seen in the 2,3-lutidine in the two different stoichiometries. In the 1:1 stoichiometry, a co-planar relative orientation can be observed and a twisted

orientation for the 2:1. The LCCL synthon units are held together in the 1:1 molecular complex by the π···π stacking interactions formed between the two lutidine - chloranilic acid molecules or two chloranilic acid molecules. For the 2:1 stoichiometry, the lutidine molecule has on one side of the ring two other lutidine molecules with which weak C-H···N and C-H···π hydrogen bonds are formed and on the other side another lutidine ring with which π···π stacking interactions are formed. These interactions hold the lutidine molecule in a twisted position relative to the chloranilic acid molecule.

The 3,4-lutidine chloranilic acid molecular complexes show similarity to the 2,4-lutidine complexes in relation to the position of the lutidine and chloranilic acid rings in the two different stoichiometries studied. The 2:1 structure contains two C-H···O weak hydrogen bonds within the LCL unit resulting in an almost co-planar unit, whereas in the 1:1 LCCL unit, only one C-H···O weak hydrogen is present and the unit is twisted. Moreover, the significantly asymmetric nature of the bifurcated hydrogen bond in the 1:1 LCCL unit facilitates an additional C-H···O weak hydrogen bond between the chloranilic acid and another lutidine molecule (Figure 6.6). The large libration at the C124 N125 C126 atoms in the plane of the ring is evidenced in the elongated shape of the thermal ellipsoids (Figure 6.8) and may perhaps also have an influence on or be a consequence of the co-planar rings in 2:1 molecular complex. A larger thermal motion can also be seen for the H125 atom (Figure 6.8) within the bifurcated hydrogen bond; this is likely to reflect the shared nature of this hydrogen atom within the symmetrical bifurcated hydrogen bond formed in this case.

The details of the hydrogen bond distances between the lutidine and chloranilic acid molecules taken from spherical refinement of the X-ray data are listed in Tables 6.13. and 6.14. The N-H···O hydrogen bond distances are, in general, shorter for the 2:1 molecular complexes compared to the 1:1 molecular complexes. This may be a consequence of the fact that in the doubly deprotonated chloranilic acid molecule there is delocalisation of the 2- charge over all four oxygen atoms, whereas in the singly deprotonated chloranilic acid, there is only a delocalisation of 1- across one side of the molecule; the charge-assisted hydrogen bonds involving CA^{2-} might therefore be expected to be stronger than those involving HCA^{-} molecules. The type of N-H···O hydrogen bond interaction formed between lutidine and chloranilic acid in all these complexes can be classified as positive negative charge assisted hydrogen bonds (+/-)CAHB N^{+}-H···O and resonance assisted hydrogen bonds RAHB N-H···O=.[55] RAHB lengths have been shown to be normally longer than CAHB. Therefore, in a doubly CAHB an increased strength of the bifurcated hydrogen interaction would be expected and shorter N-H···O hydrogen bonds are formed.

Table 6.13. The intermolecular hydrogen bonds in the supramolecular synthon units of the 1:1 chloranilic acid – lutidine molecular complexes from X-ray data (the results from neutron data are presented in Section 6.2)

D-H···A	D-H/Å	H···A/ Å	D···A/ Å	D-H···A/ º
2,3-lutidine (1:1)				
N125-H125···O2	0.89(2)	1.85(2)	2.664(2)	163(2)
C24-H24A···O2	0.969(3)	2.42(3)	3.224(2)	140(2)
C126-H126···Cl1	0.9300	3.1630	3.866(2)	133.85
2,4-lutidine(1:1)				
N125-H125···O2	0.990(11)	1.720(10)	2.6962(4)	168.0(10)
N125-H125···O3	0.991(11)	2.604(11)	3.1956(4)	118.3(8)
C24-H24A···O2	0.975(9)	2.552(9)	3.3421(4)	138.2(7)
C126-H126···O3	0.948(9)	2.820(9)	3.3341(4)	115.1(6)
2,5-lutidine (1:1)				
N125-H125···O2	0.843(10)	2.329(9)	2.9203(5)	127.5(8)
N125-H125···O3	0.843(10)	2.156(9)	2.9463(5)	156.1(9)
C24-H24A···O3	0.955(15)	2.840(16)	3.2646(6)	108.0(11)
C126-H126···O2	0.937(10)	2.281(10)	2.9098(6)	124.0(8)
2,6-lutidine(1:1)				
N125-H125···O2	0.905(10)	1.767(10)	2.6623(4)	169.7(9)
N125-H125···O3	0.905(9)	2.617(10)	3.0998(4)	114.2(7)
C24-H24A···O3	0.959(11)	2.549(11)	3.3202(5)	137.5(9)
C26-H26B···O2	0.944(11)	2.792(11)	3.1947(5)	106.7(8)
3,4-lutidine (1:1)				
N125-H125···O2	0.938(14)	1.833(14)	2.7260(7)	158.2(13)
N125-H125···O3	0.938(14)	2.430(15)	2.9237(7)	112.8(11)
C126-H126···O3	0.931(11)	2.953(11)	3.2401(7)	99.5(7)
3,5-lutidine (1:1)				
N125-H125···O2	0.889(14)	1.874(14)	2.6814(5)	150.2(13)
N125-H125···O3	0.889(14)	2.360(14)	2.9840(6)	127.3(11)
C126-H126···O2	0.939(12)	2.786(12)	3.1574(6)	104.7(8)
C124-H124···O3	0.948(11)	2.690(10)	3.1709(6)	112.1(8)

Table 6.14. The intermolecular hydrogen bonds in the supramolecular synthon units of 2:1 chloranilic acid – lutidine molecular complexes from X-ray data (the results from neutron data are presented in Section 6.2)

D-H···A	D-H/Å	H···A/ Å	D···A/ Å	D-H···A/ º
2,3-lutidine (2:1)				
N125-H125···O2	0.981(13)	2.350(14)	2.9316(5)	117.2(10)
N125-H125···O3	0.981(13)	1.706(12)	2.6556(4)	162.0(13)
C24-H24A···O2	0.948(12)	2.745(12)	3.5003(5)	134.5(9)
C24-H24A···O3	0.948(12)	2.7355(124)	3.2734(5)	115.2(9)
2,4-lutidine(2:1)				
N125-H125···O2	0.969(16)	1.69(2)	2.6470(5)	167.5(2)
N125-H125···O3	0.969(16)	2.570(16)	3.1398(6)	117.7(13)
C24-H24A···O2	0.974(16)	2.41(2)	3.2022(6)	138.0(14)
C126-H126···O3	0.940(14)	2.317(14)	3.0410(6)	133.4(11)
2,5-lutidine (2:1)				
N125-H125···O2	0.951(10)	1.7515(10)	2.6526(4)	168.0(8)
N125-H125···O3	0.951(10)	2.541(9)	3.0761(4)	115.8(7)
C24-H24A···O2	0.953(12)	2.526(12)	3.3072(6)	139.3(10)
2,6-lutidine(2:1)				
N125-H125···O2	0.916(12)	1.747(13)	2.6458(5)	166.5(12)
N125-H125···O3	0.916(12)	2.519(13)	3.0495(5)	117.3(10)
C26-H26A···O2	0.924(17)	2.785(18)	3.4438(7)	129.1(13)
C24-H24C···O3	0.914(12)	2.528(12)	3.2999(7)	142(1)
3,4-lutidine (2:1)				
N125-H125···O2	0.933(15)	1.98(2)	2.7607(6)	140.3(15)
N125-H125···O3	0.933(15)	1.998(16)	2.7439(5)	135.8(15)
C124-H124···O2	0.994(12)	2.524(11)	3.0164(6)	110.3(8)
C126-H126···O3	0.965(11)	2.630(11)	3.1077(5)	110.9(8)

The intermolecular hydrogen bonds which are formed between chloranilic acid molecules in the LCCL units of the 1:1 molecular complexes are listed in Table 6.15. An intramolecular O-H···O hydrogen bond is also formedby chloranilic acid. This interaction may be responsible for the H atom orientation pointing in the O atom direction with which the intramolecular hydrogen bond is formed (Figure 6.4.). When other shorter intermolecular interactions are present, the hydrogen atom can show a different orientation as was found in the case of the 2;3 3,5-lutidine chloranilic acid molecular complex (see

Section 6.4.3.4, below). The chloranilic acid molecules are not co-planar and are stepped relative to one another; the distances between the mean planes of each of the molecules is also given in Table 6.15. No trend between the strength of intermolecular hydrogen bonds in the chloranilic acid dimers and the twisted or planar relative orientation of lutidine ring is found.

Table 6.15 The intra and intermolecular interactions formed by chloranilic acid from X-ray data

D-H···A	D-H/Å	H···A/ Å	D···A/ Å	D-H···A/ º	Planesdi/Å
2,3lutidine (1:1)					
O5-H5···O6[1]	0.80(3)	2.04(3)	2.721(2)	144(2)	0.635
O5-H5···O6	0.80(3)	2.20(2)	2.660(2)	118(2)	
2,4lutidine(1:1)					
O6-H6···O5[2]	0.910(11)	1.923(11)	2.7193(4)	145.0(10)	0.430
O6-H6···O5	0.910(11)	2.102(11)	2.6477(4)	117.4(9)	
2,5lutidine (1:1)					
O5-H5···O6[3]	0.815(14)	2.037(14)	2.6968(5)	137.7(12)	0.334
O5-H5···O6	0.815(14)	2.141(14)	2.6452(5)	120.0(12)	
2,6lutidine(1:1)					
O5-H5···O6[4]	0.884(12)	1.936(12)	2.7225(4)	147.4(11)	0.084
O5-H5···O6	0.884(12)	2.168(13)	2.6562(5)	114.3(10)	
34lutidine (1:1)					
O5-H5···O6[5]	0.868(12)	1.952(12)	2.7143(7)	145.8(12)	0.470
O5-H5···O6	0.868(12)	2.172(11)	2.6450(6)	113.8(10)	
3,5lutidine (1:1)					
O5-H5···O6[6]	0.888(14)	1.951(14)	2.7378(5)	146.9(13)	0.100
O5-H5···O6	0.888(14)	2.134(14)	2.6408(6)	115.5(11)	

[1] *–x,-y,-z* ; [2] *x*,1-*y*,-*z* ; [3] 2-*x*, -*y*, -*z* ; [4] *–x*,1-*y*,-*z* ; [5] 1-*x*,-*y*,-*z* ; [6] 1-*x*, 1-*y*, 1-*z*

6.3.3. Crystal packing of lutidine chloranilic acid molecular complexes.

As we already discussed above, apart from the intermolecular interactions which form the LCCL (2:1) and LCL (1:1) supramolecular synthons, there are also weaker intermolecular interactions such as weak C-H···Cl, C-H···O, C-H·π· and C-H(methyl)··π hydrogen bonds or π··π stacking which may influence the relative orientation of the lutidine ring with respect to that of the chloranilic acid molecule. More details about these aspects will be

given in the following sections for each individual lutidine isomer chloranilic acid molecular complexes studied.

6.3.3.1 1:1 Lutidine Chloranilic Acid Molecular Complexes

6.3.3.1.1. 1:1 2,3-Lutidine Chloranilic Acid Molecular Complex

The hydrogen bonded supramolecular synthon in the 1:1 2,3-lutidine chloranilic acid molecular complex is almost flat apart from the fact that the two chloranilic acid rings are not exactly co-planar (Figure 6.13)). The angles formed between the planes of the two chloranilic acid molecules is 1.61(13)º. The slightly tilted LCCL layers are held together through C-H···O and C-H···Cl weak intermolecular hydrogen bonds. The lutidine and chloranilic acid molecules alternate in a zig-zag motif within the crystal packing (Figure 6.14). In this complex, there is no bifurcated hydrogen bond; this may be attributed to the packing of adjacent lutidine molecules where a methyl group forms a C-H···O weak hydrogen bond to the oxygen atom not involved in the charge-assisted N-H···O hydrogen bond (Figure 6.14)) with a C···O bond length of 3.369(3)Å.

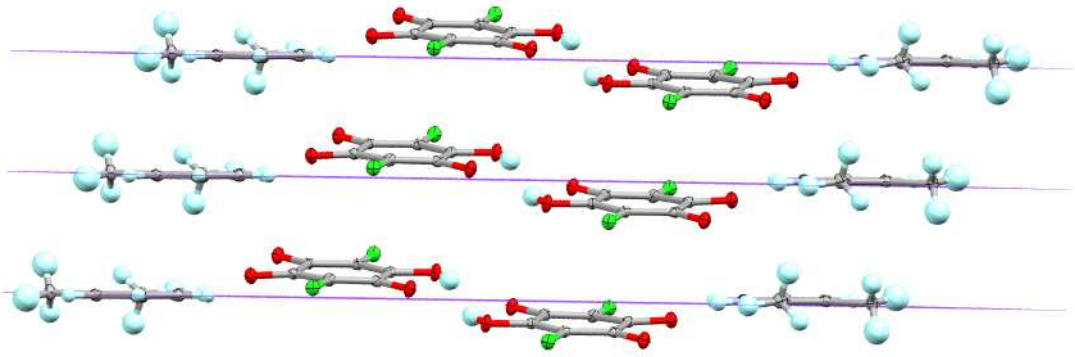

Figure 6.13. Layers of LCCL units in the 1:1 2,3-lutidine chloranilic acid molecular complex.

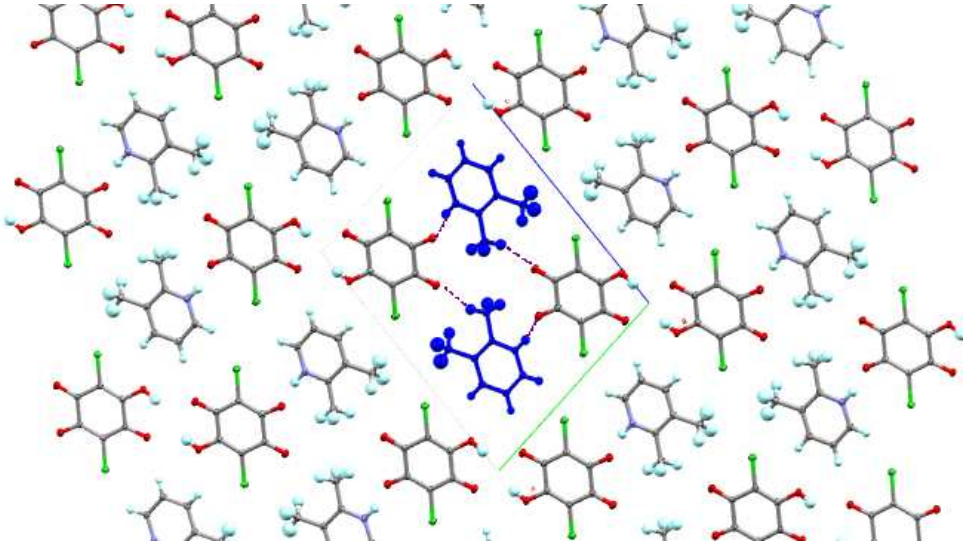

Figure. 6.14. View along the *a* axis showing the relative arrangement of lutidine molecules (blue) in adjacent LCCL units with the absence of a bifurcated hydrogen bond and weak C-H(methyl)···O hydrogen bonds in the 1:1 2,3-lutidine chloranilic acid molecular complex.

6.4.3.1.2. 1:1 2,4-Lutidine Chloranilic Acid Molecular Complex

The chloranilic acid rings which form the LCCL supramolecular synthon lie almost co-planar to each other in the 1:1 2,4-lutidine chloranilic acid molecular complex. The lutidine ring lies twisted relative to the chloranilic acid ring in this case; the LCCL motif therefore forms zig-zag layers (Figure 6.15. (a)). As the layers are tilted and the molecules are not lying on top of each other, no π···π interactions are present. Weak C-H···O and C-H···Cl hydrogen bonds are formed from the methyl groups of neighbouring LCCL units to the chloranilic acid molecule and these may have an influence on the twisting of the lutidine rings.

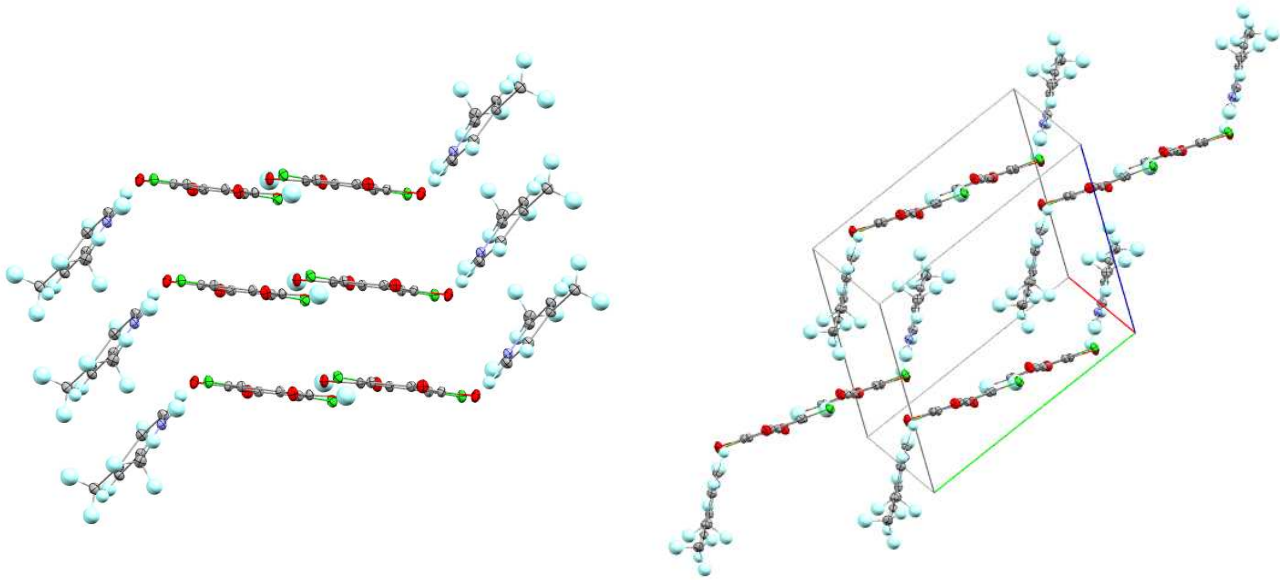

(a) (b)

Figure 6.15. (a) LCCL layers in the 1:1 2,4-lutidine chloranilic acid molecular complex; the lutidine rings twist relative to the chloranilic acid molecules. (b) The zig-zag packing motif relative to the unit cell.

6.4.3.1.3. 1:1 2,5-Lutidine Chloranilic Acid Molecular Complex

The LCCL supramolecular motifs stack upon one another in the 1:1 2,5 lutidine chloranilic acid molecular complex (Figure 6.16). In this case, the lutidine rings and the chloranilic acid molecules are approximately co-planar. The two chloranilic acid molecules lies almost co-planar in the LCCL synthon unit with an angle between the molecular planes of a 0.27(7)º. There are π··π stacking interactions formed between the units; these are formed either between lutidine and chloranilic acid molecules or between two parallel chloranilic acid molecules. These also held together through weak C-H(methyl)···Cl interactions. Other C-H···O and C-H···Cl weak hydrogen interactions connect the units into 3D (Figure 6.17). In this case, there is only one methyl group adjacent to the NH group of the lutidine; a bifurcated hydrogen bond is formed which is sandwiched by C-H···O, C-H···Cl and C-H··π weak hydrogen bonds contributing to the planarity of the LCCL synthon unit (Figure 6.18).

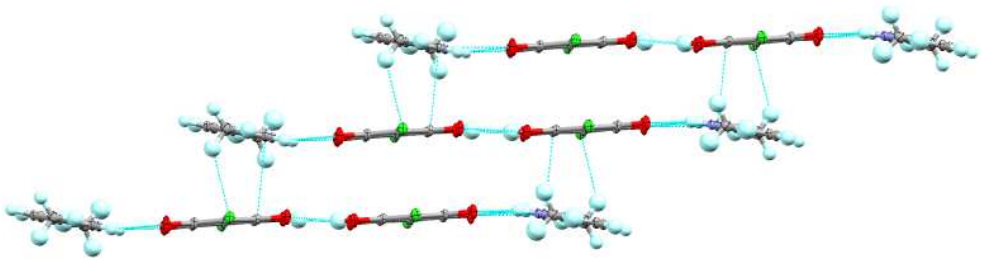

Figure 6.16. The planar supramolecular synthons stacked on each other in the 1:1 2,5-lutidine chloranilic acid molecular complex.

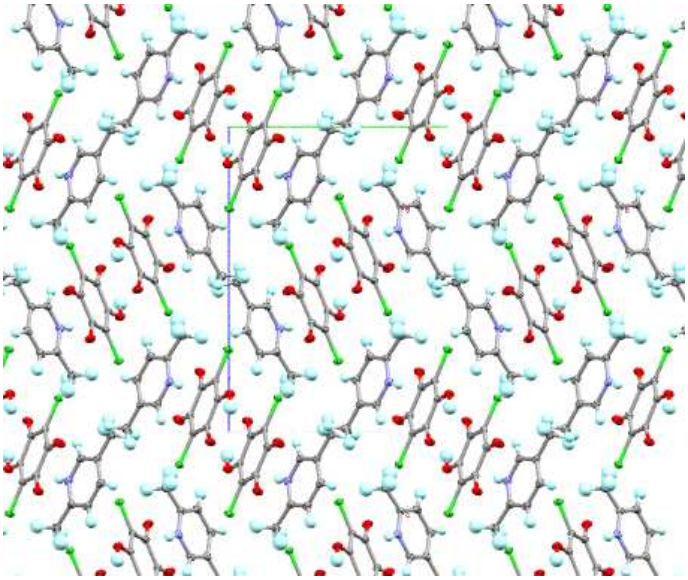

Figure 6.17. The LCCL layers connected in 3D in the 1:1 2,5-lutidine chloranilic acid molecular complex.

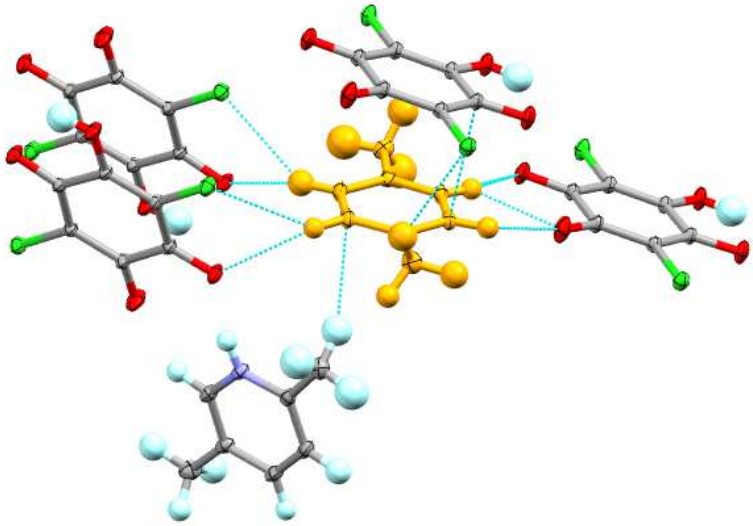

Figure 6.18. The intermolecular interactions involving the lutidine molecule (orange) and the surrounding molecules in the 1:1 2,5-lutidine chloranilic acid molecular complex.

6.4.3.1.4. 1:1 2,6-Lutidine Chloranilic Acid Molecular Complex

A similar pattern for the packing of the LCCL hydrogen-bonded synthon unit is found in the 1:1 2,6-lutidine chloranilic acid molecular complex to that of the 1:1 2,4-lutidine chloranilic acid molecular complex. The LCCL units form a zig-zag arrangement and then into layers with π··π interactions between chloranilic acid rings (Figure 6.19). The lutidine molecules are not involved in π··π interactions. The oxygen atom which is involved in the minor interaction of the asymmetric bifurcated hydrogen bond is also involved in a weak C-H(methyl)···O weak hydrogen bond with a lutidinemolecule in an adjacent LCCL unit.

The two parallel lutidine rings do not stack on top of one another (Figure 6.20)) and the two methyl groups in the same region sterically repel one another. The zig-zag layers are connected together through C-H···O and C-H···Cl weak intermolecular hydrogen bonds (Figure 6.21).

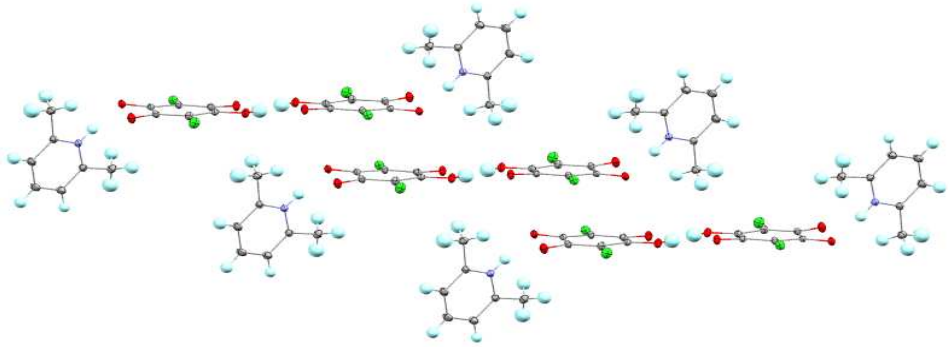

Figure 6.19. The LCCL units forming into zig-zag layers in the 1:1 molecular complex of 2,6-lutidine chloranilic acid.

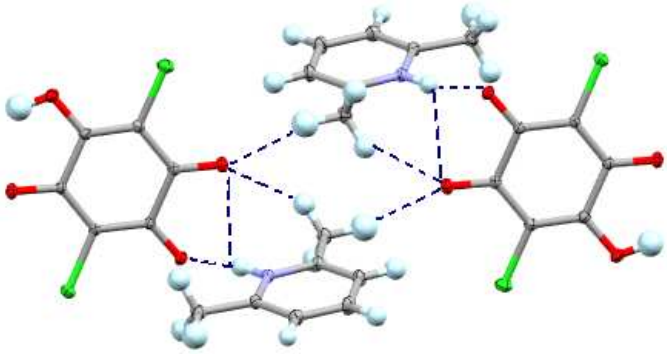

Figure 6.20. The N-H···O bifurcated hydrogen bonds within the LCCL unit and C-H···O weak hydrogen bonds connecting adjacent LCCL units in the 1:1 molecular complex of 2,6-lutidine chloranilic acid.

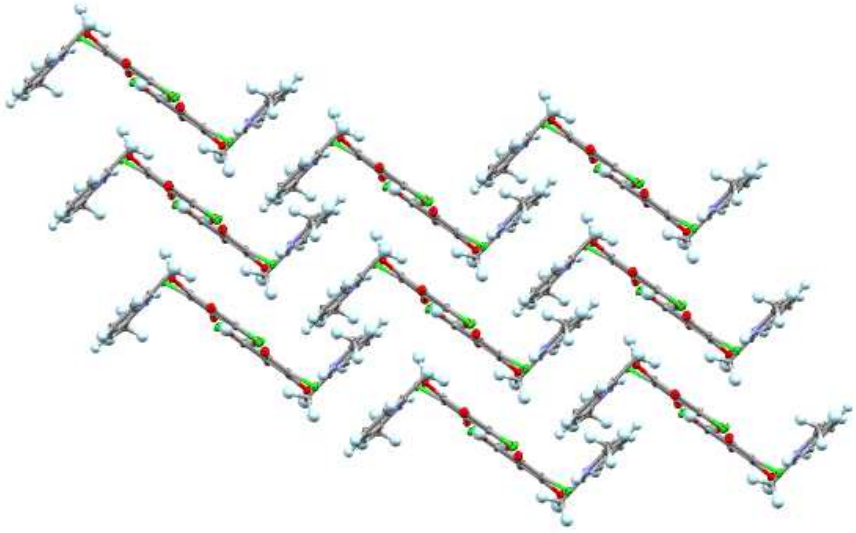

Figure 6.21. Packing of the zig-zag layers within the crystal structure in the 1:1 molecular complex of 2,6-lutidine chloranilic acid.

6.4.3.1.5. 1:1 3,4-Lutidine Chloranilic Acid Molecular Complex

The lutidine molecule in the LCCL units of the 1:1 3,4-lutidine chloranilic acid molecular complex is tilted by almost 90° relative to the chloranilic acid plane (Figure 6.22). The chloranilic acid molecules also show a slight deviation from planarity in terms molecules within the LCCL unit with the angle between the planes of 2.35(2)º. The chloranilic acid rings form Cl···π interactions within the crystal packing between the LCCL units (Figure 6.22). The LCCL units form into layers comprised of slightly tilted LCCL units (Figure 6.23) joined together through C-H···O, C-H···Cl and C-H···π weak hydrogen bonds and short Cl···O contacts (3.160 Å). The oxygen atom involved in the minor contribution to the bifurcated hydrogen bond in the LCCL unit is also involved in a weak C-H···O hydrogen bond with a lutidine molecule in an adjacent LCCL unit within the layer. The lutidine and chloranilic acid molecules alternate in a zig-zag fashion within the crystal packing (Figure 6.23). The weak C-H···O, C-H(methyl)···O, C-H···Cl and C-H···π hydrogen bonds form between lutidine and the neighbouring molecules may have a contribution to the adoption of a twisted position of the lutidine molecule relative to the chloranilic acid ring (Figure 6.24).

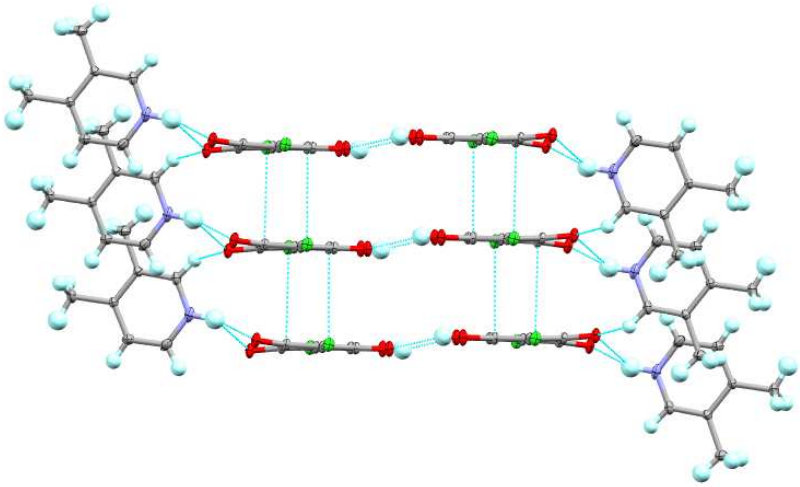

Figure 6.22. Hydrogen bonded units in the 1:1 3,4-lutidine chloranilic acid molecular complex showing Cl···π stacking interactions between the chloranilic acid molecules

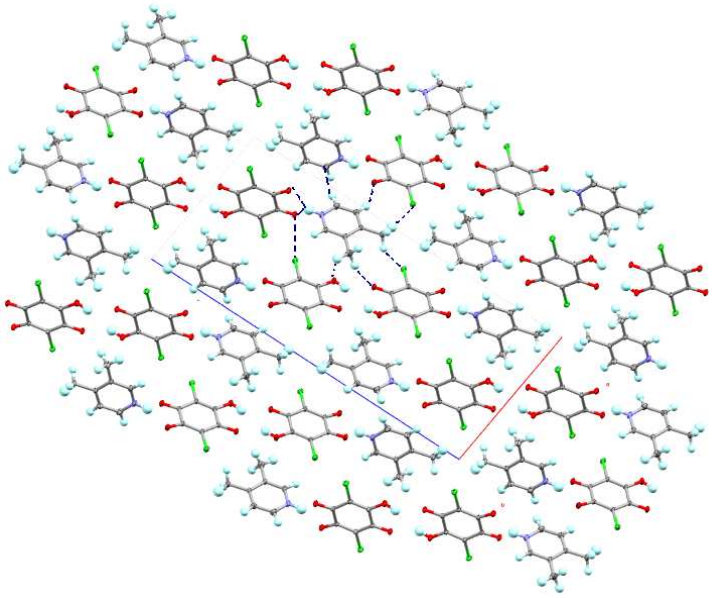

Figure 6.23. Packing of the 1:1 3,4-lutidine chloranilic acid complex, viewed along the *b* axis showing the LCCL layers within the crystal packing

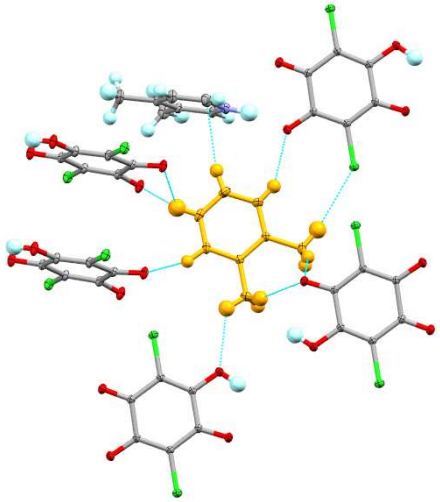

Figure 6.24. The interactions of a lutidine molecule (orange) with the surrounding molecules connected via hydrogen bonds in the 1:1 3,4-lutidine chloranilic acid molecular complex.

6.4.3.1.6. 1:1 3,5-Lutidine Chloranilic Acid Molecular Complex

The LCCL units in the 1:1 3,5-lutidine chloranilic acid molecular complex form into layers; the LCCL hydrogen bonded synthon units are significantly skewed and are held together via short O··π contacts. (Figure 6.25). The LCCL units form a zig-zag motif within the crystal packing (Figure 6.26) where they are oriented approximately perpendicular to one another and connected through C-H··π weak hydrogen bonds between one methyl group of a lutidine and a chloranilic acid molecule.

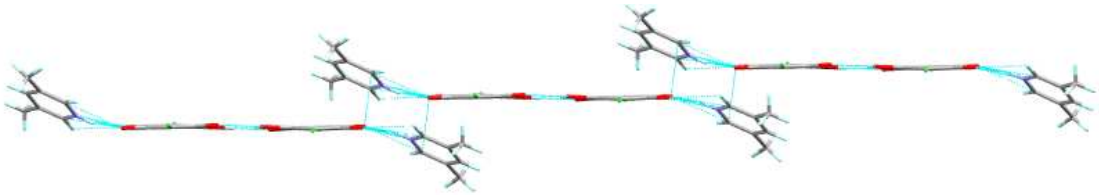

Figure 6.25. The skewed between the LCCL units forming into layers in the 1:1 3,5-lutidine chloranilic acid molecular complex.

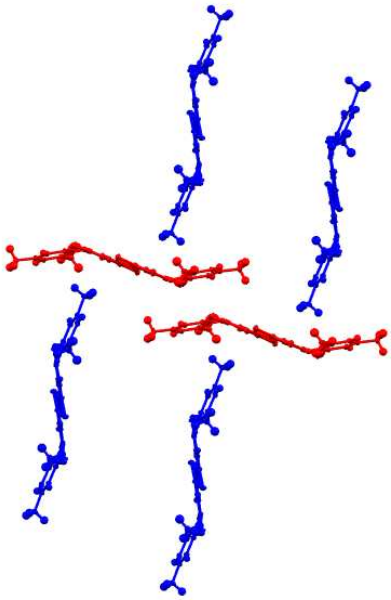

Figure 6.26. The zig-zag motif showing the alternating arrangement of LCCL units within the crystal packing in the 1:1 3,5-lutidine chloranilic acid molecular complex. The almost perpendicular LCCL units are shown in red and blue.

6.3.3.2. 2:1 Lutidine Chloranilic Acid Molecular Complexes

The hydrogen bonded synthon unit found in the 2:1 molecular complexes is the LCL unit mentioned above (Scheme 6.2). The crystal structure and the packing motifs of 5 possible isomers of lutidine with chloranilic acid will be discussed here.

6.3.3.2.1. 2:1 2,3-Lutidine Chloranilic Acid Molecular Complex

The 2,3-lutidine chloranilic acid crystal structure forms zig-zag layers comprised of LCL units where the lutidine rings lie approximately perpendicular relative to the chloranilic acid ring (Figure 6.27) The lutidine rings overlap and form π··π interactions within the crystal as they stack in a 'head to foot' manner with the adjacent LCL units. The oxygen atom involved in the minor contribution to the asymmetric bifurcated hydrogen bond also forms C-H···O and C-H(methyl)···O weak hydrogen bonds with an adjacent lutidine molecule (Figure 6.28). Layers are formed by the lutidine rings along the *ac* plane while the chloranilic acid rings lie perpendicular to this plane (Figure 6.29).

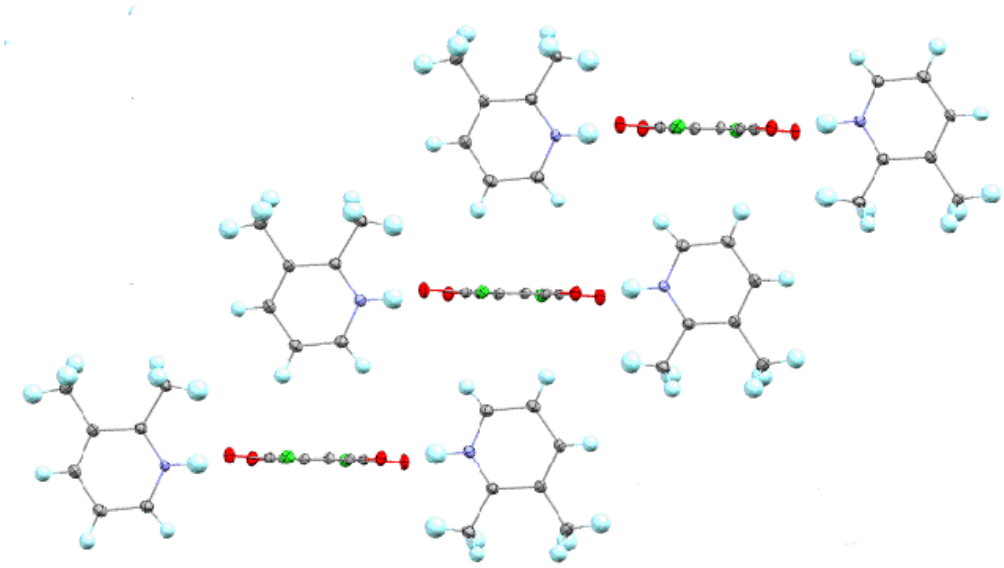

Figure 6.27. The LCL units in the 2:1 2,3-lutidine chloranilic acid molecular complex.

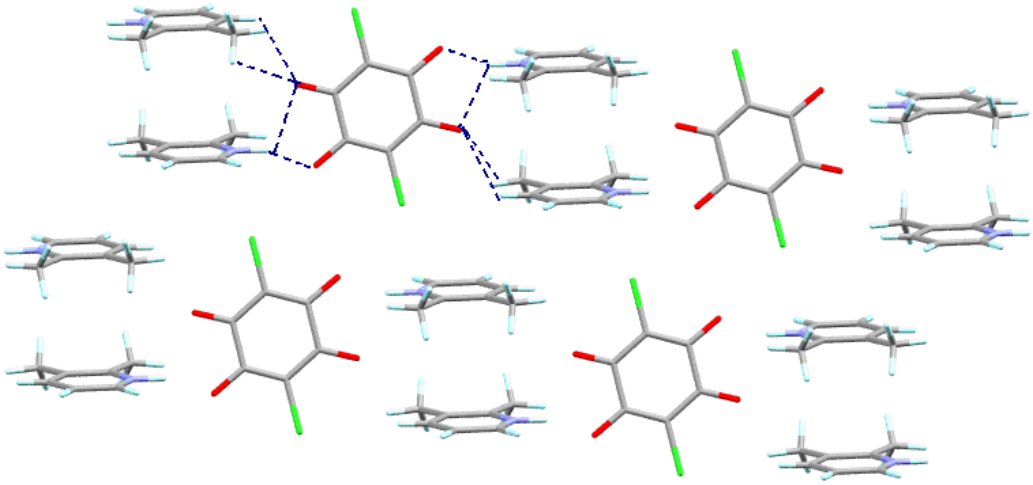

Figure 6.28. The overlapping lutidine rings stacked in a 'head to foot' motif in the 2:1 2,3-lutidine chloranilic acid molecular complex showing the hydrogen bonds formed between the chloranilic acid and lutidine molecules (blue dashed lines).

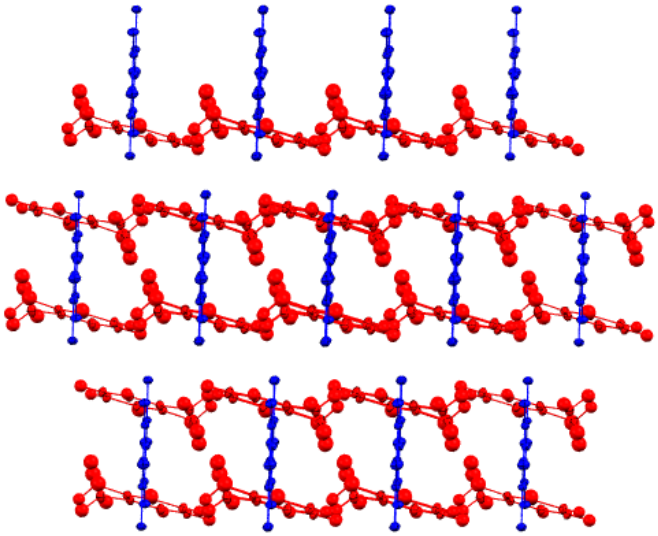

Figure 6.29. The lutidine molecules (red) forming layers along the ca plane whereas the chloranilic acid molecules (blue) lie perpendicular to this in the 2:1 2,3-lutidine chloranilic acid molecular complex

6.3.3.2.2. 2:1 2,4-Lutidine Chloranilic Acid 2:1 Molecular Complex

The 2:1 2,4 lutidine chloranilic acid molecular complex is known to crystallise in two polymorphic forms.[43] However, as no suitable crystals for high-resolution X-ray diffraction were obtained for form II, only form I was characterised in this work. The LCL hydrogen bonded motifs forms layers with the chloranilic acid parallel to the lutidine ring connected through C-H···π and C-H(methyl)···O hydrogen bond interactions (Figure 6.30). The LCL layers are tilted allowing π···π stacking interactions to form between lutidine molecules and

a chloranilic acid from an adjacent layer. The zig-zag motif is also present here and the LCL layers overlap through the crystal (Figure 6.31). The 2:1 2,4-lutidine chloranilic acid form I molecular complex is the only example from this series which crystallises in an orthorhombic crystal system with the *Pcab* space group (Figure 6.32).

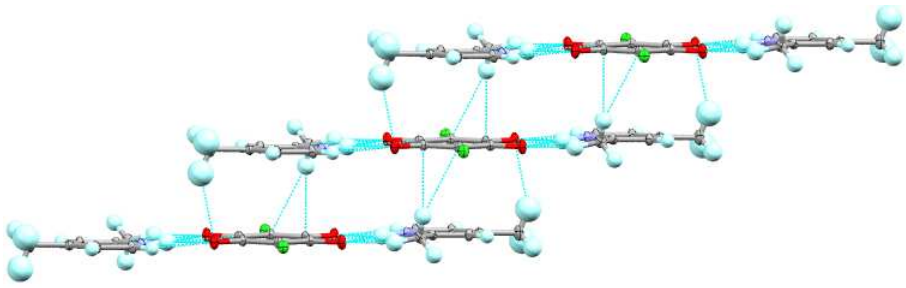

Figure 6.30. The parallel layers form by hydrogen bond units in the 2:1 2,4-lutidine chloranilic acid form I molecular complex.

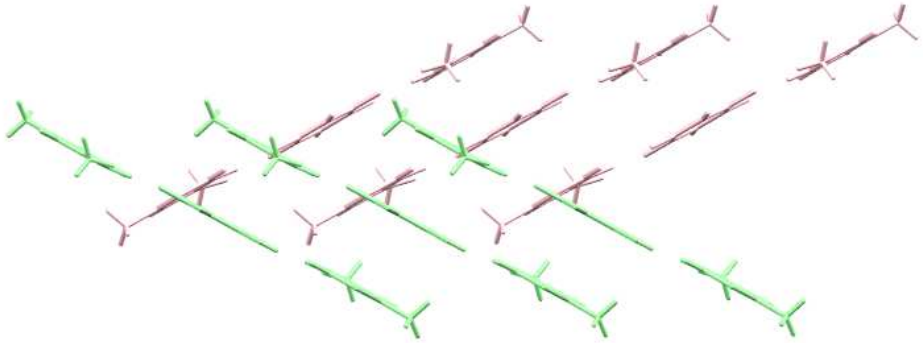

Figure 6.31. Zig-zag motif and π-π interactions between the rings in the 2:1 2,4-lutidine chloranilic acid form I molecular complex.

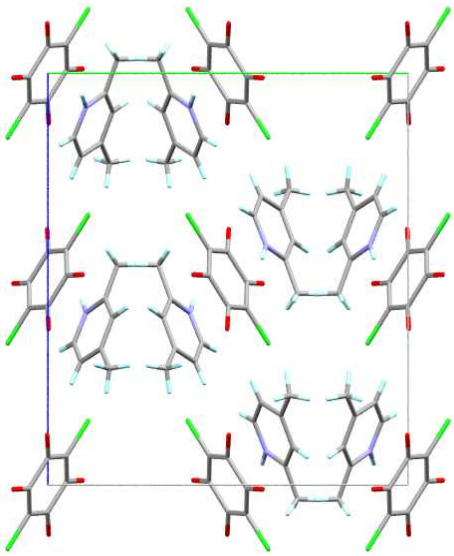

Figure 6.32. Unit cell representation of the 2:1 2,4-lutidine chloranilic acid form I molecular complex viewed along the *a* axis.

6.3.3.2.3. 2:1 2,5-Lutidine Chloranilic Acid Molecular Complex

In the 2:1 2,5-lutidine chloranilic acid molecular complex, the LCL units arrangements arranged into layers which are joined together via π··π stacking interactions between the lutidine rings stacked top-to-tail (Figure 6.33). The lutidine molecules in the LCL units form intermolecular π··π stacking and weak C-H(methyl)···π interactions with surrounding neighbour molecules. These interactions sandwich the lutidine molecules in the LCL units and this may explain why these are lying twisted relative to the chloranilic acid ring (Figure 6.34).

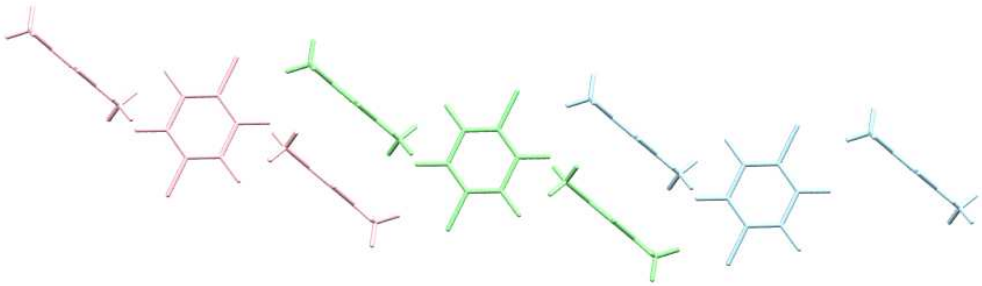

Figure 6.33. The zig-zag arrangement of the LCL units and π··π stacking interactions present in the 2:1 2,5-lutidine chloranilic acid molecular complex.

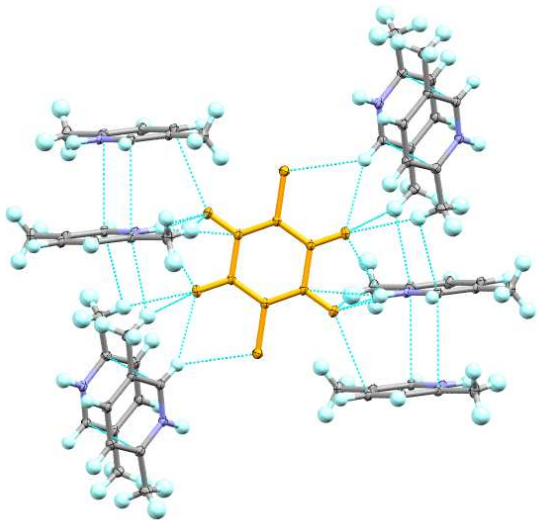

Figure 6.34. The intermolecular interactions involving the chloranilic acid molecule (orange) and the intermolecular π··π stacking interactions and C-H(methyl)··π weak hydrogen bonds which form between lutidine molecules in the 2:1 2,5-lutidine chloranilic acid molecular complex.

6.3.3.2.4. 2:1 2,6-Lutidine Chloranilic Acid Molecular Complex

The 2:1 2,6-lutidine chloranilic acid molecular complex contains an LCL unit which is similar to the 2,5-lutidine chloranilic acid unit with the rings of the molecules almost perpendicular to each other. The chloranilic acid molecules form weak C-H(methyl)···O and C-H(methyl)··π hydrogen bonds with the lutidine molecules sitting below and above the ring in the adjacent LCL units (Figure 6.35). The chlorine and oxygen atoms are involved in close contacts (3.08Å), shorter than the sum of their van der Waals radii (3.27Å), forming zig-zag chains within the crystal packing (Figure 6.36).

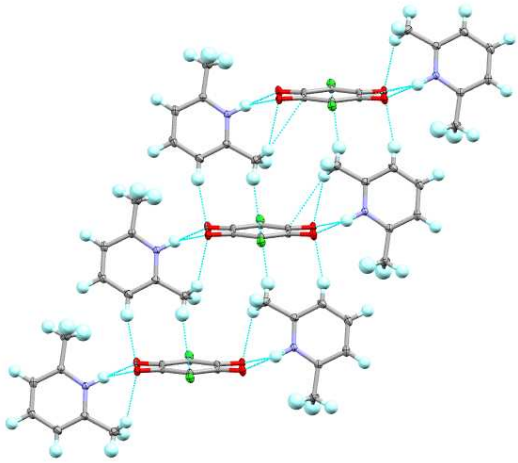

Figure 6.35. The layers of LCL hydrogen bonded units layers which form in the 2:1 2,6 lutidine chloranilic acid molecular complex.

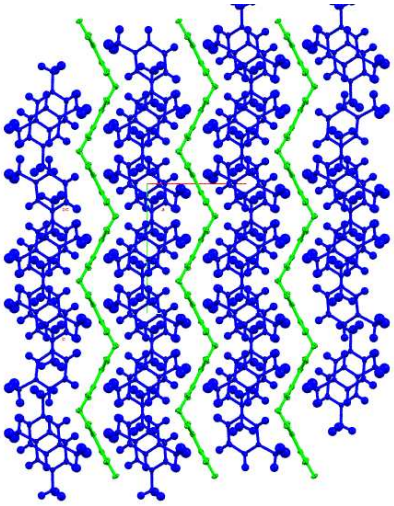

Figure 6.36. The chloranilic acid molecules form chains along the *b* axis connected through Cl···O close contacts in the 2:1 2,6-lutidine chloranilic acid molecular complex.

6.3.3.2.5. 2:1 3,4-Lutidine Chloranilic Acid Molecular Complex

In the previous studies, the 2:1 3,4-lutidine chloranilic acid molecular complex was missing from the series. The LCL unit present in the other 2:1 molecular complexes is also formed here with the lutidine and chloranilic acid rings in the same plane. The adjacent LCL units form into staggered layers held together through π··π interactions between the chloranilic acid and lutidine rings (Figure 6.37.). Weak C-H(methyl)···Cl and C-H(methyl)···O hydrogen bond interactions are also present here which may have a minor contribution on the nearly symmetric bifurcated hydrogen bond. The LCL units are joined together by weak C-H(methyl)··π and C-H···Cl interactions forming parallel layers along the *a* axis (Figure 6.38).

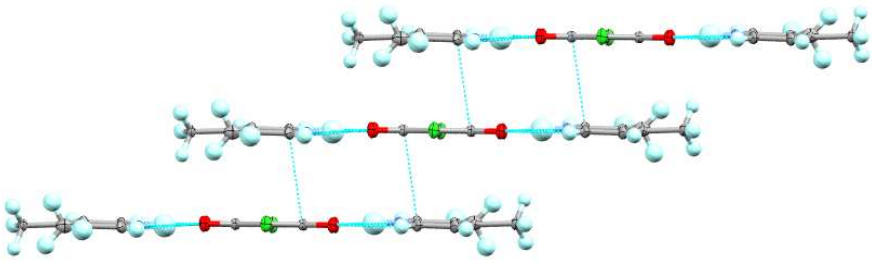

Figure 6.37. Staggered layers and π··π interactions present in the 2:1 3,4-lutidine chloranilic acid molecular complex.

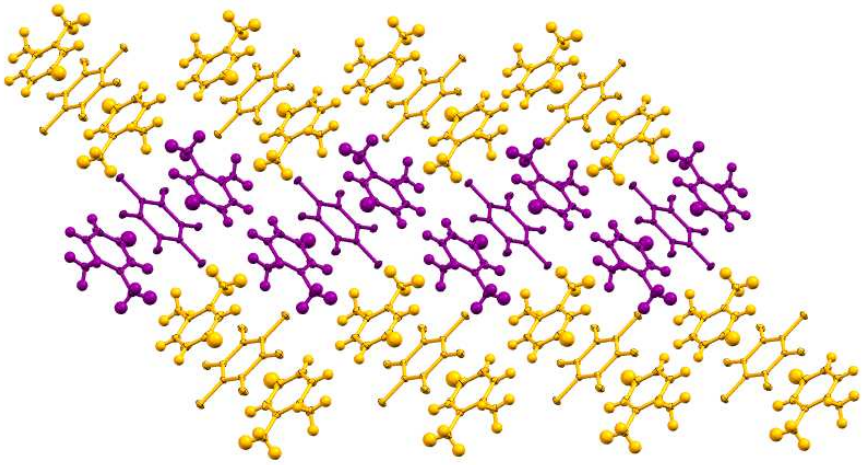

Figure 6.38. The LCL synthons forming parallel layers in the 2:1 3,4-lutidine chloranilic acid molecular complex. Purple and yellow represent the two different orientations for the LCL units within these layers.

6.3.3.3. Hydrate Forms of Lutidine Chloranilic Acid Molecular Complexes

The 2:1 3,4- and 3,5-lutidine chloranilic acid systems are known to form hydrate complexes as reported in previous work.[43] In addition, a new hydrate form for a 2:1 2,4-lutidine chloranilic acid molecular complex was determined in this work. As no suitable crystal of the 3,4-lutidine chloranilic acid hydrate were obtained, only 2,4- and 3,5-lutidine chloranilic acid hydrate forms were analysed using high resolution X-ray diffraction and the crystal packing is described below.

6.3.3.3.1. 2:1 2,4-Lutidine Chloranilic Acid Dihydrate Molecular Complex

In the 2:1 2,4-lutidine chloranilic acid dihydrate molecular complex, the chloranilic acid molecules are doubly deprotonated and the lutidine molecules protonated but the LCL unit is broken; the lutidine molecules are replaced by the water forming a new supramolecular unit, water: chloranilic acid: water (WCW) (Figure 6.39). The units are connected through symmetric bifurcated O-H···O hydrogen bonds (O···O distances 2.9710(5) and 2.9022(4)Å). The N-H···O interactions previously formed between lutidine molecules and chloranilic acid molecules are now formed between lutidine and water molecules. Instead of a 2:1 LCL unit, a seven molecule supramolecular unit is formed with the lutidine molecules connected to chloranilic acid molecules both via water molecules and directly through C-H···O and C-H···Cl weak hydrogen bond interactions. The water molecules also form O-H···O intermolecular hydrogen bonds between themselves. This creates the LWWCWWL unit (Figure 6.39)) which then form into layers. These layers are tilted (i.e.

not flat) and connected to one another through hydrogen bonding involving the water molecules (Figure 6.40).

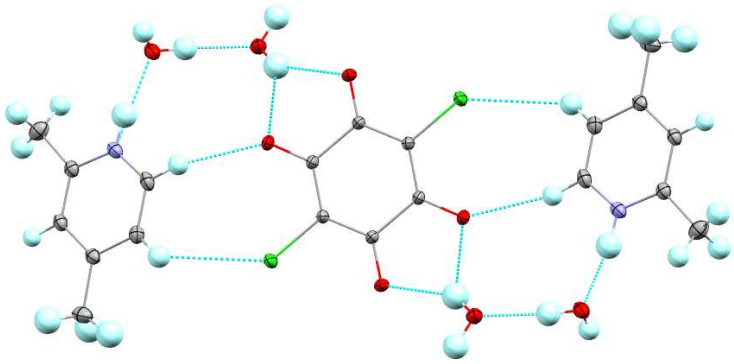

Figure 6.39. The hydrogen bonded unit LWWCWWL unit of the 2:1 2,4-lutidine chloranilic acid dihydrate molecular complex.

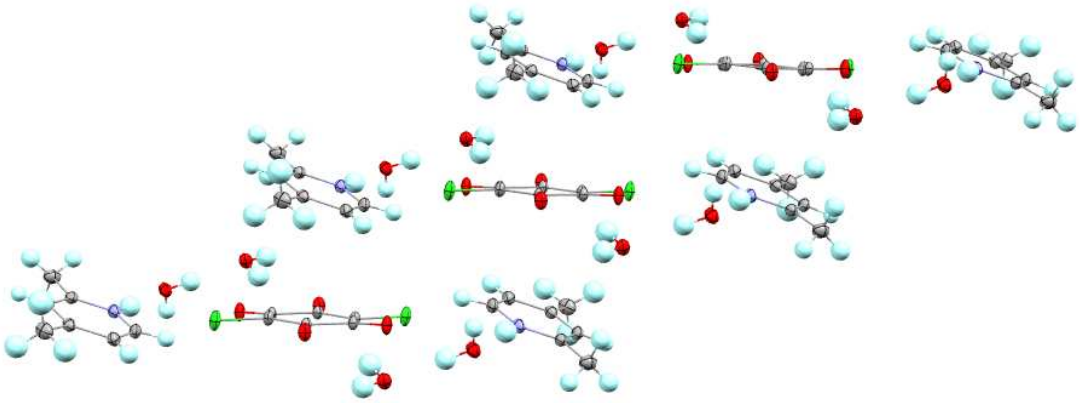

Figure 6.40. The layers formed by the supramolecular synthons in the 2:1 2,4-lutidine chloranilic acid dihydrate molecular complex; the water molecules connect the layers.

The hydrogen bonded units formed between water and chloranilic acid observed here are not unique having been reported in the molecular complexes of 1,8-bis(dimethylamino)naphthalene chloranilic acid dihydrate[55] or the 4:3:2 3-picoline chloranilic acid hydrate.[28] In the latter, only one picoline molecule was replaced by water forming picoline chloranilic acid water units (PCW).

6.3.3.3.2. 2:1 3,4-Lutidine Chloranilic Acid Trihydrate Molecular Complex

The 2:1 3,4-lutidine chloranilic acid trihydrate molecular complex forms the LCL hydrogen bonded synthon present in all of the 2:1 anhydrous molecular complexes of this series. For each chloranilic acid molecule, three water molecules are found. The lutidine

and chloranilic molecules lie coplanar relative to one another within the LCL units forming, consistent with the symmetric N-H···O bifurcated hydrogen bond on one side of the unit (2,7733(5) and 2.8203(5)Å). However, on the other side of the LCL unit, an asymmetrical N-H···O bifurcated hydrogen bond is formed (2.6788(5) and 2.9523(5)Å). The water molecules are also involved in hydrogen bond interactions with the chloranilic acid molecule, the lutidine molecules, and between themselves (Figure 6.41) reinforcing the planarity of the LCL unit. The LCL units are connected to one another through hydrogen bonding involving the water molecules (Figure 6.42)).

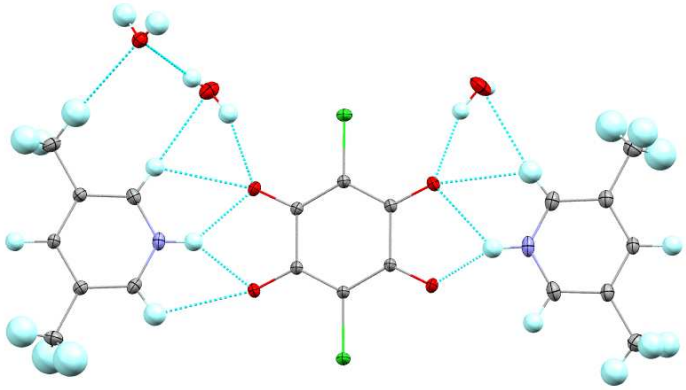

Figure 6.41. The hydrogen bonded unit of the 2:1 3,4-lutidine chloranilic acid trihydrate molecular complex

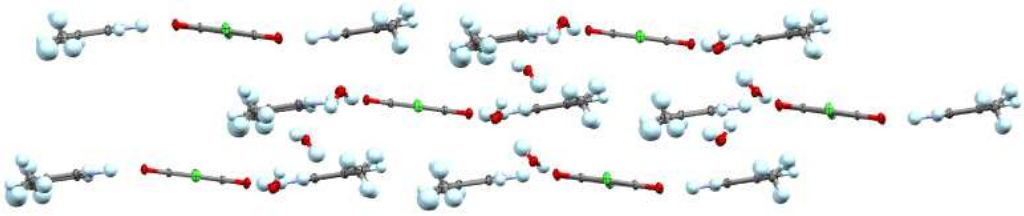

Figure 6.42. The layers formed by the supramolecular synthons alternating in a wave fashion in the 2:1 3,4-lutidine chloranilic acid trihydrate molecular complex.

6.3.3.4. Other Lutidine Chloranilic Acid Molecular Complexes

In an attempt to produce the 2:1 3,5-lutidine chloranilic acid molecular complex, two new anhydrous molecular complexes of 3,5-lutidine chloranilic acid have been determined: one of them containing the LCCL motif and a neutral chloranilic acid molecule in a 2:3 ratio of lutidine to chloranilic acid; the other one forms LCCCL motifs with singly deprotonated

chloranilic acid molecules and neutral chloranilic acid molecules with a 4:5 ratio of lutidine to chloranilic acid.

The additional neutral chloranilic acid molecules attached to the LCCL motif in the 2:3 complex have a different conformation to that of chloranilic acid found in its native crystal structure; instead of an intramolecular hydrogen bond being formed between oxygen atoms, an intramolecular O-H···Cl hydrogen bond isformed (Figure 6.43). This facilitates a short intermolecular interaction of this OH group with an oxygen atom of the deprotonated chloranilic acid molecule (O···O distance 2.556(3)Å). This type of H behaviour was observed previously in literature for chloranilic acid in combination with metals such as Cs and Rb.[57] In both cases presented in the literature, for each chloranilic acid molecule, three water molecules were present forming short O-H···Ointermolecular interactions with the H atom of chloranilic molecule.

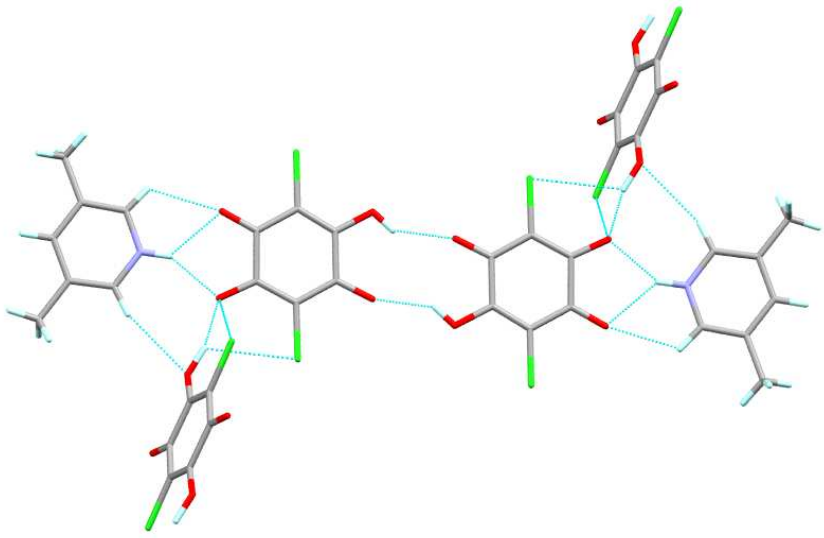

Figure 3.43. 1:2 LCCL motif formed in the 2:3 3,5-lutidine chloranilic acid molecular complex showing the additional neutral chloranilic acid molecules present in the crystal structure.

The 4:5 molecular complex forms an LCCCL motif where a hydrogen bonded unit contains three partially deprotonated HCA^- chloranilic acid molecules. In the LCCCL unit, the middle chloranilic acid ring is twisted relative to the other two chloranilic acid molecules (Figure 6.44); this middle chloranilic acid molecule is connected to the other two chloranilic acid molecules in the LCCCL unit through moderate O-H···O hydrogen bonds (O···O distance, 2.6260(15)Å). The neutral chloranilic acid molecules form O-H···O hydrogen bonds (O···O distance, 2.6075(14)Å) and O··Cl short contacts (3.141(11)Å), shorter than the sum of the van der Waals radii of the two atoms (3.27Å), with the singly

deprotonated chloranilic acid molecules. The neutral chloranilic acid molecule lies twisted relative to the other two singly deprotonated chloranilic acid rings (Figure 6.45).

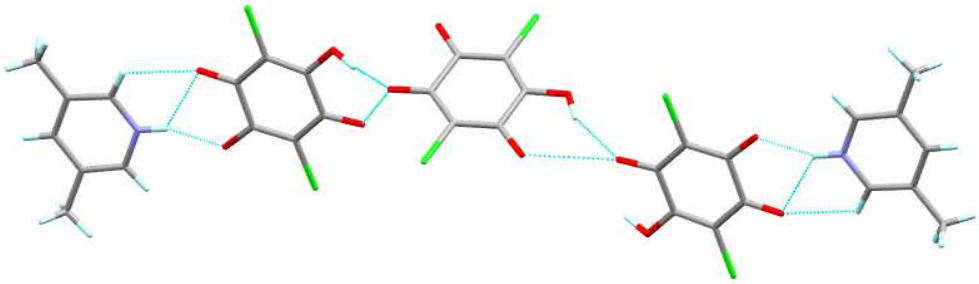

Figure 6.44. LCCCL motif present in the 4:5 3,5-lutidine chloranilic acid molecular complex.

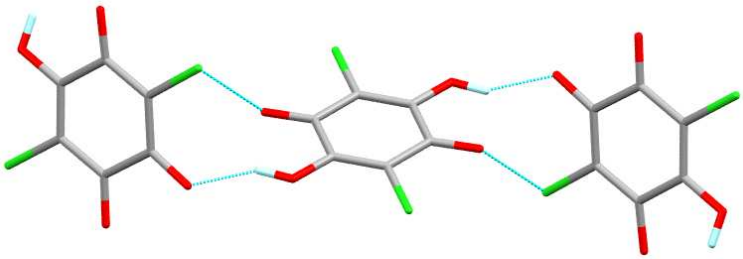

Figure 6.45. The intermolecular interactions formed between the partially and neutral chloranilic acid molecules present in the 4:5, 3,5-lutidine chloranilic acid molecular complex.

A 2:3 2,4-lutidine chloranilic acid crystal structure containing the LCL motif and a fully deprotonated chloranilic acid molecule was also found in this work. The lutidine molecules within the LCL unit are co-planar with the chloranilic acid molecules and are held together via bifurcated hydrogen bonds (Figure 6.46). In addition a neutral chloranilic acid molecule is also present. The deprotonated chloranilic acid molecules are tilted relative to the neutral chloranilic acid molecule and form O-H···O intermolecular hydrogen bond interactions (Figure 6.47)

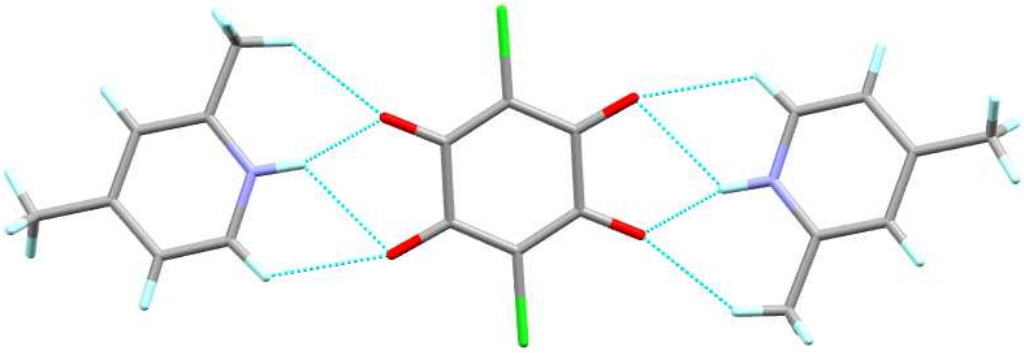

Figure 6.46. Hydrogen bonded LCL unit in the 2:3 2,4-lutidine chloranilic acid molecular complex.

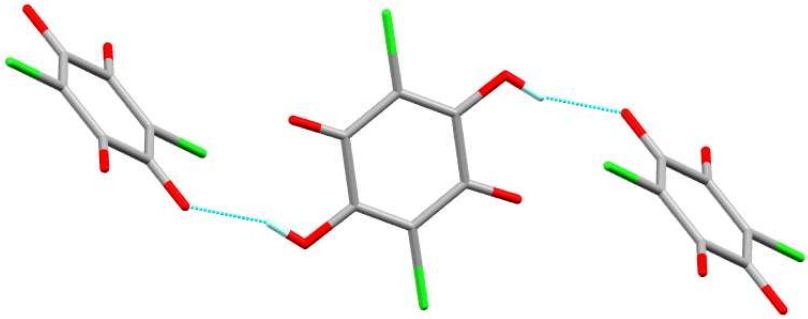

Figure 6.47. The intermolecular interactions form between the deprotonated and neutral chloranilic acid molecules formed in the 2:3 2,4-lutidine chloranilic acid molecular complex.

6.4. Neutron Diffraction Experimental Results

Four crystal structures of chloranilic acid with lutidine have been determined using neutron data collected on D19 at the ILL neutron source: 1:1 complexes of 2,4-, 2,5-, 2,6- lutidine with chloranilic acid and the 2:1 2,6- lutidine chloranilic acid molecular complex. The molecular structure together with the labelling scheme for the lutidine molecules are presented in Figures 6.48-6.51 below. The labelling scheme for the chloranilic acid is the same as was used for the X-ray data. As expected the acceptor hydrogen bond length (A···H) becomes shorter than that determined usingX-rays due to the difference in nuclear and electronic positions and the consequent D-H elongation.

A comparison between the neutron and X-ray diffraction hydrogen bonds of the 1:1 2,4-lutidine chloranilic acid molecular complex are given in Table 6.16. The neutron data show well-defined hydrogen atom behaviour for all of the hydrogen atoms including those involved in the intermolecular hydrogen bonds (Figure 6.48).

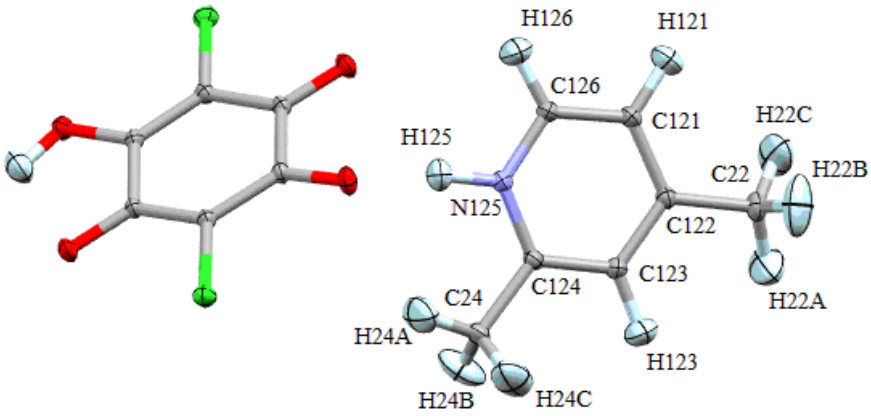

Figure 6.48. The 1:1 2,4-lutidine chloranilic acid molecular complex showing the anisotropic thermal ellipsoids for all atoms including hydrogen determined from neutron diffraction.

Table 6.16. A comparison between the hydrogen bond lengths in the 1:1 molecular complex of 2,4 lutidine with chloranilic acid determined by neutron and X-ray diffraction refinements.

Neutron	D-H/Å	H···A/ Å	D···A/ Å	D-H···A/ º
N125-H125···O2	1.0630(15)	1.6492(16)	2.6966(8)	167.42(12)
N125-H125···O3	1.0630(15)	2.5677(14)	3.1953(8)	117.10(10)
X-ray				
N125-H125···O2	0.990(11)	1.720(10)	2.6962(4)	168.0(10)
N125-H125···O3	0.991(11)	2.604(11)	3.1956(4)	118.3(8)

The 1:1 2,5-lutidine chloranilic acid molecular complex determined by neutron diffraction shows significant elongation of one of the methyl hydrogen atoms attached to C24 and high Q peaks were observed around this atom which were modelled as disordered at a 50:50 level; it is equally possible that this disorder could be described by libration of the methyl groups and anisotropic thermal parameters provide an inadequate model for this "banana" shaped motion. The disordered positions for the hydrogen atoms were not observed in the X-ray diffraction refinement and no obvious signs of libration were noticed

from the isotropic hydrogen atom refinement. The large atomic displacement parameters observed in this case are not surprising due to the freedom of the methyl group rotation (Figure 6.49).

The symmetrical bifurcated hydrogen bond in this case is confirmed by the neutron experiment (Table 6.17).

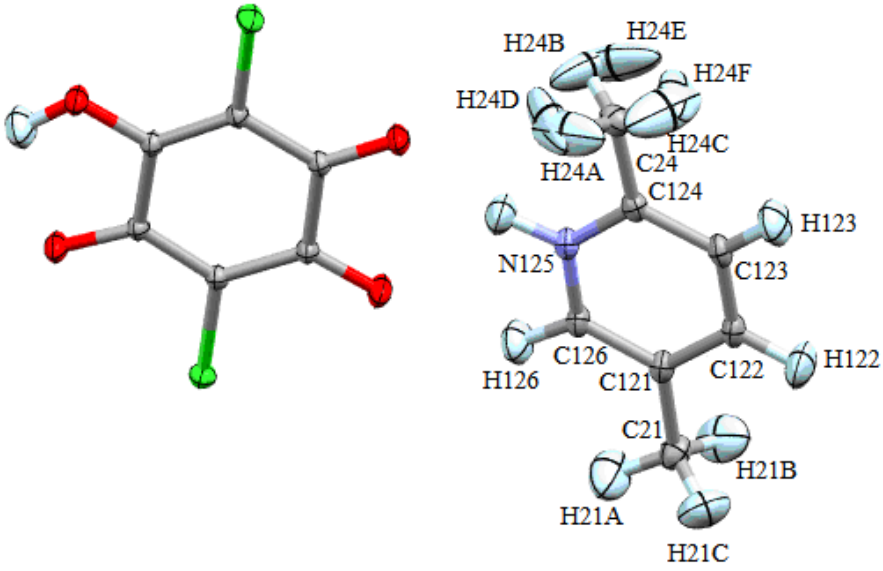

Figure 6.49. The 1:1 2,5-lutidine chloranilic acid molecular complex showing the anisotropic thermal ellipsoids from neutron diffraction.

Table 6.17. A comparison of the hydrogen bond lengths in the 1:1 molecular complex of 2,5-lutidine chloranilic acid determined using neutron and X-ray diffraction refinements

Neutron	D-H/Å	H···A/ Å	D···A/ Å	D-H···A/ º
N125-H125···O2	1.0448(15)	2.2481(16)	2.9204(9)	120.49(10)
N125-H125···O3	1.0448(15)	1.9518(16)	2.9477(8)	158.22(12)
X-ray				
N125-H125···O2	0.842(10)	2.330(9)	2.9203(5)	127.5(8)
N125-H125···O3	0.842(10)	2.157(9)	2.947(9)	156.1(9)

In case of the 1:1 2,6-lutidine chloranilic acid neutron crystal structure, one of the methyl groups has also been modelled as disordered at a 70:30 level and large thermal motion can be also spotted from the ellipsoid size due to thermal libration (Figure 6.50); again, this could also be modelled as libration rather than disorder.

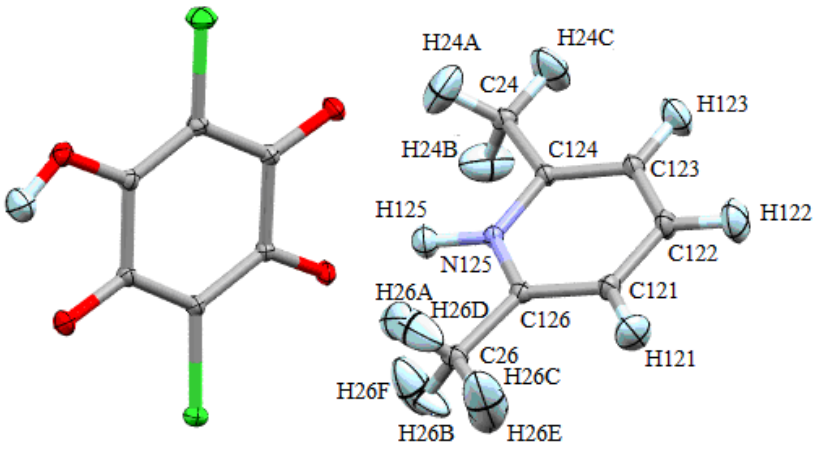

Figure 6.50. The 1:1 2,6-lutidine chloranilic acid molecular complex showing the anisotropic thermal ellipsoids from neutron diffraction.

The disordered hydrogen atoms of the methyl group also lie in this case, on the side of the shorter N-H···O bond distance of the bifurcated hydrogen bond (Table 6.18).

Table 6.18. Comparison of the hydrogen bond lengths in the 1:1 2,6-lutidine chloranilic acid molecular complex determined using neutron and X-ray diffraction refinements

Neutron	D-H/Å	H···A/ Å	D···A/ Å	D-H···A/ º
N125-H125···O2	1.0697(12)	1.6118(12)	2.6634(7)	166.40(11)
N125-H125···O3	1.0697(12)	2.5325(13)	3.1006(7)	112.30(8)
X-ray				
N125-H125···O2	0.905(10)	1.767(10)	2.6623(4)	169.7(9)
N125-H125···O3	0.905(9)	2.617(10)	3.0998(4)	114.2(7)

All the atoms have been identified as ordered for the 2,6-lutidine chloraniclic acid 2:1 molecular complex obtained from neutron diffraction data collection. The thermal ellipsoids still show large libration of the hydrogen atoms of both methyl groups (Figure 6.51).

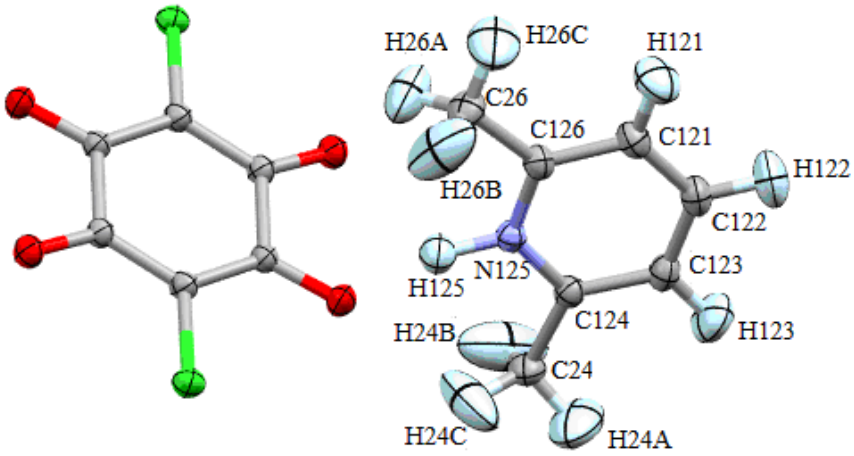

Figure 6.51. The 2:1 2,6-lutidine chloranilic acid molecular complex showing the anisotropic thermal ellipsoids from neutron diffraction.

Table 6.19. Comparison of the hydrogen bond lengths in the 2:1 2,6 lutidine chloranilic acid molecular complex determined using neutron and X-ray diffraction refinements

Neutron	D-H/Å	H···A/ Å	D···A/ Å	D-H···A/ º
N125-H125···O2	1.080(3)	1.604(4)	2.646(2)	160.3(3)
N125-H125···O3	1.080(3)	2.399(4)	3.052(2)	117.6(2)
X-ray				
N125-H125···O2	0.916(12)	1.747(13)	2.6458(5)	166.5(12)
N125-H125···O3	0.916(12)	2.519(13)	3.0495(5)	117.3(10)

6.5. Charge Density Studies

6.5.1. Multipole Refinement Analysis

Multipole refinements were carried out for the crystal structures using high resolution X-ray diffraction data apart from for the hydrate structures. These refinements were performed in order to obtain a more accurate description of the charge density and hence a more accurate description of the atomic positions and their thermal motion. The nature of the bifurcated hydrogen bond will be also investigated using the molecular graphs analysis, deformation density and Laplacian maps. In addition the singly and doubly deprotonated chloranilic acid molecules will be investigated using the charge density tools. The results were also used to estimate the lattice energy for both 1:1 and 2:1 molecular ratio (Section 6.6). The multipole refinements based on different models used are summarized in Table 6.20. The implementation of the adps for the hydrogen models obtained from SHADE[50] web interface or neutron diffraction (where possible) clearly shows an improvement in the

R_{val} values. For the 2,4-lutidine 1:1 complex, the R_{val} for models 4 and 5 are slightly lower compared with models 2 and 3, indicating a better refinement when adps from neutron data were used. As the adps for the methyl groups in the molecular complexes of 2,5-lutidine and 2,6-luditine from neutron diffraction show high thermal motion, only the adps obtained from SHADE[50] were used. However, estimating the adps for H atoms using the SHADE[50] web interface, in this case, are not entirely realistic.

Table 6.20. Summary of the multipole model refinements of the chloranilic acid luditine molecular complexes.

	R_{val}		R_{val}
2,4-lutidine1:1		2,4-lutidine2:1	
1	1.72	1	1.78
2	1.66	2	1.73
3	1.65	3	1.73
4	1.65		
5	1.64		
2,5-lutidine1:1		2,5-lutidine2:1	
1	1.96	1	2.98
2	1.91	2	2.93
3	1.90	3	2.91
3,4-lutidine1:1		3,4-lutidine2:1	
1	2.74	1	1.64
2	2.69	2	1.56
3	2.68	3	1.55
3,5-lutidine1:1		3,5-lutidine2:1	
1	2.66	1	2.45
2	2.60	2	2.41
3	2.58	3	2.40

6.5.2. The residual density maps representations

The residual electron density maps for charge density studied lutidines chloranilic acid molecular complexes are shown in Figures 6.52 and 6.53 for both the lutidine and chloranilic acid planes. The residual densities for all of the studied lutidine chloranilic acid molecular complexes do not exceed 0.378 $eÅ^{-3}$, indicating good quality of the multipole refinements.

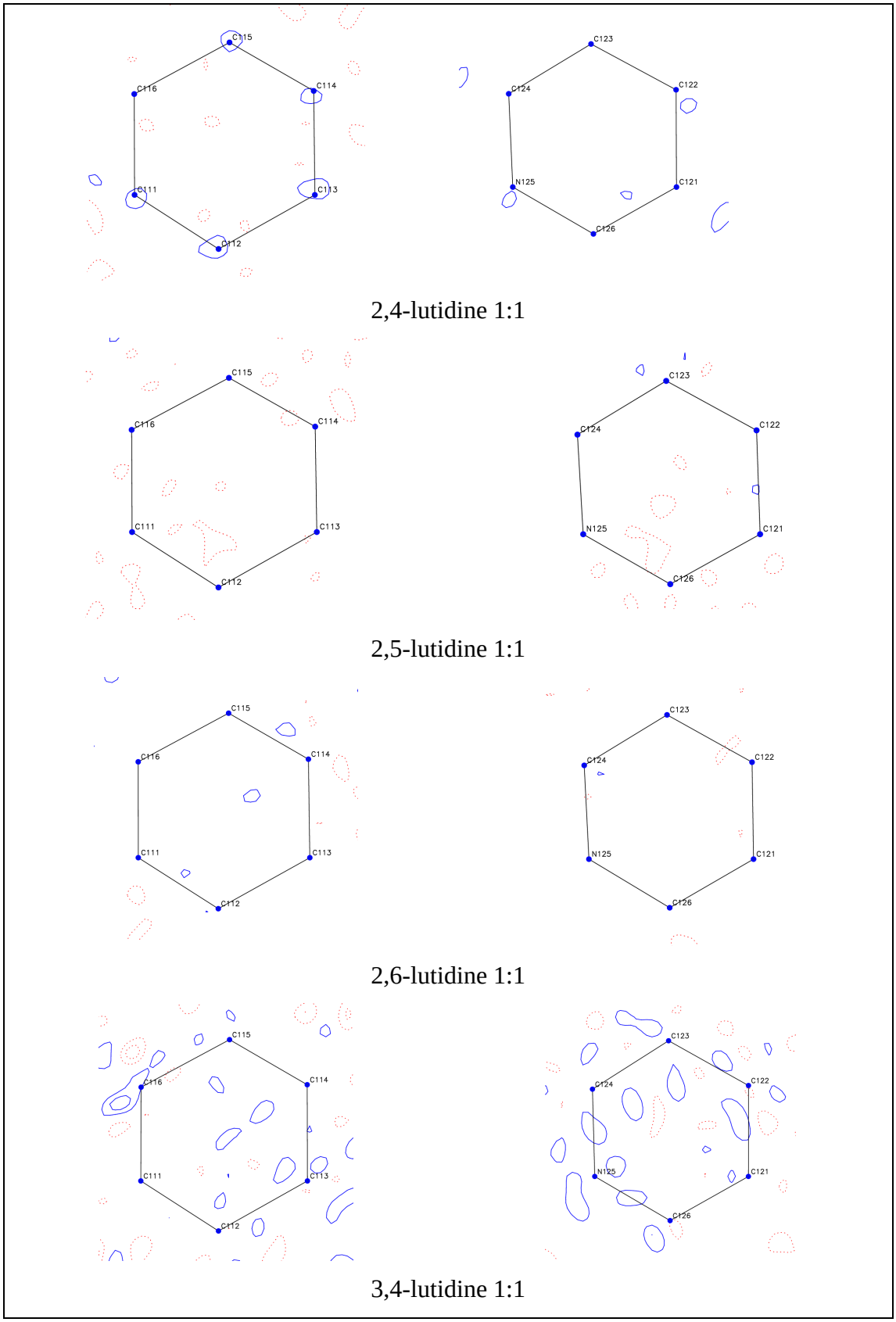

Figure 6.52. . Residual electron density maps for the 1:1 lutidine chloranilic acid molecular complexes (left –chloranilic acid rings right – lutidine rings). Contour levels are ±0.1eÅ^{-3}

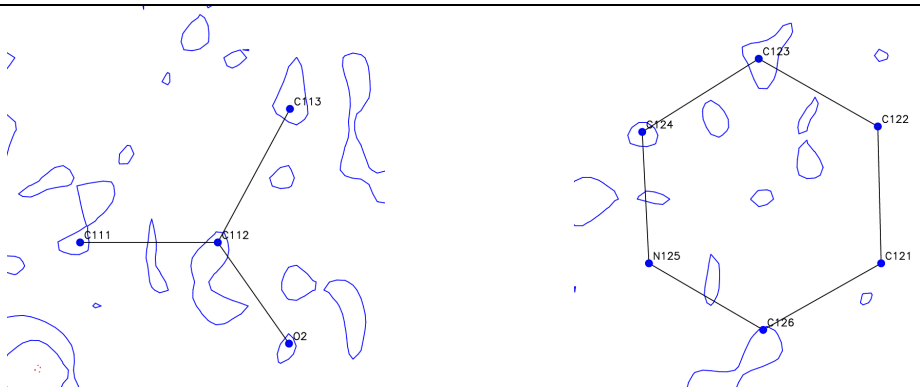

2,3-lutidine 2:1

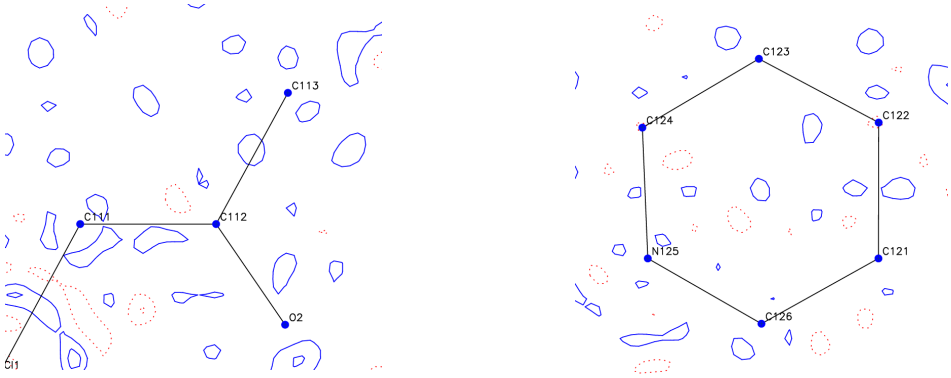

2,4-lutidine 2:1

2,5-lutidine 2:1

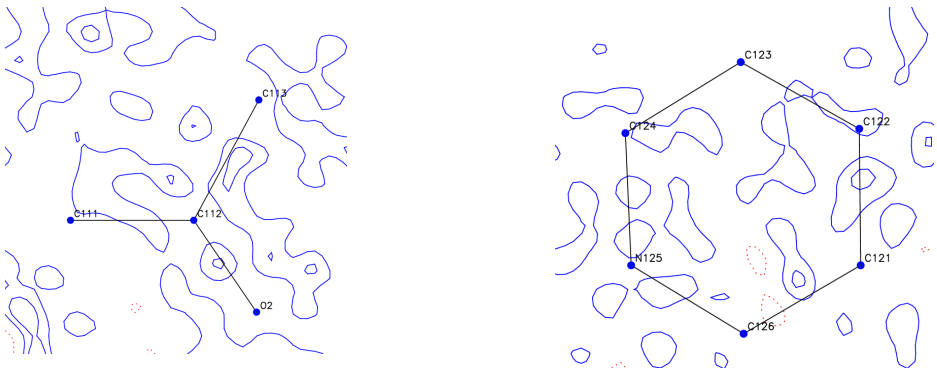

2,6-lutidine 2:1

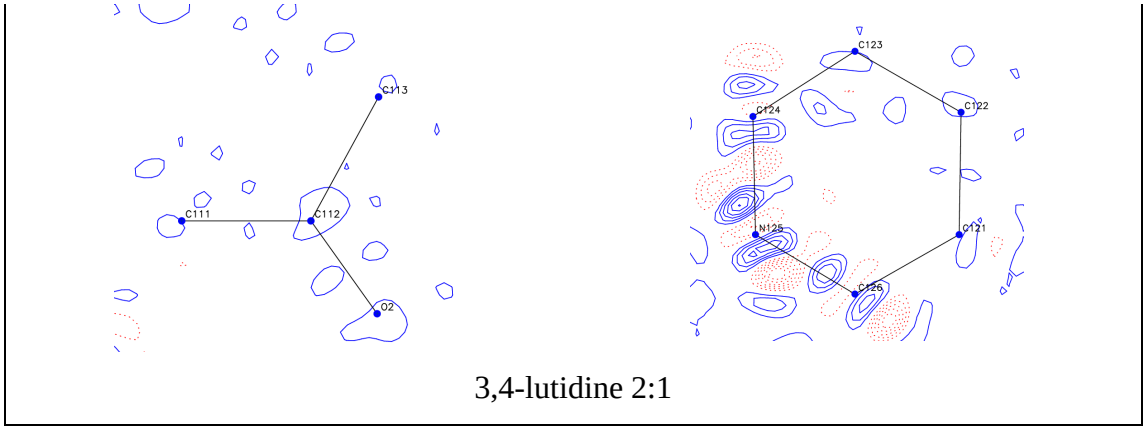

3,4-lutidine 2:1

Figure 6.53. Residual electron density maps for the 2:1 lutidine chloranilic acid molecular complexes (left –chloranilic acid rings right – lutidine rings). Contour levels are ±0.1eÅ^{-3}

An exception was noticed in the case of 2:1 3,4-lutidine chloranilic acid molecular complex where high residual density was observed around the C124-N125-C126 bond. This is not surprising as high thermal motions were observed for these atoms and this clearly has some effect on the multipole model refinement.

6.5.3 Description of molecular graphs

The molecular graphs description including BCPs formed between the atoms in the various stoichiometries of lutidine chloranilic acid molecular complexes are illustrated in Figure 6.54 and 6.55. The molecular graphs were analysed in order to investigate the existence of the bifurcated hydrogen bond formed between lutidine and chloranilic acid molecules. This type of bifurcated hydrogen bond was identified for all molecular complexes studied in this project according to the D···A distancies obtainedfrom X-ray data and analysed in Section 6.32 (except 1:1 2,3 lutidine chloranilic acid). The presence of BCPs between the H (nitrogen) and oxygen atoms will therefore confirm the existence of interatomic interactions between those atoms and these can be associated with the hydrogen bond formations. For all ‘compositional’ polymorphs, the molecular graphs obtained from each type of multipole model refinement are shown. For the 1:1 2,4 lutidine chloranilic acid molecular complex, models 4 and 5 were not included. This shows identical BCPs between lutidine chloranilic acid molecules with model 2 and 3. The BCPs present between the two molecules are different in model 1 compared with models 2 and 3 apart for the 2:1 2,3–lutidine chloranilic acid molecular complex showing similar trends in all 3 models. The

formation of bifurcated hydrogen bond between the lutidine and chloranilic acid molecule were confirmed from the molecular graphs of model 1. An exception to this was found for the 2,4-lutidine chloranilic acid molecular complexes in both stoichiometries; only one BCP was observed between the H(nitrogen) atom and one O atom in this case (Figures 6.54 and 6.55). In models 2 and 3, the formation of the bifurcated hydrogen bond was not confirmed by the molecular graph description (Figure 6.54). The weak hydrogen bond formation between the C-H(methyl)···O or C-H···O are also confirmed by the presence of BCPs, but not in all the cases. These interactions are also affected by the multipole model refinement strategy used; model 1 shows disagreements with models 2 and 3.

The high thermal libation of the N and C atoms in the 2:1 3,4 lutidine chlornailic acid molecular complex shows a strong influence on the molecular graph path and BCP positions. The path between these atoms is not a straight line as observed in all the other molecular complexes, but slightly curved (Figure 6.55).

Therefore these experimental charge density results suggest that the existence of BCPs between the atoms involved in intermolecular hydrogen bonds are sensitive to the type of multipole refinement used. Introducing quadrupole, κ, κ´ parameters for the refinement of the hydrogen atoms in model 2 and 3 clearly affects the molecular graph descriptions between the lutidine and chloranilic acid molecules.

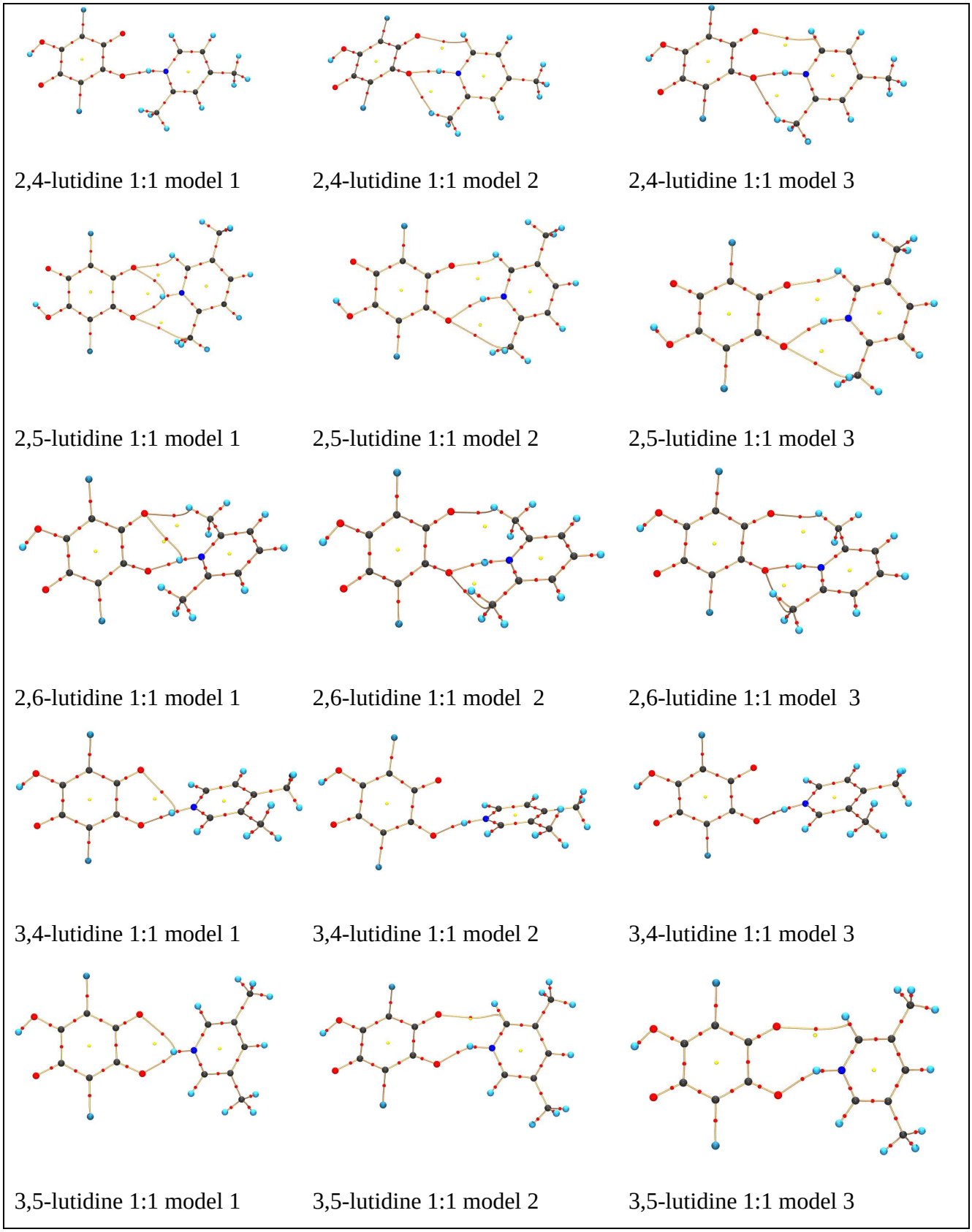

Figure 6.54. Molecular graphs of 1:1 lutidine chloranilic acid molecular complexes showing the BCPs formed between the two molecules

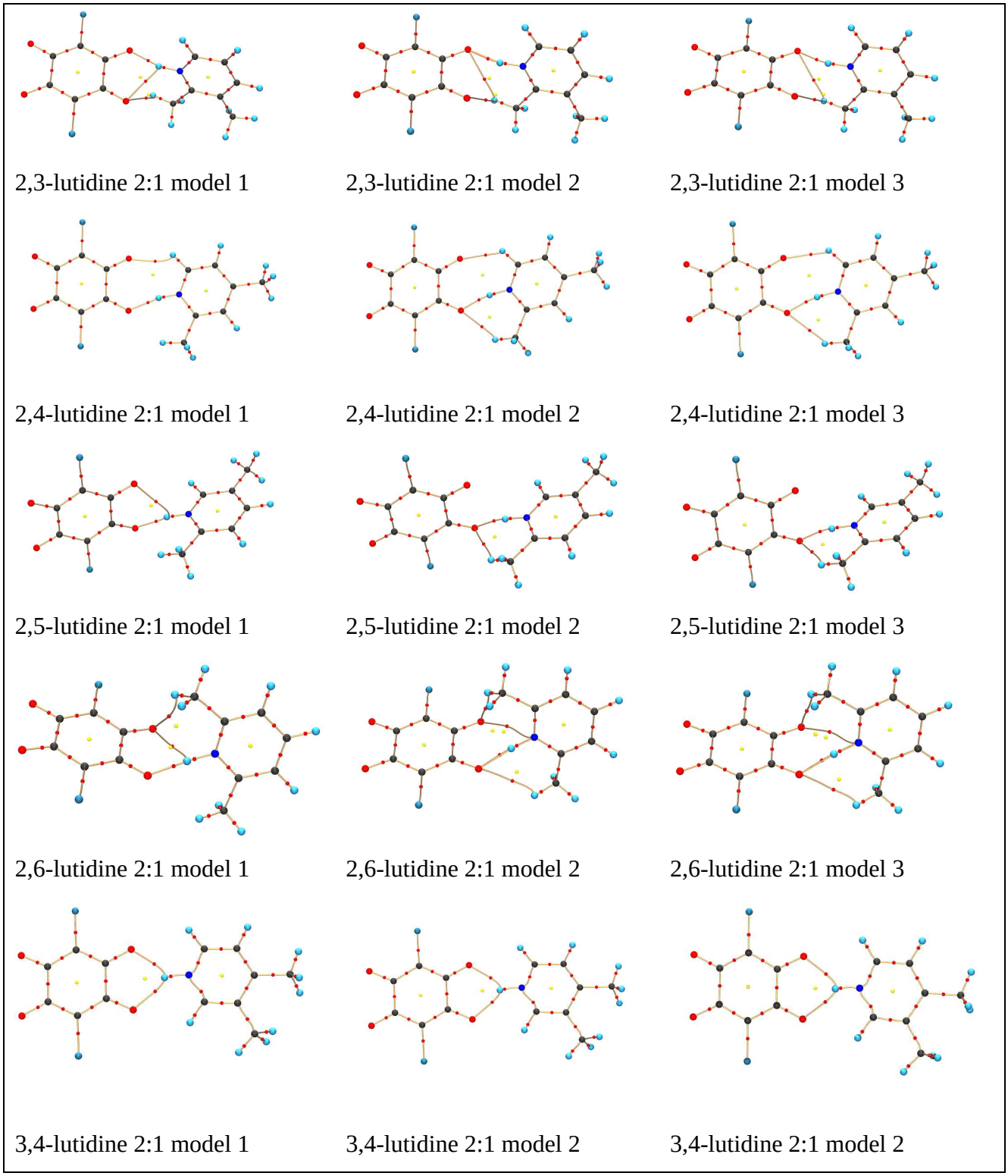

Figure 6.55. Molecular graphs of 2:1 lutidine chloranilic acid molecular complexes showing the BCPs formed between the two molecules

6.5.4 Deformation density representation

In order to further investigate the possibility of bifurcated hydrogen bond formation, the deformation density maps were plotted. Two molecular complexes were selected 2:1 2,4-lutidine chloranilic acid for which no bifurcated hydrogen bond were confirmed by the molecular graph (Figure 6.56) and 1:1 2,5-lutidine chloranilic acid (Figure 6.57) for which a symmetrical bifurcated hydrogen bond was confirmed for model 1 in the molecular graph. The lone pairs of the O atoms clearly point in the H(nitrogen) atom direction. These confirm the possibility of a bifurcated hydrogen bond formation in both cases.

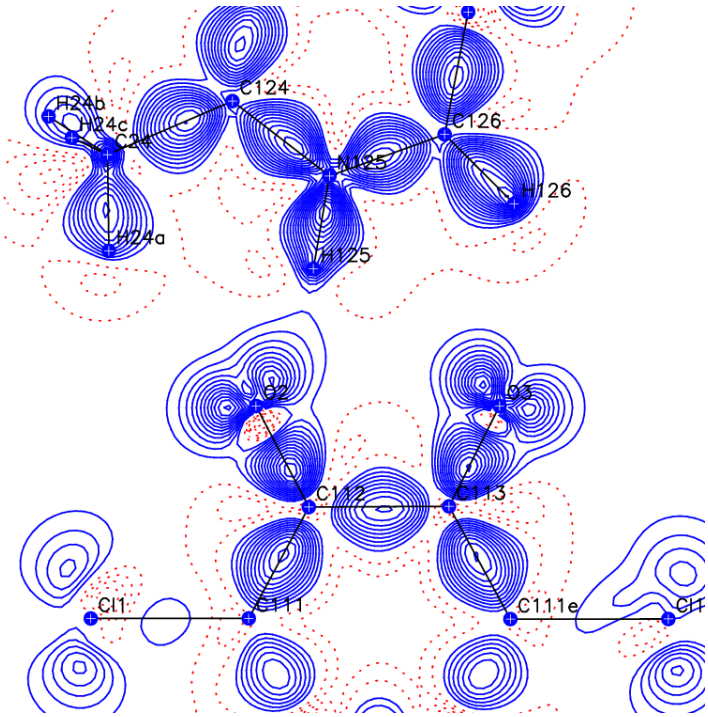

Figure 6.56. Deformation density map for 2:1 2,4-lutidine chloranilic acid showing the lone pair of the O atoms pointing in the H(nitrogen) direction. Contour levels at 0.08 eÅ^{-3}

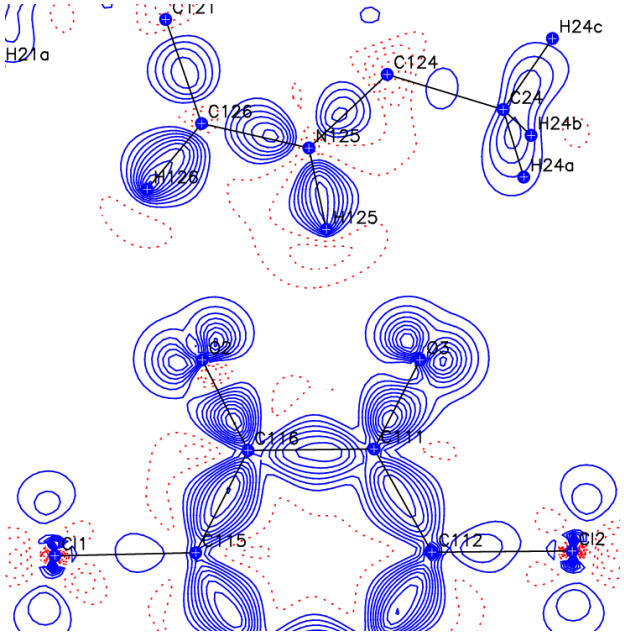

Figure 6.57. Deformation density map for 1:1 2,5-lutidine chloranilic acid showing the lone pair of the O atoms pointing in the H(nitrogen) direction (dashed line –negative contours, solid blue line – positive contours). Contour levels at 0.08 eÅ^{-3}

The deformation density maps in the plane of chloranilic acid ring were also plotted for all the molecular complexes studied using charge density analysis (Figure 6.58.and 6.59) Maps were plotted in order to investigate the delocalisation of the charge in the single and doubly deprotonated chloranilic acid molecules. The results for the singly deprotonated chloranilic acid molecule show negative deformation density (red dashed lines) at the O2 and O6 atoms in the direction of the O2-C112 and C116-O6 bonds (Figure 6.58). This is as expected for a delocalization of charge around the O2-C112-C111-C116-O6 bonds. For the O3 atom still involved in a double bond with C113 atom, no negative deformation density is observed along this bond. An exception for this rule was found for the 1:1 3,4-lutidine chloranilic acid molecular complex where a slightly negative charge was observed for the O3-C113 bond. The lone pair of electrons were also less pronounced in this case for O2 atom in the direction of the H125 atom and asymmetrical compared with the other complexes where symmetrical lone pairs were observed at this atom (Figure 6.58).

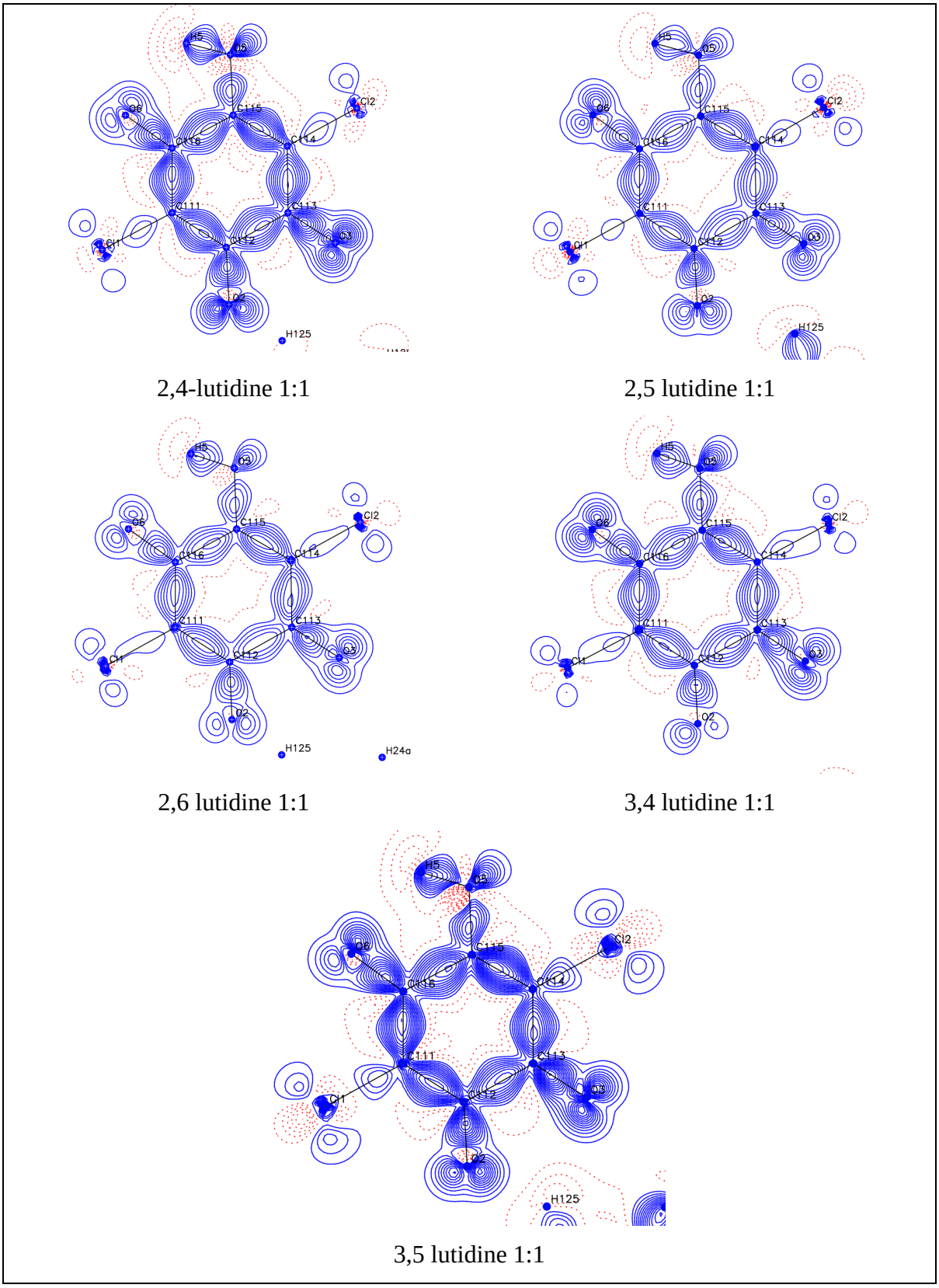

Figure 6.58. Deformation density maps in plane of chloranilic acid molecule for the 1:1 molecular complexes. (dashed red line – negative contours, solid blue line – positive contours). Contour levels at 0.08 eÅ^{-3}

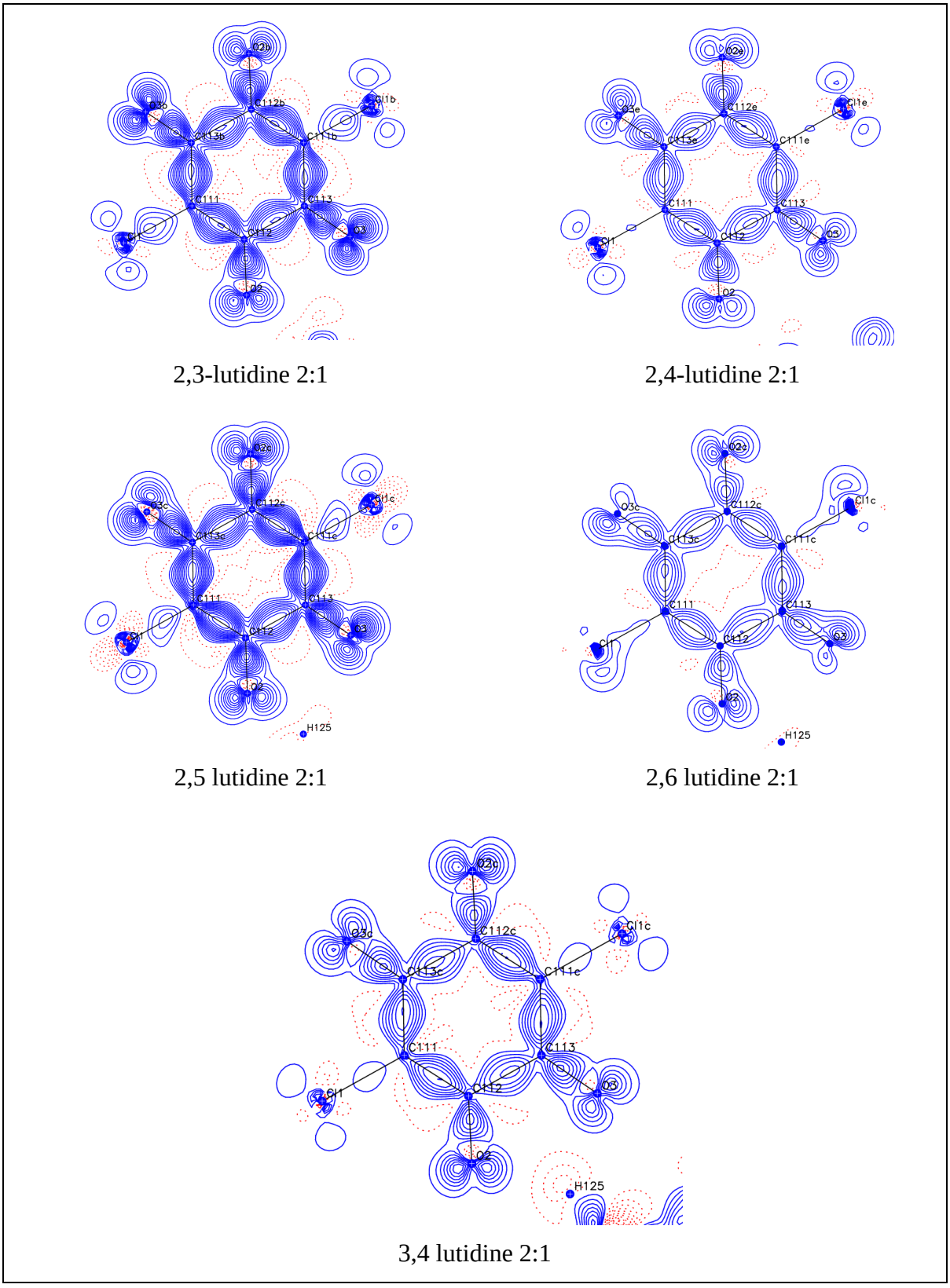

Figure 6.59. Deformation density maps in plane of chloranilic acid molecule for the 2:1 molecular complexes. (dashed red line – negative contours, solid blue line – positive contours). Contour levels at 0.08 eÅ^{-3}

For the 2:1 molecular complexes, negative deformation density can be noticed for all O atoms confirming the delocalization of the double bond for all of these atoms (Figure

6.59). An exception was found for the O3-C113 bond of the 2,6-lutidine chloranilic acid molecular complex (Figure 6.59). No negative deformation density can be observed in this case. The lone pairs of electrons of the O3 atom also show asymmetry and are less pronounced in the H125 directions. For the other molecular complexes the lone pairs of the O3 atom are symmetrical.

6.5.5 Laplacian representation

The Laplacian maps were also plotted in the O···H···O plane for the 2:1 2,4-lutidine chloranilic acid (Figure 6.60) and 1:1 2,5-lutidine chloranilic acid molecular complexes (Figure 6.61) The lone pair of the O atoms are also confirmed by these plots to be directed towards the H(nitrogen) atom direction. Hence, the possibility of the bifurcated hydrogen bond formation is also emphasised by the Laplacian representation plots.

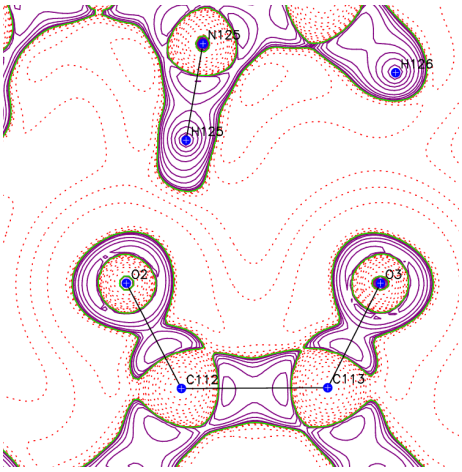

Figure 6.60 Plots of the negative Laplacian, $L(\mathbf{r})$ in the O···H···O planes of 2:1 2,4-lutidine chloranilic acid molecular complex. Positive contours – solid purple line; negative contours – dotted line. The contour levels are at -1.0×10^{-3}, $\pm 2.0 \times 10^{n}$, $\pm 4 \times 10^{n}$, $\pm 8 \times 10^{n}$ (n = -3, -2, -1, 0, +1, +2) eÅ^{-5}

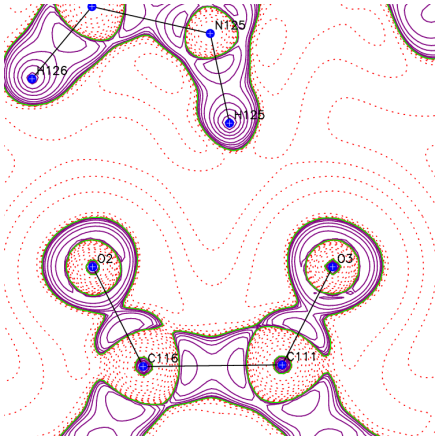

Figure 6.61. Plots of the negative Laplacian, $L(\mathbf{r})$ in the O···H···O planes of 1:1 2,5-lutidine chloranilic acid. Positive contours – solid purple line; negative contours – dotted line. The contour levels are at -1.0 x 10^{-3}, ±2.0 x 10^{n}, ±4 x 10^{n}, ± 8 x 10^{n} (n = -3, -2, -1, 0, +1, +2) eÅ^{-5}

The Laplacian maps of the chloranilic acid molecular plane were also plotted for the singly and doubly deprotonated molecules (Figure 6.62 and 6.63). They all show similar trends of the charge distribution around the atoms.

The Laplacian for the 2:1 3,4-lutidine chloranilic acid molecular complex which posses high thermal motion at the C124 N125 C126 and H125 atoms were also plotted in the plane of these atoms (Figure 6.64). A charge concentration can be observed around the H125 atom and a more spherical density compared with the charge density around the other H atoms of the lutidine chloranilic acid molecular complexes (Figure 6.62 and 6.63). The C126-N125 bond shows charge depletion at the N125 part of the bond. The N125-C124 bond also shows charge depletion, but this time at the C124 part of the bond.

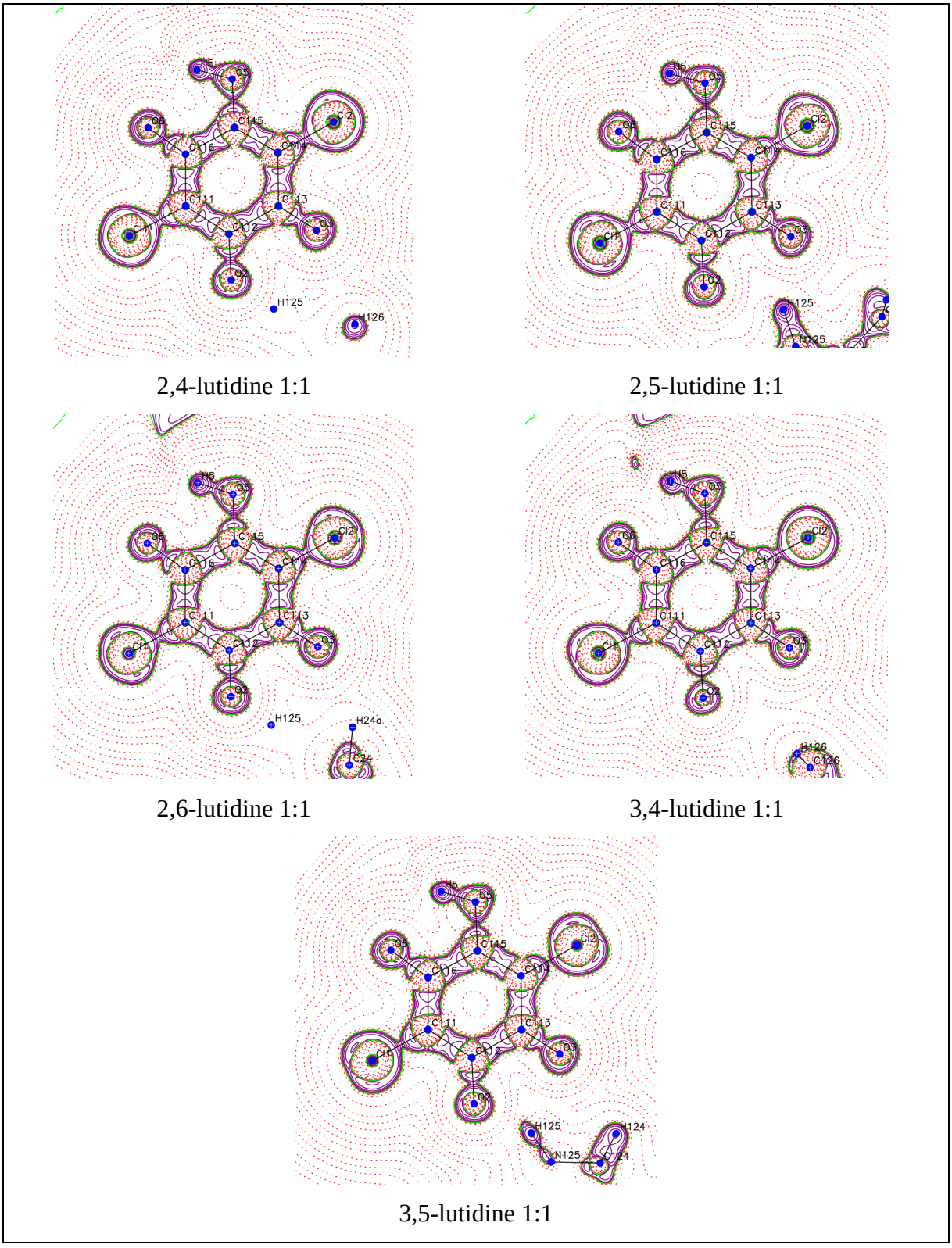

Figure 6.62. Plots of the negative Laplacian, $L(r)$ in the chloranilic acid molecule plane of 1:1 lutidine chloranilic acid molecular complexes. Positive contours – solid purple line; negative contours – dotted line. The contour levels are at -1.0×10^{-3}, $\pm 2.0 \times 10^{n}$, $\pm 4 \times 10^{n}$, $\pm 8 \times 10^{n}$ (n = -3, -2, -1, 0, +1, +2) eÅ^{-5}

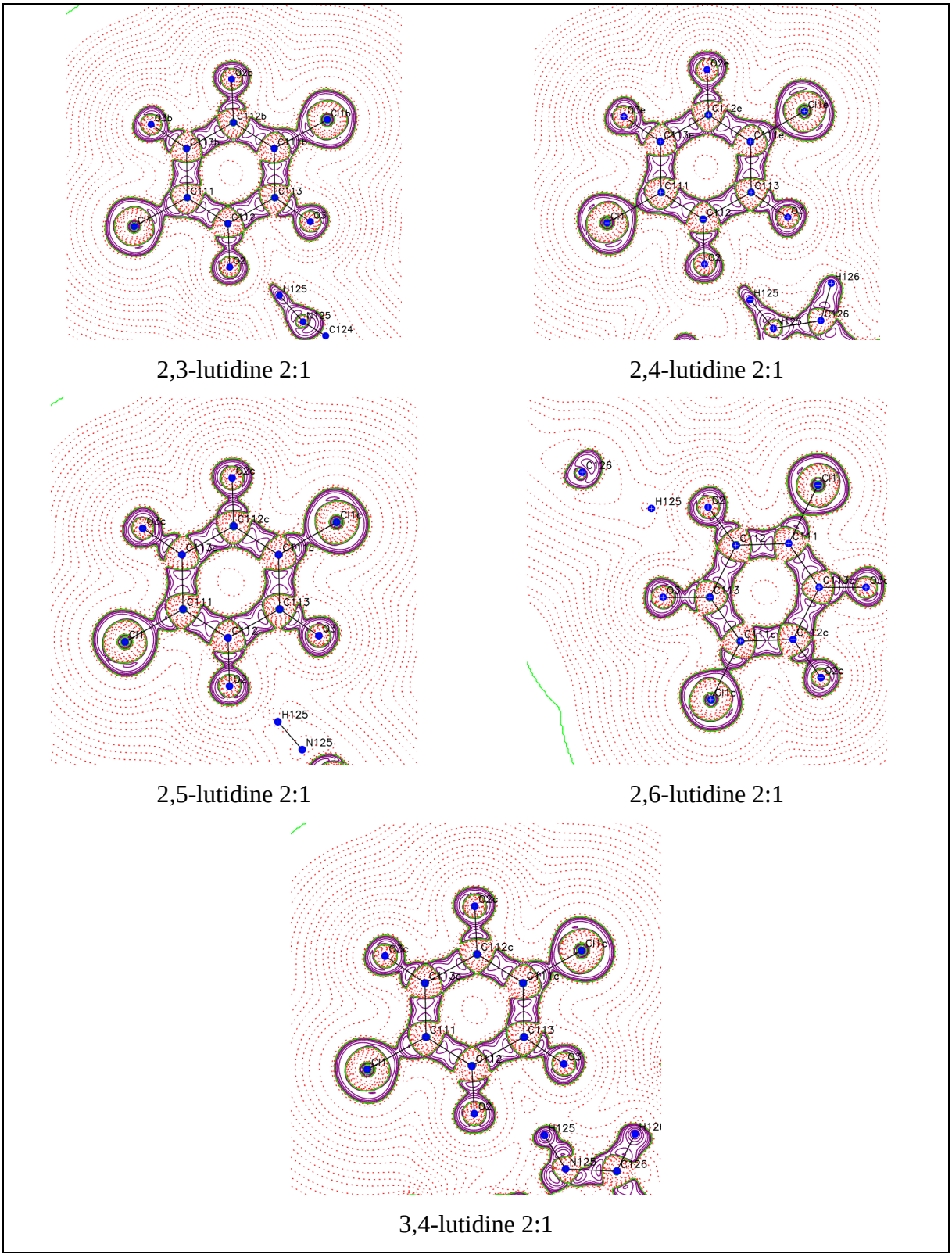

Figure 6.63. Plots of the negative Laplacian, $L(r)$ in the chloranilic acid molecule plane of 1:1 lutidine chloranilic acid molecular complexes. Positive contours – solid purple line; negative contours – dotted line. The contour levels are at -1.0 x 10^{-3}, ±2.0 x 10^{n}, ±4 x 10^{n}, ± 8 x 10^{n} (n = -3, -2, -1, 0, +1, +2) eÅ^{-5}

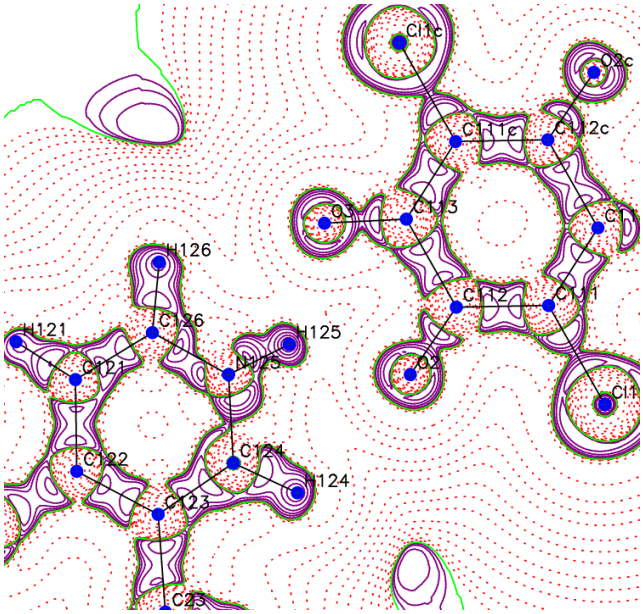

Figure 6.64. Plots of the negative Laplacian, $L(r)$ in the N125···O3···O2 plane of 2:1 3,4-lutidine chloranilic acid molecular complexes. Positive contours – solid purple line; negative contours – dotted line. The contour levels are at -1.0 x 10^{-3}, ±2.0x 10^{n}, ±4 x 10^{n}, ± 8 x 10^{n} (n = -3, -2, -1, 0, +1, +2) e Å^{-5}

6.5.6. Atomic net charge calculations

The atomic net charge using the Bader's QTAIM[58] method implemented in the XD[49] program was calculated for selected atoms in the chloranilic acid singly and doubly deprotonated molecules. These calculations were made with the aim to investigate the difference in terms of the charge distribution in both the single and doubly deprotonated chloranilic acid molecules. The results are listed in Tables 6.21 and 6.22. In the 1:1 stoichiometry, the O3 atom involved in the localised double bound shows higher charge compared with the O2 atom where the charge is delocalised. For the 2:1 cases, the charge on both O2 and O3 atoms are more equal. The C111 atom was expected to be more charged compared to C114 (Scheme 6.3) from a bond length argument. However, this happens only for 2,6-, 3,4-, and 3,5- lutidine, whereas for 2,4- and 2,5-lutidine, C114 is more charged compared with C111. There are no specific trends for C111 in the two different stoichiometries studied.

Table 6.21. Experimental Atomic Charges Q_{QTAIM} (e) for the 1:1 lutidine chloranilic acid molecular complexes

	1 :1 Q_{QTAIM}									
	C111	C112	C113	C114	C115	C116	O2	O3	O5	O6
2,4-	0.0149	0.669	0.799	0.008	0.433	0.697	-0.864	-0.955	-0.923	-0.881
2,5-	-0.005	0.704	0.698	-0.065	0.501	0.675	-0.797	-0.918	-1.017	-0.813
2,6-	-0.052	0.656	0.812	-0.040	0.455	0.766	-0.894	-0.941	-1.002	-0.810
3,4-	-0.023	0.680	0.756	0.104	0.470	0.721	-0.827	-0.970	-1.015	-0.838
3,5-	-0.060	0.787	0.809	0.020	0.403	0.738	-0.815	-0.912	-0.937	-0.843

Table 6.22. Experimental Atomic Charges Q_{QTAIM} (e) for the 2:1 lutidine chloranilic acid molecular complexes

	2 :1 Q_{QATM}				
	C111	C112	C113	O2	O3
2,3-	-0.077	0.613	0.724	-0.887	-0.901
2,4-	0.014	0.728	0.812	-0.974	-0.975
2,5-	-0.082	0.585	0.705	-0.885	-0.874
2,6-	-0.023	0.662	0.626	-0.966	-0.958
3,4-	-0.021	0.799	0.620	-0.860	-0.876

6.5.7. Charge density analysis at the BCPs formed between the atoms of the singly and doubly deprotonated chloranilic acid molecules

The ρ at the BCPs observed between the singly and doubly deprotonated chloranilic acid molecules are listed in Tables 6.23 and 6.24. As expected (Scheme 6.3), the ρ at the BCP between the C114 and C115 atoms are higher for all 1:1 lutidine chloranilic acid molecular complexes compared with the other C-C bonds. This indicates denser density of the double C114-C115 bond while for the partially delocalised C111-C112 and C111-C116 the ρ is less dense. For the single C112-C113 and C115-C116 bonds the ρ values are smaller compared with the double and partially delocalised bonds. The same can be observed for the localised C113-O3 double bond with denser density compared with the partially delocalised C112-O2, C116-O6 or the single C115-O5 bond. The ρ are more equal for the C112-O2 and C113-O3 in the 2:1 molecular complexes and smaller in magnitude compared with those of the C112-O2 in the 1:1 stoichiometry. The ρ at the BCPs between the C111 and C112 atoms or C114 and C115 atoms which form partially delocalised bonds are equal in the 2:1 stoichiometry, due to the inversion centre symmetry present. These are smaller in magnitude compared with the ρ at the BCPs between C114 and C115 atoms in the 2:1 stoichiometry. This is however normal as the localised double bonds are shorter compared with the partially delocalised bonds therefore higher density is expected for the localised double bonds.

Table 6.23. The ρ at the BCPs formed between the atoms of the singly deprotonated chloranilic acid molecules

	$\rho(r_b)$[a]				
Bond	2,4-	2,5-	2,6-	3,4-	3,5-
C(111)-C(112)	2.12	2.12	2.12	2.09	2.11
C(112)-C(113)	1.68	1.64	1.64	1.67	1.63
C(113)-C(114)	1.92	1.94	1.94	1.98	1.93
C(114)-C(115)	2.30	2.32	2.33	2.27	2.36
C(115)-C(116)	1.74	1.69	1.73	1.73	1.74
C(116)-C(111)	2.10	2.12	1.08	2.08	2.11
C(112)-O(2)	2.69	2.83	2.77	2.76	2.74
C(113)-O(3)	2.90	2.89	2.97	2.94	2.93
C(115)-O(5)	2.24	2.25	2.31	2.33	2.25
C(116)-O(6)	2.75	2.74	2.78	2.76	2.76

[a] *In units of e Å^{-3}*

Table 6.24. The ρ at the BCPs formed between the atoms of the doubly deprotonated chloranilic acid molecules

	$\rho(r_b)$[a]				
Bond	2,3-	2,4-	2,5-	2,6-	3,4-
C(111)-C(112)	2.11	2.11	2.17	2.14	2.08
C(112)-C(113)	1.67	1.65	1.65	1.67	1.61
C(112)-O(2)	2.71	2.79	2.70	2.70	2.67
C(113)-O(3)	2.81	2.79	2.79	2.81	2.71

6.6. Lattice Energy Calculations

The lattice energies for the chloranilic acid lutidine molecular complexes were estimated using the XD,[49] CRYSTAL09[51] and CLP[52] programs in order to investigate the influence of the position of the methyl groups and different stoichiometries relative to the 'compositional' polymorph stabilities.

The lattice energy calculations obtained using the experimental charge density approach (XD[49] software) for the different models used are listed in Tables 6.25 and 6.26. The initial energy was estimated for the lutidine-chloranilic acid (LC) fragment in case of 1:1 molar ratio; the total energy was obtained by adding the intermolecular interaction energies between the two lutidine chloranilic acid molecules. A variation of the lattice energy with the model used is evident. For the 2:1 molecular complexes, the entire LCL fragment was selected for the initial lattice energy estimation. The intermolecular interaction between lutidines and chloranilic acid in the LCL fragment were added in order to obtain the total lattice energy. As a consequence, the 2:1 molecular complex lattice energies are substantially different in magnitude compared with the 1:1 molecular complexes. The

XD[49] program provides the flexibility of choosing the specific atoms or molecules to be isolated in a lattice energy calculation. When there are more molecules selected in the isolated fragment, the program does not calculate the intermolecular interactions between these molecules. Therefore these should be calculated in a separate run.

The lattice energies obtained using experimental charge density results show a high dependence with the model used with no transferable trend. Therefore, is difficult to make an accurate analysis and interpretation of these results.

Table 6.25 The lattice energy calculations using the experimental charge density approach for the 1:1 chloranilic acid lutidine molecular complexes (kJ/mole).

	E_L (kJ/mole)	E_{int} (kJ/mole)	Sum (kJ/mole)
2,4-lutidine 1:1			
1	-241.07	-229.69	-335.91
2	-252.60	-334.94	-420.07
3	-255.63	-335.74	-423.5
4	-251.9	-332.57	-417.97
5	-254.76	-331.91	-420.71
2,5-lutidine 1:1			
1	-238.81	-253.6	-365.61
2	-248.15	-296.50	-396.4
3	-242.47	-302.41	-544.88
2,6-lutidine 1to1			
1	-170.44	-221.44	-281.16
2	-176.08	-313.1	-332.63
3	-179.56	-323.28	-341.2
3,4-lutidine 1:1			
1	-235.32	-222.00	-346.32
2	-259.37	-289.98	-404.36
3	-267.46	-291.76	-413.34
3,5-lutidine 1:1			
1	-218.35	-200.70	-318.7
2	-234.87	-267.50	-368.62
3	-242.66	-270.10	-337.71

Table 6.26 The lattice energy calculations using the experimental charge density approach for 2:1 lutidine chloranilic acid molecular complexes (kJ/mole).

	E_L (kJ/mole)	E_{int} (kJ/mole)	Sum (kJ/mole)
2,3-lutidine 2:1			
1	-503.36	-459.77	-963.13
2	-486.29	-531.15	-1017.44
3	-478.25	-535.36	-1013.61
2,4-lutidine 2:1			
1	-592.75	-275.08	-867.83
2	-708.65	-291.49	-1000.14
3	-687.04	-470.76	-1157.8
2,5-lutidine 2:1			
1	-544.90	-403.04	-947.94
2	-496.84	-515.64	-1012.48
3	-496.63	-516.75	-1013.38
2,6-lutidine 2:1			
1	-543.55	-406.96	-950.51
2	-523.17	-534.89	-1058.06
3	-515.19	-541.89	-1057.08
3,4-lutidine 2to1			
1	-414.60	-427.76	-842.36
2	-387.22	-459.41	-846.63
3	-380.68	-471.87	-852.55

The fully theoretical results for lattice energies obtained using CLP[52] and CRYSTAL09[51] programs are summarised in Table 6.27 for the 1:1 stoichiometries. For the 2:1 molecular ratio, calculations using the CLP[52] program are not possible due to the presence of half a chloranilic acid molecule in the asymmetric unit. Problems were also found in attributing the charge to the half chloranilic acid molecule in the 2:1 case when CRYSTAL09[51] was used.

The lattice energy calculations for the 1:1 molecular ratio show a discrepancy between the two programs used in terms of the ranking of the relative stabilities of the lutidine chloranilic acid molecular complexes. The CLP[52] program gives the most stable 'compositional' polymorph with the lowest lattice energy for 2,3-lutidine this is followed by 2,5-, 3,4-, 2,4-, 3,5-, 2,6- lutidine. The lattice energy calculations using CRYSTAL09[51] give the most stable 'compositional' polymorphs for 2,6-lutidine, followed by 3,4-, 3,5-, 2,5-, 2,4-, 2,3-lutidine. Both programs show similarity in the magnitude of the lattice energy results. Also there are close values between the different lutidine isomers in the molecular complexes. These results tentatively suggest a minor contribution of the positions of the methyl groups in the lutidine molecules and the relative stabilities of the 'compositional' polymorphs. However, an accurate description of the relative stabilities of the 'compositional' polymorphs is difficult to make due to the discrepancies between the results obtained using the two different fully theoretical programs.

Table 6.27. Lattice energy calculations for the 1:1 lutidine chloranilic acid molecular complexes using the CLP[52] program and CRYSTAL09[51] programs (kJ/mole).

	CLP[52] (kJ/mole)	CRYSTAL09[51] (kJ/mole)
2,3-lutidine 1:1	-634.0	-594.7
2,4-lutidine 1:1	-592.8	-595.5
2,5-lutidine 1:1	-598.8	-596.0
2,6-lutidine 1:1	-589.0	-600.4
3,4-lutidine 1:1	-593.4	-599.7
3,5-lutidine 1:1	-590.4	-597.0

6.7. Conclusions

New 1:1 molecular complexes of chloranilic acid with 2,3- and 3,5- lutidine and a 2:1 3,4 – lutidine and a new hydrate form of 2:1 2,4- lutidine with chloranilic acid were found. Molecular complexes containing neutral chloranilic acid coexisting with deprotonated CA^- were also found for 2,4- and 3,5-lutidine. In the 1:1 molecular complexes, the chloranilic acid is only singly deprotonated and in the 2:1 molecular complexes each chloranilic acid loses both protons. In both the 1:1 and 2:1 molecular complexes, the chloranilic acid and lutidine molecules are linked by N-H···O bifurcatedhydrogen bonds apart from in the 1:1 2,3-lutidine chloranilic acid complex where no bifurcated hydrogen bond was observed. In the 1:1 complexes, there are additional O-H···O hydrogen bonds linking dimers of chloranilic acid molecules, forming LCCL units. In the 2:1 complexes only three molecules are present in the hydrogen bonded unit (LCL).

For the 1:1 ratio molecular complexes, the lutidine ring lies almost coplanar with the chloranilic acid ring in the case of the 2,3-, and 2,5-lutidines, whereas for the 2,4- 2,6-, 3,4- and 3,5-lutidines, the LCCL unit is twisted. In the case of the 2:1 molecular complexes the lutidine ring lies in the same plane as the chloranilic acid in the 2,4- and 3,4-lutidine complexes, whereas for 2,3-, 2,5- and 2,6-lutidine complexes, the LCL unit is twisted. Therefore, no consistency between the stoichiometry and the position of the lutidine molecule relative to the chloranilic acid ring was observed apart from for 2,6-lutidine. In this case, the two methyl groups are situated next to the NH group creating steric repulsions which dictate the twisted position of the lutidine molecule relative to the chloranilic acid ring in both 1:1 and 2:1 complexes. The twisted and coplanar positions of the lutidine and chloranilic acid rings are significantly influenced by other weak interactions with the surrounding units.

In case of 1:1 lutidine chloranilic acid molecular complexes, five crystal structures were collected using high resolution X-ray diffraction: 2,4-,2,5-,2,6-,3,4- and 3,5-lutidine with chloranilic acid. For 2:1 molar ratio molecular complexes five out of the six possible crystal structure: 2,3-,2,4-,2,5-, 2,6- and 34-lutidine with chloranilic acid were collected using high resolution X-ray diffraction. These data collected were analysed for the first time using an experimental charge density approach.

The results from the multipole refinement reveal the influence of the strategy used in the refinements to the observation of BCPs in the molecular graphs. Consistency with the model used was observed only for both stoichiometries of the 2,4-lutidine chloranilic acid molecular complexes.

The different delocalisation of the charge in the single and doubly deprotonated chloranilic acid molecules were also confirmed from the deformation density and Laplacian plots.

The lattice energy of the chloranilic acid lutidine molecular complexes were estimated using XD,[49] CRYSTAL09[51] and CLP[52] programs. The results obtained using the experimental charge density approach show a high dependence of the lattice energies on the multipole model used. These dependencies were also observed in the others chapters. The relative stabilities of the molecular complexes in the 1:1 molecular ratio are also difficult to estimate using fully theoretical programs where no consistency between the two programs was obtained regarding the relative stabilities of the molecular complexes. Therefore, an accurate description on the influence of the position of the methyl groups in the different molecular complexes studied is difficult to make.

References

1. G. M. J. Schmidt, *Pure Appl. Chem.*, 1971, **27**, 647-678.
2. C. B. Aakeröy, N. R. Champness and C. Janiak, *CrystEngComm*, 2010, **12**, 22-43.
3. M. Nishio, *CrystEngComm*, 2004, **6**, 130–158.
4. C. A. Hunter, K. R. Lawson and J. Perkins and C. J. Urch, *J. Chem. Soc., Perkin Trans.*, 2001, **2**, 651–669.
5. L. Brammer, G. Mínguez Espallargas and S. Libri, *CrystEngComm*, 2008, **10**, 1712-1727.
6. P. Metrangolo, T. Pilati and G. Resnati, *CrystEngComm*, 2006, **8**, 946–947.
7. K. Rissanen, *CrystEngComm*, 2008, **10**, 1107–1113.

8. S. Samai and K. Biradha, *CrystEngComm*, 2009, **11**, 482–492.
9. P. Metrangolo, T. Pilati, G. Terraneo, S. Biella and G. Resnati, *CrystEngComm*, 2009, **11**, 1187.
10. V. Thalladi, B. S. Goud, V. J. Hoy, F. H. Allen, J. A. K. Howard and G. R. Desiraju, *Chem. Comm.*, 1996, 401-402.
11. P. Vishweshwar, A. Nangia and V. M. Lynch, *CrystEngComm*, 2003, **5**, 164-168.
12. N. Shan, A. D. Bond and W. Jones, *Tetrahed. Lett.* 2002, **43**, 3101-3104.
13. C. B. Aakeröy and A. M. Beatty, *Aust. J. Chem.*, 2001, **54**, 409-421.
14. M. Müller, X. Zhang, Y. Wang and R. A. Fischer, *Chem. Comm*., 2009, 119-121.
15. S. S. Iremonger, P. D. Southon and C. J. Kepert, *Dalton Trans*., 2008, 6103-6105.
16. H. Li, M. Eddaoudi, M. O'Keeffe and O. M. Yaghi, *Nature*, 1999, **402** 276-279.
17. O. M. Yaghi, G. Li, and H. Li, *Nature*, 1995, **378**, 703-706.
18. T. Sakaki, M. Inoue, S. Senda and K. Tomita, *Biochem. Biophys. Res. Comm*., 1978, **83**, 21.
19. M. Polito, E. D'Oria, L. Maini, P. G. Karamertzanis, F. Grepioni, D. Braga and S. L. Price, *CrystEngComm*, 2008, **10**, 1848.
20. C. Gatti and P. Macchi, Modern Charge-Density Analysis, Springer Dordrecht *Heidelberg London New York, Chapter **16**, Charge densities and crystal Engineering*, M. A. Spackman, 2012.
21. S. L. Childs, G. P. Stahly and A. Park, *Molec. Pharm.*, 2007, **4**, 323-338.
22. B. R. Bhogala, S. Basavoju and A. Nangia, *CrystEngComm*., 2005, **7**, 551-562.
23. B. Sarma, N. K. Nath, B. R. Bhogala and A. Nangia, *Cryst. Grow. Des*., 2009, **9**, 1546-1557.
24. K. S. Huang, D. Britton, M. C. Etter and S. R. A. Byrn, *J. Mater. Chem*., 1997, **7**, 713-720.
25. T. Murata, Y. Morita, Y. Yakiyama, K. Fukui, H. Yamochi, G. Saito and K. Nakasuji, *J. Am. Chem. Soc.*, 2007, **129**, 10837-10846.
26. E. K. Andersen, *Acta Cryst.*, 1967, **22**, 188.
27. E. K. Andersen, *Acta Cryst*., 1967, **22**, 191.
28. M. S. Adam, A. Parkin, L. H. Thomas and C. C. Wilson, *CrystEngComm*, 2010, **12**, 917-924.
29. K. Molčanov and B. Kojić-Prodic, *CrystEngComm*, 2010, **12**, 925-939.
30. Md. B. Zaman, M. Tomura and Y. Yamashita, *Chem. Comm.*, 1999, 999.
31. K. Gotoh, R. Ishikawa and H. Ishida, *Acta Cryst*. *E*, 2006, **62**, 4738.
32. De-Jun Yang and Shao-hua Qu, *Acta Cryst*. *E*, 2006, **62**, 4720.
33. H. Ishida and S. Kashino, *Acta Cryst*. *C*, 2001, **57**, 476.

34. K. Gotoh, T. Asaji and H. Ishida, *Acta Cryst. C*, 2007, **63**, 17.
35. H. Ishida and S. Kashino, *Acta Cryst. C*, 1999, **55**, 1714.
36. F. H. Allen, *Acta Cryst. B*, 2002, **58**, 380-388.
37. H. Ishida and S. Kashino, *Acta Cryst. C*, 1999, **55**, 1714.
38. S. Horiuchi, R. Kumai and Y. Tokura, *Chem. Comm.*, 2007, **23**, 2321-2329.
39. D. A. Haynes, Z. F. Weng, W. Jones and W. D. S. Motherwell, *CrystEngComm*, 2009, **22**, 254-260.
40. M. Schmidtmann and C. C. Wilson, *CrystEngComm*, 2008, **10**, 177-183.
41. D. A. Haynes, W. Jones and W. D. S. Motherwell, *CrystEngComm*, 2006, **8**, 830-840.
42. Lin-Heng Wei, *Acta Cryst. E*, 2007, **63**, 368.
43. M.S. Adam, *An investigation of hydrogen bonded molecular systems using X-ray and neutron diffraction. PhD thesis, University of Glasgow*, 2009.
44. Zvi Rappoport: *CRC Handbook of Tables for Organic Compound Identification, Third Edition, CRC Press, Boca Raton, Florida,* 1984, ISBN 0-8493-0303-6, p. 438.
45. Md. K. Kabir, H. Tobita, H. Matsuo, K. Nagayoshi, K. Yamada, Keiichi Adachi, Y. Sugiyama, S. Kitagawa and S. Kawata, *Cryst. Grow. Des.*, 2003, **3**, 791-798.
46. H. R. Blessing, *J. Appl. Cryst.*, 1997, **30,** 421-426.
47. A. Altomare, G. Cascarano, C. Giacovazzo and A. Guagliardi, *J. Appl. Cryst.*, 1994, **27**, 435.
48. L. J. Farrugia, *J. Appl. Cryst.*, 2012, **45**, 849-854.
49. A. Volkov, P. Macchi, L. J. Farrugia, C. Gatti, P. R. Mallinson, T. Richter, T. Koritsanszky, *XD-2006*, 2006, http://xd.chem.buffalo.edu/.
50. Ø. A. Madsen, *J. Appl. Cryst*., 2006, **39**, 757-758.
51. (a) A. D. Becke, *Phys. Rev. A*, 1988, **38**, 3098; (b) A. D. Becke, *J. Chem. Phys.*, 1993, **98**, 5648; (c) C. Lee, W. Yang and R. G. Parr, *Phys. Rev. B*, 1988, **37**, 785. (d) P. J. Stephens, J. F. Devlin, C. F. Chabalowski and M. J. Frisch, *J. Phys. Chem.*, 1994, **98**, 11623.
52. R. Dovesi, R. Orlando, B. Civalleri, C. Roetti, V. R. Saunders, and C. M. Zicovich-Wilson, *Z. Kristallogr.*, 2005, **220**, 571; R. Dovesi, V. R. Saunders, C. Roetti, R. Orlando, C. M. Zicovich-Wilson, F. Pascale, B. Civalleri, K. Doll, N. M. Harrison, I. J. Bush, P. D'Arco, and M. Llunell, CRYSTAL09 (CRYSTAL09 User's Manual. University of Torino, Torino, Italy, 2009).
53. A. Gavezzotti, *New J. Chem*., 2011, **35**, 1360-1368.

54. G. Dutkiewicz, H. S. Yathirajan, Q. N. M. H. Al-arique, B. Narayana and M.Kubicki, *Acta Cryst*. *E*, 2010, **66**, 497.
55. G. Gilli and P. Gilli, *J. Mol. Struct* , 2000, **552**, 1.
56. J. A. Kanters, A. Schouten, A. J. M. Duisenberg, T. Glowiak, Z. Malarski, L. Sobczyk, E. Grech, *Acta Cryst*. *C*, 1991, **47**, 2148.
57. K. Molčanov, I. Sabljic, B. Kojic-Prodic, *CrystEngComm,* 2011, **13**, 4211.
58. R. F. W. Bader, *Atoms in Molecules: A Quantum Theor.*, Oxford: Claredon Press.

7. $[Ni(en)_3]^{2+}(NO_3^-)_2$ (en = 1,2-diaminoethane) complex

7.1. Introduction

The general aim of this project is to study systems which exhibit polymorphism or undergo phase transitions. For this purpose, this chapter will describe a material which undergoes a displacive phase transition.

The coordination complex $[Ni(en)_3]^{2+}(NO_3^-)_2$ (en = 1,2-diaminoethane) (**6**) has been identified as a material which undergoes a displacive phase transition around 109 K, involving a change of space group from $P6_322$ (**6a**) above the transition temperature to $P6_522$ (**6b**) below.[1] As a practical application it has been suggested as being a suitable material for a liquid-nitrogen cryo-calibrant.[1]

The first crystal structure of **6a** was reported at room temperature by Swink *et al.*[2] in 1960 and re-examined by Korp *et al.*[3] in 1980, again at room temperature. The phase transition of the $[Ni(en)_3]^{2+}(NO_3^-)_2$ complex was first identified by Farrugia *et al.* (2002).[1] Both phases crystallise in the hexagonal crystal system with the $P6_322$ space group for the 123 K phase and $P6_522$ or $P6_122$ corresponding to the 100 K phase. The X-ray data for both phases were re-examined recently using Mo *Kα* radiation and also using an aluminium filter to remove the low-energy contaminant photons.[4] The crystallographic data for the phases of **6** (obtained from the present experiment) are summarised in Table 7.1. The corresponding reference codes from the previous determinations in the CSD are also noted in this table, as well as the measurement temperature.

The extremely accurate data for the two phases of **6** obtained by high resolution X-ray diffraction (θ_{max} = 50°) as part of this work will be presented. More accurate determinations of the hydrogen atom positions were provided for both phases by neutron diffraction measurements. The crystal structure of the **6a** phase was also examined using synchrotron radiation. Periodic and aperiodic single point calculations were performed and the derived topological parameters were compared with the best experimental multipole refinements. The lattice and intermolecular interactions energy of the phases of **6** were used in evaluating the thermodynamically most stable phase – as mentioned in Chapter 1, this should be the phase obtained at the lower temperature.

Table 7.1. Summary of the crystallographic data of the two phases of **6**, above and below the 109 K phase transition temperature

Phase	**6a**	**6b**
CSD ref. code	TEANIN (RT)[2]	YUXZIBO03(100K)[4]
	TEANIN01 (RT)[3]	YUXZIBO04 (100K)[4]
	YUXZIBO (173K)[4]	
	YUXZIBO01(RT)[4]	
	YUXZIBO02(RT)[4]	
	YUXZIBO05(RT)[4]	
Temp of present data collection	123 K	100 K
SP	$P6_322$	$P6_122$
a/ Å	8.8305(9)	8.8246(2)
c/ Å	11.0816(17)	33.1433(9)
V/Å^{-3}	748.35(16)	2235.20(9)
Z	2	6
ρ/g cm^{-3}	1.611	1.618

**The presented data were collected at 100K*

7.2. Experimental and Theoretical

7.2.1. Sample preparation

The racemic labile coordination complex $[Ni(en)_3]^{2+}(NO_3^-)_2$ (en = 1,2-diaminoethane) was prepared as described previously in the literature[1] using a mixture of an aqueous solution of $Ni(NO_3)_2$ and a slight stoichiometric excess of ethylenediamine. The resultant deep-purple solution was allowed to evaporate in air. Suitable crystals for X-ray and neutron diffraction were obtained within 7-8 hours as the solution became concentrated. The homochiral crystals obtained contained either the Δ or Λ isomer of the tris-chelate cation, as the racemic complex spontaneously resolves on crystallisation.

7.2.2. Data collection and Conventional (Spherical atom) refinement

Single crystals of suitable size were selected, prepared and cooled to 123 K and 100 K on the diffractometer, using an Oxford Cryosystems Cryostream cooling device, in order to measure the two phases. High resolution X-ray data were collected for each of the two phases, **6a** and **6b**, on a Bruker-Nonius Kappa CCD diffractometer (Mo K_α radiation) over a period of one week for each data collection. The integration of intensities was performed using the DENZO[5] software. The effects of the absorption were corrected using the local

program GAUSSIAN.[6] The observed reflections were merged using SORTAV.[7] The structures were solved using SIR92[8] and refined initially in the spherical-atom formalism with full-matrix least squares on F^2. Non-hydrogen atoms were refined with anisotropic displacement parameters. Structure solution refinements were performed using the WinGX[9] package of crystallographic programs. The two phases of the Λ isomer were obtained. The structure of the **6a** phase was also measured using two different synchrotron sources: Diamond – beamline I19 and Soleil – CRYSTAL beam line. In both cases the Δ isomer was studied. The data collected at Diamond were integrated using three different software packages: D*TREK, Bruker ApexII and CrysAlisPro, in order to evaluate which data integration gives the best refinement. When the CrysAlisPro program was used for integration, a SADABS[10] absorption correction was also applied. The Soleil data were integrated using CrysAlisPro and no SADABS[10] absorption correction was applied in this case.

Neutron diffraction data were collected for two different crystal samples of $[Ni(en)_3]^{2+}(NO_3)_2$ at 120 (±2) K, and 100K on the SXD instrument[11] at the ISIS spallation neutron source, using the time-of-flight Laue diffraction method. A total of eleven frames, each containing information from eleven detectors, were collected, with a typical frame exposure time of 3.5 h (600 μA h) at 120 K and ~6 h (1000 μA h) at 100 K. Reflection intensities were reduced to structure factors using standard SXD procedures, as implemented in the computer program SXD2001.[12] Refinements were carried out using SHELXL97[13] using anisotropic displacement parameters for all atoms, including the H atoms.

The details of data collections and refinements for the data collected on X-ray laboratory and synchrotron sources, along with the neutron data, are given in Tables 7.2.-7.3. For the synchrotron and neutron data the same unit cell was used as those obtained initially from laboratory X-ray data collection, to allow for the scaling of adps for the H atoms between the neutron and X-ray data.

Table 7.2. Experimental crystallographic data for $[Ni(en)_3]^{2+}(NO_3^-)_2$ (en = 1,2-diaminoethane) complex, **6a**, at 123K

Compound formula	$C_6H_{24}N_8NiO_6$	$C_6H_{24}N_8NiO_6$	$C_6H_{24}N_8NiO_6$	$C_6H_{24}N_8NiO_6$
Temperature / K	123	123	123	123
M_r	363.00	363.00	363.00	363.00
Space group	$P6_322$	$P6_322$	$P6_322$	$P6_322$
Crystal system	Hexagonal	Hexagonal	Hexagonal	Hexagonal
a/ Å	8.8305(9)	8.8305(9)	8.8305(9)	8.8305(9)
c/Å	11.0816(12)	11.0816(12)	11.0816(12)	11.0816(12)
V/Å^{-3}	748.35(1)	748.35(1)	748.35(1)	748.35(1)
Z	2	2	2	2
D_{calc}/g cm^{-3}	1.61	1.60	1.60	1.61
F(000)	384	-	384	384
Radiation	Mo Kα	TOF neutron	Synchrotron	Synchrotron
λ/Å	0.71073	0.42-7.64	0.4859	0.45760
μ(Mo-K_a)/mm^{-1}	1.338	0.222	0.46	0.36
Crystal size/mm	0.13x0.35x0.56	2.0x2.0x8.0	0.05x0.09x0.09	0.05x0.10x0.10
θ range/deg	2.7-50.1	8.2-84.0	1.8-32.1	1.7-30.2
Max sin(θ)/ λ	1.07	0.13	1.09	1.09
No. of data used for merging	216602	260774	160272	241239
No. of unique data	2641	17583	2701	2700
hkl range	$0 \le h \le 16$	$-23 \le h \le 23$	$0 \le h \le 16$	$0 \le h \le 16$
	$0 \le k \le 9$	$-23 \le k \le 21$	$0 \le k \le 9$	$0 \le k \le 9$
	$-23 \le l \le 23$	$-19 \le l \le 11$	$-23 \le l \le 24$	$-23 \le l \le 24$
R_{int}	0.0438	-	0.0668	0.0945
R_σ	0.0240	0.0383	0.0461	0.0355
Spherical atom refinement				
No. of data in refinement	2641	17583	2701	2700
No. of refined parameters	49	70	51	51
Final *R* [$I > 2\sigma(I)$]	0.019	0.074	0.021	0.030
R_w [$I > 2\sigma(I)$]	0.049	0.196	0.053	0.076
Goodness of fit *S*	1.118	1.052	1.041	1.039
Extrema in residual map	-0.482 → 0.807eÅ^{-3}	-1.995 → 2.821fmÅ^{-3}	-0.541→ 1.451eÅ^{-3}	-1.330 → 0.569eÅ^{-3}
Max shift/esd in last cycle	0.000	0.000	0.000	0.001
Multipole refinement				
No. of data in refinement	2590	-	2587	2562
No. of refined parameters	100	-	100	100
Final *R* [$I > 3\sigma(I)$]	0.0142	-	0.0158	0.0210
R_w[$I > 3\sigma(I)$]	0.0218		0.0199	0.0239
Goodness of fit *S*	1.5323	-	0.9366	1.0859
Extrema in residual map/ eÅ^{-3}	-0.439→0.253	-	-0.292 → 0.262	-0.308→0.773
Max shift/esd in last cycle	0.644920E-05	-	0.941417E-05	0.249359E-05

Table 7.3. Experimental crystallographic data for $[Ni(en)_3]^{2+}(NO_3)_2$ (en = 1,2-diaminoethane) complex, **6b**, at 100K

Compound formula	$C_6H_{24}N_8NiO_6$	$C_6H_{24}N_8NiO_6$
Temperature / K	100	100
M_r	363.00	363.00
Space group	$P6_122$	$P6_122$
Crystal system	Hexagonal	Hexagonal
a/ Å	8.8246(2)	8.8246(2)
c/Å	33.1433(9)	33.1433(9)
V/Å^{-3}	2235.20(1)	2235.20(1)
Z	6	6
D_{calc}/g cm^{-3}	1.62	1.62
F(000)	1152	-
Radiation	Mo Kα	TOF neutron
λ/Å	0.71073	0.42-7.64
μ(Mo-K_a)/mm^{-1}	1.344	0.224
Crystal size/mm	0.14x0.32x0.52	2.0x2.0x8.0
θ range/deg	2.7-51.6	2.7-81.5
Max sin(θ)/ λ	1.1	0.12
No. of data used for merging	260774	20302
No. of unique data	8379	1848
hkl range	$0 \le h \le 16$	$-10 \le h \le 0$
	$0 \le k \le 9$	$0 \le k \le 22$
	$-72 \le l \le 73$	$0 \le l \le 57$
R_{int}	0.0387	0.1726
R_σ	0.0262	0.0662
Spherical atom refinement		
No. of data in refinement	8379	1848
No. of refined parameters	145	204
Final *R* [$I > 2\sigma(I)$]	0.020	0.072
R_w [$I > 2\sigma(I)$]	0.055	0.161
Goodness of fit *S*	1.042	1.018
Extrema in residual map	-0.575 →0.428 eÅ^{-3}	-1.719 →2.189 fmÅ^{-3}
Max shift/esd in last cycle	0.002	0.000
Multipole refinement		
No. of data in refinement	8197	-
No. of refined parameters	278	-
Final *R* [$I > 3\sigma(I)$]	0.0166	-
R_w [$I > 3\sigma(I)$]	0.0221	
Goodness of fit *S*	1.3664	-
Extrema in residual map/ eÅ^{-3} (all data)	–0.282→0.350	-
Max shift/esd in last cycle	0.542436E-04	-

7.2.3. Multipole refinement

The multipole refinements were performed using the XD package.[14] The multipole expansion was truncated at the octupole level for all non-H atoms, apart from the Ni atom for which the refinement of hexadecapoles were allowed. Five different multipole refinements were carried out for both phases. The first refinement (model 1), for **6a**, was performed applying extensive chemical constraints with an imposed local 32 point symmetry at the Ni atom, local 3-fold axis symmetry to the N atom of the nitrate group, and local mirror plane symmetry to the N and C atoms of the cation. For the **6b** phase, local 2-fold axis symmetry was applied for the Ni atom and local mirror plane symmetry for the N atom of the nitrate group and the N and C atoms of the cation. The results from these refinements were used to estimate the H-atom adps by the Madsen method using the SHADE web interface.[15] The calculated adps for the H-atoms were used in a subsequent refinement (model 2) as fixed parameters. In the final cycles (model 3) the multipole constraints were released. The same refinement strategies were adopted for the case where the adps for the H atoms were obtained from the scaled X-ray and neutron data (models 4 and 5). The hydrogen distances obtained from the neutron experiments were used in all refinements. Multipole populations and *k* parameters were grouped in all refinements according to the chemical similarity of the atoms. The initial charges were set and kept fixed to 2+ for Ni atoms and 1– for each nitrate group.

The tabulated scattering factors for both the $4s^0$ and $4s^2$ populations were tested in the case of the Ni atom, in order to examine the best fit obtained for the neutral Ni atom and the Ni^{2+} ion scattering factors and confirm the charge assigned to the Ni atom. These were applied to the multipole refinement of theoretical single point gas phase calculations (see below, Table 7.4.). The residual density map shows the lowest values for the deepest hole in the case of the neutral Ni atom. However, the highest peak shows lower values when the 4s population was set to 0, while the R(%) is also lower for the $4s^2$ multipole refinement. Therefore it is hard to make a clear distinction between the two $4s^0$ and $4s^2$ electrons population based on the modelling of the diffraction data. In the present study the 4s population for Ni atom was fixed at 2.0 and is not varied in the final model.

Table 7.4. The residual electron density peaks and R(%) summary for the different charge scattering factor refinements tested on phase **6a** using the theoretical structure factors derived from Gaussian03[9] wave function calculations.

	Multipole refinement of theoretical single point gas phase calculations	
Scattering factor	Ni $4s^2$	$Ni4s^0$
Highest peak	0.167	0.155
Deepest hole	-0.184	-0.268
R(%)	0.0035	0.0036

7.2.4. Theoretical calculations

Gas-phase single point calculations were performed using the DFT method. The Wachters+f[16] basis set was used for the Ni atom, with def2-TZVP basis set employed for all remaining atoms. The subsequent topological analyses were performed using the AIMPAC[17] program. Theoretical structure factors were computed from the resultant wave-functions and used in a multipole refinement within XD,[14] where all thermal parameters were set to zero and all positional parameters were kept fixed. Periodic single point calculations were also performed using the CRYSTAL09[18] program with the DFT method and the B3LYP[19] functional. The Wachters+f[16] basis set was used for the Ni atom and 6-31G** for the remaining atoms. The intermolecular interaction energies were calculated using the TURBOMOLE6.2[20] software with the DFT method, B97-d[21] functional, and def2-TZVPP[22] basis set.

7.3. Results and discussion

7.3.1. Structural details and description of intermolecular interactions

The structural details of the known phases of **6** have been discussed previously in the literature;[1] a summary of this information is given here. The intermolecular interactions involving hydrogen contacts analysed using the bond distance details obtained from neutron diffraction experiments will be examined at the end of this section.

The ORTEP view of the Λ-$[Ni(en)_3]^{2+}$ cation shows the atomic displacement ellipsoids for all atoms and the numbering scheme used in this study (Figure 7.1). The **6a** phase, which crystallise in the $P6_322$ space group, contain either Δ or Λ isomer and by cooling below 109 K transforms into one of the two subgroups: $P6_522$ for crystals containing the Δ isomer of the chelate, or $P6_122$ for crystals containing the Λ isomer. A modification in the

length of the *c* axis can also be observed due to the phase transition. This axis is three times longer for the **6b** phase. The *a* axis is slightly contracted at the lower temperature.

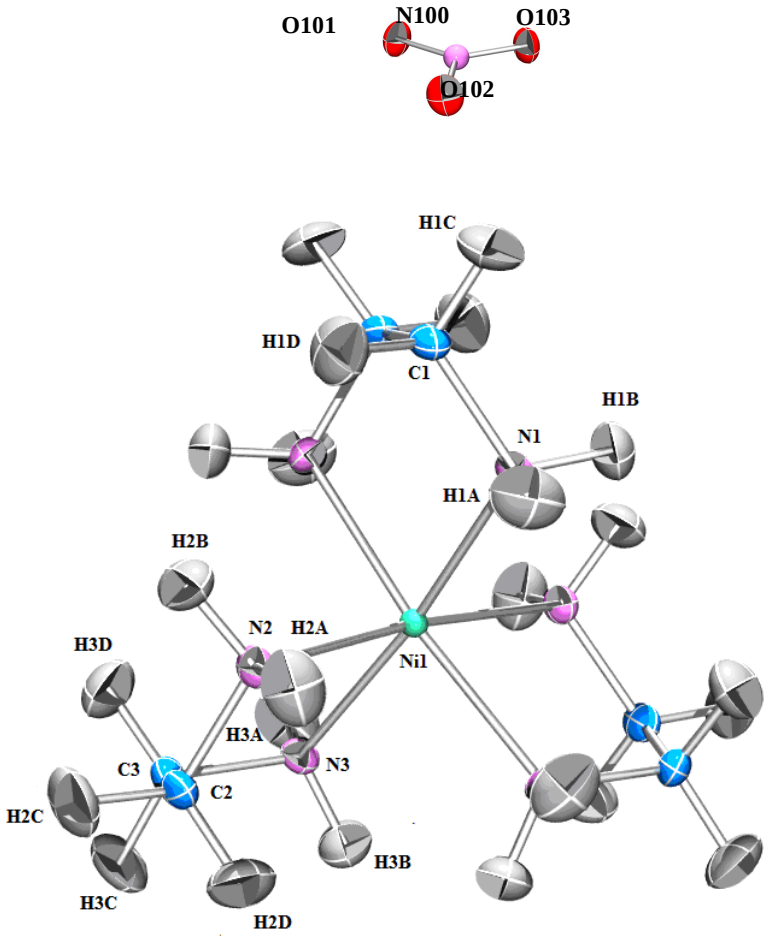

Figure 7.1. *ORTEP* view of the Λ-$[Ni(en)_3]^{2+}(NO_3^-)_2$ isomer at 123K (phase **6a**)

In phase **6a** the Ni atom lies on a special position of 32 symmetry while in **6b** it lies on the twofold symmetry position. The nitrate nitrogen atom lies on a threefold axis in **6a** and in a general position in **6b**. The projections perpendicular and along the *c* axis of the two phases are illustrated in Figure 7.2. It is evident from the unit cell packing views that a displacement of the Ni atoms away from the 3_1 axis occurs in the $P6_122$ phase (**6b**, Λ isomer). For the $P6_322$ (phase **6a**), the displacement of the Ni atom, away from the 3-fold axis, can be also seen from this view.

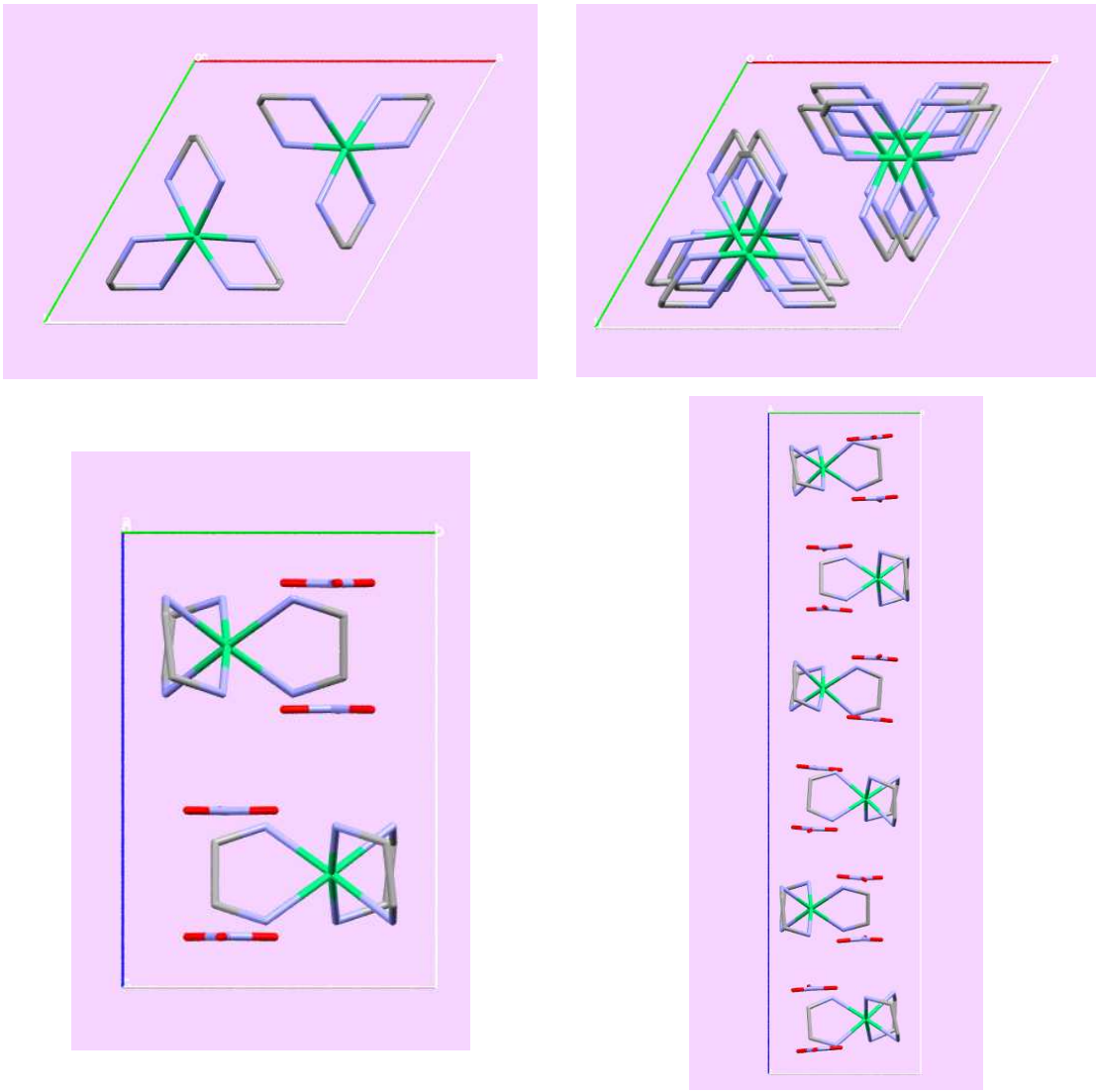

Figure 7.2. The packing motif in the $[Ni(en)_3]^{2+}(NO_3^-)_2$ complex at 123 K (left, **6a**) and 100 K (right, **6b**).

The molecular structure of the cation remains substantially similar in both phases. The superposition of the cations emphasises the very good structural agreement between them (Figure 7.3). The Ni-N distances at 100 K lie between 2.1399(4) Å and 2.1359(4) Å and at 123 K they are 2.1348(4) Å. A high degree of similarity can be also observed between the N-C-C-N torsion angles within the bidentate N ligand: at 100K these are in the range of 54.62(6) to 55.53(5)°, while at 123K the unique torsion angle is 54.77(8)°.

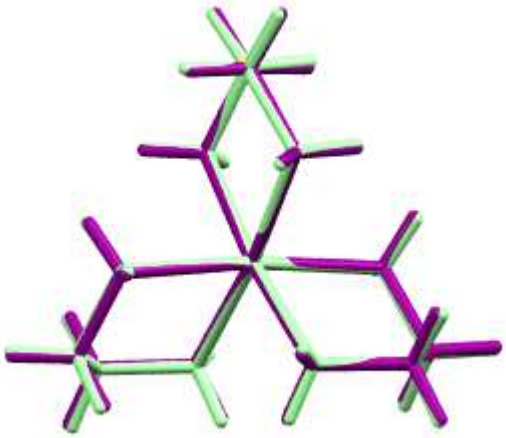

Figure 7.3. Best fit of the $[Ni(en)_3]^{2+}(NO_3^-)_2$ complex measured in its two phases at two different temperatures, 123K (purple; **6a**) and 100K (green; **6b**)

The hydrogen bond interactions present in **6a** and **6b** can be classified according to their H···A (acceptor) distances as moderate and weak interactions. There are two types of donor atoms, C and N of the cation, and three types of acceptor atoms, N and O of the nitrate group and the C atom of the cation. The most important hydrogen bond interactions and the corresponding distances obtained from neutron diffraction measurements are listed in Table 7.5. A slight elongation in the hydrogen bond interactions N1-H1A···O101 and N1-H1B···O103 can be observed in the case of **6b**. However, similar N-H···O hydrogen bond interactions present in **6b** are shorter compared with their equivalents in **6a**. Some of the N-H···O hydrogen bonds have somewhat shorter distances indicating stronger interactions. The length of the C-H···O hydrogen bond interactions varies in **6b** from 2.304(2) to 2.347(12) Å, while the unique distance in **6a** is found to be 2.326(2) Å. Overall, the distances of the hydrogen bonding interactions present in **6a** and **6b** have good similarity.

Table 7.5. Hydrogen bond interactions present in the $[Ni(en)_3]^{2+}(NO_3^-)_2$ complex at 123 and 100 K

Hydrogen bonds present	Neutron H•••A distance (Å)	
	100K	**123K**
N1-H1A•••O101	2.201(8)	2.181(2)
N1-H1A•••O103	2.511(11)	2.542(2)
N1-H1B•••O103	2.354(9)	2.246(2)
N2-H2A•••O101	2.519(10)	
N2-H2A•••O102	2.136(12)	
N2-H2B•••O102	2.166(11)	
N2-H2B•••O103	2.561(10)	
N3-H3B•••O101	2.257(11)	
N3-H3A•••O103	2.202(10)	
C1-H1D•••O102	2.304(10)	2.326(2)
C2-H2D•••O101	2.339(11)	
C3-H3D•••O103	2.347(13)	

7.3.2. Analysis of the electron density distribution

7.3.2.1. Analysis of the topological parameters

The topological parameters from the experimental data were compared with the multipole refinement of the theoretical structure factors of both single point gas phase calculations and periodic calculations. The distance (Å) of the BCP to the nuclei denoted by d_1 and d_2, the electron density ρ, the Laplacian at the BCP and the three eigenvalues λ_1, λ_2, λ_3 of the Hessian matrix for the atoms present in the asymmetric unit of both phases are listed in Tables 7.6-7.7. The topological parameters from the multipole refinement of the synchrotron data integrated using different software are also listed here. The experimental topological parameters are in general in good agreement with the theoretical ones for the **6a** phase. For example, in the case of the Ni(1)-N(1) bond, a relatively minor difference can be observed between the experimental $\rho(r_b)$ and $\nabla^2\rho(r_b)$ and both periodic and gas phase calculations. A slight variation of the value of $\nabla^2\rho$ for the N(100)-O(101) bond from –0.61 to –6.54 $eÅ^{-3}$ can be observed for the experimental data. In some cases, the $\nabla^2\rho$ values are correlated better with the results from the multipole refinement of the theoretical structure factors compared with the results extracted from the wave function. The $\nabla^2\rho$, in case of the atoms involved in the hydrogen bond interactions of the N-H and C-H groups,

are mostly found to vary with the type of integration and source used, giving in some cases a slightly larger difference between experimental and theoretical data, but with no clear evidence of $\nabla^2\rho$ variations in the case of bonds involved in moderate hydrogen bonds.

For phase **6b** the $\nabla^2\rho$ for the experimental data are found to be in good agreement with the results from multipole refinement of the theoretical structure factors. On the other hand, there is considerable discrepancy between the $\nabla^2\rho$ of the experimental data and the results extracted from the wave function.

Table 7.6. Topological Analysis of Bond Critical Points for phase **6a**

Bond	$\mathbf{d_1}^a$	$\mathbf{d_2}^a$	$\boldsymbol{\rho(r_b)}^b$	$\boldsymbol{\nabla^2\rho(r_b)}^c$	$\boldsymbol{\lambda_1}^c$	$\boldsymbol{\lambda_2}^c$	$\boldsymbol{\lambda_3}^c$
Ni(1)-N(1)	1.0138	1.1238	0.46	7.02	-1.49	-1.44	9.95
	1.0036	1.1358	0.42	6.92	-1.31	-1.17	9.39
	1.0086	1.1327	0.41	6.86	-1.28	-1.15	9.28
	0.9998	1.1362	0.42	7.02	-1.29	-0.93	9.24
	1.0235	1.1113	0.47	6.98	-1.63	-1.40	10.01
	1.0044	1.1560	0.37	5.61	-2.26	-1.04	8.92
	1.0028	*1.1338*	*0.437*	*6.6610*	*-1.4130*	*-1.3760*	*9.4490*
	1.0154	*1.1214*	*0.42*	*6.78*	*-1.48*	*-1.44*	*9.70*
N(100)-O(101)	0.6127	0.6380	3.11	-5.95	-26.74	-24.80	45.59
	0.6209	0.6288	3.06	-0.61	-25.79	-22.54	47.72
	0.6167	0.6330	3.06	-1.00	-25.53	-21.97	46.49
	0.6213	0.6281	3.15	-1.48	-27.04	-24.13	49.70
	0.6146	0.6352	3.10	-6.54	-26.94	-23.04	43.44
	0.6249	0.6256	3.09	4.56	-27.81	-22.47	54.84
	0.5995	*0.6507*	*3.237*	*-24.9390*	*-31.8270*	*-28.2890*	*35.1770*
	0.6235	*0.6267*	*3.10*	*-2.95*	*-27.89*	*-25.17*	*50.10*
C(1)-N(1)	0.6440	0.8335	1.70	-8.94	-11.48	-10.68	13.22
	0.6067	0.8713	1.62	-10.59	-11.21	-8.97	9.60
	0.6087	0.8691	1.60	-10.19	-10.72	-9.31	9.84
	0.6482	0.8312	1.79	-9.84	-12.46	-11.12	13.75
	0.6543	0.8240	1.66	-7.11	-11.31	-10.86	15.05
	0.6419	0.8376	1.82	-11.87	-13.92	-10.03	12.08
	0.6056	*0.8716*	*1.739*	*-15.1790*	*-12.6750*	*-12.3970*	*9.8930*
	0.6500	*0.8272*	*1.65*	*-7.28*	*-11.35*	*-11.18*	*15.26*
H(1A)-N(1)	0.2926	0.7255	2.20	-27.02	-27.63	-26.34	26.95
	0.2893	0.7288	2.20	-25.71	-27.53	-26.07	27.89
	0.2862	0.7319	2.10	-21.74	-25.49	-24.24	27.99
	0.2760	0.7436	2.22	-28.82	-28.27	-27.02	26.47
	0.2747	0.7434	2.31	-30.21	-31.09	-29.78	30.66
	0.3238	0.6942	2.18	-20.65	-24.79	-23.18	27.33
	0.2549	*0.7631*	*2.270*	*-42.8520*	*-31.9920*	*-31.1630*	*20.3030*
	0.2752	*0.7428*	*2.13*	*-22.65*	*-27.21*	*-26.17*	*30.72*

Table 7.6 Continued

H(1A)-N(1)	0.2926	0.7255	2.20	-27.02	-27.63	-26.34	26.95
	0.2893	0.7288	2.20	-25.71	-27.53	-26.07	27.89
	0.2862	0.7319	2.10	-21.74	-25.49	-24.24	27.99
	0.2760	0.7436	2.22	-28.82	-28.27	-27.02	26.47
	0.2747	0.7434	2.31	-30.21	-31.09	-29.78	30.66
	0.3238	0.6942	2.18	-20.65	-24.79	-23.18	27.33
	0.2549	*0.7631*	*2.270*	*-42.8520*	*-31.9920*	*-31.1630*	*20.3030*
	0.2752	*0.7428*	*2.13*	*-22.65*	*-27.21*	*-26.17*	*30.72*
H(1B)-N(1)	0.2953	0.7243	2.17	-25.60	-26.67	-25.81	26.88
	0.2897	0.7294	2.19	-25.22	-27.10	-26.05	27.93
	0.2850	0.7342	2.09	-21.14	-25.20	-24.24	28.30
	0.2924	0.7297	2.08	-23.88	-25.46	-24.27	25.85
	0.2874	0.7319	2.21	-26.41	-28.33	-27.56	29.49
	0.3263	0.6931	2.13	-20.02	-24.79	-22.80	27.57
	0.2748	*0.7443*	*2.269*	*-37.7530*	*-30.1160*	*-29.2380*	*21.6010*
	0.2982	*0.7211*	*2.15*	*-18.55*	*-25.38*	*-24.45*	*31.28*
H(1C)-C(1)	0.3920	0.7061	1.92	-20.79	-17.70	-17.27	14.18
	0.3697	0.7287	1.85	-20.73	-17.96	-16.81	14.03
	0.3809	0.7174	1.84	-19.21	-17.37	-16.29	14.46
	0.4006	0.6983	1.94	-18.88	-17.05	-16.42	14.59
	0.4201	0.6782	2.01	-21.80	-18.09	-17.81	14.11
	0.3263	0.6931	2.13	-20.02	-24.79	-22.80	27.57
	0.3917	*0.7084*	*1.893*	*-23.5480*	*-18.4210*	*-17.9480*	*12.8210*
	0.3765	*0.7236*	*1.79*	*-15.30*	*-17.00*	*-16.18*	*17.89*
H(1D)-C(1)	0.4170	0.6833	1.77	-18.06	-15.64	-15.16	12.74
	0.4011	0.6995	1.68	-17.15	-15.10	-14.28	12.24
	0.4262	0.6742	1.61	-15.34	-13.82	-13.03	11.51
	0.4336	0.6667	1.73	-14.87	-13.95	-13.63	12.72
	0.4648	0.6356	1.74	-17.54	-14.88	-14.43	11.77
	0.3684	0.7320	1.78	-15.87	-16.33	-15.15	15.61
	0.3904	*0.7075*	*1.901*	*-23.7270*	*-18.5470*	*-18.0850*	*12.9050*
	0.3749	*0.7230*	*1.80*	*-15.38*	*-16.88*	*-16.43*	*17.93*

The order of the lines for each bond is as follows:
1. KappaCCD/DENZO model 4
*2. Diamond/D*TREK*
3. Diamond/CrysAlisPro
4. Diamond/CrysAlisPro sadabs
5. Diamond/Bruker ApexII
6. Soleil/ CrysAlisPro
7. Gas phase calculation - reference density from the wave function (Gaussian03)
8. Gas phase calculation - reference density from the theoretical structure factor (Gaussian03)

[a] In units of Å. [b] In units of e Å^{-3}. [c] In units of e Å^{-5}

Table 7.7. Topological Analysis of Bond Critical Points for phase **6b**

Bond	d_1[a]	d_2[a]	$\rho(r_b)$[b]	$\nabla^2 \rho(r_b)$[c]	λ_1[c]	λ_2[c]	λ_3[c]
Ni(1)-N(1)	1.0184	1.1222	0.44	6.52	-1.56	-1.39	9.47
	1.0044	*1.1360*	*0.432*	*6.5990*	*-1.3890*	*-1.3500*	*9.3380*
	1.0328	*1.1075*	*0.45*	*5.95*	*-1.89*	*-1.88*	*9.72*
Ni(1)-N(2)	1.0124	1.1258	0.44	6.69	-1.56	-1.41	9.67
	1.0033	*1.1341*	*0.439*	*6.6200*	*-1.4230*	*-1.3850*	*9.4280*
	1.0307	*1.1065*	*0.45*	*6.00*	*-1.91*	*-1.90*	*9.81*
Ni(1)-N(3)	1.0213	1.1161	0.45	6.57	-1.66	-1.46	9.69
	1.0028	*1.1343*	*0.439*	*6.6270*	*-1.4160*	*-1.3820*	*9.4250*
	1.0303	*1.1067*	*0.45*	*6.00*	*-1.91 -*	*1.89*	*9.81*
N(100)-O(101)	0.6075	0.6454	3.09	-5.62	-26.15	-24.59	45.11
	0.6008	*0.6514*	*3.219*	*-24.5230*	*-31.5710*	*-28.0620*	*35.1090*
	0.6223	*0.6299*	*3.08*	*-2.22*	*-27.50*	*-24.80*	*50.08*
O(102)-N(100)	0.6145	0.6418	3.19	-4.75	-27.84	-25.25	48.33
	0.6034	*0.6524*	*3.190*	*-23.8710*	*-31.1930*	*-27.7390*	*35.0610*
	0.6269	*0.6289*	*3.07*	*-2.55*	*-27.75*	*-24.80*	*50.00*
O(103)-N(100)	0.6197	0.6304	3.10	-2.75	-26.81	-22.03	46.09
	0.5994	*0.6506*	*3.236*	*-24.9110*	*-31.7850*	*-28.2790*	*35.1530*
	0.6229	*0.6272*	*3.10*	*-2.99*	*-27.96*	*-25.24*	*50.21*
C(1)-N(1)	0.6726	0.8054	1.67	-8.57	-11.57	-10.31	13.32
	0.6076	*0.8696*	*1.744*	*-15.2140*	*-12.7190*	*-12.4680*	*9.9730*
	0.6560	*0.8212*	*1.66*	*-6.92*	*-11.27*	*-11.13*	*15.48*
H(1A)-N(1)	0.2830	0.7382	2.21	-29.62	-27.66	-26.41	24.45
	0.2561	*0.7649*	*2.253*	*-42.1640*	*-31.6100*	*-30.8330*	*20.2790*
	0.2847	*0.7363*	*2.16*	*-23.94*	*-27.15*	*-26.26*	*29.48*
H(1B)-N(1)	0.2769	0.7382	2.24	-31.01	-28.46	-27.57	25.02
	0.2732	*0.7419*	*2.295*	*-38.7250*	*-30.6250*	*-29.7970*	*21.6970*
	0.2919	*0.7232*	*2.15*	*-18.59*	*-25.53*	*-24.65*	*31.59*
C(2)-N(2)	0.5822	0.8963	1.53	-8.53	-9.58	-7.25	8.30
	0.6078	*0.8706*	*1.737*	*-15.1250*	*-12.7100*	*-12.3420*	*9.9270*
	0.6496	*0.8288*	*1.67*	*-7.75*	*-11.65*	*-11.17*	*15.06*
H(2A)-N(2)	0.2878	0.7245	2.18	-28.70	-26.65	-26.18	24.13
	0.2513	*0.7606*	*2.303*	*-44.5790*	*-32.8720*	*-31.9840*	*20.2770*
	0.2755	*0.7364*	*2.23*	*-27.76*	*-29.16*	*-28.15*	*29.55*
H(2B)-N(2)	0.2889	0.7312	2.17	-27.83	-26.10	-25.88	24.15
	0.2741	*0.7459*	*2.262*	*-37.7740*	*-30.0850*	*-29.1740*	*21.4850*
	0.2946	*0.7255*	*2.11*	*-17.35*	*-24.91*	*-23.97*	*31.52*
C(3)-N(3)	0.6832	0.7968	1.79	-10.32	-12.44	-12.11	14.23
	0.6051	*0.8746*	*1.724*	*-14.9120*	*-12.5240*	*-12.1910*	*9.8040*
	0.6497	*0.8301*	*1.65*	*-7.23*	*-11.33*	*-10.94*	*15.05*
H(3A)-N(3)	0.2896	0.7297	2.19	-29.04	-26.68	-26.01	23.65
	0.2559	*0.7632*	*2.263*	*-42.4040*	*-31.8040*	*-30.9030*	*20.3030*
	0.2754	*0.7437*	*2.21*	*-27.82*	*-28.89*	*-27.98*	*29.05*
H(3B)-N(3)	0.2778	0.7457	2.23	-30.07	-28.27	-26.98	25.18

Table 7.7 Continued

	0.2754	*0.7476*	*2.242*	*-36.9950*	*-29.6710*	*-28.7280*	*21.4040*
	0.3007	*0.7223*	*2.21*	*-23.54*	*-27.01*	*-25.89*	*29.36*
H(1C)-C(1)	0.4004	0.7015	1.74	-16.92	-16.33	-14.49	13.89
	0.3915	*0.7085*	*1.892*	*-23.4990*	*-18.3900*	*-17.9270*	*12.8180*
	0.3799	*0.7201*	*1.79*	*-15.32*	*-16.71*	*-16.19*	*17.58*
H(1D)-C(1)	0.3990	0.6963	1.73	-16.15	-15.24	-15.00	14.09
	0.3903	*0.7047*	*1.915*	*-24.0120*	*-18.7200*	*-18.2310*	*12.9390*
	0.3887	*0.7063*	*1.86*	*-18.43*	*-17.61*	*-17.25*	*16.43*
C(3)-C(2)	0.7031	0.8189	1.68	-11.71	-11.03	-10.38	9.70
	0.7592	*0.7617*	*1.741*	*-16.3570*	*-12.7670*	*-12.1700*	*8.5800*
	0.7594	*0.7615*	*1.67*	*-10.22*	*-11.38*	*-10.82*	*11.99*
H(2C)-C(2)	0.3972	0.6991	1.75	-16.85	-16.14	-14.84	14.13
	0.3902	*0.7059*	*1.908*	*-23.8470*	*-18.6400*	*-18.1610*	*12.9540*
	0.3838	*0.7123*	*1.85*	*-17.93*	*-17.59*	*-17.13*	*16.79*
H(2D)-C(2)	0.3795	0.7153	1.85	-18.99	-18.10	-16.30	15.41
	0.3900	*0.7040*	*1.915*	*-24.0400*	*-18.7480*	*-18.2210*	*12.9290*
	0.3752	*0.7188*	*1.82*	*-16.13*	*-17.14*	*-16.66*	*17.66*
H(3C)-C(3)	0.3739	0.7238	1.89	-20.30	-18.63	-17.40	15.72
	0.3901	*0.7069*	*1.906*	*-23.8210*	*-18.6160*	*-18.1570*	*12.9510*
	0.3863	*0.7107*	*1.86*	*-18.21*	*-17.63*	*-17.20*	*16.62*
H(3D)-C(3)	0.3785	0.7189	1.87	-19.89	-18.14	-17.00	15.24
	0.3903	*0.7067*	*1.906*	*-23.8510*	*-18.6200*	*-18.1330*	*12.9020*
	0.3842	*0.7129*	*1.86*	*-18.33*	*-17.65*	*-17.31*	*16.63*

The order of the lines for each bond is as follows:
1. KappaCCD/DENZO model 4
2. Gas phase calculation - reference density from the wave function (Gaussian03)
3. Gas phase calculation - reference density from the theoretical structure factor (Gaussian03)

[a] In units of Å. [b] In units of e Å^{-3}. [c] In units of e Å^{-5}

7.3.2.2. Multipole refinements analysis

Five different multipole model refinements were performed for the X-ray laboratory and synchrotron sources data for **6a**, as described in Section 7.2.3. The results listed in Tables 7.8 and 7.9 show a lower R factor for the unrestricted model (3 and 5) in the case of both **6a** and **6b**. However, the values of minimum and maximum peaks in the Fourier map are almost indistinguishable (Table 7.11). In the absence of clear evidence for improved agreements, the models with lowest R values were analysed in more detail. The topological parameters of the experimental charge density refinements were compared with those from (a) the wave-functions of gas phase, (b) the multipole model based on the refinements of the theoretical structure factors of the gas phase calculation and (c) periodic calculations. A global residual factor (calculated as described in Chapter 2, equation 2.9) was estimated in order to provide a quantitative measure for the fit of the experimental data and theoretical

calculations of topological parameters. Good agreements of the values of ρ between experimental charge density and theoretical calculations results can be seen for both phases and in general when adps for H atoms were used. The $R_{\nabla 2}$ results in case (a) show significantly larger discrepancies between experimental data and theoretical calculations, especially for model 1. On the other hand, as expected, the Laplacian at the BCPs for all bonds present in **6a** and **6b** give better agreements in case (b). An improvement can also be observed when anisotropic displacement parameters for H atoms are used either from SHADE[14] or neutron diffraction experiments. The multipole refinement against the theoretical structure factors obtained from periodic calculations gives noticeably good agreement with the experimental data for models 2-5. The full optimisation of both molecules in the asymmetric unit – Ni-en and nitrate – simultaneously is not possible, therefore only single point calculations were carried out in this study.

Table 7.8. The residual factors of the experimental data vs theoretical data for phase **6a**

(a) Reference density from wave function	**Model**	$\mathbf{R_{values}}$	$\mathbf{R_{\rho}}$	$\mathbf{R_{\nabla 2(\rho)}}$
	1	0.0152	0.0603	0.534
	2	0.0145	0.0509	0.451
	3	0.0143	0.0520	0.456
	4	0.0144	0.0420	0.435
	5	0.0142	0.0438	0.450
(b) Reference density from theoretical structure factor	**Model**	$\mathbf{R_{values}}$	$\mathbf{R_{\rho}}$	$\mathbf{R_{\nabla 2(\rho)}}$
	1	0.0152	0.0153	0.051
	2	0.0145	0.0055	0.171
	3	0.0143	0.0067	0.106
	4	0.0144	0.0038	0.152
	5	0.0142	0.0020	0.119

Table 7.9. The residual factors of the experimental data vs theoretical data for phase **6b**

(a) Reference density from wave function	**Model**	$\mathbf{R_{values}}$	$\mathbf{R_{\rho}}$	$\mathbf{R_{\nabla 2(\rho)}}$
	1	0.0171	0.0514	0.4765
	2	0.0167	0.0361	0.3616
	3	0.0166	0.0303	0.3401
	4	0.0167	0.0406	0.3630
	5	0.0166	0.0342	0.3396
(b) Reference density from theoretical structure factor	**Model**	$\mathbf{R_{values}}$	$\mathbf{R_{\rho}}$	$\mathbf{R_{\nabla 2(\rho)}}$
	1	0.0171	0.0148	0.0631
	2	0.0167	0.0011	0.1426
	3	0.0166	0.0072	0.1820
	4	0.0167	0.0035	0.1400
	5	0.0166	0.0031	0.1820

The spherical and multipole refinements from the synchrotron X-ray sources data have been compared with the X-ray laboratory data in order to reveal any discrepancies between the results from the two type of sources. The R(%) factor resulting from the spherical atom and multipole refinements are lower for the X-ray laboratory data (Table 7.10 and 7.11).

Table 7.10. Spherical atom refinement results for **6a**, comparing the values from X-ray laboratory source and synchrotron sources with different integration programs.

Spherical atom refinement	R(%)
Diamond/D*TREK	2.05
Diamond/CrysAlisPro	2.24
Diamond/CrysAlisPro -sadabs	2.10
Diamond/Bruker - ApexII	2.37
Soleil/CrysAlisPro	3.02
KappaCCD/DENZO	1.91

Table 7.11. The experimental charge density refinements for **6a**, including the R(%) values and the minimum and maximum peaks in the residual map, tabulated for various integration programs.

Model	1	2	3	4	5
KappaCCD/DENZO					
Highest Peak	0.252	0.239	0.247	0.246	0.253
Deepest hole	-0.425	-0.435	-0.432	-0.437	-0.439
R(%)	1.52	1.45	1.43	1.44	1.42
Diamond/D*TREK					
Highest Peak	0.832	0.829	0.846	0.828	0.839
Deepest hole	-0.506	-0.495	-0.498	-0.490	-0.498
R(%)	1.68	1.64	1.59	1.63	1.58
Diamond/CrysAlisPro					
Highest Peak	0.229	0.235	0.225	0.238	0.224
Deepest hole	-0.769	-0.725	-0.665	-0.718	-0.657
R(%)	1.70	1.66	1.59	1.65	1.58
Diamond/CrysAlisPro – sadabs					
Highest Peak	0.242	0.262	0.264	0.260	0.262
Deepest hole	-0.287	-0.295	-0.291	-0.301	-0.292
R(%)	1.71	1.63	1.58	1.62	1.58
Diamond/Bruker - ApexII					
Highest Peak	0.350	0.361	0.361	0.355	0.359
Deepest hole	-0.647	-0.666	-0.655	-0.671	-0.660
R(%)	2.12	2.07	2.00	2.06	1.99
Soleil/CrysAlisPro					
Highest Peak	0.823	0.756	0.775	0.749	0.773
Deepest hole	-0.367	-0.358	-0.319	0.352	0.308
R(%)	2.46	2.22	2.11	2.29	2.10

The lowest R(%) for the synchrotron data was obtained when the D*TREK software was used for integration of the data. Overall there are no major discrepancies between these R(%) values: all of these lie in a range between 2.05 and 3.02% for the spherical atom refinement. As is expected, an improvement in terms of R(%) and residual map peaks was obtained when anisotropic parameters for H atoms are used in the multipole refinements.

On the other hand, it is hard to make a clear distinction between the restricted multipole model and those where the restrictions imposed by local symmetry were released (2 and 3 or 4 and 5).

It should be noted that the highest resolution data were obtained for the synchrotron radiation sources, as high as $\sin\theta/\lambda = 1.5$ Å^{-1}. Because the quality of the synchrotron data at very high angle were not satisfactory (Figure 7.4 - a), they were truncated at the same resolution as the laboratory source data (1.1 Å^{-1}). Therefore a direct comparison can be carried out between the results from the two sources. The scale factor plots (Figure7.4 b,c) and shelx summary included below (Table 7.12), from the synchrotron data integrated with D*TREK software, show a high degree of similarity between the two experiments, but this is the case only when the data were truncated at the same resolution. Hence, it can concluded that for this system, the synchrotron data do not improve the results in terms of the resulting model, with the advantage being only in terms of data collection time. In addition, the R factor obtained from the laboratory radiation source is slightly lower compared with that obtained from the synchrotron sources.

(a)

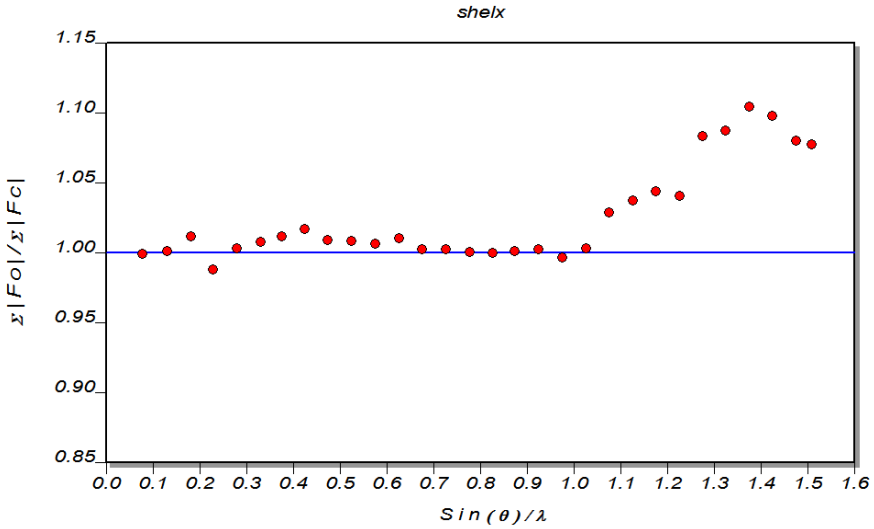

(b)

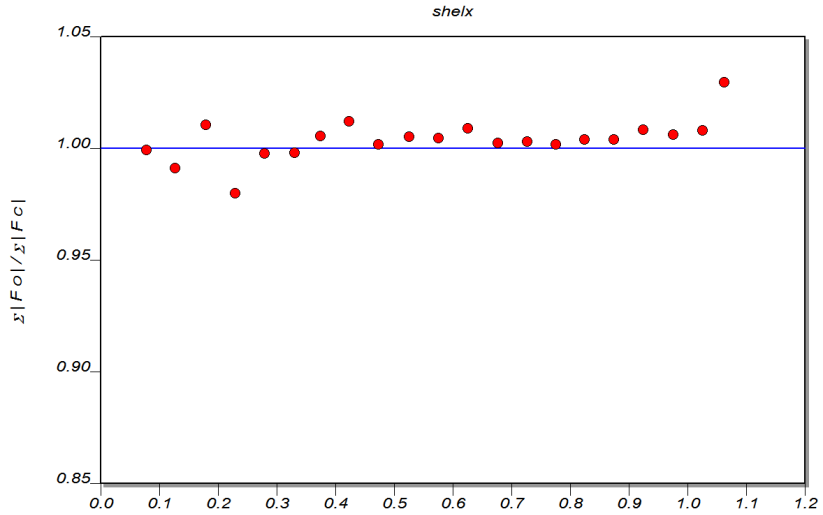

(c)

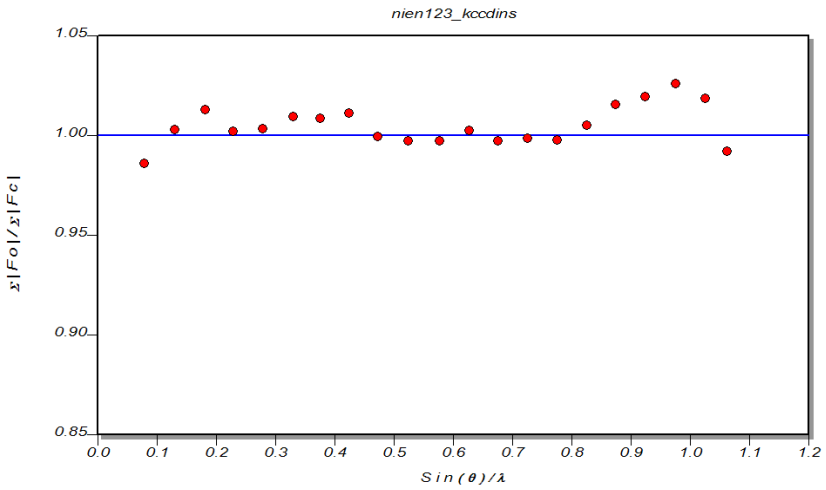

Figure 7.4. Scale factor plots for the various data on **6a** (a) synchrotron data to sinθ/λ =1.519 $Å^{-1}$ and (b) data truncated at sinθ/λ = 1.1 $Å^{-1}$; (c) X-ray laboratory source data at sinθ/λ = 1.1 $Å^{-1}$

Table 7.12 SHELXL final cycle data for the various refinements of **6a**

(a) SHELXL refinement for D*TREK data to sinθ/λ = 1.1 Å^{-1}

No of data	R1	R1 (Fo>4σ(Fo)	wR2	GooF	Flack parameter
2512	0.0212	0.0205 (2440 data)	0.0656	0.704	0.022(0.018)

Analysis of variance for reflections employed in refinement K = Mean[Fo^2] / Mean[Fc^2] for group

Fc/Fc(max)	0.000	0.011	0.019	0.026	0.034	0.043	0.055	0.069	0.096	0.144
Number in group	262	264	227	252	252	262	241	254	245	253
GooF	0.886	0.757	0.908	0.766	0.670	0.620	0.624	0.593	0.580	0.545
K	1.177	1.001	0.983	0.974	0.978	1.003	1.009	1.010	1.023	1.005

Resolution(A)	0.47	0.48	0.50	0.52	0.55	0.59	0.63	0.69	0.79	1.00
Number in group	260	245	251	252	255	244	255	248	249	253
GooF	0.838	0.796	0.714	0.690	0.683	0.593	0.583	0.702	0.680	0.722
K	1.032	1.000	1.014	1.017	1.016	1.009	1.008	1.018	1.010	1.005
R1	0.041	0.038	0.033	0.028	0.025	0.021	0.018	0.021	0.016	0.017

Final difference Fourier

No of unique data	R1 for unique data	Highest peak	Deepest hole
1584	0.0216	0.71 e/A^3	-0.79 e/A^3

(b) SHELXL refinement for reference data (KappaCCD) to sinθ/λ = 1.1 Å^{-1}

No of data	R1	R1 (Fo>4σ(Fo)	wR2	GooF	Flack parameter
2641	0.0198	0.0191	0.0492	1.118	0.0794(0.0085)

Analysis of variance for reflections employed in refinement K = Mean[Fo^2] / Mean[Fc^2] for group

Fc/Fc(max)	0.000	0.016	0.026	0.036	0.045	0.056	0.068	0.083	0.110	0.158
Number in group	266	264	265	265	275	250	263	264	266	263
GooF	1.652	1.231	1.001	0.991	0.941	0.897	0.926	1.098	0.930	1.282
K	1.449	1.095	1.035	0.996	1.002	1.010	0.994	0.994	0.996	1.006

Resolution(A)	0.46	0.48	0.50	0.52	0.55	0.58	0.63	0.69	0.79	1.01
Number in group	268	262	264	264	264	268	258	266	261	266
GooF	1.081	0.945	1.004	1.031	1.261	1.042	0.960	0.994	1.007	1.659
K	0.988	1.019	1.030	1.016	1.008	0.992	0.990	0.995	0.992	1.009
R1	0.042	0.034	0.033	0.028	0.027	0.021	0.016	0.014	0.013	0.015

Final difference Fourier

No of unique data	R1 for unique data	Highest peak	Deepest hole
1599	0.0189	0.81 e/A^3	-0.48 e/A^3

On the other hand, the Fourier maps plotted in the Ni-N-C plane show large differences depending on the software used for integrating the synchrotron data and the X-ray laboratory data for spherical refinements, with the exception of those using CrysAlisPro and CrysAlisPro-sadabs (Figure 7.5). The discrepancies may arise from the different scaling scheme obtained from each individual program. These differences persist also in the multipole refinement (Figure 7.6.) which may be influenced by the quality of the data and the multipole refinement schemes employed.

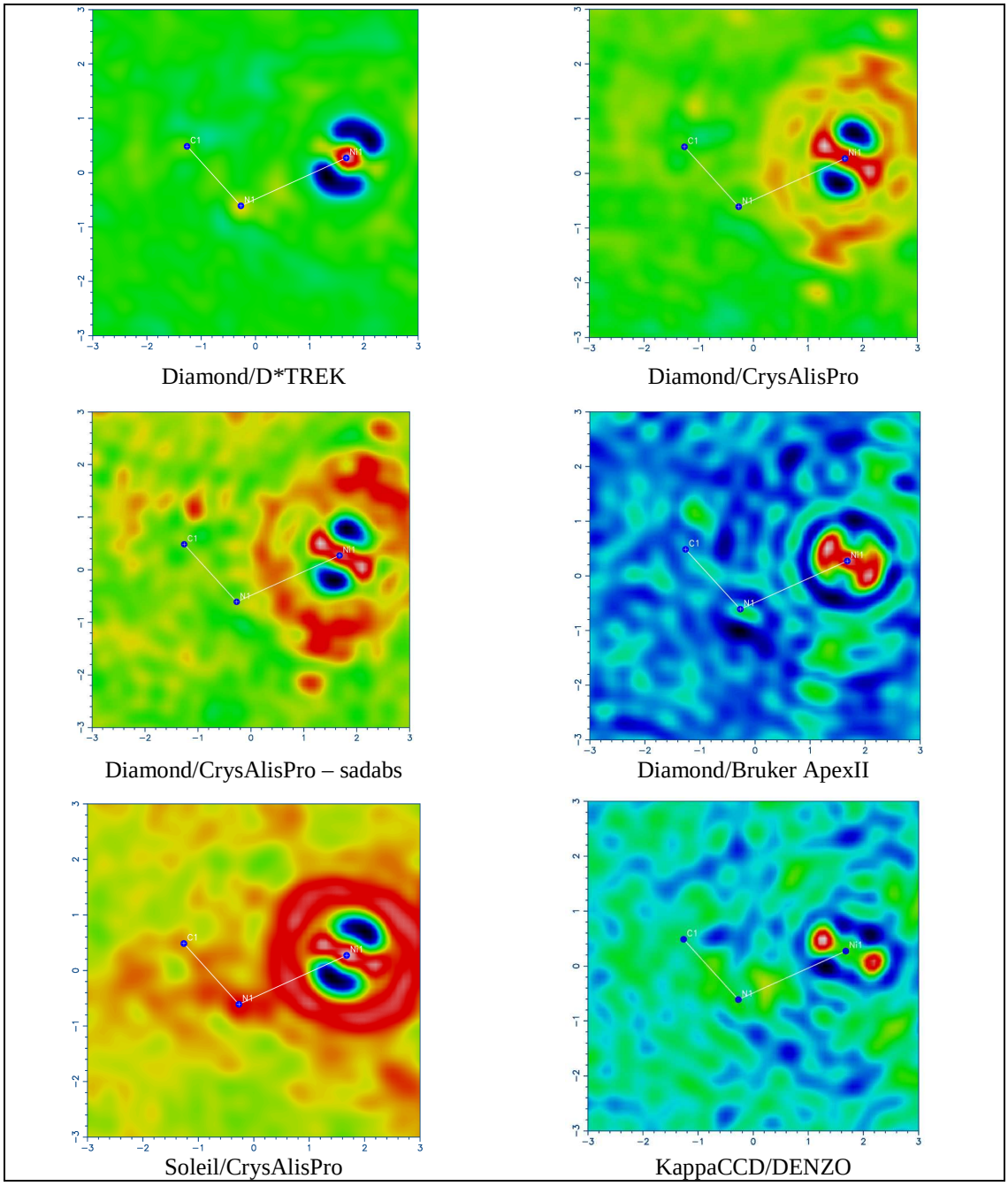

Figure 7.5. Residual density maps of phase **6a** obtained from spherical atom refinements of data integrated by various methods.

To illustrate this, one example is the residual map from the KappaCCD/DENZO data set. Here the residual map looks almost flat with only few peaks, whereas the Soleil/CrysAlisPro residual map from the multipole refinements contains positive charge around the Ni atom. In any case, the deformation density maps look very similar for the various types of experimental data apart for those obtained with Soleil/CrysAlisPro. Some disagreement can also be seen in the experimental charge density deformation maps compared with the theoretical periodic and gas phase calculations. Only two lobes (colour code blue) around Ni atom are found in the experimental data (apart from in the Bruker ApexII data) whereas in the theoretical calculations four lobes are present.

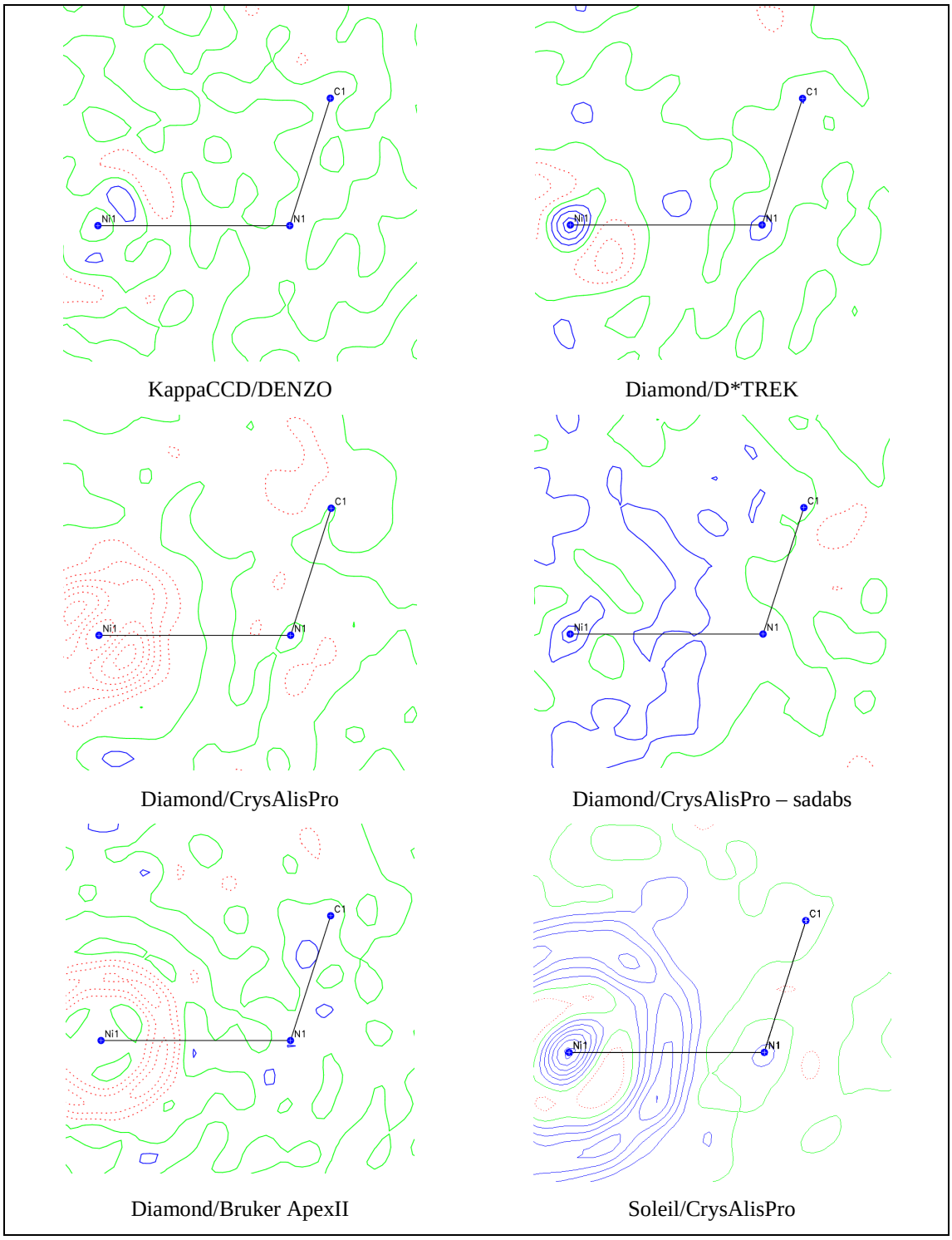

Figure 7.6. Residual density maps of multipole model refinements for various integrations of the data from the two radiation sources obtained for **6a**. Contours level at 0.1 eÅ^{-3}

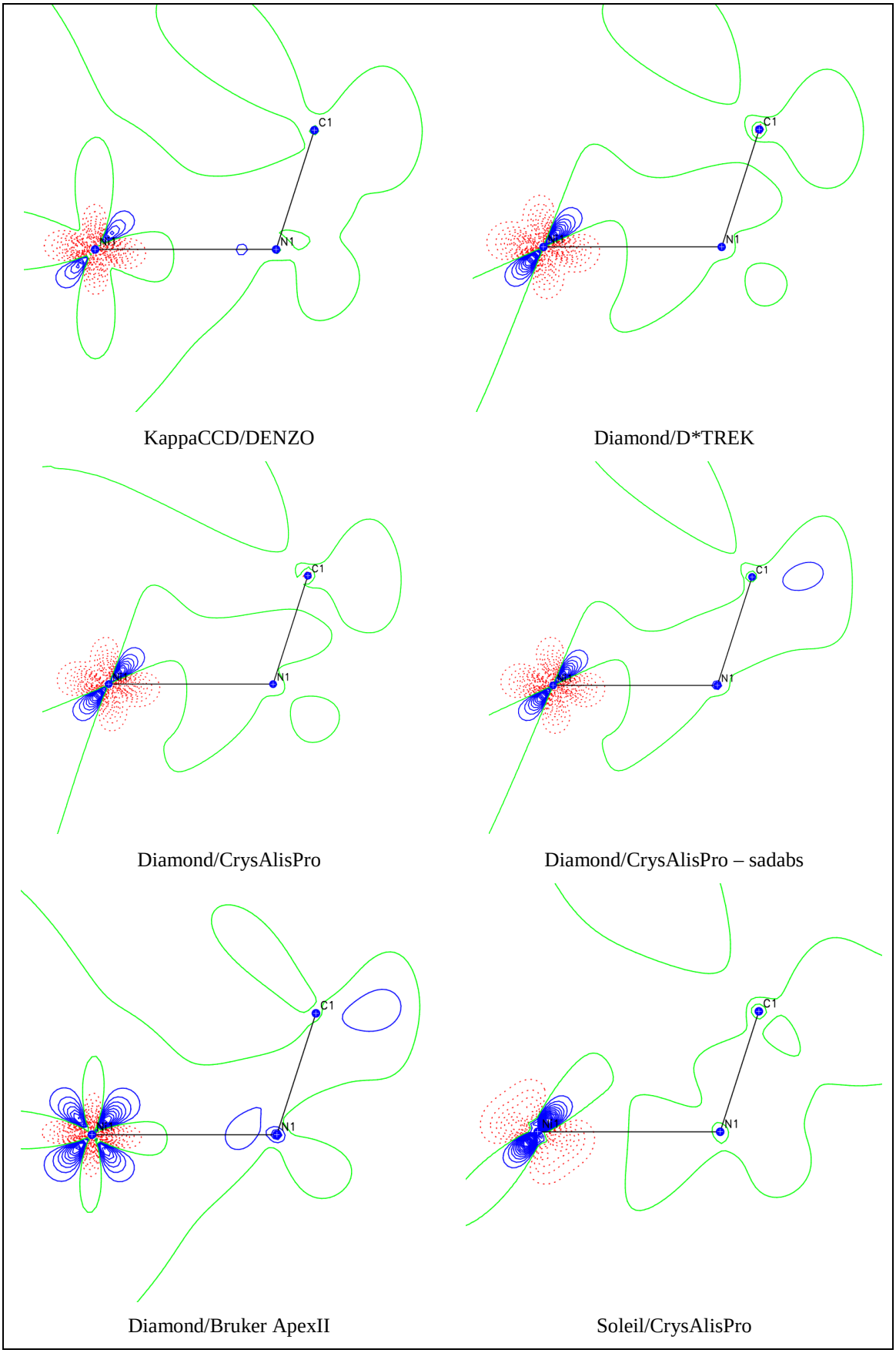

Figure 7.7a. Experimental deformation density maps in the Ni-N-C plane for **6a**. Contours level at 0.08eÅ^{-3}

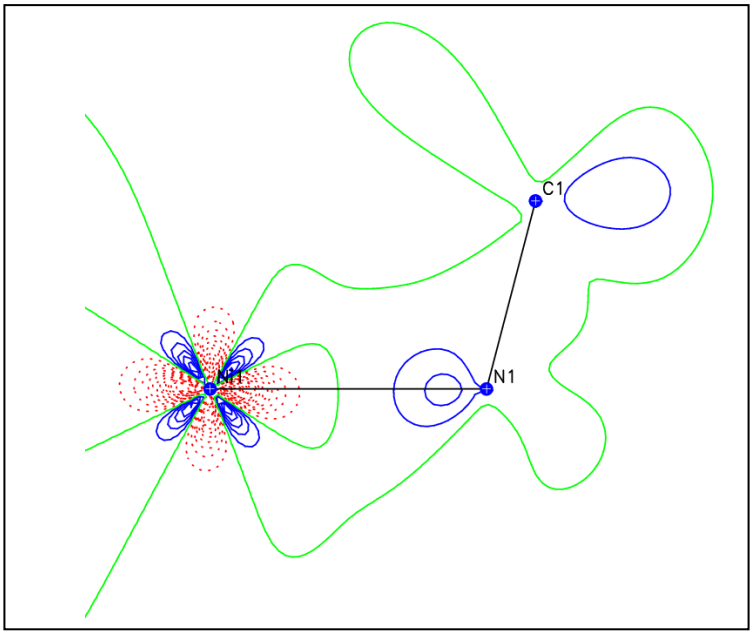

Figure 7.7b. Deformation density maps in the Ni-N-C plane for the theoretical structure factors calculated using CRYSTAL09,[18] for complex **6a**.

The negative Laplacian maps in the Ni-N-C plane resulting from theoretical gas phase calculations and experimental data of **6a** (model 4) were also examined (Figure 7.8.). Good agreement can be observed between the two Laplacian pictures plotted in Figure 7.8 (a) and (b). Clear separation in the 'lone pair' of the N atom can be observed in both the experimental and the theoretical Laplacian maps. The Ni atom shows a cuboidal disposition of charge concentrations (in both cases) that has been experimentally observed in many octahedrally (or pseudo-octahedrally) coordinated transition metals. As is expected from simple ligand-field theory, the eight charge concentrations on the Ni atom maximally avoid the ligand charge concentrations. The six charge concentrations of the N atoms align with the six charge depletions on the Ni atom.

(a)

(b)

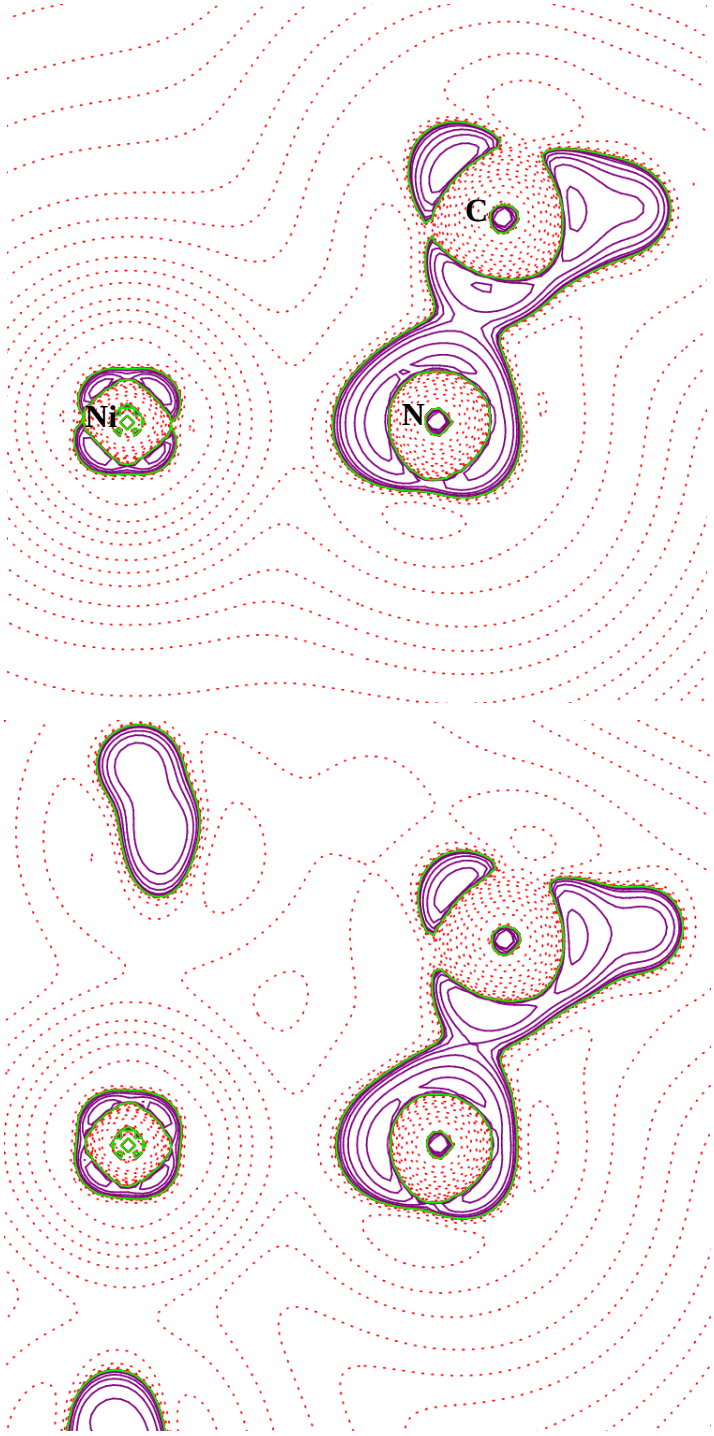

Figure 7.8. The Laplacian plot in the Ni-N-C plane of the $[Ni(en)_3]^{2+}(NO_3^-)_2$ complex phase **6a**, (a) experimental data, (b) theoretical data (Gaussian03[9]).

7.3.3. Lattice and intermolecular interaction energy calculations

The lattice energy calculations and the intermolecular interactions energy results for phases **6a** and **6b** will be analysed in this section. As in the previous chapters, the lattice energy was calculated using both experimental charge density and fully theoretical calculation methods. In this case, the lattice energy was provided only by the periodic calculations using CRYSTAL09[18] program. The lattice energy can not be achieved using the CLP[18]

program when more than two molecules are present in the asymmetric unit. In this case, the entire molecules are not present in the asymmetric unit and to make the calculations feasible, the whole molecules need to be generated. However, applying the corresponding symmetry to generate the entire Ni-en molecule will also result two nitrate molecules. Hence, there will be three molecules in the generated asymmetric unit and this type of calculation is not possible in the CLP program, in which only up to two molecules in the asymmetric unit are allowed. Also CLP[18] can be applied only for crystal systems of lattice symmetry up to orthorhombic and phases **6a** and **6b** crystallise in hexagonal crystal systems.

The lattice energy results calculated using the XD[14] program for phases **6a** and **6b** are summarised in Table 7.13. The E_L term represents the lattice energy of the $[Ni(en)_3]^{2+}(NO_3^-)_2$ fragment. The total lattice energy is obtained by adding to the value of E_L the intermolecular interaction energy (Int. en.) between the cation and nitrate fragments. The **6a** phase shows a considerably lower lattice energy in all models compared with that calculated for **6b** from the X-ray laboratory source data. In the refinements where no adps for H are implemented, substantially higher energy values were obtained for the KappaCCD/DENZO data set for both **6a** and **6b**. Relatively small differences can be noted in the lattice energies resulting from the KappaCCD/DENZO, Diamond/D*TREK and Diamond/CrysAlisPro-sadabs data sets. The lattice energy estimated for the data integrated with Diamond/CrysAlisPro and Diamond/Bruker ApexII gives an unusual higher energy, much closer to those obtained for **6b**, while an unusual lower lattice energy can be observed for the Soleil/CrysAlisPro results, especially for model 3 and 5, compared with all the other synchrotron and X-ray laboratory source data. These experimental charge density lattice energy calculations suggest a high dependence of the results upon the model imposed, the integration software and the radiation source used.

Table 7.13. The lattice energy (kJ/mol) for the phases of **6** calculated for data from X-ray laboratory source and synchrotron radiation sources.

KappaCCD/DENZO		**6a**	
	E_L	Int. en.	Sum
1	-323.45	-542.98	- 866.43
2	-347.35	-595.08	- 942.43
3	-369.49	-612.84	- 982.33
4	-344.52	-592.91	- 937.43
5	-365.14	-608.49	- 973.63
KappaCCD/DENZO		**6b**	
1	-335.77	-411.68	-747.45
2	-374.93	-433.47	-808.40
3	-371.84	-438.58	-810.42
4	-372.14	-433.34	-805.48
5	-369.62	-440.27	-809.89
Diamond/D*TREK		**6a**	
1	-274.96	-543.25	-818.21
2	-318.30	-598.12	-916.42
3	-344.78	-608.27	-953.05
4	-302.32	-587.65	-889.98
5	-337.89	-598.12	-936.01
Diamond/CrysAlisPro		**6a**	
1	-248.67	-539.96	-788.63
2	-232.25	-553.86	-786.11
3	-268.30	-571.65	-839.95
4	-221.31	-550.74	-772.05
5	-262.08	-568.40	-830.48
Diamond/CrysAlisPro - sadabs		**6a**	
1	-414.20	-623.36	-1037.56
2	-359.43	-628.24	-987.67
3	-424.29	-598.91	-1023.2
4	-361.33	-626.95	-988.28
5	-410.18	-606.77	-1016.95
Diamond/Bruker ApexII		**6a**	
1	-207.32	-478.89	- 686.21
2	-207.90	-507.81	- 715.71
3	-262.18	-526.31	- 788.49
4	-198.30	-505.41	- 703.71
5	-255.63	-523.61	- 779.24
Soleil/CrysAlisPro		**6a**	
1	-392.53	-660.26	-1052.79
2	-326.48	-750.37	-1076.85
3	-433.78	-717.90	-1151.68
4	-332.68	-743.43	-1076.11
5	-453.64	-716.38	-1170.02

In order to support and further assess the lattice energy calculations obtained using experimental charge density, single point periodic calculations were performed using the

CRYSTAL09[18] software. The positions of the atoms for both phases were taken from the best multipole refinement model (5). The lattice energy was calculated as described in Chapter 2 and the results are listed in Table 7.14. As mentioned in Chapter 1, it is expected that the most stable phase will be the one obtained at the lowest temperature. The results are not in agreement with this expectation, instead the most stable phase with the lowest lattice energy was found to be **6a**, although the difference between the two phases in terms of lattice energy is only 0.7 kJ/mol. The fully theoretical results show a large discrepancy with the experimental data in the magnitude of the lattice energies, especially for models 2-5. Model 1 shows in general closer agreement with the values from the fully theoretical calculations.

Table 7.14. Lattice energy calculations of the phases of **6** using the CRYSTAL09[18] software (kJ/mol).

	CRYSTAL09[18]
6a	-737.07
6b	-736.37

In addition, for a comparison between the relative stabilities of the phases, all the closer neighbour molecules which show intermolecular interactions with the cation were generated according to their symmetry. For each phase, a central cation is found to be connected to six others through very weak C-H···H intermolecular contacts (Table 7.15 – the neighbour molecules are numbered as 1,2…6), and to eight nitrates through moderate N-H···O and weak C-H···O hydrogen bonds (Table 7.15– the neighbour molecules are numbered as 1,2…8), (Figure 7.9 (a, b)). The intermolecular interaction energies between the cation-cation (repulsive) or cation-nitrate group were calculated using the TURBOMOLE6.2.[20] program at the DFT/B97-d/def2-TZVPP level. As can be seen from Table 7.15, in the case of the **6a** phase, the nitrate groups give an overall lower interaction energy of –4931.3 kJ/mol when compared with the **6b** phase where weaker intermolecular interactions are formed, with a value of –4640.3 kJ/mol. The repulsive cation-cation interactions are found to be stronger in the case of phase **6b**, with a value of 3635 kJ/mol. In terms of the intermolecular interactions of the nearest neighbouring molecules, the most stable phase can be considered to be phase **6a** with the lower overall intermolecular

interaction energy of –1299.06 kJ/mole. This is surprising as the lower temperature phase in normally expected to be the most stable one.

In the **6a** phase, the two nitrate groups sitting above and below the cation will give identical contributions to the intermolecular interaction energy due to the asymmetric unit construction (Figure 10 (a)). All the nitrates surrounding the cation in the lateral position will also give the same intermolecular interaction energy. All the cation intermolecular interactions are the same in **6a** as they are all situated at the same distance from the central cation. The energy of the intermolecular interactions between the cation and the nitrates will give three different contributions, based on the asymmetric unit present in **6b** (Figure 10 (b)).

Table 7.15. The intermolecular interaction energies for the **6a** and **6b** phases

	DFT		**XD**[14]	
	6a	**6b**	**6a**	**6b**
cation-cation				
1	605.3	606.0	628.8	367.5
2	605.4	606.3	628.8	346.3
3	605.8	606.0	628.6	351.8
4	605.2	606.0	628.8	388.9
5	605.3	605.3	628.8	392.7
6	605.2	605.4	628.6	373.7
Sum	3281.5	3635	3772.4	2220.9
cation-nitrate				
1	-691.9	-692.0	-608.4	-440.2
2	-589.6	-521.6	-523.0	-297.4
3	-588.5	-599.2	-522.9	-377.7
4	-588.5	-599.2	-522.7	-290.7
5	-593.1	-522.0	-523.2	-318.8
6	-599.3	-509.2	-525.0	-315.4
7	-588.6	-505.1	-525.3	-301.6
8	-691.8	-692.0	-607.8	-369.6
Sum	-4640.3	-4931.3	-4358.3	-2711.4
Total	-1658.8	-1296.3	-585.9	-490.5

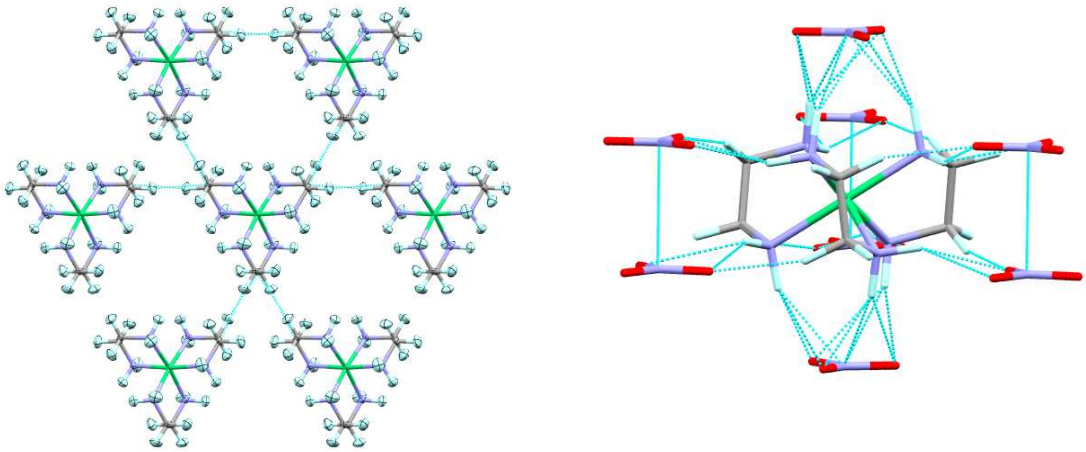

(a) (b)

Figure 7.9 The intermolecular interactions involving neighbouring molecules in the phases of **7,** (a) cation-cation interactions, (b) cation-nitrate interactions.

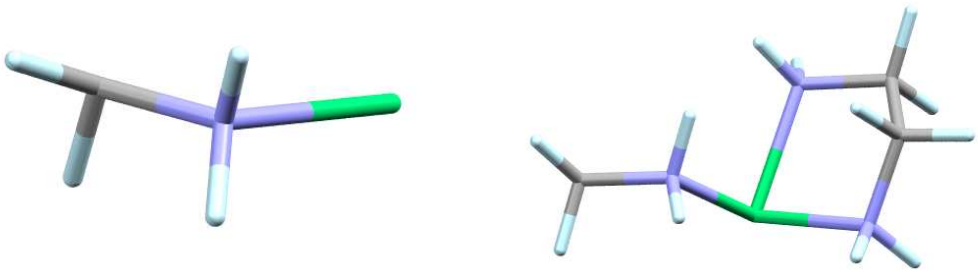

6a **6b**

Figure 7.10. The asymmetric unit present in the **6a** and **6b** phases.

In examining the crystal packing, Figure 7.11 shows by colour codes the asymmetric unit and the atoms obtained by applying the corresponding symmetry for constructing the whole molecules of the **6b** phase. The nitrates sharing the same intermolecular interaction distances are also sorted by colour codes. The nitrate groups located above and below the cation give the stronger intermolecular interactions and are almost identical for the **6a** and **6b** phases with energies of –691.9, –691.8 and –692.0, –692.0 kJ/mol, respectively. These are noted in Table 7.15 as cation-nitrate interactions 1 and 8. Two nitrates located in the lateral position in the **6b** phase have stronger intermolecular interactions (with energies –599 kJ/mol), corresponding to the cation forming the shorter intermolecular hydrogen bond interactions (N-H···O, 2.1506(6) and 2.6073(8) Å, C-H···O 2.2975(8) Å) (Figure 7.11 - nitrate colour code pink). These N-H···O and C-H···O bonds are slightly elongated in the **6a** phase, with equivalent distances of 2.674(1), 2.2402(7) and 2.317(1) Å, respectively, and this is reflected in the intermolecular energy being slightly weaker in this case (–588 kJ/mol). The other nitrate groups located in

the lateral position form weaker intermolecular interactions with slightly longer N-H···O and C-H···O hydrogen bonds in **6b** (Figure 7.11 colour code orange and light blue). On the other hand, despite the N-H···O and C-H···O hydrogen bonds being slightly shorter for the nitrate with the colour code light blue, their intermolecular interactions are found to be weaker (–505.1, –509.2 kJ/mol) compared with those for the orange coded nitrate (–521.6, –522.0 kJ/mol) in which the N-H···O and C-H···O are slightly elongated. However, the difference in these hydrogen bond distances is small, and the differences in the Ni(cation)···N(nitrate) distances, which are shorter for the 'light blue' nitrate (5.337 Å) compared with the 'orange' nitrate molecule (5.427 Å), may also make a contribution to the final intermolecular interaction energy.

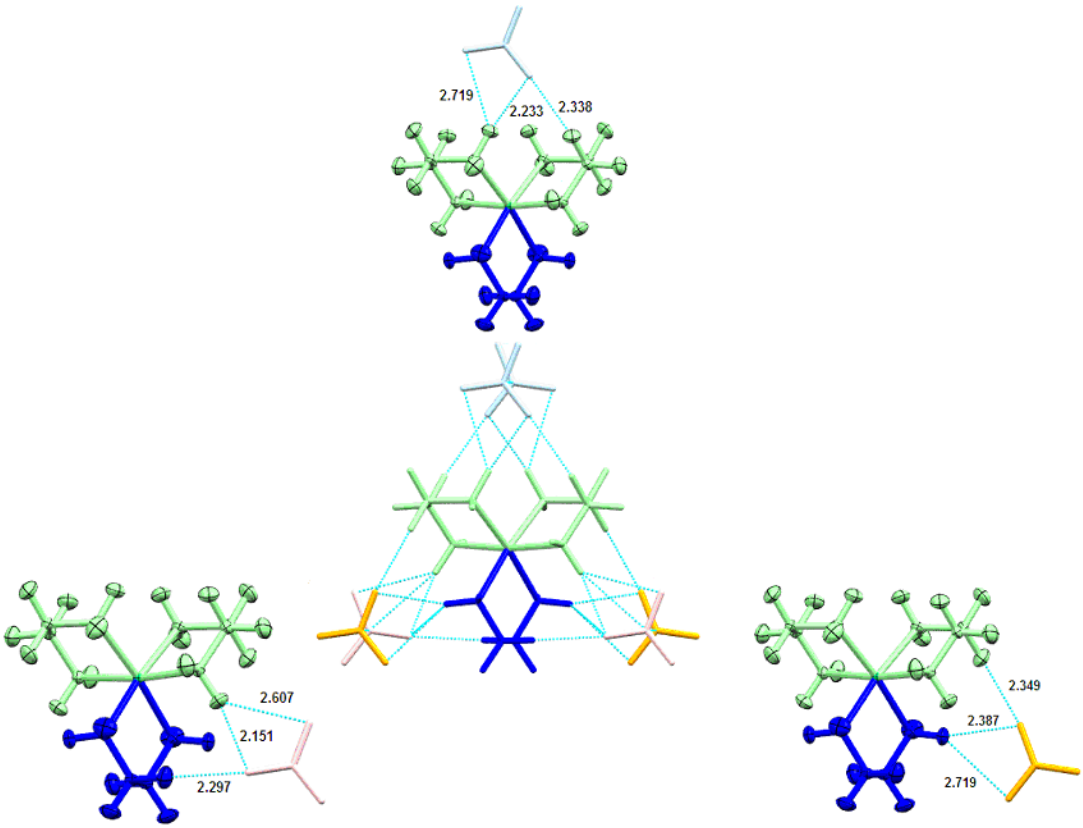

Figure 7.11. The cation-nitrate intermolecular interactions in the **6b** phase, with the asymmetric unit of the cation coloured blue.

The cation-cation interactions are similar for all six surrounding neighbour molecules, which are arranged as shown in Figure 7.12. The cations located along the *a* axis form slightly elongated intermolecular C-H···C contacts (H···C distance of 2.9851(5) Å) compared with the other four cations (2.8795(5) Å and 2.8227(4) Å). On the other hand, the unique C···C intermolecular distances do not mirror this trend, at 3.9082(9) Å for the

cations located along the *a* axis and 3.8964(8), 3.9394(8) Å for the other cation-cation interactions formed. In consequence the intermolecular interaction energies are almost identical between the different neighbours. The unique C-H···C interaction present in the **6a** phase, with length 2.8688(7) Å, gives an intermolecular interaction energy of ~ -605 kJ/mol between the cations. The intermolecular interaction energies were also calculated using the XD[14] program for the best multipole model refinement (5). The results show a considerably larger difference in magnitude compared with the theoretical calculations. Despite this difference the same order of stability between the two phases was obtained.

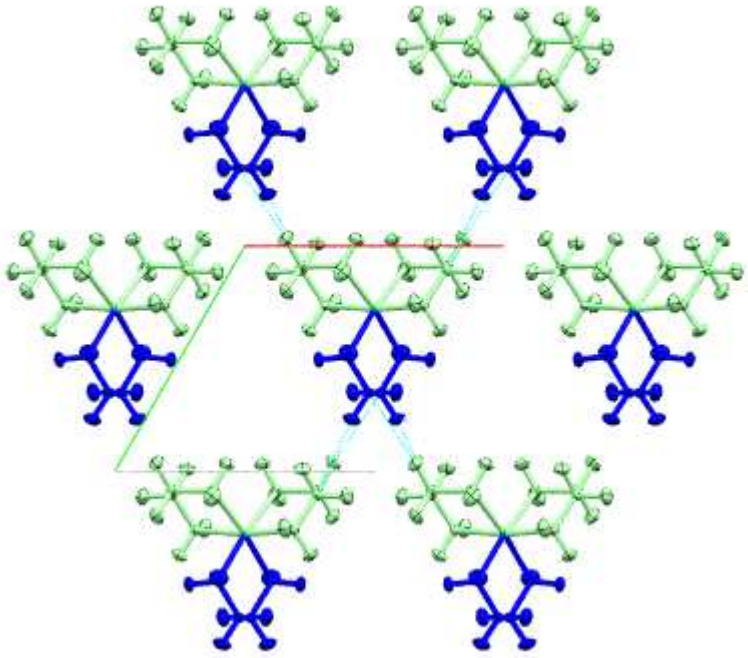

Figure 7.12 The cation-cation intermolecular interactions formed in the **6b** phase.

In order to investigate the contribution of the hydrogen bonds to the stability of the phases of **6**, the energies at the bond critical points were calculated for each intermolecular interaction present for the best multipole model (Table 7.16 – the six cation-cation intermolecular interactions are labelled 1,2,…,6 and the eight cation-nitrate intermolecular interactions present are labelled 1,2,…,8). The intermolecular interaction energy calculated with the TURBOMOLE6.2[20] program shows stronger interactions between the cation-nitrate molecules for the **6a** phase, with the energies at the bond critical points lower for the **6b** phase.

As mentioned above, the cations in **6b** located along the *a* axis with slightly longer C-H···C contacts gives higher (less stabilising) energy at the BCP (−26.25 kJ/mol) compared with the other four cation-cation interactions (with interaction energies of −52.51 kJ/mol). Also the energies at the BCP for the 'light blue' nitrate-cation interactions (Figure 7.11) are lower (−131.27 kJ/mol) compared with those for the "orange' nitrate-cation interactions (–91.89 kJ/mol). These results are in the opposite order to the values of the total intermolecular interactions between these molecules.

Table 7.16. Energies (kJ/mol) at the BCP of the intermolecular interaction hydrogen bonds for the phases of **7**.

	6a	**6b**
cation-cation		
1	-26.25	-52.51
2	-26.25	-26.25
3	-26.25	-52.51
4	-26.25	-52.51
5	-26.25	-26.25
6	-26.25	-52.51
cation-nitrate		
1	−236.295	−262.55
2	−118.14	−91.89
3	−118.14	−170.65
4	−118.14	−170.78
5	−118.14	−91.89
6	−118.14	−131.27
7	−118.14	−131.27
8	−236.295	−262.55
Sum	**−1338.93**	**−1575.39**

7.5. Conclusions

The two phases of compound **6** have been analysed for the first time using high resolution X-ray diffraction above and below the 109 K phase transition temperature. In addition, neutron data were collected for both phases. The 123 K phase was also analysed using data from two synchrotron X-ray sources: Diamond and Soleil. Both phases crystallise in the hexagonal crystal system with the $P6_322$ space group for the 123 K phase (**6a**) and $P6_522$ or $P6_122$ (depending on the isomer adopted by the complex) corresponding to the 100 K phase (**6b**). In **6a** the Ni atom lies on a special position of 32 symmetry while in 6**b** it is

sitting on the twofold symmetry axis. The nitrate nitrogen atom lies on a threefold axis in **6a** and in a general position in **6b**.

The multipole refinement against theoretical structure factors obtained from periodic calculations gives noticeably good agreement with the experimental data for models 2-5. These good agreements obtained here are not surprising, the experimental data have been compared with single point gas phase calculations and the geometry of both molecules compared is identical.

The experimental charge density lattice energy calculations suggest a high dependence of the results on the refinement model imposed the integration software and the radiation source used. The fully theoretical results obtained from the CRYSTAL09[18] software gave the most stable phase with the lowest lattice energy for **6a**. These results are not in agreement with expectation: the most stable form is expected for the lowest temperature phase crystal structure. Large discrepancies are observed in terms of the magnitude of the lattice energy between the results obtained from experimental charge density and fully theoretical approaches.

The intermolecular interaction energies between the cation-cation and cation-nitrate groups were calculated using the TURBOMOLE6.2[20] program. The results again show that, contrary to expectation, the 123 K phase is indicated as the most stable one from these calculations, showing the strongest intermolecular interaction energy.

References

1. L.J. Farrugia, P. Macchia and A. Sironi, *J. Appl. Cryst*, 2003, **36**, 141-145
2. L. N. Swink and M. Atoji, *Acta Crys*t., 1960, **13**, 639.
3. J. D. Korp, I. Bernal, R. A. Palmer and J. C. Robinson, *Acta Cryst. B,* 1980, **36**, 560.
4. P. Macchi, H. -B.Burgi, A. S. Chimpri, J. Hauser and Z. Gal, *J. Appl .Cryst*., 2011, **44**, 763.
5. Z. Otwinowski and W. Minor, Processing of X-ray Diffraction Data Collected in Oscillation Mode, in Methods in Enzymology, Vol., *Macromolecular*

Crystallography, part A, edited by C. W. Carter Jr & R. M. Sweet, New York: Academic Press. 1997, **276**, 307-326.

6. P. R. Mallinson, K. W. Muir, *J. Appl. Cryst*., 1985, **18**, 51-53.
7. R. H. Blessing, *J. Appl. Cryst*.. 1997, **30**, 421.
8. A. Altomare, G. Cascarano, C. Giacovazzo and A. Guagliardi, *J. Appl. Cryst.*, 1994, **27**, 435.
9. L. Farrugia, *J. Appl. Cryst.*, 2012, **45**, 849-854.
10. SADABS: Area-Detector Absorption Correction; Siemens Industrial Automation, Inc.: Madison, WI, 1996.
11. D. A. Keen, M. J. Gutmann and C. C. Wilson, *J. Appl. Cryst.*, 2006, **39**, 714-722.
12. M. J. Gutmann, *SXD2001. ISIS Facility, Rutherford Appleton Laboratory, Oxfordshire, England*, 2005.
13. G. M. Sheldrick, *Acta Cryst. A*, 2008, **64**, 112-122.
14. A. Volkov, P. Macchi, L. J. Farrugia, C. Gatti, P. R. Mallinson, T. Richter and T. Koritsanszky, *XD-2006*, 2006, http://xd.chem.buffalo.edu/.
15. Ø. A. Madsen, *J. Appl. Cryst*., 2006, **39**, 757-758.
16. A. J. H. Wachters, *J. Chem. Phys*., 1970, **52**, 1033-1036.
17. F. W. Biegler-Konig, R. F .W. Bader and T. Tang, *J. Comput. Chem*, 1982, **3**, 317
18. R. Dovesi, R. Orlando, B. Civalleri, C. Roetti, V. R. Saunders, and C. M. Zicovich-Wilson, *Z. Kristallogr.*, 2005, **220**, 571; R. Dovesi, V. R. Saunders, C. Roetti, R. Orlando, C. M. Zicovich-Wilson, F. Pascale, B. Civalleri, K. Doll, N. M. Harrison, I. J. Bush, P. D'Arco, and M. Llunell, CRYSTAL09 (CRYSTAL09 User's Manual. University of Torino, Torino, Italy,2009).
19. (a) A. D. Becke, *Phys. Rev. A*, 1988, **38**, 3098; (b) A. D. Becke, *J. Chem. Phys.*, 1993, **98**, 5648; (c) C. Lee, W. Yang and R. G. Parr, *Phys. Rev. B*, 1988, **37**, 785. (d) P. J. Stephens, J. F. Devlin, C. F. Chabalowski and M. J. Frisch, *J. Phys. Chem.*, 1994, **98**, 11623.
20. TURBOMOLE V6.2 2010, a development of University of Karlsruhe and Forschungszentrum Karlsruhe GmbH, 1989-2007, TURBOMOLE GmbH, since 2007; available from http://www.turbomole.com.
21. S. Grimme, *J. Comput. Chem.* 2006, **27**, 1787.
22. (a) F. Weigend, R. Ahlrichs, *Phys. Chem. Chem. Phys.*, 2005, **7**, 3297. (b) F. Weigend, *Phys. Chem. Chem. Phys.*, 2006, **8**, 1057.
23. A.Gavezzotti, *New J. Chem*., 2011, **35**, 1360-1368.

8. Dichlorotetrakis(dimethylsulphoxide) ruthenium(II)

8.1. Introduction

This chapter addresses the polymorphic nature of dichlorotetrakis(dimethylsulphoxide) ruthenium (II) (**7**) $RuCl_2(Me_2SO)_4$ (Scheme 8.1). The material has been reported to possess magnetic properties[1] and biological activity, exhibiting antineoplastic activity against several murine metastasizing tumors.[2] Moreover, 'in vitro' it interacts with DNA and forms covalent bonds with nucleobases such as guanine.[3] Complex **7** was synthesized in both *cis* and *trans* configurations.[4-9] The *cis* configuration is known to crystallise in four different forms,[4-9] three monoclinic and one orthorhombic, while the *trans*-configuration is known to crystallise only in a tetragonal form[6,10] (Table 8.1.).

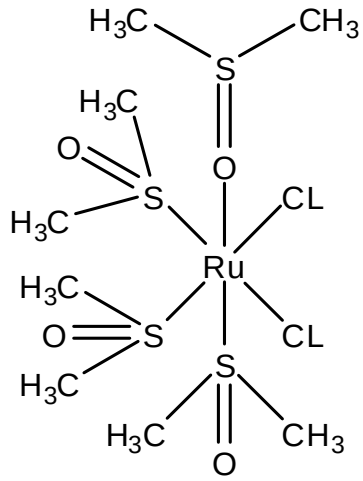

Scheme 8.1. The molecular structure of dichlorotetrakis(dimethylsulphoxide) ruthenium (II), **7**.

The first crystal structure (form I) of the *cis* configuration was reported in 1975.[4] This was followed by the structure of form IV, first reported in 1987.[5] The crystal structure of form II was first analysed using X-ray diffraction in 1988,[6] while the structure of form III was reported in 2008.[7] Form I was re-examined in 2005[8] and form IV in 2003.[9] The crystal structure of the *trans* configuration was determined in 1988[6] and 1990.[10] In Table 8.1, a summary of the crystallographic data is given for all forms (form I and IV experimental data from this work, while form II and III are data from the CSD).

Table 8.1. Crystallographic data and data collection temperatures for the *cis* (Forms I-IV) and *trans* polymorphs of dichlorotetrakis(dimethyl sulphoxide) ruthenium (II), **7**.

Form	**I**	**II**	**III**	**IV**	
			cis		***trans***
CSD refcode	CDMSOR[4] (RT) CDMSOR04[8] (170K)	CDMSOR02[6] (RT)	CDMSOR05[7] (290K)	CDMSOR01[5] (RT) CDMSOR03[9] (120K)	KACNOR[6] (RT) KACNOR01[10] (RT)
SP	$P2_1/n$	$P2_1/n$	$P2_1/c$	$Pccn$	$I4/m$
a / Å	8.8685(10)	8.417(2)	10.148(<1)	10.8062(29)	9.121(3)
b / Å	17.8300(29)	27.695(4)	10.463(<1)	11.6335(40)	9.121(3)
c / Å	11.2842(20)	8.598(2)	10.428(<1)	28.1743(90)	11.167(4)
α / °	90.00	90.00	90.00	90.00	90.00
β / °	91.993(8)	116.88(3)	99.80(1)	90.00	90.00
γ / °	90.00	90.00	90.00	90.00	90.00
V/ Å^3	1783.24(7)	1787.71	1928.042	3541.9(19)	464.506
Z'	1	1	1	1	0.13
ρ/g cm^{-3}	1.80	1.8	1.669	1.82	1.732

**The presented data were collected at 100K*

High-resolution X-ay diffraction was used in this project to characterize form I and IV; it was not possible to prepare suitable crystals for high resolution analysis of the other forms.

8.2. Experimental and Theoretical

8.2.1 Sample preparation

Compound **7** is described in the literature as being prepared by refluxing ruthenium trichloride trihydrate in dimethylsulphoxide for a few minutes.[11] The various forms can be obtained by recrystallising the product from different solvents: form I in methanol; form II in a hot mixture of DMSO:acetone (1:6),[6] form III by the cooling of a hot DMSO solution followed by slow diffusion of acetone and adding a few drops of diethyl ether into the solution;[7] form IV by cooling of a hot DMSO solution.[5]

In the attempts in this work to obtain the polymorphs of **7** using the formulations from the literature as noted above, only crystals of form I and IV could be obtained. In contrast to the published preparation, Form IV was in fact obtained in a hot mixture of DMSO:acetone (1:6) solution.

8.2.2 Data collection and Conventional (Spherical atom) refinement

Single crystals of suitable size were selected and mounted onto a goniometer and cooled to 100K on the diffractometer. High resolution X-ray data of forms I and IV were collected on a Bruker-Nonius Kappa CCD diffractometer (Mo K_α radiation), equipped with a Oxford Cryosystems Cryostream cooling device, over a period of one week. The Collect software

was used for monitoring the data collection. The low-resolution X-ray data were measured prior to the high-resolution data. The integration of intensities was carried out using the software DENZO.[12] The reflection measurements were merged and empirical absorption corrections were performed using SORTAV.[13] The structures were solved using SIR92[14] and refined initially in the spherical-atom formalism with full-matrix least squares on F^2. The non-hydrogen atoms were refined with anisotropic displacement parameters. Structure solution and refinement were performed using the WinGX[15] package of crystallographic programs. The details of the data collection and refinements are provided in Table 8.2.

Synchrotron data were also collected for form IV at Diamond – Beam line I19 and integrated using CrysAlisPro software. The results of this data collection and their comparison with laboratory X-ray data collections are presented in Section 8.6.

8.2.3 Multipole refinements

The XD[16] software package was used for the multipole refinements. The multipole expansion was truncated at the octupole level for C, N and O atoms. For S, Cl and Ru atoms, the refinement of hexadecapoles were allowed. The radial terms used for the Ru atom were of the Fourier-Bessel order of the Volkov-Macchi model.[17] Three different multipole refinements were performed for forms I and IV. In the first refinement (model 1) extensive constraints with imposed local mirror symmetry were applied for the Ru and S atoms. For the Cl, O and C atoms free multipole refinement was allowed. Only the first monopole and last dipole were refined in this model for H atoms. These were used to estimate the H-atom adps by the method of Madsen using the SHADE web interface.[18] The calculated H-atom adps were used in subsequent refinements (model 2) as fixed parameters. In the final cycles (model 3) the multipole constraints were released. The hydrogen atoms were set to the standard neutron distances from their parent atom in all refinements. Multipole populations and κ parameters were grouped in all refinements according to the chemical similarity of the atoms.

Table 8.2. Experimental crystallographic data for **7**, form I and IV.

Compound formula	$RuCl_2S_4O_4C_8H_{24}$	$RuCl_2S_4O_4C_8H_{24}$	$RuCl_2S_4O_4C_8H_{24}$
Form	I	IV	IV
M_r	484.5	484.5	484.5
Space group	$P2_1/n$	*Pbnb*	*Pccn*
Crystal system	Monoclinic	Orthorhombic	Orthorombic
a/ Å	8.8685(10)	10.8062(29)	10.8288(4)
b/ Å	17.8300(29)	11.6335(40)	28.2117(8)
c/Å	11.2842(20)	28.1743(90)	11.6686(3)
β/deg	91.993(8)	90.00	90.00
V/Å^{-3}	1783.24(7)	3541.9(19)	3564.74(19)
Z	4	8	8
D_{calc}/g cm^{-3}	1.80	1.82	1.81
F(000)	984	1968	1968
Radiation	Mo Kα	Mo Kα	Synchrotron
λ/Å	0.71073	0.71073	0.48590
μ(Mo-K_a)/mm^{-1}	1.651	1.663	2.014
Crystal size/mm	0.19x0.32x0.42	0.17x0.29x0.37	0.02x0.03x0.03
θ range/deg	2.1-53.5	2.0-50.2	1.8-29.0
Max sin(θ)/ λ	1.13	1.08	0.99
No. of data used for merging	462143	344183	221985
No. of unique data	21348	18436	14663
hkl range	$-19 \le h \le 19$	$0 \le h \le 23$	$0 \le h \le 20$
	$0 \le k \le 40$	$0 \le k \le 25$	$0 \le k \le 56$
	$0 \le l \le 25$	$0 \le l \le 60$	$0 \le l \le 23$
R_{int}	0.0420	0.0530	0.0670
R_σ	0.0269	0.0316	0.0403
Spherical atom refinement			
No. of data in refinement	21348	18436	14663
No. of refined parameters	269	269	180
Final *R* [$I > 2\sigma(I)$]	0.025	0.025	0.046
R_w [$I > 2\sigma(I)$]	0.062	0.060	0.109
Goodness of fit *S*	1.052	1.042	1.076
Extrema in residual map/ eÅ^{-3}	-2.370→2.314	-0.983→ 0.785	-1.708→4.900
Max shift/esd in last cycle	0.004	0.003	0.002
Multipole refinement			
No. of data in refinement	19811	16105	12912
No. of refined parameters	579	579	490
Final *R* [$I > 3\sigma(I)$]	0.0239	0.0248	0.0452
R_w [$I > 3\sigma(I)$]	0.0302	0.0261	0.0404
Goodness of fit *S*	1.7803	1.3474	1.8195
Extrema in residual map/ eÅ^{-3} (all data)	-2.133 →1.869	-0.664 →0.778	-2.076→4.279
Max shift/esd in last cycle	0.188325E-02	0.359652E-03	0.566747E-04

8.2.4 Theoretical calculations

Gas-phase structure optimisations were performed using the DFT method at the B3LYP[19]/Def2-TZVPP[20] level of theory, within the Gaussian03 program.[21] Basis sets were

obtained from EMSL.[22] The subsequent topological analyses were performed using the AIMPAC program.[23] Theoretical structure factors were computed from the resultant wave functions and used in a multipole refinement within XD,[16] where all thermal parameters were set to zero and all positional parameters were kept fixed.

8.3. Results and discussion

8.3.1. Molecular structure and conformation details

The *ORTEP* diagram of 7 (at 100 K) showing the thermal ellipsoids and the labeling scheme used in this work is illustrated in Figure 8.1.

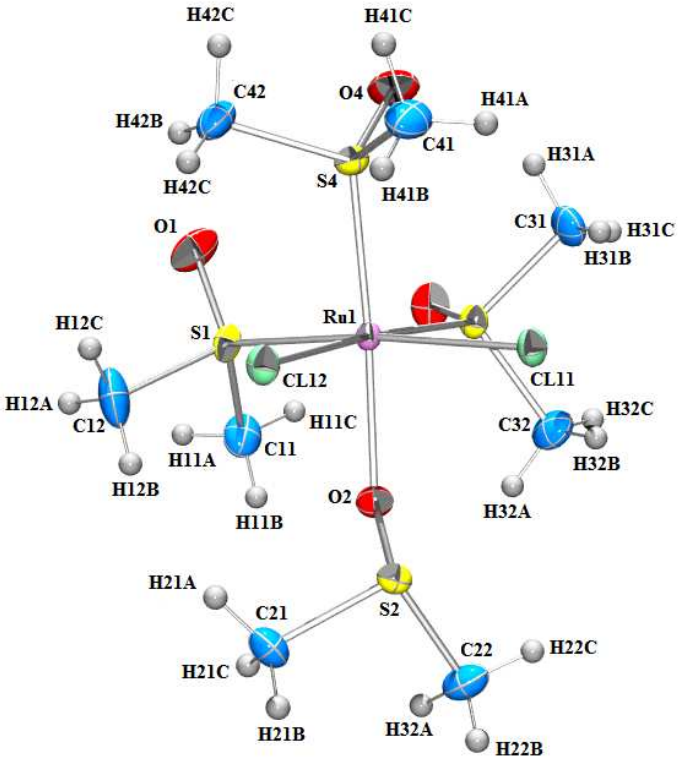

Figure 8.1. The *ORTEP* diagram of form I of 7 at 100 K, showing the thermal ellipsoids and the labeling scheme used in this work.

In the molecular structures of **7** the Ru atom has a distorted octahedral coordination with the two chlorine ligands atoms orientated either in *cis* or *trans* configuration and four dimethylsulfoxide ligands occupying the remaining coordination sites. Three of the dimethylsulfoxide groups are S-bonded while the fourth is O-bonded. The best-fit overlay plot of the molecules of the two studied polymorphs of 7 is illustrated in Figure 8.2. A slight conformational difference can be observed between the two forms due to the orientation of the methyl groups of the sulfoxide O-bonded ligand. The optimised gas phase molecule using the DFT method at the B3LYP[19]/Def2-TZVPP[20] level of theory/basis

set shows a better conformational agreement with form IV. The two methyl groups of the sulfoxide O-bonded ligand again give a slight deviation between the optimised gas phase molecule and form I.

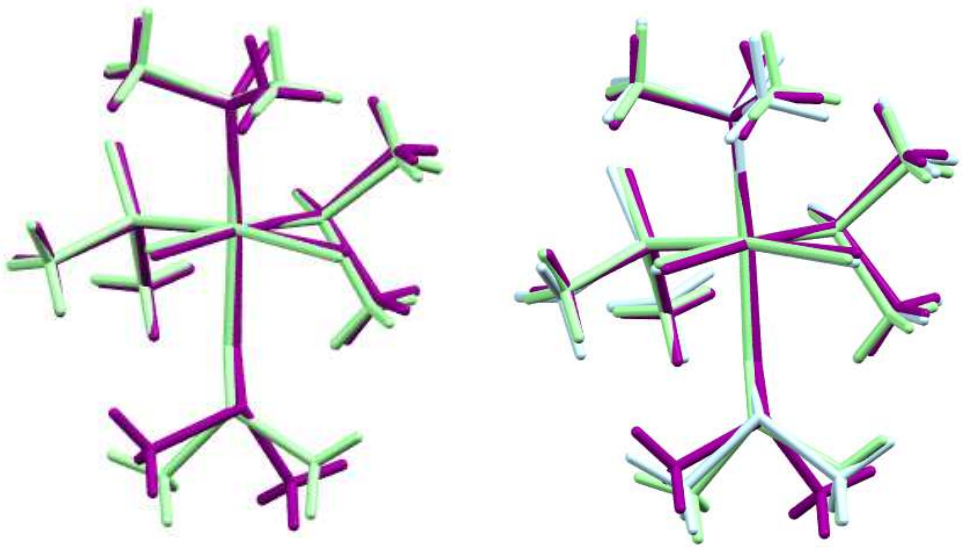

(a) (b)

Figure 8.2. Best fit overlays of (a) forms I and IV, (b) form I, IV and optimised gas phase molecule of *cis*-**7**. Colour code: form I - purple, form IV – green, optimised – blue

Table 8.3. Selected torsion angles of forms I and IV of **7** from experimental X-ray data, in comparison with the CSD data and optimised gas phase calculations.

Torsion angle	**Form I**		**Form IV**		**Optimised structure**
	This work	**CSD data**	**This work**	**CSD data**	
S1-Ru1-S4-O4	-84.11(5)	-84.30	-77.35(4)	-77.62	-88.92
S3-Ru1-S4-O4	8.66(5)	8.58	16.93(4)	16.52	4.9
S4-Ru1-S1-O1	22.18(4)	22.12	17.17(4)	17.17	14.34
O2-Ru1-S1-O1	-161.92(4)	-161.72	-163.87(4)	-163.81	-171.47
S4-Ru1-S3-O3	-84.35(4)	-84.16	-81.62(3)	-81.46	-86.53
S1-Ru1-S3-O3	8.98(4)	9.30	11.95(3)	12.01	8.88
O2-Ru1-S3-O3	94.73(4)	94.80	96.66(3)	96.83	96.28

Selected torsion angles of forms I and IV from the present experimental results are compared with those from the CSD in Table. 8.3. The optimised gas phase calculations are

also included in the table. The experimental results show very good agreement with the previous CSD data. However, there are slight differences in torsion angles of the different forms. For instance, the S3-Ru1-S4-O4 torsion angle is 8.66(5)° for form I while in form IV this angle is almost double this value (16.93(4)°). The torsion angles for the optimised gas phase molecule give in general better agreement with those in form I. The main conformational difference between the optimised gas phase molecule and those in the solid state forms arises from the orientation of the O2 atom. This is reflected in the O2-Ru1-S1-O1 torsion angle which is −171.47° for the optimised gas phase molecule and −161.92(4), −163.87(4) for forms I and IV, respectively.

8.3.2. Intermolecular interactions and crystal packing

The molecules in Form I are linked to form two distinct dimer motifs: γ and ζ, which are linked through C_{methyl}-H···Cl and C_{methyl}-H···C_{methyl} weak interactions (Figure 8.3). The dimer designated γ forms an $R_2^2(12)$ ring linked by C_{methyl}-H···Cl interactions. The C_{methyl}-H···Cl present in the γ dimer also forms $R_2^2(8)$ rings, designated α in Figure 8.3(a). The second dimer comprises an $R_2^2(12)$ ring formed by C_{methyl}-H···C_{methyl} weak interactions and is designated ζ in Figure 8.3(b).

There are also two O···H-C_{methyl} interactions, represented as β in Figure 8.3(c), comprising an $R_2^2(6)$ ring. Two O atoms acting as acceptors and two H-C_{methyl} donors form a further, more extended, $R_2^2(13)$ ring designated as ε in Figure 8.3(c). Finally, three methyl groups acting as donors and one O atom and one Cl atom acting as acceptors form the $R_3^2(12)$ ring, designated τ in Figure 8.3(d).

(a)

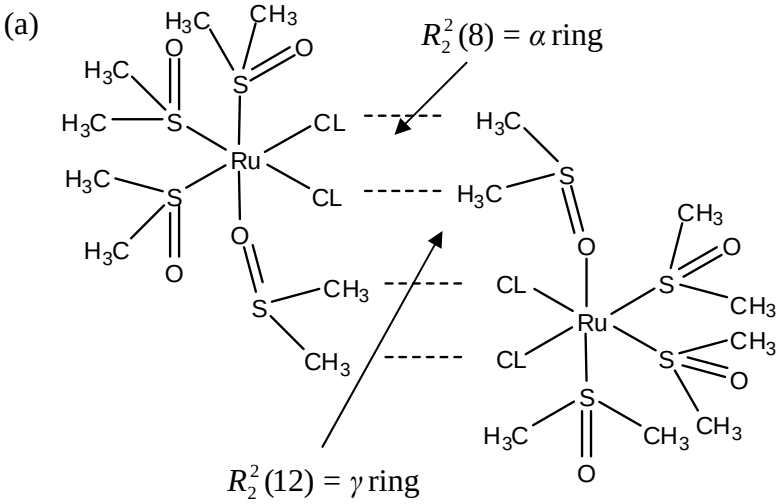

(b)

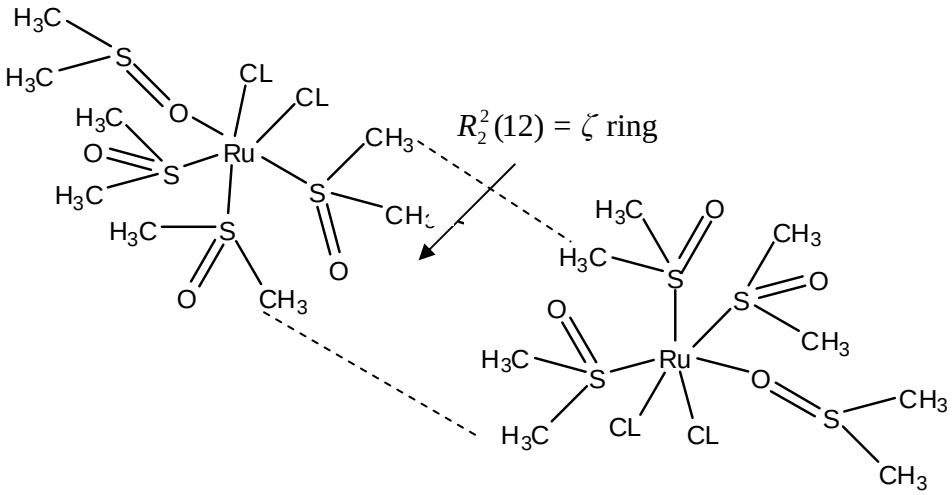

Figure 8.3. Hydrogen bonding motifs in form I of **7**: (a) form I dimer illustrating α and γ rings; (b) form I showing the ζ ring representation of hydrogen bond intermolecular interactions.

(c)

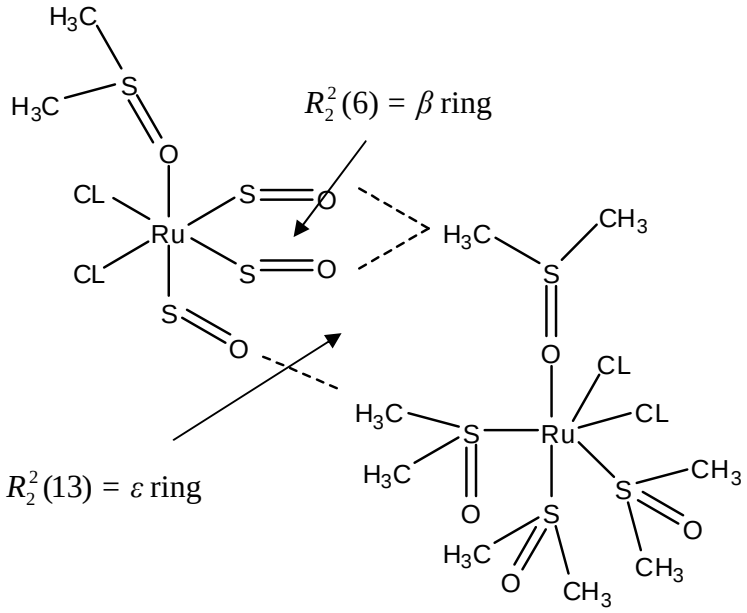

(d)

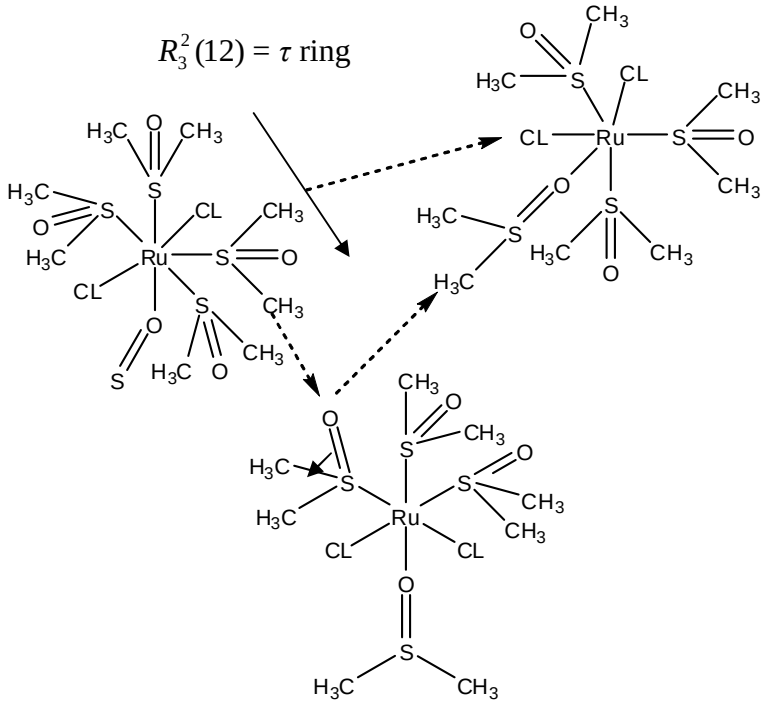

Figure 8.3, continued**.** Hydrogen bonding motifs in form I of **7**: (c); form I hydrogen bond interactions illustrating β and ε rings. (d) form I showing the τ ring representation.

In form IV, a dimer is formed through hydrogen bond interactions between Cl···H-C and C-H···C. These interactions form an $R_2^2(7)$ ring designated π in Figure 8.4 and a further $R_2^2(13)$ ring, denoted μ. There are also an O···H-C and Cl···H-C_{methyl} bifurcated hydrogen bonds, resulting in a total of seven different acceptors for the intermolecular interactions (two Cl, both of them involved in the bifurcated hydrogen bond, two O – one involved in

the bifurcated hydrogen bond – and three C_{methyl}). The bifurcated hydrogen interaction between Cl ···H-C and O···H-C is illustrated in Figure 8.5 (a) and (b) (*Mercury* view).

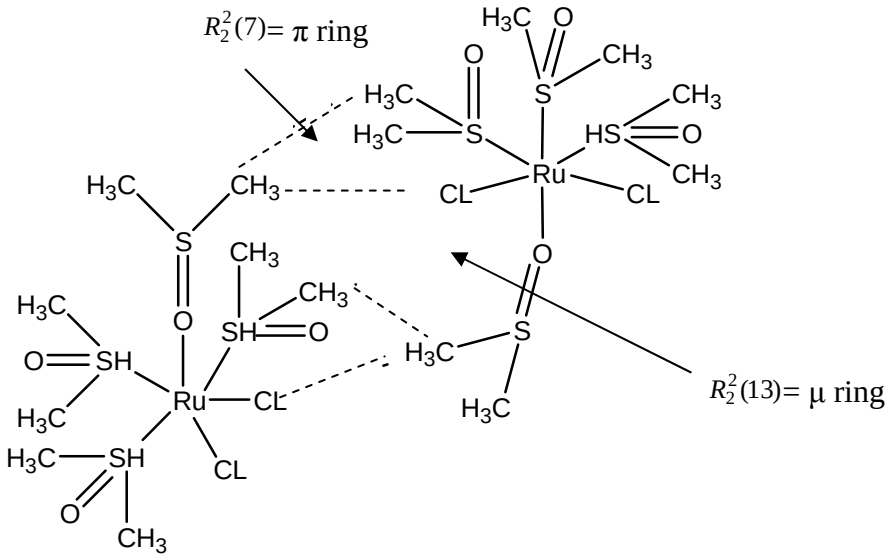

Figure 8.4. Hydrogen bonding motifs in form IV of **7**, showing the π and μ rings in the dimer and their graph set notation.

(a)

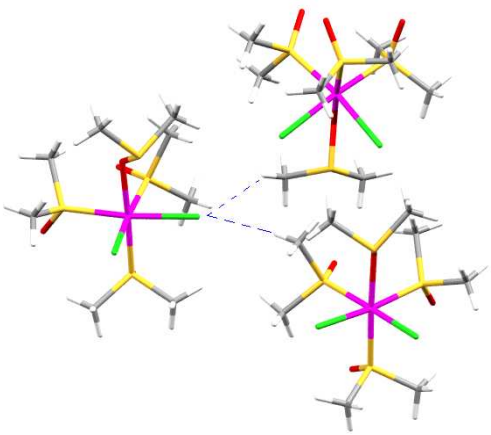

Figure 8.5. The hydrogen bonded intermolecular interactions in Form IV of **7**, showing the bifurcated Cl··· H-C_{methyl} (a) and O··· H-C_{methyl} (b) motifs (below).

(b)

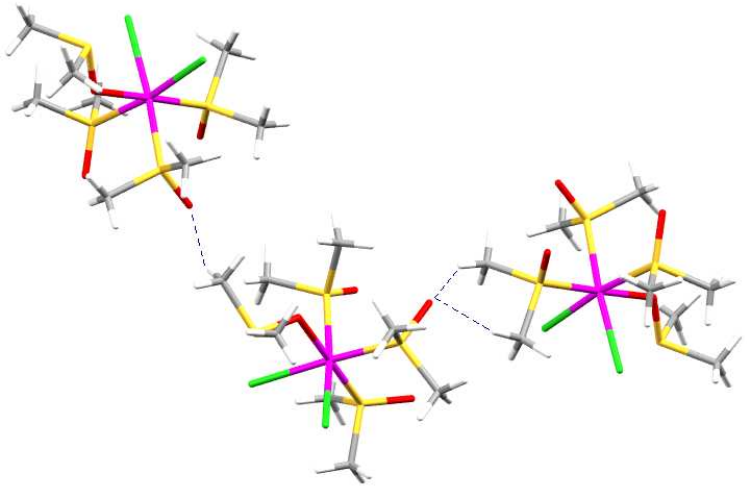

Figure 8.5. continued, The hydrogen bonded intermolecular interactions in Form IV of **7,** O··· H-C_{methyl} motifs

A summary of all hydrogen bond interactions observed in forms I and IV and their corresponding A···D distances are given in Table 8.4. The hydrogen bond interaction distances in forms I and IV lie between 3.128(1) and 3.809(1) Å. The shortest interaction length is for the C(32)-H(32A)···O(1) contact which forms the τ ring in form I. Another relatively short hydrogen bond involved in a dimer interaction (β ring) was found for the C(12)-H(12A)···O(4) contact (3.2398(14) Å). The other dimer involved in this ring gives a slightly longer hydrogen bond interaction – C(21)-H(21C)···O(3), 3.3374(12) Å. The C-H···Cl contacts, which form the α ring, are slightly elongated (3.6747(9) - 3.5790(12) Å) compared with the dimers in the β ring where C-H···O bonds are present. The bifurcated C-H···Cl intermolecular interactions present in form IV are similar in length (3.580(1) and 3.6498(15) Å) to those present in form I. In addition, there are two other C-H···Cl contacts present in form IV which show longer hydrogen bond interactions (3.8094(1) and 3.707(1) Å). The C-H···O contacts present in form IV are also slightly elongated compared with those present in form I, apart from the C(42)-H(42A)···O(1) hydrogen bond interaction.

Table 8.4. Hydrogen bond and other intermolecular interactions in forms I and IV of **7**.

Label	Graph set symbol	Hydrogen bonds present	Polymorph	D···A distance
α	$R_2^2(8)$	C(21)-H(21B)···Cl(11)	I	3.6747(9)
α	$R_2^2(8)$	C(22)-H(22B)···Cl(12)	I	3.5790(12)
τ	$R_2^2(12)$	C(31)-H(31C)···Cl(12)	I	3.5611(10)
β	$R_2^2(6)$	C(12)-H(12A)···O(4)	I	3.2398(14)
β	$R_2^2(6)$	C(21)-H(21C)···O(3)	I	3.3374(12)
τ	$R_2^2(12)$	C(32)-H(32A)···O(1)	I	3.1284(12)
π	$R_2^2(7)$	C(12)-H(12A)···Cl(12)	IV	3.8094(1)
		C(21)-H(21A)···Cl(12)	IV	3.707(1)
	bifurcated	C(31)-H(31A) ···Cl(11)	IV	3.580(1)
	bifurcated	C(22)-H(22A) ···Cl(11)	IV	3.6498(15)
	bifurcated	C(41)-H(41C)···O(1)	IV	3.555(1)
	bifurcated	C(42)-H(42A)···O(1)	IV	3.2414(17)
		C(22)-H(22C)···O(3)	IV	3.421(2)
π	$R_2^2(7)$	C(11)-H(11B)···C(21)	IV	3.668(1)
		C(31)-H(31A)···C(22)	IV	3.603(2)

8.3.3. Hirshfeld surfaces and fingerprint plots analysis of the intermolecular hydrogen bond interactions of the studied forms of 7

The Hirshfeld surface analysis with the derived two-dimensional fingerprint plots will be examined in this section. The resulting two dimensional fingerprint plots of the hydrogen bond interactions in forms I and IV are illustrated in Figure 8.6. The external long sharp peaks representing the Cl···H interactions show a high degree of similarity in both forms. The other two peaks, in the 1.2-1.4 Å d_e/d_i region, also give similar results for both forms. The main difference arises from the H···H short contacts which are represented by the middle sharp peak in form I, while in form IV this peak is more diffuse. This is due to the fact that in form IV there are two short H···H contacts formed while in form I there is only one.

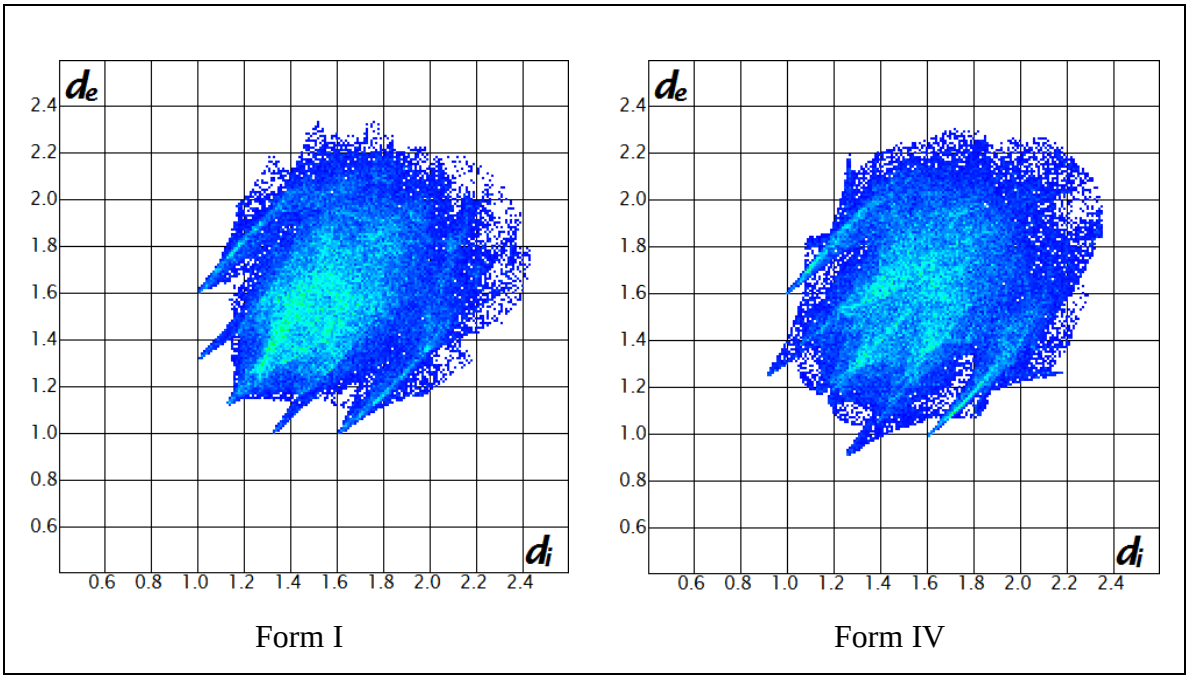

Figure 8.6. Fingerprint plots of forms I and IV of **7**.

8.4. Analysis of the electron-density distribution

8.4.1. Analysis of topological parameters

A detailed comparison between the topological parameters obtained from experimental data and those obtained from theory is now given. The topological parameters from the experimental data were compared with those directly determined from the wave functions of the gas phase calculations and also with the multipole model based on the theoretical structure factors. The distance (Å) of the BCP to the nuclei denoted by d_1 and d_2, the electron density ρ, the Laplacian at the BCP, $\nabla^2\rho$ and the three eigenvalues $\lambda_1, \lambda_2, \lambda_3$ of the Hessian matrix of some atoms of the two forms are listed in Table 8.5 for form I and in Table 8.6 for form IV.

The agreements between experimental data of form I and the theoretical results will first be discussed. The bonds in which there are the largest differences between experiment and theory are the S-O bonds, perhaps due to the involvement of the O atom in strong hydrogen bonding. For instance in case of the S(3)-O(3) bond, the $\nabla^2\rho(r_b)$ parameter from the experimental data (–13.23 eÅ^{-3}) shows significant discrepancy with that derived from the pure wave function (+13.7 eÅ^{-3}). A slightly better agreement is observed when the

density reference is taken from the multipole refinements of the theoretical structure factor ($\nabla^2\rho(r_b)$ = −20.27 eÅ^{-3}). The same can be observed for S1-O1 and S1-O2, where the experimental $\nabla^2\rho(r_b)$ parameters give better agreement with those obtained from the multipole refinements of theoretical structure factors, whereas a large discrepancy can be observed in comparison with those derived from the pure wave function. On the other hand, the S4-O4 bond shows closer values of the experimental $\nabla^2\rho(r_b)$ with those derived from the pure wave function and a larger discrepancy with those obtained from the multipole refinements of theoretical structure factors. On the other hand, in general, the experimental Laplacian parameters fit better with the theoretical data obtained from the mutipole refinements compared with those derived from the pure wave function. Some of the C-H bonds also show significant discrepancy between experimental and theoretical results, including H22A-C22, H22C-C22, H41A-C41, H41B-C41, although these atoms are not involved in strong hydrogen bonds. The bonds containing the transition metal atom, including Cl-Ru, S-Ru and O-Ru, yield good agreement between experimental and theoretical topological parameters. The experimental topological parameters of the C-S bonds overall are also in good agreement with theoretical data, especially with those obtained from multipole refinement of the theoretical structure factors.

Table 8.5. Topological Analysis of Bond Critical Points for form I of **7**.

Bond	**d_1[a]**	**d_2[a]**	**$\rho(r_b)$[b]**	**$\nabla^2\rho(r_b)$[c]**	**λ_1[c]**	**λ_2[c]**	**λ_3[c]**
Cl(11)-Ru(1)	1.2134	1.2229	0.44	5.59	-1.29	-0.81	7.70
	1.1765	*1.3046*	*0.410*	*4.6660*	*-0.9030*	*-0.8870*	*6.4570*
	1.2326	*1.2435*	*0.35*	*4.78*	*-1.07*	*-0.66*	*6.51*
Cl(12)-Ru(1)	1.2075	1.2262	0.47	5.80	-1.21	-0.86	7.87
	1.1699	*1.3056*	*0.409*	*4.5260*	*-1.0180*	*-0.9110*	*6.4550*
	1.2416	*1.2417*	*0.35*	*4.59*	*-1.04*	*-0.81*	*6.45*
S(1)-Ru(1)	1.1118	1.1616	0.74	7.17	-2.80	-2.15	12.11
	1.1153	*1.2462*	*0.574*	*6.4260*	*-1.3280*	*-1.1950*	*8.9490*
	1.1351	*1.2255*	*0.62*	*6.01*	*-2.28*	*-1.80*	*10.09*
S(3)-Ru(1)	1.1038	1.1684	0.82	7.95	-2.96	-2.56	13.47
	1.1158	*1.2456*	*0.576*	*6.3630*	*-1.3620*	*-1.2260*	*8.9520*
	1.1327	*1.2281*	*0.62*	*6.11*	*-2.33*	*-1.74*	*10.18*
S(4)-Ru(1)	1.1263	1.1397	0.71	6.18	-2.67	-2.19	11.04
	1.1003	*1.2185*	*0.640*	*6.4560*	*-1.7000*	*-1.4820*	*9.6390*
	1.0801	*1.2408*	*0.62*	*8.77*	*-1.56*	*-1.31*	*11.64*
O(2)-Ru(1)	0.9852	1.1577	0.54	8.37	-2.21	-1.75	12. 33
	1.1094	*1.1434*	*0.371*	*6.8590*	*-0.9820*	*-0.8610*	*8.7020*
	1.0848	*1.1772*	*0.30*	*6.68*	*-0.73*	*-0.52*	*7.93*
S(1)-O(1)	0.6771	0.7952	2.20	-18.34	-14.96	-13.81	10.43
	0.5878	*0.8901*	*1.930*	*14.2410*	*-11.1060*	*-11.0500*	*36.397*

Table 8.5 Continued

	0.6458	*0.8325*	*2.15*	*-14.52*	*-14.64*	*-12.52*	*12.64*
C(11)-S(1)	0.8297	0.9619	1.23	-3.99	-7.11	-6.63	9.75
	0.8247	*0.9795*	*1.331*	*-9.1070*	*-7.9630*	*-7.6130*	*6.4690*
	0.8117	*0.9925*	*1.26*	*-5.36*	*-7.26*	*-7.03*	*8.94*
C(12)-S(1)	0.7887	1.0066	1.30	-3.59	-7.53	-6.74	10.68
	0.8307	*0.9758*	*1.329*	*-9.1320*	*-7.9680*	*-7.6170*	*6.4530*
	0.8277	*0.9788*	*1.26*	*-5.39*	*-7.42*	*-7.00*	*9.03*
S(2)-O(2)	0.7428	0.8049	1.77	-9.72	-9.64	-9.08	9.00
	0.6108	*0.9253*	*1.736*	*5.2230*	*-9.6610*	*-9.5560*	*24.439*
	0.7197	*0.8167*	*1.95*	*-15.95*	*-13.75*	*-12.40*	*10.20*
C(21)-S(2)	0.8500	0.9324	1.34	-5.92	-7.76	-6.96	8.80
	0.8392	*0.9671*	*1.319*	*-8.9040*	*-7.8470*	*-7.3800*	*6.3230*
	0.8194	*0.9867*	*1.25*	*-5.33*	*-7.61*	*-6.84*	*9.12*
C(22)-S(2)	0.8422	0.9507	1.30	-5.62	-7.77	-6.89	9.04
	0.8390	*0.9673*	*1.318*	*-8.8970*	*-7.8430*	*-7.3810*	*6.3270*
	0.8116	*0.9946*	*1.26*	*-5.03*	*-7.53*	*-6.88*	*9.38*
S(3)-O(3)	0.6729	0.8132	2.07	-13.23	-13.14	-11.05	10.96
	0.5889	*0.8922*	*1.920*	*13.7000*	*-11.0460*	*-11.0180*	*35.764*
	0.6503	*0.8308*	*2.23*	*-20.27*	*-16.51*	*-14.83*	*11.08*
C(31)-S(3)	0.7588	1.0214	1.29	-3.60	-7.20	-6.90	10.50
	0.8148	*0.9854*	*1.337*	*-9.1330*	*-8.0030*	*-7.6390*	*6.509*
	0.7903	*1.0099*	*1.30*	*-5.08*	*-7.54*	*-6.97*	*9.43*
C(32)-S(3)	0.8826	0.9062	1.22	-4.13	-6.91	-6.52	9.31
	0.8323	*0.9747*	*1.327*	*-9.1150*	*-7.9560*	*-7.5980*	*6.440*
	0.8158	*0.9914*	*1.27*	*-5.58*	*-7.54*	*-7.11*	*9.06*
S(4)-O(4)	0.6187	0.8648	1.79	5.39	-10.90	-8.62	24.91
	0.5878	*0.8906*	*1.929*	*14.2170*	*-11.1590*	*-11.1350*	*36.512*
	0.6473	*0.8316*	*2.16*	*-13.71*	*-13.95*	*-12.33*	*12.57*
C(42)-S(4)	0.8218	0.9721	1.29	-5.09	-7.85	-6.70	9.45
	0.8190	*0.9818*	*1.339*	*-9.2300*	*-8.0380*	*-7.6820*	*6.4910*
	0.7943	*1.0067*	*1.34*	*-5.55*	*-7.65*	*-7.38*	*9.47*
C(41)-S(4)	0.8828	0.9103	1.28	-5.18	-7.60	-6.85	9.28
	0.8195	*0.9826*	*1.338*	*-9.2120*	*-8.0090*	*-7.7010*	*6.4980*
	0.7987	*1.0036*	*1.32*	*-6.11*	*-7.87*	*-7.39*	*9.15*
H(11A)-C(11)	0.3563	0.7101	1.83	-17.84	-17.71	-17.01	16.87
	0.3881	*0.7010*	*1.889*	*-23.2110*	*-18.0310*	*-17.9140*	*12.734*
	0.4126	*0.6764*	*1.86*	*-22.28*	*-17.35*	*-17.17*	*12.23*
H(11B)-C(11)	0.3848	0.6813	1.65	-14.79	-15.49	-14.12	14.81
	0.3858	*0.7029*	*1.893*	*-23.3890*	*-18.1970*	*-18.0100*	*12.818*
	0.4032	*0.6856*	*1.88*	*-23.28*	*-17.93*	*-17.75*	*12.40*
H(11C)-C(11)	0.3485	0.7175	1.86	-17.87	-17.99	-17.63	17.75
	0.3713	*0.7157*	*1.928*	*-24.4900*	*-19.0650*	*-19.0110*	*13.587*
	0.4019	*0.6850*	*1.93*	*-24.70*	*-18.35*	*-18.14*	*11.79*
H(12A)-C(12)	0.4005	0.6665	1.75	-17.32	-16.59	-14.35	13.62

Table 8.5 Continued

	0.3876	*0.7018*	*1.892*	*-23.2910*	*-18.0810*	*-18.0040*	*12.794*
	0.4212	*0.6682*	*1.87*	*-22.59*	*-17.31*	*-17.05*	*11.77*
H(12B)-C(12)	0.4018	0.6650	1.67	-13.63	-14.12	-13.87	14.36
	0.3861	*0.7009*	*1.900*	*-23.5420*	*-18.2880*	*-18.1360*	*12.883*
	0.4146	*0.6723*	*1.87*	*-22.38*	*-17.54*	*-17.08*	*12.24*
H(12C)-C(12)	0.3744	0.6917	1.90	-20.73	-19.32	-16.68	15.27
	0.3775	*0.7075*	*1.926*	*-24.297*	*-18.889*	*-18.786*	*13.379*
	0.3958	*0.6892*	*1.87*	*-22.17*	*-17.84*	*-17.56*	*13.23*
H(21A)-C(21)	0.4057	0.6608	1.83	-18.71	-16.69	-15.33	13.32
	0.3815	*0.7065*	*1.909*	*-23.8410*	*-18.5210*	*-18.4360*	*13.117*
	0.4166	*0.6714*	*1.88*	*-23.14*	*-17.54*	*-17.28*	*11.68*
H(21B)-C(21)	0.4154	0.6508	1.76	-17.86	-15.75	-15.07	12.96
	0.3882	*0.7021*	*1.883*	*-23.1270*	*-17.9620*	*-17.8490*	*12.684*
	0.4305	*0.6597*	*1.86*	*-21.91*	*-16.87*	*-16.65*	*11.61*
H(21C)-C(21)	0.3843	0.6818	1.95	-21.13	-18.53	-17.50	14.89
	0.3865	*0.7031*	*1.890*	*-23.3070*	*-18.1180*	*-18.0470*	*12.858*
	0.4139	*0.6758*	*1.86*	*-21.18*	*-16.94*	*-16.87*	*12.63*
H(22A)-C(22)	0.4107	0.6563	1.76	-15.53	-15.62	-14.34	14.43
	0.3864	*0.7031*	*1.891*	*-23.3180*	*-18.1270*	*-18.0540*	*12.863*
	0.4096	*0.6800*	*1.86*	*-20.51*	*-16.97*	*-16.74*	*13.20*
H(22B)-C(22)	0.4142	0.6529	1.77	-17.53	-16.21	-15.12	13.80
	0.3883	*0.7021*	*1.882*	*-23.1180*	*-17.9530*	*-17.8400*	*12.676*
	0.4354	*0.6549*	*1.87*	*-21.68*	*-16.79*	*-16.57*	*11.68*
H(22C)-C(22)	0.4242	0.6434	1.67	-12.63	-13.38	-12.91	13.65
	0.3814	*0.7063*	*1.911*	*-23.8690*	*-18.5410*	*-18.4610*	*13.133*
	0.4083	*0.6794*	*1.90*	*-21.71*	*-17.57*	*-17.30*	*13.16*
H(31A)-C(31)	0.3662	0.6999	1.89	-20.20	-18.30	-17.66	15.77
	0.3717	*0.7149*	*1.927*	*-24.4880*	*-19.0800*	*-18.9800*	*13.572*
	0.3921	*0.6944*	*1.95*	*-23.87*	*-18.66*	*-18.57*	*13.36*
H(31B)-C(31)	0.3698	0.6965	1.88	-19.78	-18.08	-17.19	15.49
	0.3798	*0.7080*	*1.907*	*-23.8190*	*-18.5790*	*-18.3920*	*13.152*
	0.3968	*0.6911*	*1.91*	*-22.20*	*-17.90*	*-17.80*	*13.49*
H(31C)-C(31)	0.3852	0.6824	1.80	-18.92	-17.20	-16.07	14.36
	0.3883	*0.7009*	*1.888*	*-23.1910*	*-18.0090*	*-17.8910*	*12.710*
	0.4090	*0.6803*	*1.86*	*-20.60*	*-17.13*	*-16.85*	*13.39*
H(32A)-C(32)	0.4039	0.6625	1.77	-18.41	-16.46	-15.05	13.10
	0.3839	*0.7027*	*1.910*	*-23.7780*	*-18.4460*	*-18.3370*	*13.005*
	0.4216	*0.6652*	*1.88*	*-22.32*	*-17.55*	*-17.00*	*12.23*
H(32B)-C(32)	0.3760	0.6905	1.91	-20.80	-18.44	-17.47	15.12
	0.3802	*0.7069*	*1.910*	*-23.8670*	*-18.5740*	*-18.4620*	*13.169*
	0.4166	*0.6706*	*1.87*	*-21.84*	*-17.31*	*-16.76*	*12.22*
H(32C)-C(32)	0.3884	0.6777	1.84	-19.08	-17.11	-16.15	14.17
	0.3871	*0.7021*	*1.892*	*-23.2960*	*-18.0710*	*-18.0310*	*12.807*
	0.4165	*0.6727*	*1.87*	*-22.64*	*-17.42*	*-17.17*	*11.96*

Table 8.5 Continued

H(42A)-C(42)	0.3819	0.6845	1.89	-22.57	-18.53	-17.50	13.47
	0.3878	*0.7015*	*1.889*	*-23.2210*	*-18.04*	*-17.9310*	*12.750*
	0.4050	*0.6842*	*1.85*	*-20.04*	*-17.09*	*-16.81*	*13.86*
H(42B)-C(42)	0.3903	0.6758	1.89	-24.31	-19.07	-17.61	12.37
	0.3814	*0.7069*	*1.903*	*-23.6970*	*-18.46*	*-18.29*	*13.06*
	0.4035	*0.6849*	*1.90*	*-22.90*	*-18.08*	*-17.46*	*12.64*
H(42C)-C(42)	0.3681	0.6981	2.01	-26.91	-21.13	-19.60	13.82
	0.3734	*0.7135*	*1.924*	*-24.3680*	*-18.9580*	*-18.8840*	*13.473*
	0.3958	*0.6910*	*1.90*	*-21.24*	*-17.77*	*-17.34*	*13.87*
H(41A)-C(41)	0.3733	0.6929	1.70	-13.23	-15.98	-13.89	16.64
	0.3775	*0.7083*	*1.922*	*-24.2000*	*-18.8380*	*-18.7100*	*13.349*
	0.4187	*0.6672*	*1.93*	*-23.12*	*-17.87*	*-17.54*	*12.29*
H(41B)-C(41)	0.3670	0.6991	1.72	-13.24	-15.86	-14.77	17.38
	0.3780	*0.7097*	*1.910*	*-23.9400*	*-18.6800*	*-18.5210*	*13.261*
	0.4029	*0.6848*	*1.90*	*-23.65*	*-18.05*	*-17.56*	*11.96*
H(41C)-C(41)	0.3596	0.7069	1.84	-17.88	-18.28	-16.75	17.15
	0.3884	*0.7010*	*1.890*	*-23.2390*	*-18.0180*	*-17.9400*	*12.719*
	0.4139	*0.6756*	*1.86*	*-22.65*	*-17.53*	*-17.04*	*11.92*

First line corresponds to Form I experimental data. The second and the third lines (italic) correspond to reference density from the wave function and reference density from the theoretical structure factors, respectively. [a] *In units of Å.* [b] *In units of e Å*$^{-3}$. [c] *In units of e Å*$^{-5}$

In the case of form IV (Table 8.6), the bonds containing the metal transition atom Ru also show good agreement between the topological parameters of the experimental and theoretical data. The same can be observed for the C-S bonds. The experimental Laplacian parameters for the S-O bonds show a large discrepancy with those derived from the pure wave function, whereas good agreement is obtained with those from the multipole refinement of the theoretical structure factors. The experimental parameters of the C-H bonds show in general good agreement with the theoretical data especially with those obtained from multipole refinement of the theoretical structure factors. The most affected bond, showing the most extensive discrepancy between experimental and theoretical data, is H24C-C42 ($\nabla^2\rho(r_b)$ = –14.47 and –24.196 eÅ^{-3}).

Table 8.6. Topological Analysis of Bond Critical Points for form IV of **7**.

Bond	$\mathbf{d_1}^{a}$	$\mathbf{d_2}^{a}$	$\boldsymbol{\rho(r_b)}^{b}$	$\boldsymbol{\nabla^2\rho(r_b)}^{c}$	$\boldsymbol{\lambda_1}^{c}$	$\boldsymbol{\lambda_2}^{c}$	$\boldsymbol{\lambda_3}^{c}$
Cl(11)-Ru(1)	1.1886	1.2266	0.46	5.84	-1.07	-0.98	7.89
	1.1695	*1.3050*	*0.411*	*4.6710*	*-0.9050*	*-0.8930*	*6.4680*
	1.1861	*1.2916*	*0.31*	*5.66*	*-0.50*	*-0.38*	*6.54*
Cl(12)-Ru(1)	1.2080	1.2317	0.45	5.59	-1.15	-1.00	7.74
	1.1768	*1.3049*	*0.409*	*4.5180*	*-1.0230*	*-0.9100*	*6.4500*
	1.2114	*1.2857*	*0.32*	*5.02*	*-0.79*	*-0.53*	*6.34*

Table 8.6 Continued

S(1)-Ru(1)	1.1052	1.1662	0.76	6.63	-2.53	-2.30	11.46
	1.1155	*1.2454*	*0.576*	*6.3880*	*-1.3590*	*-1.2180*	*8.9640*
	1.0977	*1.2639*	*0.56*	*7.86*	*-1.30*	*-1.16*	*10.32*
S(3)-Ru(1)	1.1105	1.1636	0.78	6.25	-2.62	-2.57	11.44
	1.1156	*1.2459*	*0.574*	*6.4050*	*-1.3430*	*-1.2040*	*8.9520*
	1.0975	*1.2634*	*0.57*	*7.85*	*-1.31*	*-1.16*	*10.32*
S(4)-Ru(1)	1.0954	1.1549	0.83	6.34	-3.01	-2.77	12.13
	1.1001	*1.2185*	*0.640*	*6.4610*	*-1.6970*	*-1.4810*	*9.6390*
	1.0780	*1.2416*	*0.63*	*8.76*	*-1.55*	*-1.34*	*11.64*
O(2)-Ru(1)	1.0027	1.1310	0.56	9.13	-1.96	-1.82	12.92
	1.1097	*1.1437*	*0.371*	*6.8510*	*-0.9790*	*-0.8590*	*8.6890*
	1.0839	*1.1773*	*0.30*	*6.65*	*-0.74*	*-0.53*	*7.92*
S(1)-O(1)	0.6384	0.8471	2.16	-13.75	-13.05	-12.62	11.91
	0.5888	*0.8921*	*1.920*	*13.7090*	*-11.0470*	*-11.0180*	*35.774*
	0.6440	*0.8371*	*2.14*	*-15.31*	*-13.96*	*-13.89*	*12.54*
C(11)-S(1)	0.8232	0.9693	1.35	-5.73	-7.86	-7.13	9.27
	0.8150	*0.9856*	*1.336*	*-9.1170*	*-7.9960*	*-7.6300*	*6.5100*
	0.7986	*1.0020*	*1.29*	*-4.96*	*-7.25*	*-6.99*	*9.28*
C(12)-S(1)	0.7979	0.9895	1.39	-6.26	-8.28	-7.55	9.58
	0.8327	*0.9743*	*1.327*	*-9.1230*	*-7.9580*	*-7.6010*	*6.4370*
	0.8213	*0.9858*	*1.27*	*-5.63*	*-7.41*	*-7.18*	*8.95*
S(2)-O(2)	0.7235	0.8164	2.13	-16.97	-13.59	-13.08	9.69
	0.6109	*0.9254*	*1.736*	*5.21*	*-9.661*	*-9.548*	*24.419*
	0.7121	*0.8241*	*1.92*	*-14.52*	*-12.25*	*-12.12*	*9.85*
C(21)-S(2)	0.8060	0.9832	1.36	-5.21	-7.85	-7.05	9.69
	0.8387	*0.9676*	*1.318*	*-8.8880*	*-7.8400*	*-7.3800*	*6.3320*
	0.8227	*0.9835*	*1.25*	*-4.86*	*-7.21*	*-6.84*	*9.18*
C(22)-S(2)	0.8250	0.9596	1.38	-5.72	-7.71	-7.63	9.62
	0.8395	*0.9667*	*1.319*	*-8.9090*	*-7.8490*	*-7.3780*	*6.3180*
	0.8233	*0.9829*	*1.24*	*-5.09*	*-7.25*	*-6.83*	*9.00*
S(3)-O(3)	0.6510	0.8292	2.26	-19.99	-14.60	-14.23	8.84
	0.5879	*0.8901*	*1.929*	*14.2330*	*-11.1050*	*-11.0500*	*36.388*
	0.6413	*0.8367*	*2.17*	*-14.86*	*-14.32*	*-13.55*	*13.01*
C(31)-S(3)	0.8134	0.9670	1.44	-7.18	-8.31	-8.19	9.32
	0.8305	*0.9762*	*1.328*	*-9.1210*	*-7.9640*	*-7.6130*	*6.4550*
	0.8259	*0.9809*	*1.26*	*-5.45*	*-7.34*	*-7.07*	*8.96*
C(32)-S(3)	0.8201	0.9720	1.39	-6.45	-7.98	-7.70	9.22
	0.8249	*0.9794*	*1.331*	*-9.1120*	*-7.9670*	*-7.6140*	*6.4680*
	0.8123	*0.9920*	*1.27*	*-5.55*	*-7.31*	*-7.11*	*8.86*
S(4)-O(4)	0.6358	0.8436	2.22	-17.19	-15.24	-14.35	12.40
	0.5878	*0.8906*	*1.928*	*14.1920*	*-11.1570*	*-11.1310*	*36.481*
	0.6428	*0.8358*	*2.22*	*-16.07*	*-14.60*	*-14.00*	*12.53*
C(42)-S(4)	0.8355	0.9494	1.34	-4.55	-7.42	-6.66	9.53
	0.8199	*0.9825*	*1.337*	*-9.2080*	*-8.0060*	*-7.6990*	*6.4970*

Table 8.6 Continued

	0.8135	*0.9889*	*1.28*	*-5.45*	*-7.36*	*-6.97*	*8.88*
C(41)-S(4)	0.7861	0.9989	1.46	-7.96	-9.11	-8.31	9.46
	0.8183	*0.9824*	*1.340*	*-9.2250*	*-8.0360*	*-7.6820*	*6.4940*
	0.8020	*0.9987*	*1.30*	*-4.97*	*-7.18*	*-6.99*	*9.20*
H(11A)-C(11)	0.4016	0.6645	1.87	-21.32	-17.45	-16.81	12.94
	0.3717	*0.7149*	*1.927*	*-24.4830*	*-19.0750*	*-18.9770*	*13.569*
	0.3890	*0.6976*	*1.94*	*-23.85*	*-18.70*	*-18.59*	*13.44*
H(11B)-C(11)	0.4092	0.6570	1.83	-20.18	-16.50	-16.17	12.49
	0.3797	*0.7080*	*1.907*	*-23.8250*	*-18.5830*	*-18.3950*	*13.153*
	0.3956	*0.6922*	*1.90*	*-22.02*	*-17.86*	*-17.76*	*13.60*
H(11C)-C(11)	0.3959	0.6706	1.91	-21.87	-17.79	-17.35	13.27
	0.3883	*0.7010*	*1.888*	*-23.1950*	*-18.0140*	*-17.8940*	*12.712*
	0.4128	*0.6764*	*1.87*	*-20.75*	*-17.10*	*-16.87*	*13.22*
H(12A)-C(12)	0.3865	0.6795	1.91	-21.28	-18.09	-17.22	14.02
	1.1047	*1.6185*	*1.892*	*-23.2970*	*-18.0730*	*-18.0330*	*12.809*
	0.4227	*0.6665*	*1.87*	*-22.66*	*-17.30*	*-17.07*	*11.71*
H(12B)-C(12)	0.3946	0.6715	1.88	-21.35	-17.61	-17.02	13.27
	1.2518	*1.7056*	*1.910*	*-23.8500*	*-18.5580*	*-18.4480*	*13.155*
	0.4179	*0.6692*	*1.87*	*-21.86*	*-17.30*	*-16.74*	*12.18*
H(12C)-C(12)	0.3878	0.6784	1.91	-21.59	-17.96	-17.48	13.85
	0.3839	*0.7026*	*1.910*	*-23.7770*	*-18.4430*	*-18.3360*	*13.003*
	0.4173	*0.6694*	*1.926*	*-24.2970*	*-18.8890*	*-18.7860*	*13.379*
H(21A)-C(21)	0.3999	0.6662	1.89	-21.95	-17.94	-16.97	12.96
	0.3810	*0.7066*	*1.912*	*-23.8970*	*-18.5650*	*-18.484*	*13.152*
	0.4072	*0.6803*	*1.90*	*-21.81*	*-17.64*	*-17.32*	*13.16*
H(21B)-C(21)	0.3883	0.6785	1.92	-21.50	-18.11	-17.49	14.10
	0.3883	*0.7021*	*1.882*	*-23.1090*	*-17.9480*	*-17.8340*	*12.673*
	0.4323	*0.6580*	*1.87*	*-21.72*	*-16.89*	*-16.58*	*11.76*
H(21C)-C(21)	0.3916	0.6745	1.95	-22.90	-18.31	-17.97	13.38
	0.3865	*0.7031*	*1.891*	*-23.3140*	*-18.1230*	*-18.0490*	*12.859*
	0.4085	*0.6811*	*1.86*	*-20.73*	*-17.02*	*-16.88*	*13.16*
H(22A)-C(22)	0.4027	0.6641	1.94	-21.96	-17.88	-17.12	13.04
	0.3864	*0.7033*	*1.890*	*-23.3070*	*-18.1200*	*-18.0510*	*12.863*
	0.4121	*0.6776*	*1.87*	*-21.55*	*-17.11*	*-17.07*	*12.62*
H(22B)-C(22)	0.4082	0.6582	1.91	-21.62	-17.22	-17.10	12.70
	0.3881	*0.7021*	*1.883*	*-23.1390*	*-17.9690*	*-17.8580*	*12.688*
	0.4286	*0.6616*	*1.86*	*-21.83*	*-16.87*	*-16.67*	*11.71*
H(22C)-C(22)	0.4116	0.6550	1.91	-22.36	-17.55	-17.11	12.31
	0.3819	*0.7061*	*1.909*	*-23.8140*	*-18.4970*	*-18.4120*	*13.094*
	0.4137	*0.6743*	*1.88*	*-23.07*	*-17.61*	*-17.30*	*11.85*
H(31A)-C(31)	0.3818	0.6851	1.79	-18.41	-16.98	-15.93	14.50
	0.3712	*0.7158*	*1.928*	*-24.4970*	*-19.0720*	*-19.0170*	*13.592*
	0.4042	*0.6828*	*1.93*	*-24.61*	*-18.28*	*-18.07*	*11.73*

Table 8.6 Continued

H(31B)-C(31)	0.3752	0.6909	1.82	-18.28	-17.19	-16.08	14.99
	0.3861	*0.7026*	*1.893*	*-23.3700*	*-18.1780*	*-17.9930*	*12.801*
	0.3981	*0.6907*	*1.88*	*-23.52*	*-18.04*	*-17.88*	*12.40*
H(31C)-C(31)	0.3615	0.7045	1.94	-21.61	-18.89	-18.29	15.57
	0.3880	*0.7011*	*1.889*	*-23.2120*	*-18.0350*	*-17.9160*	*12.738*
	0.4196	*0.6695*	*1.87*	*-22.30*	*-17.24*	*-17.03*	*11.97*
H(32A)-C(32)	0.3893	0.6773	2.00	-21.82	-18.65	-18.10	14.93
	0.3876	*0.7018*	*1.892*	*-23.2860*	*-18.0800*	*-17.9990*	*12.793*
	0.4276	*0.6618*	*1.87*	*-22.27*	*-17.00*	*-16.94*	*11.68*
H(32B)-C(32)	0.4110	0.6560	1.81	-17.20	-15.82	-15.36	13.98
	0.3863	*0.7007*	*1.900*	*-23.5230*	*-18.2720*	*-18.1190*	*12.869*
	0.4187	*0.6683*	*1.87*	*-22.04*	*-17.27*	*-16.95*	*12.18*
H(32C)-C(32)	0.4247	0.6415	1.76	-16.89	-15.87	-13.77	12.75
	0.3770	*0.7080*	*1.927*	*-24.3240*	*-18.9160*	*-18.8130*	*13.404*
	0.3979	*0.6871*	*1.87*	*-21.92*	*-17.69*	*-17.43*	*13.20*
H(42A)-C(42)	0.3999	0.6665	1.85	-18.76	-16.53	-16.00	13.78
	0.3884	*0.7010*	*1.890*	*-23.2400*	*-18.0180*	*-17.9420*	*12.720*
	0.4134	*0.6761*	*1.85*	*-22.24*	*-17.27*	*-17.01*	*12.03*
H(42B)-C(42)	0.3969	0.6697	1.83	-17.05	-17.13	-14.29	14.37
	1.2360	*1.7311*	*1.910*	*-23.9420*	*-18.6800*	*-18.5230*	*13.261*
	0.4097	*0.6780*	*1.91*	*-23.60*	*-17.93*	*-17.47*	*11.80*
H(42C)-C(42)	0.4072	0.6624	1.69	-14.47	-15.07	-13.96	14.57
	0.3777	*0.7080*	*1.922*	*-24.1960*	*-18.8310*	*-18.7040*	*13.340*
	0.4142	*0.6717*	*1.92*	*-22.68*	*-17.79*	*-17.47*	*12.58*
H(41A)-C(41)	0.3626	0.7034	1.87	-19.59	-17.65	-17.20	15.26
	0.3733	*0.7136*	*1.925*	*-24.3800*	*-18.9690*	*-18.8920*	*13.482*
	0.3889	*0.6979*	*1.92*	*-22.08*	*-18.14*	*-18.00*	*14.06*
H(41B)-C(41)	0.3671	0.6991	1.85	-19.10	-17.38	-16.66	14.93
	0.3810	*0.7073*	*1.904*	*-23.7150*	*-18.4810*	*-18.3130*	*13.080*
	0.4027	*0.6856*	*1.91*	*-23.48*	*-18.10*	*-17.91*	*12.53*
H(41C)-C(41)	0.3724	0.6939	1.82	-19.36	-17.26	-16.55	14.45
	0.3879	*0.7014*	*1.889*	*-23.2200*	*-18.0370*	*-17.9280*	*12.745*
	0.4042	*0.6851*	*1.86*	*-20.04*	*-17.08*	*-16.94*	*13.97*

First line corresponds to Form IV experimental data. The second and the third lines (italic) correspond to reference density from the wave function and reference density from the theoretical structure factors, respectively. [a] *In units of Å.* [b] *In units of e Å^{-3}.* [c] *In units of e Å^{-5}*

8.4.2. Analysis and comparison of the multipole refinements.

In this section, the improvement in the agreements between the experimental and theoretical data with the increase of the model sophistication will be discussed. Three different multipole models were used in refinements of the experimental data (1, 2, 3), as described in Section 8.2.3. These were compared with (a) the topological analysis of the

wave functions of the gas phase calculations, and (b) the multipole model based on the refinements of the theoretical structure factors. The charge density and the Laplacian at the BCPs of each experimental and theoretical model have also been compared. Since the volume of data is too great to be able to see the trends clearly (Table 8.5 and 8.6), a residual factor R_{Par} was calculated in order to describe the global measurement of the agreement between experimental and theoretical parameters, using equation 2.9, Chapter 2. The R_{val}, R_{ρ} and $R_{\nabla 2(\rho)}$ values for the studied forms I and IV of **7** are summarized in Table 8.7. An improvement of the R_{values} term can be noticed with the increase of the sophistication of the multipole model, such that the lowest R_{values} were found for model 3 followed by 2 and 1. The best agreement of the ρ between experimental and theoretical results for form I and IV in both cases (a) and (b) were found for model 2, followed by 3 and 1. The $\nabla^2(\rho)$ shows the same trend as for ρ in both cases (a) and (b) for form I. For form IV, the lowest $R_{\nabla 2(\rho)}$ was found for model 3 followed by 2 and 1 for both cases (a) and (b). The R_{ρ} are quite similar in magnitude for form I in both cases, while for form IV the density from the theoretical structure factors gives slightly higher values as compared with the density from the pure wave function. The $R_{\nabla 2(\rho)}$ are slightly higher in magnitude when the density reference from the theoretical structure factors is chosen, compared with the density reference from wave function. It can be concluded that using the adps evaluated using the SHADE[18] methodology, which allows multipole refinement of the H atoms at the quadrupole level, improves the agreement level between experimental and theoretical topological parameters.

Table 8.7. The residual factors for the various multipole model refinements of both the experimental and theoretical data for forms I and IV of **7**.

(a) Reference density from wave function	**Model**	$\mathbf{R_{values}}$	$\mathbf{R_{\rho}}$	$\mathbf{R_{\nabla 2(\rho)}}$
I	1	0.0243	0.0564	0.3129
	2	0.0242	0.0208	0.1512
	3	0.0239	0.0251	0.1524
IV	1	0.0254	0.0398	0.2596
	2	0.0252	0.0072	0.0765
	3	0.0248	0.0269	0.0029
(b) Reference density from theoretical structure factor				
I	1	0.0243	0.0560	0.3658
	2	0.0242	0.0204	0.2178
	3	0.0239	0.0211	0.2184
IV	1	0.0254	0.0355	0.2265
	2	0.0252	0.0117	0.0877
	3	0.0248	0.0315	0.0590

8.5. Lattice and intermolecular interaction energy calculations

The lattice energy of forms I and IV of **7** was calculated using the XD[16] software. The two theoretical approaches used for these calculations in the previous chapters (CRYSTAL09[22] and CLP[23]) were not able to be applied in this case. For CRYSTAL09[22], the convergence criteria were not met during the SCF cycles, while the CLP[23] program can not provide calculations for compounds containing transition metal atoms. The lattice energy calculations using the various experimental charge density approaches are listed in Table 8.8. As noted in the previous chapters, the lattice energy shows high sensitivity to the type of multipole model used. Lower values for the lattice energy were obtained when a more sophisticated multipole model was used; this is especially true for the unrestricted models. A large discrepancy between the lattice energy of forms I and IV can be noticed from Table 8.8. According to these results, the most stable form, showing the lowest lattice energy, is form I.

Table 8.8. The lattice energy calculation results (kJ/mol) using experimental charge density approach.

Form	I	IV
Model		
1	-308.174	-199.54
2	-368.017	-247.21
3	-463.941	-294.48

A multipole refinement was also performed for both forms, in which the x,y,z and U_{ij} parameters were refined only once and in a different block from the multipole parameters. However, the result does not show any significant difference in the lattice energies calculated for the different forms. In this case the values for lattice energy obtained were –346.5 kJ/mol for form I and –230.57 kJ/mol for form IV.

8.6. Synchrotron radiation source results

In this section, the results of the refinements of synchrotron data for form IV of **7** will be compared to those from the X-ray laboratory source (KappaCCD). The synchrotron data were collected at Diamond – beamline I19, giving high resolution X-ray diffraction resolution at $\sin\theta/\lambda$ = 1.12 $Å^{-1}$ and integrated using the CrysAlisPro software. The spherical and multipole refinements are summarised in Table 8.9. In the scale factor plot

for synchrotron data at the sinθ/λ = 1.15 $Å^{-1}$ resolution cut off, the F_{obs}/F_{calc} calculation reveals a large deviation from the standard value at the higher angles of data collection (Figure 8.7 (a)). The synchrotron data were also truncated at 1.0 $Å^{-1}$ resolution to allow a direct comparison between the data from the laboratory and synchrotron sources (Figure 8.7 (b) and (c)). A high residual is observed in the difference Fourier map resulting from the spherical synchrotron data refinement (deepest hole = −1.708, highest peak = 4.9 $eÅ^{-1}$). This may be associated with the fact that the synchrotron data were collected at a wavelength, λ = 0.4859Å, at which the imaginary component of the anomalous dispersion is significantly high. Anomalous dispersion occurs when the frequency of the primary beam is near the field created between the nucleus and electron forces, which are considered as oscillators with natural frequencies; in presence of such a natural frequency resonance will take place. In the presence of anomalous dispersion effects, the values of the structure factors are modified from their non-resonant values. The data collected using X-ray laboratory radiation source shows lower values for the deepest hole and highest peak present in the residual difference Fourier density map (minimum and maximum values of −0.983 and 0.785 $eÅ^{-3}$). This is not surprising as the second component of the anomalous dispersion is significantly lower for the wavelength of the laboratory data collection, at λ = 0.71073 Å, f″= 0.8363, while at λ = 0.4859Å – the wavelength used for the synchrotron data collections f″= 2.884139. The reason for using the 0.4859Å wavelength is that the imaginary component of the anomalous dispersion is in general lower for the other elements.

Table 8.9. Spherical and multipole model refinements for form IV of **7** including synchrotron and laboratory X-ray source radiation.

Spherical atom refinement	R(%)	**Multipole refinement**	R(%)
CrysAlisPro (sinθ/λ =1.15 $Å^{-1}$)	5.91	CrysAlisPro (sinθ/λ =1.12 $Å^{-1}$)	5.94
CrysAlisPro (sinθ/λ =1.0 $Å^{-1}$)	4.59	CrysAlisPro (sinθ/λ =1.0 $Å^{-1}$)	4.52
X-ray laboratory source (KappaCCD)	2.54	X-ray laboratory source (KappaCCD)	2.54

On the other hand, the Fourier maps plotted in the Cl-Ru-Cl plane show a large difference between the synchrotron and the X-ray laboratory data for spherical and multipole model refinements (Figure 8.8.) These discrepancies might be due to the different scaling scheme obtained for each individual program.

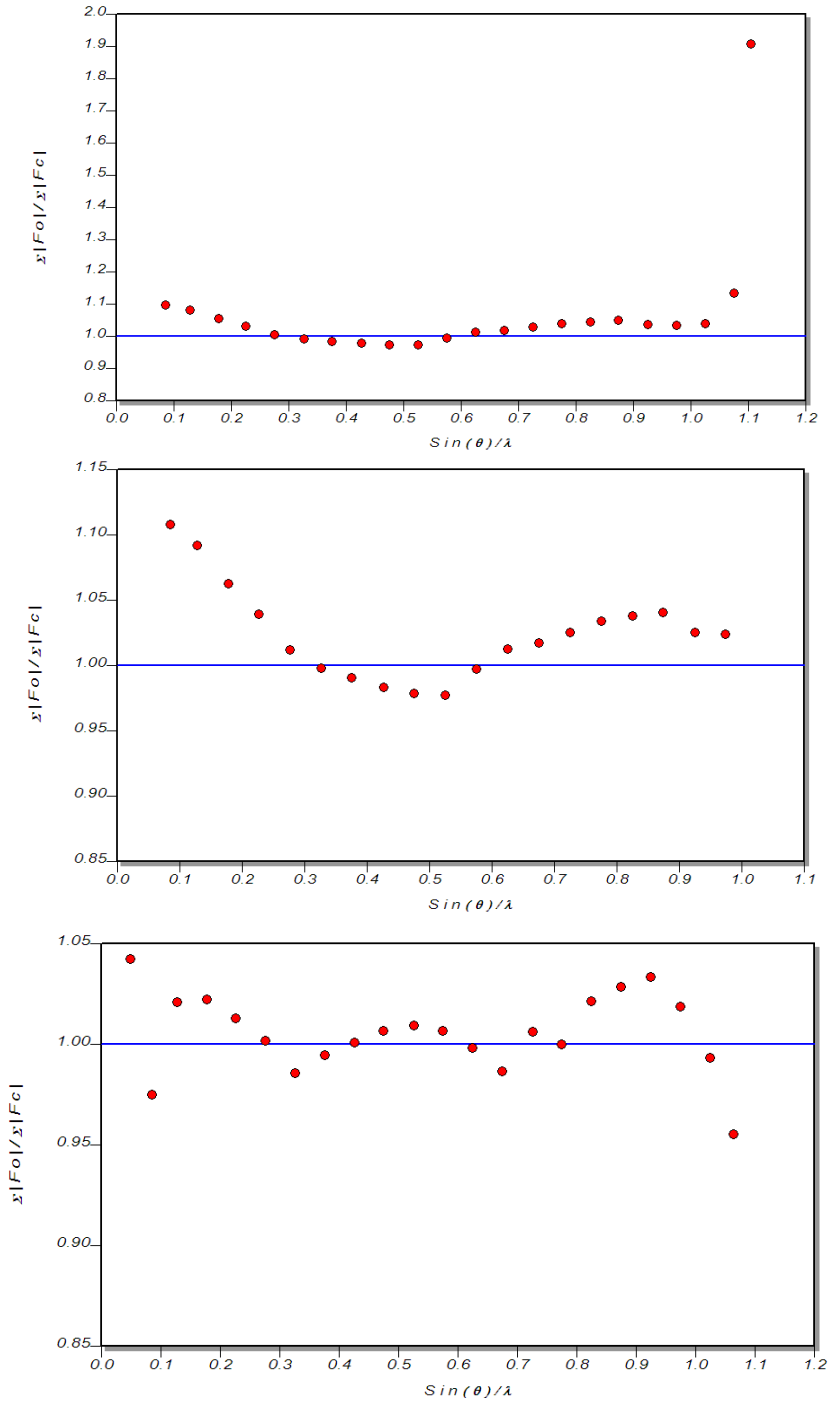

Figure 8.7. Scale factor plots (a) for synchrotron data to sinθ/λ =1.15 $Å^{-1}$ and (b) on data truncated at data sinθ/λ = 1.0 $Å^{-1}$; (c) X-ray laboratory source data at sinθ/λ = 1.1 $Å^{-1}$

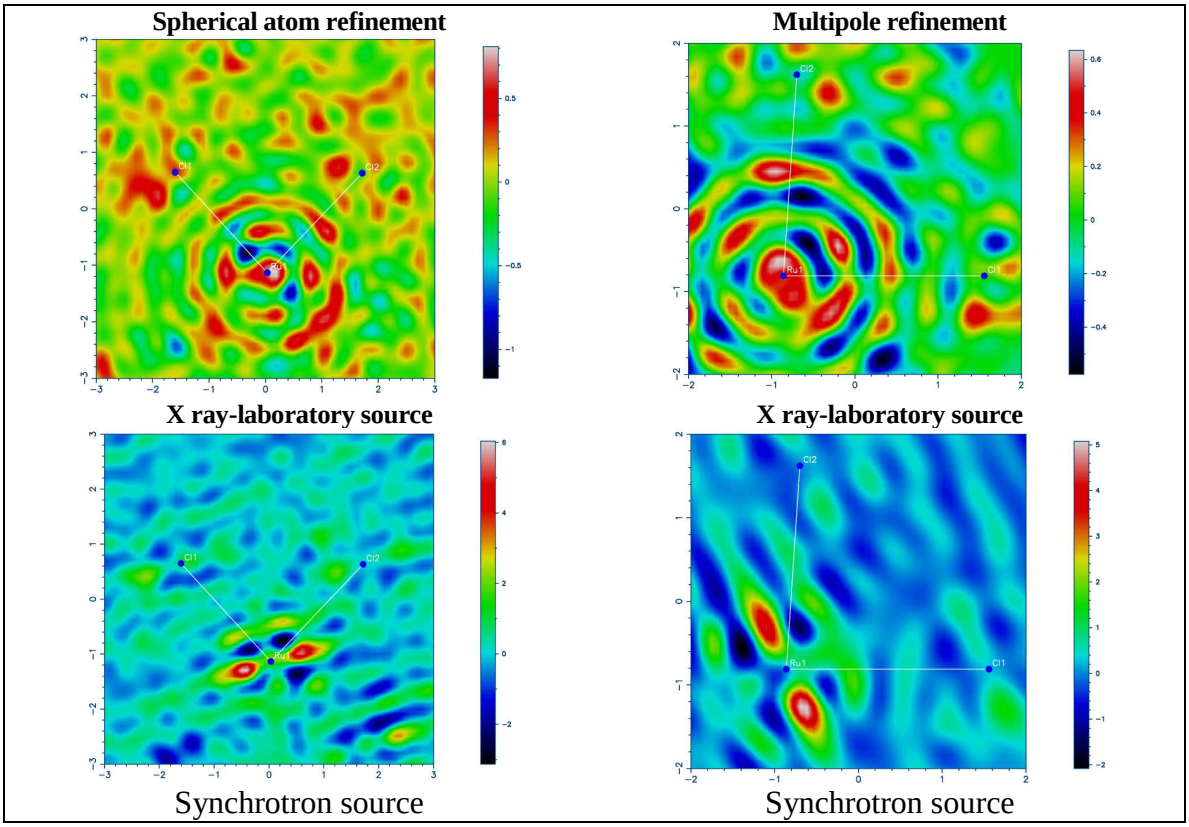

Figure 8.8. Residual Fourier density maps of form IV from synchrotron and X-ray laboratory sources for spherical and multipole refinements.

8.7. Conclusions

Forms I and IV of **7** have been analysed for the first time using high resolution X-ray diffraction.

An improvement of the R_{values} term can be noticed with the increase of the sophistication of the multipole model employed in the refinement, such that the lowest R_{values} were found for model 3 followed by 2 and 1. Using the adps obtained from the SHADE methodology, which allows multipole refinement of the H atoms at the quadrupole level, improves the agreement between experimental and theoretical topological parameters. As noted in the previous chapters, the lattice energy shows high sensitivity to the type of multipole model used. Lower values for the lattice energy were obtained when a more sophisticated multipole model was used, especially for the unrestricted models. According to the experimental charge density results, the most stable form with the lowest lattice energy was found to be form I.

References

1. C. Monti-Bragadin, M. Giacca, L. Dolzani and M. Tamaro, *Inorg. Chim. Acta*, 1987, **137**, 31.
2. G. Sava, S. Zorzet, T. Giraldi, G. Mestroni and G. Zassinovich, *Eur. J. Cancer Clin. Oncol.*, 1984, **20**, 841.
3. S. Cauci, E. Alessio, G. Mestroni and F. Quadrifoglio, *Inorg. Chim. Acta*, 1987, **137**, 19.
4. A. Mercer and J. Trotter, *Dalton Trans.*, 1975, 2480.
5. W. M. Attia and M. Calligaris, *Acta Cryst. C*, 1987, **43**, 1426.
6. E. Alessio, G. Mestroni, G. Nardin, W. M. Attia, M. Calligaris, G. Sava and S. Zorzet, *Inorg. Chem.*, 1988, **27**, 4099.
7. G. Georgieva, G. Gencheva, B. L. Shivachev and R. P. Nikolova, *Acta Cryst. E*, 2008, **64**, 1023.
8. F. C. Pigge, J. J. Coniglio and N. P. Rath, *Organometallics*, 2005, **24**, 5424.
9. R. S. Srivastava and R. Fronczek, *Acta Cryst. E*, 2003, **59**, 427.
10. J. S. Jaswal, S. J. Rettig and B. R. James, *Can. J. Chem.*, 1990, **68**, 1808.
11. I. P. Evans, A. Spencer and G. Wilkinson, *J.C.S. Dalton*, 1973, 204-209.
12. Z. Otwinowski, W. Minor, *Methods in Enzymology, Macromolecular Crystallography, Part A;* W. C. Carter and M. R. Sweet, *Academic Press New York*, 1997, **279**, 307-326.
13. H. R. Blessing, *J. Appl. Cryst.*, 1997, **30,** 421-426.
14. L. J. Farrugia, *J. Appl. Cryst.*, 1999, **32**, 837-838.
15. A. Altomare, G. Cascarano, C. Giacovazzo and A. Guagliardi, *J. Appl. Cryst.*, 1994, **27**, 435.
16. A. Volkov, P. Macchi, L. J. Farrugia, C. Gatti, P. R. Mallinson, T. Richter and T. Koritsanszky, *XD-2006*, 2006, http://xd.chem.buffalo.edu/.
17. A. Volkov and P. Macchi, VM databank of scattering factors in XD2006, unpublished results.
18. Ø. A. Madsen, *J. Appl. Cryst.*, 2006, **39**, 757-758.
19. (a) A. D. Becke, *Phys. Rev. A*, 1988, **38**, 3098; (b) A. D. Becke, *J. Chem. Phys.*, 1993, **98**, 5648; (c) C. Lee, W. Yang and R. G. Parr, *Phys. Rev. B*, 1988, **37**, 785. (d) P. J. Stephens, J. F. Devlin, C. F. Chabalowski and M. J. Frisch, *J. Phys. Chem.*, 1994, **98**, 11623.
20. (a) F. Weigend. and R. Ahlrichs., *Phys. Chem. Chem. Phys.*, 2005, **7**, 3297; (b) F. Weigend, *Phys. Chem. Chem. Phys.*, 2006, **8**, 1057.

21. M. J. Frisch, G. W. Trucks, H. B. Schlegel, G. E. Scuseria, M. A. Robb, J. R. Cheeseman, J. A. Montgomery, T. V. Jr., K. N. Kudin, J. C. Burant, J. M. Millam, S. S. Iyengar, J. Tomasi, V. Barone, B. Mennucci, M. Cossi, G. Scalmani, N. Rega, G. A. Petersson, H. Nakatsuji, M. Hada, M. Ehara, K. Toyota, R. Fukuda, J. Hasegawa, M. Ishida, T. Nakajima, Y. Honda, O. Kitao, H. Nakai, M. Klene, X. Li, J. E. Knox, H. P. Hratchian, J. B. Cross, V. Bakken, C. Adamo, J. Jaramillo, R. Gomperts, R. E. Stratmann, O. Yazyev, A. J. Austin, R. Cammi, C. Pomelli, J. W. Ochterski, P. Y. Ayala, K. Morokuma, G. A. Voth, P. Salvador, J. J. Dannenberg, V. G. Zakrzewski, S. Dapprich, A. D. Daniels, M. C. Strain, O. Farkas, D. K. Malick, A. D. Rabuck, K. Raghavachari, J. B. Foresman, J. V. Ortiz, Q. Cui, A. G. Baboul, S. Clifford, J. Cioslowski, B. B. Stefanov, G. Liu, A. Liashenko, P. Piskorz, I. Komaromi, R. L. Martin, D. J. Fox, T. Keith, M. A. Al-Laham, C. Y. Peng, A. Nanayakkara, M. Challacombe, P. M. W. Gill, B. Johnson, W. Chen, M. W. Wong, C. Gonzalez and J. A. Pople, GAUSSIAN03, Wallingford, CT., US, 2004.
22. Basis sets were obtained from the Extensible Computational Chemistry Environment Basis Set Database, Version 02/25/04, as developed and distributed by the Molecular Science Computing Facility, Environmental and Molecular Science Laboratory which is part of the Pacific Northwest Laboratory, P.O. Box 999, Richland, WA 99352, U.S.A., and funded by the U.S. Department of Energy.
23. F. W. Biegler-Konig, R. F .W. Bader and T. Tang, *J. Comput. Chem*, 1982, **3**, 317.
24. R. Dovesi, R. Orlando, B. Civalleri, C. Roetti, V. R. Saunders, and C. M. Zicovich-Wilson, *Z. Kristallogr.*, 2005, **220**, 571; R. Dovesi, V. R. Saunders, C. Roetti, R. Orlando, C. M. Zicovich-Wilson, F. Pascale, B. Civalleri, K. Doll, N. M. Harrison, I. J. Bush, P. D'Arco, and M. Llunell, CRYSTAL09 (CRYSTAL09 User's Manual. University of Torino, Torino, Italy, 2009).
25. A. Gavezzotti, *New J. Chem*., 2011, **35**, 1360-1368.

9. Conclusions

Four polymorphs of sulfathiazole have been studied for the first time using high-resolution X-ray diffraction. Forms II, III and IV were also determined for the first time using the neutron diffraction technique. The results were analysed using the experimental charge density approach. In addition, periodic and aperiodic calculations were carried out, in order to support the experimental results. A minor disorder/twin was noticed for the S atom in the thiazole ring which was not observed in the previous studies. However, the minor disorder/twin has no effect on the topological parameters derived from experimental electron density. An unusual intramolecular BCP was found between the O and S (thiazole ring) atoms in each molecule of forms I, II, III and IV of sulfathiazole**,** both in the experimental data and the theoretical results. The nature of the S···O interaction was investigated using the electrostatic potential plots which showed an electrostatic type of interaction. In particular, the positive value of the Laplacian at the BCP suggest the possibility of an electrostatic S···O interaction. The lattice energy calculations from the experimental density were found to show a significant discrepancy compared with the theoretical results. Manipulating the multipole refinement strategy reduced the dissimilarity between the experimental charge density and theoretical results. The lattice energies difference between the experimental charge density and theoretical calculations are relatively small, and it is found that predicting the stability order of the polymorphs, which are known to present very small energy differences as small as 5 kJ/mol or less, it is rather difficult even when using only fully theoretical programs. It has been shown that the relative stability of sulfathiazole polymorphs cannot be estimated only on the basis of the hydrogen bond interactions; this may also be more generally the case for polymorphic materials of organic compounds.

Three anhydrous polymorphs of piracetam, together with the monohydrate form, have been characterised using high-resolution X-ray diffraction. Forms II and III were also determined for the first time using the neutron diffraction technique. In contrast to previous reports, the crystals of form I produced in this work have been identified to be stable over a period of six months at ambient conditions. A disorder of one methylene group in the pyrrolidone ring was found at the 70% level, corresponding to a different orientation of the molecule in the unit cell. In the previous study three of the methylene groups of the pyrrolidone ring were identified with disorder. The lattice energy calculations, as found for sulfathiazole, show significant dependence on the multipole model strategy used in the refinements. Even the magnitudes of the lattice energies of the forms were significantly

different for the fully theoretical approaches used, although all showed the same ranking stabilities. Form III was identified with the lowest lattice energy, followed by forms II and I.

Form III of carbamazepine was determined for the first time using high-resolution X-ray diffraction and neutron diffraction. In addition the dihydrate form was also determined using neutron diffraction. It was shown in the present work, based on both X-ray and neutron data, that the orthorhombic interpretation of the dihydrate form is more reliable. In some of the previous interpretations, the monoclinic crystal system was attributed to this form. The neutron data also offer the possibility to make a clear distinction between the O and N atoms which were identified to exhibit disorder in the orthorhombic crystal system. In addition, in the neutron data one hydrogen atom of the water molecule was also identified as disordered. The same conclusion can be drawn here regarding the lattice energy calculations.

Two conformational polymorphs of octakis(phenylsulfanyl)naphthalene were analysed for the first time using high resolution X-ray diffraction. The two polymorphs can be distinguished by their different colours, yellow and red. The topological parameters reveal unusual BCPs between the S atom and the C-C bond of the benzene ring in both forms of octakis(phenylsulfanyl)naphthalene. In the red form an additional BCP was identified between two S···S atoms. This intramolecular interaction may be responsible for the different conformational polymorphs that octakis(phenylsulfanyl)naphthalene can adopt. The high sensitivity of the lattice energies to the multipole refinement strategy used was also observed in this case. However, due to the large difference in magnitude of the lattice energy between the two forms, it can be clearly distinguished that the red form is most stable one. On the other hand, the gas phase optimised energy calculations indicated that the yellow conformation would be the most stable one for an isolated molecule.

The molecular complexes of the isomers of lutidine (dimethylpyridine) with chloranilic acid (2,5-dichloro-3,6-dihydroxy-*p*-benzoquinone) in both 1:1 and 2:1 stoichiometries have been studied for the first time using high-resolution X-ray diffraction. Four of the chloranilic acid – lutidine molecular complexes were also measured for the first time using neutron diffraction at the ILL using monochromatic radiation on the D19 instrument: 2,4-lutidine (1:1), 2,5-lutidine (1:1) and 2,6-lutidine (1:1 and (2:1)). The neutron results showed large thermal motion of the hydrogen atoms of the methyl groups in 2,5-lutidine (1:1), 2,6-lutidine (1:1 and (2:1)) molecular complexes and some of these atoms were

identified as showing potential disorder. New 1:1 molecular complexes of chloranilic acid with 2,3- and 3,5- lutidine, a 2:1 complex with 3,4 – lutidine and a new hydrate form of 2:1 2,4- lutidine with chloranilic acid were also found. Molecular complexes containing neutral chloranilic acid coexisting with deprotonated CA^- were also found for 2,4- and 3,5-lutidine. The delocalization of the charge in the singly and doubly deprotonated chloranilic acid molecules were confirmed by the charge density analyses.

The discrepancy of the lattice energies between the experimental charge density and the theoretical calculations were also noticed here. It has been shown that estimating the relative stabilities of the molecular complexes for the 1:1 stoichiometry is also difficult even with fully theoretical programs. No consistency between the two programs used was obtained regarding the relative stabilities of the molecular complexes. In consequence, an accurate description on the influence of the position of the methyl groups in the different molecular complexes studied is difficult to make.

The coordination complex $[Ni(en)_3]^{2+}(NO_3^-)_2$ (en = 1,2-diaminoethane), a material which undergoes a displacive phase transition around 109 K, has been also studied in this work and characterised using high-resolution X-ray diffraction as well as neutron diffraction. The highest temperature phase was also characterised using data from two synchrotron sources: Diamond and Soleil. The lattice calculation results indicate, contrary to expectation, the 123 K phase to be the most stable one.

Forms I and IV of $RuCl_2(Me_2SO)_4$ were analysed for the first time using high resolution X-ray diffraction. As noted for the previous compounds, the lattice energy once again shows high sensitivity to the type of multipole model used.

In summary, it appears from this work that it is currently difficult to determine accurate lattice energies, and even the relative stability ranking, of polymorph energy differences. It is clear that further work in this area is required, for example in improving the energy calculations from determined electron densities, or in making the modelling of these electron densities using multipole methodologies more accurate.